

Tailoring of Iron Oxide Nanoparticle Surfaces: Application of Phosphonic Acid Derivatives to Control Particle Properties and Synthesis of Stable Self-Healing Organic- Inorganic Nanocomposites

Dissertation

zur Erlangung des Grades

des Doktors der Naturwissenschaften

der Naturwissenschaftlich-Technischen Fakultät

der Universität des Saarlandes



**UNIVERSITÄT
DES
SAARLANDES**

vorgelegt von

Bastian Oberhausen, M. Sc.

Saarbrücken

2023

Tag des Kolloquiums:	19. April 2024
Prodekan:	Prof. Dr. -Ing Michael Vielhaber
Berichterstatter:	Prof. Dr. Guido Kickelbick
	Prof. Dr. -Ing Markus Gallei
Vorsitz	Prof. Dr. Marc Schneider
Akad. Mitarbeiter:	Dr. Andreas Rammo

Die vorliegende Arbeit wurde im Zeitraum von Mai 2018 bis Februar 2022 im Arbeitskreis von Herrn Prof. Dr. Guido Kickelbick im Fachbereich Anorganische Festkörperchemie an der Universität des Saarlandes angefertigt.

Danksagung

An dieser Stelle möchte ich mich bei allen bedanken, die mich auf dem Weg zu meiner Promotion begleitet und unterstützt haben.

An erster Stelle gilt mein Dank Herrn Prof. Dr. Guido Kickelbick, der mir die Möglichkeit gegeben hat die Promotion in seinem Arbeitskreis durchzuführen. Insbesondere bedanke ich mich für die Vergabe des interessanten Themas und die zahlreichen Anregungen und Diskussionen im Rahmen des Arbeitskreiseminars und der Mitarbeiterbesprechungen. Nicht zuletzt möchte ich mich für den Freiraum und die Unterstützung bei der Umsetzung eigener Ideen bedanken. Auch für die mühevollen Arbeit des Korrekturlesens und Begutachtens der Dissertation möchte ich mich bedanken.

Herrn Priv.-Doz. Dr.-Ing habil. Guido Falk und Herrn Prof. Dr.-Ing. Markus Gallei danke ich für die wissenschaftliche Begleitung der Arbeit. Weiter bedanke ich mich bei Herrn Prof. Dr.-Ing. Markus Gallei für die Übernahme des Koreferats.

Mein besonderer Dank gilt meinen Kolleginnen und Kollegen der gesamten Arbeitsgruppe Kickelbick, sowie der WASTE und Water Gruppe für die freundliche Arbeitsatmosphäre und die fachlichen und nichtfachlichen Gespräche. Insbesondere möchte ich Lucas für die vielen konstruktive Diskussionen und Überlegungen danken.

Für die XRD-Messungen danke ich Robert, Dennis, Mana, Tobias, Anna und Stefan Engel. Oliver danke ich für die konstruktiven Tipps und Hinweise und sein Engagement, sowie seine Unterstützung bei der Auswertung der Pulverdiffraktogramme, insbesondere im Bereich der organisch-anorganischen Perowskite.

Kristina und Sandra danke ich für die Durchführung der ICP-MS Messungen. Susanne Harling danke ich für die Durchführung der CHN-Analysen.

Frau Sahra Schumacher danke ich für die Durchführung der Zeta Potential Messungen. Für die Durchführung und Auswertung der SAXS-Messungen bedanke ich mich bei Bart-Jan Niebuur und Björn Kuttich. Ich bedanke mich beim AK Diebels für die Durchführung der Zugversuche und bei Prof. Dr.-Ing. Dr. rer. nat. Anne Jung für die Unterstützung bei der Interpretation der Ergebnisse. Aylin Koldemir danke ich für die Durchführung der Mößbauer Spektroskopie Untersuchungen.

Meinen Forschungspraktikanten Alexander, Emanuel, Yannic und Simon, sowie unseren Laboranten Ajda und Matthias danke ich für die Unterstützung im Labor. Ferdinando Bassato und Siyang He danke ich für die Zusammenarbeit im Rahmen ihrer Masterarbeiten.

Traudel und Christel danke ich für ihren unverzichtbaren Beitrag im Rahmen der Praktikumsbetreuung. Susanne Limbach danke ich für die freundliche Unterstützung bei organisatorischen Fragen.

Sylvia und Steffan Blank danke ich für die Anfertigung passgenauer Aufbauten und für die Wartung und Instandsetzung diverser Laborgeräte.

Nicht zuletzt gilt mein Dank meiner Familie und den Kellerkindern. Insbesondere danke ich meinen Eltern Tanja und Patrick, meinen Brüdern Kevin und Mirko sowie meinen Großeltern Karin und Rüdiger für ihre stetige Unterstützung und Ermutigung.

Kurzzusammenfassung

Materialermüdung und daraus resultierendes Versagen sind Probleme, die bei allen Werkstoffen auftreten. Um die Lebensdauer der Materialien zu verlängern, werden im Wesentlichen zwei Ansätze verfolgt. Während im ersten Ansatz die Robustheit der Werkstoffe verbessert wird, werden im zweiten Ansatz so genannte selbstheilende Materialien entwickelt, die entstandene Schäden eigenständig oder durch Energiezufuhr reparieren. In dieser Arbeit wurden selbstheilende Nanokomposite basierend auf superparamagnetischen Eisenoxid-Nanopartikeln und Methacrylat basierten Polymermatrizes hergestellt. Als Heilmechanismen wurden ionische Wechselwirkungen, Wasserstoffbrückenbindungen, sowie dynamische kovalente Bindungen in Form von Diels-Alder/Retro-Diels-Alder-Reaktionen genutzt. Durch gezieltes Design der Partikeloberflächen mit funktionalisierten Phosphonsäuren konnte eine stabile Einbettung in die Polymermatrix erreicht werden. *N,N,N*-Trimethyl-6-phosphono-hexan-1-ammoniumbromid- und (10-(3-Propylureido)decyl)phosphonsäure-funktionalisierte Partikel, kombiniert mit Sulfonat- oder Urethyl-funktionalisierten Polymeren wurden eingesetzt, um den Heilmechanismus an die Partikel-Polymer-Phasengrenze und damit genau an die Schwachstelle herkömmlicher Verbundwerkstoffe zu verlagern. Darüber hinaus wurde gezeigt, dass die Nanokomposite durch induktive Erwärmung der Nanopartikel sowohl räumlich aufgelöst als auch bei niedrigeren Temperaturen als bei konventioneller Ofenheizung ausgeheilt werden können.

Abstract

Material fatigue and subsequent failure are problems that affect all materials. While one approach is to improve robustness to prevent damage from occurring, self-healing materials can repair damage autonomously or through energy input. This can greatly improve the service life of these materials. In this work, self-healing nanocomposites based on superparamagnetic iron oxide nanoparticles and methacrylate-based polymer matrices were synthesized. Ionic interactions, as well as hydrogen bonding and dynamic covalent bonding in the form of Diels-Alder/retro-Diels-Alder reactions, were used to induce self-healing properties in the composites. By carefully designing the particle surfaces using functional phosphonic acids, stable incorporation into the polymer matrices was achieved. *N,N,N*-Trimethyl-6-phosphonohexyl-1-ammonium bromide and (10-(3-propylureido)-decyl)phosphonic acid functionalized particles were used in combination with sulfonate or ureylene functionalized polymers to shift the healing mechanism to the particle-polymer-phase interface, thereby relocating it precisely to the weak point of conventional composites. Key parameters such as polymer composition and particle content in the composite were optimized to tailor the mechanical properties and healing efficiency. Furthermore, magnetic field-induced heating of the particles allowed spatially resolved healing of the nanocomposites at lower macroscopic temperatures than conventional oven heating.

List of Publications

Within this work:

- *“Induction Heating Induced Self-Healing of Nanocomposites Based on Surface-Functionalized Cationic Iron Oxide Particles and Polyelectrolytes”* (DOI: 10.1039/D1NA00417D)
- *“Self-Healing Iron Oxide Polyelectrolyte Nanocomposites: Influence of Particle Agglomeration and Water on Mechanical Properties”* (DOI: 10.3390/nano13232983)

Others:

- *“Surface-Charged Zirconia Nanoparticles Prepared by Organophosphorus Surface Functionalization with Ammonium or Sulfonate Groups”* (DOI: 10.1021/acs.langmuir.9b01093).
- *“HBr or not HBr? That is the Question: Crystal Structure of 6-Hydroxy-1,4-diazepane-1,4-dium dibromide Redetermined”* (DOI: 10.1107/S2053229619005321)

Abbreviations

AIBN	azobisisobutyronitrile
AMF	alternating magnetic field
APTES	(3-aminopropyl)triethoxysilane
ATRP	atom transfer radical polymerization
ARGET ATRP	activators regenerated by electron transfer ATRP
BIBB	α -bromoisobutyryl bromide
2,2'-Bipy	2,2'-bipyridine
BMA	butyl methacrylate
BSE SEM	backscattered electron imaging scanning electron microscopy
CTA	chain transfer agent
COH1	composites based on poly(FMA-co-H1-co-MIMA-co-BMA) and urea functionalized particles
COH2	composites based on poly(FMA-co-H2-co-MIMA-co-BMA) and urea functionalized particles
CX_Y	ionic self-healing nanocomposites, based on ATRP polymers, X refers to the polymer composition (DEGMA:SMBS), Y refers to the particle content in wt% (1-20)
DA	Diels-Alder
DBPO	dibenzoyl peroxide
DEA	2-(diethylamino)ethyl methacrylate
DEGMA	di(ethylene glycol) methyl ether methacrylate
DMAEMA	2-(dimethylamino)ethyl methacrylate
DPA	2-(diisopropylamino)ethyl methacrylate
DTRP	degenerative transfer radical polymerization
EBriB	ethyl- α -bromisobutyrate
E	E-modulus
FMA	furfuryl methacrylate
FRP	free radical polymerization
FTIR	Fourier-transform infrared spectroscopy
HEMA	hydroxyethyl methacrylate
HMTETA	1,1,4,7,10,10-hexamethyltriethylenetetramine
HOMO	highest occupied molecular orbital
H1	2-acetamidoethyl methacrylate
H2	2-(4-butylureido) ethyl methacrylate
I_{bkg}	constant scattering background

ICAR ATRP	initiators for continuous activator regeneration ATRP
ICP-MS	inductively coupled plasma - mass spectrometry
$I_g(q)$	Gaussian distribution, accounting for the Bragg peak in paracrystalline polymers
IL	ionic liquid
$I_P(q)$	generalized Porod law
ITRP	iodine transfer radical polymerization
LbL	layer-by-layer deposition
LOQ	limit of quantification
LUMO	lowest unoccupied molecular orbital
m	fractal dimension of agglomerates
MALDI-TOF	matrix-assisted laser desorption/ionization time-of-flight mass spectrometry
METAC	2-(methacryloyloxy)-ethyl-trimethyl-ammonium chloride
MIMA	maleimidoalkyl methacrylate
NCX	ionic self-healing nanocomposites, based on FRP polymers, X refers to the particle content in wt% (2-20)
NMP	nitroxide mediated polymerization
PALS	phase-analysis light scattering
pH_{PZC}/PZC	point of zero charge
pH_{IEP}/IEP	isoelectric point
PH1	poly(FMA-co-H1-co-MIMA-co-BMA)
PH2	poly(FMA-co-H2-co-MIMA-co-BMA)
pK_A	negative decadic logarithm of the acid dissociation constant
pK_B	negative decadic logarithm of the base dissociation constant
PMDETA	<i>N,N,N',N'',N'</i> -pentamethyl diethylenetriamine
$P_{pS}(q)$	form factor of polydisperse spheres
RAFT	reversible-addition-fragmentation chain transfer polymerization
R_{HS}	hard sphere radius
$R_{p0.2}$	tension at which the permanent elongation after unloading is 0.2 %
rDA	retro-Diels-Alder
SAM	self-assembling monolayers
SAR	specific absorption rate
SAXS	small angle X-ray scattering
$S_{HS}(q)$	disordered hard sphere structure factor
SI ATRP	surface initiated ATRP

SLP	specific loss power
SMBS	sodium-4-(methacryloyloxy)butane-1-sulfonate
SRMP	stable radical mediated polymerizations
$\tan(\delta)$	dissipation factor
TEM	transmission electron microscopy
TEMPO	2,2,6,6-tetramethylpiperidin-1-oxyl
T_g	glass transition temperature
TPMA	tris(2-pyridylmethyl)amine
T_{95}	temperature at 5 wt% mass loss in thermogravimetric analysis
Upy	2-ureido-4-pyrimidone
XRD	X-ray diffraction
^xPol	poly(SMBS-co-DEGMA), synthesized via ATRP, 1:X = SMBS:DEGMA monomer ratio
$^x\text{PolF}$	poly(SMBS-co-DEGMA), synthesized via FRP, 1:X = SMBS:DEGMA ratio determined from CHN
$^x\text{AIP@Fe}_x\text{O}_y$	Non-polar initiator functionalized iron oxide nanoparticles, X = mmol P/150 mg particles
$^x\text{P@Fe}_x\text{O}_y$	cationic functionalized iron oxide nanoparticles, X = mmol P/150 mg particles
$^x\text{PA@Fe}_x\text{O}_y$	anionic functionalized iron oxide nanoparticles, X = mmol P/150 mg particles
$^x\text{PIP@Fe}_x\text{O}_y$	polar initiator functionalized iron oxide nanoparticles, X = mmol P/150 mg particles
$^x\text{UP@Fe}_x\text{O}_y$	urea functionalized iron oxide nanoparticles, X = mmol P/150 mg particles
ϵ_c	dielectric constant
ϵ_{\max}	maximum strain the material can withstand
σ_{\max}	maximum stress the material can withstand

Content

1.	Introduction and Theoretical Background.....	1
1.1.	Nanocomposites	2
1.2.	Synthetic Approaches to Organic-Inorganic Nanocomposites	3
1.2.1.	Grafting-to Polymerization	4
1.2.2.	Grafting-from Polymerization	11
1.3.	Inorganic Fillers for Incorporation into Organic Matrices	19
1.3.1.	Iron Oxide Nanoparticles.....	20
1.3.2.	Synthesis Routes for Iron Oxide Nanoparticles	23
1.3.3.	Functionalization of Iron Oxide Nanoparticles	25
1.4.	Introduction of Charges to Metal Oxide Nanoparticle Surfaces	30
1.4.1.	Generation of Surface Charges by pH Adjustment.....	31
1.4.2.	Generation of Surface Charges by Functionalization	32
1.5.	Mechanisms and Advances in Self-Healing Polymers.....	38
1.5.1.	Dynamic Covalent Bond Chemistry in Self-Healing.....	40
1.5.2.	Dynamic Non-Covalent Bond Chemistry in Self-Healing.....	46
1.6.	Self-Healing Nanocomposites.....	52
2.	Research Goals	58
2.1.	Objective.....	58
2.2.	Concept	58
3.	Results and Discussion.....	61
3.1.	Synthesis and Characterization of the Metal Oxide Nanoparticles	61
3.2.	Synthesis of Permanently Charged Nanoparticles	72
3.2.1.	Synthesis of the Cationic Functionalization Reagent.....	73
3.2.2.	Cationic Particle Functionalization	73
3.2.3.	Synthesis of the Anionic Functionalization Reagent.....	82
3.2.4.	Anionic Particle Functionalization.....	83
3.2.5.	Comparison of the Cationic and Anionic Functionalized Particles	87
3.3.	Synthesis of Switchable Cationic Surfaces	89
3.4.	Ionic Self-Healing Nanocomposites	98

3.5.	Self-Healing Nanocomposites via Ionic Interactions at the Particle-Polymer Interface.....	99
3.5.1.	Synthesis and Characterization of Anionic Polymers by ARGET ATRP	101
3.5.2.	Synthesis and Characterization of Ionic Nanocomposites based on the ATRP Polymers.....	104
3.5.3.	Self-Healing Studies on the Ionic Nanocomposites based on the ATRP Polymers	111
3.5.4.	Investigation of the Influence of Storage Conditions on the Properties of the ATRP Polymers and Composites	119
3.5.5.	Synthesis and Characterization of Anionic Polymers by FRP.....	124
3.5.6.	Synthesis and Characterization of Ionic Nanocomposites based on the FRP Polymers.....	141
3.5.7.	Self-Healing Studies on the Ionic Nanocomposites based on the FRP Polymers	150
3.6.	Synthesis of Nanocomposites via SI ATRP.....	154
3.6.1.	Synthesis of a Phosphonic Acid-Based ATRP Initiator with a Non-Polar Linker	156
3.6.2.	Synthesis of a Phosphonic Acid-Based ATRP Initiator with a Polar Linker.....	159
3.6.3.	Synthesis of ATRP Initiator Functionalized Particles	161
3.6.4.	SI ATRP of Model Monomers	166
3.7.	Self-Healing Nanocomposites Based on Two Healing Mechanisms.....	168
3.7.1.	Synthesis and Characterization of Double Self-Healing Polymers Based on DA and Hydrogen Bond Chemistry	168
3.7.2.	Synthesis and Characterization of the Ureylene Functionalized Iron Oxide Nanoparticles.....	174
3.7.3.	Synthesis and Characterization of the Double Self-Healing Composites Based on DA and Hydrogen Bond Chemistry	179
3.7.4.	Advances in the Synthesis of Double Self-Healing Polymers Based on DA and Ionic Bond Chemistry.....	183
4.	Conclusion and Perspective.....	192
5.	Experimental.....	195
5.1.	Materials	195

5.2.	Characterization.....	196
5.3.	Synthetic Procedures.....	199
6.	References	233

1. Introduction and Theoretical Background

The field of nanomaterials, and nanoparticles in particular, is an extremely bright field that has generated a steadily growing interest in recent decades. The prefix nano comes from the ancient Greek word *nános*, meaning dwarf. The research field of nanoscience thus encompasses the disciplines that deal with materials in the nanometer size range. This includes 0D nanomaterials such as nanoparticles and quantum dots, which have diameters < 100 nm in all dimensions, as well as materials that are only in one (nanosheets and nanofilms) or two dimensions (nanorods, nanotubes and nanowires) in the nanoscale. However, the modern definition also includes 3D "nanomaterials", although technically no dimension of these materials is tied to the nanoscale. These include agglomerates of nanoparticles, polycrystals or bundles of nanowires (see Figure 1).

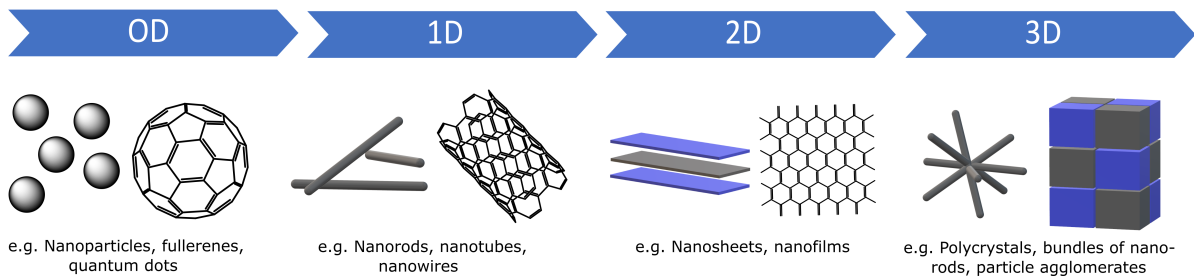


Figure 1: Overview of the types of nanomaterials. Adapted from [1].

Although the research field of nanoscience is relatively new, the history of nanoparticles and nanostructures used by humans traces back centuries and includes color pigments in art and glassmaking, as well as clay-based pottery building materials.[2,3] What all these materials have in common is that they exhibit extraordinary properties that could only be explained much later as a result of the development of advances in analytical techniques, such as electron spectroscopy, which made it possible to detect nanoscale components. Although there had been previous studies, such as Ostwald's 1914 work "*The World of Neglected Dimensions*", in which he discussed the then modern colloid chemistry, which was centrally concerned with nanoparticle dispersions [4], today the lecture "*There's Plenty of Room at the Bottom*" by Nobel laureate Richard Feynman is generally regarded as the starting point for the scientific consideration of nanoscience. Here Feynman emphasized the importance of nanomaterials: "*In the year 2000, when they look back at this age, they will wonder why it was not until the year 1960 that anybody began seriously to move in this (nano) direction.*" Indeed, in the years since then, a steadily growing interest in research has been observed. Since the early 1990s, the number of publications has increased from less than 100 publications per year to several thousand without any signs of a slowing down (see Figure 2).

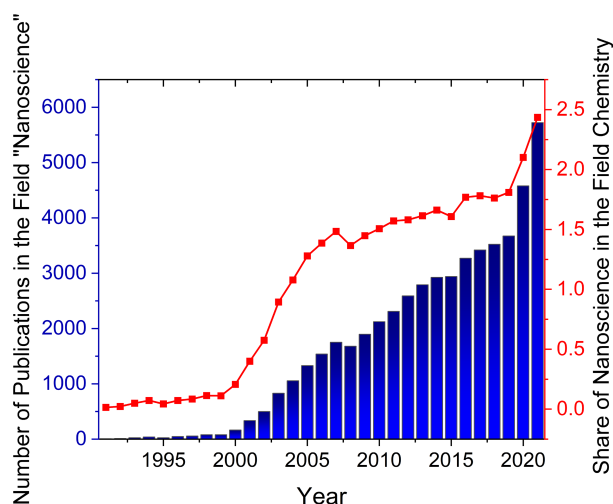


Figure 2: Development of the number of publications in the field of nanoscience (source: SciFinder database, as of July 22, 2022).

This interest is rooted in the unique physical and chemical properties of nanosized materials, which are often very different from those of bulk materials. This can be attributed to the high surface area-to-volume-ratio and the resulting high surface energy of nanoparticles. As a result, nanoparticles tend to form larger agglomerates. Therefore, a central research focus is the stabilization of the particles. Further, applications of nanomaterials often require a homogeneous distribution in a matrix. These materials are called nanocomposites and synergistically combine the advantageous physicochemical properties of both the filler and the matrix component. The conjunction of inorganic fillers with organic matrices is therefore of particular interest because it covers a wide range of properties. The crux of these materials are the phase boundaries they contain, which represent weak points of the systems. The aim of this work is to contribute to the understanding and optimization of this organic-inorganic interface.

1.1. Nanocomposites

IUPAC defines composites as materials comprised of multiple different (non-gaseous) phase domains in which at least one domain is continuous. If at least one dimension of one phase is in the nanometer size range, the term nanocomposites is used.[5] In recent years, organic-inorganic nanocomposites have attracted considerable attention. Here, mostly metal or metal oxide nanoparticles as well as carbon based inorganic fillers are used.[6–9] Organic-inorganic composites offer the advantage of synergistically combining the advantageous physicochemical properties of both the inorganic and the organic or polymeric component.[10] By introducing an inorganic filler, the mechanical and thermal stability of the polymers can be increased, while the flexibility of the polymer component is maintained, which gives access to lifetime improvements.[11–15] Further, the organic component allows the introduction of functional groups that allow the control of the composite properties. In addition to applications

in the field of drug transport and self-assembly, the improvement of properties gives access to numerous applications, including use as gas barriers [16,17], in catalysis [18,19], in energy storage [20] for optical or magnetic applications [21] and self-healing among other things. Since self-healing is a central research topic in this work, this aspect will be discussed separately in chapters 1.5 and 1.6. First, however, the synthetic approaches to organic-inorganic nanocomposites will be discussed in more detail.

1.2. Synthetic Approaches to Organic-Inorganic Nanocomposites

The simplest approach to organic-inorganic nanocomposites is the embedding of nano-objects into a polymer matrix. Polymer nanocomposites can be prepared in several ways, which are divided into two categories: *ex situ* and *in situ*. In the *ex situ* methods, the organic and inorganic components are synthesized separately and the inorganic component is simply mixed with either the melt of a thermoplastic polymer or a polymer solution.[22,23] *In situ* synthesis involves dispersing the inorganic component in the monomer, which is then polymerized, or the reverse, where the inorganic phase is formed in a solution or gel of the polymer.[24,25] In these approaches, both strong or weak interactions can occur between the organic and inorganic components. In particular, the latter can cause the two components to separate over time. In this context, the strategy of nanoarchitectonics for the construction of nanocomposites is promising, as it involves a well-defined sequential assembly process that allows the optimization of the phase interface and the synthesis of reliable nanocomposites. This requires synthetic techniques that allow control at the molecular level, known as grafting techniques.[26] Three approaches of graft polymerization are used for the preparation of organic-inorganic nanocomposites. These are grafting-from, grafting-to and grafting-through polymerizations. A schematic representation of the synthesis strategies is shown in Figure 3.

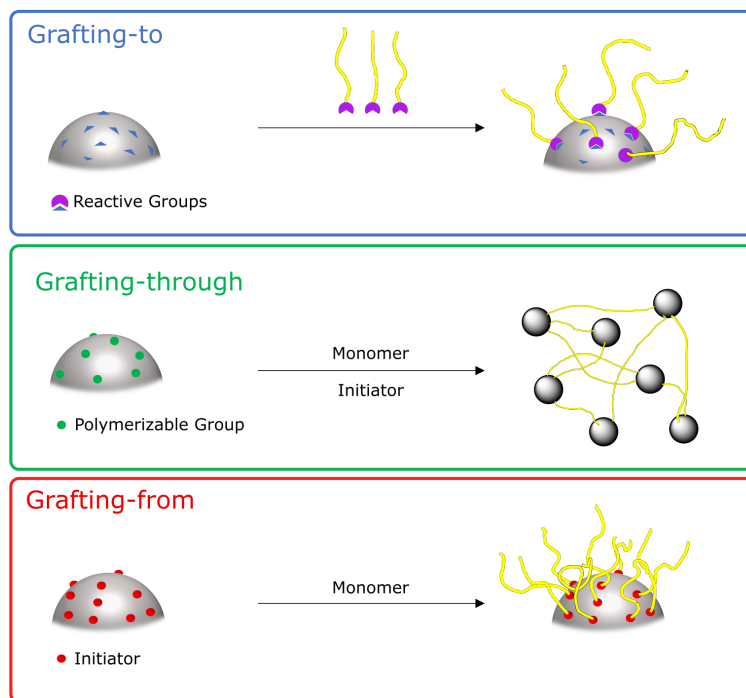


Figure 3: Synthetic approaches to grafted nanocomposites. Adapted from [26].

One of the major differences between the composites obtained from grafting-from and grafting-to techniques is the grafting density achieved. Grafting-to often produces lower grafting densities due to the diffusional effects and the steric demand of the polymer chains.[26,27] Often this is not even investigated, although it has significant influences on many of the solution phase properties of nanocomposites. Depending on the grafting density, pancake, mushroom, or brush type chain arrangements are formed. The number of stabilizing groups thus governs in particular the properties in solution, such as their colloidal stability and hydrodynamic diameter.[28] In the following the synthetic approaches will be described in more detail.

1.2.1. Grafting-to Polymerization

The grafting-to method involves polymerization remote from the particle surface. For this purpose, polymers are used which have anchor groups that can bind to the surface of the paired particles. These anchor groups are either introduced during polymerization or generated by subsequent functionalization.[29] The advantage of this method is that the synthetic effort is often low, and in addition almost any surface can be functionalized by suitable selection of the anchor group. Therefore, the focus here will be on the polymerization processes. A detailed discussion of the particles and anchor groups relevant to this work can be found in section 1.3.3. A large variety of polymerization options are available for the synthesis of the polymer components. Polymers are formed by polyreactions, which in turn are divided into chain-growth and step-growth reactions. The reactions differ in that in chain growth reactions the reactive center remains at the end of the chain and thus an active state is permanently present, while in step growth the ground state is passed through again after each reaction step.[30] Since the

two chain growth reactions free radical and controlled radical polymerization were applied in this work, they are described in more detail below.

Free radical reaction: Free radical polymerization is the most common chain growth reaction, consisting of the elementary reactions chain initiation, chain growth and chain termination. The chain reaction is started by radicals which are formed thermally, photolytically or by chemical reaction of an initiator. A monomer radical is formed by reaction with the monomer, which thereby itself turns into the active or reactive center. During the growth reaction, the previously formed monomer radical accumulates further monomers in the form of multiple additions. In the process, a macromolecular chain is formed. The more resonance-stabilized the polymer radical is, the slower the chain growth proceeds. Furthermore, the growth rate depends on steric and polar effects of the reaction partners.[30] Chain termination means the end of the growth of the polymer chain. This takes place through recombination or disproportionation. The main advantage of this type of polymerization is its robustness: not only can it be used for a wide range of monomers in many different solvents, but it is also tolerant towards most functional groups. In addition, polymerizations are possible on a large scale, so that free radical polymerization is the most important polymerization technique in industry. The disadvantage of free radical polymerization is that it is difficult to control due to chain termination and transfer reactions. This lack of reaction control means that it is not possible to tailor the composition and architecture of the polymers formed or their molecular weight distribution.[31,32]

Living polymerization and controlled radical polymerization: Ideal living polymerizations are chain reactions without transfer and termination reactions.[33,34] This reaction control leads to a constant number of active centers over the reaction period.[34] As a result, narrow molar mass distributions are obtained for the polymers. Furthermore, the molecular weight of the polymer chains increases linearly with the monomer consumption (see Figure 4). This linear relationship means that the molecular weight of the polymers can be precisely controlled. In comparison, in free radical polymerization, the molar mass of the polymer strands increases abruptly, which prevents good controllability, and in step-growth reactions, such as polycondensation, the formation of high molecular weight polymers only occurs at a high conversion rate of almost 100 %.[35,36]

Introduction and Theoretical Background

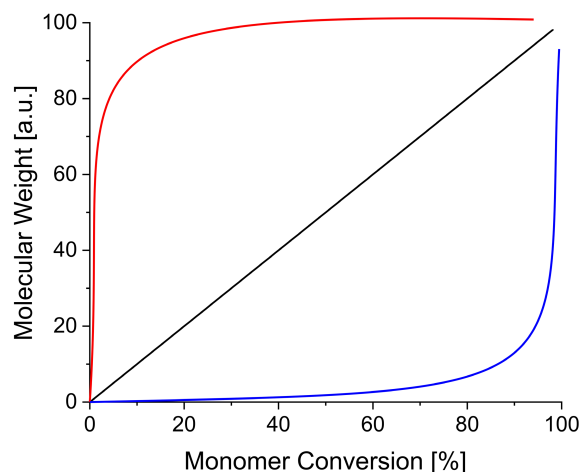


Figure 4: Polymer molecular weight as a function of monomer conversion for free radical (red), controlled radical/living (black) and condensation (blue) polymerization. Adapted from [35].

Assuming a highly pure reaction system, polymerization stops only after complete consumption of the monomer. The chain ends that are still active are referred to as dormant. This means that polymerization can be resumed after the monomer has been added again, enabling the synthesis of complex structures and block-like polymers.[36] Depending on the mechanism, a distinction is made between living cationic and living anionic polymerizations. In these ionic polymerization techniques, the reaction is initiated by a cation/anion and proceeds via ionic intermediates. Poly(styrene) was first synthesized through an anionic polymerization by Szwarc in 1956.[33] While chain termination can often be prevented under high purity reaction conditions in anionic polymerization, living cationic polymerization often proves difficult even in high purity systems. The main reason for this is that cationic propagation centers at the chain end tend to undergo β -proton transfer to the monomer, counterion or other basic species in the reaction system under chain termination.[32] Therefore, strictly speaking, cationic polymerization is not a living reaction, but the requirement is only approximately fulfilled by this chemical equilibrium. Therefore, this type of polymerization should be called quasi-living.[37]

This balance between active and dormant species is also used in living free radical polymerizations. The living free radical polymerizations described below and used in this work will be referred to as controlled free radical polymerization, in agreement with the literature. However, it should be noted that this term does not conform to the IUPAC recommendation, which advocates the term reversible-deactivation polymerization. They define this as “*Chain polymerization, propagated by chain carriers that are deactivated reversibly, bringing them into active-dormant equilibria of which there might be more than one*”.[38] The first controlled radical polymerization was described in 1982 by Otsu *et al.* for vinyl polymerization.[39,40] This work involved so-called iniferter polymerizations. An iniferter is a chemical compound that acts as initiator, transfer agent and terminator.[41,42] Tetraethylthiuram disulfide and, in later

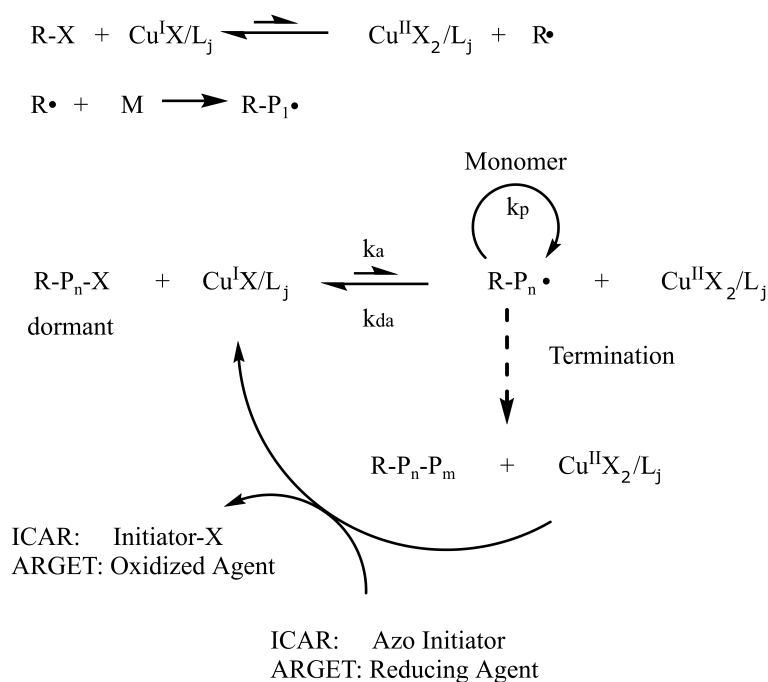
reports, triphenylphenylazomethane or S-benzyl-*N,N*-diethyldithiocarbamate were used as iniferters for vinyl polymerization.

Since then, a variety of controlled radical polymerization techniques have been developed. They can be distinguished by the way of achieving the required dynamic equilibrium between active and dormant species. One approach is a transfer between the propagating radicals and a dormant species. The most important representatives of these degenerative transfer radical polymerizations (DTRP) are reversible-addition-fragmentation chain transfer polymerization (RAFT) and iodine transfer radical polymerization (ITRP). Since these processes play only a very minor role in this work only the relevant literature will be referenced at this point.[43–48]

The second approach to achieve dynamic equilibrium is the reversible deactivation of radicals to form dormant species. The short-term reactivation can occur spontaneously, as in the case of stable radical mediated polymerizations (SRMP), or by a catalytic manner. One of the best-known examples of SRMP is the so-called nitroxide mediated polymerization (NMP). Here, the principle of reversible chain termination is exploited by using stable radicals based on linear or cyclic nitroxides. If the reaction between the stable radical and the polymeric radical is sufficiently reversible, the termination is reversible. Furthermore, when the number of active chains is low enough, the polymerization is controlled. The most commonly used nitroxide is the radical scavenger (2,2,6,6-tetramethylpiperidin-1-yl)oxyl (TEMPO).[49] However, the foremost important polymerization technique of the SRMP is the atom transfer radical polymerization (ATRP). Since this polymerization technique is the most relevant for this work, it will be explained in more detail below.

Atom transfer radical polymerization was developed independently by Matyjaszewski and Sawamoto in the 1990s.[50,51] IUPAC defines ATRP as a “*Controlled reversible-deactivation radical polymerization in which the deactivation of the radicals involves reversible atom transfer or reversible group transfer catalyzed usually, though not exclusively, by transition-metal complexes.*”[38] Since this development, a large number of variations of the polymerization have been described in the literature. The basic mechanism, as well as the progress in the polymerization of ionic monomers, which is of particular relevance for this work, will be described in more detail. In ATRP halogenated alkanes serve as initiators. Furthermore, a transition metal complex is added, consisting of a transition metal salt and nitrogen- or phosphorus-based chelating ligands. The mechanism of ATRP is shown in Scheme 1.

Introduction and Theoretical Background



Scheme 1: Schematic mechanism of the copper based ATRP reaction.

ATRP is mechanistically closely related to atom transfer radical addition, which is commonly used in organic synthesis for carbon-carbon bond formation and is based on inner sphere electron transfer.[50] In the first step, a reversible reaction takes place between the halogen alkane and the copper salt. This results in the abstraction of the halide. More precisely, it is a homolytic halogen transfer in which a radical is generated, and the transition metal is oxidized. Further, the coordination of the released halide to the transition metal takes place with expansion of the inner coordination sphere. Copper is the most commonly used transition metal, but a number of different transition metals have been described which allow a one-electron transfer redox cycle.[52] These include among others: titanium(III/IV) [53], iron(II/III) [54,55], cobalt(II/III) [56,57], nickel(II/III) [58], molybdenum(III/IV) [59,60], ruthenium(II/III) [61,62], palladium(II/III) [63,64] and rhenium(V/VI) [65]. The radical released during the halogen transfer can then react with the monomer and lead to the growth of the polymer chain. These chain radicals likewise can react with the oxidized transition metal complex and are thus in equilibrium with the dormant halogenated species. The controllability of the reaction is defined by the activation-deactivation equilibrium ($K_{\text{ATRP}} = \frac{k_{\text{a}}}{k_{\text{da}}}$). For the reaction to proceed in a controlled manner, the radical concentration should be low, to reduce radical-radical termination reactions. This is the case when K_{ATRP} is small. As a result, the reaction times are often significantly longer compared to free radical polymerization. There are several parameters to control the reaction rate. The first is the reaction temperature. Activation rates increase with increasing temperature. In general, reactions of less active alkyl halides are accelerated further than those of higher active initiators.[66] A second way to control the

Introduction and Theoretical Background

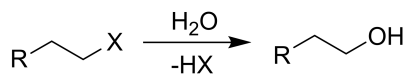
reaction comes from the choice of solvent. Braunecker *et al.* have shown that the activation rate increases with the polarity of the solvent.[67] Also the choice of the ligand is crucial. In addition to solubilizing the catalytic system, the ligand system also affects redox chemistry through electronic effects and selectivity through steric/electronic effects. Thus, K_{ATRP} decreases linearly with the redox potential of the complexes.[66] The activation rate for copper complexes with nitrogen-based ligands decreases from tetradentate (cyclic-bridged > branched > cyclic > linear) over tridentate to bidentate.[68] Finally, the initiator also has an influence on the activation. There are three influencing factors: For the most commonly used α -bromo esters and benzyl halides, the activation rate increases with the degree of substitution. At the same time, the activation rate follows the ability to stabilize radicals. Therefore, phenyl esters are more reactive than cyanides, esters, benzyls, and amides. For initiator systems with the same structure, the activation rate decreases with increasing binding energy from iodine to bromine to chlorine. SCN and NCS represent the worst leaving groups and therefore show the lowest activity.[69] Usually, a structure similar to the monomer is chosen for the alkyl structure of the initiator.[52]

However, ATRP also offers a number of challenges. Since the oxidation state of the transition metal plays a central role in the reaction, degassing of the reaction medium is necessary to avoid oxidation by dissolved oxygen. Thus, originally, large amounts of catalyst had to be used.[50] In newer approaches small amounts supporting agents in form of azo initiators or reducing agents are added to continuously regenerate the catalyst.[70,71] The former is called initiators for continuous activator regeneration (ICAR) ATRP and the later activator regenerated by electron transfer (ARGET) ATRP. In ARGET ATRP Sn(II) 2-ethylhexanoate, glucose [71,72] or hydrazine derivatives[73,74] are usually used as the reducing agent. Further, if chosen appropriately, the ligand or the monomer can also function as the reducing reagent to provide a controlled reaction.[75,76] If taken to the extreme, it is possible to start with the oxidized catalyst species, and the reduced species is then generated *in situ*. This is often referred to as reversed ATRP. The big advantage here is that residual oxygen is not a problem. The disadvantage of this reaction route is that only homopolymers and no complex architectures can be produced via this route.

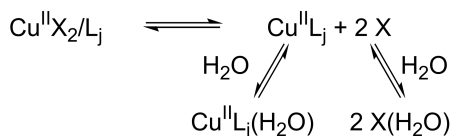
Another problem for ATRP is the controlled polymerization in polar and protic solvents, especially water.[77,78] In aqueous media, K_{ATRP} values are several orders of magnitude higher than in organic media. This implies high radical concentrations and thus increased termination reactions and low control.[67,79] However, this is not the only aspect that restricts the controllability of the ATRP in water. Several equilibria occur during polymerization in the aqueous medium. One is the dissociation of the initiator or the dormant chain. A second

problem is the disproportionation of the $\text{Cu}^{\text{I}}\text{X}/\text{L}$ activator. Finally, the lability of the $\text{Cu}^{\text{II}}\text{X}_2/\text{L}$ deactivator often hampers controllability.[79,80] These processes are shown in Scheme 2.

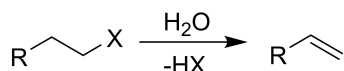
Hydrolysis of the dormant species:



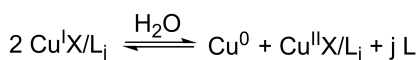
Dissociation and hydrolysis of the deactivator complex:



Elimination reaction of the dormant species:



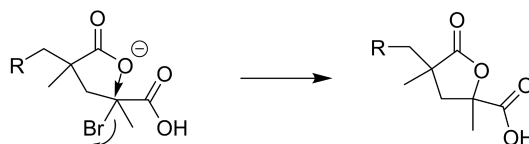
Disproportionation of the activator complex:



Scheme 2: Side reactions in aqueous ATRP.

Aqueous polymerization, however, is of great interest. Not only is water a cheap, green solvent, but also the synthesis of water-soluble polymers, such as those used in biomedical and pharmaceutical applications or in self-assembly, is of enormous interest. Also for the synthesis of ionic polymers, such as those in this work, water compatibility of the ATRP is indispensable. Over the years, several approaches have been taken to circumvent the problems. In their publication, Tsarevsky *et al.* describe two possible approaches.[81] It was shown that the stability of the ternary $\text{Cu}^{\text{II}}\text{L}_j$ complex in methanol-water mixtures decreases with increasing water content. By optimizing the solvent composition, successful polymerization could be achieved in partially aqueous systems. It was further shown that the deactivation step in ATRP, can be accelerated significantly by increasing the total concentration of the copper(II) halide. However, not only the solvent poses a central problem in the preparation of ionic polymers, but also the ionic groups themselves. While the synthesis of cationic systems has already been described many times, be it through polymerization of the cationic monomers directly [82,83], or subsequent conversion into cationic systems by pH adjustment [84,85], the synthesis of monomers carrying acidic groups was long considered as an exclusion criterion for the use of ATRP as a polymerization technique. These acidic groups often destroy the catalyst complex by protonation of the ligands or by replacing the ligands completely, especially when low catalyst amounts are used. The resulting complexes, which are usually much less redox active, prevent successful polymerization. Furthermore, displacement of the halide ligands in the copper(II) deactivator complex can occur.[79,86,87] The most elegant solution would be to develop catalyst systems that are stable and maintain their equilibrium dynamics in the acidic medium. However, this represents a major challenge, so that, similar to the aqueous ATRP polymerizations, an optimization of the reaction conditions is preferred in most cases. For sulfonic acids, the problems appear to be less widespread than for carboxylic acids. Iddon *et al.* already described in 2004 the controlled polymerization of sodium 4-styrenesulfonate via ATRP by simply adjusting the composition of the methanol-water solvent mixture and using an

anionic initiator.[88] Thereafter the synthesis of fluorinated aromatic monomer with pendant sulfonate groups were reported both by introducing the acidic groups before and after polymerization.[89,90] Block copolymers were also produced by adapting the solvent composition.[91] The production of carboxylate-based systems required a higher degree of optimization, since intramolecular reactions such as lactonization can lead to a loss of chain end functionality and thus to polymerization failure (see Scheme 3).



Scheme 3: Lactonization of poly(methacrylic acid) in ATRP.[92]

Nevertheless, poly(methacrylic acid) was obtained by careful protonation (pH = 0.9) and utilization of the more stable chloride initiators and catalysts. However, a prerequisite for good control is still the use of stable binding complex ligands such as tris(2-pyridylmethyl)amine (TPMA) and operation at quite high polymerization rates.[92] More recently the utilization of a very stable porphyrin-iron catalyst complex was also described, showing a promising progress based on the path of catalyst optimization in contrast to optimizing reaction conditions.[93] Nevertheless, optimization of the reaction conditions is also necessary for these systems. For this reason and the pH stability of the negative charge of the sulfonate group, sulfonate-based anionic polymers were investigated in this work. Based on these advances, a variety of monomer systems are accessible which can subsequently be converted to the corresponding composites using the grafting-to technique.

The same polymerization techniques are also used in grafting-through polymerization. Here, the particle surface carries polymerizable groups, which are then incorporated into the chains of the growing polymer.[94,95] Since grafting-through was not used in this work, a more detailed description will not be given here.

1.2.2. Grafting-from Polymerization

The grafting-from method is a surface-initiated (SI) polymerization. Here, initiator molecules are immobilized on the particle surface. The functionalized particles are dispersed in the monomer or monomer-containing solutions. The same polymerization strategies are available for grafting-from polymerization as for polymerization in solution. For surface-initiated variants of free-radical polymerization, studies can be found early in the literature.[96] Ruhe and Pruckler reported the polymerization of poly(styrene) from silica particle surfaces using a surface-bound azo initiator as early as 1998.[97,98] Free radical polymerization has even been used to produce Janus particles, i.e. particles with significant anisotropy in their properties.[99] The advantages of free radical polymerization, such as the accessibility of many monomers,

are retained in SI polymerization.[100] A central disadvantage of the mostly AIBN-based initiator design is that two radicals are formed. One at the particle surface and one diffusing into the solution, so that free polymerization always takes place in solution as a side reaction. This can be circumvented by using controlled polymerizations. Despite the good controllability, ionic polymerizations are rarely used for the SI production of nanocomposites. The strongly alkaline and nucleophilic chain ends used in the reaction and the strongly alkaline and nucleophilic chain ends formed from them already severely limit the choice of surfaces that can be used. Furthermore, the components are extremely sensitive to impurities, especially protic reagents, which cause chain termination by protonation. Nevertheless, some examples of anionic polymerization from carbon, silicon and clay surfaces are described.[101–105] Although large efforts have been put into the anionic polymerization of silica particles, the polymerization of metal oxide surfaces poses a major challenge. A central problem are the Si-OH surface functionalities, which lead to termination of the chain ends. Furthermore, polymerization in solution is often observed as a side reaction due to unbound initiator molecules or butyllithium, which is often used to prepare the initiator and could not be completely removed. As a result, polymers with lower molecular weights and higher polydispersity are obtained than in ionic polymerization in solution.[106–109]

Living radical polymerization are particularly suitable for SI polymerization. This is due to the fact that the bonding of the initiator to the surface creates a mobility barrier that restricts termination.[110] SI RAFT and SI ATRP are the most widely used techniques today. Due to the abundance of publications and extensive reviews in this area, it should be referred to these here.[111–118] As the ATRP is used in this work, a few selected examples, which represent milestones in SI ATRP or are of particular relevance to this work, will be highlighted in the following paragraph. These include polymerizations of ionic monomers and polymerizations from iron oxide surfaces.

The first descriptions of SI ATRP can be found at the end of the 1990s. Ejaz *et al.* describe the graft polymerization of methyl methacrylate from silicon substrates.[119] In this study, 2-(4-chlorosulfonylphenyl)ethyltrimethoxysilane was used as the initiator. The initiator was immobilized by hydrolysis of the methoxy group and subsequent attachment to the oxidized silicon substrate. CuBr and 2,2'-bipyridine (2,2'-Bipy) were used as the initiator complex.

Surface-initiated polymerization has been applied to a variety of monomers and particle systems. Due to their properties, iron oxide particles are one of the most commonly used particles. Another practical advantage of iron oxide particles is that they can be dissolved in acid under comparatively mild conditions and allow subsequent characterization of the polymers, while other particle systems such as SiO₂ require much harsher reagents such as hydrofluoric acid.[120,121]

Introduction and Theoretical Background

First reports on surface-initiated ATRP from iron oxide surfaces can be found in the early 2000s. Wang *et al.* and Gravano *et al.* describe the production of Fe₂O₃-poly(styrene) based core-shell nanoparticles, which can be used as macroinitiators for ATRP.[122,123] This interest in macroinitiators already points to a central criterion of SI ATRP. Due to the space requirements of polymerization, it is often advisable to choose a large spacer to gain a certain distance to the surface and thus free space for the chains.

While in these cases the initiator functionality was mostly attached to the particle surface via carboxylate functionalities, more stable anchor groups such as silanes [124], dopamines [125] or phosphonic acids [126] were also used.

One of the most common areas of application is the biomedical sector. Due to their suitability for use as contrast agents in magnetic resonance imaging or for drug transport, the iron oxide particles are of central interest. Therefore, the functionalization with polar systems such as poly(2-hydroxyethyl methacrylate), poly(methacrylic acid) or poly(2-(methyl sulfinyl)ethyl acrylate) is often described, which allows the application under physiological conditions.[127,128]

Also the syntheses of more complex systems such as block copolymers or Janus-type nanocomposites via SI-ATRP from iron oxide particles have been described.[129,130]

As already mentioned, the influence of termination reactions on the properties of the composites is a central problem of multifunctional initiators. Termination can occur both by intermolecular reactions, leading to crosslinked, gel-like networks, and intermolecularly, leading to broader distributions of the polymer chains. Therefore, great efforts have been made to find ways to minimize the termination reactions and gel formation during the grafting-from process by optimizing the polymerization conditions. This includes adding a larger amount of monomer and applying conditions to slow down the redox rate or adding the redox conjugate to the reaction mixture, further facilitating the exchange between the active radicals and the dormant species. Adding sacrificial initiator to the solution provides both a means of monitoring the reaction and controlling the initiation from the surface. Other approaches include stopping the reaction at low conversions or reaction in dilute solutions.[131,132]

As with ATRP in solution, SI ATRP also had to be carried out under strict deoxygenation. Due to the development of ARGET ATRP, SI ATRP could later also be carried out in the presence of limited amounts of oxygen even with small amounts of catalyst by adding an appropriate excess of reducing agent. Matyjaszewski *et al.* describe for the first time the application of ARGET ATRP for the synthesis of poly(butyl acrylate) and poly(butyl acrylate)-*block*-poly(styrene) from silicon wafers.[117]

Further application of high pressure allows controlled ARGET ATRP due to an increased propagation rate constant, while the deactivation rate constant is reduced. As a result, the reaction rate is increased, while good control is maintained.[121] Since the persistent radical effect is avoided, low catalyst concentrations are possible and no reducing agents are necessary.[133]

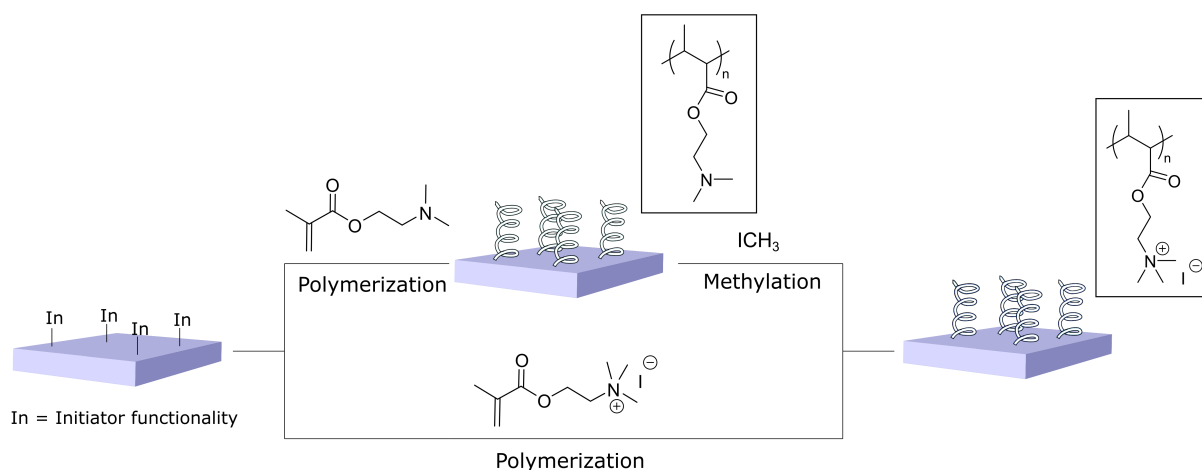
Comparable results have also been obtained for polymerization in mini emulsions.[134] Due to the compartmentalization of the reaction medium radical termination and gelation are minimized while deactivation is increased, yielding in good control. Bombalski *et al.* describe high yields and reaction speed without macroscopic gelation.[135] As a result, the polymerization technique is still widely used today.[136,137]

ATRP polymerizations in solution have shown that external stimuli can increase the control over polymerizations. The reason for this is that the reaction rate can be adjusted by setting the properties of the stimuli. Further, the stimulus can be turned off completely, allowing precise temporal control over polymerization. Various stimuli have been applied in solution, including electric current [138–140], ultrasonication [93,141,142] and more recently mechanical initiation by ball milling.[143]

Another important technique, particularly in relation to SI ATRP, is photoinduced ATRP. Initial work on photoinduced initiation of an ATRP employed the reverse ATRP procedure in combination with a standard photo initiator.[144] Today, however, photo initiators are usually no longer utilized. Instead, regeneration of the activator complex is achieved by photochemical reduction of the deactivator complex by a free aliphatic amine.[145,146] For this purpose, the ligand is usually added in excess. This reaction control was also applied to the SI ATRP.[147] Although relatively high catalyst concentrations were required to obtain good control over polymerization, the extremely low amount of alkyl halide functionality provided good control, allowing the synthesis of methyl methacrylate and oligo-(ethylene glycol) methyl ether methacrylate polymer films grafted from silica substrates.

Lastly, the progress made in the SI ATRP-based synthesis of ionic nanocomposites will be described here. There are two basic possibilities to produce ionic nanocomposites. The first possibility is the use of ionic monomers. The second possibility is the polymerization of a non-ionic monomer which has functional groups that can be converted into charge-bearing groups by further reactions. The synthesis strategies are shown schematically using the example of poly(2-(methacryloyloxy)ethyltrimethylammonium iodide) in Scheme 4.

Introduction and Theoretical Background



Scheme 4: Schematic representation of the synthesis strategies of ionic nanocomposites using the example of poly(2-(methacryloyloxy)ethyltrimethylammonium iodide).

The synthesis of cationic functionalized nanocomposites is often carried out by introducing the cationic groups after the actual polymerization process. For the direct SI ATRP polymerization of cationic monomers, polymerizations of 2-(methacryloyloxy)ethyltrimethylammonium chloride (METAC) are almost exclusively described in the literature. The polymerization from flat substrates [148–154] has been studied in more detail than the polymerization from particle surfaces.[155].

Osborne *et al.* described the controlled growth of METAC-sodium methacrylate block copolymer brushes on gold-coated silicon substrates.[148] The initiator was immobilized using thiol groups. Polymerization was carried out in a methanol-water mixture (4:1) at room temperature using CuCl, 2,2'-Bipy and CuCl₂ as catalyst system. By ellipsometry, layer thicknesses of 70 nm were determined after 80 minutes of reaction time, potentially enabling application in biosensors or smart coatings.

Based on the Osborne protocol, Dunlop *et al.* described the polymerization of METAC from mica surfaces.[149] Here, the initiator was immobilized by silane anchor groups. In contrast to the previous synthesis, the polymerization was carried out in water. As a result of the reduced excess of CuCl₂ and 1,1,4,7,10,10-hexamethyltriethylenetetramine (HMTETA) as ligand, polymer films of 15-40 nm thickness were synthesized in 15 minutes reaction time. In another work, analogous polyelectrolyte brushes were polymerized from sapphire after a gas phase deposition of the initiator on the Ar/H₂O plasma activated surface.[151]

Ramos and Moya investigated the influence of the grafting density of ω-mercaptopundecyl bromoisobutyrate-thiol on gold surfaces.[150] A mixture of DMF and water (3:2, v:v) was used as solvent and METAC was catalyzed with 2,2'-Bipy and CuCl. A combination of spectroscopic ellipsometry and quartz crystal microbalance with dissipation (QCM-D) allowed determination of water content. Water content values varied in a range between 55 % and 79 % for each graft fraction and showed no clear correlation with grafting density.

Introduction and Theoretical Background

Li *et al.* investigated the electrochemically induced SI ATRP of METAC.[153] In this work, the polymerization was observed *in situ* by atomic force microscopy. CuCl_2 and 2,2'-Bipy were used as the catalyst system. Layer thicknesses of 60 nm were achieved within 15 minutes. Dramatic enhancement of poly(METAC) growth was observed by shielding the charge of the end group by adding a counterion electrolyte such as 1-methyl-3-butylimidazolium bromide or 1-methyl-3-butylimidazolium tetrafluoroborate in aqueous solution.

One of the few exceptions in which particle surfaces are used as substrates is the work of Tan *et al.*[155] Here, cationic poly(2-(methacryloyloxy)-ethyl-trimethyl-ammonium chloride) brushes were grafted by ATRP from silica nanoparticle surfaces (≈ 320 nm). BIBB was immobilized on the particle surface via a trichlorosilane. 2,2'-Bipy, CuBr, and CuCl_2 were used as catalyst complexes. The polymerization of METAC was carried out in a mixture of isopropyl alcohol and water (4:1) at room temperature. The obtained particles were used to stabilize water-oil Pickering emulsions.

The subsequent introduction of cationic groups usually takes place via amines, which are converted into the corresponding ammonium ion or quaternary amine either by pH adjustment or by alkylation.

The first descriptions of this can be found in 2003. Chen *et al.* describe the polymerization of 2-(dimethylamino)ethyl methacrylate (DMAEMA) and 2-(diethylamino)ethyl methacrylate (DEA) from silica nanoparticles (≈ 300 nm) in addition to the surface-initiated ATRP polymerization of styrene sulfonate.[156] The polymerization of DMAEMA was carried out in water at 20 °C with 2,2'-Bipy and CuBr as catalyst complex. The particles showed an increase in hydrodynamic radius of 32.5 nm within 2 hours reaction time. DEA was polymerized in methanol at 50 °C. HMTETA was used as a complex ligand for this polymerization. An increase in hydrodynamic radius of 21 nm was obtained at 50 °C. The authors demonstrated that below the isoelectric point (pH 8), the particles are stabilized in the aqueous medium by electrostatic repulsion.

Fielding *et al.* put this concept into practice.[157] In her work, 2-(diisopropylamino)ethyl methacrylate and methacrylic acid 2-diethylaminoethyl ester were polymerized from silicon wafers via ATRP with CuBr and 2,2'-Bipy. Brushes with thickness of 150 and 170 nm were grown within 22 hours at 20 °C. The obtained brushes showed smart swelling behavior in response to pH changes, allowing their application as acidic vapor sensors.

In a similar approach, Topham *et al.* further investigated the relationship between charge density and polyelectrolyte brush profile with neutron reflectance and *in situ* ATR IR.[158] For this purpose, poly(2-(diethylamino)ethyl methacrylate) brushes were grown from a silicon crystal, which served as a substrate for neutron reflection experiments, and from a

spectroscopy crystal. At $\text{pH} < \text{p}K_{\text{B}}$ of the free polymer chain, the polymer brushes are protonated and show an expanded structure, while at $\text{pH} > \text{p}K_{\text{B}}$ the chains collapse.

In their studies, Cheesman *et al.* investigated the influence of substrate curvature on polyelectrolyte brush growth.[159] Poly(2-(diethylamino)ethyl methacrylate) was polymerized from silica particles in the size range 120 – 840 nm, as well as silica wafers. The film thickness was determined by TGA and ellipsometry. The rate of surface-initiated polymer brush growth increased significantly with curvature for the particles with diameters below 450 nm. The increasing curvature of the substrate results in a larger distance between the active chain ends, which decreases the break-off rate.

Quaternary amines are also commonly used to create permanent charges in the polymer. For example, Wang *et al.* describe the synthesis of a cationic macroinitiator by functionalizing SiO_2 nanoparticles either with (3-aminopropyl)triethoxysilane (APTES), which is then reacted with BIBB, or directly with APTES-BIBB to obtain initiator-functionalized particles.[160] 2-(Dimethyl amino)ethyl methacrylate (DMAEMA) was then polymerized from the particle surface. Cationic functionalities were obtained by quaternization of the amine with 1-bromohexane under ambient conditions. Similar investigations are also known for iron oxide-based systems.[161,162]

Kirillova *et al.* investigated the aggregation and self-assembly behavior of hairy core-shell particles with different architectures consisting of a hard silica core and soft polymer brush shells.[163] Uniformly functionalized as well as Janus particles with different hemispheres, including hydrophilic positively charged poly((2-(dimethylamino)ethyl methacrylate) brushes and negatively charged poly(acrylic acid) brushes, as well as uncharged hydrophilic polymers and hydrophobic polymers were synthesized via SI ARGET ATRP or grafting-to process. CuBr_2 and TPMA catalyst complexes in a DMF solution were used in the ATRP process. Sn(II) 2-ethylhexanoate was used as a reducing reagent. Polymerization was carried out at 70 °C for 120 minutes. Layer thicknesses between 8 and 15 nm were obtained for different particle architectures.

One of the first reports on the polymerization of anionic methacrylate-based monomers dates to 2004. Here, Masci *et al.* described the surface-initiated polymerization of potassium 3-sulfopropyl methacrylate, as well as the preparation of the amphiphilic block copolymer with methyl methacrylate by means of ATRP at 20 °C.[164] Again, 2,2'-Bipy was used as a ligand for the catalyst complex. While a high polydispersity was observed in pure water, a DMF-water mixture and an excess of CuBr_2 allowed good control and gave polydispersities in the range of 1.15 - 1.25.

Introduction and Theoretical Background

A few years later, Wan *et al.* described the grafting of poly(3-sulfopropyl methacrylate) brushes from patterned Sylgard-184 silicone elastomer negative imprints and resorcinol formaldehyde positive imprints of natural trifolium using ATRP.[165] For this purpose, a monolayer of 3-(trichlorosilyl)propyl-2-bromo-2-methylpropanoate was immobilized on the surface as an initiator and a catalyst complex of CuBr and 2,2'-Bipy was used. The polymerization was carried out at room temperature in a water-methanol-mixture (2:1). The obtained materials showed that both the structure and the chemical composition of the surface adjusted by the polymer brush modification improved the anti-algae fouling and foul release.

Lattuada and Hatton described both the polymerization of an ionic monomer and the polymerization of non-ionic precursors, which are subsequently converted into ionic components.[166] For this purpose, they use HMTETA and CuBr as a metal complex. Hereby, the ionic 4-styrenesulfonic acid sodium salt was directly polymerized. Further, hydroxyethyl methacrylate (HEMA), as well as trimethylsilyl acrylates and trimethylsilyl methacrylates were polymerized as nonionic precursors. Poly(HEMA) was converted into a carboxylate by ring opening of succinic anhydride. Trimethylsilyl acrylates and trimethylsilyl methacrylates were converted into the anionic methacrylate by deprotection.

In addition to methacrylate-based systems, there are mainly reports on the polymerization of styrene sulfonate. Multiple literature reports exist varying in the used substrates, such as SBA-15 molecular sieve (SiO₂), halloysite nanotubes or poly(glycidyl methacrylate) microspheres and the used catalyst complex.[167–169]

Foster *et al.* undertook major efforts to optimize the ARGET surface initiated ATRP process for poly(styrene sulfonate).[170] For this purpose, 11-(trichlorosilyl) undecyl 2-bromo-2-methylpropanoate was immobilized on titanium substrates. Styrene sulfonate was polymerized from the surface in a reverse ATRP setup using vitamin C as reducing agent and CuBr₂/2,2'-Bipy as catalyst complex. A solvent mixture of methanol and water (1:2) was used. The parameters (A) reaction time of initiator immobilization, (B) polymerization time, (C) CuBr₂ concentration, and (D) vitamin C concentration were optimized in a 2⁴-factorial design approach. The results can be summarized as follows: No chemical, structural, or morphological changes were observed in the polymer films with longer reaction times for immobilization. Minimal reaction times (< 24 h) should be used for ATRP, as film quality may suffer with longer reaction times due to corrosion of the titanium substrates. Furthermore, minimal CuBr₂ concentrations (< 0.5 mg/nm²) and excess vitamin C are optimal. Overall, the reaction conditions are consistent with those of ARGET ATRP in solution. The authors also observed two-way interactions between (A)(C) and (B)(D), although these correlations are not robust because interpretation of the results and the regression model is somewhat problematic, according to the authors.

In contrast to cationic systems, the subsequent introduction of anionic groups is less common. Nevertheless, some approaches to this are described. One possibility already discussed in the framework of Lattuada's systems is the incorporation of protected carboxylates, such as trimethylsilyl acrylates and trimethylsilyl methacrylates, which are subsequently deprotected, or the introduction of a nucleophile species such as amines or alcohols which can be used to ring-open cyclic systems such as succinic anhydride to create the anionic functionality.[166] Conversely, Bondar *et al.* describe the opening of the epoxide group of previously polymerized poly(glycidyl methacrylate) with sodium hydrogen sulfite.[171] So far, this strategy has not been described for nanocomposites. Another strategy for introducing polymeric groups after polymerization is the sulfonation of styrene.[172–175] However, often the efficiencies are quite low or require harsh conditions, which is why the reactions are rarely used for composites production.

Over the last few years, great efforts have been put into the investigation of organic-inorganic nanocomposites. In addition to free radical polymerization, which has already been well studied, a number of controlled polymerization techniques have come to the forefront. In particular, ATRP plays an important role, for which a wide range of polymerizable monomers and suitable reaction media have been developed by optimizing the polymerization conditions. ATRP is a particularly potent synthesis route for surface initiated polymerizations. Similar to ATRP polymerization in solution, solvent mixtures of water and alcohols, as well as DMF, have proven to be particularly suitable for the controlled conversion of ionic monomers. In addition, small additions of CuCl_2 have been shown to increase the controllability of the reaction. Both HMTETA and 2,2'-Bipy were successfully used as ligands in the SI ATRP of ionic systems. The ability to synthesize ionic systems has now opened up areas of application that were not originally possible using ATRP-based composites. In the following section, the fillers used in the nanocomposites and their functionalization will be discussed in more detail.

1.3. Inorganic Fillers for Incorporation into Organic Matrices

The applications of nanomaterials are numerous and heterogeneous. As a result, a comprehensive market analysis of nanomaterials is a challenge. In a study by *Risk & Policy*, it is assumed that between 500 and 2000 different nanomaterials exist on the market.[176–178] These studies date back several years and today the quantities are certainly significantly higher. By far the largest share is represented by carbon-based systems, especially carbon black ($\approx 85\%$).[176] The main applications here are mostly based on the physical properties of the starting material. In the automotive industry in particular, carbon black is used as a reinforcing filler. Other applications include the use as a black pigment, as an antistatic additive and UV absorber.[179] A second important group of nanomaterials are metal oxide particles. Semimetal and metal oxide nanoparticles have been used for decades, not only in research,

but also in various industries, where they are produced annually on a kiloton scale and used in a wide variety of products. Furthermore, they are often physiologically compatible and are therefore frequently used in the medical field.[180–183] The most important representatives and their applications are described in more detail below.

Silicon dioxide is the second most widely used nanomaterial, accounting for approx. 12 % of the total. The pertinent crystalline forms are α -quartz ($P3_121$), β -quartz ($P3_221$), α -cristobalite ($P4_12_12$), β -cristobalite ($Fd\bar{3}m$), Tridymite (β , α , OS, OP, MC, MX), coesite ($C2/c$) and stishovite ($P4_2/mnm$), where α -quartz represents the stable phase at normal temperature and pressure.[184] Crystalline SiO_2 accounts only for a relatively small proportion of technical applications. In contrast to crystalline SiO_2 , amorphous SiO_2 has a greater tolerance towards impurities. The main applications are in the field of color pigments in paints and toners, cosmetics and foods.[185–188] Silica nanoparticles are of great interest for applications such as catalysis, pharmaceuticals and drug delivery.[189] They are also used to fabricate electronic substrates, thin film substrates, electrical and thermal insulators, as well as moisture sensors [190]. Further they serve as fillers to reinforce composites [190] or concrete [191].

Titanium dioxide is a polymorphic oxide that occurs in three crystalline modifications (rutile, anatase and brookite). The titanium atom is octahedrally coordinated in all modifications and the oxygen is surrounded by three titanium atoms in each case. The modifications differ in the number of edge linkages. Anatase and rutile crystallize in the tetragonal space group $I4_1/amd$ and $P4_2/mnm$, respectively, while brookite crystallizes in the orthorhombic space group $Pbca$. In technical application are mainly anatase and rutile. Again, one of the main applications is the use as a white pigment.[192,193] Rutile is also used in sunscreens due to its ability to absorb UV radiation.[194–196] TiO_2 is further used due to its photocatalytic ability for example in photoactive cement, which is able to bind NO and NO_2 or in photovoltaic cells.[197–200] In addition, TiO_2 -based materials are often employed in self-cleaning materials.[201] The self-cleaning is achieved with its photo-induced superhydrophilicity. Further, it is commonly used as an antimicrobial substance and similar to SiO_2 for mechanical strengthening of a variety of materials.[201]

Iron oxides are also indispensable in many areas today. In the following chapters, iron oxide nanoparticles and the possibilities of their surface functionalization will be discussed in more detail, as they are primarily used in this work.

1.3.1. Iron Oxide Nanoparticles

Iron oxides are another metal oxide of growing research interest. The most common oxidation states of iron are +1, +2, and +3. Fe_2O is an unstable compound that forms under high pressure and is therefore of little importance.[202] Much more important are the oxides wüstite (FeO),

maghemite (Fe_2O_3), and the mixed oxide magnetite (Fe_3O_4). The incorporation of iron oxide into a material offers another distinct advantage in addition to improving the mechanical and thermal properties. The nanoparticles induce magnetism into the material. While bulk wüstite exhibits antiferromagnetic properties [203], magnetite and maghemite are ferrimagnetic in bulk.[204–206] Both states are cooperative magnetic phenomena. Antiferromagnetic materials consist of two magnetic sublattices. In both sublattices, the magnetic moments of the atoms are ferromagnetically coupled and thus aligned in parallel. Due to the antiparallel ordering of the sublattices, no net magnetization is observed. In the case of ferrimagnetism, the magnetic moments of the sublattices are different and do not completely cancel each other out, resulting in a permanent magnetization. The magnetic properties change during the transition from bulk to nanomaterial. Magnetic nanoparticles are divided into multi and single domain particles. The term domain describes individual areas in the material in which the spins are arranged collinearly. The domains are separated from each other by domain walls. Whether a domain wall is formed depends on the magnetostatic energy and the domain wall energy. If the cost of the magnetostatic energy is greater than the domain wall energy, a new domain wall is nucleated. The domain wall energy is dependent on the inter-domain areas, whereas the magnetostatic energy is proportional to the particle volume. As a result of that if the particle volume is decreased under a certain threshold, the so called single-domain size threshold, the magnetostatic energy cost falls below the domain wall energy, making single domain particles more favorable.[207] In addition to the size, the magnetic properties also depend on the morphology of the particles, their composition, and their surface functionalization.[208–213] As an example, the formation of a single-domain structure for Fe_3O_4 in cubic morphology occurs only below a size of 76 nm [214], but for spherical Fe_3O_4 nanoparticles already from a diameter of 128 nm.[215] Superparamagnetism represents the lower limit for these single-domain particles. In superparamagnetic materials the balance between thermal fluctuation and magnetic anisotropy determines the dynamics. The magnetic properties are therefore strongly dependent on the temperature. In the case of superparamagnetic particles, the anisotropy energy is in the range of the thermal energy. This leads to random flipping of the spins around the anisotropy axis, which is referred to as Néel relaxation. The temperature at which this transition takes place is called blocking temperature. The frequency with which the relaxations take place is defined by its energy barrier, which in turn is proportional to the particle volume. Therefore, there is a critical particle volume, below which the blocking temperature is below room temperature, and a superparamagnetic material is obtained. For iron oxide nanoparticles this is in the range of 20 – 25 nm.[216]

Superparamagnetic materials exhibit properties of both paramagnetic and ferromagnetic materials: Like paramagnetic materials they do not have a permanent arrangement of the dipoles. But since the magnetic moments in a single particle are already pre-oriented as a

group with a much larger net moment, superparamagnetic materials exhibit a significantly higher magnetic susceptibility, similar to ferromagnetic materials. With a permanent magnetization particles tend to agglomerate due to the magnetic interaction.[217] Therefore, another advantage of superparamagnetism is that the risk of agglomeration of the particles is lower, though of course agglomeration due to van der Waals interactions are still commonly observed.[218] Since good dispersibility of the particles is often a prerequisite for application, superparamagnetic nanoparticles are often times preferred despite their weaker magnetizability.[219] The introduction of magnetic properties potentially offers the opportunity for spatially resolved introduction of heat with an alternating magnetic field (AMF), to which the nanoparticles respond with a physical particle rotation (Brownian relaxation) and/or an internal dipole inversion (Néel relaxation). Which relaxation mechanism is preferred is dependent on particle size, magneto crystalline anisotropy and matrix viscosity.[220] Both mechanisms are associated with an increase in temperature, which can be used as a trigger for other processes. The heating efficiency is described by the specific loss power (SLP), which is defined as electromagnetic power lost per mass of magnetic material and carries the unit watts per kilogram. Alternatively, the specific absorption rate (SAR) is used, which is derived from the slopes of heating curves (see Equation (1)).

$$\text{SAR} = \frac{C_s m_s}{m} \frac{dT}{dt} \quad (1)$$

C_s = Specific heat capacity of the solvent

$m_s = V_s \cdot \rho_s$ = Sample mass

m = Mass of magnetic material

dT/dt = Slope of the heating curve

Due to the dependence of SAR on the strength and frequency of the alternating magnetic field, it is difficult to directly compare SAR values between different test setups. Typically for iron oxide particles in the 10 nm size range, SAR values are in the range of 10-90 W/g, although values up to several hundred have been reported for specific functionalizations, field strengths, and frequencies.[221] Further, this experimental dependence makes it difficult to exactly evaluate the exact influence of parameters such as particle size, anisotropy, composition and crystallinity on SAR. Nevertheless, the following trends can be identified: Generally if the size of the particles is reduced, the total magnetic moment decreases and therefore often the heating efficiency decreases.[222,223] It should be noted that, in contrast to that, some studies suggest that there is an ideal particle size for a maximum SAR after which a further increase will decrease the SAR again.[210,224] This value depends on the material and the properties of the magnetic field. The heating efficiency also depends on the morphology of the particles.

With an increase in the anisotropy of the particles, the magnetic anisotropy increases, which generally increases the SLP.[225–227] Furthermore, it was shown that an improvement of the SLP or SAR can be achieved with the transition from Fe_3O_4 to the mixed oxides MnFe_2O_4 , CoFe_2O_4 and ZnFe_2O_4 or core-shell systems.[228,229] In addition, an increase in crystallinity increases the SAR.[230]

Because of the unique properties and the resulting applications, especially the magnetic field induced heating, iron oxide particles were chosen as the nanofiller in this work. In addition, the particles allow magnetic decantation, which facilitates easy clean up procedure for the functionalized particles. In the following chapter, the possible synthesis routes of the iron oxide particles will be described in more detail.

1.3.2. Synthesis Routes for Iron Oxide Nanoparticles

A large number of synthesis routes are available for the synthesis of iron oxide particles. With a few exceptions, such as synthesis by ball milling[231], synthesis is carried out using the bottom-up approach. The most important methods will be briefly explained below.

Co-precipitation: Co-precipitation is certainly the synthetically simplest method. Here, the iron(II)/iron(III) salts, mostly as chlorides or nitrates, are added together in an alkaline medium. The synthesis takes place either at room temperature or under gentle heating. Besides the simple set-up, this synthesis also convinces with its high yields. However, the reaction requires good control of the pH and inhomogeneous sizes and shapes are often obtained. Furthermore, poor crystallinity and many times agglomerates are often observed due to lack of stabilization.[232–235]

Hydrothermal reaction: In hydrothermal synthesis, the metal oxides are produced above the boiling point of the solvent and at pressures exceeding 1 bar.[236] The increased temperature and pressure often lead to highly crystalline particles with a high surface activity.[237–239] Here, too, iron chlorides or nitrates are used, but also alkoxides or acetates. Synthesis takes place in two steps. First, the starting compounds are hydrolyzed, followed by condensation. The hydrothermal process allows precise control of the nucleation and growth rate by the reaction conditions (e.g. pH). Thus a precise adjustment of the particle size and morphology is possible. However, the synthesis is usually coupled with long reaction times.[237]

Sol-gel reaction: The sol-gel process, originally developed for SiO_2 -based inorganic ceramics and glass materials, was quickly transferred to a variety of colloidal metal oxides.[240,241] The process consists of the steps hydrolysis and condensation of metal alkoxides or salt precursors. In this, first colloidal solutions, so called sols are formed followed by the formation of solvent swollen integrated networks, which are called gels. These gels can be nanoparticles or three-dimensional polymer networks.[242] Precise control of the size and structure of the

particles is possible through precise adjustment of the reaction conditions. The disadvantages include sometimes long reaction times and often high costs of the metal alkoxides.

Micro emulsions: The use of microemulsion technology allows the most precise control of particle size. The reaction principle in microemulsions is that of co-precipitation. It differs only in the reaction medium used. It consists of an aqueous phase emulsified in an organic phase. Surfactants are added for stabilization of the micro droplets. The water-soluble precursors are in the water phase. Precipitation is initiated by the addition of a base. Due to the well-defined shape and volume of the micelles, as well as the concentration of the precursors, precise control of the particle size is possible.[243–245] The major disadvantages are the low yields, the large quantities of solvent required and the time required due to more extensive work up.

Thermal decomposition: Thermal decomposition is another solution-based synthesis option. Due to the good control of size and morphology, combined with high yields, this synthesis route is a popular method of choice and was also used in this work. This synthesis route relies on the pyrolysis of organometallic precursors, such as carboxylates, carbonyls or most commonly iron acetylacetonate ($\text{Fe}(\text{acac})_3$).[246–249] Usually, the reactions are carried out in the temperature range of 200 – 300 °C, which limits the solvent selection. These include benzyl ethers, phenyl ethers and longer-chain hydrocarbons such as octadecene. As a result of the high temperatures, highly crystalline iron oxide particles are obtained. In the core these mostly show the magnetite structure, while the degree of oxidation increases towards the surface and a transition towards maghemite is observed.[208,250] The reaction is usually carried out in two temperature steps in order to better control nucleation and growth and thus obtain narrow particle distributions. For the heat up methods it was suggested that in a first step initially a decomposition of precursors takes place forming poly iron oxo clusters. These serve as building blocks for the nucleation and growth of the particles.[251,252] As a result of this finding, particle preparation has also been carried out in two steps.[210] As already described by LaMer, the key to narrow particle distributions is a burst-like nucleation, whereby nucleation can be separated from particle growth.[253] One approach to this is hot injection methods, in which the precursor is added to the already hot solution, thereby obtaining a high supersaturation.[254,255] Another promising approach is the continuous addition of a precursor that allows selective control of particle size, which the authors describe as "*extended LaMer mechanism*".[210] Another possibility for an almost instantaneous temperature increase is the use of induction heating of steel balls, which are placed in the reaction medium.[256] Usually, in thermal decomposition methods capping agents are added at the beginning of the reaction. While they ensure the dispersibility of the particles in selected solvents and thus prevent agglomeration, they also have a major influence on the control of size and shape for example by preferential binding to certain crystal facets. Sometimes the ligands also function

as reducing agents and are therefore required for a successful synthesis.[257] Further the choice influences the possibility for post-synthetic functionalization. The most commonly used combination consists of oleic acid and oleyl amine.[258] Oleic acid and oleyl amine are both hard Lewis bases, which can both form complexes with the metal ions and bind to the particle surface. However, Klokkenburg *et al.* reported that oleic acid has a greater affinity towards the iron oxide surface and the amine only facilitates this bonding through deprotonation of the carboxylic acid group.[259,260] Later, Sun *et al.* developed a synthesis in which very monodisperse nanoparticles could be obtained by adding 1,6-hexanediol.[261] Qiao *et al.* have carried out an extensive study of the influences of the individual components. It was shown that, in addition to the concentration ratios of oleyl amine, oleic acid and the type and amount of diol used, the selected solvent, which is partially oxidized at the high temperatures, also has an influence on the size and morphology of the particles.[209] Since carboxylates and amines bind to the particle surface via coordinative or ionic interactions, subsequent exchange for other ligands is possible, which opens up a multitude of possible particle properties.[262]

1.3.3. Functionalization of Iron Oxide Nanoparticles

In the following, the functionalization process and the functionalization reagents used will be described in more detail. The focus will again be on iron oxide particles, although literature on other metal oxides has also been taken into account in some cases, in order to describe the binding modes of certain ligands. In principle, these can be transferred well to the iron oxide particles, but it should be considered that slight deviations are possible due to the deviating metal centers.

The functionalization of nanoparticles has played a central role since the beginning of the investigation of nanomaterials. The fundamental tendency to agglomeration due to the high surface energy is one of the central challenges in dealing with nanomaterials, which can be bridged by suitable functionalization.[263] The concept of stabilization by functionalization was first described by Schmidt in the context of the synthesis of SiO₂ nanoparticles via a sol-gel approach.[264] There are two possibilities to counterbalance the attractive van der Waals forces: steric stabilization and electrostatic stabilization. In the first case, a steric barrier is created by attaching sterically demanding ligands to the particle surface, which prevents the particles from approaching each other. In the second case, kinetic stabilization is achieved by introducing charges to the particle surface. This can be achieved by pH adjustment or by attaching permanently charged molecules. The introduction of charges leads to Coulomb repulsion between the equally charged particles and thus to stabilization. The stabilization can be estimated well by means of DLVO theory.[265] Since electrostatic stabilization plays a central role in the following investigations, it will be discussed again in more detail in chapter 1.4.

Introduction and Theoretical Background

In addition to reducing the tendency to agglomeration, functionalization is often accompanied by a reduction in reactivity towards other chemical reactions. For example, the oxidation sensitivity can be reduced.[266] Further, functionalization can improve compatibility with the surrounding medium, resulting not only in improved stabilization in solution, but also in improved distribution of the particles in a polymer matrix to form a composite material.[267] Furthermore, new particle properties can be generated by functionalization. Due to the large number of functional groups available, almost any particle property can be generated. In order not to go beyond the scope of this work, only the application of initiator functionalities for polymerization and the adjustment of the polarity by ionic groups are mentioned here, since these are of particular relevance for the following investigations.[168,169,268–270] Figure 5 shows the basic structure of the functionalization reagents.

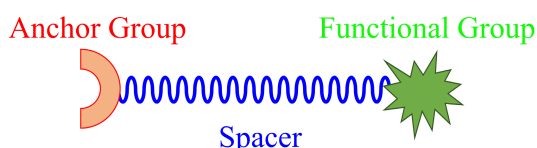


Figure 5: Structure of functionalization reagents.

While the functional group has a major influence on the particle properties, the spacer primarily serves to increase the steric demand of the ligands and thus to stabilize the particles. To a lesser extent, however, the polarity of the particles or the reactivity of the functional groups can also be influenced by the choice of the spacer. Since the functional groups are often used as reaction centers, the space available there plays a major role. Thus, lengthening the spacer by a few atoms can significantly influence the reaction rate and efficiency.[271]

The anchor groups in particular play a central role with regard to the stability of the functionalization. The following section will therefore describe the available anchor groups in more detail. These include carboxylic acids, amines, sulfonic acids, cysteines, dopamines, alkoxy/chlorosilanes and phosphonic acids.[272–274] The individual possibilities will be discussed in more detail below.

Carboxylic acids: Carboxylates are one of the most frequently used functionalization reagents. As described above, especially oleic acid, is added for stabilization during synthesis. Carboxylates are particularly popular because they can be exchanged easily and almost completely under mild conditions.[275] The reason for this is the rather weak interactions. Four bonding modes can be observed: electrostatic, monodentate, and bridging or chelating bidentate. The strength of the interaction can be assessed by the wavenumber separation of the symmetric and asymmetric COO^- IR vibrations.[262,276,277] Here, the monodentate binding exhibits the largest separation. For the other binding mechanisms, smaller separations

(<180 cm⁻¹) are observed. A precise assignment of the vibrations is often difficult here, since even the relative order of the binding modes is inconsistent in literature reports.[278,279]

Amines: While amines are a popular functionalization for metal particles, they play only a minor role in the case of metal oxides, often serving only as reducing agents that further facilitate the binding of other functionalization reagents.[260] Amines can bind to the surface either via hydrogen bonding or electrostatic interactions, though accurate identification is difficult, especially in the presence of adsorbed water.[262]

Sulfonic acids: Rarely, poly sulfonates are also added directly during particle synthesis for stabilization.[280] Again, the binding mode can be identified by IR spectroscopy. A distinction is made between inner-sphere and outer-sphere complexes. While in the former the asymmetric S-O stretching vibration splits into two or three signals for monodentate and bidentate coordination, respectively, due to the reduction in symmetry, the signal for the outer-sphere complexes is shifted to higher wavenumbers compared to free sulfonate groups. Electrostatic interactions are also described.[262] Due to the stronger interactions with the metal oxide surface, carboxylic acids are preferred when a refunctionalization is intended.

Cysteines/dopamines: Cysteines and dopamines are both used particularly in the biomedical field. Both groups are biocompatible and outperform other functionalization reagents such as carboxylates due to more stable binding. For the dopamine derivatives the improved orbital overlap (sigma- and π -donor bonding) results in a five membered ring.[281,282] Therefore a complete exchange is possible.[275] In the case of cysteine, bidentate linkage occurs through the thiol and carboxylate groups, which under certain circumstances may also lead to reductive dissolution of the particle surface.[283,284] Oxidation of the thiol groups can lead to the formation of disulfide crosslinked ligands, resulting in stable functionalized particles.[285]

Alkoxy-/chlorosilanes: One of the most frequently used functionalization reagents are alkoxy- and chlorosilanes. Bonding is achieved by the reaction of hydroxy groups on the particle surface with the alkoxy/chlorosilane groups. This leads to the formation of stable Fe-O-Si bonds with elimination of water or hydrochloric acid.[286] In addition to mono-, di- and tridentate bonds, crosslinking events lead to the formation of interconnected silica layers and poly condensed disordered layers on the surface, resulting in core shell systems.[287,288] However, during the crosslinking, the irreversible formation of aggregates can often be observed. To avoid this, mono alkoxy silanes are often used for functionalization. In addition, the by-products (dimers) formed by homo condensation can also be readily separated in solution.[289]

Phosphonic acids: Phosphonic acids are used as coupling agents due to their affinity towards a vast variety of surfaces, such as metal- / transition metal- oxides, hydroxides, carbonates

and phosphates.[290] Less frequently, phosphates are also used for functionalization. However, phosphates show lower hydrolytic and thermal stability due to the more labile P-O-C bond, which is why they will not be discussed further here.[291] The M-O-P bond formed during the attachment of the phosphonic acid is known for its tremendous stability. Thus, it is often not possible to achieve a detachment of the phosphonate group by increasing the temperature. Only the decomposition of the attached organic group occurs.[269,271] Further, the bond is generally described as pH stable. Compared to silanes, phosphonates form monolayers, since they do not show a tendency to intermolecular reaction and therefore do not form networks. Nevertheless, the binding mechanisms are diverse and have been the subject of many investigations.[126,290,292,293] Pujari *et al.* describe two routes for surface binding, which depend in particular on the Lewis acidity of the metal surface, but also on temperature, pH value, concentration and the solvent used.[293] In both cases, the bonding takes place via condensation processes. However, in the case of high Lewis acidic surfaces, initial coordination of phosphoryl oxygen occurs first, while in the case of less Lewis acidic surfaces, bonding is promoted by hydrogen bonding. This results in a variety of bonding modes: monodentate (a and b), bridging bidentate (c and d), bridging tridentate (e), chelating bidentate (f and g), chelating tridentate (h) and mechanisms with additional hydrogen bonding (i-l). These are outlined in Figure 6.

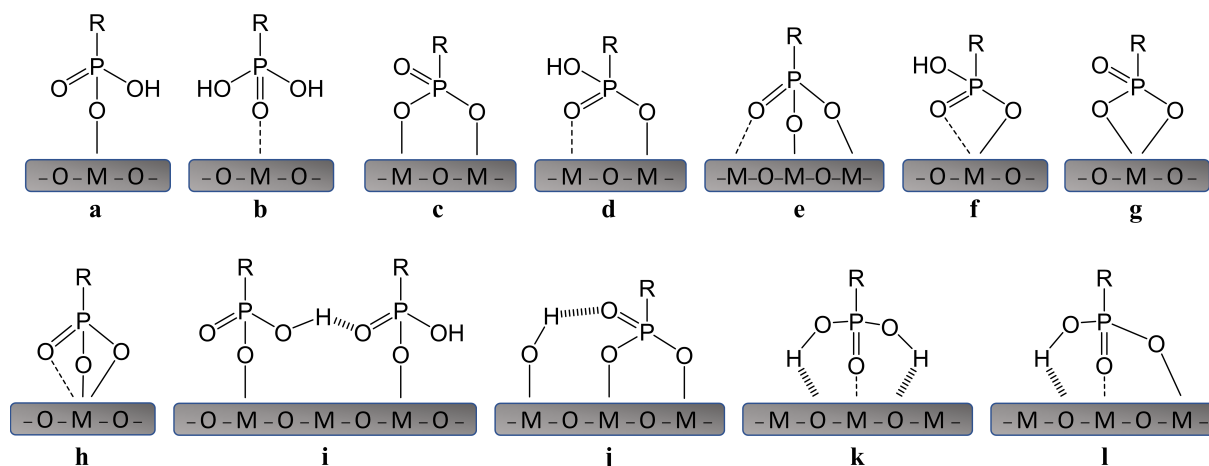


Figure 6: Bonding mechanisms of phosphonic acids. Adapted from [293] and [294].

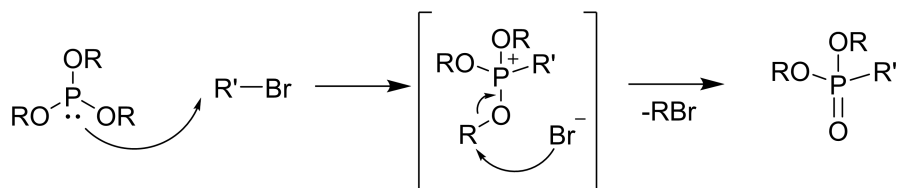
However, the determination of the binding modes is difficult. A simple disappearance of specific vibrational bands in IR, such as P-OH or P=O, does not allow a differentiation between a bonding to the surface or formation of hydrogen bonds. Also, the shift in ^{31}P NMR is often times not conclusive. It has been shown, that solid state NMR of ^{17}O can be utilized to determine the binding modes.[294] Due to the interactions of the alkyl chains, ordering occurs on the surface. As a result, high packing densities can be achieved.[295–297] Calculations based on the space requirement of the phosphate/phosphonate group a value of 4.16 molecules/nm² was determined for a maximally densely packed monolayer.[271,297,298]

Davis *et al.* have investigated the exchange of radiolabeled oleic acid for phosphonic acid derivatives and have shown that this exchange is almost complete under ambient conditions.[275] Furthermore, it has been shown that both metal and metal oxide surfaces are stabilized by functionalization with phosphonic acid and thus, for example, can be protected from oxidation.[266,299,300]

Another advantage is the synthetic accessibility of phosphonic acid derivatives. The most important synthetic routes for phosphonic acids are the Michaelis-Arbusow reaction, the Michaelis-Becker reaction, and radical additions to olefins, which are shown in Scheme 5 to Scheme 7.

The Michaelis-Arbusow reaction was originally discovered by Michaelis and further developed by Arbusow.[301,302] Here, alkyl or aryl halides are reacted under reflux, usually with alkyl phosphites, to form the corresponding phosphonic acid ester. The reaction proceeds via an S_N2 mechanism with formation of the positively charged phosphonium ion. The advantage of the reaction lies in the simplicity of execution and the high yields.

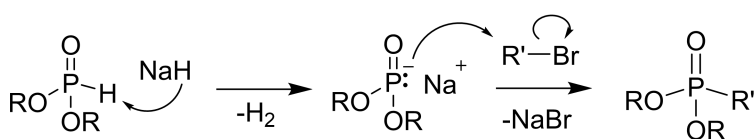
Michaelis-Arbusow Reaction:



R = alkyl
R' = alkyl, aryl

Scheme 5: Reaction mechanism of the Michaelis-Arbusow reaction.

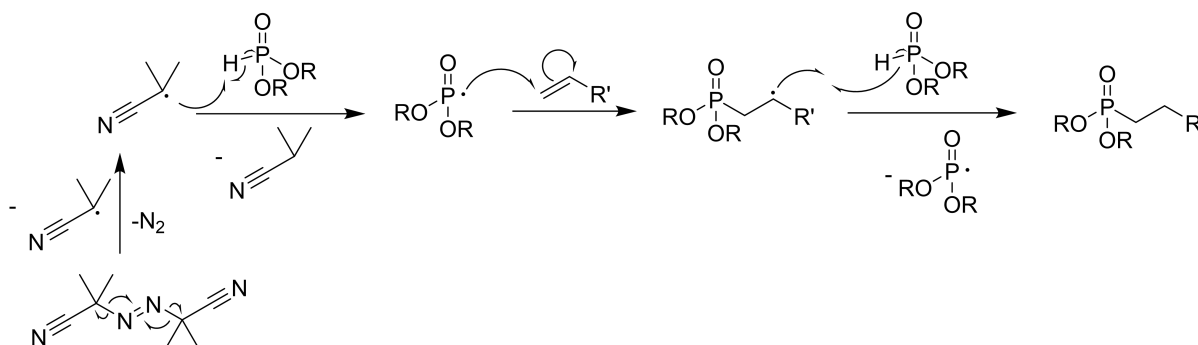
An alternative to the Michaelis-Arbusow reaction is the Michaelis-Becker reaction. The reaction proceeds in two steps. First, the hydrogen phosphonate is deprotonated by means of a base. Then, analogous to the Arbusow variant, a nucleophilic substitution on a haloalkane takes place. While this method often results in lower yields than the Michaelis-Arbusow method, it allows to work at lower temperatures, which is why this synthesis route is used for more sensitive substances.[303]

Michaelis-Becker Reaction:

R = alkyl
R' = alkyl, aryl

Scheme 6: Reaction mechanism of the Michaelis-Becker reaction.

Radical addition to double bonds is used less frequently. In most cases, AIBN is used as the radical initiator. Although the addition of hydrogen phosphonic acid to carbon double bonds is also described in the literature, hydrogen phosphonates are also frequently utilized here, whereby the corresponding phosphonic acid esters are obtained. [304–306]

Radical Addition to Olefins:

Scheme 7: Reaction mechanism of the radical addition to olefins.

Since the acid hydrolysis of phosphonic esters often requires high temperatures, their hydrolysis is usually carried out via the silyl ester.[293,307] Due to their enormous stability and accessibility, phosphonic acids were used as coupling reagents in this work.

1.4. Introduction of Charges to Metal Oxide Nanoparticle Surfaces

The generation of charges on particle surfaces is a much-studied topic. The reason for the interest in nanoionics is both due to the fundamental, as well as technological importance. A key application is that the particles can be stabilized by the surface charge in polar media.[308] This enables application in the biomedical sector, where compatibility under physiological and thus aqueous conditions is a prerequisite.[270,309] Furthermore, compatibility with polar polymer matrices is ensured by ionic functionalization. This not only often times results in a mechanically more stable material, but also self-healing and shape memory could be induced by the electrostatic interactions.[310] Another application is electrostatically driven self-assembly. The design of functional nanoobjects, so-called supramolecular structures, through electrostatic interactions is a rapidly advancing field.[311–313] Applications include the synthesis of isolated nanostructures, but also layered or patterned structures.[314] The

structures are built up by layer-by-layer deposition (LbL). The layer-by-layer technique refers to the successive deposition of oppositely charged polyelectrolytes on charged substrates. This technique for the flexible production of thin layers was first described by Iler in 1966.[315] The particles are either applied as building blocks or as pre-oriented multilayers. The properties that can be generated from the structure include antireflecting, antifogging, and self-cleaning properties.[316–318] Depending on the application, stable or switchable charges are preferred. In the following, the possibilities for the generation of charges on nanoparticle surfaces will be explained in more detail.

1.4.1. Generation of Surface Charges by pH Adjustment

A commonly used method for generating surface charges is to exploit the pH dependence of the surface chemistry of metal oxide particles. Metal oxide particles form a monolayer of surface hydroxyl groups in aqueous dispersions. These can be protonated or deprotonated. Due to this acid-base property (amphiphilicity), the surface charge, both in its sign and magnitude, is dependent on the pH of the surrounding medium.[319,320] The pH value at which the surface charge drops to zero is called the point of zero charge (PZC, better pH_{PZC}). This can be determined by potentiometric titration and is largely dependent on the metal cation of the particle. The properties that play a particular role here are electronegativity, charge and ionic radius of the metal, but to a lesser extent also those of oxygen.[321] The surface charge is negative at $\text{pH} > \text{pH}_{\text{PZC}}$ and positive at $\text{pH} < \text{pH}_{\text{PZC}}$ (see Figure 7). Therefore, pH values in the range of the pH_{PZC} should be avoided to obtain electrostatic stabilization.

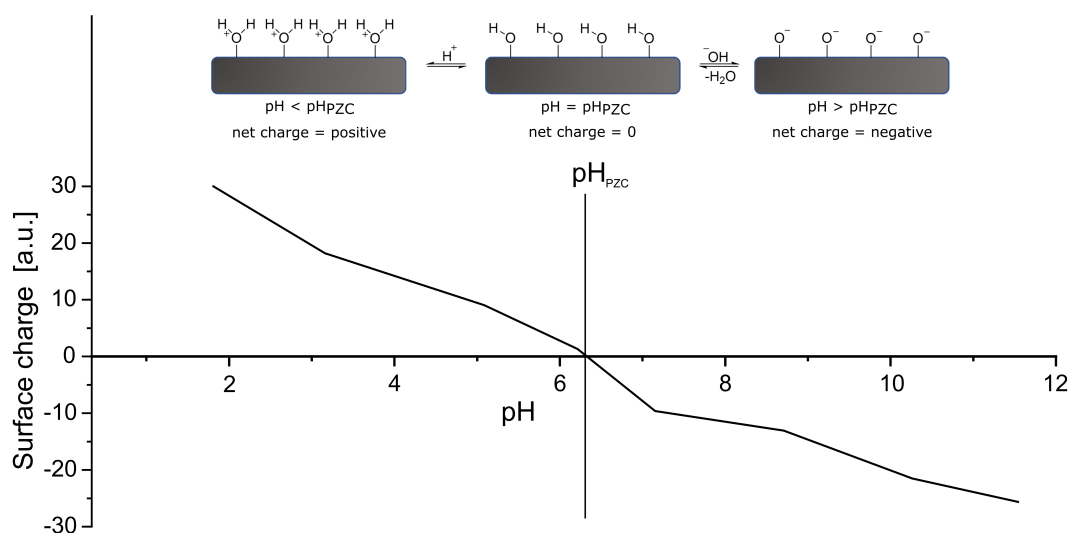


Figure 7: Schematic representation of the protonation/deprotonation process on metal oxide surfaces and its influence on the surface charge.

A more detailed investigation was carried out by Clavier *et al.*[322] They investigate the surface charging behavior of nanoparticles based on a simple coulomb model using Monte Carlo simulations. They considered how the change in pH affects the charging behavior including

parameters like site distribution and density as well as the dielectric constant. It was shown that the site distribution is playing a major role and that a homogeneous distribution leads to the most efficient ionization degrees. With the decrease of the surface site density, deprotonation processes become easier due to less repulsion thus shifting the titration curves towards an isolated monomer situation. The acid base properties also have an influence, especially if two deprotonation steps are possible. If the negative logarithms of the acid dissociation constants (pK_A) are too close to each other ($\Delta pK_A < 2$), no pH_{PZC} is obtained, but a value is obtained at which the net charge is zero. This so-called isoelectric point is of high significance for the characterization of ionic functionalization of nanoparticles and is therefore described in more detail in section 1.4.2. However, it should already be emphasized here that the point of zero charge and the isoelectric point are not equivalent, and the methods for determining them are quite different. The dielectric constant has been identified as another factor influencing charging behavior. For particles with low dielectric constant like hematite ($\epsilon_c = 12$) sites are less electrostatically screened and therefore coulomb repulsion is higher. This results in a lower deprotonation efficiency even at strong alkaline pH values compared to materials with higher dielectric constants such as TiO_2 ($\epsilon_c = 130$).^[322] Even though the composition of the particles in combination with the pH of the surrounding medium have the main influence on the particle charge, other influencing factors are discussed in the literature. For example, Barisk *et al.* describe the influence of the particle size on the charge density.^[323] They use a multi-ion surface charge-regulation model, which includes protonation and deprotonation steps to calculate the local charge density, though still not considering Stern layer effects. It was observed that the surface charge density increases with an increase in the particle size and reaches a plateau when the particle size exceeds a critical value.

The studies show that metal oxide particles can be stabilized in the charged state by pH adjustment over long periods of time and can be used as dispersions for further conversion.^[324–327] However, the choice of the metal oxide already fundamentally determines the surrounding medium in order to stabilize the charges and there is little room for adjustment, which significantly limits the scope of application. Therefore, there is a tendency to generate surface charges by suitable functionalization, which allows a precise adjustment of the charges. The possibilities available for this are explained in more detail in the following chapter.

1.4.2. Generation of Surface Charges by Functionalization

The possibilities for introducing surface charges by functionalization are arbitrarily large. In addition to the bonding possibilities described in chapter 1.3.3, the entire range of organic functional groups and inorganic ions that adsorb to the surface are available. In this way, almost any application area can be served. The stability of the charge is determined by the

selection of the functional group. Acidic/alkaline groups are frequently used here, which can be present in the charged or uncharged state depending on external conditions. While the stability of the ionic group is crucial for some applications, for others it is precisely the change between charged and neutral states in response to a change in pH that makes the system suitable for use. Therefore, careful selection and tailoring of the functionalization reagents is indispensable. Here, too, the characterization of the charge state of the particles will be briefly discussed first.

While the pH_{PZC} is often still well suited for describing unfunctionalized particle surfaces, it has little relevance for ionically functionalized particles, since the hydroxyl groups may react differently or not at all to pH changes, due to covalent, electrostatic or hydrogen bonds. In addition, the charges introduced by functionalization have a strong influence on the total charge of the particles. In practice, therefore, the zeta potential is frequently used to evaluate the particle charge. In the following, the concept of zeta potential and its determination will be explained.

If a charged particle is in an electrolyte solution, an oppositely charged layer of ions is formed on the surface. This layer is in turn composed of two parts. The inner strongly bonded layer is called the Stern layer. With increasing distance from the surface, the attractive interaction decreases progressively. Due to the thermal movement of the ions in solution, a diffuse layer is formed. If the charged particle now moves, the surrounding ions within a certain boundary move with the particle, while the ions outside the boundary do not move. This results in a shear. The boundary at which this process occurs is called the slipping plane. The potential at this interface is called the zeta potential. For the determination of the zeta potential, there are several approaches and processes that can be investigated [328]:

- **Electrophoresis:** Electrophoresis is the movement of a charged particle relative to the surrounding medium under the influence of an electric field
- **Electroosmosis:** Electroosmosis is the movement of a liquid relative to a stationary charged surface
- **Sedimentation potential:** The sedimentation potential is the electric field generated when charged particles move relative to a stationary liquid
- **Streaming potential:** The streaming potential is the electric field generated when a suspension medium is forced to flow along a stationary charged surface by a pressure difference

All of them are electrokinetic methods. In the following, the electrophoresis method will be briefly explained in more detail since it is used in this work. By applying an electric field, the suspended charged particles are accelerated to the oppositely charged electrode. This

movement is counteracted by friction/viscous forces. After equilibrium is reached, the particles move at a constant speed (electrophoretic mobility). This is dependent on the strength of the electric field, the dielectric constant and the viscosity of the surrounding medium, as well as the zeta potential. Therefore it can be converted into the zeta potential via the Henry equation.[329]

$$U_E = \frac{2\varepsilon\zeta f(\kappa\alpha)}{3\eta} \quad (2)$$

$$\Leftrightarrow \zeta = \frac{2\varepsilon f(\kappa\alpha)}{3\eta U_E} \quad (3)$$

U_E = Electrophoretic mobility

ε = Dielectric constant

ζ = Zeta Potential

η = Solvent viscosity

$f(\kappa\alpha)$ = Henry's function

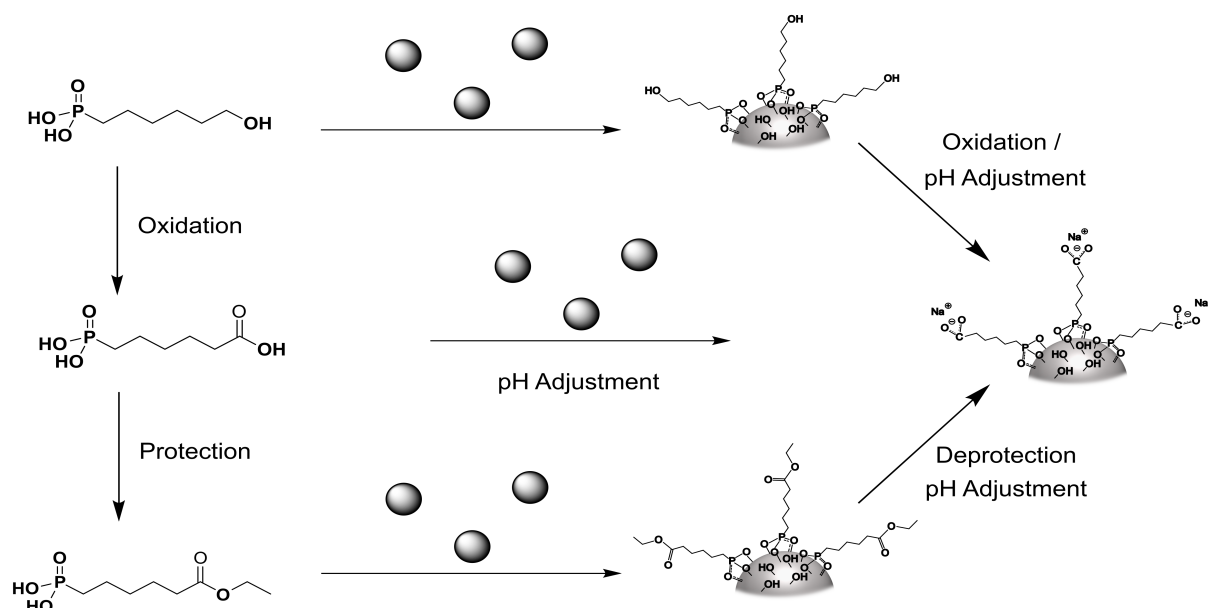
Electrophoretic light scattering is commonly used as an analytical technique for determining electrophoretic mobility. Most commonly used are the laser Doppler velocimetry, phase analysis light scattering (PALS) techniques or combinations of those.[328] A detailed explanation of these detection methods will not be given here, but reference should be made to the relevant literature.[330,331]

If a pH-dependent investigation of the zeta potential is now carried out, conclusions can be drawn about the stability of the particle dispersions. Analogous to the pH_{PZC} , the isoelectric point (IEP) is defined here. The IEP describes the point at which the velocity is zero for particles exposed to an external electric field, i.e., the zeta potential drops to zero. The net surface charge is negative at $pH > pH_{IEP}$ and positive at $pH < pH_{IEP}$. For naked particles, IEP and PZC mostly match ($\Delta(pK_{A1}-pK_{A2}) \geq 2$), while deviations can be expected in case of successful functionalization with adsorbed ions or ionic ligands. As discussed above, the stability of nanofluids is directly linked to their electrokinetic properties. Therefore, pH control can increase stability due to strong repulsive forces. Particles exhibiting a zeta potential between - 30 mV to + 30 mV tend to coagulate.[332] As a result investigations at various pH values for a fixed nanofluid lead to the observation that especially in the range of the IEP agglomeration is to be expected.[333,334]

The pK_A and pK_B values of the functional group in particular play a central role in the stability of the charge as a function of the pH value. For anionic functionalization, strong acids are used, which are present in the deprotonated, ionic form over a wide pH range. The most common representatives are carboxylates, organosulfates and sulfonates. Of this group, carboxylates have the highest pK_A values and are therefore protonated most rapidly. Depending on the neighboring groups, the pK_A values for aliphatic carbonic acids are in the range of 1 - 5. For carboxylic acids, a variety of synthesis methods exist. These include oxidation reactions of alcohols, aldehydes and ketones, or from Grignard compounds by reaction with CO_2 . [335–338] In practice, however, ω -bromo or hydroxy carboxylic acid derivatives are usually utilized, in which the anchor group is subsequently attached in the ω position, which is often possible under mild conditions. Nevertheless, protection of the carboxylic acid functionality is often necessary in these cases. [339,340] In comparison with carboxylic acids, sulfates and sulfonates are significantly more acidic. Even though pK_A values of up to 2.5 are described, these acids usually exhibit values in the negative range. [341–343] The organosulfates are usually prepared by esterification of lauryl alcohol with sulfuric acid, sulfurochloridic acid or sulfur trioxide and subsequent neutralization. [344] For aromatic sulfonic acids, which can be prepared via sulfonation or sulfochlorination followed by hydrolysis, the reaction conditions are often too harsh for the remaining components of the coupling reagents. Also, the synthesis of phosphonoalkylsulfonates, e.g., by the reaction of halogenalkanes with Na_2SO_3 , often takes place under rather harsh conditions and leads to low yields despite long reaction times. [345,346] Although the oxidation of thiols to sulfonic acids has been known for some time, the synthesis of phosphonoalkylsulfonic acid coupling reagents by this route has only recently been reported. The method allowed for short reaction times and resulted in high yields. [269]

A problem of the carboxylate and sulfonate groups is that they can bind to the particle surface as an anchor group, functioning as a crosslinker and thus leading to agglomeration of the particles. This can occur despite the phosphonic acids used in this work have a higher affinity towards the particle surfaces, so that the replacement of the weaker and dynamic bonding via coulomb interactions of the carboxylates and sulfonates would be expected to occur. [262,273] To circumvent this problematic, a second approach is to generate the anionic charges on the particle surface through post modification. This can be achieved either by using a precursor or a protected derivative of the acid group. Scheme 8 graphically illustrates the different possibilities using the example of carboxylic acid.

Introduction and Theoretical Background



Scheme 8: Schematic representation of the possible synthesis routes of ionic functionalized nanoparticles.

The simplest possibility is certainly the preparation of the ionic coupling reagent and its subsequent application to the surface of the particles. Since the pK_A of the carboxylic and sulfonic acids is lower than that of the phosphonic acid, it is not possible to deprotonate the phosphonic acid by adjusting the pH value, without also deprotonating the other acids, to generate an electrostatic preference towards the positive particle surface. It should be mentioned at this point that the stability of the bond also depends on the particle system. By using a precursor or the protected ionic group, the competitive reaction with the particle surface can be prevented. If the particle surface is completely covered with phosphonic acid during functionalization, the ionic group can then be generated without the risk of binding. However, the range of possible reactions that can be carried out on the particle surface is limited. Another advantage is that the occupation density for ionic functionalization reagents is often significantly lower than that of uncharged systems, which can be increased via the post introduction of the ionic group.[296,347] The reaction path via the protected group is somewhat more complex, but has the advantage that the oxidation reactions required to produce the carboxylate and sulfonate groups do not have to be carried out in the presence of the particles. This circumvents the risk of oxidation of the nanoparticles. Liu *et al.* utilize 3,4-dihydroxyhydrocinnamic acid to functionalize FePt, cubic Fe₃O₄, Pd, CdSe, and NaYF₄ (Yb 30 %, Er 2 %, Nd 1 %) nanoparticles.[270] Thus converting the initially hydrophobic surfaces into hydrophilic negatively charged surfaces after pH adjustment, making the particles water dispersible. Syntheses of sulfonate-based systems by this route are also known.[348,349] On the route of ionic group generation after functionalization, examples were described as early as 1996. Maoz *et al.* reported on the self-assembly of trichloro(nonadecyl)silane on SiO₂ substrates, followed by oxidation of the double bond with KMnO₄ and 18-crown 6 to a

carboxylate functionality.[350,351] For the synthesis of sulfonates, comparative studies have been carried out in which the ionic groups were introduced directly with and after the functionalization of ZrO_2 . [269]

On the cationic side, amines are commonly used functionalities. The pK_B values of the amines are in the range of 3 - 5 for aliphatic amines.[352,353] Even at a neutral pH of 7, the ammonium ion is predominant in solution. The basicity decreases significantly for the aromatic aniline derivatives. pK_B values of > 7 are observed.[354] As a result of that at neutral pH the systems are only partially protonated. In the case of amines, permanently positively charged systems can also be generated by the production of quaternary ammonium salts. The methods of preparation of the amines are diverse and can therefore be selected on the basis of the stabilities of the corresponding spacers and anchor groups. Halogen compounds are frequently used as the starting point. Here, the corresponding halogen alkanes are reacted with ammonia, primary, secondary or tertiary amines, whereby the protonated primary, secondary, tertiary or quaternary amine compounds are obtained.[269] The primary amine can also be obtained via a number of other reactions. These include the Gabriel synthesis and the Delepine reaction, both of which also start from the halogenalkane.[355,356] Furthermore, amines are accessible through the reduction of nitriles, azides, nitro compounds or carboxylic acid amides, as well as their degradation.[341,357–361] Among the most important technical methods is the reductive amination of carbonyles.[362] It should also be mentioned here that it is possible to convert primary amines into more highly substituted ones. Besides the conversion with alkylation reagents, such as methyl iodide, which often yields a mixture of products, more controlled reactions such as the Eschweiler-Clarke methylation are applied.[363,364] Due to this good synthetic accessibility, as well as the stable, and in the case of the quaternary ammonium compounds even permanent, charge over wide pH ranges, these systems are frequently used.[365–367] With these systems also anisotropic functionalized, Janus-like systems have been realized.[368] Amines are used, especially when switchable charges are necessary on the surfaces.[270] Here, too, the synthesis of the amines reagent usually takes place before functionalization and the charge is introduced afterwards by pH adjustment. An interesting approach was recently published by Siek *et al.*[369] Here gold particles were uniformly functionalized with positively charged *N,N,N*-trimethyl(11-mercaptoundecyl)ammonium chloride and negatively charged mercaptoundecanoic acid. While the positive charges are permanent, the negative charges can be generated in a pH-dependent manner. Thus, systems can be generated that allow precise switching between positive, neutral and negative surfaces. In addition, by varying the ratios of the two functionalization reagents, a second control variable is introduced for tailoring the switchability of the charge ratios. There are also post-functionalization strategies for cations. One possible strategy for generating amine functionality on surfaces or on cubic spherosilicates is the

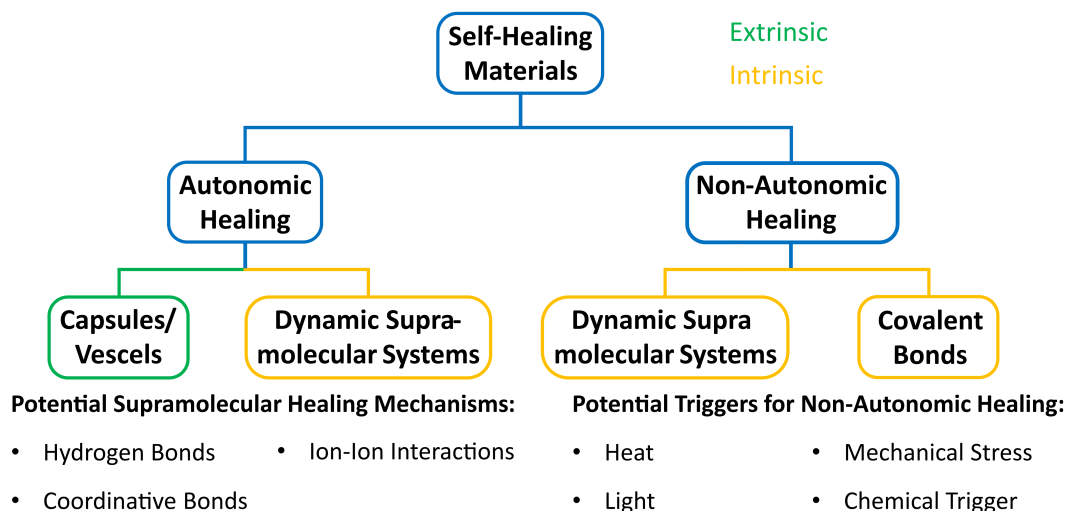
reduction of azide precursors.[370–372] Syntheses by nucleophilic substitution of halogens by amine functionalities at the particle surface are also known.[269]

In addition to molecular functionalization reagents, functionalization with ionomers and polyelectrolytes also plays a major role. According to IUPAC, ionomers are macromolecules in which a small but significant portion of the constitutional units bear ionizable or ionic groups, or both. In contrast, polyelectrolytes carry a substantial amount of the constitutional units bear ionizable or ionic groups.[34] The charges can occur both in the polymer backbone or in the side chains. Analogous to acids and bases, polyelectrolytes are also divided into weak and strong electrolytes. Strong electrolytes are dissociated over wide pH ranges, so that the charge density is largely independent of the surrounding medium. As discussed above, this applies to systems carrying sulfonate groups, such as poly(styrene sulfonate), or permanently cationic systems such as poly(diallyldimethylammonium chloride) or poly(methacryloyloxyethyl trimethyl ammonium chloride). Copolymers are also frequently used.[174,373,374] Weak polyelectrolytes, on the other hand, have dissociation constants > 2 and are therefore only partially dissociated at intermediate pH values. These include poly(allylamine), poly(ethyleneimine) and poly(acrylic acid). The polyelectrolytes are prepared either by polymerization of ionic monomers or by modifications after polymerization of uncharged monomers. By taking the polymer route, the system is not so limited by the surface area of the particles and thus more charges can be applied. These systems are mostly used in the field of self-assembly or drug transport and release.[309,375] Another possible application is self-healing nanocomposites. In the following chapter, the material class of self-healing materials and the underlying mechanisms will be explained in more detail.

1.5. Mechanisms and Advances in Self-Healing Polymers

All materials, whether natural or synthetic, are exposed to environmental stresses. These lead to degradation over time and deterioration of the materials properties up to complete failure. This usually occurs initially in the form of microcracks, which develop into larger defects.[376,377] In the case of nanocomposites, the phase boundaries are often the weak points. Initial progress has been made here by transferring the often adsorption-based bonding to covalent bonding.[97,98] Nevertheless, the interfaces still represent weak points of the materials. This is particularly the case when agglomerates are formed, which represent stress concentration points.[378–380] While today most materials are still designed for damage prevention, another potential solution to enhance the lifetimes of materials is the introduction of self-healing properties. Inspired by numerous biological models, the long-term reliability of self-healing materials has made their investigation a rapidly growing field of research. Blaiszik *et al.* define self-healing materials as the ability to repair damage and restore lost or degraded

properties, utilizing resources inherently available to the system.[381] Scheme 9 shows an overview of the classification of self-healing materials.



Scheme 9: Overview of the self-healing mechanisms. Adapted from [382].

In general, a distinction is made between intrinsic and extrinsic healing. Intrinsic healing means that the healing functionalities are incorporated within the matrix on a molecular level. This is the case when chemical bonds are responsible for the healing process. The term self-healing is somewhat misleading, as most intrinsic healing materials need an external trigger to conduct the healing process. These materials are classified as non-autonomic healing materials and are more accurately described as healable materials. However, in accordance with the literature, the term self-healing material is also used in this work. But there are also examples of autonomic healing based on supramolecular interactions, where no external trigger is necessary for healing. Further extrinsic self-healing materials also represent a large part of the autonomic self-healing materials. Extrinsic healing materials rely on an external healing agent, which is released when the material is damaged.[381,382] Though not first published these so called first generation self-healing materials have the disadvantage of only supporting a single healing cycle. In the case of polymers extrinsic mechanisms have been used mostly in thermosets [383–388], while the intrinsic healing is more commonly used in elastomers.[389–392] The intrinsic healing mechanism of polymers and organic-inorganic nanocomposites theoretically allows infinite healing cycles. Therefore, these second-generation self-healing materials have attracted increasing interest and will therefore be described in more detail below.

Intrinsic healing mechanisms: The efficiency for such intrinsic healing is fundamentally defined by three aspects: localization, chain mobility and temporality. Localization refers to the scale and the position of the damage. Intrinsic self-healing takes place at the molecular level. The systems contain functional groups that can interact reversibly and thus restore the initial state after damage. As a result of that it is apparent that healing only occurs on a nanoscale,

as that is the proximity of atomic interactions. Therefore, the central prerequisite for intrinsic healing is contact. Chain mobility is another key prerequisite for healing. Mobility accelerates both the transport of healing agents within the polymer, as well as the rearrangement of polymer strands responsible for healing. In rigid materials, these hurdles cannot be overcome due to the static surface, so that proximity and mobility through heating or addition of a suitable solvent is necessary. This may also be necessary for soft materials or at least lead to a strong improvement of the curing efficiency. Temporality describes the time between the damage and repair. The speed with which healing occurs is of course closely linked to the concept of mobility and localization.[393,394]

While a phenomenological examination of the healing of scratches can often already be carried out optically, mechanical measurements are often performed before and after healing to quantify the healing efficiency. Although the results of microscopy and recovery of mechanical properties usually coincide.[395] The efficiency is usually evaluated as a ratio of healed and initial properties (See Equation (4)).[389]

$$\eta(\%) = \frac{E_{\text{healed}}}{E_{\text{initial}}} \quad (4)$$

As early as 1970, Malinskii *et al.* published one of the first studies describing the self-healing properties of a polymer.[396–398] In the three-part study, they investigated factors such as temperature, crosslinking, molecular weight and layer thickness on the self-healing properties of poly(vinyl acetate). Sometime later, Jud *et al.* and Wool *et al.* described the healing of cracks in poly(methyl methacrylate), poly(styrene), and hydroxy terminated poly(butadiene).[395,399,400] All these studies were based on chain interdiffusion, which is a well-known effect for polymer systems and is achieved by increasing the temperature above the glass transition temperature (T_g) of the materials. This effect has been theoretically described by different models by de Gennes and Prager *et al.*[401,402] In more recent studies specific reversible interactions were applied to increase the self-healing speed and efficiency. These dynamic bonds can be divided into covalent and non-covalent interactions.

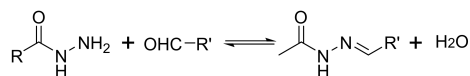
1.5.1. Dynamic Covalent Bond Chemistry in Self-Healing

In general, covalent bonds are restricted in their reversibility due to the stability of these bonds. However, there are dynamic covalent bonds where thermodynamically controllable formation or cleavage of a bond is achieved by a trigger such as temperature, light or pH. Temperature changes are most used in self-healing materials because higher temperatures promote chain mobility, which increases healing efficiency. Reversible reactions can be found in condensation, exchange or addition reactions. An overview of the most commonly used dynamic covalent bonds for self-healing is shown in Scheme 10.

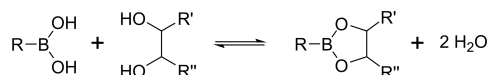
Dynamic Covalent Bonds Utilized in Self-Healing

Condensation reactions

Acyl hydrazone condensation:

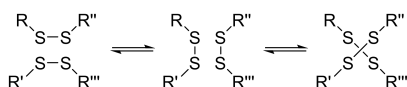


Esterification of boronic acid

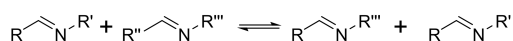


Exchange reactions

Disulfide metathesis:

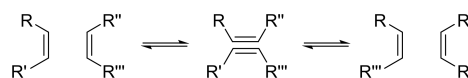


Imine/oxime metathesis:

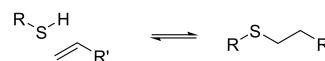


Addition reactions

Cycloaddition:



Thiol-ene reaction:



	T	pH	Light
Boronic ester	●	●	●
Acyl hydrazone	●	●	●
Imine/Oxime	●	●	●
Siloxanes	●	●	●
Disulfides	●	●	●
Radical exchange	●	●	●
Thiol-ene	●	●	●
Cycloaddition	●	●	●

Scheme 10: Overview of the most commonly used dynamic covalent bonds for self-healing. Adapted from [403].

Since condensation and exchange reactions play only a minor role in this work, they will be explained only briefly. In the field of condensation reactions, two moieties react under the elimination of water or alcohols. The most used mechanisms are the reversible formation of acyl hydrazones or boronic esters. Lehn *et al.* describe for the first time the preparation of poly(acyl hydrazone)-based reversible covalent polymers.[404,405] In this process, both a supramolecular and a molecular linkage is achieved through the acyl hydrazone functionality. The systems were switchable in response to temperature. Though initially this effect was used to obtain control over the physical properties of these polymers, Kuhl *et al.* used this reversible bond formation for self-healing.[406,407] The system of reversible boron/borate ester formation is more commonly used in the field of self-healing. Boron/borate esters are formed by a reaction of boric acid with 1,2- or 1,3-diols to form five- or six-membered rings, respectively. pH changes are used as a trigger, since boric acid and diols predominate at low pH values, while ester formation is preferred at higher pH values.[408] In 2017, Wang *et al.* described the synthesis of a dual self-healing hydrogel by integrating borate esters and acyl hydrazone bonds into an interpenetrating network.[409] Though the healing mechanisms based on condensation are efficient and often allow healing under mild conditions, they are mostly applicable in hydrogels, which display overall low mechanical strength.

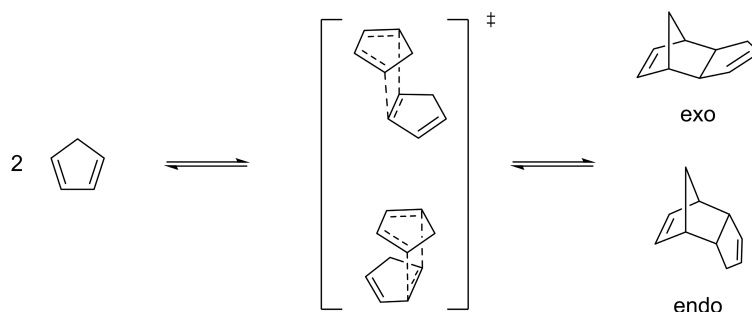
Exchange reactions utilize reactive isofunctional groups. During the reaction, atoms which were partners in the reactants are interchanged in the products. A wide range of chemical groups are available for this metathesis. One of the most used mechanisms is the metathesis of disulfide bonds. The healing mechanism is attributed to the thiol-disulfide exchange reaction

rather than a disulfide-disulfide exchange. This mechanism allows healing at low temperatures, although the lability of the bonds limits their application, especially at high temperatures.[410,411] Radical exchange in alkoxyamines is also commonly used. Although some systems are described as labile to oxygen and several side reactions are reported in the literature due to the high reactivity of the $\text{NO}\cdot$ radical.[412] Nonetheless, optimization allowed the preparation of systems that show room temperature healing and are resistant to air due to the fast cleavage and recombination equilibrium of C-ON bonds.[413,414] Imine [415,416] and oxime metathesis [417,418] are commonly used for the synthesis of self-healing hydrogels and often show a high healing efficiency under mild conditions, but are concurrent with low mechanical stability. Systems with siloxane-based metathesis also frequently exhibit low mechanical stability, but are significantly more chemically stable in comparison.[419,420] Olefin metathesis is highly efficient at shuffling strong carbon-carbon double bonds under ambient conditions, but requires the use of transition metal catalysts which make the materials inherently toxic and expensive.[421,422] The individual healing systems are intrinsically associated with advantages and disadvantages. The selection of the healing mechanism is therefore based on the desired properties and application of the material.

The third category, addition reactions, is probably the most studied area. The thiol-ene reaction is an important example. This is a Michael type addition, which was found to occur rapidly and in a reversible manner.[423,424] The disadvantage of the healing mechanism is that the sulfur-carbon bond is relatively weak and decomposition is observed at elevated temperatures.[423,425] Therefore, the majority of addition reactions in the field of self-healing are additions that produce stable carbon-carbon bonds. These are mainly cycloadditions. The most common cycloadditions are the [2+2]-cycloaddition [426–428], the [4+4]-cycloaddition [429] and most importantly the [4+2]-cycloaddition, the so-called Diels-Alder (DA) reaction. The [2+2]- and [4+4]-cycloadditions, like all $4n\pi$ electron obeying cycloadditions, are photochemically conductible. This allows healing under mild conditions, but poses the problem of superficial healing in thicker samples due to the low penetration depth of the radiation.[403] Since photoinduced cycloadditions were not used in this work, a detailed description of these will not be given here. In addition to the thermal controllability and the stability of the carbon-carbon bonds formed, DA-based self-healing also offers the advantage of robustness. High yields are obtained for both Diels-Alder and retro-Diels-Alder (rDA) reactions and due to the absence of side reactions, a large number of healing cycles can be run. Furthermore, the DA chemistry is already very well studied, so that versatile chemical modification of the components is already described in the literature, which can be used to set the reaction parameters such as the reaction temperatures. Furthermore, no additives are necessary for the healing process. Because of this flexibility and robustness, DA curing was chosen as one

of the healing mechanisms in this work. Therefore, the mechanism itself, as well as the state of the literature on its use in the field of self-healing, will be described in more detail below.

Diels-Alder based self-healing: The reason for the applicability DA/rDA chemistry in self-healing materials is a thermally controlled equilibrium between the combination of a diene and a dienophile and the corresponding cycloadduct. As a Click reaction, the DA reaction exhibits a high thermodynamic driving force. The DA reaction takes place in a single step via a six centered transition state. In this state, a concerted pericyclic rearrangement of the six π -electrons occurs by a positive overlap of the highest occupied molecular orbital (HOMO) of the diene and the lowest unoccupied orbital (LUMO) of the dienophile. This transition state is accompanied by a steric demand, which can limit the reversibility of the reaction.[271] Scheme 11 schematically shows the reaction course of the homo cycloaddition of cyclopentadiene.



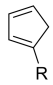
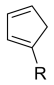

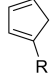
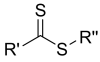
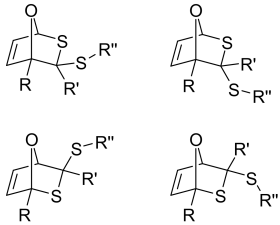
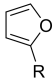
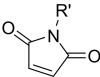
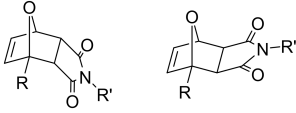
Scheme 11: Homo DA reaction of cyclopentadiene.

As shown in the example of cyclopentadiene, two products can be obtained in the DA reaction, the exo and the endo product. Despite the steric advantage and thus the higher thermodynamic stability of the exo configuration, the endo product is usually obtained. This is due to kinetic effects. The most widely accepted rationale for this is secondary orbital interactions that cause a pre-orientation of the diene and the dienophile in the endo position.[430] Sakata and Fujimoto studied the prototypical DA reaction of cyclopentadiene and maleic anhydride as well as other polarizable dienophiles, where the C=O functionality was replaced by C=NH or C=CH₂ moieties.[431,432] In their work, they showed that orbital interactions play only a minor role, and the control between exo and endo product is through electrostatic attractions introduced by the polarized C=O group. The C=O bond lifts the electron population from the carbon atom, creating the attraction between the dienophile and the diene in the endo transition state. Furthermore, the choice of substituents, which interact via steric or electrostatic interactions, can determine whether the endo or exo reaction pathway is preferred.[431]

Only a small number of DA pairs are suitable for use in self-healing. Cyclic dienes and dienophiles are used almost exclusively. The reason for this is that most non-cyclic addition pairs are not suitable for reversible reaction control. The thermally induced rDA reaction often requires high temperatures. However, at these elevated temperatures, decomposition of the

Introduction and Theoretical Background

cycloadduct often occurs rather than the corresponding retro reaction in which the original components are recovered. Furthermore, the cyclic systems offer the advantage that the substituents on the double bond are trapped in the cis configuration, so that no rotation around the connecting σ -bond is necessary to perform the reaction. Three types of DA pairs are commonly used. These are summarized in Scheme 12.

Diene	Dienophile	DA-Adducts	Advantages/Disadvantages
			<ul style="list-style-type: none"> + only one functionality is needed - high rDA temperature - long reaction times
			<ul style="list-style-type: none"> + low healing temperatures + short reaction times - low thermal stability
			<ul style="list-style-type: none"> + easy chemical modification + tailorable healing temperatures - long reaction times

Scheme 12: Suitable DA pairs for self-healing materials.

The first one is the homo-addition of cyclopentadiene. Cyclopentadiene can both act as a diene as well as a dienophile, which is an advantage as only one functionality is needed to induce the self-healing behavior. In the homo-addition a bridged bicyclic compound is obtained, which itself can react in a cycloaddition. Though the polymerizability of cyclopentadiene was already known much earlier [433,434], the first work on the DA/rDA based healable polymers was described by Kennedy and Castner in the late 70s.[435,436] Although healing was possible, only two healing cycles could be performed, probably due to partial decomposition at the required high rDA temperature of 170 °C.[437] Interestingly the reaction temperature for the rDA can be reduced by functionalization of the cyclopentadiene rings. For this purpose, α,ω -bis(cyclopentadiene) monomers were prepared in which the cyclopentadiene unit is attached via a carboxylate group.[438] The systems obtained in this way allow more healing cycles due to the less harsh conditions.

The second group of DA reactions suitable for self-healing are the hetero DA reactions. These cyclopentadiene-thiocarbonyl systems operate at a lower temperature range. In most cases, dithioesters are used for this purpose. The DA reaction of thioaldehydes with cyclopentadiene was first described by Vedejes in 1986.[439] Here, the hetero DA proceeded within minutes, though the yields were lackluster depending on the substitution pattern. By adding trifluoroacetic acid or $ZnCl_2$ as a catalyst, the reaction rates were further increased.[440–442]

McGregor and Sherrington were one of the first describing the reversibility of hetero DA.[443] Hetero DA is mainly used for reversible crosslinking of RAFT polymers, since they already contain the thiocarbonyl functionality in the form of the CTA.[441,444–446] The major drawback of these hetero DA systems is the restriction to the low temperature range, as the materials decompose at lower temperatures already.[441,447] In an interesting example Oehlenschlaeger *et al.* used the dithioester-cyclopentadiene DA pair.[447] The system prepared showed to be curable in multiple cycles within 10 minutes at 120 °C and 1 kN pressure. In addition to the healing ability also the mechanical properties were tunable through crosslinking.

The last approach of DA-based self-healing is the reaction of heterocycles, mainly the combination of maleimide and furan. Compared to hetero DA, these systems are much more temperature stable. In addition, the temperature range for DA and rDA is in a good range for a variety of polymer matrices. The usual temperature range for DA reactions is between room temperature and 80 °C depending on the electronic activation. Overall, higher reactivity is observed as the LUMO of the dienophile and the HOMO of the diene approach each other. This is the case when the electron density of the diene increases, and the electron density of the dienophile decreases. In the case of the maleimide, the electron density is greatly reduced by the two conjugated C=O groups. The aromatic stabilization of the furan ring further allows the rDA to occur at lower temperature range of 80 °C – 120 °C.[448] However, this aromatic stabilization is also the reason why the kinetic preference of the endo product is less pronounced. Often times both the endo as well as the exo product are obtained or the equilibrium is completely shifted to the exo product.[449] Furthermore, both the furan and maleimide components allow easy chemical modification and integration into polymer networks. For these reasons, the maleimide furan system was chosen for this work. In the following, an overview of these materials will be given.

The maleimide-furan DA pair was first mentioned as a polymer crosslinker in a patent from 1966, in which several polymer networks bearing furan functionalities were described. The crosslinking took place either via bi- or trifunctional maleimides.[450] In the following years, more and more studies on crosslinking with this DA pair were published. For example, Stevens *et al.* and Goussé *et al.* describe the crosslinking of poly(styrene).[451,452] Both attached maleimide functionalities to poly(styrene) and use α,ω -bifuran linkers for the DA crosslinking. This strategy of incorporating the DA functionality after the polymerization process is typical for the early studies.[453] The reversibility of crosslinks via DA reaction was first described by Canary and Stevens.[454] Two approaches were used to study reversible crosslinking. One was poly(styrene) substituted with maleimido methyl groups using difuryl adipate as the crosslinker, and the other was poly(styrene) containing both maleimide and furan groups in the

polymer backbone. Both approaches allowed reversible crosslinking, but problems were observed regarding stability, especially of the furan-containing polymers. Despite these promising early studies, the first reports on the use of reversible crosslinking in the field of self-healing did not appear until ten years later. Chen *et al.* described a reversibly covalently crosslinked network consisting of a tetrafunctional furan monomer with a trifunctional maleimide linker.[455] The material showed healing on a macroscopic scale. When the material was heated to 150 °C, a 30 % degree of rDA was observed within 15 minutes. Subsequent cooling to DA temperature showed curing of the material, although mechanical testing showed that only 57 % of the original breaking load was restored after healing. The materials demonstrated the ability to withstand multiple healing cycles. Subsequently the system was further optimized and expanded to other maleimide linkers, which have lower melting points and thus often allow better healing due to the increased mobility.[456] The healing tests are supported by calculations suggesting that the time required for healing is dictated by the kinetics of the DA reaction rather than diffusion-driven processes.

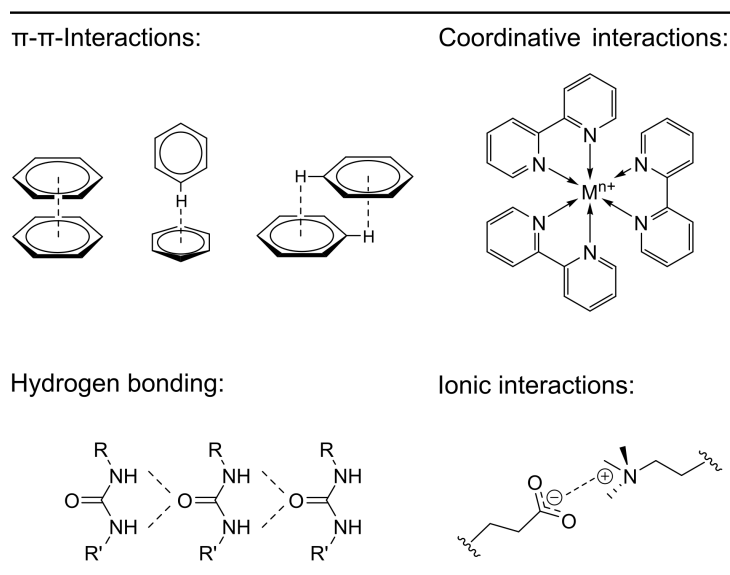
Today, however, self-healing polymers are far from being limited to the dendrimer-like systems. Based on the work of Stevens, a variety of systems have been described in the literature in which self-healing polymer networks are obtained either based on polymers with crosslinkers [457–465], the integration of both DA functionalities in one polymer [466,467], or the use of two polymer strands, each with one DA functionality [468–471]. These systems have the advantage that the material properties can be tuned via the selection of the polymer backbone and self-healing is added via the integration of the DA groups without changing the properties too much. The investigated systems include backbone polymers such as methacrylates [461,463,466,470], styrene derivatives [457], epoxides [458,472], siloxanes [464,465,471] or polyurethanes [460,462]. The systems are thus tailored to the requirements of the desired applications, which range from thermosets over thermoplastics and elastomers to hydrogels. In addition to DA healing, a variety of dynamic non-covalent interactions are also used for self-healing in polymers. These will be discussed in the following.

1.5.2. Dynamic Non-Covalent Bond Chemistry in Self-Healing

Dynamic non-covalent bond chemistry offers the advantage that these often do not require an external stimulus for self-healing and therefore healing occurs immediately after damage and is often very fast. Furthermore, the interactions are weaker than the covalent bonds, so that these represent predetermined breaking points that subsequently heal efficiently. Despite the individually weak interactions, strong networks can be formed in the aggregate. Nevertheless, the interactions are mainly used in soft systems such as hydrogels. However, when moving to systems with higher mechanical strength, an external energy supply is often required to increase the chain mobility, to enable self-healing. The four most common interactions used in

Introduction and Theoretical Background

this context are π - π -stacking [473–478], coordinative interactions [389,479–483], ionic interactions and hydrogen bonding. An overview of the non-covalent interactions used is shown in Scheme 13.



Scheme 13: Non-covalent interactions used for self-healing.

As both ionic interactions as well as hydrogen bonding are used healing mechanisms in this work, the state of the literature will be explained in more detail.

Self-healing based on ionic interactions. Although ionomers have been known since the mid-60s, they are still extensively studied today, as the mechanical properties of ionically crosslinked networks are often superior to those of conventional hydrogels. Surprisingly, they are rarely studied for self-healing.[484–491]

An important material that can be classified between coordinative and ionic interactions is poly(ethylene-co-methacrylic acid).[492] This material is mainly responsible for the fact that ionomer-based self-healing materials are widely regarded as one of the most efficient healing systems, as they recover independently from devastating damage in a very short time. The copolymer is marketed in various molar masses, compositions, and degrees of neutralization by Dupont under the names Surlyn®, Norel® or React-A-Seal®, among others. The polymer responds to ballistic impacts with self-healing. Two inherent material reactions are responsible for the healing process. The first is an elastic reaction that provides the rebound and shape memory effect of the polymer. In addition, a viscous reaction provides the final seal. Both effects depend on the thermal friction forces during the impact. The repeatability of the healing process supports the assumption that the healing originates from inherently formed structures. In further work, Varley and van der Zwaag showed that ionic clusters which form in the polymer are crucial for the healing process.[493] These so-called multiplets are usually almost spherical in their arrangement and consist of fewer than 10 ion pairs, which in turn overlap to form

clusters.[494–496] Several practical and theoretical studies have been performed to characterize the structure of this cluster. These include hard sphere models or core-shell models.[497–500] In the following, the influence of the degree of neutralization on self-healing was investigated. Moderate ionic contents proved to be most efficient for healing below 40 °C, while above healing improved with increasing ionic content.[501] Based on this work, other ionic self-healing materials have been described. Zhang *et al.* developed a block copolymer of poly(methyl methacrylate) and poly(butyl methacrylate-co-2-acrylamido-2-methyl-1-propanesulfonic acid).[502] The monomer choice and polymer architecture lead to microphase separation, resulting in two networks, the vitrified PMMA and the supramolecular interactions from the sulfonate component. The material exhibited excellent shape memory and self-healing properties. In a similar approach, Das *et al.* were able to generate cationic polymer strains by reacting a commercial bromo butyl rubber with butyl imidazole, which induced excellent self-healing into the material.[503]

The obvious approach of achieving self-healing by combining ionic dendrimer systems or using two complementary polyelectrolytes or polyampholytes has hardly been investigated. The first descriptions of ionic self-healing systems can be found in the work of Wang from 2014.[504] Here, a layer-by-layer deposition of branched poly(ethyleneimine) and poly(acrylic acid) was carried out. In addition, cetyltrimethylammonium bromide micelles loaded with triclosan were integrated by post-diffusion. The transparent and antibacterial films allowed self-healing after immersion in water or spraying the damaged films with water under ambient conditions.

In general, it has been observed with self-healing ionic polymers that the chain mobility must be increased for successful healing. This is usually done by wetting, which proved to be particularly effective when NaCl-containing solutions were used.[505,506] This can be understood by considering that the cooperative separation of oppositely charged chains is required prior to the healing process to induce new crosslinks across the cut edge. This is done by neutralizing the charge with the salt. Furthermore, it has been shown that adjusting the pH to acidic or alkaline conditions can also be used to reduce the crosslink density and thus improve healing.[507] One problem with this wetting technique is that the polymers often swell and lose their structural integrity when exposed to water.[506] Elevated temperatures have also been shown to improve healing.[508]

In a promising recent example, Zhang *et al.* reported a mechanoresponsive self-healing ionic elastomer based on poly(methacrylic acid) as the anionic component and zwitterionic crosslinks, including betaine, dimethylglycine, L-proline, sarcosine, and trimethylamine oxide.[509] The obtained material showed 100 % healing within 12 hours at a humidity of 80 %. Mechanical tests confirmed that multiple healing cycles could be run.

As a second non-covalent bonding mechanism, hydrogen bonds were used in this work. Their applications in the field of self-healing will therefore also be described in the following.

Self-healing based on hydrogen bonds. Hydrogen bonds are physical interactions that are much weaker than covalent bonds and even ionic interactions. Nevertheless, they are probably the most used dynamic non-covalent bonds in the field of self-healing because they form stable networks collectively. Like ionic interactions, hydrogen bonds are in a state of equilibrium and reconnect after damage at room temperature.[510,511] Even though hydrogen bonds have been explored extensively as a healing mechanism [512–514], only a few selected examples will be discussed here.

Although supramolecular crosslinked polymers based on hydrogen bonds have been known since the early 90s [515], the first description of a self-healing material based on hydrogen bonding can be found much later. In 2008, Cordier *et al.* described a first example of this.[391] In this work, di- and tricarboxylic acids were first condensed with diethylene triamine, followed by a reaction with urea. Thus, a mixture of oligomers with amidoethylimidazolidone, di(amidoethyl) urea and diamidotetraethyltriurea groups was obtained, showing self-healing at room temperature. However, it was pointed out that the rubbers obtained in this way could not hold stress without creep. Also, solvent resistance of the materials is rather low, although similar to the ionic systems, the addition of water as a plasticizer significantly improved the healing.

Hentschel *et al.* synthesized the first hydrogen-based self-healing block copolymers.[516] The ulterior motive of this system is that these are composed of a hard poly(styrene) blocks and soft poly(butyl methacrylate) blocks, which are known to show microphase separation, resulting in advantageous mechanical properties. To prevent permanent damage due to covalent bond breaking, 2-ureido-4-pyrimidinone was integrated as a hydrogen bond based crosslinking capping agent. The thermoplastic elastomer obtained showed an almost quantitative recovery of both E-modulus and maximum stress. This approach of using hydrogen bonds at the chain ends has also been applied to other polymers such as perfluoropolyethers or siloxanes and showed good applicability in different chemical environments.[517,518]

But the hydrogen bonds are not only used in the chain ends, but also in the side chains. For example, Song *et al.* report the synthesis of a self-healing polyurethane elastomer with 2-ureido-4-pyrimidinone as side groups.[519] In this work, they showed that the mechanical properties improved with increasing number of crosslinks. At 20 mol% 2-ureido-4-pyrimidinone groups, healing degrees of up to 90 % were observed.

Lastly, there is the integration of hydrogen bonding groups into the main chain. In a recent study, elastomers with excellent tensile strength, toughness and elongation were synthesized by three-step polyadditions using poly(tetramethylene ether glycol), isophorone diisocyanate, 2,6-pyridinedimethanol and 4,4'-methylenebis(2-chloroaniline), again applying the soft/hard segment approach.[520] The materials showed a healing efficiency of more than 83 % in tensile strength, toughness and elongation at room temperature within 48 hours.

In a very interesting approach, Zhou *et al.* reported the synthesis of a self-healing crosslinked elastomer with urea-urethane moieties.[521] The materials exhibit extreme extensibility and high toughness and heal excellently in several cycles at room temperature in a short time (10 minutes). The authors attribute this behavior to the synergistic effect of the robust dynamic urea bonds and the hydrogen bonds between and within the chain. Although not the first example, this approach of combining different healing modes is one of the major breakthroughs in the field of self-healing materials and achieves the goal of combining good mechanical properties and high healing efficiencies.

Combination of intrinsic healing interactions. Materials that use multiple healing mechanisms are grouped together in the so-called fourth generation of healing materials.[393] Their origin dates back to a work of Burattini from 2010. In this work a polyimide and a polyurethane with pyrenyl end groups were applied for both hydrogen bonding based and π - π -stacking based healing.[475] Since then, the literature utilizing two healing mechanisms has been growing steadily. The materials can be divided into three groups: Combined covalent healing, combined non-covalent systems and combined covalent/non-covalent systems. The combined covalent systems are scarcely studied and refer almost exclusively to the combination of disulfide and imine bonds.[522–524] Even less frequently, the combination of disulfide bonds with acyl hydrazone [525] and borate ester bonds [526] are described. Significantly more studied are the systems with two non-covalent healing mechanisms. While these systems often show good healing efficiencies, their mechanical properties are often times lacking. The most common combinations are hydrogen bonding and ionic interactions [527–531], as well as hydrogen bonding and metal/ligand interactions.[532–535] More rarely, systems are also described in which all three interactions are used.[536]

Much more interesting are the combinations of covalent and non-covalent healing mechanisms due to the orthogonality of the healing mechanisms. To a damage the materials can autonomously respond instantly via the supramolecular mechanism, while the mechanical properties are improved via the reversible covalent crosslink, further allowing a trigger based second healing. Again, a variety of combinations are used, including hydrogen bonds with disulfide [537–541] or imine bonds [542–544], metal ligand coordination with disulfide bonds [545] or DA chemistry [546] and many more. However, due to the relevance to this work, only

the combinations of hydrogen bonds and DA reactions, as well as ionic groups and DA, will be considered here.

The combination of hydrogen bonds and DA healing was first described by Araya-Hermosilla *et al.*[459] In their work aliphatic ketones were modified via a Paal-Knorr reaction introducing both furan as well as amine functionalities. In addition to the hydrogen bond forming amines and keto groups, DA healing was introduced by adding a maleimide crosslinker. As initially side reactions in the form of the formation of imines was observed the group later improved the polymer system by using hydroxides instead of amines as the hydrogen bond donor.[547]

Based on this, the healing mechanisms have been applied to a number of different polymer systems, including methacrylates [548], siloxanes [549], and urethanes [550], all showing improved mechanical properties and good healing efficiencies. Willocq *et al.* further showed that the healing efficiency of their polyurethanes was tunable based on the polymer composition.[550] Comparisons between interpenetrating networks and single polymer networks containing both healing functionalities showed that the interpenetrating networks often times outperformed the single network in its properties which was attributed to the greater dynamics.[548] The decoupling between the two networks allows for better energy dissipation and the increased mobility improves the self-healing of the interpenetrating system. The influence of the matrix polymer was then further investigated by Cummings *et al.* In their work they synthesized interpenetrating networks in which one network had covalent DA bonds and the other provided hydrogen bonds via 2-ureido-4-pyrimidinone.[551] The matrix polymers used were nonpolar poly(ethyl acrylate) on the one hand and polar poly(2-hydroxyethyl acrylate) on the other hand, which itself can form further hydrogen bonds. It was shown that self-healing, toughness, and fracture energies were weaker for the poly(2-hydroxyethyl acrylate) system, although there were more hydrogen bonds. This suggests that the quality of the hydrogen bonds between two 2-ureido-4-pyrimidinones outweighs the total amount of hydrogen bonds. For material design, this means that the selection of the forming group of hydrogen bonds is crucial for both mechanical and self-healing properties.

In contrast to the hydrogen bond-based systems, combined DA healing and ionic interactions are almost not studied. The only work in this area to date is by Lindenmeyer, Johnson and Miller. In their work they used a trifuran functionalized crosslinker in combination with either an imidazolium mono or bis maleimide.[552] DA reaction was performed at 120 °C in an oven, which is a rather high temperature for the DA of the furan maleimide system. Healing experiments were performed by heating previously halved samples for up to 4 hours for the bismaleimide and 1.5 hours for the mono maleimide sample, at which point almost complete healing was observed determined with tensile testing (max. stress/strain recovery > 90 %). Although the healing speed is better in the second system, the first one showed a factor four

higher maximum stress of almost 8 MPa. Unfortunately, no NMR or IR studies were performed at the different points in time of the healing process, so that an assignment of the healing to DA/rDA or ionic interactions cannot be conclusively clarified.

To summarize, the combination of dynamic covalent and non-covalent bonds leads to a trade-off between mechanical properties and healing efficiency. Another way to improve the mechanical properties of self-healing systems while retaining high healing efficiencies is the use of nanocomposites in which the mechanical properties are improved through the integration of an inorganic component. This strategy will be explained in more detail in the following chapter.

1.6. Self-Healing Nanocomposites

While the concept of self-healing is well-known for polymeric systems, pure inorganic materials like ceramics and metals lack potential healing mechanisms, or require high energy input to work due to the bonding situation in inorganic solids.[553,554] The use of organic-inorganic nanocomposites allows the limited inorganic healing mechanisms to be replaced by the dynamic bond formation of the polymeric systems. The flexibility of the healing mechanisms of the polymeric component can thus be maintained, while particularly increasing the mechanical and thermal stability compared to conventional polymers. Due to the excellent properties of the self-healing nanocomposites, they are of great interest and are extensively reviewed in the literature.[555–559] Two strategies are available for the self-healing nanocomposites. Self-healing can either take place in the polymer network or at the phase interface. If the healing mechanism takes place in the polymer, the inorganic components are usually physically incorporated into the healing polymer matrix. Fibers, coils, nanosheets and particles of various compositions are used for this purpose. At this point, however, due to the relevance to the topic of this work, the focus will be on iron oxide nanoparticle-based systems and their application as nano heaters.

In the case of nanocomposites, too, there have been studies on chain interdiffusion-based healing, analogous to those of polymers. A first example is the work of Corten and Urban, in which superparamagnetic Fe₂O₃ nanoparticles (d = 12 nm) were incorporated in a copolymer of methacrylate, butyl methacrylate and heptadecafluorodecyl methacrylate.[560] With a particle content of 14 wt%, the composites were completely healed by the heat input induced in an alternating magnetic field. Since then, the approach was also carried over to other polymeric systems, including poly(styrene) [561], poly(propylene) [562], poly(ethylene-co-vinyl acetate) [563] or poly(ethylene-co-methacrylic acid) [564]. While it has been shown that particle amounts of less than 0.1 vol% are sufficient to heal small scale damage, e.g., caused by electrical treeing [568], for μm scale damage, typically 3-20 wt% particles are used to induce the required temperature.[561,563]

However, the magnetic field induced heat was not only used for healing via chain interdiffusion. In a first paper, Hohlbein *et al.* describe the synthesis of a nanocomposite healing via coordinate bonds consisting of poly(butyl acrylate-co-methyl acrylate) using zinc(II) as a complex central atom.[565,566] Integration of superparamagnetic Fe₃O₄ or CoFe₂O₄ particles, both in the size range of 15 nm, enhanced self-healing by inductively heating the composites in an alternating magnetic field, even at low filler contents (0.05 vol%) and temperatures below the melting point of the polymer. This indicates that the ionic interactions are the responsible self-healing mechanism.

In a recent example, Zhang *et al.* synthesized a self-healing hydrogel based on gelatin and agarose.[567] Fe₃O₄@PSS-co-MA@SiO₂ nanoparticles were integrated into the hydrogel. Healing was possible both in an alternating electromagnetic field and photothermally. Due to the choice of polymer, a very low overall mechanical strength was observed with a maximum stress of about 0.005 MPa. Recovery of approximately 55 % of maximum stress and 75 % of strain was observed. Although the healing mechanism is not discussed further in the paper, hydrogen bonding and chain interdiffusion appear to be the main healing mechanisms.

While the approach of simply physically incorporating the nanoparticles in the polymer network is synthetically easier to access, moving the healing mechanism to the phase interface has the advantage that the inorganic material is often better distributed in the polymer and the healing mechanism is located at the phase boundary, which is usually the weak point of the materials. In the following, the state of the literature will be presented where DA healing, hydrogen bonding or ionic interactions are used as a healing mechanism at the phase boundary.

In the case of DA healing, one functionality is bound to the inorganic surface, while the orthogonal DA functionality is bound to the polymer matrix. Here, too, the focus will be on particulate fillers since fibers and sheets are prone to fracture and no healing has yet been described for the reinforcement itself.

Several self-healing nanocomposites have been investigated in our group. In one example, Engel and KICKELBICK describe the SI ATRP of a butyl methacrylate-furfuryl methacrylate copolymer from SiO₂ (d = 42 nm) nanoparticle surfaces.[568] The obtained core-shell particles were incorporated into a copolymer of butyl methacrylate and maleimidoalkyl methacrylate and then crosslinked by DA reaction. The material showed the ability to heal scratches on a μm-scale.

The role of the matrix in the self-healing process was also investigated. Schäfer and KICKELBICK investigated the self-healing ability of DA-functionalized silica nanoparticles used as crosslinking agents in poly(butyl methacrylate) and poly(siloxane) matrices, both of which contain the orthogonal DA functionality either as a capping agent or in the side chain.[569] The

samples were able to heal μm -scale scratches after being heated to 120 °C for rDA and then to 60 °C for the DA reaction. Methacrylate thermoplastics showed a lower tendency to crosslink reactions compared to elastomeric siloxanes, which can be attributed to the higher T_g and stiffness of the methacrylates.

Further, fundamental studies have been performed to investigate the feasibility of DA chemistry on silica and iron oxide particle surfaces.[271,570] For this purpose, maleimide or furane functionalities were immobilized on the particle surfaces. Overall, it was found that the higher the grafting density and steric effects near the reaction site, the lower the DA conversion. This means that as the chain length of the DA group bound to the surface is increased, the DA efficiency increases. Similarly, as the steric demand of the DA group in solution was increased, it was found that an increase reduced the DA efficiency at the surface. The results suggest that the DA reaction is not the most suitable healing mechanism for the phase boundary of the nanocomposite systems due to the steric demands.

One approach to circumvent this problem is to switch to non-covalent interactions, such as ionic interactions. Similar to the polymer systems, the materials are also well studied here.[571–575] However, the suitability for self-healing is rarely considered, although thin films of self-suspended liquids of ionic nanoparticles are known to form self-healing conductive lubricant layers for contacts in microelectromechanical systems.[576,577]

The first descriptions of a self-healing nanocomposite based on ionic interactions come from Zheng *et al.* in 2015.[578] The authors describe the synthesis of silica nanoparticles modified with poly(2-dimethylaminoethyl methacrylate) brushes that introduce cationic charges to the particle surfaces. The particles act as a crosslinker for an anionic poly(acrylic acid) network. The electrostatic interactions between the cationic particles and the anionic polymer give the material self-healing capabilities at the μm scale.

Further investigations were carried out by Odent *et al.* In their work, the authors describe the synthesis of anionic silica nanoparticles ($d = 18 \text{ nm}$) by functionalization with 3-(trihydroxy silyl)-1-propane sulfonic acid.[579] The particles were embedded in a commercial polylactide, an imidazolium-terminated PLA and in a poly(ϵ -caprolactone-co-D,L-lactide) polymer network. The electrostatic interactions allow good dispersion of the particles in the polymers. The ionic hybrids are much more deformable compared to the neat PLA though creep compliance tests suggest that the ionic interactions prevent permanent slippage, which is responsible for significant shape-memory loss. In a second study the authors integrated the previously developed particles into a cationic, imidazolium-functionalized, polyurethane polymer matrix. Particle loadings of 5-40 wt% were used.[310] As a result, stiff, tough, and highly extensible nanocomposites were obtained. Scratches with a razor blade were healed at 50 °C within 5 hours. The tensile tests performed showed a maximum elongation at break of 463 % for the

composites at 20 wt% particle loading, which is 11 times that of the neat polymer. In addition, a 40-fold increase in tensile strength and a 2.5-fold increase in stiffness was obtained. Subsequent theoretical studies have confirmed that the excellent toughness of IPNCs is due to the electrostatic interaction between polymers and nanoparticles, and not to the mobility of nanoparticles or polymer entanglements.[580]

Recently, Mugemana *et al.* reported the synthesis of poly siloxane-based self-healing nanocomposites.[581] For this purpose, they again used 3-(trihydroxy silyl)-1-propanesulfonic acid-functionalized silica particles and integrated them into a poly(dimethylsiloxane) grafted with trimethylammonium bromide either as an end group or in the side chain. Higher thermal stability but poorer particle dispersion was observed for the end-group functionalized systems. Rheology studies showed a significant viscosity fraction for the sidechain functionalized systems, while end-group functionalized systems showed solid like behavior. The highest elongation at break of 120 % was observed for side-chain functionalized polymers with a nano silica loading of 10 wt%. The nanocomposite also showed self-healing at 80 °C within 30-60 minutes in a humid environment.

In addition to ionic interactions, hydrogen bonds are also used for crosslinking inorganic and organic components. Although like for ionic systems, the application of the interaction at the phase boundary is rarely investigated for self-healing. Here, too, carbon-based materials are frequently used.[582–584]

Less commonly, metal oxide and metal hydroxide nanoparticles are used. Depending on the pH value, these automatically exhibit the ability to form hydrogen bonds without functionalization. Jiang *et al.* describe the synthesis of a zirconium hydroxide-based self-healing nanocomposite.[585] For this 2-acrylamido-2-methyl propane sulfonic acid and acrylamide were randomly copolymerized in the presence of zirconium hydroxide (d = 10-15 nm) nanoparticles. Mechanical properties and healing efficiency could be tuned by the polymer composition and particle content. With a particle content of 12 wt% a tensile strength of 404.3 KPa was obtained and showed 86 % recovery in healing experiments within 24 hours at room temperature.

In another example, Hu *et al.* describe the use of calcium hydroxide nanoparticles (< 5 nm).[586] The particles act as crosslinkers in poly(acrylic acid) networks via hydrogen bonds. Materials with excellent mechanical properties were obtained with a particle content of 200 ppm. A maximum tensile elongation of 2300 %, a maximum tensile strength of 72 kPa and a toughness of 0.611 MJ/m³ were obtained. In curing tests, > 91 % of tensile elongation and > 98 % of tensile strength were recovered.

Introduction and Theoretical Background

In a study by Bian *et al.*, the authors discuss the functionalization of SiO₂ with amino functionalities.[587] Bifunctional and trifunctional amines were reacted with a mixture of dicarboxylic and tricarboxylic acids to obtain a hydrogen-bonding polyamide. The polyamide and functionalized particles were combined with a two-component epoxy resin. The obtained material was then studied in self-healing tests. The hydrogen bonding system prevents electrical treeing. Although good healing was observed visually, tensile testing showed that tensile strength recovery was less than 17 % and continued to decrease with further healing cycles.

The previously theoretically described advantage of the combination of dual crosslinked nanocomposites [588] has been put to practice in a study from Schäfer and Kickelbick.[73,370] In this work, hydrogen bonds were used as the first self-healing mechanism between the inorganic filler and the polymer matrix. In addition, DA/rDA healing was completely shifted into the polymer network. In this work, urea functionalized spherosilicates were used in random copolymers of butyl methacrylate, furfuryl methacrylate, 2-(1,3-dioxo-3a,4,7,7a-tetrahydro-1H-4,7-epoxyisoindol-2(3H)-yl)ethyl methacrylate and 2-acetamidoethyl methacrylate/2-(2-hydroxyethyl)-3a,4,7,7a-tetrahydro-1H-4,7-epoxyisoindole-1,3(2H)-diones. The healing by reversible bond formation of DA chemistry could thereby be supported and accelerated by the self-assembling/self-healing effect of the hydrogen bonds between the organic and the inorganic components.

Since then, several approaches have been taken to utilize this double self-healing, mainly in the field of self-healing hydrogels. Different combinations of self-healing mechanisms have been investigated, including hydrogen bonds with coordination bonds or reversible covalent bonds, including imine and boronate ester bonds.[589–592]

In summary, the field of self-healing nanocomposites is less explored than the field of self-healing polymers, although the introduction of inorganic fillers brings many advantageous properties such as mechanical and thermal stability or even facilitates the introduction of new properties in the field of magnetism or optics, thus opening up new application areas and triggering possibilities for the self-healing materials. The major challenge is that this rigidity caused by the inorganic components reduces the flexibility and chain mobility required for self-healing. In addition, phase interfaces can act as stress focus points, causing weak points in the material. Integrating the healing mechanism into these phase interfaces is a promising approach to develop materials that heal at their weak points. This approach requires careful design of both the particle surface and the polymer matrix. Interestingly, iron oxide particles have only been used as magnetic field-triggered nano heaters in systems where chain interdiffusion or other healing mechanisms are confined to the polymer matrix rather than the interface. Another promising approach in the field of self-healing polymers is the combination

Introduction and Theoretical Background

of covalent, non-covalent crosslinking networks, which have been shown to exhibit enhanced self-healing properties. Surprisingly, this approach has been rarely applied to composite systems. These aspects were therefore defined as the core motifs of this work and will be elaborated in more detail below.

2. Research Goals

2.1. Objective

The objective of this work is the synthesis and characterization of self-healing nanocomposites. Ionic interactions and hydrogen bonding and their combination with DA/rDA healing were chosen as healing mechanisms. The self-healing composites are composed of three main components: the inorganic filler, the polymer matrix and the coupling agent. The first section of this work therefore deals with the synthesis and optimization of suitable particle systems. Two requirements must be met and therefore determine the particle choice. The first requirement is that the particles can be heated by introduction into an alternating magnetic field to potentially trigger the healing process. Compared to healing in a conventional oven, this offers the advantage that healing can be performed spatially resolved, which does result in a lower thermal load on the intact material. Furthermore, the heat is generated intrinsically so that, unlike diffusion-controlled heating in an oven, a uniform temperature increase in the material can be achieved. This allows healing at macroscopically lower temperatures. The second requirement is that the particles can be well incorporated into the polymer matrix. Therefore, the following section deals with the tailoring of the particle surface to improve this incorporation or even allowing the particles to be part of the self-healing process itself. The next aspect is the design of polymer matrices including the synthesis of suitable functional monomers and the optimization of the polymerization process. Finally, self-healing nanocomposites were obtained by combining the organic and inorganic components. In the following, the performed studies will be described in more detail.

2.2. Concept

Selection of a suitable particle system

Iron oxide nanoparticles were chosen as the particle system, which, in addition to their thermal and mechanical stability, also introduce interesting magnetic properties with their superparamagnetic behavior, including heating in an alternating magnetic field. Mixed iron oxides were synthesized via thermal decomposition. The particles were characterized using DLS, TEM, XRD, FTIR spectroscopy, TGA and CHN analysis. The chemical composition and magnetic properties of particles was determined using ICP-MS and Mößbauer spectroscopy, respectively. The SARs of the particles were determined by induction heating experiments to determine the suitability of the systems for the further use as nano heaters.

Ionic self-healing nanocomposites

With regard to the ionic functionalization of the particles, the molecular phosphonic acid derivatives 6-phosphonohexylsulfonic acid and *N,N,N*-trimethyl-6-phosphonohexane-1-

Research Goals

ammonium bromide were used, which generate charged surfaces that are largely independent of pH. In addition to the permanent attachment of these ionic groups to the particles, systems for the reversible attachment of ionic groups were designed in order to achieve switchability of the surface polarity. This was achieved by using phosphonic acid derivatives that allow the reversible introduction of ionic groups via DA/rDA reactions. The obtained systems permit temperature-controlled switching of the surface polarity and a high stability of the charge towards pH changes, which is an advantage over the unfunctionalized metal oxide particle systems. The coupling agents were characterized by NMR, FTIR and CHN analysis. The particle functionalization was studied by FTIR spectroscopy, TGA, CHN, and ICP-MS. The stability of the charges was investigated using zeta potential measurements.

The ionic interaction between positively functionalized particles and negatively charged polymers, prepared via ATRP or FRP of sodium 4-(methacryloyloxy)butane-1-sulfonate and di(ethylene glycol) methyl ether methacrylate, was used as the healing mechanism. The systems were characterized using NMR and FTIR spectroscopy, as well as TGA, CHN analysis and DSC. Polymer composition and particle content of the composites were investigated as parameters to adjust the composite properties. Furthermore, it was examined whether the heating of the particles in the alternating magnetic field is suitable to induce the healing process. This was examined optically with a microscope and quantitatively using tensile tests. Another central aspect is the investigation of environmental influences, especially humidity and temperature, on the mechanical properties and particle distribution within the polymer systems. This was done by means of rheological studies, tensile tests, backscattered electron imaging (BSE) SEM and SAXS.

In addition, preliminary studies were conducted to investigate whether the stability and healing efficiency of ionic nanocomposites are better when the ionic interactions are located at the phase boundary or in the polymer network. Therefore, in addition to the systems described in the last section, composites should be prepared in which the ionic interactions take place purely within the polymer. This was to be done by SI-ATRP in order to control the system as well as possible to avoid competing processes such as polymerization in solution. For this purpose, two suitable initiator systems were synthesized and immobilized on the particle surface. In initial investigations, composites were prepared by SI ATRP of non-ionic model monomers. The initiators were characterized by NMR and FTIR spectroscopy, as well as CHN analysis. The functionalized particles and composites were characterized by FTIR spectroscopy, ICP-MS, TGA, CHN analysis and TEM.

Double self-healing systems

In the last section, the alternating magnetic field triggered healing was transferred to an established self-healing system based on both hydrogen bonding and DA/rDA chemistry,

Research Goals

where the former already occurs at room temperature and the latter is thermally triggered. The polymers were characterized by NMR, FTIR spectroscopy and DSC. An urea-terminated phosphonic acid was synthesized and immobilized on the surface of iron oxide nanoparticles to achieve a stable incorporation of the particles in the polymer matrix via hydrogen bonding. Characterization was performed by NMR, FTIR spectroscopy and CHN analysis for the coupling agent and by TGA, CHN analysis, DLS, ICP-MS and FTIR spectroscopy for the functionalized particles. The self-healing of the nanocomposites was verified by optical microscopy, FTIR spectroscopy and DSC. Lastly, preliminary studies on the copolymerization of ionic and DA monomers to obtain an ionic double self-healing system were performed.

3. Results and Discussion

In the following, the results obtained during the doctorate will be presented. Details of the experimental procedure and the NMR and FTIR spectra of all compounds can be found in the experimental and a separate appendix. The zeta potential, SAXS and electron microscopy measurements were performed at the INM - Leibniz Institute for New Materials in Saarbrücken. The zeta potential measurements were conducted by Sarah Schumacher. The SAXS data were recorded and fitted by Dr. Björn Kuttich and Dr. Bart-Jan Niebuur. The TEM and SEM measurements were performed by M.Sc. Lucas Niedner, Dr. Nadja Klippel, Dr. Thomas Klein, Dr. Christina Odenwald or M.Sc. Mana Mohammed from the Inorganic Solid State Chemistry group at Saarland University. The tensile tests were performed by the Applied Mechanics group at Saarland University under the direction of Prof. Dr.-Ing. Stefan Diebels and Prof. Dr.-Ing. Dr. rer. nat. Anne Jung. The Mößbauer spectroscopy was performed and evaluated by M.Sc. Aylin Koldemir at the institute of Inorganic and Analytical Chemistry at the University Münster.

3.1. Synthesis and Characterization of the Metal Oxide Nanoparticles

This chapter contains the synthesis and characterization of the iron oxide, as well as cobalt- and manganese-iron mixed oxide nanoparticles. All three types of metal oxides are suitable for induction heating, which can potentially be used to trigger healing or initiate reactions on the particle surface. The goal of the synthesis was to produce superparamagnetic particles. The magnetic properties are significantly influenced by the particle size. While the magnetic moment increases with particle size [222,223], a transition from ferrimagnetism to superparamagnetism is typically observed for particle sizes < 20 nm.[216] The loss of permanent magnetization increases the chances of obtaining well-distributed particles, as the particles with permanent magnetization often undergo pre-orientation and cluster together. Therefore, the targeted particle size was in the range of 5 nm - 15 nm. A variety of methods are available for the synthesis of metal oxide particles. The starting compounds are usually chlorides, nitrates, organic complexes or alkoxides. In these studies, acetylacetonate complexes of iron, cobalt and manganese were used. In the case of the mixed oxides, an M:Fe ratio of 1:2 was chosen. Since the exact composition of the particles was not determined for each batch, the systems will be referred to below as Fe_xO_y , $Mn_{1-x}Fe_{2+x}O_4$ and $Co_{1-y}Fe_{2+y}O_4$. The particles were obtained by thermal decomposition in the presence of oleylamine, oleic acid, and 1,2-dodecanediol, using benzyl ether as a solvent. The synthesis was carried out according to literature procedure with minor modifications.[261] The particles were prepared in two 30-minute temperature steps at 200 °C and 300 °C. This method was chosen because it provides a narrow size distribution even in the < 20 nm range and allows easy purification by magnetic decantation. All particles used in this work were stored as dispersions and under an

Results and Discussion

argon atmosphere to avoid irreversible agglomeration and oxidation of the particles. To allow for a subsequent introduction of other surface functionalities by ligand exchange, the weakly binding oleic acid was added during synthesis for particle stabilization.

The size of the prepared particles was measured by DLS using *n*-hexane as the dispersion medium (see Figure 8).

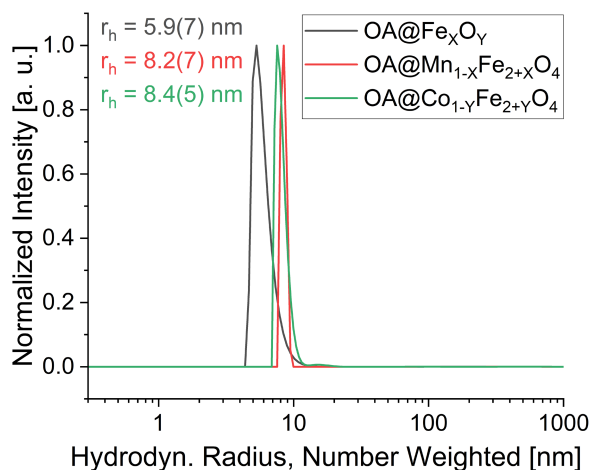


Figure 8: DLS measurement of OA@Fe_xO_y, OA@Mn_{1-x}Fe_{2+x}O₄ and OA@Co_{1-y}Fe_{2+y}O₄ in *n*-hexane.

The number-averaged hydrodynamic diameters of the obtained particle systems were 11.8 nm for the Fe_xO_y, 16.4 nm for the Mn_{1-x}Fe_{2+x}O₄ and 16.8 nm for the Co_{1-y}Fe_{2+y}O₄ particles, respectively. Thus, the hydrodynamic diameter is within the targeted range and no agglomerates are obtained.[271] It should be noted, that although DLS is well suited for checking whether the particles are agglomerated, the hydrodynamic diameters determined by DLS give only a rough estimate of the particle size. The hydrodynamic radius corresponds to the radius of a hypothetical solid sphere that has the same diffusion properties in the dispersion medium as the particle described by the hydrodynamic radius. As a result of that, the actual particle diameter can be significantly smaller depending on the functionalization and the strength of the interaction with the surrounding solvent, making the hydrodynamic radius unsuitable for calculating surface loadings. Therefore, additionally TEM was carried out. The micrographs are shown in Figure 9.

Results and Discussion

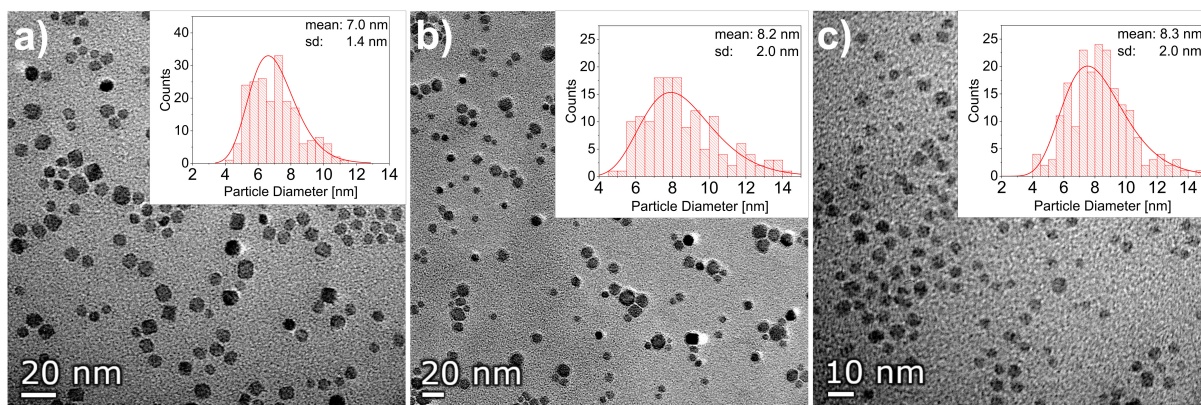


Figure 9: TEM images of a) $OA@Fe_xO_y$, b) $OA@Mn_{1-x}Fe_{2+x}O_4$ and c) $OA@Co_{1-y}Fe_{2+y}O_4$. Histograms: Statistical size distribution of the particles ($N = 200$).

For all samples, well dispersed particles are obtained even after drying on the TEM grids. The micrographs were analyzed using the program imageJ.[593] For each sample, 200 particles were measured. A log-normal distribution was obtained for all three metal oxides. With a mean diameter of 7.0 nm, the iron oxide particles are slightly smaller than the mixed oxides, which have a mean diameter of 8.2 nm and 8.3 nm for the manganese and cobalt mixed oxides, respectively.

The good stabilization in *n*-hexane during DLS also indicates that the functionalization with oleic acid was successful. This was further investigated by FTIR spectroscopy. Figure 10 shows the FTIR spectra of the synthesized particles in comparison with that of pure oleic acid.

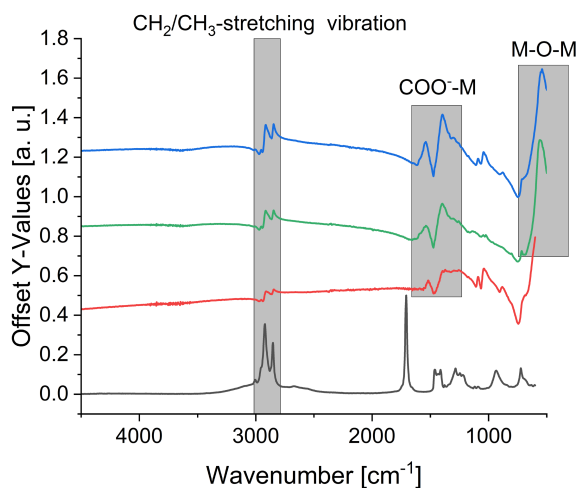


Figure 10: FTIR spectra of oleic acid (black), $OA@Fe_xO_y$ (red), $OA@Mn_{1-x}Fe_{2+x}O_4$ (green) and $OA@Co_{1-y}Fe_{2+y}O_4$ (blue).

The symmetric and asymmetric C-H stretching vibrations at 2855 cm^{-1} and 2932 cm^{-1} are clearly visible in all particle samples. Furthermore, the signals of the bound carbonyl functionality can be detected, although they are strongly damped, indicating a successful functionalization. Finally, the signal of the particle framework oscillation (Fe-O-Fe) can be seen at 533 cm^{-1} . To quantify the organic content, the particles were analyzed using TGA and CHN

analysis. For the TGA, the particles were first heated to 880 °C under N₂ and then to 1000 °C under synthetic air. The curves obtained are shown in Figure 11 a).

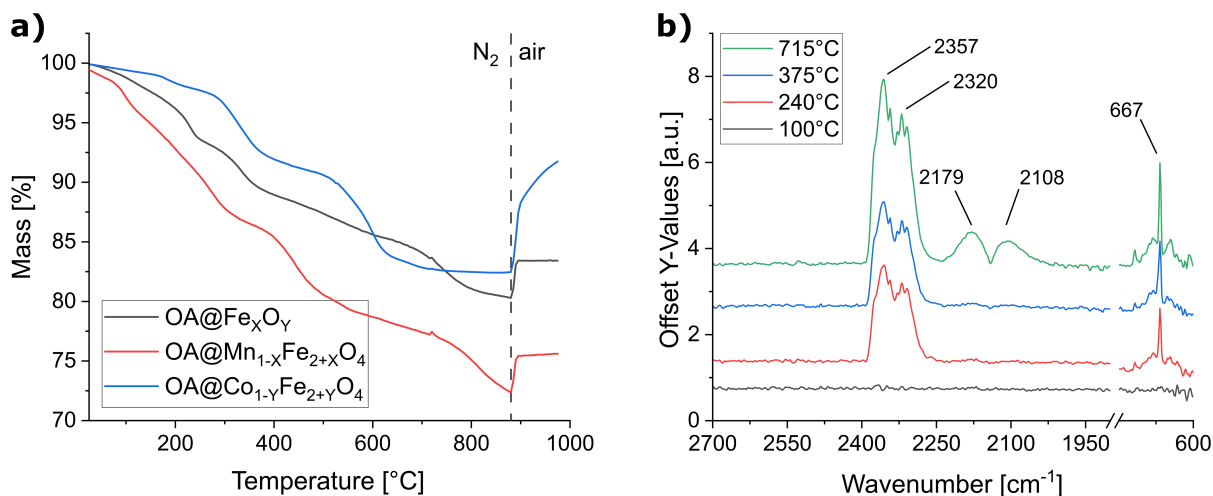


Figure 11: a) TGA curves of the oleic acid functionalized nanoparticles. The samples were heated from room temperature to 880 °C under nitrogen atmosphere, followed by heating to 1000 °C under a mixture of nitrogen and oxygen (4:1) with a rate of 10 K/min. b) FTIR spectra of the gas phase of OA@Fe_xO_y during the decomposition steps, temperatures as indicated.

For all samples a three-step mass loss is observed in the N₂ segment. The largest differences between the three particle systems result from the first two mass loss steps where the physical, adsorbed and covalently bound OA is largely decomposed.[594] The third mass loss, which occurs at significantly different temperatures for the three particle systems, is due to the reduction of the particles. The varying temperatures can therefore be attributed to the different redox potentials of the particles. Lai *et al.* showed that iron oxide nanoparticles without the OA coating showed no mass loss in this range.[595] This means that during the pyrolytic decomposition of OA in the first two steps, some residual organic material is left on the surface. This is oxidized to CO and CO₂ in the third step as the particles are reduced. Both the formed CO₂ (667 cm⁻¹, 2320 cm⁻¹, 2357 cm⁻¹) and CO (2108 cm⁻¹, 2179 cm⁻¹) were observed in coupled TG-FTIR measurements, which is shown exemplarily for the OA@Fe_xO_y system in Figure 11 b). The lowest total mass loss of 17.55 % is observed for the cobalt-based system. The pure iron oxide system also shows a comparable mass loss of 19.71 %, while a higher loss of 27.64 % is observed for the manganese-doped sample. The reason for this significant deviation of manganese mixed oxide has not yet been identified. For all systems, a significant increase in mass is observed in TGA after the introduction of synthetic air. This is due to oxidation of the particles. The samples were examined by CHN both before and after heating to 880 °C under nitrogen, as well as after the air segment. A summary of the TGA and CHN data (before heating) is shown in Table 1.

Results and Discussion

Table 1: TGA and CHN results of the oleic acid functionalized nanoparticles.

Sample	TG Residual Mass [%]		CHN [%]		
	25-880 °C	880-1000 °C	C	H	N
	N ₂	air			
OA@Fe _x O _y	80.29	83.42	9.09	1.71	-
OA@Mn _{1-x} Fe _{2+x} O ₄	72.36	75.61	13.30	1.52	-
OA@Co _{1-y} Fe _{2+y} O ₄	82.45	91.75	6.40	1.22	-

After the heating segment under N₂ no carbon or hydrogen was detected by CHN, indicating a complete decomposition of the organic, even before contact with oxygen. In agreement with the TGA results, the CHN results for OA@Mn_{1-x}Fe_{2+x}O₄ also show a higher organic content. It is also noteworthy that TGA based calculations yield significantly higher surface coverages than the CHN. The reason for this is the previously described partial reduction of Fe(III) to Fe(II) in the N₂ segment. This is accompanied by a reduction of the particle mass and thus simulates a higher organic content. A more detailed discussion of the processes during TGA can be found in the XRD section below.

In order to accurately determine the particle loading by TGA, it is necessary to identify the particle composition and its change in the N₂ segment. For this purpose, XRD measurements were performed. The Rietveld method was used for fitting. The diffractograms of the initial particles are shown in Figure 12.

Results and Discussion

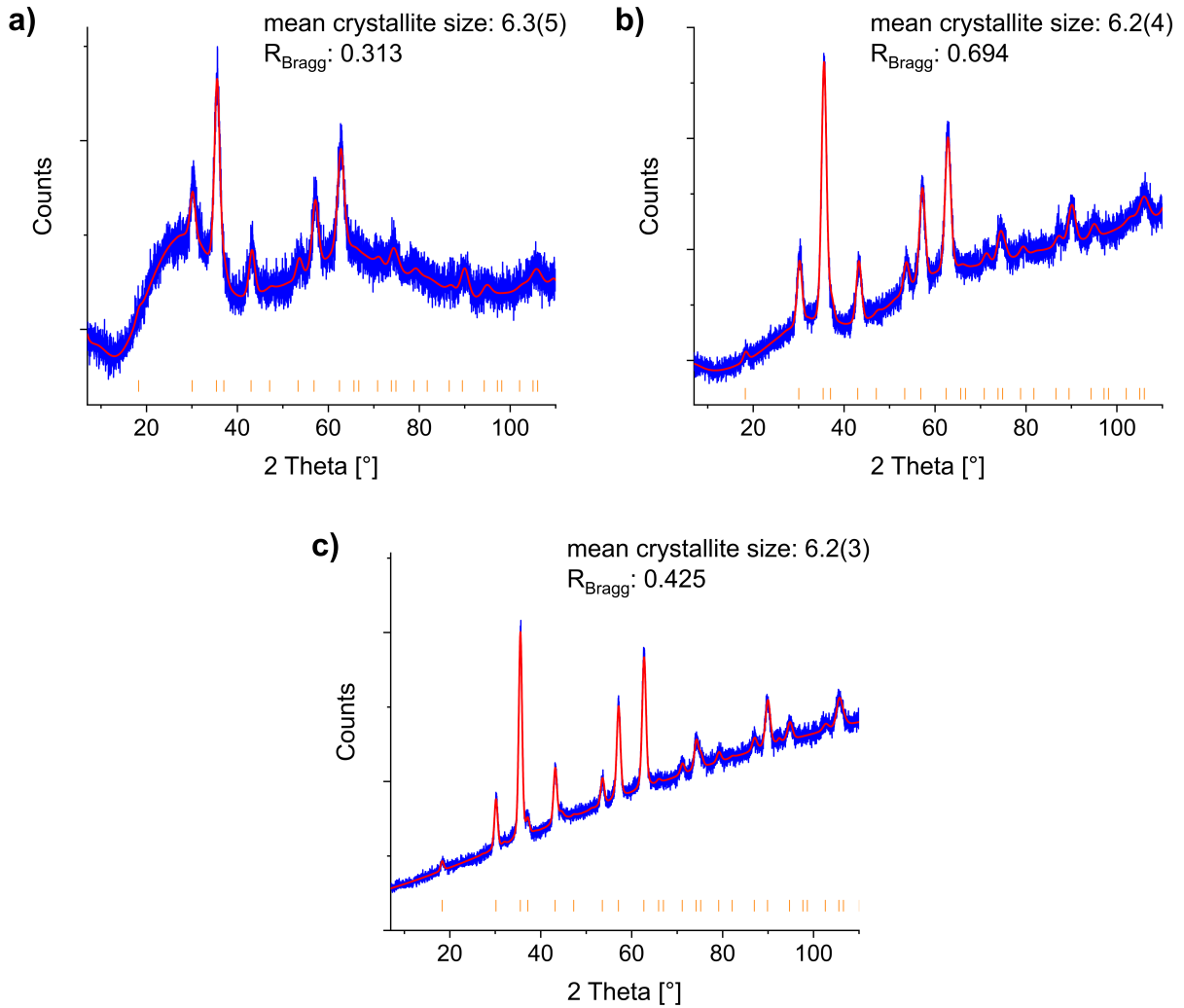


Figure 12: X-ray diffractograms and Rietveld refinements of a) OA@Fe_xO_y, b) OA@Mn_{1-x}Fe_{2+x}O₄ and c) OA@Co_{1-y}Fe_{2+y}O₄. Blue: experimental data, red: Rietveld refinement, orange: hkl-values. Reference taken from COD1513301/ COD2300618/ COD1533163.[596–598]

The broad signals at 30° and 60°, particularly pronounced in the case of OA@Fe_xO_y, originate from the glass slides on which the samples were prepared and are not from the product phase. In general, broad reflexes are obtained for the samples, indicating nanocrystalline materials. The three systems obtained crystallize phase-pure in the space group $Fd\bar{3}m$. The size of the crystalline ordered domains was determined from the integral breadth of the signals. With a crystallite size of 6.3 nm for OA@Fe_xO_y and 6.2 nm for the two mixed oxides, these agree not only with each other but also with the particle sizes determined in TEM, showing that almost completely crystalline particles are obtained. Due to the coinciding structure of maghemite and magnetite (the maghemite phase corresponds to a cation-deficient magnetite), the similar electronic situation and the small crystallite size, it is difficult to distinguish between the two phases. The same applies to the cobalt- and manganese-iron mixed oxides, which prevents an accurate characterization of the particle composition by XRD.

Nevertheless, in the next step, a temperature dependent XRD measurement was performed to see if other phase transitions occur during TGA. For this exemplarily the OA@Fe_xO_y system

Results and Discussion

was used. The sample was heated to 800 °C in vacuum ($5 \cdot 10^{-3}$ mbar) and an XRD measurement was taken every 100 °C. The results are shown in Figure 13.

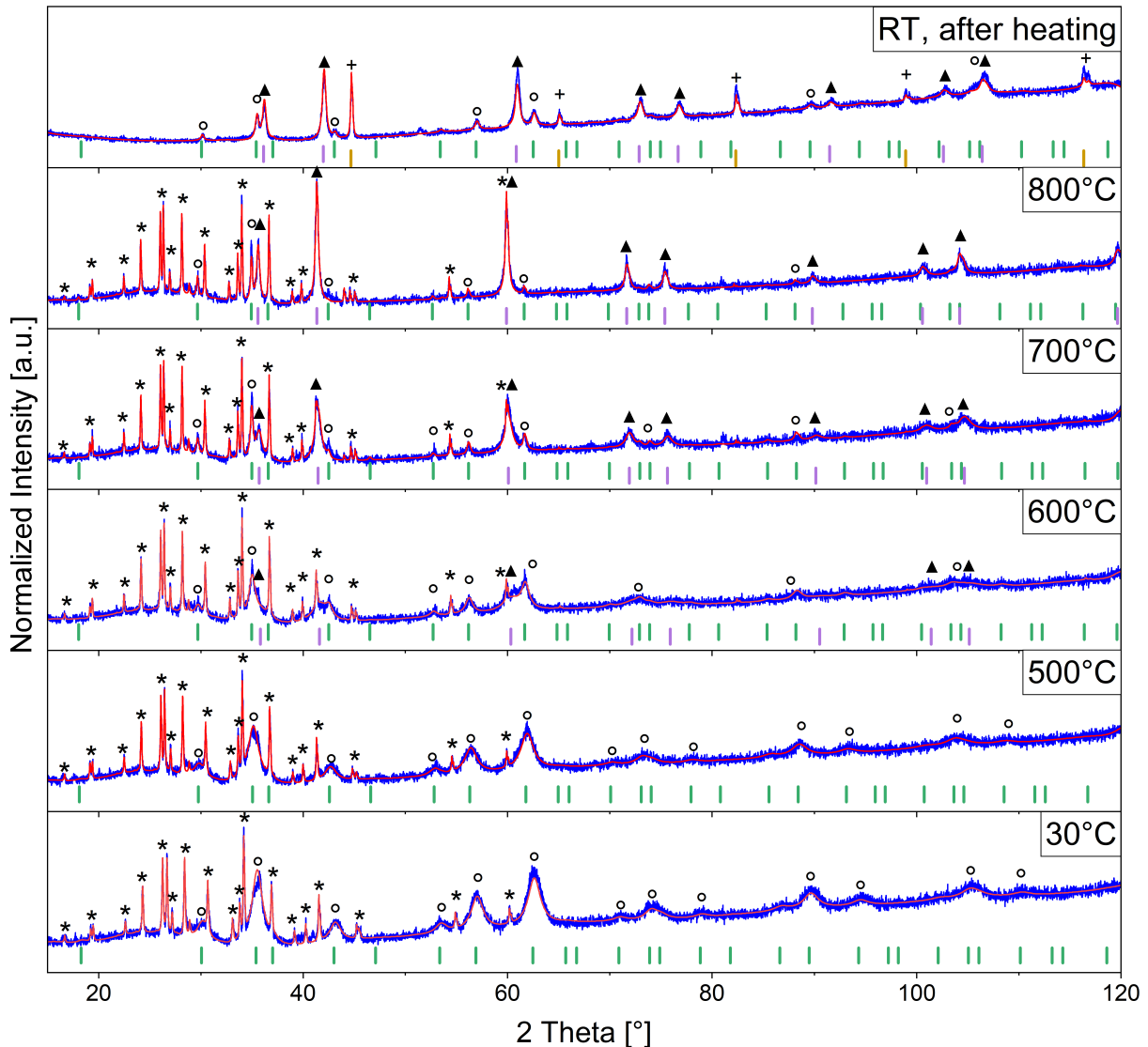


Figure 13: Temperature dependent XRD of OA@Fe_xO_y. * = Signals of the sample holder, ▲/green = reflections/hkl values of Fe₃O₄, ▲/purple = reflections/hkl values of FeO, ▲/orange = reflections/hkl values of Fe. Temperatures are as indicated in the graph. Reference taken from COD1513301, COD1011169 and COD2300202.[596,599,600]

Contrary to previous measurements, the samples were prepared on a heat resistant Macor® sample holder. This is a crystalline material that causes sharp reflections in the small angle range. These are marked with stars. An exception to this is the measurement at room temperature after heating, which was measured on a silicon single crystal holder. Examination of the particle reflections shows that they are entirely represented by the maghemite or the magnetite phase at temperatures up to 500 °C. However, it should be pointed out that a partial reduction from maghemite to magnetite in this temperature range cannot be excluded by XRD and seems likely in view of the CO₂ and water signals in the FTIR spectrum of the gas phase observed during this initial mass loss at 240 °C (Figure 11 b). When the particles are heated, no changes in crystallite size can be detected within the range of the measurement accuracy.

Results and Discussion

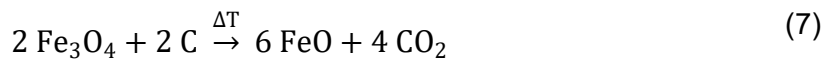
The lattice parameter of the cubic system shows an increase from 8.403(3) nm to 8.485(2) nm, which is within the expected range due to the thermal expansion of the material. Starting from 600 °C, a significant decrease in the initial reflections is observed. Furthermore, additional reflections occur. Because of the difficulty in identifying the phases due to the superposition of the sample holder reflections, the sample was removed from the sample holder after heating and measured on a silicon single crystal holder. In addition to magnetite (24.09 %), wüstite (63.33 %) and elemental iron (12.58 %) were identified as product phases. These phases were then used to fit the diffractograms at the higher temperatures. At 600 °C, only 50.30 % of the material is present as Fe₃O₄. With further temperature increases to 700 °C and 800 °C, the fraction decreases further to 26.68 % and 14.14 %, respectively. No elemental iron was observed. The rest of the material was reduced to FeO. Lai *et al.* propose the following mechanism [595]:



Further the literature regularly refers to a second superimposed signal in this reduction step, which is often times described as a result of the following reaction [595,601]:



However, the temperature dependent analysis showed that no elemental iron is formed during the heating step. The appearance of both CO and CO₂ in the TG-FTIR during this mass loss at > 600 °C (Figure 11 b) suggests that the second superimposed signal is more likely to be caused by the following reaction:



Subsequently, the obtained FeO disproportionates to elemental iron and magnetite upon cooling back to room temperature, explaining the renewed increase in Fe₃O₄ content and the appearance of iron in the measurement on the single crystal holder. The disproportionation occurs according to the following equation:



Due to the reactions (5) and (7) during TGA, the number of oxygen atoms in the particle lattice and thus the particle mass decreases, simulating a higher organic content. Since both the initial particle compositions are not constant from batch to batch and even depend on the storage time of the particles, calculated surface coverage based on TGA data should be used with caution, although they are well suited for relative comparisons within a particle batch.

ICP-MS measurements were performed to further characterize the cobalt- and manganese-iron mixed oxides. For the cobalt containing particles, an M:Fe ratio of 1:7.8 was obtained, and for manganese only a ratio of 1:29.7. This is significantly lower than the initially used precursor

Results and Discussion

ratio of 1:2 (M:Fe) and rather deviating from the ratio reported by Sun *et al.*[261] This effect is known from the literature for both mixed oxides. It is due to the different decomposition temperatures of the metal acetylacetonates.[602] Especially for $\text{Mn}(\text{acac})_2$, which initiates decomposition at $\approx 250\text{ }^\circ\text{C}$, a temperature $\approx 50\text{ }^\circ\text{C}$ higher than that of $\text{Fe}(\text{acac})_3$ [603,604], this can lead to an incomplete decomposition of the precursor or the formation of manganese-rich phases, which are removed during the washing steps. This results in low manganese concentrations in the remaining particles.[605] The poor reproducibility of the mixed oxides can be attributed to the lack of temperature control with the highly contact-dependent heating mantle setup. Nevertheless, all three particle samples were investigated for their suitability for magnetic field induced heating, as the main application of the particles will later be as nano heaters for self-healing. For this purpose, 2 wt% particle dispersions were prepared in xylene and introduced into an alternating magnetic field. The 2 wt% refer to the magnetic material, so the weight was corrected for the determined organic on the surface. Due to the previously described problem with the TGA data, the CHN data was used for this purpose. It was assumed that the carbon content originates entirely from the bound oleic acid. To minimize heat exchange with the environment during induction heating, a sealed double-walled vessel was used. The temperature was measured using a fiber optic temperature sensor which was placed directly in the dispersion through a septum. The temperature evolution was determined at a field strength of 0.62 kA/m generated by a 1997 1G 5/3000 high frequency generator. In Figure 14 the time-dependent temperature evolution of the samples in the magnetic field is shown.

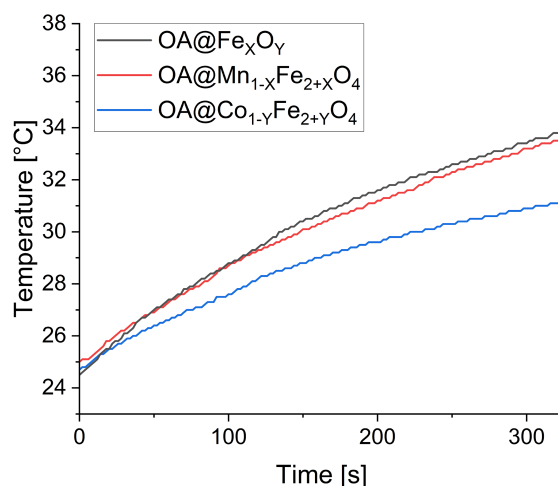


Figure 14: Heating studies for 2 wt% oleic acid functionalized particles in xylene in an alternating magnetic field. Frequency: 1.95 MHz, field strength: 0.62 kA/m.

Overall, the particle systems showed a comparable heat generation, which is surprising at first, since higher saturation magnetizations and thus higher heating efficiencies are expected for the mixed oxides. However, this is explained by the fact that only very small amounts of cobalt and manganese could be incorporated into the iron oxide lattice. For the $\text{OA@Fe}_x\text{O}_y$ system a maximum temperature of $33.4\text{ }^\circ\text{C}$ was measured after five minutes. In the case of

Results and Discussion

OA@Mn_{1-x}Fe_{2+x}O₄, a temperature of 33.2 °C and in the case of OA@Co_{1-y}Fe_{2+y}O₄ a temperature of 30.9 °C was determined after the same heating time. The SAR values for the three particle systems were determined from the temperature increase in the first 60 s using Equation (1). The values for OA@Fe_xO_y, OA@Mn_{1-x}Fe_{2+x}O₄ and OA@Co_{1-y}Fe_{2+y}O₄ were 63.5 W/g, 51.6 W/g and 41.9 W/g respectively. This is in the usual range for iron oxides rather than the mixed oxides, again supporting the observations from ICP-MS.[221,606,607] Nonetheless, all three particle systems are usable for magnetic field-induced heating.

Finally, the magnetic properties of the particle systems were investigated by Mößbauer spectroscopy. Figure 15 shows the spectra obtained for the OA@Fe_xO_y particles at room temperature and at 78 K.

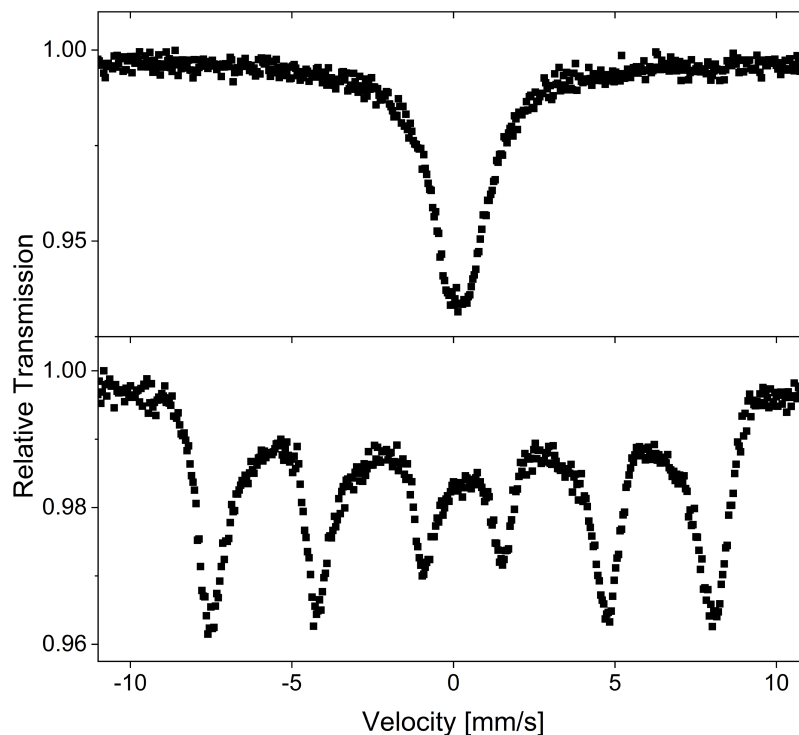


Figure 15: ⁵⁷Fe Mößbauer spectra of OA@Fe_xO_y, recorded at room temperature (top) and 78 K (bottom).

No hyperfine field splitting is observed for the OA@Fe_xO_y particles at room temperature. Instead, a poorly resolved quadrupole doublet is detected. This is because of fast superparamagnetic relaxation.[608–611] An isomeric shift of 0.14(2) mm/s was observed. Due to the nanocrystalline nature and the resulting poorly defined coordination, a rather high linewidth is obtained, which does not allow a definitive statement about coordination or oxidation state, although the characteristic black color of the particles strongly suggests the presence of the mixed oxide. After cooling the sample to 78 K, a moderately well resolved magnetic hyperfine splitting is observed, even without applied field. This means that the Brownian and Néel relaxation are suppressed and thus the magnetic moments are frozen in

the ordered ferrimagnetic state. The observed uneven baseline indicates that the system is in the region of the blocking temperature. However, further measurements are needed to determine the exact temperature.

Likewise, the $\text{OA@Co}_{1-y}\text{Fe}_{2+y}\text{O}_4$ and $\text{OA@Mn}_{1-x}\text{Fe}_{2+x}\text{O}_4$ systems were investigated. The results are shown in Figure 16.

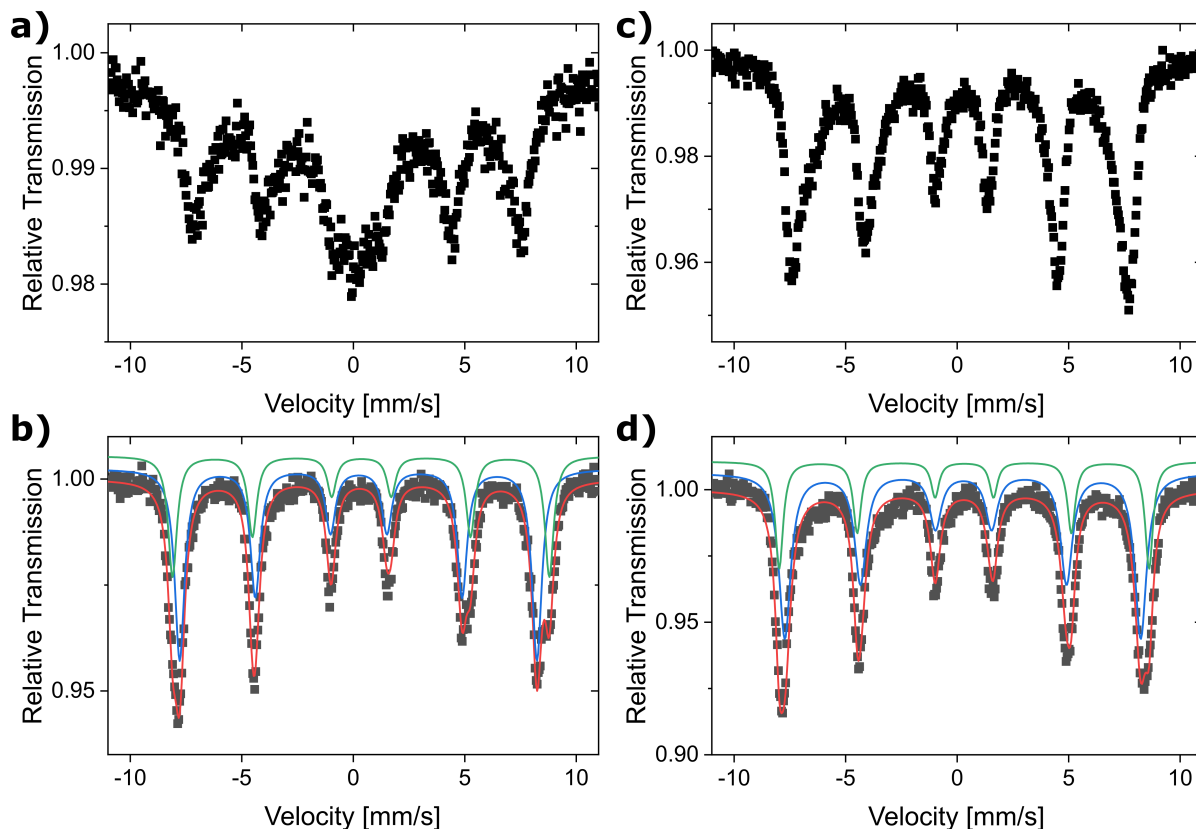


Figure 16: Experimental (data points) and simulated (colored lines) ^{57}Fe Mößbauer spectra of a)/b) $\text{OA@Co}_{1-y}\text{Fe}_{2+y}\text{O}_4$ and c)/d) $\text{OA@Mn}_{1-x}\text{Fe}_{2+x}\text{O}_4$ recorded at room temperature (top) and 78 K (bottom).

In contrast to the $\text{OA@Fe}_x\text{O}_y$ particles, the cobalt- and manganese-iron mixed oxides exhibit hyperfine splitting at room temperature. In the case of the $\text{OA@Co}_{1-y}\text{Fe}_{2+y}\text{O}_4$, a superposition of the Zeeman sextet of the blocked component and the quadrupole doublet of the superparamagnetic component is obtained. This indicates that the blocking temperature is close to room temperature. Thus, depending on their size, some of the particles are in the blocked state and some are in the superparamagnetic state.[610] The manganese-containing samples, on the other hand, already show a well resolved hyperfine structure at room temperature. This means that the magnetic properties seem to change from superparamagnetism to a permanent magnetic state. This observed increase in the blocking temperature of the mixed oxides is in good agreement with literature reports [612–614], although it is surprising that the small amounts of cobalt and manganese have such a large influence. At 78 K, a well resolved hyperfine structure is obtained for both mixed oxides. In contrast to the $\text{OA@Fe}_x\text{O}_y$ particles, a flat baseline is obtained, confirming that the systems

are well below the blocking temperature. In addition, the introduction of cobalt or manganese makes it possible to distinguish between tetrahedral (blue) and octahedral (green) coordinated iron by a stronger splitting of the signals. However, the low resolution and high width of the signals does not allow a precise quantification of the occupation of the octahedral and tetrahedral gaps.

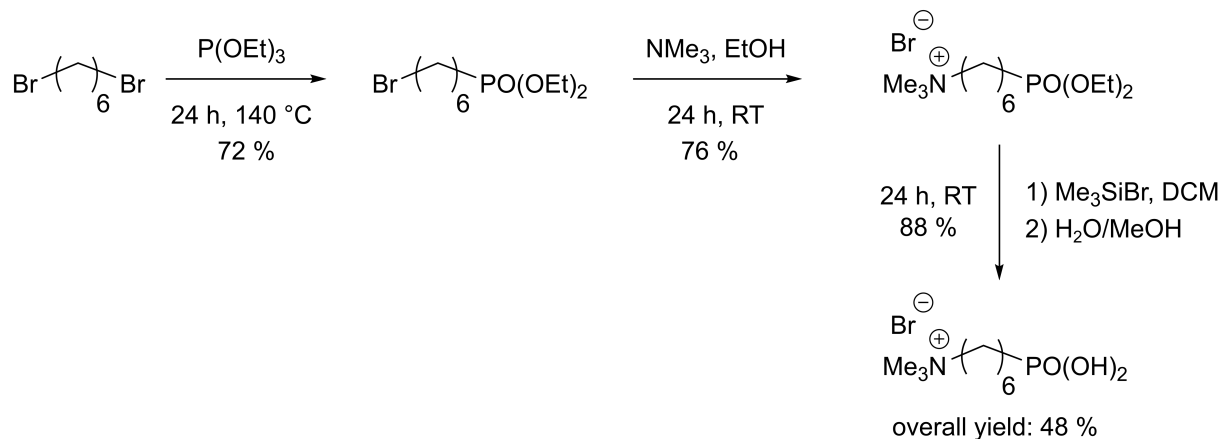
In summary, it can be said that with the addition of cobalt and manganese, even in small amounts where the heating efficiency still seems to be largely unaffected, the magnetic properties change from superparamagnetism for the $\text{OA@Fe}_x\text{O}_y$ to a permanent magnetic state for the $\text{OA@Co}_{1-y}\text{Fe}_{2+y}\text{O}_4$ and $\text{OA@Mn}_{1-x}\text{Fe}_{2+x}\text{O}_4$ at room temperature. Since the integration of cobalt and manganese does not change the structure of the iron oxide, but only involves a partial substitution of Fe(II), a monotonic structure-property relationship should result. Therefore, it is to be expected that if more cobalt and manganese are integrated the blocking temperature rises further and thus a permanent magnetization prevails. This is associated with the risk of particle agglomeration due to magnetic interactions. For this reason, the $\text{OA@Fe}_x\text{O}_y$ particles were used exclusively for the following studies and no further optimization of the cobalt and manganese systems was carried out.

3.2. Synthesis of Permanently Charged Nanoparticles

The aim of this study was to synthesize iron oxide nanoparticles with a permanent ionic charge that is not or only slightly affected by changes in the surrounding medium. Therefore, carboxylic acids and amines are not good choices because their protonation and thus their charge is strongly pH dependent. Quaternary amines are excellent groups to introduce positive charges to the particle surface due to their pH-independent positive charge and synthetic accessibility. Sulfonates were used as anionic groups, which are negatively charged over a wide pH range due to their low pK_A value.[343] All functionalization reagents used here have the same structure. The desired ionic group is attached via a spacer, in this case a C_6 linker, to an anchor group that binds to the particle surface. This spacer length of 6 was chosen because shorter functionalization reagents do not generate the necessary steric repulsion to maintain stable particle dispersions and thus often lead to agglomeration. In addition, the corresponding 1,6-dibromohexane, which is needed as the starting compound for the synthesis, is readily available, unlike the longer-chain derivatives. Organophosphorus molecules bearing functional groups are ideal molecules for the surface-functionalization of transition metal oxide systems, due to their strong binding to the surface, their high chemical stability and the variety of functions that can be incorporated into the molecules.[273,347] In the following, the synthesis routes for the ionic phosphonic acid derivatives and the subsequent functionalization of the particles are described.

3.2.1. Synthesis of the Cationic Functionalization Reagent

The synthesis of the cationic phosphonic acid is shown in Scheme 14 and was performed according to literature procedure.[269]



Scheme 14: Synthesis route for *N,N,N*-trimethyl-6-phosphonohexan-1-ammonium bromide.[269]

The synthesis of the cationic phosphonic acid was carried out in three steps. As described above, the starting material is the commercially available 1,6-dibromohexane. In a Michaelis-Arbusow reaction it is converted to the corresponding phosphonic acid ester. The product was obtained in 72 % yield as a colorless oil. In the next step a positive charge is introduced by a nucleophilic substitution of the bromo functionality using trimethylamine. After filtration, a white solid was obtained in 76 % yield. Finally, the phosphonic acid ester was hydrolyzed. For this purpose, the phosphonic acid ester is first converted to the less stable silyl ester and then hydrolyzed with a water/methanol mixture. The reaction was carried out in 88 % yield. CHN analysis as well as NMR and FTIR spectroscopy confirmed the product formation with an overall yield of 48 %.

3.2.2. Cationic Particle Functionalization

An exchange protocol for the oleic acid molecules against the *N,N,N*-trimethyl-6-phosphonohexan-1-ammonium bromide was developed. The functionalization of the iron-oxide particles was carried out in a dispersion, which allowed an isotropic functionalization. The exchange with the organophosphorus coupling reagent was optimized to achieve a maximum densely packed monolayer. Phosphonic acid to particle ratios between 0.025 to 0.6 mmol per 150 mg nanoparticles were investigated, to cover the gradual substitution of the oleic acid. The upper limit was chosen in accordance with literature reports to achieve maximum surface loading.[271] The value of 0.6 mmol per 150 mg of particles corresponds to the 5-fold excess necessary for maximum dense monolayer on the particle surface. The calculation was performed according to equation (9), assuming that the phosphonate group

Results and Discussion

occupies an area of 24 \AA^2 [298] and that the phase pure Fe_3O_4 particles have a uniform size of 10 nm.

$$R = \frac{A_{\text{Phos,tot}}}{A_{\text{Part,tot}}} = \frac{\rho_{\text{Fe}_3\text{O}_4} \cdot r_{\text{Part}} \cdot N_A \cdot A_{\text{Phos}} \cdot n_{\text{Phos}}}{m_{\text{ref}} \cdot 3} \quad (9)$$

R = R-fold excess necessary for maximum dense monolayer

$A_{\text{Phos,tot}}$ = Total area that can be covered by the phosphonate

$A_{\text{Part,tot}}$ = Total particle surface area in reference mass

$\rho_{\text{Fe}_3\text{O}_4}$ = Density of Fe_3O_4 [g/m^3]

r_{Part} = Particle radius [m]

N_A = Avogadro constant [mol^{-1}]

A_{Phos} = Space requirement phosphonic acid group [m^2]

n_{Phos} = Number of moles of phosphonic acid per reference mass [mol]

m_{ref} = Reference mass = 0.150 g

These samples are hereafter referred to as $^{0.025}\text{P@Fe}_x\text{O}_y$ - $^{0.600}\text{P@Fe}_x\text{O}_y$. The oleic acid functionalized particles are easily dispersible in *n*-hexane, while the ionic functionalized particles are easily dispersible in polar solvents such as ethanol or water. As a result, the polarity of the particles increases significantly with increasing functionalization. Therefore, a mixture of *n*-hexane/ethanol (1:2) proved as a suitable dispersion medium to ensure stable dispersions of the particles throughout the entire exchange process. The stability of the particle dispersions in different solvents is shown as an example for the $\text{OA@Fe}_x\text{O}_y$ and $^{0.200}\text{P@Fe}_x\text{O}_y$ particles in Figure 17.

Results and Discussion

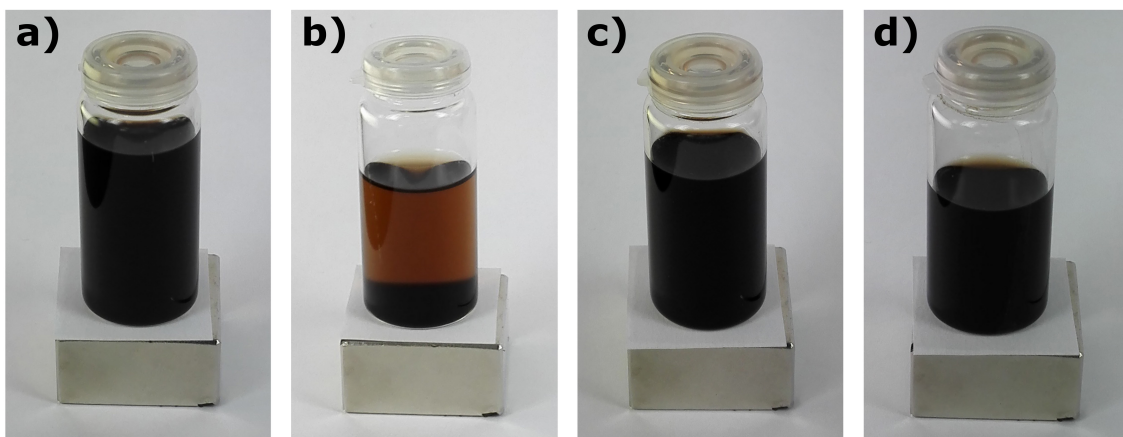


Figure 17: Particle dispersions of a) $OA@Fe_xO_y$ and b) $^{0.002}P@Fe_xO_y$ in *n*-hexane, as well as c) $^{0.002}P@Fe_xO_y$ and d) $OA@Fe_xO_y$ in *n*-hexane:ethanol (1:2).

Although the exchange typically occurs within a short time, the reaction medium was stirred for 24 hours to achieve as complete an exchange as possible. FTIR spectroscopy was used to characterize the cationic functionalized particles. For better comparability of the signals, all spectra were normalized to the Fe-O-Fe vibration at 536 cm^{-1} . The spectra obtained are shown in Figure 18.

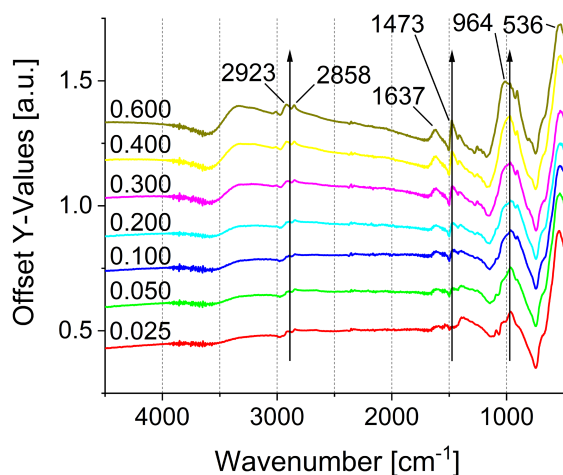


Figure 18: FTIR spectra of the cationic functionalized particles ($^{0.025}P@Fe_xO_y$ - $^{0.600}P@Fe_xO_y$).

The main characteristic of the modified particles is the signal at 964 cm^{-1} , which originates from the oscillation of the PO_3 unit, thus confirming the binding to the particle surface. The intensity of the signal increases successively with the amount of phosphonic acid added, indicating a progressing functionalization.[294,615,616] Furthermore, the FTIR spectra show an increase of the C-H stretching and deformation vibrations at $2945 - 2813\text{ cm}^{-1}$ and $1645 - 1402\text{ cm}^{-1}$. The C=O stretching vibration which is present in all samples as a broad signal at 1637 cm^{-1} proves a non-quantitative exchange of the oleic acid. Although the overall low signal intensity implies a low concentration of oleic acid on the surface. It nevertheless suggests that a significantly larger proportion of oleic acid remains on the surface than in similar exchange

Results and Discussion

protocols described in literature for DA or poly(ethylene glycol) based phosphonic acid derivatives.[271,275] This effect may result from the electrostatic repulsion of the cationic groups which increases with increasing surface coverage. In this context, Schmitt showed that functionalization with the charged 6-phosphonohexanoic acid leads to significantly lower functionalization densities than with alkyl phosphonic acids of comparable steric demand.[617] However, this influence is not entirely clear, as for this functionalization, in addition of the binding of the phosphonic acid, additional binding of the carboxylic acid to the particle surface is described, which may lead to faster saturation of the particle surface and thus to lower functionalization densities. ^{31}P NMR spectroscopy was performed on the supernatant solutions of the functionalization reaction mixtures (Figure 19), showing residual unreacted phosphonic acid starting from sample $^{0.100}\text{P}@Fe_xO_y$. This means that the particle surface is saturated.

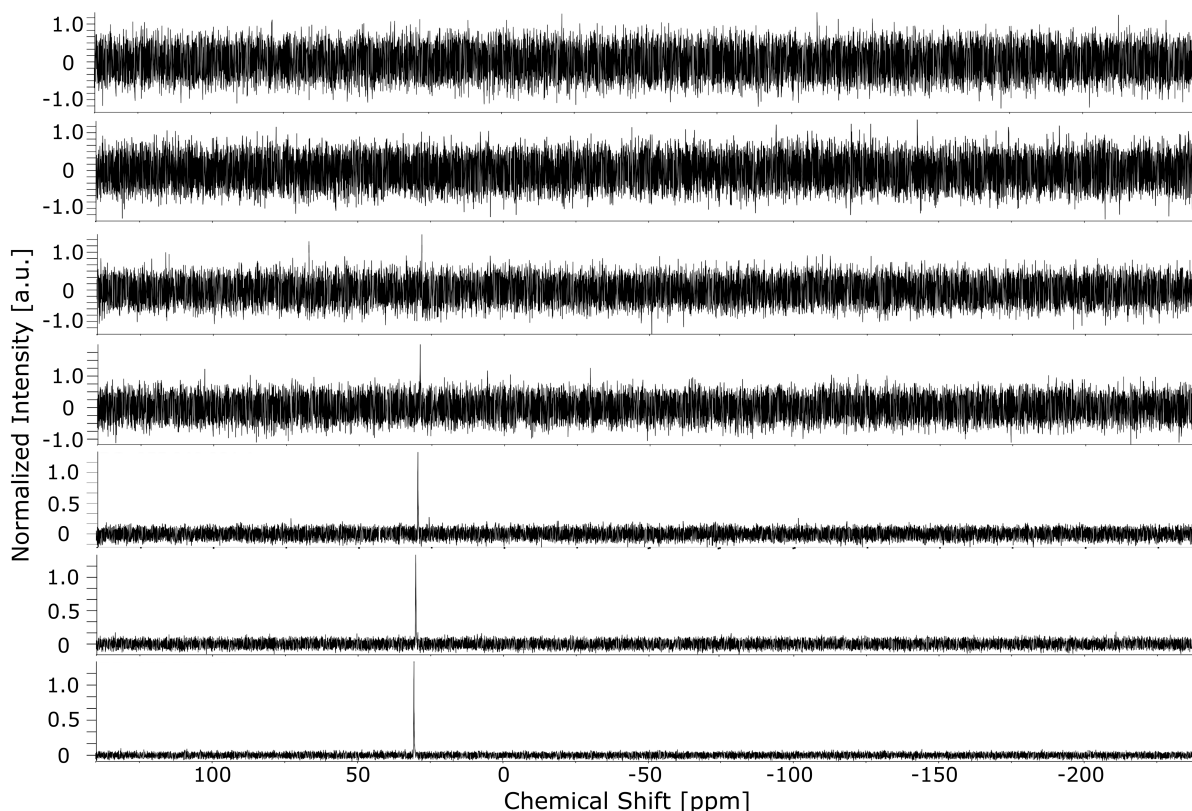


Figure 19: ^{31}P NMR spectra of the supernatant solutions of the functionalization reaction mixtures of $^{0.025}\text{P}@Fe_xO_y$ (top) - $^{0.600}\text{P}@Fe_xO_y$ (bottom).

The surface coverage after the exchange reaction was investigated by TGA and CHN analysis. The obtained TGA curves obtained are shown in Figure 20 a). Prior to the TGA measurements a 10-minute vacuum step at 100 °C was performed to remove residual solvent adsorbed on the particle surface. The actual measurement then consisted of two steps. First, the samples were heated to 880 °C under nitrogen. In this first section, the cationic particles show a mass loss between 50 °C and 200 °C. This is most likely due to the desorption of solvent, which could not be removed even in the preheating step due to the strong interactions with the

positively charged particle surface. The decomposition of the phosphonic acid starts at a temperature of 230 °C and takes place in several steps. This mass loss is observed for all samples. The mass loss is increased for all cationic modified particle samples compared to the oleic acid functionalized particles, indicating an increase in organic material bound to the surface. The mass loss increases from sample $^{0.025}\text{P@Fe}_x\text{O}_y$ to $^{0.600}\text{P@Fe}_x\text{O}_y$. The organic fraction obtained at the end of the N_2 segment (char yield) varies between 22 % and 34 %. In the second step, the temperature is raised further to 1000 °C under synthetic air. For all samples, an increase in mass can be observed in the air segment, which is due to the oxidation of the particles. Again, the mass change is more pronounced for the cationic functionalized particles, with an increase of 7 % - 12 %, than for the oleic acid functionalized particles (~3 %). This suggests an additional oxidation mechanism. While a complete desorption/decomposition is expected for the oleic acid upon heating, the phosphonic acid anchoring group remains on the particle surface even at higher temperatures.[269] This is confirmed by the vibration of the phosphonate group at 964 cm^{-1} , observed in FTIR spectra recorded subsequent to the TGA measurements (Figure 20 b). By switching to oxygen-containing atmosphere the phosphonate is oxidized to the phosphate in addition to particle oxidation. As a result, the mass increase is magnified with phosphonic acid functionalization.

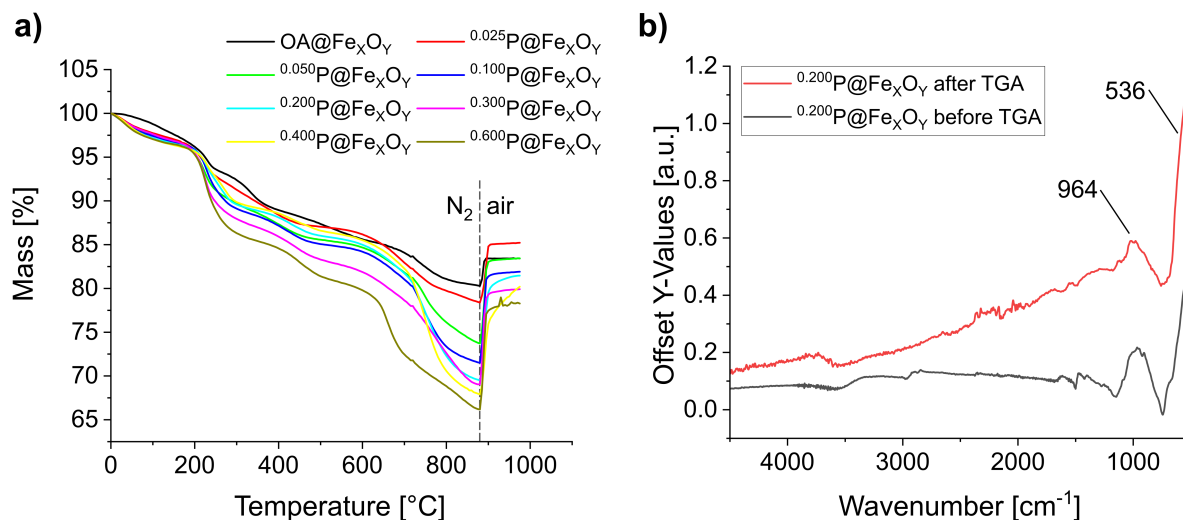


Figure 20: a) TGA curves of oleic acid and the cationic functionalized nanoparticles. The samples were heated from room temperature to 880 °C under nitrogen atmosphere, followed by heating to 1000 °C under a mixture of nitrogen and oxygen (4:1) with a rate of 10 K/min. b) FTIR spectra of $^{0.200}\text{P@Fe}_x\text{O}_y$ before and after TGA.

In combination with the TGA results, CHN analysis was used to calculate the surface coverage. Due to the aforementioned oxidation that occurs at elevated temperatures in TGA when synthetic air is used, the residual mass at the end of the N_2 segment (carbon/hydrogen content below the CHN detection limit) was used to calculate the surface coverage. The following equation was applied:

Results and Discussion

$$n_{ca} = \frac{X}{Y} \times \frac{1000}{M \times N} \quad (10)$$

where n_{ca} is the amount of coupling agent per particle in mmol/g, X is the percentage of the respective element from CHN analysis, Y is the residual mass from TGA in %, M is the molar mass of the respective element and N is the number of that element in the molecule. However, these calculations are subjected to several small errors. First, the FTIR data suggests that trace amounts of oleic acid remain on the particle surface, which is not considered in the calculation. In addition, as mentioned above, the desorption behavior of the two coupling agents is different. While the oleic acid desorbs completely during heating, the anchoring group of the phosphonic acid remains on the particle surface, what skews the determination of the organic content. Lastly the partial reduction of the particles within the N₂ segment during TGA was not considered either. The used TGA and CHN data, as well as the calculated surface coverage are shown in Table 2.

Table 2: TGA and CHN results of the oleic acid and the cationic functionalized nanoparticles (^{0.025}P@Fe_xO_y - ^{0.600}P@Fe_xO_y).

Sample	TG Residual Mass [%]		CHN [%]			Surface Coverage [mmol/g]		
	25-880°C N ₂	880-1000°C air	C	H	N	C	H	N
OA@Fe _x O _y	80.28	83.41	9.09	1.71	-	0.52	0.62	-
^{0.025} P@Fe _x O _y	78.38	84.95	8.93	1.63	0.48	1.05	0.90	0.44
^{0.050} P@Fe _x O _y	73.71	83.30	9.34	1.88	0.73	1.17	1.10	0.71
^{0.100} P@Fe _x O _y	71.51	81.64	10.45	2.34	0.89	1.35	1.41	0.89
^{0.200} P@Fe _x O _y	69.50	80.68	11.30	2.48	1.00	1.50	1.54	1.03
^{0.300} P@Fe _x O _y	69.04	79.62	11.94	2.51	1.11	1.60	1.57	1.15
^{0.400} P@Fe _x O _y	67.90	79.04	12.31	2.64	1.10	1.68	1.68	1.16
^{0.600} P@Fe _x O _y	66.18	77.84	12.44	2.53	1.26	1.74	1.65	1.36

The mass loss in the N₂ segment observed in TGA increases with the amount of phosphonic acid used for functionalization. The same trend is observed for the CHN data as well and consequently in the n_{ca} values. For all samples, a lower coverage was calculated based on the nitrogen content obtained from the CHN analysis than for the values calculated on the basis of the carbon and hydrogen content. This supports the argument that additional organic matter or water is still present on the surface. To calculate the remaining organic ligand on the particle surface, the carbon and hydrogen contents derived from the phosphonic acid were subtracted from the total mass of carbon and hydrogen. Since nitrogen is only present in the phosphonic

Results and Discussion

acid, the corresponding carbon and hydrogen contents were calculated from the nitrogen content of the CHN analysis and the elemental composition of the phosphonic acid. As expected, the amount of remaining carbon (5.23 % - 2.73 %) and hydrogen (0.84 % - 0.45 %) gradually decreases as the amount of phosphonic acid added is increased. This confirms that the equilibrium of the exchange can be advanced by increasing the phosphonic acid concentration. However, in all cases, some oleic acid still remains on the particle surface. Looking at the corrected carbon to hydrogen ratio, it is noticeable that the ratio in several samples does not match the ratio in oleic acid ($C:H_{OA} = 6.31$). This indicates the presence of additional organic material on the particle surface, e.g. adsorbed solvent that could not be removed during the drying process ($C:H_{ethanol} = 3.97$). Therefore, an exact quantification of the remaining oleic acid was not possible.

In the next step, the influence of the cationic modification on the size of the particles was examined. For this purpose, XRD, TEM and DLS investigations were carried out in analogy to the oleic acid functionalized particles. The results are shown in Figure 21 for the $^{0.200}P@Fe_xO_y$ system in comparison with the initial oleic acid functionalized particles.

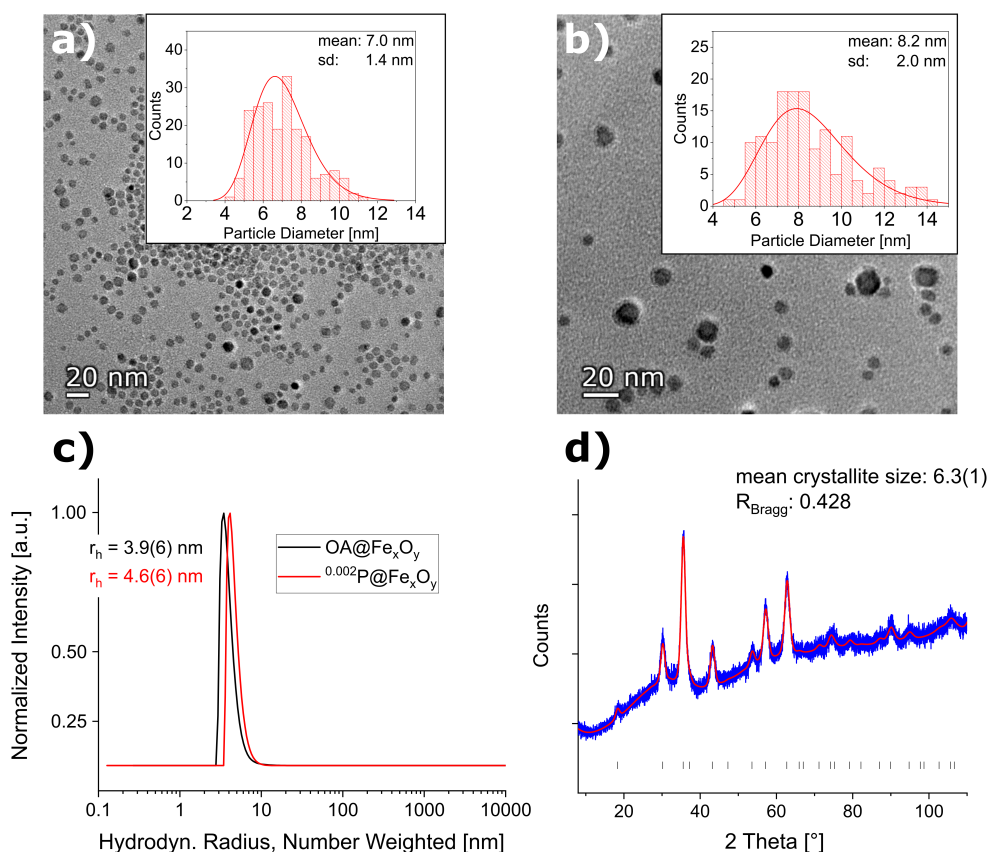


Figure 21: TEM images of a) $OA@Fe_xO_y$ and b) $^{0.002}P@Fe_xO_y$. Histograms: Statistical size distribution of particles ($N = 200$). c) DLS measurements of $OA@Fe_xO_y$ in *n*-hexane and $^{0.002}P@Fe_xO_y$ in water. d) X-ray diffractogram of the phosphonic acid functionalized particles ($^{0.200}P@Fe_xO_y$). Blue: experimental data, red: Rietveld refinement, black hkl-values. Reference taken from COD1513301.[596]

Results and Discussion

The particles show no change in the size of the hydrodynamic radius by DLS, nor in the crystallite size determined by XRD, nor in the particle size determined by TEM within the measurement accuracy. Furthermore, no color change was observed during functionalization, indicating that the composition of the iron oxide did not change significantly.

In the last step, zeta potential measurements were carried out. This allows to determine both the isoelectric point and the pH stability of the positive charge. In Figure 22 the zeta potential curve of the $^{0.002}\text{P}@Fe_xO_y$ is shown in comparison to the oleic acid functionalized particles.

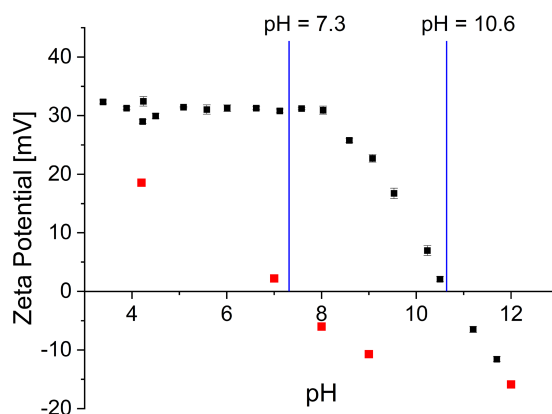


Figure 22: Zeta potential of $^{0.002}\text{P}@Fe_xO_y$ in water (black) and OA@ Fe_xO_y in ethanol (red) as a function of pH.

The zeta potential of the oleic acid functionalized particles starts at approx. 17 mV at pH 4. Subsequently, a linear decrease of the zeta potential down to -17 mV at pH 12 can be observed. In the literature, a zeta potential range of about -40 mV to 40 mV is described for naked iron oxide particles.[618,619] The smaller range observed for OA@ Fe_xO_y can be attributed to the number of hydroxyl functionalities available on the particle surface, which are reduced by the binding of oleic acid. However, a direct comparison of the absolute values is difficult, since the zeta potential depends on a number of parameters such as particle size, concentration, pH, temperature, pressure, and method of sample preparation.[620] By interpolation, an IEP of 7.3 was determined, which agrees quite well with the values described in the literature for non-ionic functionalized iron oxide nanoparticles, which are in the range of 5.6 - 7.9.[621–623] However, it should be mentioned here that the zeta potential of these particles could not be determined in an aqueous system due to their poor dispersibility. The measurements were performed in a water:ethanol mixture, for which, strictly speaking, the pH value is not defined. O'Brien and White showed in their work that the electrophoretic mobility and thus the zeta potential of ionic colloidal particles is independent of the dielectric properties and the electrostatic boundary conditions on the particle surface. Instead it is mainly dependent on the particle size, their shape and the charge in or the potential on the shear plane and thus the electrolyte solution.[624] Consequently, not only the initial counterion but also the choice of acid/base used in the titration plays a role, especially in view of the fact that an exchange of

Results and Discussion

the counterion can also take place. Therefore, there is a dependence between the zeta potential and the concentration and type of ions in solution [620,625], though it is not possible to separate concentration effects from pH effects.[620,626] The pH affects protonation/deprotonation equilibria at the surface and affects charge density, while counterion concentration affects the degree to which the surface charge is screened. For the choice of counterion, higher charged counterions generally lead to compression of the diffuse double-layer and thus a reduction in zeta potential. In contrast, the size of the ions at the same charge does not seem to be well correlated with the zeta potential.[620] These dependencies further complicate the comparison of zeta potential absolute values of charged particles, so no detailed literature comparison is made here. The ionically modified particles are readily dispersible in water and show a higher positive zeta potential of 30 mV in the low pH range. For the investigated cationic particles, the zeta potential remains constant up to pH 8. This confirms the positive surface charge. Subsequently, a linear decrease of the zeta potential is observed. An IEP of 10.6 was determined, which is significantly higher than that of the oleic acid functionalized particles. The result is nevertheless quite surprising, since a permanent positive surface charge should be provided by the quaternary ammonium groups. To further investigate this observation, the pH value of a new batch of cationic modified particles was adjusted to 11.5. The particles were then characterized by CHN, which confirmed the absence of nitrogen containing groups at high pH values. However, some organic matter remained on the surface. Since the previous studies suggested that a considerable amount of oleic acid was still present on the surface, an analogous study was performed with the oleic acid functionalized particles. And indeed, the CHN confirmed that the oleic acid is only partially removed at high pH. The CHN results are shown in Table 3.

Table 3: CHN analysis results of $^{0.200}\text{P}@Fe_xO_y$ and $\text{OA}@Fe_xO_y$ before and after base treatment (pH = 11.5).

Sample	CHN [%]		
	C	H	N
$^{0.200}\text{P}@Fe_xO_y$	11.30	2.48	1.00
$^{0.200}\text{P}@Fe_xO_y$ (pH = 11.5)	3.97	1.18	-
$\text{OA}@Fe_xO_y$	9.09	1.71	-
$\text{OA}@Fe_xO_y$ (pH = 11.5)	8.19	1.58	-

To further investigate the absence of nitrogen content on the particle surface, the supernatant solution of the cationic functionalized particles was analyzed by NMR spectroscopy at pH 11.5 (see Figure 23). In the supernatant solution, both the proton NMR and phosphorus NMR showed the signals of the intact phosphonic acid, confirming that a desorption process rather than a decomposition process is responsible for the absence of nitrogen on the particle

surface. This is quite remarkable, as the binding of a variety of phosphonic acid derivatives to metal oxide nanoparticles has been described as very stable.[269,275,627]

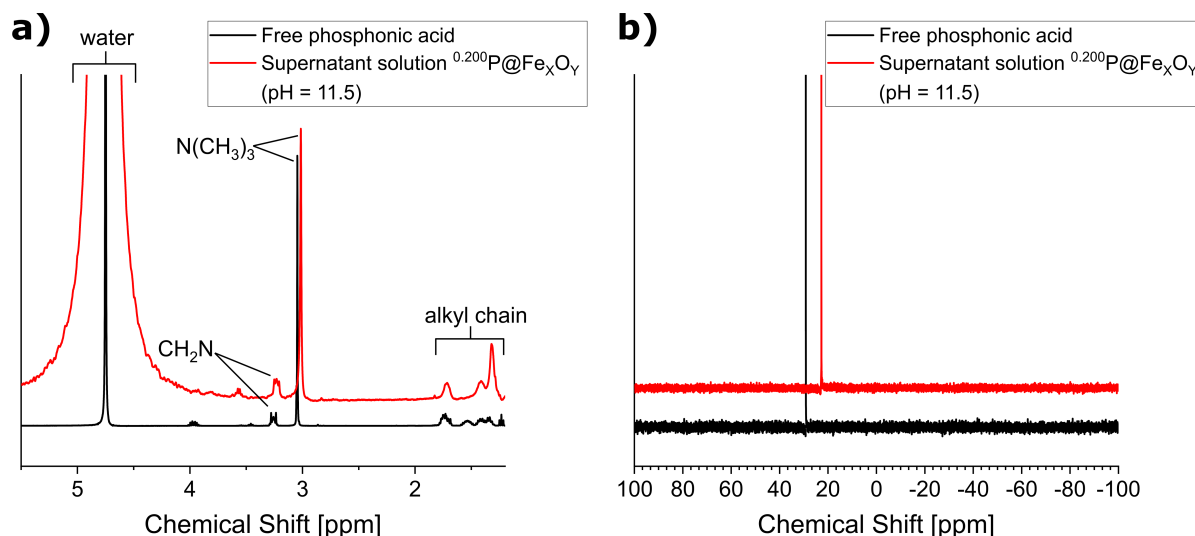
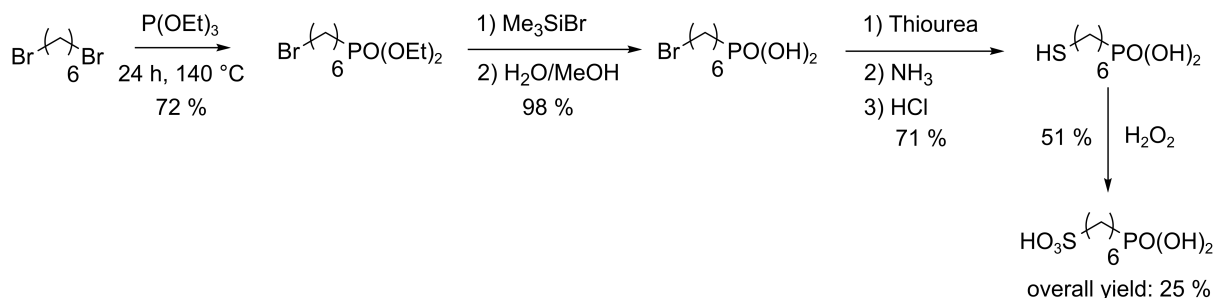


Figure 23: a) ^1H and b) ^{31}P NMR spectra of the supernatant solution of $^{0.200}\text{P}@Fe_xO_y$ at $\text{pH} = 11.5$ (red), in comparison with the free phosphonic acid (black).

In summary, positively charged particles have been synthesized. The particles are readily dispersible in common polar solvents such as water or alcohols. They are even redispersible after drying due to the electrostatic repulsion, which is rare for iron oxide nanoparticles in this size range. The particles have a positive surface charge at least in the pH range from 3.3 to 10.6, which is limited by particle dissolution in the low pH range and desorption of phosphonic acid in the high pH range. In the following, negatively charged particles are to be produced in an analogous manner.

3.2.3. Synthesis of the Anionic Functionalization Reagent

The synthesis of the anionic phosphonic acid derivative is shown in Scheme 15 and was performed according to literature procedure.[269]



Scheme 15: Synthesis route for 6-phosphonohexylsulfonic acid.[269]

The anionic coupling reagent was synthesized in four steps. The first step of the synthesis coincides with that of the cationic phosphonic acid to give the 6-bromohexylphosphonic acid. In the next step, the phosphonic acid ester was hydrolyzed via the silyl ester intermediate with

a yield of 98 %. Subsequently, the 6-bromohexylphosphonic acid was converted to 6-mercaptohexylphosphonic acid by an S-alkylation reaction. For this purpose, the isothiuronium salt was first prepared by adding thiourea, which was then hydrolyzed. The synthesis was carried out with a yield of 51 %. In the final step, the thiol was oxidized to the sulfonic acid. The last step was carried out with a yield of 71 %. CHN analysis as well as NMR and FTIR spectroscopy confirmed the product formation with an overall yield of 25 %.

3.2.4. Anionic Particle Functionalization

The anionic functionalization of the particles was carried out in the same way as for the cationic systems. The systems obtained are hereafter referred to as $^{0.025}\text{PA@Fe}_x\text{O}_y$ - $^{0.600}\text{PA@Fe}_x\text{O}_y$. The anionic particles were examined by FTIR spectroscopy (see Figure 24). For better comparability, the spectra were normalized to the particle vibration at 575 cm^{-1} .

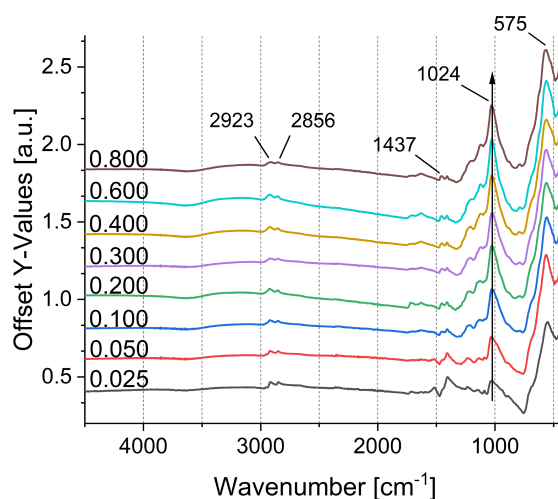


Figure 24: FTIR spectra of the anionic functionalized particles ($^{0.025}\text{PA@Fe}_x\text{O}_y$ - $^{0.600}\text{PA@Fe}_x\text{O}_y$).

The spectra show the C-H stretching and deformation vibrations at 2923 cm^{-1} , 2856 cm^{-1} and 1437 cm^{-1} , respectively. While in samples $^{0.025}\text{PA@Fe}_x\text{O}_y$ and $^{0.050}\text{PA@Fe}_x\text{O}_y$ the C-H deformation vibrations at 1437 cm^{-1} are still superimposed by the signals of the carbonyl vibration of the oleic acid, the signal of the carbonyl vibration is no longer visible starting from $^{0.100}\text{PA@Fe}_x\text{O}_y$. The successive functionalization by the phosphonic acid can be confirmed by the increasing signal of the PO_3 vibration at 1024 cm^{-1} .

TGA and CHN analysis were used to quantify surface occupancy. Equation (10) was again applied to calculate the surface coverage. The results are presented in Table 4.

Results and Discussion

Table 4: TGA and CHN results of the anionic functionalized nanoparticles ($^{0.025}\text{PA@Fe}_x\text{O}_y$ - $^{0.600}\text{PA@Fe}_x\text{O}_y$).

Sample	TG Residual Mass [%]		CHN [%]			Surface Coverage [mmol/g]		
	25-880°C	880-1000°C	C	H	S	C	H	S
	N ₂	air						
$^{0.025}\text{PA@Fe}_x\text{O}_y$	76.87	85.84	8.48	1.50	0.44	1.53	1.29	0.18
$^{0.050}\text{PA@Fe}_x\text{O}_y$	76.44	84.80	6.82	1.53	1.48	1.24	1.32	0.60
$^{0.100}\text{PA@Fe}_x\text{O}_y$	71.97	81.16	7.88	1.76	1.92	1.52	1.62	0.83
$^{0.200}\text{PA@Fe}_x\text{O}_y$	70.78	80.51	8.30	1.88	2.16	1.63	1.76	0.95
$^{0.300}\text{PA@Fe}_x\text{O}_y$	70.44	79.93	8.56	1.93	2.41	1.69	1.81	1.07
$^{0.400}\text{PA@Fe}_x\text{O}_y$	68.92	77.79	9.45	2.14	2.71	1.90	2.05	1.23
$^{0.600}\text{PA@Fe}_x\text{O}_y$	66.75	76.74	9.81	2.36	3.02	2.04	2.34	1.41

For the anionic systems, a significant increase in mass loss can be observed in the N₂ segment of the TGA due to the addition of the anionic phosphonic acid to the particle surface which is decomposed during this step. A similar effect can be seen in the CHN data and consequently for the particle loading. Here the surface coverage can be determined from the sulfur contents obtained from CHN analysis. The loading densities calculated from the sulfur content are significantly lower than those derived from the carbon and hydrogen content, again indicating additional organic matter on the surface, although the FTIR spectra show no signs of residual oleic acid from sample $^{0.100}\text{PA@Fe}_x\text{O}_y$ onwards.

Subsequently, the influence of the functionalization on the particle size was investigated. TEM, DLS and XRD measurements were carried out for this purpose. The results are shown in Figure 25 exemplary for the $^{0.200}\text{PA@Fe}_x\text{O}_y$, since it can be expected that an almost complete surface coverage of the particles has been reached at this point.

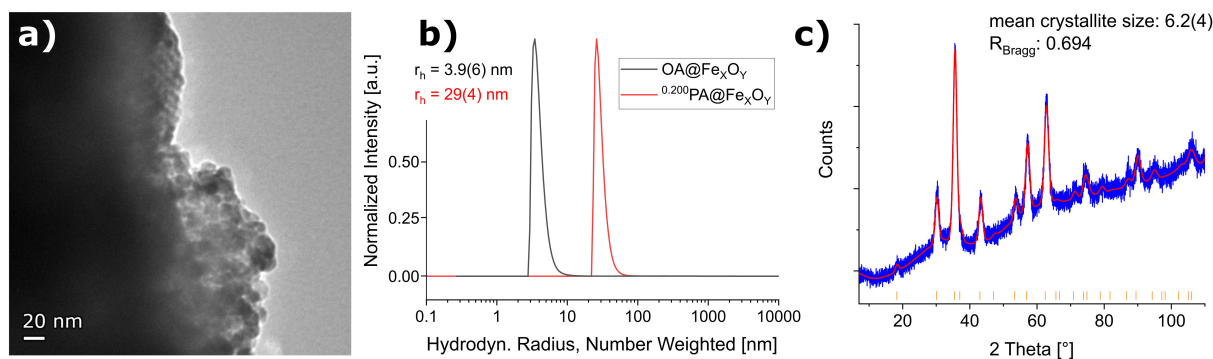


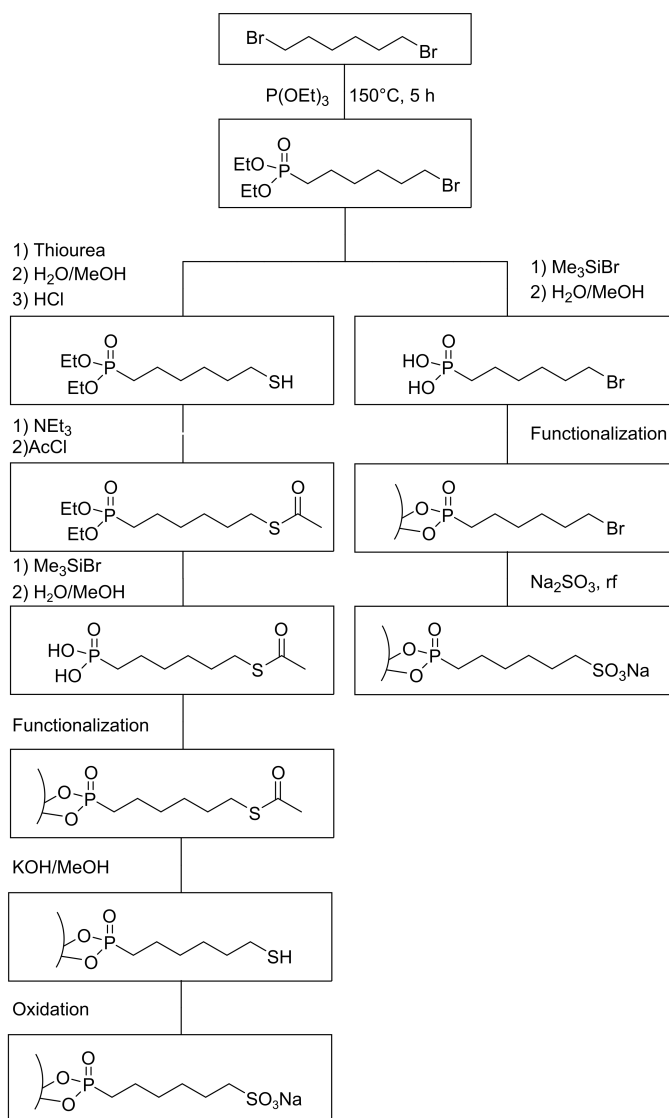
Figure 25: a) TEM image of $^{0.002}\text{PA@Fe}_x\text{O}_y$, b) DLS measurement of $\text{OA@Fe}_x\text{O}_y$ in *n*-hexane and $^{0.002}\text{PA@Fe}_x\text{O}_y$ in water and c) X-ray diffractogram of the phosphonic acid functionalized particles ($^{0.200}\text{PA@Fe}_x\text{O}_y$). Blue: experimental data, red: Rietveld refinement, orange *hkl*-values. Reference taken from COD1513301.[596]

Results and Discussion

The X-ray diffractogram shows no change in crystallite size upon functionalization. In contrast, the DLS differs from the oleic acid functionalized particles. The mean hydrodynamic radius shifts from 3.9 nm, corresponding to a single particle, by a factor more than seven to 29 nm, indicating agglomeration of the particles. Agglomerates are also observed in the corresponding transmission electron micrographs, although here the agglomeration is further increased by the drying process. Agglomerates of up to 2 μm in diameter are obtained. The formation of the agglomerates is surprising, as the electrostatic repulsion of the sulfonate groups should stabilize the particles.[269] To exclude the possibility that the agglomeration during functionalization is due to the choice of an unfavorable dispersant, the polarity of the solvent was adjusted by varying the composition between *n*-hexane, ethanol, methanol and water. However, agglomerates were still observed in all cases. Furthermore, an attempt was made to vary the surface charge of the particles and the degree of protonation of the acid groups by adjusting the pH. In the pH range of 4.4 to 6.3 as well as in the range from 10.0 to 11.8, very broad distributions with an average size of more than 100 nm were observed. At pH 2, in addition to the larger agglomerates, another much narrower signal is obtained at about 58 nm. In the case of this sample, a slight yellowish coloration was visible in the dispersion, indicating the dissolution of the particles in the acidic medium. In agreement with the first study, narrower distributions are observed in the pH range of the PZC of the iron oxide particles (6.9 - 8.3). However, no system could be obtained without agglomerate formation. The reason for the agglomerates is probably that not only the phosphonate but also the sulfonic acid binds to the particle surface. This is surprising, as the sulfonate binds via electrostatic interactions and should therefore be easily exchanged by the phosphonate, which forms more stable and irreversible bonds.[262,293] This was shown in particular in studies investigating the binding of phosphate in competition with sulfate on iron oxide surfaces, in which a negligible effect of sulfate was observed.[628–630] However, there is also a study by Yu *et al.* investigating phosphate adsorption on sodium dodecyl sulfonate-functionalized magnetite in which, even at high phosphate concentrations, signals of sodium dodecyl sulfonate were found in the FTIR spectra, indicating an incomplete exchange.[631] Further it has also been described that a second intraparticle binding occurs via the even weaker binding carboxyl group of 6-phosphonohexanoic acid, which led to the agglomeration of alumina coated silica nanoparticles.[632] In contrast, zirconium oxide nanoparticles have indeed been stabilized by 6-phosphonohexylsulfonic acid.[269] Thus, it appears that not only the surface charge but also the particle composition strongly influences the binding of the acid groups. Whether this is an effect of the stability of the sulfonate binding to the different metal centers, or the accessibility of OH surface functionalities that facilitate the desorption of the sulfonate [633], has not been conclusively determined. To avoid this competitive binding by the sulfonate, a transition to weaker-binding sulfonate precursors was made. If the surface is then saturated by the

Results and Discussion

phosphonic acid, no crosslinking via the sulfonic acid group should take place after its synthesis. Two synthetic approaches were used for this purpose. These are shown in Scheme 16.



Scheme 16: Synthetic approaches to anionic functionalized iron oxide nanoparticles via weakly binding sulfonic acid precursors.

In the first route, an acetyl-protected thiol in the form of (6-(acetylthio)hexyl)phosphonic acid is attached to the particle surface as a non-binding precursor. Analogous to the previous syntheses, the phosphonic acid ester group was introduced in the first step via a Michaelis-Arbusow reaction. Then the thiol group was introduced. This was achieved by an S-alkylation in 92 % yield. The synthesis of the acetyl-protected thiol was carried out by reaction of the thiol with acetyl chloride. The product was obtained in 44 % yield as a pale-yellow liquid. In the subsequent hydrolysis step of the phosphonic acid ester, only a product mixture was obtained. The signal integrals show that the alkyl backbone is still present in the by-product. Whether the by-product is a result of the partial hydrolysis of the thioester to the thiol or a cyclic system similar to that described by Odinet *et al.* is obtained could not be fully clarified yet.[634] Since

characterization at the particle surface is difficult due to the superparamagnetic properties of the iron oxide core, the subsequent reaction to the sulfonic acid was therefore first tested in solution. The conversion took place in two steps. First, the sulfonic acid ester was hydrolyzed with potassium hydroxide, followed by the oxidation to the thiol with hydrogen peroxide to obtain the desired product. A total yield of 1.8 % was obtained.

In the second route, the ω -bromo functionalized precursor, the introduction and subsequent hydrolysis of the phosphonic acid ester took place analogous to the initial synthetic procedure described earlier. The sulfonate group was obtained according to the literature procedure by reaction with sodium sulfite for 72 hours in water under reflux.[635] A yield of 13 % was obtained. The overall yield was 8.4 %.

In the next step, both reaction pathways were carried out analogously on the particle surface. Unfortunately, agglomerates were also observed for the anionic particle systems prepared in both approaches (see Figure 26). In addition, the oxidation with H_2O_2 in the first approach also led to an oxidation of the particles, as indicated by the discoloration from black to brown. Since NMR spectroscopy was not possible due to the superparamagnetic particles and from FTIR spectroscopy due to the low signal intensity, no conclusions could be drawn regarding the successful introduction of the sulfonate group or whether a subsequent attachment to the particle surface occurs after its introduction.

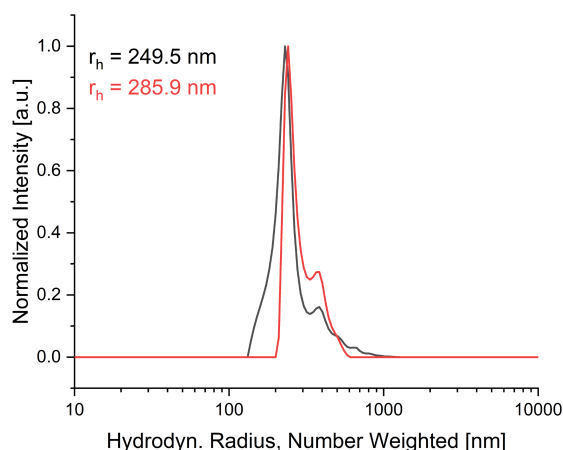


Figure 26: DLS measurements of the $^{0.002}PA@Fe_xO_y$ particles in water, synthesized via the 6-bromohexyl- (black) and the (6-(acetylthio)hexyl) phosphonic acid (red).

Due to problems with the post-functionalization approaches, the anionic particles produced by the original route were used for the further investigations.

3.2.5. Comparison of the Cationic and Anionic Functionalized Particles

As described in the previous section, the main difference between the two ionic particle systems is in their agglomeration behavior. In contrast to the cationic systems, the anionic particles could not be stabilized by electrostatic repulsion, even after extensive optimization.

Results and Discussion

This appears to be due to the different ways in which the two phosphonic acids interact with the particle surface (Figure 27).

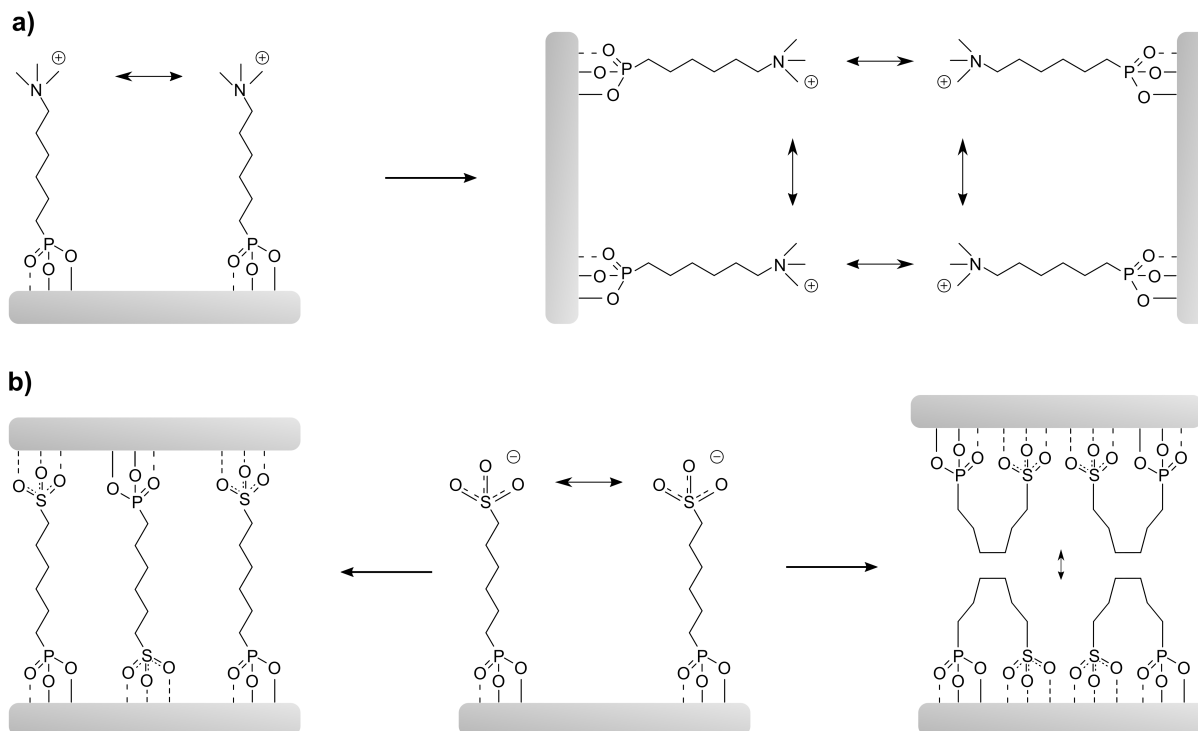


Figure 27: Overview of the possible interactions between the synthesized ionic phosphonic acids and the iron oxide surfaces.

While in the case of cationic phosphonic acid only repulsive interactions can occur leading to the stabilization of the particles, in the case of anionic phosphonic acid additionally intra- and interparticle binding by the sulfonic acid can take place. In both cases, the stabilization of the particles due to electrostatic repulsion is lost. Although some weak steric repulsion is expected after the intraparticle interaction, it can be assumed that this is insufficient to stabilize the particles. In the case of interparticle binding, agglomeration of the particles is even forced by the bridging ligand. Comparison with literature shows that deviating interactions of the sulfonic acid can be obtained for different particle systems.[269]

A comparison of the two FTIR spectra of the $^{0.200}\text{PA}@Fe_xO_y$ and $^{0.200}\text{P}@Fe_xO_y$ samples shows that the signal of the carbonyl stretching vibration of the surface bound oleic acid (1637 cm^{-1}) decays faster in the case of the anionic particles (Figure 28 a). This indicates a more complete exchange than in the case of the cationic systems. However, it seems unlikely that these residual amounts of oleic acid in the cationic systems are related to the better stabilization, since agglomeration is also observed at lower amounts of anionic phosphonic acid, where some residual oleic acid is still observed on the particle surface. Despite the differences in particle surface coverage with oleic acid, comparable surface coverage is observed for the phosphonic acids, calculated based on the nitrogen and sulfur content, respectively (Figure 28 b). The curves resemble that of typical sorption models. After an initial sharp increase in

occupancy, less sorbate can be absorbed as the sorption surfaces of the sorbent become more heavily loaded. Whether this is due to the space requirement of the anchor group or to the fact that the positive and negative charge have an equal effect on the particle coverage, has not yet been clarified.

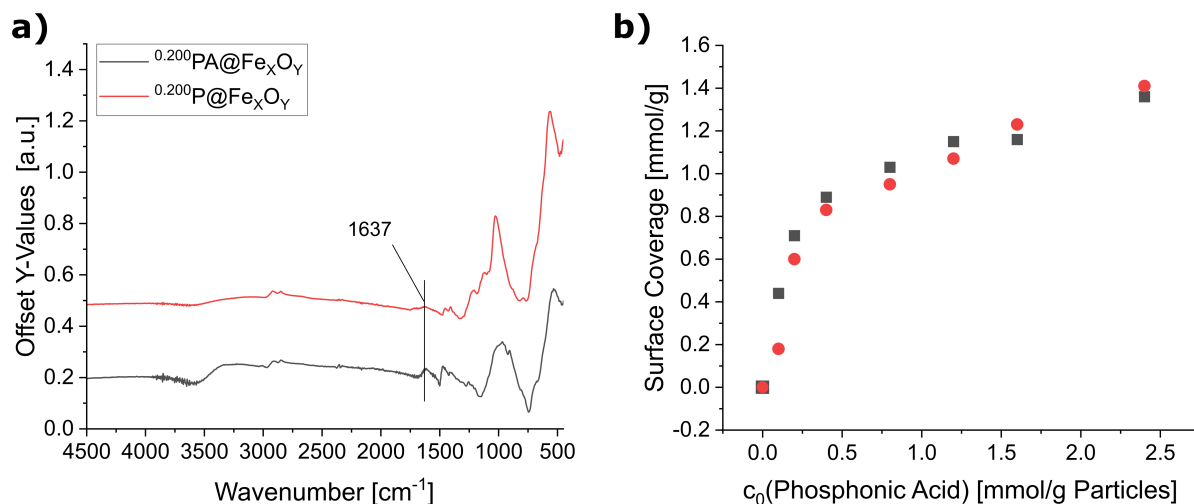


Figure 28: a) FTIR spectra of $^{0.200}\text{PA@Fe}_x\text{O}_y$ and $^{0.200}\text{P@Fe}_x\text{O}_y$. b) Calculated surface coverage of the synthesized cationic (black) and anionic (red) functionalized particles based on the nitrogen and sulfur content determined from CHN as a function of the initial phosphonic acid-particle-ratio.

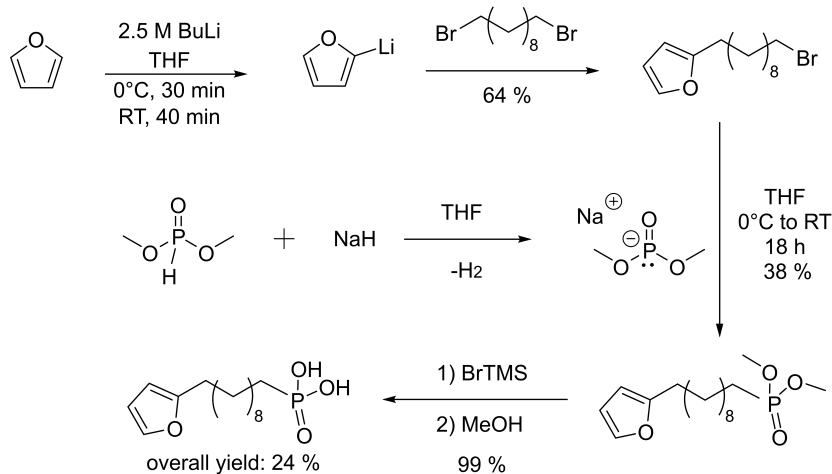
Since well-dispersed particles are beneficial for applications in the field of self-assembly and agglomerates are less suitable for self-healing materials, as they often act as stress concentration points and thus significantly reduce the loading capacity [378–380], the investigation of ionic self-healing materials was focused on the cationic particle systems. For the self-healing studies, the $^{0.200}\text{P@Fe}_x\text{O}_y$ system was selected, since no further strong increase in surface loading density was observed afterwards. In the following, systems with temperature-controlled surface charges were prepared.

3.3. Synthesis of Switchable Cationic Surfaces

In recent years, interest in smart surfaces has increased significantly. One of the properties being investigated is switchable surface wettability.[636] These systems are used in a variety of areas ranging from microfluidic devices to oil-water separating systems and biomedical applications.[637] These switchable surfaces can be realized via self-assembled monolayers of functionalized nanoparticles, that change their properties upon an external trigger such as temperature, light or pH changes.[638–640] Here the heating of the metal oxide particles in an alternating magnetic field is to be investigated as an alternative trigger. In this work, organic functionalization reagents were prepared for the synthesis of iron oxide nanoparticles that reversibly carry an ionic group on the surface. The reversibility of the functionalization is based on a temperature-controlled DA/rDA reaction. For this purpose, DA active groups are immobilized on the particle surface, to which any organic moiety can be attached in a temperature-controlled and reversible manner via the respective DA counterpart. The

Results and Discussion

furan/maleimide diene/dienophile pair was chosen for this work because of its high stability and reversibility. Scheme 17 shows the synthesis route for the furan component which is anchored to the particle surface by a phosphonic acid group. The synthesis was carried out according to literature procedure.[271]

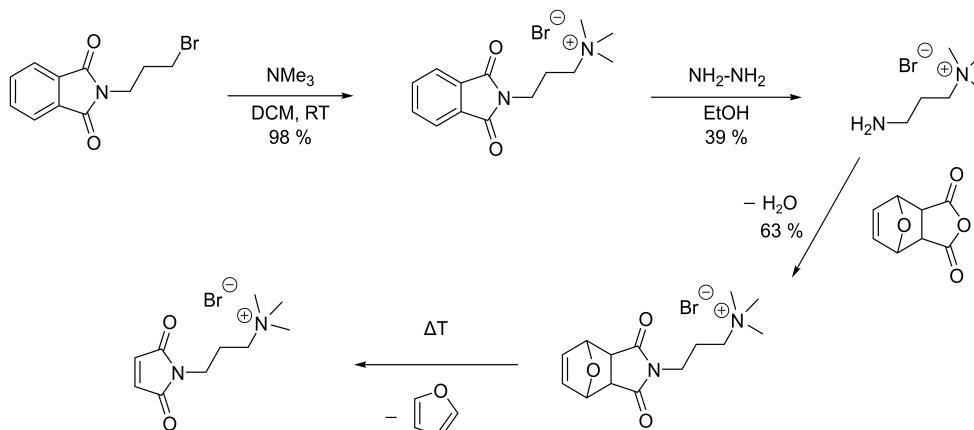


Scheme 17: Synthesis route for (10-(furan-2-yl)decyl)phosphonic acid.[271]

The investigations by Schäfer and Kickelbick showed that a large distance from the particle surface is necessary to meet the steric requirements of the DA reaction. Therefore, in comparison to the permanently ionic systems, an increased spacer length (C₁₀) was used here. The synthesis was carried out in four steps. The starting material was furan, which was reacted with butyl lithium to form 2-lithium furanide. The furanide was used without further purification and directly reacted in excess with 1,10-dibromodecane in a Michaelis-Becker reaction. After work-up by column chromatography, the product was obtained in 64 % yield. The bromoalkylfuran was then reacted with a slight excess of freshly prepared sodium dimethylphosphite to form the phosphonic acid ester. A yield of 38 % was achieved. In the final step, almost quantitative hydrolysis of the phosphonic acid ester took place. The product was recrystallized from a methanol-hexane mixture. An overall yield of 24 % was obtained. The purity of the obtained product was verified by ¹H, ¹³C, ³¹P and FTIR spectroscopy.

On the side of the maleimide functionality, a shorter spacer length between the ionic group and the maleimide was chosen, as longer chains generally tend to hamper the DA reactions at the surface due to steric repulsion.[271] Whether this assumption also remains true for the ionic systems is not certain, since the charges come closer to each other with shorter chain lengths, thus increasing electrostatic repulsion. It can therefore be assumed that in the case of ionic systems an optimum exists in the range of medium chain lengths. A C₃ spacer was used for the initial investigation. The synthesis route is shown in Scheme 18.

Results and Discussion



Scheme 18: Synthesis route for the 3-maleimido-*N,N,N*-trimethylpropan-1-ammonium bromide.

For the preparation of the ionic DA component, (3-bromopropyl)phthalimide was used as starting material and converted to the cationic species by nucleophilic substitution with trimethylamine. The product precipitated during synthesis as a white solid in 98 % yield. The 3-amino-*N,N,N*-trimethylpropan-1-ammonium bromide is obtained via hydrazinolysis. A yield of 39 % was obtained. In the subsequent step, the protected maleimide was obtained by reaction with the previously prepared 3a,4,7,7a-tetrahydro-4,7-epoxyisobenzofuran-1,3-dione. Despite the additional reaction step required for the subsequent deprotection, this reaction route is usually preferable to the direct reaction with maleic anhydride, since the preset geometry prevents a ring opening of the maleic anhydride. The reaction took place in 63 % yield. The final step was to thermally initiate the rDA reaction. The reaction was carried out in the solid state in the form of a TGA study to determine the optimum rDA temperature. The results are shown in Figure 29.

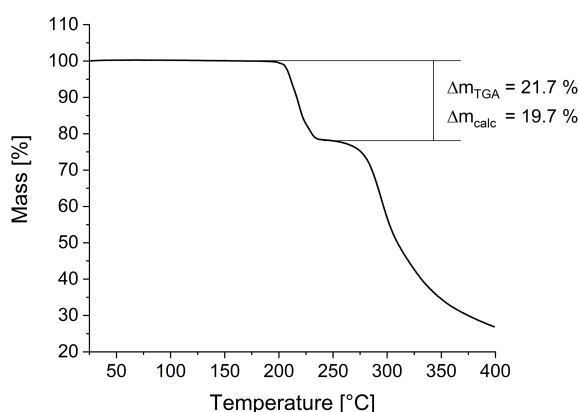


Figure 29: TGA curve of the 3-(1,3-dioxo-1,3,3a,4,7,7a-hexahydro-2H-4,7-epoxyisoindol-2-yl)-*N,N,N*-trimethylpropan-1-ammonium bromide. The sample was heated from room temperature to 400 °C under nitrogen atmosphere with a rate of 10 K/min.

The TGA curve shows a first mass loss starting at a temperature of approx. 200 °C, which is very high for the rDA reaction of the furan-maleimide DA pair. Subsequently, an almost complete decomposition of the compound takes place. The initial mass loss of 21.7 % is in

good agreement with the calculated value expected due to the rDA reaction and the subsequent evaporation of the furan ring ($\Delta m_{\text{calc}} = 19.7\%$). Based on the TGA results, the prepared compound was thermally treated in an alumina crucible at 210 °C for 1 hour in a tube furnace to perform the rDA reaction. The initially white compound turned yellow and was subsequently poorly soluble in common NMR solvents. The product was analyzed by FTIR spectroscopy. The FTIR spectrum obtained is shown in Figure 30.

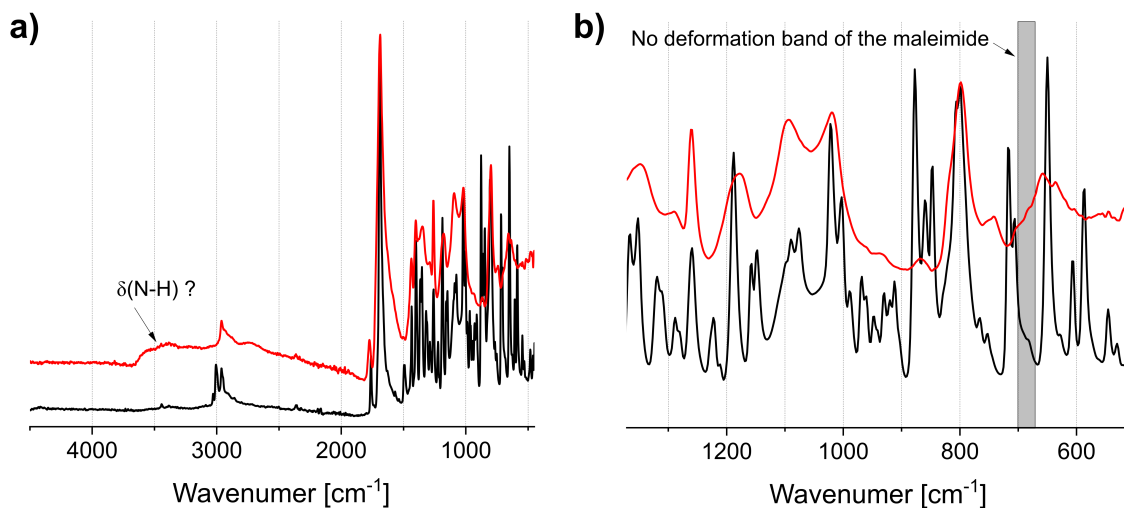
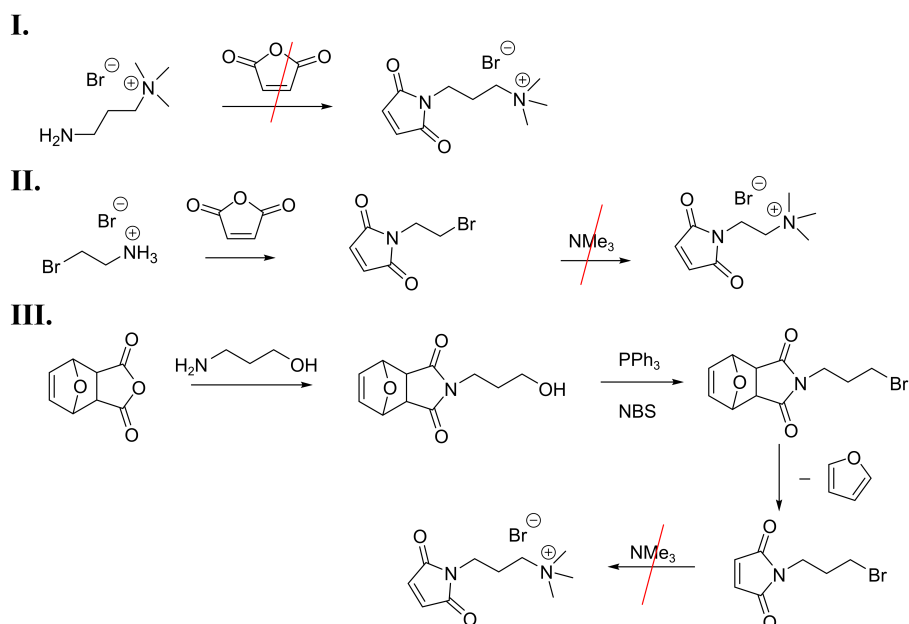


Figure 30: FTIR spectra of 3-(1,3-dioxo-1,3,3a,4,7,7a-hexahydro-2H-4,7-epoxyisoindol-2-yl)-N,N,N-trimethylpropan-1-ammonium bromide before (black) and after (red) temperature treatment.

The FTIR spectrum of the oven-treated sample shows no signal of the free maleimide, whose ring deformation band is expected at approx. 690 cm^{-1} . In addition, a signal appears at 3500 cm^{-1} . This is in the typical range of O-H or N-H stretching vibrations, indicating an opening of the maleimide ring. Since the synthesis in the bulk material was not successful, a deprotection in solvent was subsequently attempted. First, water was used as the solvent. The protected maleimide was dissolved and heated to reflux. The reaction mixture was then rapidly cooled to room temperature with an ice bath in order to prevent DA reaction. NMR analysis showed that no retro-DA reaction took place. Since the rDA reaction often only occurs in the range $> 100^\circ\text{C}$, the compound was dispersed in toluene and heated under reflux. After a reaction time of two hours, hot water was added to the mixture. This procedure has the advantage that the furan, which was released during the rDA reaction, remains in the organic phase, while the ionic component transfers into the aqueous phase. Therefore, the DA components are present in separate phases to further inhibit DA reaction. In addition, the reaction mixture was again, cooled with an ice bath. Despite the adjusted reaction control, no rDA product was observed. An analogous result was also observed at 180 °C in ethylene glycol, which is much higher than the rDA temperature commonly described for the furan maleimide system ($< 150^\circ\text{C}$).^[73,455]

Results and Discussion

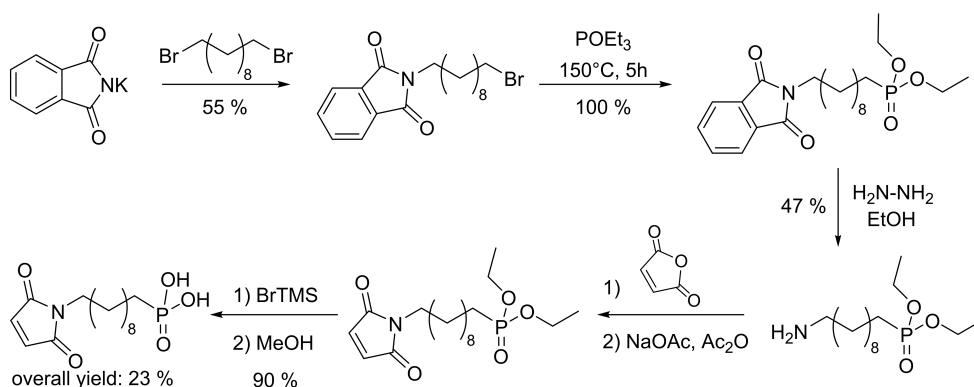
Several different approaches were then used to bypass the rDA deprotection step. First, the 3-amino-*N,N,N*-trimethylpropan-1-ammonium bromide was reacted directly with maleic anhydride. During this reaction, an opening of the maleimide ring was observed, which is a known side reaction. However, the methods commonly described in the literature have failed to close the ring.[641–643] Alternative strategies were also pursued by first introducing the maleimide and only then generating the ionic group. The starting materials were 2-bromoethane-1-ammonium bromide on the one hand and protected maleimide itself on the other. An overview of the synthetic routes tested is shown in Scheme 19. In all routes, the maleimide ring opening arose either during the addition to the maleic anhydride itself or during the introduction of the cationic group. In each case, a subsequent closure of the ring was not possible.



Scheme 19: Alternatively tested synthesis routes for the cationic maleimide.

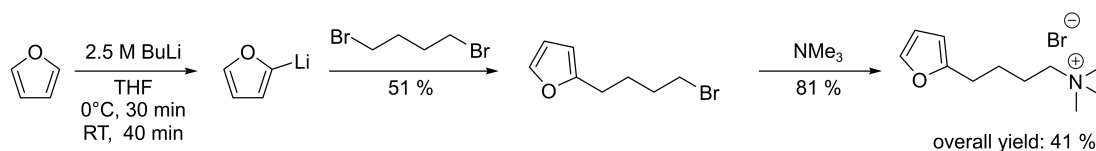
As a result, it was attempted to reverse the system and immobilize the maleimide functionality on the surface and synthesize a furan-based cationic component. The synthesis of the phosphonic acid was again conducted according to literature procedure with minor modifications.[271] The synthesis route is shown in Scheme 20.

Results and Discussion



Scheme 20: Synthesis route for the maleimide decyl phosphonic acid.[271]

The synthesis was carried out in five steps. In this process, 1,10-dibromodecane is reacted with potassium phthalimide in a Gabriel-like reaction, whereby potassium bromide is cleaved to give the *N*-alkyl phthalimide. A yield of 55 % was obtained in this step. The hydrazinolysis is led by a Michaelis-Arbusow reaction, which proceeds quantitatively. The hydrazinolysis takes place in 47 % yield by refluxing in ethanol for one hour. Subsequently, the maleimide is synthesized by reaction with maleic anhydride. Since ring opening occurs during this reaction, ring closure is achieved by stirring with sodium acetate in acetic anhydride. Complete separation of the by-products was not possible. Therefore, the crude product was used as received for the final reaction step. In the last step, the phosphonic acid ester was hydrolyzed. A yield of 90 % was obtained over the last two reaction steps. This results in an overall yield of 23 %. The product was characterized by ^1H , ^{13}C , ^{31}P NMR and FTIR spectroscopy. The synthesis route of the cationic component is shown in Scheme 21.



Scheme 21: Synthesis route for the 4-(furan-2-yl)-*N,N,N*-trimethylbutan-1-ammonium bromide.

The synthesis was carried out in three steps. First, the 2-lithium furanide was synthesized. The furanide was used without further purification and reacted directly in excess with 1,4-dibromobutane in a Michaelis-Becker reaction to obtain the 2-(4-bromobutyl)furan. A product mixture of the single and double furanated alkanes was obtained. Using the integrals from the ^1H NMR spectrum, a yield of 51 % was estimated. In the next step, the cationic group was introduced by an $\text{S}_{\text{N}}2$ reaction with trimethylamine. A conversion of 81 % was obtained. The overall yield was 41 %. The product formation was again confirmed by ^1H , ^{13}C , ^{31}P and FTIR spectroscopy. In addition, the molecular structure of the product was determined by single crystal X-ray diffraction analysis (see Figure 31).

Results and Discussion

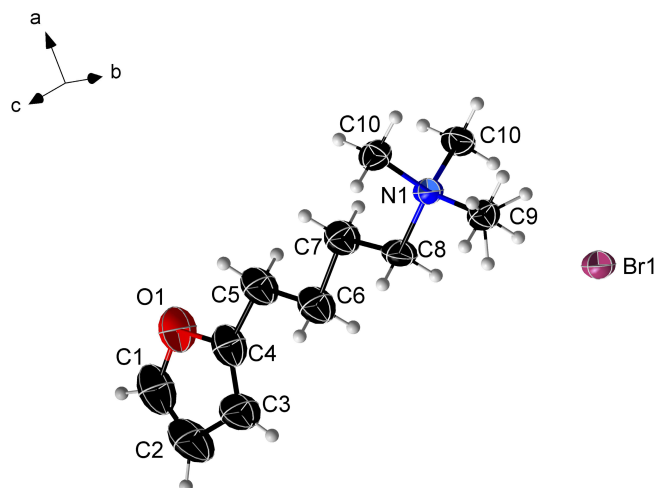


Figure 31: Crystal structure of 4-(furan-2-yl)-N,N,N-trimethylbutan-1-ammonium bromide.

In the next step, the DA reaction between the cationic furan derivative and the maleimido phosphonic acid was attempted in solution. For this purpose, the two components were added to a mixture of water and methanol in a 1:1 ratio and heated to 100 °C for two days. Figure 32 shows the downfield region of the ^{13}C NMR spectrum of the DA product in comparison with the starting compounds.

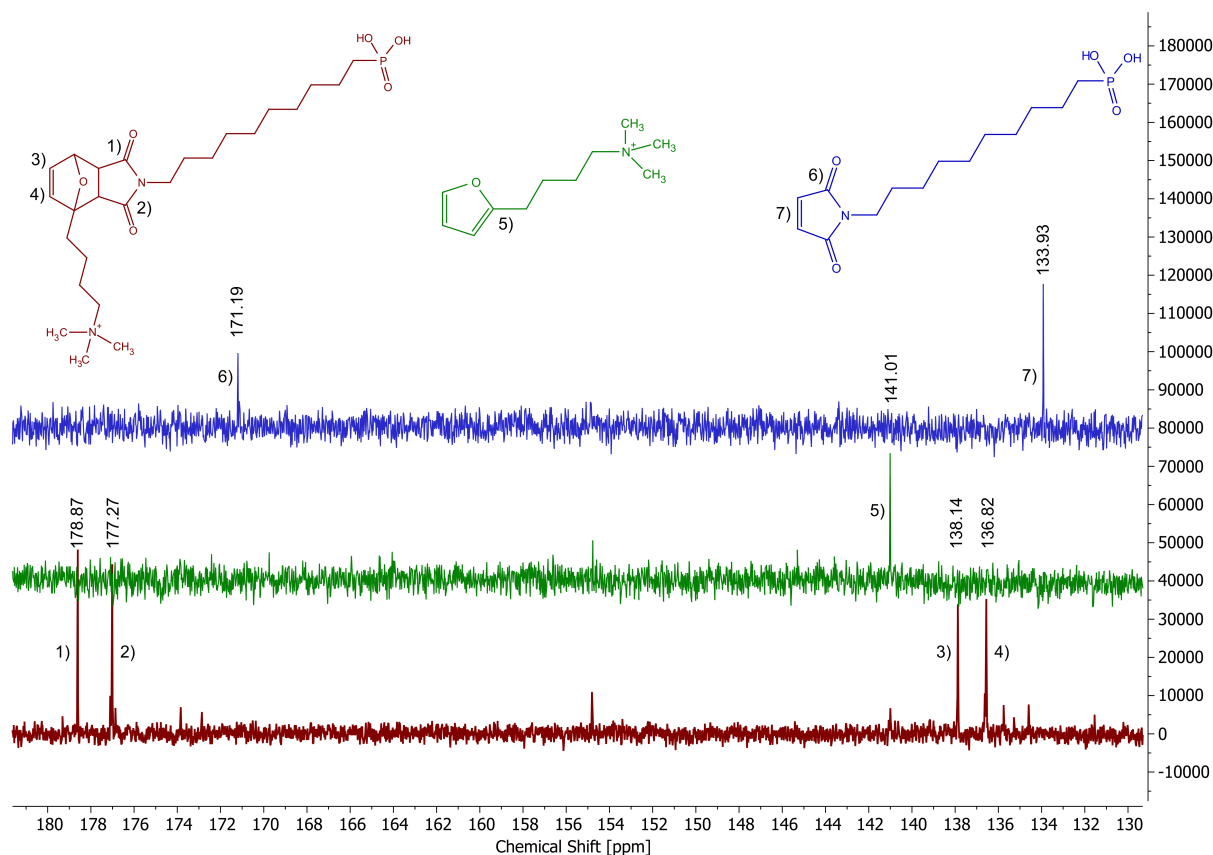


Figure 32: ^{13}C NMR spectra of maleimide decyl phosphonic acid (blue), 4-(furan-2-yl)-N,N,N-trimethylbutan-1-ammonium bromide (green) and the DA product (red).

Results and Discussion

The disappearance of the furan and maleimide signals indicates that the reactants are completely converted. In the product spectrum, the signals of the carbonyl groups and the newly formed double bond of the DA adduct are clearly visible. The NMR spectrum also shows slightly shifted signals of the same structure, indicating the presence of both the endo and the exo product. However, impurities can also be detected in the product. The overlapping of the signals of the by-products and the endo-exo mixture complicate the interpretation of the ^1H NMR spectrum. Examination of the ^{31}P NMR spectrum confirms the presence of several by-products at low concentrations. Purification of the product could not be carried out because workup is limited to extraction or precipitation, which do not remove the by-products. Purification by column chromatography is not feasible due to the high affinity of the phosphonic acid group towards the common stationary phases. Further distillation was not possible due to the high boiling point of the DA-adduct. As a result, the product is first decomposed by the rDA reaction. Since it has already been shown in earlier work by Wang *et al.* [431], that the barrier of the DA reaction can be altered by electrostatic interactions, the bromide counterion was exchanged for the weaker coordinating counterions triflate and perchlorate. Since this had no effect on the reaction temperature or the observed partial decomposition during the DA reaction, this approach was not pursued further. The formation of the by-products is an indication of a poor cyclability. To take a closer look at this the reaction was repeated in the solid state in the DSC. Five cycles in the temperature range from 0 °C to 200 °C were carried out. The DSC curves of the 2nd and 5th cycles are shown in Figure 33.

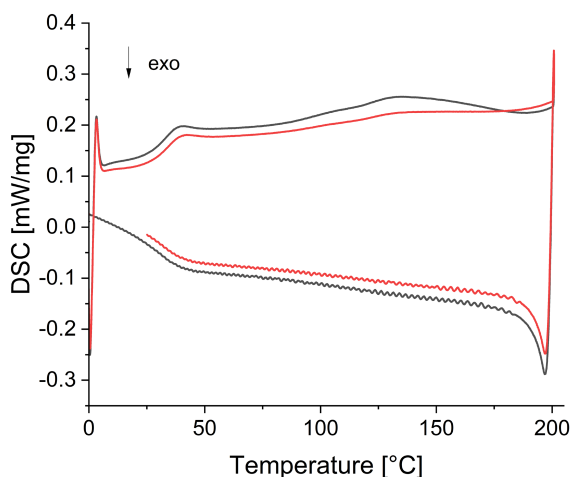


Figure 33: 2nd (black) and 5th (red) heating cycle of the cationic DA product.

The DSC curve shows the DA and rDA reaction at a temperature of 43 °C and 134 °C, respectively. The overall signal intensity is low, and broad signals are obtained especially for the rDA which is consistent with the required longer reaction time already observed in solution. Furthermore, both the heat transfer of the DA and the rDA decrease from 12.5 J/g to 7.3 J/g and 12.9 J/g to 3.6 J/g, respectively, from the second to the fifth cycle, which is consistent with

Results and Discussion

the partial decomposition observed previously. Since no further endothermic signal is observed in the high temperature range, it can be assumed that the rDA signal is superimposed by the decomposition signal.

In the following, the switchable system was transferred to the iron oxide particles. For this purpose, a ratio of 0.3 mmol phosphonic acid per 150 mg particles was chosen. The purified and dried particles were analyzed by CHN and TGA. The occupancy density was again calculated applying Equation (10). The nitrogen content from the CHN analysis was used for this. A loading density of 1.06 mmol/g was calculated. This is within the range of the occupation densities of the permanent ionic systems, indicating that the space requirement of the anchor group rather than the ionic group is responsible for the loading density. Subsequently, the DA reaction was performed on the particle surface. For this purpose, toluene was added to the maleimide-functionalized particles. Then 4-(furan-2-yl)-*N,N,N*-trimethylbutan-1-ammonium bromide dissolved in water was added. The two-phase mixture was then heated overnight at 100 °C under vigorous stirring. The reaction mixture was photographed before and after the reaction. The black, initially maleimide functionalized particles are located in the denser toluene phase. After heating, the particles are brown in color, indicating oxidation. The particles also accumulate at the phase interface and on the glass wall. This is surprising since a transition to the aqueous phase was expected during the ionic functionalization. To avoid oxidation, the experiment was carried out again under argon atmosphere. No brown coloration of the particles was observed in this reaction. In addition, a transition into the water phase was observed (see Figure 34).

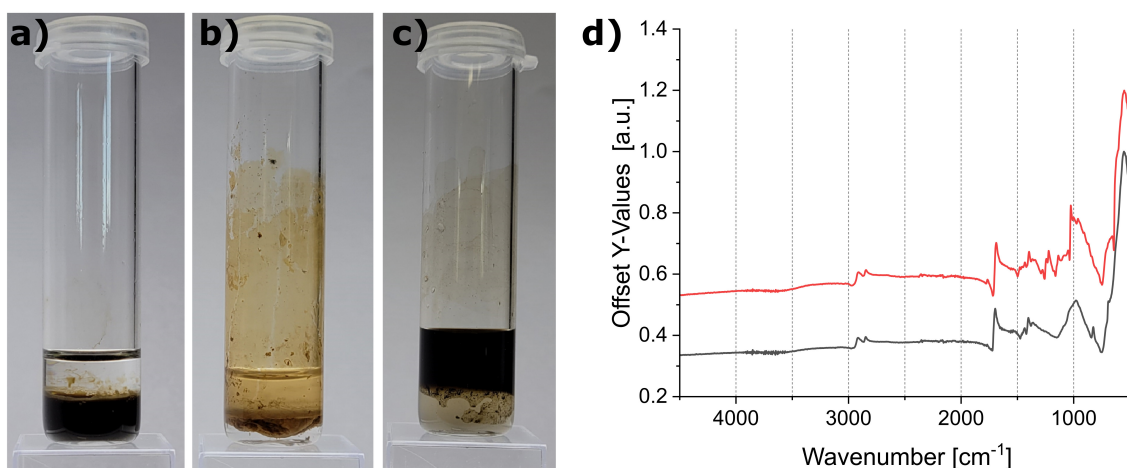


Figure 34: Maleimide functionalized particles in a toluene-water mixture a) before and after reaction with 4-(furan-2-yl)-*N,N,N*-trimethylbutan-1-ammonium bromide under b) air and c) argon atmosphere. d) FTIR spectra of the dried samples of the maleimide (black) and cationic functionalized particles (red).

Oxidation of the particles was sufficiently suppressed by conducting the reaction under inert gas. Since the particles transfer into the aqueous phase after the reaction, the cationic functionalization appears to be successful. The FTIR spectrum of the dried particles also confirms the successful DA reaction by the appearance of the symmetric and asymmetric C-O

stretching vibrations at 1025 cm^{-1} and 1216 cm^{-1} respectively. The zeta potential of the particles prepared under inert gas was also recorded. The results are shown in Figure 35.

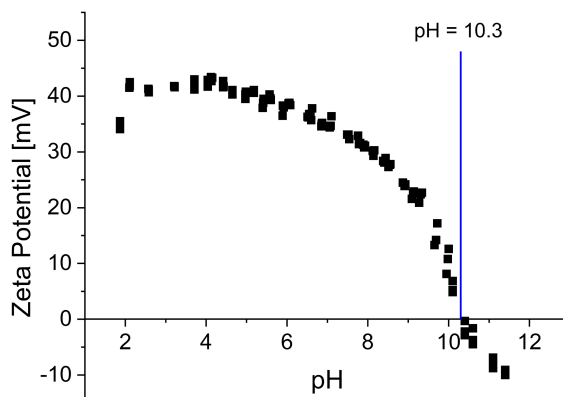


Figure 35: Zeta potential of the switchable cationic phosphonic acid functionalized iron oxide nanoparticles as a function of pH.

The zeta potential of the sample starts at about 40 mV and remains constant up to pH 4. Compared to the permanently charged particles, the positive surface charge of the switchable system seems to decrease earlier. From the range of the IEP of the oleic acid functionalized particles a stronger decrease of the zeta potential starts, analogous to the permanently charged particles. Nevertheless, a positive zeta potential is achieved over almost the entire pH range, which confirms the successful integration of positive charges on the particle surface. The IEP, with a value of 10.3, is slightly below the value for the permanently charged ones (10.6). Subsequently, an attempt was made to perform an rDA reaction. Contrary to the previous observations for the molecular system, no rDA was observed on the particle surface either in the solid state in the DSC or in the particle dispersion in ethylene glycol at $140\text{ }^{\circ}\text{C}$. Instead, thermal decomposition appears to be occurring, as no nitrogen was detected in the samples in the subsequent CHN analysis. Similar to the previously described deprotection of the cationic maleimide, the energy barrier of the rDA appears to be increased, severely limiting the performance of the rDA. Because of this problem with cyclability, the preparation of ionic self-healing nanocomposites has been limited to the permanently charged systems.

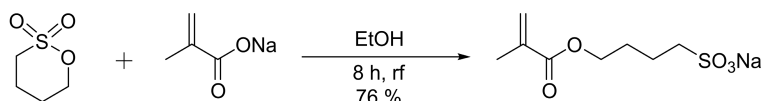
3.4. Ionic Self-Healing Nanocomposites

Self-healing is a phenomenon that has long been known and widely studied in the field of polymer chemistry. In recent years, due to the potential of composite materials, the phenomenon has also been increasingly investigated in this field as well. So far, the emphasis has been on healing mechanisms based on DA and hydrogen bonds. Due to their autonomous healing, hydrogen bond-based systems are of particular interest. Healing through ionic interactions, on the other hand, has so far only been scarcely investigated. A central goal of this work is to transfer the excellent self-healing properties known for ionomers and polyelectrolytes to composite systems. Two basic strategies for the preparation of self-healing

nanocomposites were considered in this work. On the one hand, the reversible interaction responsible for healing is brought to the particle-polymer interface and, on the other hand, the healing functionality is completely transferred to the polymer, which is covalently bound to the particle surface. The results of these two approaches will be discussed in chapter 3.5 and 3.6, respectively.

3.5. Self-Healing Nanocomposites via Ionic Interactions at the Particle-Polymer Interface

Several self-healing nanocomposites have already been investigated in our group. In these previous experiments, it was shown that the self-healing efficiency depends on the mobility and flexibility of the polymer matrix and thus on the T_g and the degrees of freedom of the functional groups on the nanoparticle surface.[73,568,569] Overall, methacrylates have proven to be advantageous as a polymerizable group due to their high flexibility, as their properties are adaptable by the choice of the side chain. In addition, the high reactivity in the polymerization process remains often times independent of the functionalization. As a counterpart to the cationic functionalized particles, an anionic polymer was required. Due to the large pH-independence of the negative charge the sulfonate group was chosen. Initially, ω -bromoalkyl alcohols were used as the starting material, which were reacted with methacryloyl chloride to give the corresponding ω -bromoalkyl methacrylates. Subsequently, the halogen was converted to the sulfonate. The advantage of this process is that the chain length can be varied. Later, the chain length was fixed at four, as this is easier accessible by ring-opening of 1,4-butane sultone (Scheme 22).[644]



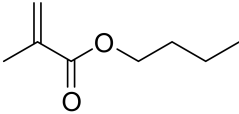
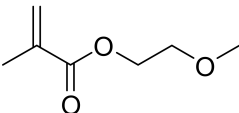
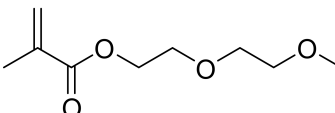
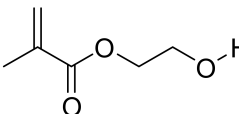
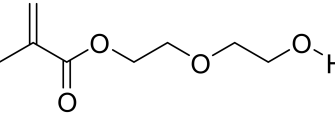
Scheme 22: Synthesis of sodium 4-(methacryloyloxy)butane-1-sulfonate.[644]

In this way, the synthesis of sodium 4-(methacryloyloxy)butane-1-sulfonate (SMBS) is achieved in good yields (76 %) and high purity. Since anionic polyelectrolytes such as poly(acrylic acid) tend to have high T_g s (> 100 °C) [627], it is often necessary to use copolymers, in which a second monomer provides a lower T_g . Butyl methacrylate (BMA), which is frequently used because of its low T_g and commercial availability, has proven to be an incompatible polymer backbone, due to the strongly differing polarity in comparison with the ionic systems. Initial studies failed to find suitable polymerization conditions, under which both monomers as well as the forming polymers can be dissolved. This resulted in poorly reproducible polymer compositions. Two approaches were tested to reduce the polarity difference between the monomers. The first one was to decrease the polarity of the SMBS via replacement of the counterion.[645] By exchanging the sodium counterion with the much less

Results and Discussion

polar tetrabutylphosphonium cation, the polarity of the sulfonate can be drastically reduced. The previously only water-soluble monomer was now also dissolvable in THF and in small amounts in toluene. However, the polymerization did not yield a copolymer with BMA, as overall, no reaction of the SMBS derivate was observed. In another approach, the BMA was replaced by a more polar system. In the context of using the polymer systems as components of self-healing nanocomposites, low T_g s were considered the key criterion for monomer selection. Table 5 shows the T_g s of some selected polymer systems.

Table 5: T_g s of some selected methacrylate polymers.

Polymer	Structural Formula of the Monomer	T_g of the Polymer
poly(BMA)		20-40 °C [646,647]
poly(MEGMA)		20-30 °C [616,648]
poly(DEGMA)		-40 °C [616]
poly(HEMA)		55-110 °C [627,649]
poly(HDEGMA)		87 °C

The T_g of poly(MEGMA) reported in the literature is in the range of that of poly(BMA). However, compared to poly(BMA), no significant increase in polarity and therefore no significant improvement in miscibility with the ionic components can be expected here either. Extending the chain by one ethylene glycol unit (DEGMA), should further increase the polarity. However, this also coincides with a very significant decrease in the T_g . Values around -40 °C are reported in the literature. The T_g of the polymer should also not be too low to maintain mechanical strength of the material and to allow a distinction between self-healing based on ionic interactions and simple chain interdiffusion. Since the introduction of the ionic and DA components is expected to increase the T_g , poly(DEGMA) was nevertheless investigated as a possible alternative to poly(BMA). Another possibility to further increase the polarity is the use of a hydroxyl terminated chain. The poly(HEMA) system has been extensively studied in the literature. A wide range of T_g values is described.[627,649] Compared to the methyl terminated

system of the same chain length, an increase in the T_g can be observed. Therefore, it is expected that poly(HDEGMA) should be well suited for application. Unlike DEGMA, HDEGMA is not commercially available and was prepared from diethylene glycol. The reaction was carried out with methacrylic acid using p-toluenesulfonic acid as a catalyst.[650] A T_g of 87 °C was determined by DSC after homo-polymerization. Surprisingly, this is significantly higher than that of poly(BMA), which is why the DEGMA system was used for the subsequent investigations. Both ATRP and free radical polymerization were used for copolymerization. The preparation and characterization of the polymers and the corresponding composites are described in more detail in the following chapters.

3.5.1. Synthesis and Characterization of Anionic Polymers by ARGET ATRP

Initially, the polymer synthesis was carried out via ATRP. This has the advantage of a high reaction control. Due to the presence of ionic groups, ATRP polymerization presents some challenges. All synthesized polymers were prepared via ARGET ATRP, using hydrazine as the reducing agent. Literature known procedures were applied, using a Cu(I) catalyst with 2,2'-Bipy as the ligand.[73] Polymerization was carried out in a water methanol mixture of 3:1 where the pH was adjusted to 0.9. The polymerization was carried out at 70 °C. In a first approach, the homopolymers for the monomers used were synthesized. Yields of 53 % for the ionic homopolymer and over 60 % for poly(DEGMA) and the synthesized copolymers were obtained after 24 h. ^1H NMR confirmed product formation and the removal of unreacted monomer during the work-up. Removal of the copper complex was achieved by dialysis against dilute HCl. Successful separation was indicated by the discoloration of the product (Figure 36).

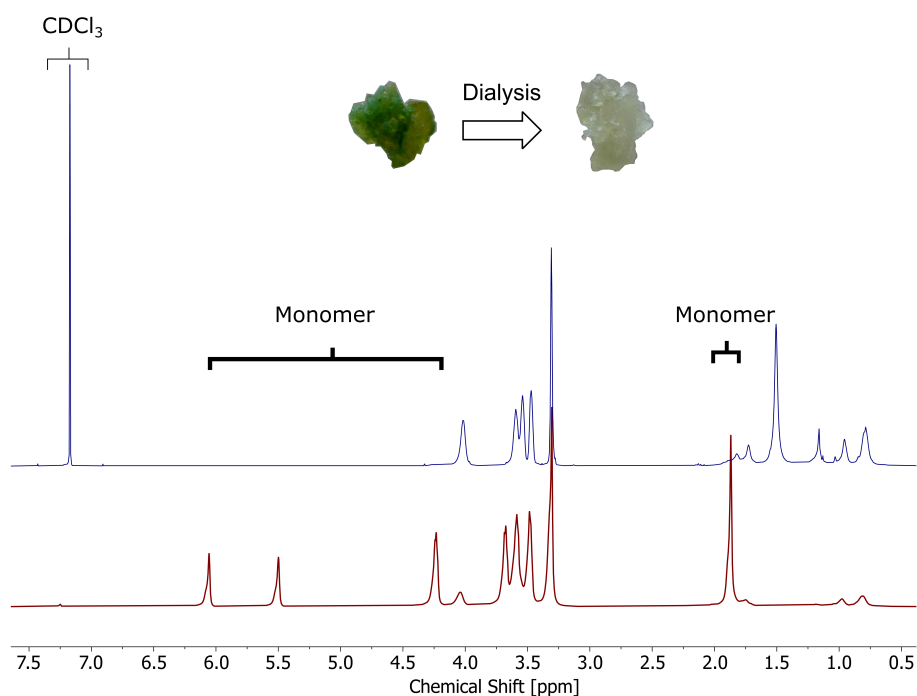


Figure 36: ^1H NMR spectra of poly(DEGMA) before (red) and after (blue) dialysis.

Results and Discussion

DSC measurements were performed on both synthesized homopolymers. The T_g was determined at $\frac{1}{2}\Delta c_p$. Poly(DEGMA) shows a very low T_g of approx. $-23\text{ }^\circ\text{C}$, which is in good agreement with literature reports.[616] Contrary the T_g of the anionic homopolymer is much higher at $126\text{ }^\circ\text{C}$. To evaluate the variability of the T_g by adjusting the polymer composition copolymers with monomer ratios of 1:10, 1:8, 1:5 and 1:3 (SMBS:DEGMA) were synthesized by weighing the respective amounts of monomer. The polymers are hereafter referred to as ^{10}Pol , ^8Pol , ^5Pol and ^3Pol , respectively. Initially, a sample with a polymer composition of 2:1 was also synthesized. However, it was not further investigated because the resulting samples were extremely brittle and could not be brought to a processable state. Figure 37 shows the ^1H NMR spectra of the obtained polymers. The spectra were normalized to the COO-CH₂ signal at 4.11 ppm.

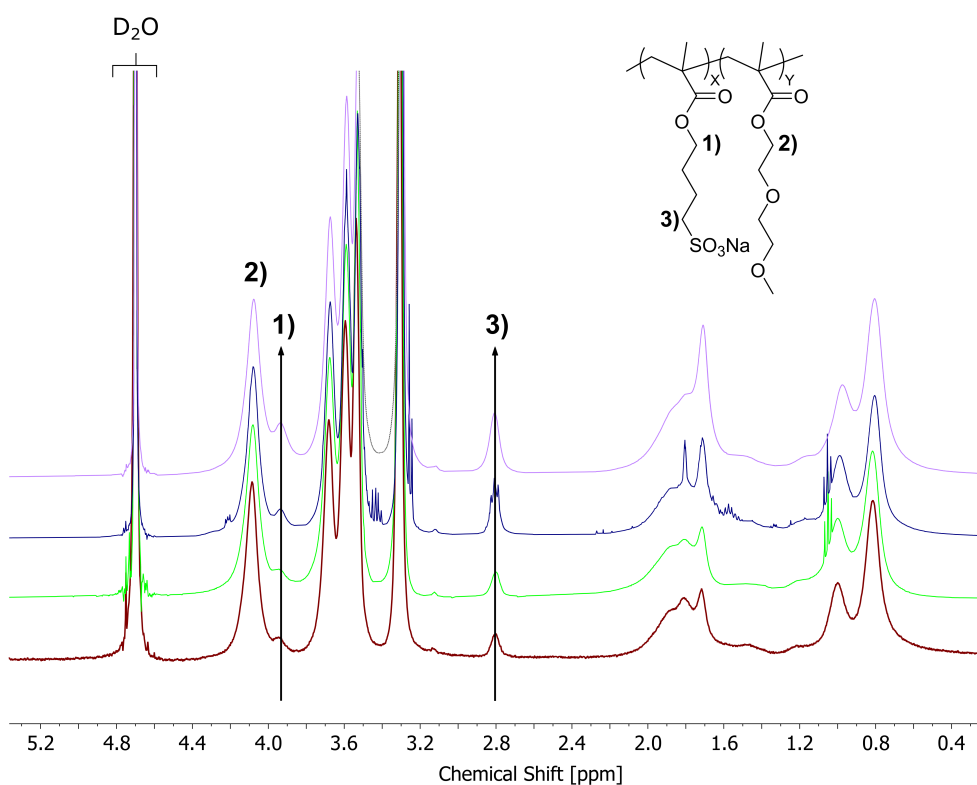


Figure 37: ^1H NMR spectra of ^{10}Pol (red), ^8Pol (green), ^5Pol (blue), ^3Pol (purple) synthesized by ARGET ATRP.

The ratio between the SMBS and DEGMA signals increases as the ionic fraction in the monomer mixture is increased. The polymer composition determined by integration of the ^1H NMR signals agrees with the initial weighted monomer ratios (see Table 6).

Results and Discussion

Table 6: Influence of the polymer composition on the T_g .

Sample	DEGMA _{theo}	SMBS _{theo}	DEGMA _{found}	SMBS _{found}	T_g [°C]
poly(DEGMA)	n	-	n	-	-23
poly(SMBS)	-	n	-	n	126
¹⁰ Pol	10n	n	11.0n	n	-18
⁸ Pol	8n	n	8.1n	n	-16
⁵ Pol	5n	n	5.2n	n	26
³ Pol	3n	n	4.0n	n	50

Subsequently, DSC measurements were carried out to determine the thermal properties, in particular the T_g s of the polymers. Figure 38 shows the obtained DSC curves in the range of the T_g for the DEGMA homopolymer and the synthesized copolymers. T_g s between -18 °C and 50 °C were determined for the copolymers. No additional signals are obtained in the DSC, confirming the formation of a random copolymer. The T_g s of the synthesized polymers increases as the proportion of ionic species increases.

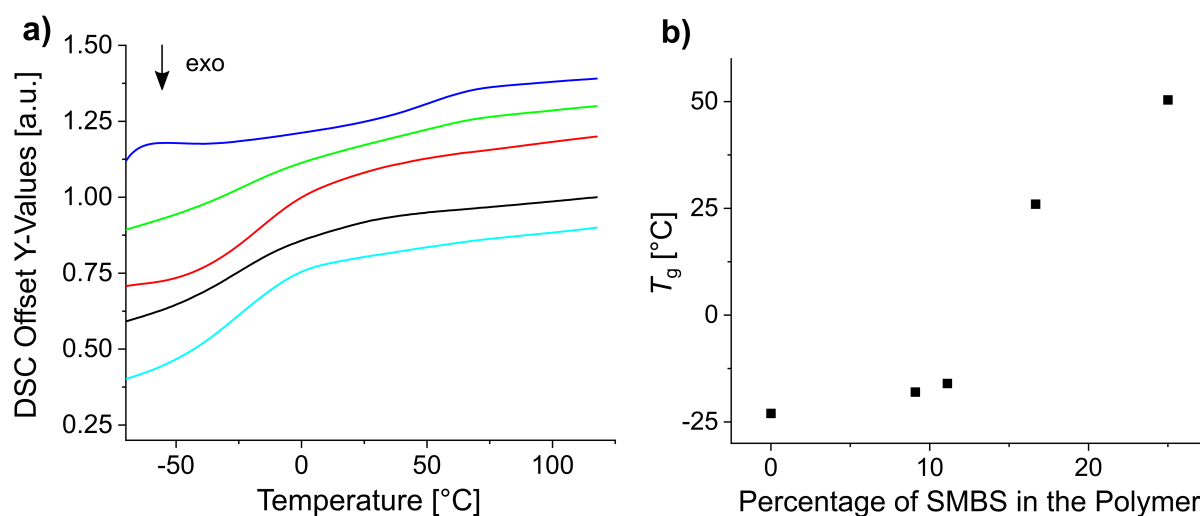


Figure 38: a) DSC curves of the synthesized copolymers via ARGET ATRP and b) influence of the polymer composition on the T_g .

The observed increase in T_g with increasing proportion of ionic species is below the rule of mixture. This is in agreement with reported copolymers and empirical models such as the Gordon-Taylor equation.[651,652] Especially at the lower molar percentages the T_g only increases very slightly, whereas at the higher molar concentrations, after a certain threshold, the increase is significantly higher.

TGA measurements were performed to evaluate the thermal stability of the polymers used. The results are shown in Figure 39.

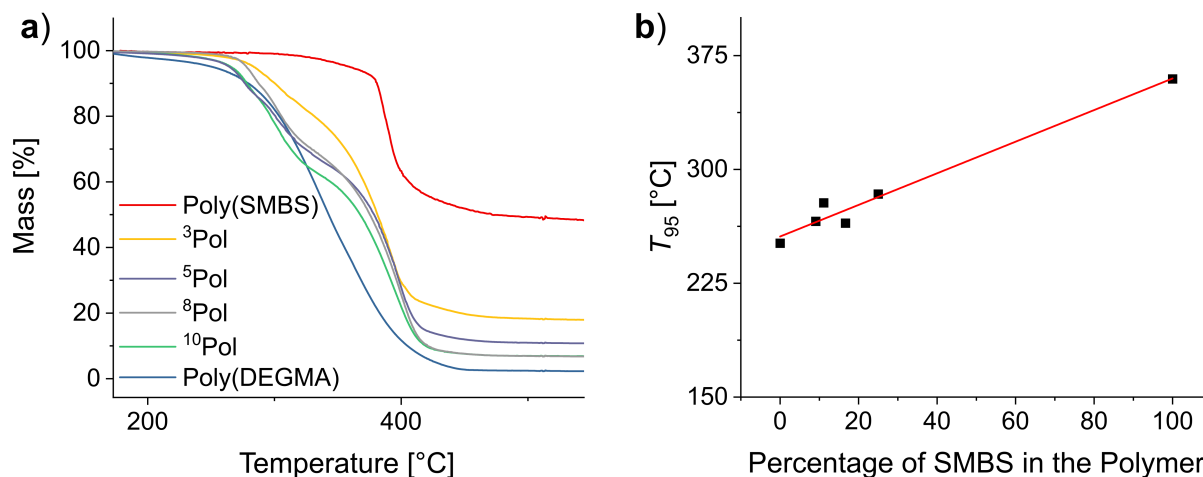


Figure 39: a) TGA of the synthesized polymers via ARGET ATRP and b) influence of the polymer composition on the T_{95} values. The samples were heated from room temperature to 880 °C under nitrogen atmosphere, followed by heating to 1000 °C under a mixture of nitrogen and oxygen (4:1) with a rate of 10 K/min.

For all polymers, decomposition begins at temperatures above 250 °C. For the matrix polymer, the onset is at 274 °C. In contrast, the temperature stability of the anionic polymer is much higher, showing decomposition at 375 °C. Consequently, the synthesized copolymers show two distinct decomposition steps at the respective decomposition temperatures of the homopolymers. The T_{95} values (temperature at 5 % mass loss) of the polymers were considered to evaluate the polymer stability. By increasing the amount of poly(SMBS) in the polymers an almost linear increase of the T_{95} values from 251 °C for poly(DEGMA) to 360 °C for poly(SMBS) is observed (see Figure 39). Furthermore, poly(DEGMA) shows an almost complete decomposition (char yield: 2 %), whereas a residual mass of 48 % is determined for the ionic poly(SMBS).

In summary, anionic copolymers were successfully prepared by ARGET ATRP. The monomer ratio of SMBS and DEGMA provides an easy way to tailor the polymer composition and thus the T_g , which is the crucial parameter for self-healing. This composition further controls the thermal stability of the polymers. With the lowest T_g s, polymers also exhibited the lowest temperature resistance. In the following, the self-healing nanocomposites were produced by combining the ionic polymers with the previously synthesized cationic nanoparticles.

3.5.2. Synthesis and Characterization of Ionic Nanocomposites based on the ATRP Polymers

Nanocomposites were obtained by mixing the synthesized copolymers with the respective amount of cationic functionalized nanoparticles in a water/THF solvent mixture (1:1). Particle contents between 1 wt% and 20 wt% were used. The solvents were evaporated at room temperature under vigorous stirring. The composite specimens were prepared by compression molding in a Teflon mold at 80 °C using a vice. The entirety of the synthesized composites is shown in Table 7.

Results and Discussion

Table 7: Composite names and compositions (C10_1-C3_20).

	¹⁰ Pol	⁸ Pol	⁵ Pol	³ Pol
1 wt% ^{0.200} P@Fe _x O _y	C10_1	C8_1	C5_1	C3_1
2 wt% ^{0.200} P@Fe _x O _y	C10_2	C8_2	C5_2	C3_2
5 wt% ^{0.200} P@Fe _x O _y	C10_5	C8_5	C5_5	C3_5
20 wt% ^{0.200} P@Fe _x O _y	C10_20	C8_20	C5_20	C3_20

Black, solid, and highly magnetic samples were obtained. All specimens show no macroscopic agglomeration of the particles within the polymer (Figure 40).

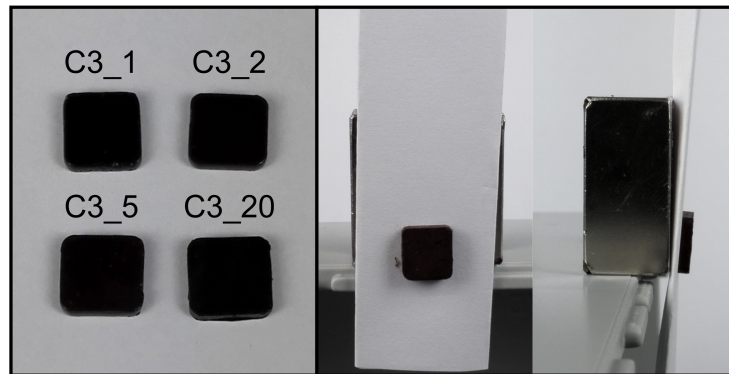


Figure 40: Image of the ³Pol based nanocomposites C3_1, C3_2, C3_5 and C3_20 (1 wt%, 2 wt%, 5 wt% and 20 wt% particle content). Dimensions: 0.5 cm x 0.5 cm x 1 mm and investigation of the magnetic properties of C3_1.

Analogous to the polymer samples, TGA measurements were performed on the composites to determine their thermal stability. The results for the ¹⁰Pol and ³Pol based systems are shown exemplarily in Figure 41. In contrast to the polymer composition, the particle content has little effect on the material's thermal stability. While a slight increase in the T_{95} value is observed for all composites, the influence seems to decrease with increasing proportion of the ionic component in the polymer. For the ¹⁰Pol based systems, the decomposition is shifted from 266 °C to 275 °C when the particle content is increased from 0 wt% to 20 wt%. For the ³Pol systems, on the other hand, the shift is only about 5 °C for the same particle contents. As already observed for the polymer systems the char yield of the ³Pol based composites is much higher than that of the ¹⁰Pol based systems. The observed increase in char yield of the composites compared to the respective polymers correlates almost linearly with the particle content. With the introduction of 20 wt% particles, the char yields increase from 6 % to 24 % for the ¹⁰Pol and from 16 % to 26 % for the ³Pol based systems, respectively.

Results and Discussion

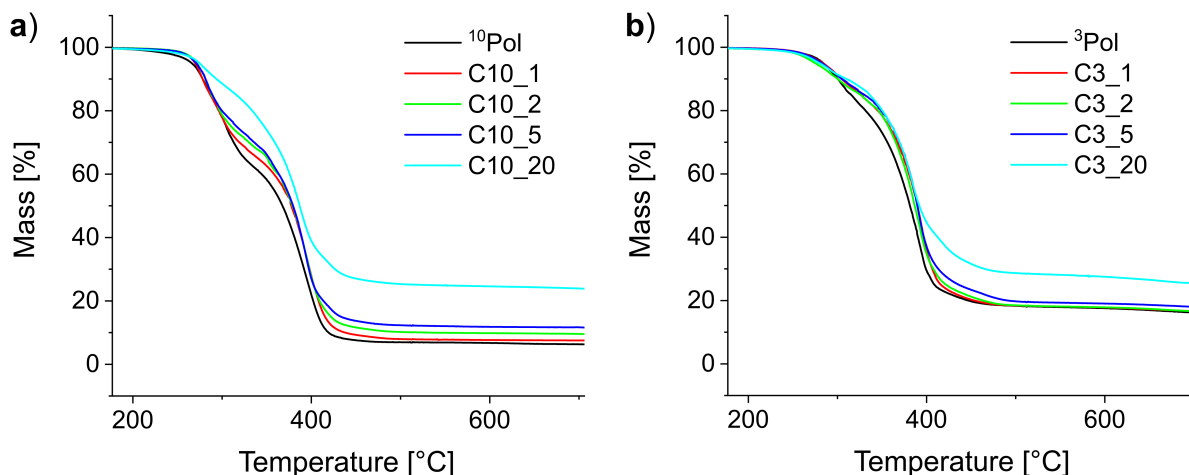


Figure 41: Thermogravimetric analysis of the a) ^{10}Pol and b) ^3Pol based composites (0-20 wt% particles). The samples were heated from room temperature to 880 °C under nitrogen atmosphere, followed by heating to 1000 °C under a mixture of nitrogen and oxygen (4:1) with a rate of 10 K/min.

Next, the influence of the particle content on the T_g was investigated. The DSC analysis showed two different effects for composites with low and high SMBS content. Figure 42 shows the curves obtained for the ^{10}Pol and ^3Pol based systems as representatives of systems with a low and high ionic character, respectively. DSC measurements revealed no changes of the T_g s for ^{10}Pol and ^8Pol based composites in comparison to the respective copolymers. These results are quite surprising, since a decrease in chain mobility and thus an increase in T_g would be expected due to the strong ionic interactions between the particles and the polymer matrix. Moll and Kumar explain the almost complete absence of a T_g shift, which has been described for many strongly interacting composite systems, by the fact that an almost irreversible bond is formed between the polymer and the filler.[653] As a result, the layer is dynamically decoupled from the rest of the "free polymer". Furthermore, they postulate this bonded layer does not relax in the time scale of the DSC measurements, whereby only the bulk polymer is recorded. For the composites with higher poly(SMBS) content, a decrease in T_g was even observed upon particle integration, with a decrease from 26 °C to - 10 °C for ^5Pol based systems and from 50 °C to - 15 °C for ^3Pol based systems, respectively. These results can be attributed to comprised solvent [654,655], which could not be removed completely, especially for the composites with higher SMBS contents. Independent of the polymer composition no deviations in the T_g were observed between the composites with 1 wt%, 2 wt%, 5 wt% and 20 wt% particle content.

Results and Discussion

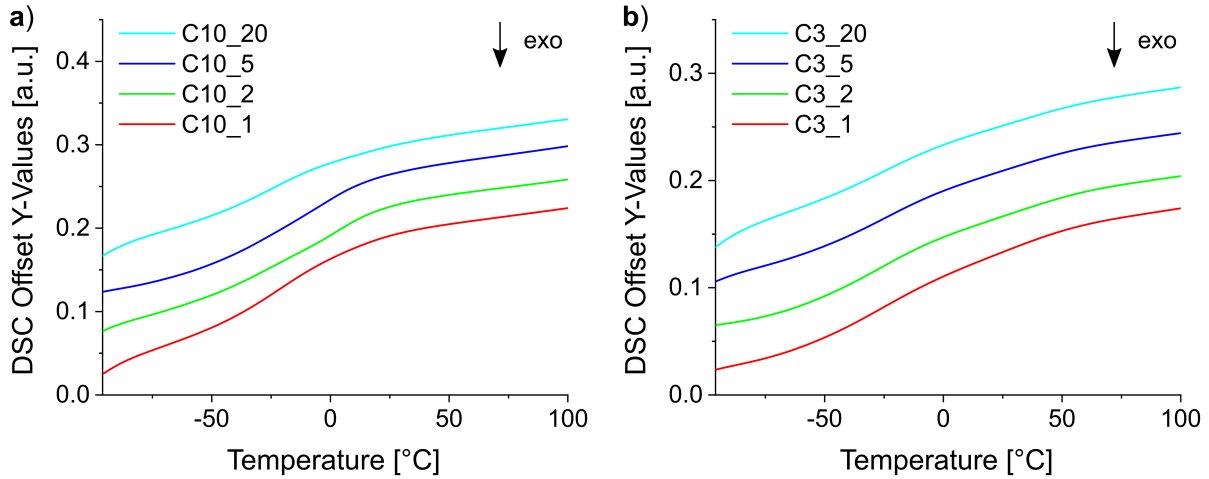


Figure 42: DSC curves of the a) ¹⁰Pol and b) ³Pol based composites (1-20 wt% particles).

The next step was to study the distribution of the particles in the polymer system. Several methods are available for this purpose. Backscattered electrons are often used in the form of BSE SEM measurements. To obtain the SEM images, the samples were cooled with liquid nitrogen and fractured. The resulting fracture edge was sputtered with gold and examined. The particles can be seen as brighter areas on the micrographs. The results for C3_1 - C3_20 are shown exemplarily in Figure 43.

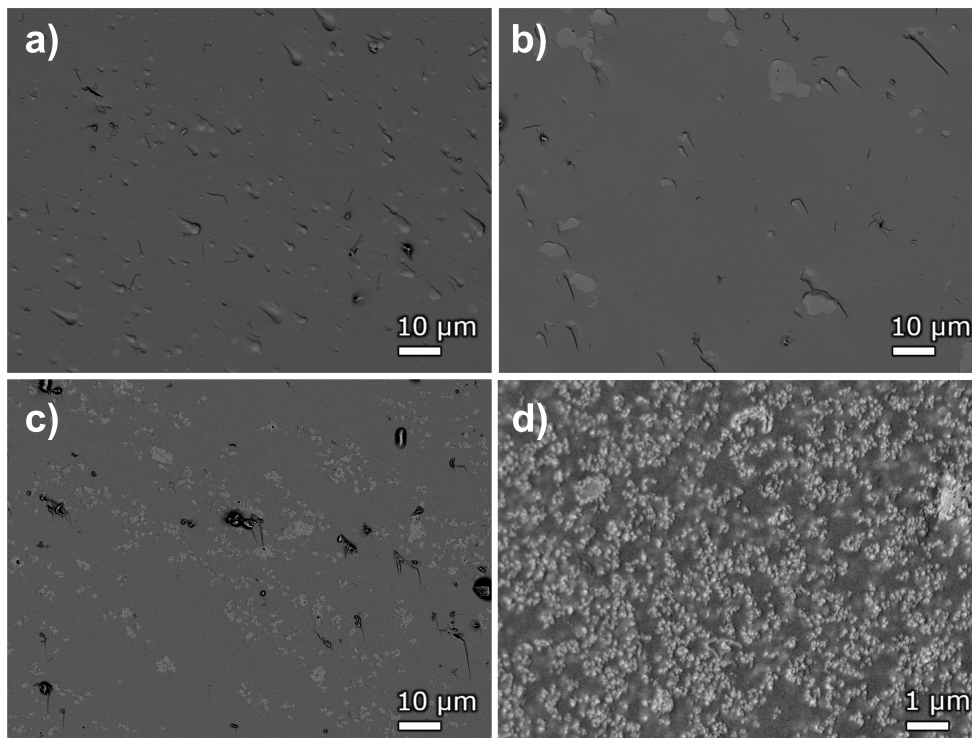


Figure 43: BSE SEM images of the a) C3_1, b) C3_2, c) C3_5 and d) C3_20 composites.

The micrographs show that particle agglomerates are obtained for all composites. At a particle content of 20 wt%, a large number of agglomerates with a size of about 100 nm (≈ 10 times the particle diameter) are present, forming an almost regular structure. At 5 wt%, the average

Results and Discussion

size of the agglomerates increases significantly. With a mean diameter of about 1 μM , this corresponds to 100 particles in diameter. In contrast to the sample with 20 wt% particles, these large agglomerates are not regularly arranged. Some of the agglomerates are further bridged to form large aggregates. As the particle concentration is reduced to 2 wt% a further increase in agglomerate size can be observed. These are several μm in size. Furthermore, it is not possible to see that they are composed of smaller units. Whether these are actually agglomerates or discoloration due to surface effects caused by the unevenness of the fracture edges cannot be said with certainty. The last composites considered, with 1 wt% particle content, again show slight variations in the agglomerates that form. They are spherical and, with an average diameter of 0.5 μm , again slightly smaller than the agglomerates of the sample with 2 wt% particles.

In addition, SAXS measurements were performed, which allow a more detailed description of the size distribution and the distribution of the particles in the network based on electron density differences. At this point, a brief explanation should be given of how the SAXS measurements were interpreted and what information can be gleaned from each of the curve features. Figure 44 shows the typical SAXS curves (scattering intensity versus scattering vector q) for several models of particle distribution in a polymer matrix. The SAXS curves are shifted along the intensity axis for better comparability.

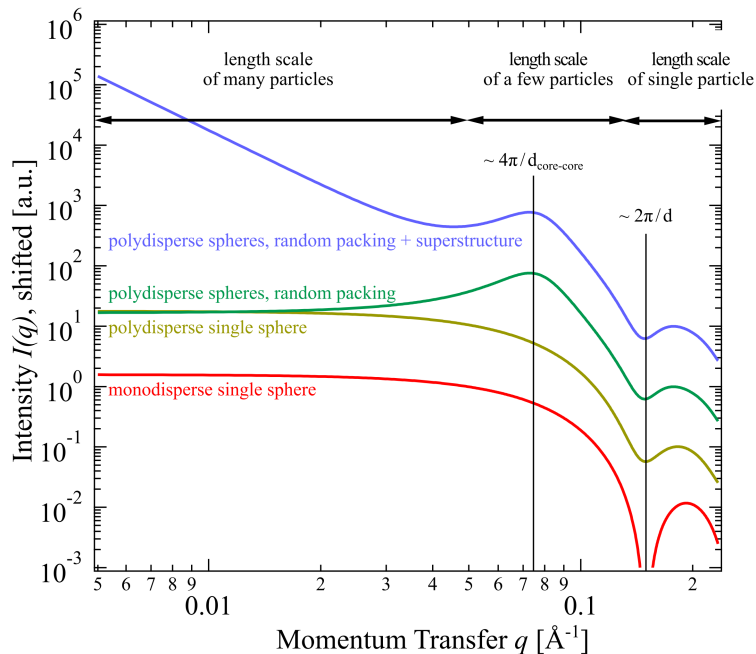


Figure 44: Expected scattering curves for the particle distribution models: monodisperse single sphere (red), polydisperse single sphere (yellow), polydisperse spheres with random packing (green) and polydisperse spheres with random packing and a superstructure (blue).

The SAXS curves can be divided into three regimes. At large q values the SAXS curve is determined by the embedded primary particles and represents the length scale of 3 - 10 nm. At the intermediate and small q values, larger ranges of first 5 – 20 nm and then 20 – 120 nm

are mapped. Thus, the SAXS measurements allow not only the description of the primary particles, but also their distribution in the material.

Scattering from dispersed nanoparticles can be described by the form factor of monodisperse spheres. The main feature of this model is a shoulder accompanied by secondary features such as minima and maxima depending on the particle distribution. When well dispersed single sphere particles are considered, a sharp minimum is observed where the intensity drops to zero (red curve). This is at $q = \frac{2\pi}{d}$, where d is the sphere diameter. Since nanoparticles in real samples have a certain size distribution, this originally sharp signal broadens and becomes less deep (yellow curve). If several spheres are considered, which are not completely randomly distributed, but whose positions show a certain regularity, an additional peak in the scattering curves is obtained (green curve). This occurs at $q = \frac{4\pi}{d_{cc}}$, where d_{cc} is the distance between two adjacent spheres (center-to-center). The more orderly the spheres are packed and thus the higher the density, the sharper and more intense this peak becomes. In agglomerates of nanoparticles, this structure is usually not arbitrarily large, but a superstructure is formed from these locally packed particles leading to an increase in scattering intensity in the low q range (blue curve). To quantify the structural properties of the nanoparticles the data was modeled using the function:

$$I(q) = I_P(q) + S_{HS}(q)P_{pS}(q) + I_{bkg} \quad (11)$$

Where $P_{pS}(q)$ is the form factor of polydisperse spheres following a Gaussian size distribution, and correlates with the radius R of the nanoparticles.[656] $P_{pS}(q)$ is multiplied by a disordered hard sphere structure factor, $S_{HS}(q)$, accounting for the nanoparticle arrangement.[657] It yields the hard sphere radius, i.e., half of the center-to-center distance of the nanoparticles, and the volume fraction that the hard spheres occupy within the agglomerates. Furthermore, a generalized Porod law, $I_P(q)$ accounts for large-scale structures. I_{bkg} is a constant background. Figure 45 shows the SAXS curves and determined fits, obtained at different particle contents for the ³Pol based systems.

Results and Discussion

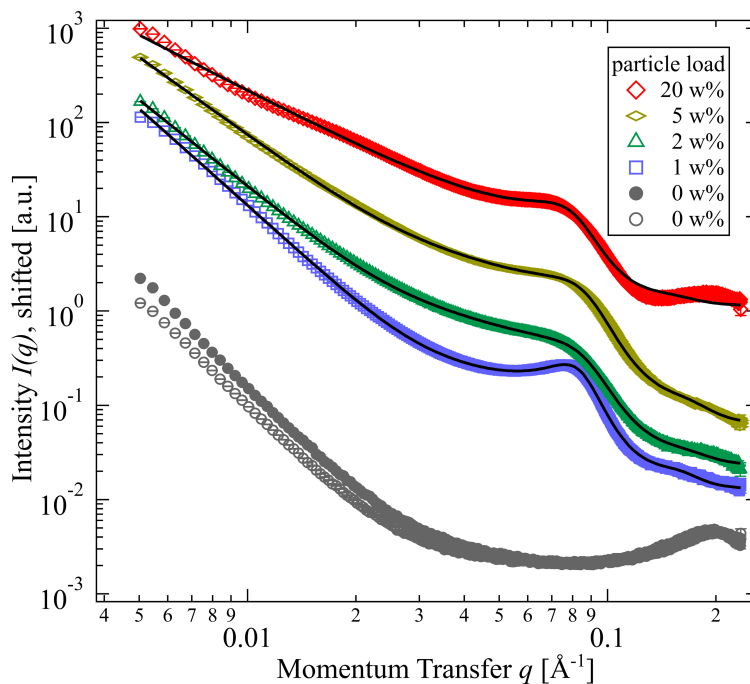


Figure 45: SAXS curves of ${}^3\text{Pol}$ and the composites C3_1-C3_20. Black lines are fits to the data using Equation (11).

The scattering curve of ${}^3\text{Pol}$ represents the base line. As the polymer showed a strong background signal, it was not possible to accurately determine the particle size from the SAXS data. Therefore, an average particle diameter of 5.9 nm, derived from TEM was assumed for the fits. The peak at about 0.08 \AA^{-1} has a lower intensity and is shifted to larger q values for the 2 wt% and 5 wt% particle content samples than for the 1 wt% and 20 wt% particle content samples. Consequently, the fitting model yields a lower local density of about 26 % and a smaller core-to-core distance of 7.0 nm. For the samples with 1 wt% and 20 wt% particle content, a local density of 33 % and a core-to-core distance of 7.5 nm were determined. The deviation of the core-to-core distances is within the standard deviation of the mean particle diameters of different particle batches. The local density does not refer to the absolute number of particles, but to how densely they are packed locally. Comparing a well-dispersed to an agglomerated particle system with the same total density/particle number, the model would yield different local densities. A lower local density for the well-dispersed system (0 for an ideally distributed system) and a higher one for the agglomerated system is obtained. A high local packing density thus means that the particles can pack especially densely. In the extreme case, for example, an FCC structure with a packing density of 74 % is formed. Conversely, if the fraction of particles is small, yet a high local density is determined, as seen for the 2 wt% and 5 wt% particle content samples, there must be large areas in the polymer where no particles are located, especially when larger agglomerates are formed. This is in good agreement with the results of the BSE SEM measurements. Furthermore, the decrease in the Porod exponents from 1 wt% to 20 wt% indicates that the superstructure is becoming more open and less compact, which can also be supported by the SEM measurements.

Since particle agglomerates were observed in all cases when mixing polymer and particles in solution, cryogenic milling was used as a second method for composite preparation. Cryogenic milling is particularly suitable for the treatment of elastic materials such as the polymers used here, which have a T_g well below room temperature. Cryogenic milling takes advantage of the fact that these materials become brittle at low temperatures, thus enabling milling. The milling jars were cooled with liquid nitrogen. Overall, based on the SEM and SAXS data, there was no significant difference in agglomeration resulting from the two manufacturing processes. Only the Porod exponent determined from the SAXS data, and the local density of the particles differed slightly, indicating a more open superstructure is present in the cryo ground composites. Since agglomerates were also observed in all cases for these systems, the solution-based preparation approach was retained in the following to exclude decomposition of the polymer during the milling process. In the next step, the self-healing of the samples was investigated.

3.5.3. Self-Healing Studies on the Ionic Nanocomposites based on the ATRP Polymers

The self-healing studies were performed on specimens measuring 1 cm x 1 cm x 0.2 cm. Two types of self-healing experiments were performed, differing in the type of heat input used to provide the energy required for the healing process. First, regular heating in an oven was performed. For the self-healing experiments, the composite specimens were cut to half their thickness. The cut ends were carefully pressed together and heated at 80 °C for 24 hours. The specimens were then placed back into the Teflon molds and heated for another 24 hours. Microscope images were taken after each step. The results are shown exemplarily for the C3_20 system in Figure 46.

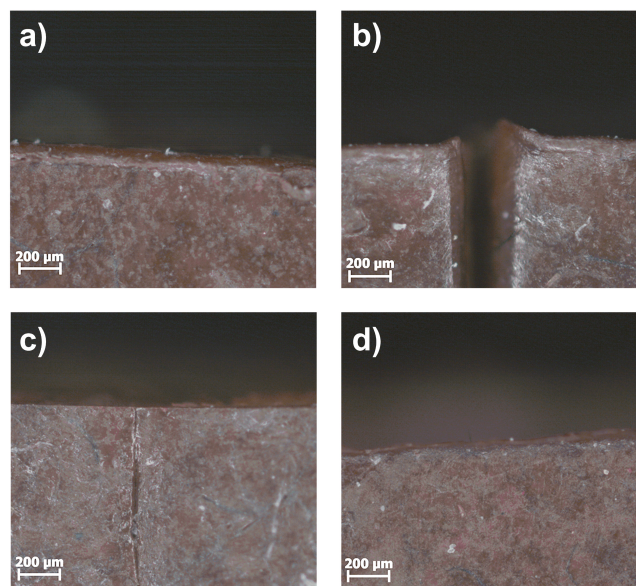


Figure 46: Microscope images of a) C3_20, b) cut through half thickness, c) gently pressed together at room temperature then heated to 80 °C for 24 hours and d) another 24 hours at 80 °C in a Teflon mold.

Results and Discussion

Within the first 24 hours an almost complete recombination of the surfaces was observed. After another 24 hours the crack completely disappeared for all samples. Overall, the healing times are rather long, which is most likely due to the strong fixation of the particles and polymer by the ionic interactions. This results in an increased rigidity and reduced chain mobility, which restrains healing. As a result, the healing is generally faster for samples with lower SMBS and particle content, due to the higher chain mobility in low T_g systems. Closely associated with this seems to be the restricted cleavage and reconnection of the ionic bond. This is a known phenomenon in ionic self-healing polymers. To overcome this problem, for ionic polymers, healing is often performed in salt solutions. Thus, the charges are partially screened, and the binding dynamics are improved.[505,506] However, since the systems investigated are partially water soluble, this is not an option here.

Instead, healing studies were performed in an alternating magnetic field. For induction heating, it has been suggested that much higher temperatures can be reached in the nano environment of the particles, far exceeding the macroscopic temperatures.[658] This might improve the binding dynamics at the particle surface. For further investigations, the ^{10}Pol based systems were excluded as they tended to melt and interflow upon heating, which did not allow the investigation of the actual healing process based on ionic interactions.

In preparation for the self-healing experiments in alternating electromagnetic fields, heating studies were performed. Figure 47 shows exemplarily the determined temperature at varying generator powers over time for the composites C3_1 – C3_20. In general, a slightly lower heat generation was observed for the composite systems than for the particle dispersions. The course of the macroscopic temperature curve is determined to a large extent by the heat capacity of the matrix as well as by the interactions at the phase interface, which significantly control heat dissipation.[659–662] As expected, the heating efficiency increases with increasing particle content. The slight decrease in temperature in the first segment can be attributed to the water cooling of the induction coil. Starting from that point with every increase of the applied power a sharp increase in temperature is observed. Within five minutes an equilibrium is reached, and the temperature stabilizes. For C3_1, with the lowest particle content of 1 wt%, a maximum of 58 °C can be reached. At 2 wt% the maximum temperature slightly increases to 63 °C. For C3_5 and C3_20 temperatures above 80 °C (temperature used in oven self-healing experiments) are possible. It should be noted again that the temperature increase of the immediate nano environment around the magnetic nanocrystals is significantly higher than the macroscopic temperature.[658]

Results and Discussion

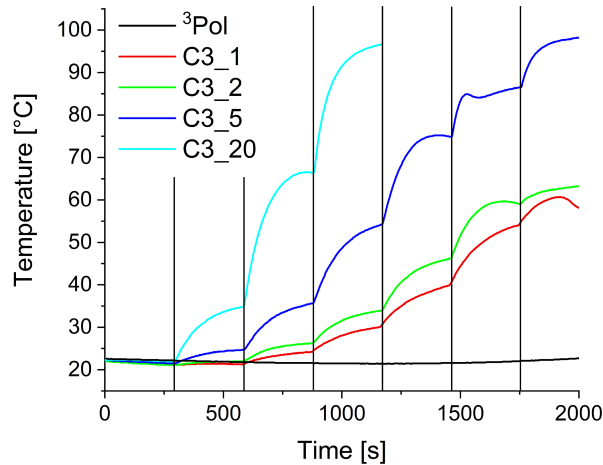


Figure 47: Heating studies for composites C3_1-C3_20 in alternating magnetic fields in comparison with the pure polymer. Frequency: 1.95 MHz, field strength: 0.5 - 1.1 kA/m, percentage values refer to the applied part of the total generator power of 3000 W for the respective heating segment.

The influence of the electromagnetic field on the ^3Pol sample was also investigated as a control experiment. Even at full power, no significant heating of the sample was observed. At this point the heating mechanism for the composites is not fully clarified yet, as for the used small particles used, a lower heating efficiency due to Néel and Brown relaxation can be expected. At higher frequencies heating might also occur due to eddy currents. Eddy currents are swirling loops of electric current induced in a conductor by a change in magnetic field. Conversely, they also occur when a conductor remains in the same position in a changing field. As a result, the current flowing through the resistance of the conductor dissipates energy as heat in the material.[663]

In the next step induction heating was used as a stimulus to initiate the healing process. The field strengths were adjusted to reach a macroscopic temperature of 58 °C, thus lying below the healing experiments in the regular oven. Analogously to the healing experiments in the regular oven, microscope images were recorded after pressing the edges together, after 24 hours and after 48 hours healing time. The results are shown in Figure 48 for the C3_20 system.

Results and Discussion

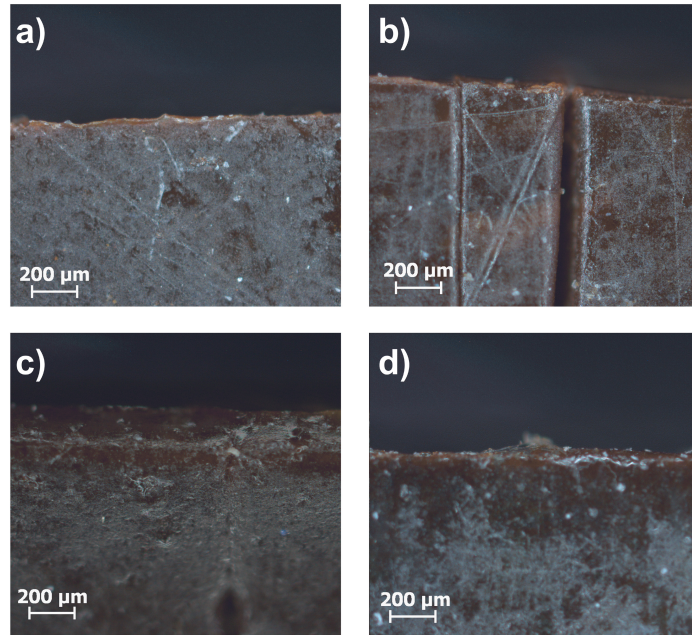


Figure 48: Microscope images of the a) untreated sample C3_20, b) the cut sample and the healed sample after c) 24 hours and d) 48 hours at 58 °C in the induction furnace.

As shown in Figure 48 the cut healed completely. A control experiment was performed with the polymer sample ³Pol, where no crack healing was observed. Due to the absence of the particles, the alternating magnetic field does not induce heat in the sample, which is necessary for the healing process. In addition, the removal of the ionic interactions, that occur between the particles and the polymer in the composites, hampers the self-healing. A comparison of the conventional oven heating and heating in the alternating magnetic field shows, that the induction heating allows faster and more efficient healing at lower macroscopic temperatures. This indicates that the locally generated high temperatures improve the healing process. To quantify the healing efficiency uniaxial tensile tests were performed.

First, the pristine composites were examined to determine the influence of polymer composition and particle content on the mechanical properties. Figure 49 shows the geometry of the specimens for the tensile tests. The measurements were carried out at a constant temperature of 20 °C and a displacement rate of 0.2 mm/s. Force-distance curves were recorded, which were converted to stress-strain curves taking into account the specimen geometry. Triplicate specimens were prepared for the measurements. Since good agreement was obtained between the triplicates, the average values of the measurements are given below for better clarity (Figure 49).

Results and Discussion

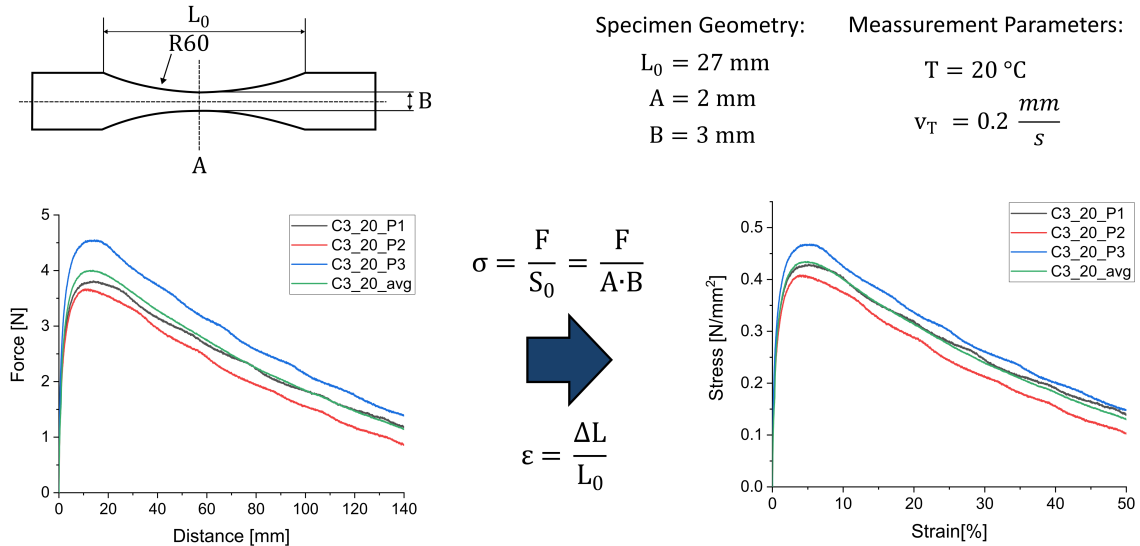


Figure 49: Sample geometry and evaluation of tensile tests.

Three parameters were considered to characterize the materials. First, the E-modulus (E), which describes the materials resistance to elastic deformation and is determined from the slope in the linear elastic region of the stress-strain plot. Second, the ultimate tensile strength (σ_{\max}), which describes the maximum stress the material can withstand and finally 0.2 % proof stress ($R_{p0.2}$) which is the stress at which the permanent elongation after unloading is 0.2 % of the initial length. In the first step, the influence of the polymer composition on the mechanical properties of the composites was investigated. The polymer composition was varied at a constant particle content of 5 wt%. Figure 50 shows the stress-strain curves of the composites C8_5-C3_5, as well as the plot of E-modulus, σ_{\max} and $R_{p0.2}$ against the polymer composition.

Results and Discussion

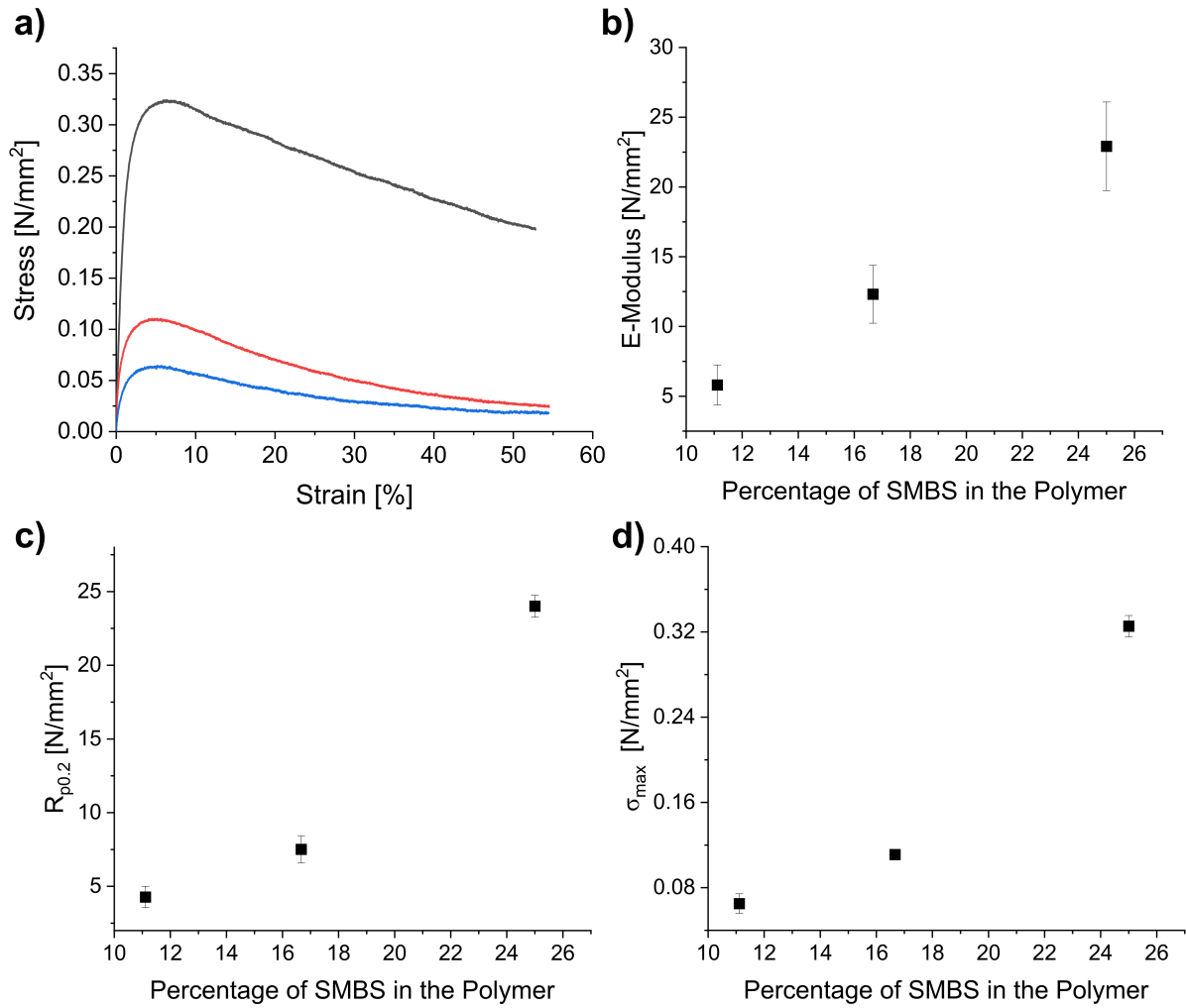


Figure 50: a) Stress-strain curves of ³Pol (black), ⁵Pol (red) and ⁸Pol (blue) based nanocomposites (5 wt% particles), as well as the determined b) E-moduli, c) $R_{p0.2}$ and d) σ_{max} values.

The materials exhibit the typical behavior of a viscoelastic solid. Initially, an elastic region is observed with a steep linear increase in the stress-strain curves. The samples are highly elastic regardless of the polymer composition. At a certain point (σ_{max} /yield point) the material undergoes significant elongation with a reduction in the stress due to the reduction in cross-sectional area. Despite the severe necking, no samples teared during the measurements within the maximum elongation possible on the tensile test rig. E-modulus, $R_{p0.2}$ and σ_{max} increase linearly with increasing ionic content in the polymer (Figure 50). For the E-modulus, an increase of about a factor of 4 is observed from 6 N/mm² to 23 N/mm², which are surprisingly low values. The $R_{p0.2}$ is also in a similar range. Both the $R_{p0.2}$ and the σ_{max} show a slightly better reproducibility within the triplicates.

Analogously, the influence of the particle content on the composite properties was investigated. For this samples with varying particle contents and a constant polymer composition of 1:3 (SMBS:DEGMA) were prepared. Particle contents from 0 to 20 wt% were investigated. The results are shown in Figure 51.

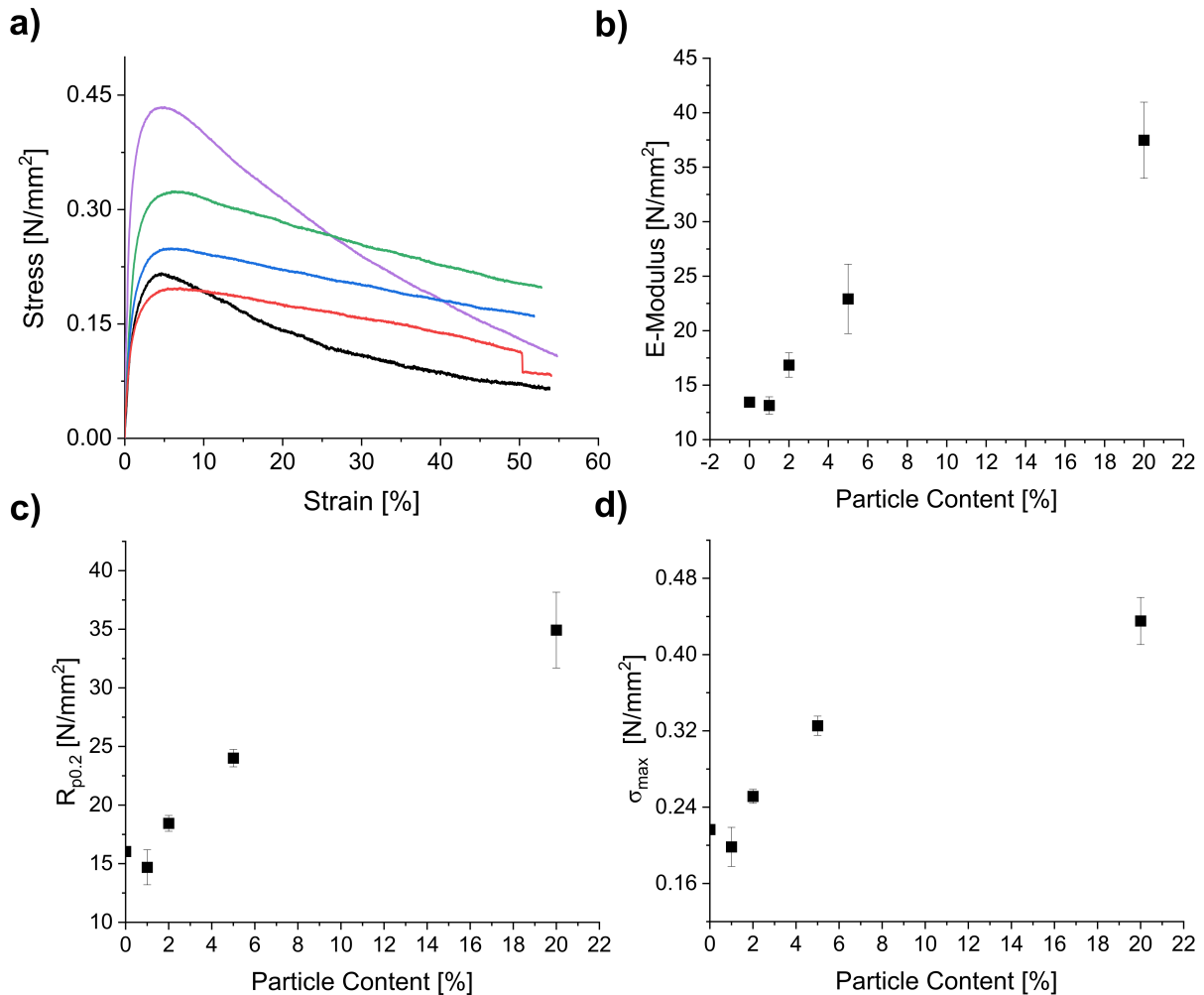


Figure 51: a) Stress-strain curves of the ³Pol based composites with particle contents of 0 wt% (black), 1 wt% (red), 2 wt% (blue), 5 wt% (green) and 20 wt% (purple), as well as the determined b) E-moduli, c) $R_{p0.2}$ and d) σ_{max} values.

In general, an increase in E-modulus and tensile strength is observed with increasing particle content. However, an exception arises in the case of the pure polymer system, where the tensile strength is slightly higher than the composite system with 1 wt% particles. In addition, the initial polymer, and the system with 20 wt% particles show different failure behavior. It is plausible that the particles at high concentrations facilitate the polymer chains to slide past each other more easily, similar to a solid lubricant, and thus change the damage behavior. This could be due to better distribution of the agglomerates in the polymer matrix observed for the 20 wt% particle system. Figure 51 also shows the plot of the E-modulus and tensile strength as a function of particle content. In contrast to the effect of polymer composition, the relationship here is not linear. Instead, the mechanical properties seem to reach a plateau at higher particle contents.

Subsequently, a second batch of specimens was prepared in the same manner. However, these were incised and then healed in an oven at 80 °C for 48 hours prior to measurement. As before, no further damage could be detected under the microscope after healing. Additionally,

Results and Discussion

two samples were prepared from the same ³Pol batch, one with 12 wt% and one with 30 wt% particle content, in order to check whether the mechanical properties actually plateau at higher particle levels. Only the sample at 12 wt% could be examined in tensile testing, since the sample obtained with 30 wt% particle content was extremely brittle and it was not possible to produce a crack free test specimen. Surprisingly, all ³Pol based specimens from the second batch, regardless of whether they were healed specimens or the newly prepared 12 wt% specimen, fractured even at low strains (< 30 %). Figure 52 a) shows the influence of the polymer composition on the E-moduli of the healed specimens (red) compared to the results from the first batch (black). Again, a linear increase of the E-modulus with the ionic content in the polymer is observed, although the healed samples have a much higher tensile strength overall. With E-moduli between 24 N/mm² and 413 N/mm², the values are in the initially expected range. The deviation between the healed and initial samples increases with increasing ionic content in the polymer. This can also be seen in all other specimens used to investigate the influence of the particle content (Figure 52 b). Again, the mechanical properties of the healed specimens are significantly higher. In contrast to the ionic content, the percentage deviation for low particle contents is higher than that for high particle contents. Significantly larger deviations between triplicates were also observed. Additionally, the E-modulus of the newly prepared 12 wt% unhealed sample is shown as a blue triangle. The E-modulus of this sample fits more closely to the healed samples (factor 0.5) than to the first batch (factor 10), although it does not align with any of the data.

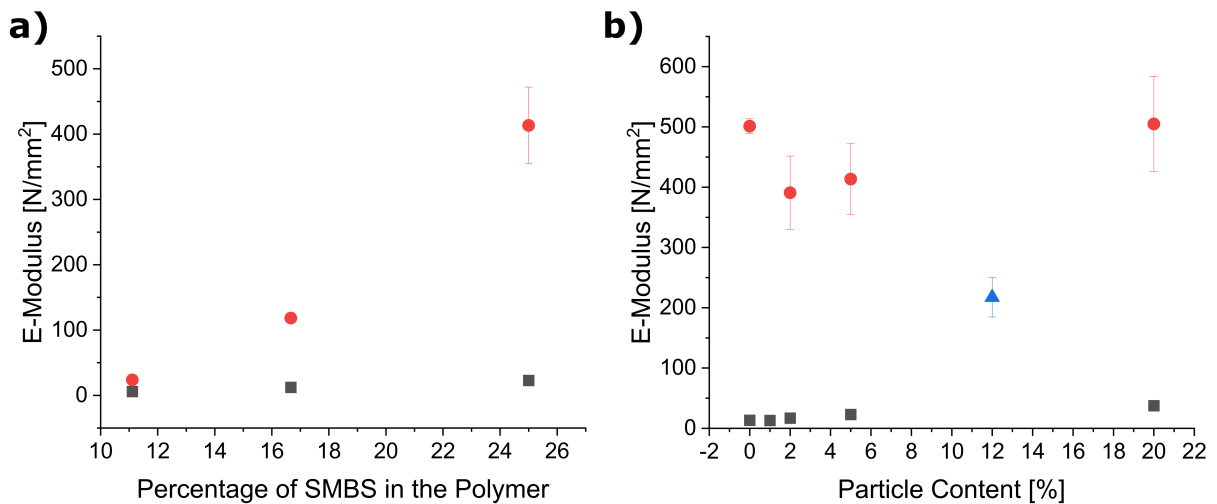


Figure 52: Plot of the mean E-moduli of the healed (red) and initial composites (black) as a function of a) polymer composition and b) particle content.

In summary, within a batch the expected trends can be observed, but the significant increase in hardness and brittleness of the samples during the curing process is surprising. The cause of the large deviations between the composite samples from different batches and the healed samples was subsequently investigated in more detail. The SMBS:DEGMA ratio and T_g s are consistent between different batches as determined by NMR spectroscopy and DSC, thus

eliminating polymer composition as a cause of the deviations. In addition, the particles for the entire series of experiments came from a single batch, eliminating the possibility of differences in the particle properties. Previous studies have shown that both poly(DEGMA) and polyelectrolytes tend to adsorb water from ambient air [664,665] and have even been used as moisture sensors because of the reversibility and rapidity of water uptake.[666] Due to this known affinity, it seems evident that the deviations in the properties are due to the water content of the samples. The influence of the water content on a variety of properties such as mechanical strength, stiffness and ion conductivity has been described in the literature.[665,667–669] The water content mostly depends on the storage conditions such as storage duration, temperature or ambient humidity. The self-healing experiments can be considered as an extreme case of these deviating storage conditions. During healing, the samples are exposed to an elevated temperature of 80 °C for a prolonged period of time. This might reduce the water content of the samples and lead to the observed increase in hardness and brittleness compared to the initial samples. Therefore, the influence of different storage conditions on water content and the material properties was subsequently investigated.

3.5.4. Investigation of the Influence of Storage Conditions on the Properties of the ATRP Polymers and Composites

Since the water content of the samples was identified as a key factor in the performance of the systems, the first step was to develop a method for determining the water content of the samples. A coupling of TGA and mass spectrometry was used for this purpose. MS measurements were performed in multiple ion detection mode. The ion currents belonging to H_2O^+ ($m/z = 18$), CO^+ ($m/z = 28$) and CO_2^+ ($m/z = 44$) were detected as a function of time. The sample was heated to 400 °C under nitrogen atmosphere. Figure 53 shows the TGA-MS measurement of a ^3Pol sample stored under humid conditions.

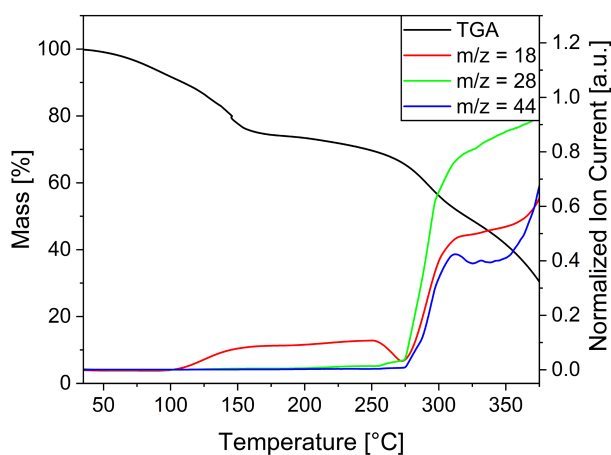


Figure 53: TGA-MS measurement of ^3Pol stored under high humidity. The sample mass (TGA curve) is depicted as a black line. The colored lines are the ion currents for $m/z = 18$, 28 and 44.

Results and Discussion

The TGA curve shows a strong mass loss of almost 30 % in the range from 50 °C to 200 °C and a second one starting at 250 °C. In the region of the first drop an increase of the ion current corresponding to H_2O^+ is observed. Afterwards the signal falls back to almost zero. On the other hand, in the region of the second mass loss, the increase of the ion current of $m/z = 18$ is accompanied by an increase of the ion currents of both $m/z = 28$ and 44, which correspond to CO^+ and CO_2^+ , respectively. This indicates that the polymer is decomposed in this region. The absence of these signals at low temperatures indicates that only the adsorbed water evaporates from the sample in the temperature range up to 200 °C. As a result, the water content of the sample can be easily assessed by determining the initial mass loss in TGA, allowing a precise study of the effect of water content on polymer properties.

To investigate the effect of storage on material properties, two extreme storage situations were considered: First, storage at elevated temperature and second, storage at high humidity. Both the polymers and the composites were studied. All samples were dried in a high vacuum for two days prior to the following series of measurements.

First, typical measurement variations were investigated using the vacuum-dried polymer sample ^3Pol . Figure 54 shows the TGA curves obtained, and the water content determined from the individual measurements.

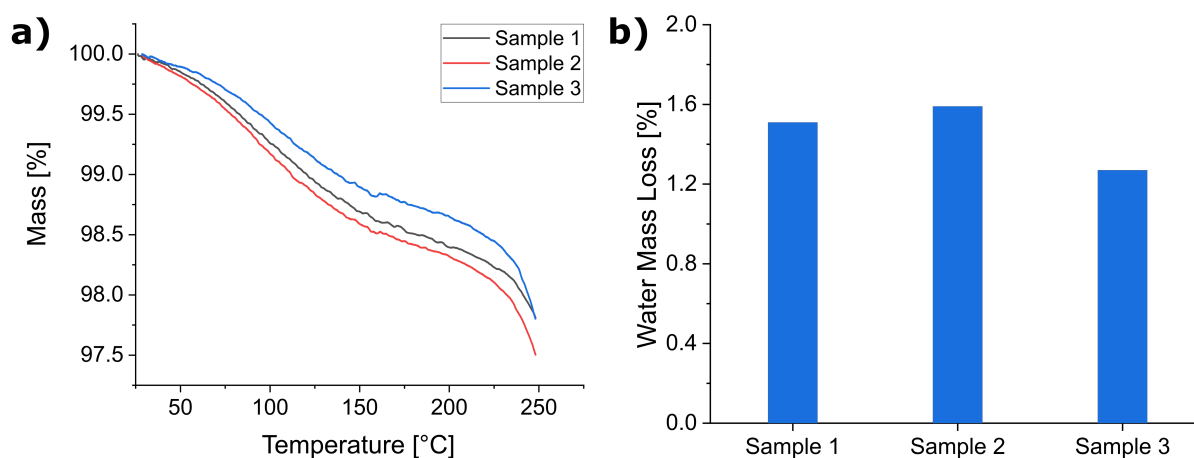


Figure 54: a) TGA curves of the vacuum-dried ^3Pol triplicates and b) their determined water content. The samples were heated from room temperature to 250 °C under nitrogen atmosphere with a rate of 10 K/min.

Even after vacuum drying, the samples still contain an average of 1.46 wt% water. A standard deviation of 0.12 wt% was obtained from the tests.

To study the influence of healing experiments the polymer samples were stored at 80 °C, which corresponds to the temperature of the healing experiments. Storage times of 5, 10, 15, 30, 60, 120, 180, and 4320 minutes were used. Subsequently, the polymer systems were analyzed by TGA. Figure 55 a) shows the water content of the polymer samples determined by TGA.

Results and Discussion

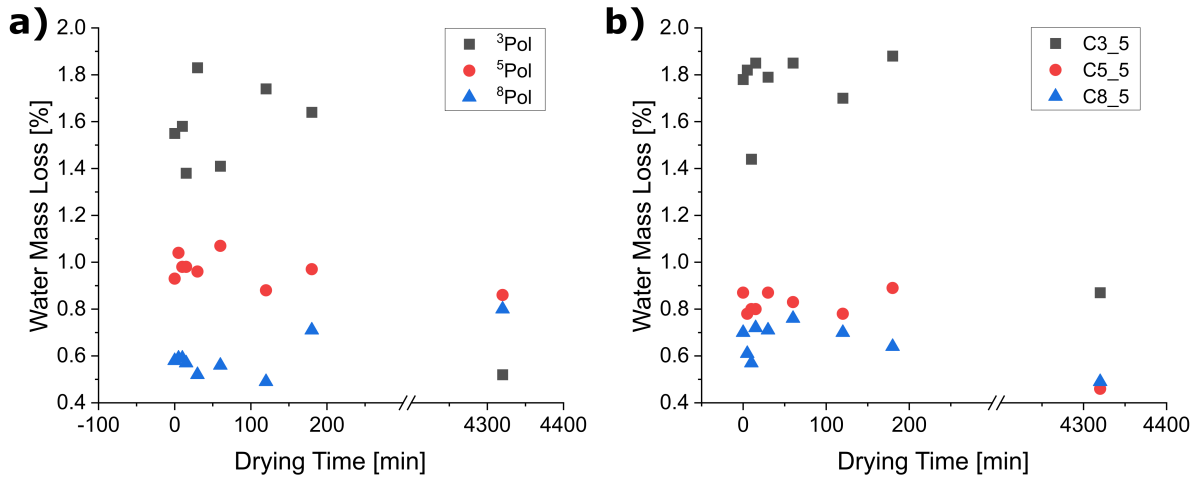


Figure 55: Determined water content of a) the polymer samples and b) their composites with a particle content of 5 wt% after different storage times at 80 °C.

All samples still contain residual amounts of water after storage under vacuum. The higher the ionic content in the polymer, the higher the water content. For the polymer compositions 1:3, 1:5 and 1:8 (SMBS:DEGMA), the initial water content was determined to be 1.55 wt%, 0.93 wt% and 0.58 wt%, respectively. During storage at 80 °C, the ⁵Pol and ⁸Pol systems show almost no changes in water content within the previously determined standard deviation, while for the 1:3 ratio a significant decrease is observed with long storage times. The respective composite systems were also tested with 5 wt.% particles each. The results are presented in Figure 55 b). For the composite samples with 5 wt% particle content, a behavior similar to that of the polymer systems is observed. The higher the ionic content in the polymer, the higher the initial water content. While only a slight decrease in the water content is observed for the ⁸Pol and ⁵Pol based composites even after a longer drying time, the differences are significantly higher in the ³Pol based system. This observation is consistent with the fact that the mechanical measurements for these composites also show the largest differences between the batches.

In a next step, the influence of the particle content was investigated further. For this purpose, ³Pol-based composite samples with particle contents between 0 wt% and 12 wt% were prepared and their water content was investigated under the same drying conditions. The water content of the samples determined from the TGA data is shown in Figure 56. Within the standard deviation of the determination method, the particle content has no influence on the residual amount of water in the system. Only the systems with 2 wt% particles show a slightly lower water content. The reason for this is still unknown.

Results and Discussion

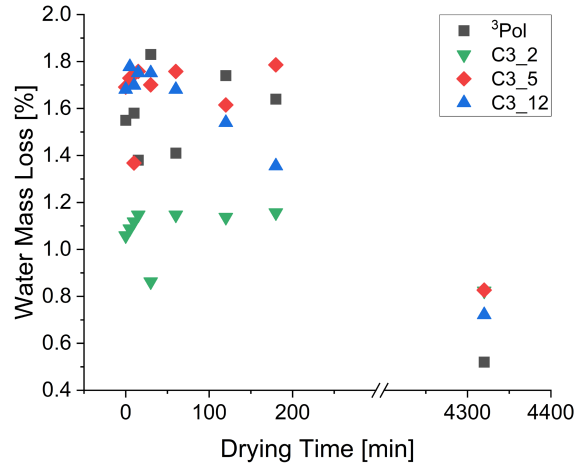


Figure 56: Determined water content of the ³Pol based composite samples with different particle contents (0-12 wt%) after different storage times at 80 °C.

In the following, the influence of storage under high humidity was investigated. To ensure constant conditions the storage under increased humidity was carried out in a desiccator over water. To further increase the humidity, the desiccator was evacuated to 600 mbar at the beginning. Storage times of 5, 10, 15, 30, 60, 120, 180 and 1140 minutes were investigated. Figure 57 shows the water contents determined for the polymer systems as well as their composites with 5 wt% particle content.

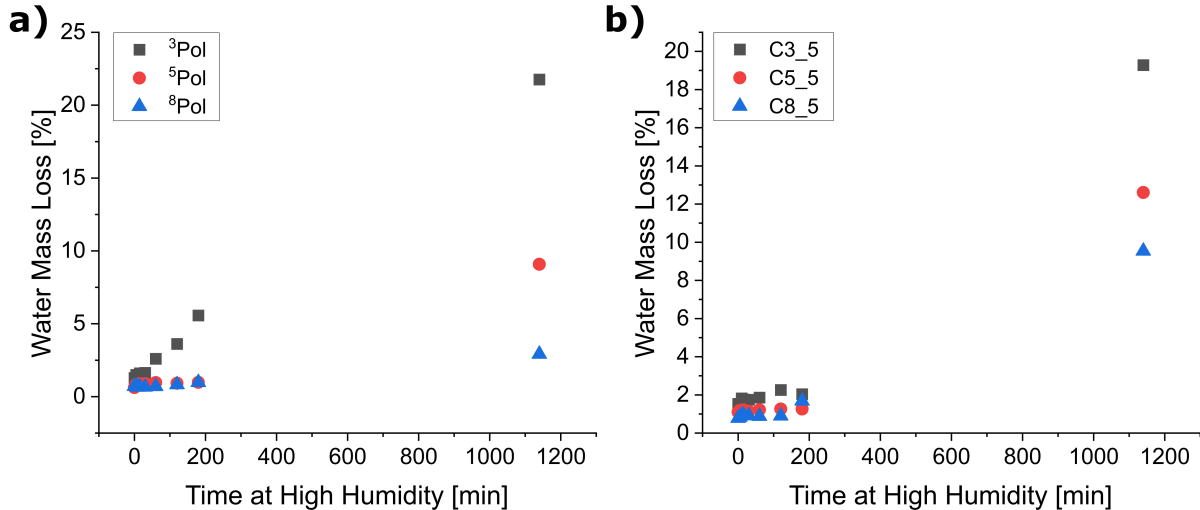


Figure 57: Determined water content of a) the polymer samples and b) their composites with a particle content of 5 wt% after different storage times at elevated humidity.

All samples show a significant increase in water content with increasing storage time. The samples with a high ionic content in the polymer show the highest affinity for water uptake. At a storage time of 19 hours, water contents of up to 21.8 wt% are found for the ³Pol system. For the ⁵Pol system, the water content after the same storage time was 9.1 wt% and for the ⁸Pol system only 2.9 wt%. The water absorption correlates almost linearly with the mass fraction of the ionic species in the sample. Already at a water content of 2.9 wt% (⁸Pol system

Results and Discussion

at maximum storage time), viscous, sticky samples are obtained, which are unsuitable for further tensile tests or electron microscopic investigations. Again, the trends in the results of the composite systems with 5 wt% particle content agree well with those of the polymers. The higher the ionic content in the original polymer, the faster and more water is absorbed by the respective composite. However, the overall water contents are lower than those of the respective polymer systems. To investigate this effect, composites with varying particle contents were prepared for the ³Pol system (0-12 wt%), stored at elevated humidity and then analyzed by TGA. The results of the TGA measurements are shown in Figure 58.

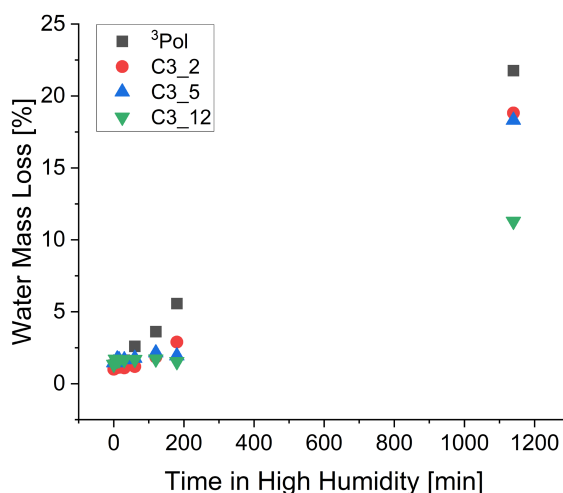


Figure 58: Determined water content of the ³Pol based composite specimens with different particle contents after different storage durations at elevated humidity.

In general, the samples with the lowest particle content had the highest water content. Based on the TGA results of the cationic particles stored under high humidity, the influence of the cationic groups appears to be negligible. Table 8 shows the measured water content compared to that which would be expected based on the proportion of anionic groups in the composite. As the particle content increases, the experimentally determined water content falls increasingly below the expected value. This is explained by the increasing screening of the anionic groups in the polymer caused by the cationic groups on the particle surface. Since the "free" anionic groups appear to be responsible for the water affinity, this decreases with increasing particle content.

Table 8: Water content of the ³Pol specimens after 19 hours of elevated humidity.

Polymer	Particle Content [%]	Water Content _{exp} [%]	Water Content _{meas} [%]
³ Pol	0	21.76	21.76
³ Pol	5	20.67	19.28
³ Pol	12	19.15	12.82

The investigations on the storage conditions clearly show that the systems prepared have a high affinity towards water and readily adsorb water from ambient air. When stored at elevated humidity, the initially firm samples lose their structural integrity after only a few hours and turn into a sticky viscous mass. Therefore, a drying procedure must be developed and storage conditions such as humidity and temperature must be strictly controlled to obtain reproducible results and to determine healing efficiencies. For this study, free radical polymerization was used to synthesize the polymers instead of ARGET ATRP, as the preparation is less complex and easily scalable. In addition, ATRP of acidic monomers presents several problems. Ligand displacement in the copper complex is frequently observed [670] and careful pH adjustment is often required to prevent it.[92,93] This pH adjustment also affects the degree of protonation of the finished polymer, which has a strong influence on the material properties and might partially be responsible for the poor reproducibility of the results.[501] Furthermore, the polymerization of ionic monomers requires the use of highly polar and often protic solvents, which can cause inefficient deactivation by dissociation of the bromine ligand from the deactivator complex.[81] The subsequent competitive coordination of the solvent with the Cu(II) complex results in little control this making the required extensive reaction preparation redundant. Finally, even when using the same catalyst and under the same conditions, each monomer has its own equilibrium constant for atom transfer, both for the active and the dormant species. As a result, the optimal polymerization conditions for different monomers are often very different and must be carefully adjusted. These parameters include the type and concentration of the transition metal, the ligand, the initiator, the reaction temperature and the composition of the solvent.[670] Even when the reaction conditions were adjusted in previous studies to make the monomer consumption of the comonomers comparable, the FRP should provide a better chance for a statistical distribution of the ionic groups in the polymer.

3.5.5. Synthesis and Characterization of Anionic Polymers by FRP

Analogous to the previous experiments, the SMBS-DEGMA monomer pair was used. Despite the hoped-for synthetic simplicity, even after transfer to FRP, optimization of the reaction conditions was necessary to obtain polymers that could be at least partially solubilized to allow characterization and synthesis of the nanocomposites. AIBN and DBPO were studied as possible initiators. The reaction temperature and the initiator to monomer ratio were optimized. The obtained polymers were characterized by ^1H NMR spectroscopy.

In a first set of experiments, polymerization was carried out under standard conditions for free radical polymerization. 1 mol% AIBN was used as the initiator. A reaction temperature of 70 °C was chosen. All polymerizations were carried out in a water-methanol solvent mixture and an overall monomer concentration of 0.63 mol/L. To determine the optimum reaction time, a kinetic study was performed using pyridine as a tracer to monitor the conversion. Monomer

Results and Discussion

ratios of 1:3, 1:5, 1:8 and 1:10 (SMBS:DEGMA) were investigated. Samples were taken after 0.5 h, 1 h, 2 h, 3 h, 4 h and 5 h reaction time. Figure 59 shows the proton NMR spectra after different reaction times as an example for the 1:3 system.

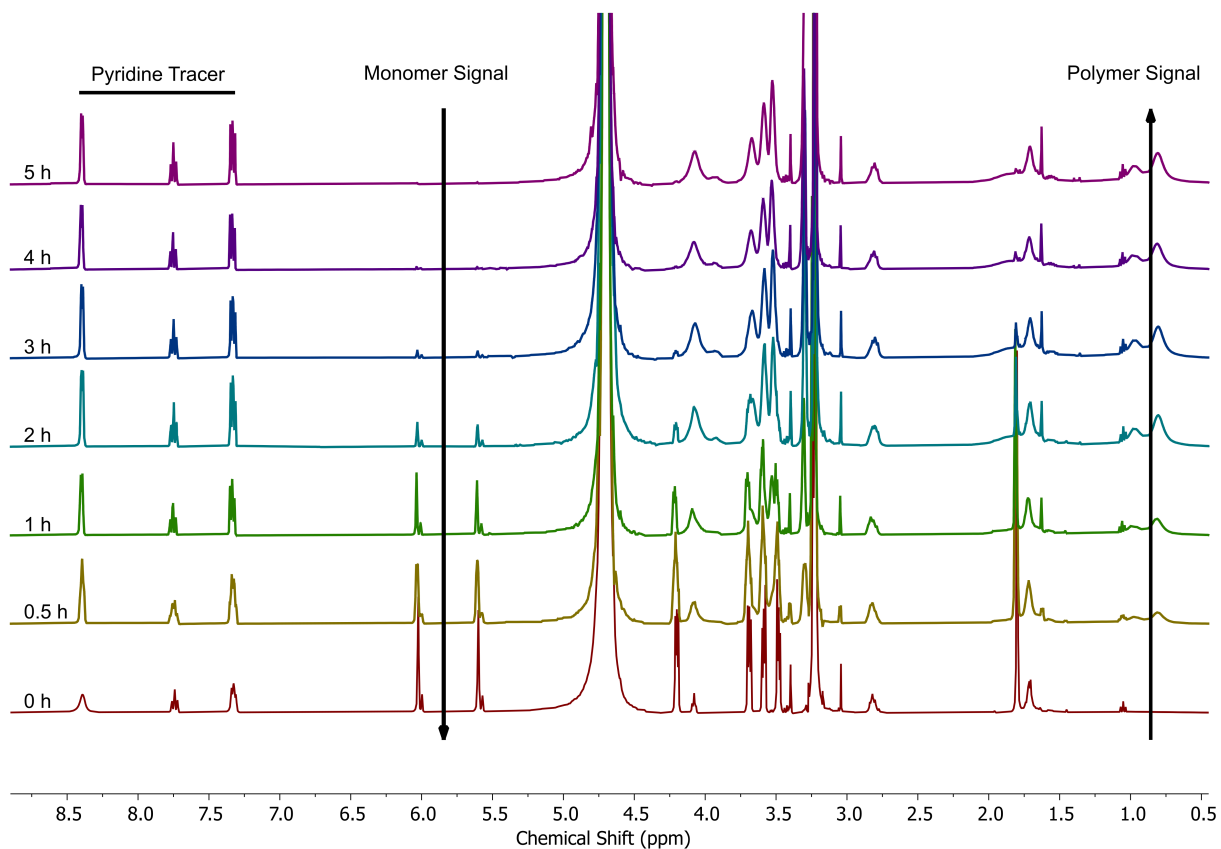


Figure 59: ¹H NMR of the reaction mixture of SMBS and DEGMA (1:3) after different reaction times; initiator: AIBN (1 mol%); Temperature: 70 °C.

The ¹H NMR spectrum shows the decrease in the signal of the protons at the double bond (5.5-6.2 ppm) of the methacrylate units, indicating the conversion of the monomers. At 0.8 ppm the signals of the polymer backbone increase. The signals were normalized to the signals of the pyridine tracer (> 7 ppm) to determine the conversion. The result is shown in Figure 60.

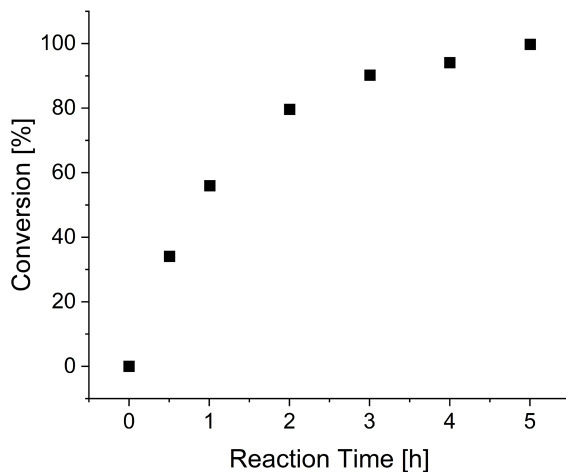


Figure 60: Conversion of SMBS and DEGMA (1:3); Initiator: AIBN (1 mol%); Temperature: 70 °C.

Results and Discussion

The resulting conversion diagram shows the typical progression for a FRP.[671,672] At low conversion, initiator radicals and oligomeric radicals are increasingly formed. The reaction rate increases rapidly and changes into a continuous reaction course. The gross reaction rate then decreases continuously as the concentration of the monomers decreases. A conversion of 80 % is reached within two hours and 100 % within five hours. With exception of the 1:3 ratio (SMBS:DEGMA), all systems precipitate during polymerization and are insoluble in all common solvents. Since solubility is required for the composite synthesis, the initiator concentration was increased to obtain shorter polymer chain lengths. The following experiments were carried out exemplarily with the 1:8 monomer ratio, as it showed the worst solubility in the previous experiment. In the first step, the amount of initiator was increased from 1 mol% to 10 mol%. The conversion obtained is shown in Figure 61.

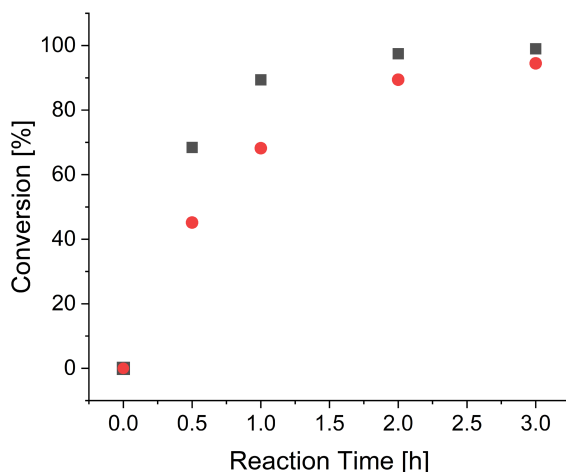


Figure 61: Comparison of the conversion of SMBS and DEGMA (1:8) at an initiator concentration of 1 mol% (red circles) and 10 mol% (black squares); Initiator: AIBN; Temperature: 70 °C.

The reaction rate increased with the amount of initiator used. After only two hours, almost 100 % conversion was achieved. However, the polymers obtained were still insoluble. Due to the already extremely high initiator-to-monomer ratio, oligomers rather than polymers are to be expected and a further increase of the ratio does not seem reasonable, since chain transfer to polymers seems to occur early and long insoluble chains are formed despite the high initiator concentration. Therefore, DBPO was used as initiator because it has a lower activation rate than AIBN, although this does not always correlate with the overall reaction speeds.[671,673] The reaction was carried out at 85 °C, which is a typical reaction temperature for DBPO. Figure 62 shows the comparison of monomer conversion using DBPO or AIBN as the initiator.

Results and Discussion

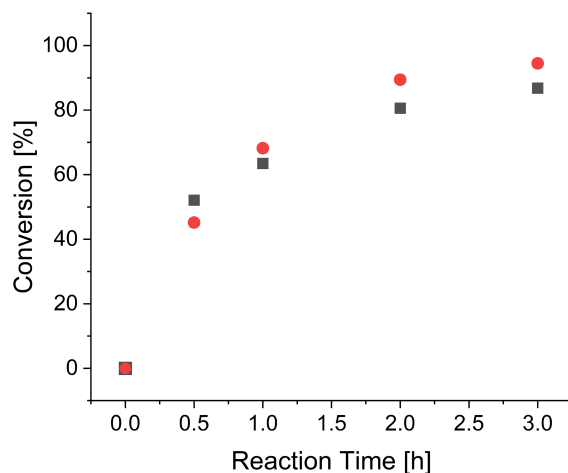


Figure 62: Comparison of the conversion of SMBS and DEGMA (1:8), using AIBN (1 mol%, $T = 70\text{ }^{\circ}\text{C}$, red circles) and DBPO (1 mol%, $85\text{ }^{\circ}\text{C}$, black squares) as initiators.

The polymerizations show comparable reaction rates for the two initiators used. The polymers obtained show swelling in contact with water but are still insoluble. In a next step, the reaction temperature was considered as an optimization parameter. To improve the control of the reaction, the reaction temperature was gradually lowered from $85\text{ }^{\circ}\text{C}$ to $70\text{ }^{\circ}\text{C}$ and then to $60\text{ }^{\circ}\text{C}$. The amount of initiator was fixed at 1 mol%. Figure 63 shows the monomer conversion for the different reaction temperatures.

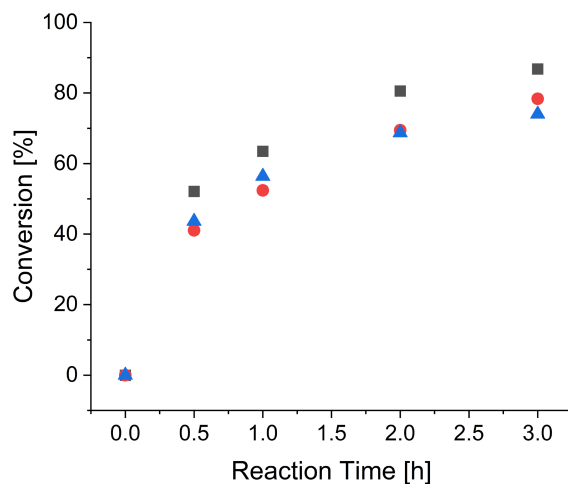


Figure 63: Comparison of the conversion of SMBS and DEGMA (1:8); Initiator: DBPO (1 mol%); Temperature: $60\text{ }^{\circ}\text{C}$ (blue triangles) / $70\text{ }^{\circ}\text{C}$ (red circles) / $85\text{ }^{\circ}\text{C}$ (black squares).

The monomer conversion rate decreases slightly from $85\text{ }^{\circ}\text{C}$ to $70\text{ }^{\circ}\text{C}$. In contrast, no major differences are observed between the reaction temperatures of $70\text{ }^{\circ}\text{C}$ and $60\text{ }^{\circ}\text{C}$. However, the polymer properties change significantly. The solubility of the polymers improves with decreasing reaction temperature. The samples synthesized at $60\text{ }^{\circ}\text{C}$ are still not completely soluble but allow further processing to the composites and show sufficiently fast reaction. Therefore, the polymers used in the later steps were synthesized at this temperature. Under

Results and Discussion

the optimized reaction conditions, the polymerizations were carried out for the SMBS:DEGMA ratios of 1:3, 1:5, 1:8 and 1:10. The conversion is shown in Figure 64.

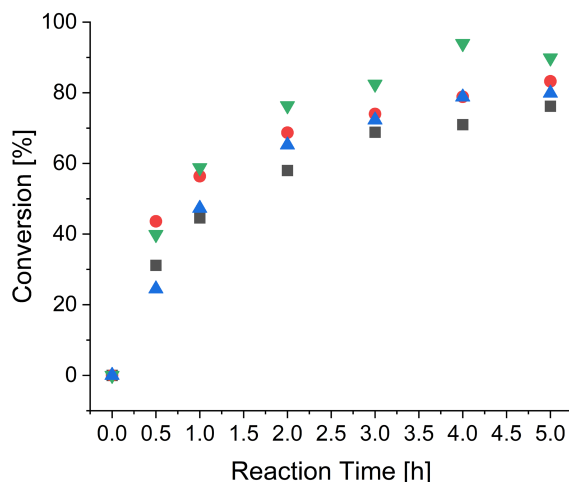


Figure 64: Comparison of the conversion of SMBS and DEGMA for the monomer ratios 1:10 (black squares), 1:8 (red circles), 1:5 (blue triangles) and 1:3 (green triangles); Initiator: DBPO (1 mol%); Temperature: 60°C.

The conversion rate increases slightly with increasing SMBS content. Similar to the 1:8 ratio, the other polymers also exhibit sufficient solubility. A reaction time of five hours was chosen. The polymerizations were carried out without the pyridine tracer under the optimized conditions. Unreacted monomer was removed by dialysis against water and methanol. The polymers were characterized by NMR spectroscopy. The ^1H NMR spectra of the synthesized polymers are shown in Figure 65. The spectra were normalized to the backbone signal at 3.4 ppm.

Results and Discussion

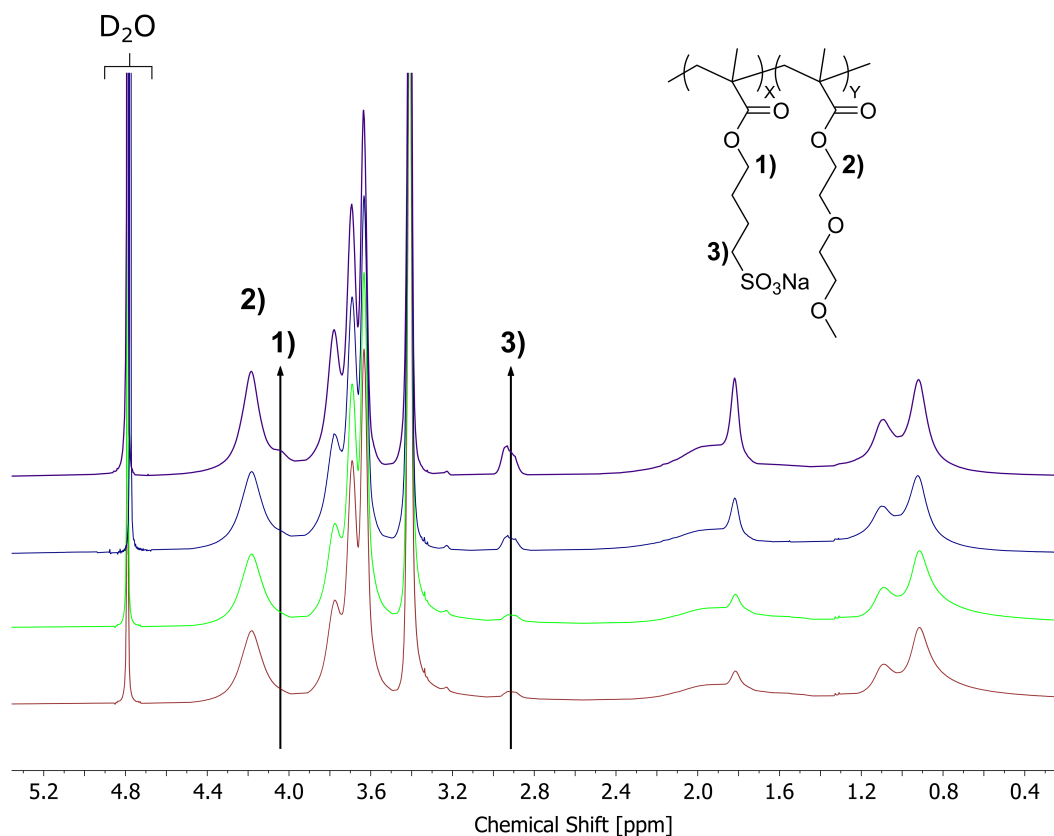


Figure 65: ^1H NMR spectra of the polymers obtained at a SMBS:DEGMA ratio of 1:10 (red), 1:8 (green), 1:5 (blue) and 1:3 (purple) via FRP.

The NMR spectra show the expected signals. The molar fraction of SMBS in the polymer was calculated from the integral ratios of the signals of the CH_2 groups adjacent to the methacrylate (4.20 ppm) and the sulfonate group (2.91 ppm). Unlike for the polymers previously prepared by ATRP, the composition determined by NMR is not consistent with the monomer ratio used (see Table 9). Since the polymers only partially dissolve, the overall composition of the polymer cannot be reliably determined from the NMR data. Therefore, additionally CHN analysis was carried out on the polymers. The mass fraction of SMBS was calculated from the determined mass fraction of sulfur. The remaining mass was assumed to be DEGMA to determine the molar fraction of SMBS in the polymer. Table 9 shows the expected ratio of DEGMA to SMBS based on the monomer ratio used and the ratios calculated from the NMR and CHN data.

Table 9: Polymer compositions (FRP) determined by NMR and CHN analysis.

Sample	DEGMA/SMBS _{theo}	DEGMA/SMBS _{NMR}	DEGMA/SMBS _{CHN}
$^{22.4}\text{PoIF}$	10	9.5	22.4
$^{19.5}\text{PoIF}$	8	5.4	19.5
$^{13.7}\text{PoIF}$	5	7.3	13.7
$^{9.4}\text{PoIF}$	3	6.6	9.4

Results and Discussion

The ratios calculated from the CHN data show that the proportion of ionic species is significantly lower than the monomer ratio used. This indicates that the reaction rate of the ionic species in the polymerization is slower and therefore less is incorporated into the polymer network than expected. The polymer compositions calculated based on the NMR data deviate significantly from both the values expected from the monomer ratio and the results of CHN analysis. For all samples the ionic content derived from the NMR data is higher than that derived from CHN. This is due to the better solubility of the polymer strands with increased amount of ionic groups in the NMR solvent used (D_2O), causing them to be over-represented in the NMR. Since the CHN data better reflects the overall polymer composition, the polymers are referred to below as $^{22.4}PoIF$, $^{19.5}PoIF$, $^{13.7}PoIF$ and $^{9.4}PoIF$, in reference to the DEGMA:SMBS ratios determined from elemental analysis.

Further, the samples were analyzed by FTIR spectroscopy. Figure 66 shows the obtained FTIR spectra, which were normalized to the asymmetric C-O stretching vibration at 1107 cm^{-1} for better comparability.

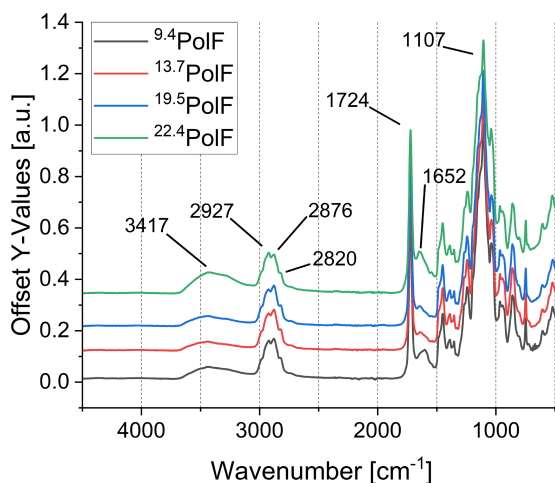


Figure 66: FTIR spectra of the $^{9.4}PoIF$ (black), $^{13.7}PoIF$ (red), $^{19.5}PoIF$ (blue) and $^{22.4}PoIF$ (green) samples.

The FTIR spectra show the expected signals. The C-H stretching vibrations at $2820 - 2927\text{ cm}^{-1}$ and the C=O stretching vibration at 1724 cm^{-1} can be seen as intense signals. Furthermore, all samples show a broad signal at 3417 cm^{-1} , which can be assigned to O-H stretching vibrations. This is indicative of incorporated water that could not be completely removed during the drying process and suggests a similar water affinity of the polymers as observed for the ATRP samples.

This water affinity and the influence of the water content on the polymer properties were investigated below. To study the influence of water content on mechanical properties, the water content of the prepared polymer samples was first determined. Analogous to the characterization of the ATRP polymers, TGA studies were performed for this purpose. The dry

Results and Discussion

polymer samples were stored above water in a desiccator at reduced pressure (600 mbar) for different periods of time. TGA measurements were performed after 2 h, 5 h, 8 h and 24 h. The curves obtained are shown in Figure 67.

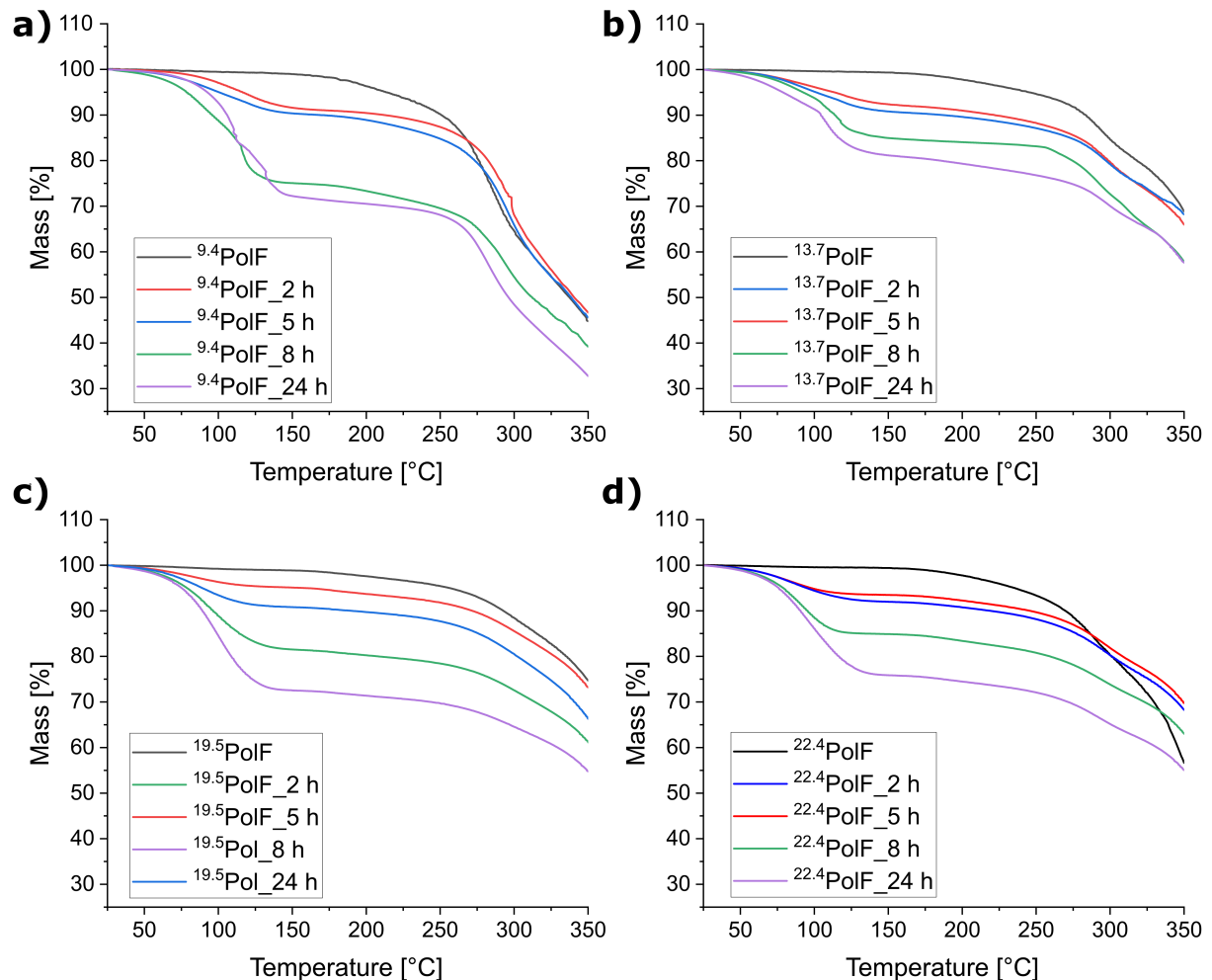


Figure 67: TGA curves of the a) $^{9.4}\text{PolF}$, b) $^{13.7}\text{PolF}$, c) $^{19.5}\text{PolF}$ and d) $^{22.4}\text{PolF}$ systems after varying storage times under humid conditions. The samples were heated from room temperature to 350 °C under nitrogen atmosphere, with a rate of 10 K/min.

Irrespective of the polymer composition, all TGA curves show a strong decrease in mass between 100 °C and 150 °C with increasing storage time at high humidity. At this temperature the physically adsorbed water is removed. To quantify the water content, the mass loss was again determined in the range < 200 °C. The obtained water contents of the polymer samples are shown in Figure 68 as a function of the storage time.

Results and Discussion

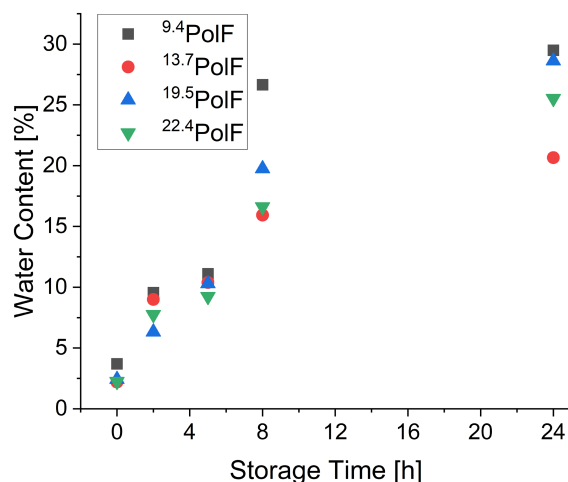


Figure 68: Determined water content of the FRP polymer samples after varying storage periods under increased humidity.

As expected, the water content of the samples increases with increasing storage time. After an initial rapid water uptake, the adsorption rate slows down and almost reaches saturation. However, the saturation concentration does not seem to correlate directly with the number of ionic groups, which is in contrast to the observed results for the ATRP polymers. After just two hours, the samples are noticeably softer and swollen. A more detailed interpretation of this observation will be given in the context of the structure elucidation of the polymers in the context of the SAXS measurements.

Subsequently, rheological studies were carried out and the dynamic modulus as well as the shear modulus of the samples was determined in oscillation experiments to determine the effect of the adsorbed water on the mechanical properties. During the tests the samples were heated to 52.5 °C and then cooled back down to room temperature. To assess the reproducibility of the measurements, the commercial polysiloxane DOW Corning OE6630 was tested first, which is comparable in terms of softness and allows the production of more uniform samples. Storage-, loss- and the shear modulus were determined at 50 °C for four separately prepared samples. While a small deviation between the separately produced samples was observed for the loss modulus (SD < 2 %) and the shear modulus (SD = 5 %), a significantly higher deviation of almost 20 % was observed for the storage modulus. Therefore, for the interpretation of the following results, it must be considered that smaller deviations are not only related to the reproducibility of the samples but can also come from the measurement deviations.

The shear modulus of the polymer systems was determined as a function of the storage time at high humidity and thus the water content. As in the case of the model polymer, oscillation experiments were also performed here, in which the samples were first heated to 50 °C and then cooled back to room temperature. The obtained temperature dependent shear moduli are

shown exemplarily for the $^{9.4}\text{PoIF}$ system in Figure 69 a). Surprisingly after cooling back to room temperature, the initial shear modulus is no longer reached. This effect is less pronounced at higher water contents. Whether this is an actual decrease in the dynamic modulus as a result of deformation, or whether the recovery is simply not fully observed on the time scale of the measurement is not yet clear, although the latter seems likely. Figure 69 b) shows the shear modulus at 50 °C as a function of the adsorbed water.

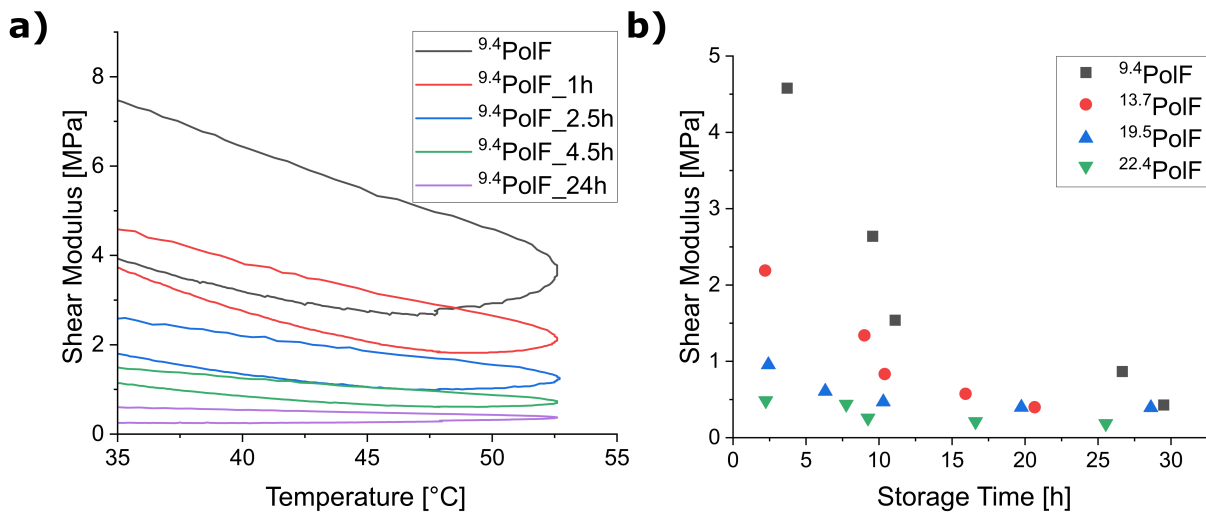


Figure 69: a) Shear modulus of the $^{9.4}\text{PoIF}$ system at different temperatures as a function of the storage time at humid conditions and b) summary of the influence of the water content of the polymers on the shear modulus.

An almost linear decrease in shear modulus with increasing water content is observed for all samples. The steepness of the decrease in hardness increases with the amount of SMBS in the polymer. While a 42 % decrease in shear modulus is observed for the $^{9.4}\text{PoIF}$ system at 5.9 % water uptake, the modulus decreases only by 9.5 % for the $^{22.4}\text{PoIF}$ system at a comparable water uptake (5.5 %). Overall, a maximum decrease between 61.9 % and 90.6 % was observed for the different polymer samples at a storage time of 24 hours. Next the dynamic modulus was examined. The storage and loss moduli as a function of storage time at elevated humidity are shown in Figure 70.

Results and Discussion

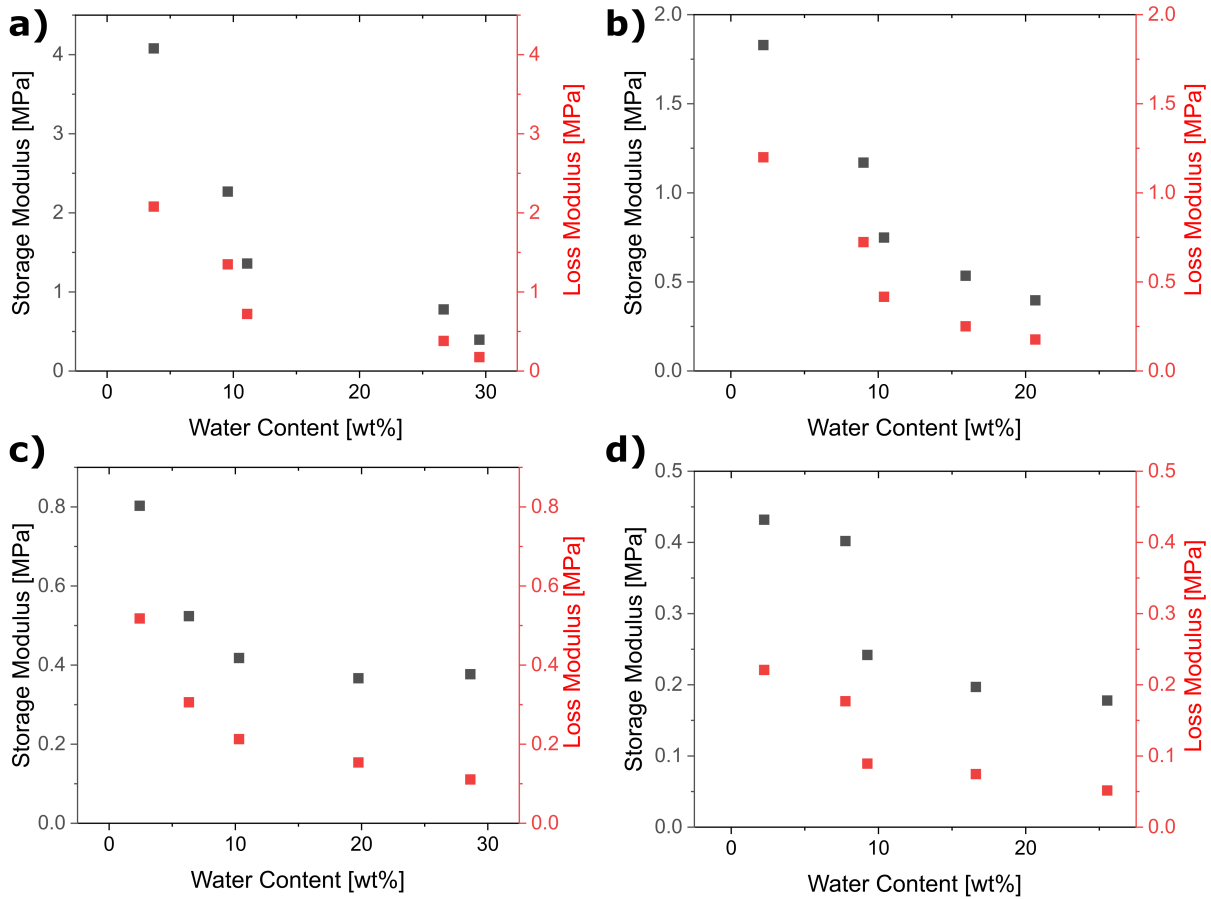


Figure 70: Storage and loss moduli for a) ${}^{9.4}\text{PoIF}$, b) ${}^{13.7}\text{PoIF}$, c) ${}^{19.5}\text{PoIF}$ and d) ${}^{22.4}\text{PoIF}$ as a function of the water uptake upon storage at high humidity.

In general, the storage modulus is larger than the loss modulus, regardless of the polymer composition and water content. The stored deformation energy is therefore higher than the deformation energy dissipated by internal friction, indicating physicochemical interactions between the polymer strands. The results are typical of viscoelastic solids. For both storage and loss modulus a steep decrease with increasing water content is observed. The storage modulus decreases due to the reduced stiffness. In addition, the reduced friction between the polymer chains due to the water leads to a decrease in the dissipated heat and thus the loss modulus. The results show that as the ionic content in the polymer increases, not only does the water absorption increase, but also the dynamic modulus decreases at a faster rate. For the ${}^{9.4}\text{PoIF}$ system, a 56 % decrease in the storage modulus and a 65 % decrease in loss modulus was observed for a water uptake of about 5.9 %, while for the ${}^{22.4}\text{PoIF}$ system for a comparable water uptake (5.5 %), a decrease of 7 % and 20 % for storage and loss modulus, respectively, was observed. To classify the change in material properties, the dissipation factor $\tan(\delta)$, calculated from the ratio of loss and storage modulus, was considered. The plot of $\tan(\delta)$ versus the water uptake is shown in Figure 71. In general, the polymers with a higher ionic content exhibit a higher initial $\tan(\delta)$. All samples show a significant decrease of $\tan(\delta)$ with increasing water content of the samples, which is equivalent to a shift towards an ideal

elastic body. The adsorbed water acts as a plasticizer, as it increases the chain mobility by reducing internal interactions, such as hydrogen bonding or electrostatic interactions between polymer chains, while increasing molecular space.[674]

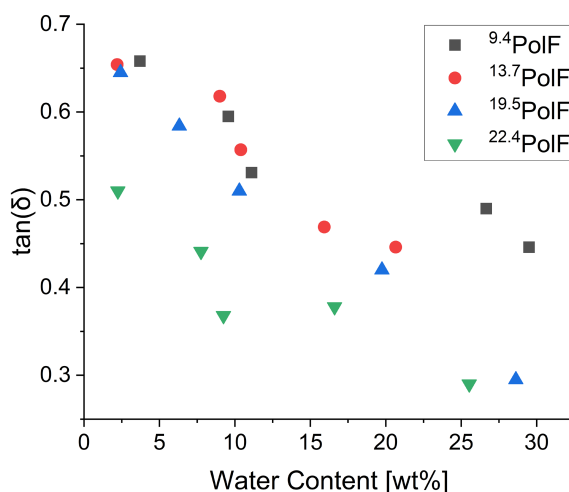


Figure 71: Plot of $\tan(\delta)$ against the amount of water comprised in the FRP polymer samples.

The combination of the TGA data and rheological measurements shows that even small differences in the water content drastically change the mechanical properties and flow behavior of the polymers. The largest change in dynamic modulus is always observed in the first few hours of storage at high humidity. Subsequently, the dynamic modulus decreases only slightly, which is due to the then decreasing water uptake, rather than a reduced influence of the absorbed water, as an almost linear relationship between water content and dynamic modulus can still be observed thereafter. These results again emphasize the need for an optimized drying process.

For this purpose, an analogous series of measurements was carried out to investigate the influence of the storage time at 80 °C on the water content of the polymer samples. When stored for 8 hours or longer, the polymers changed from colorless to pale yellow, indicating partial degradation. After drying, the samples were analyzed by TGA. Overall, the measurements show only minor differences in water content of less than 2 % in the low temperature range (< 200 °C). To avoid decomposition and since only small amounts of water are removed after longer drying times the samples for the following studies were dried for two hours at 80 °C. Thereafter they were stored in a desiccator at reduced pressure (15 mbar) over phosphorus pentoxide for at least one week prior to use.

Figure 72 shows the shear moduli determined at 50 °C as a function of the polymer composition after the optimized drying process. The shear modulus increases linearly with the proportion of ionic groups in the polymer, which is expected since the ionic homopolymer exhibits a much higher rigidity as the DEGMA-based homopolymer.

Results and Discussion

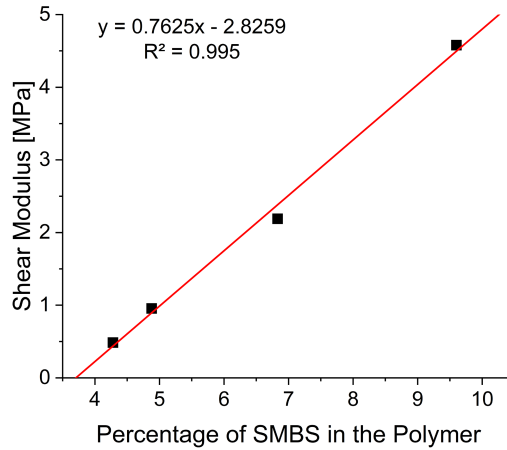


Figure 72: Shear modulus as a function of the polymer composition.

In addition, the dry polymers were examined by TGA. The T_{95} values were determined to evaluate the thermal stability. Figure 73 shows both the TGA curves as well as the T_{95} values as a function of the polymer composition. The TGA curves indicate no water loss in the range below 100 °C, which confirms the successful drying. Regardless of the polymer composition, degradation starts above 250 °C. As expected from the polymer composition, the decomposition is primarily defined by the degradation of the DEGMA, while the degradation of the SMBS can only be seen as a shoulder at about 375 °C. Surprisingly, the T_{95} values decrease with increasing ionic content. The copolymers show almost complete decomposition (char yield < 6.5 %) even under nitrogen atmosphere. After switching to synthetic air, the residual mass decreases to less than 3 %.

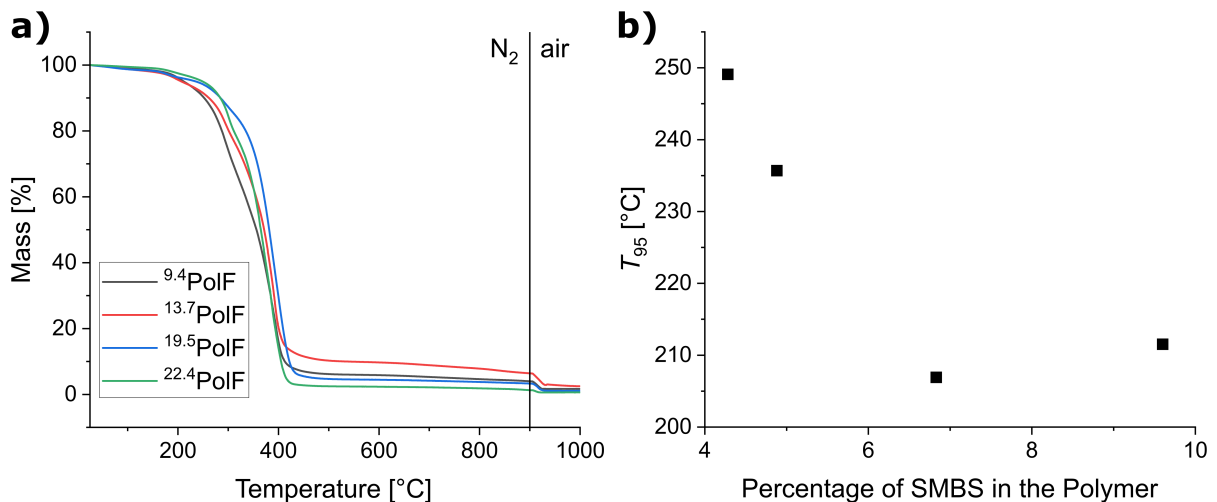


Figure 73: a) TGA curves of the $^{9.4}\text{PolF}$ (black), $^{13.7}\text{PolF}$ (red), $^{19.5}\text{PolF}$ (blue) and $^{22.4}\text{PolF}$ (green) polymers and b) T_{95} values in dependence of the polymer composition. The samples were heated from room temperature to 880 °C under nitrogen atmosphere, followed by heating to 1000 °C under a mixture of nitrogen and oxygen (4:1) with a rate of 10 K/min.

Furthermore, DSC measurements were also carried out. Figure 74 shows the DSC curves and the T_g s determined for the FRP prepared polymers compared to the ATRP systems. The T_g s don't vary much when the polymer composition is changed. This is consistent with the observation from the previous study of the ATRP polymers, that a certain threshold value of SMBS must be exceeded in order to cause significant changes in the T_g . Nevertheless, a slight increase in the T_g with the amount of SMBS in the polymer is also observed here. Overall, the T_g s are about 10 °C lower than for the ATRP systems described earlier. No second glass transition was observed in the region of the T_g of poly(SMBS) (125 °C). Due to the low concentration of SMBS in the polymer and the already low intensity of glass transitions in the DSC, it cannot be excluded that block-like structures or even separate ionic and non-ionic polymer strands are present, due to the different reaction rates of the monomers in FRP.

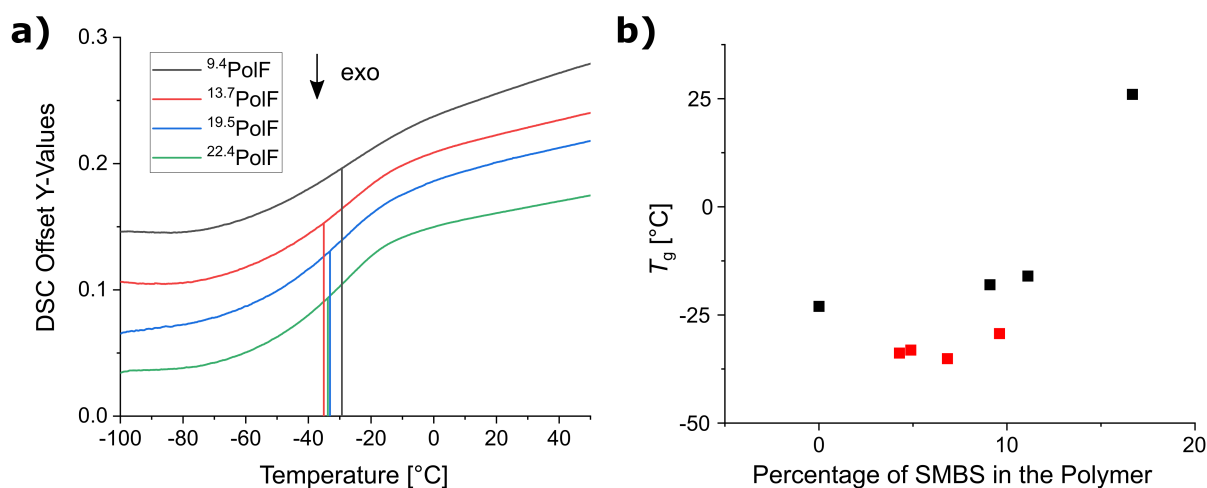


Figure 74: a) DSC curves of the $^{9.4}$ PoIF (black), $^{13.7}$ PoIF (red), $^{19.5}$ PoIF (blue) and $^{22.4}$ PoIF (green) polymers. b) comparison of the T_g s of the FRP polymers (red) with the polymers obtained by ARGET ATRP (black).

The polymers were analyzed by SAXS to determine the scattering background of the polymer for investigation of the particle distribution in the later synthesized composite samples. The results for the $^{9.4}$ PoIF system are shown in Figure 75 a).

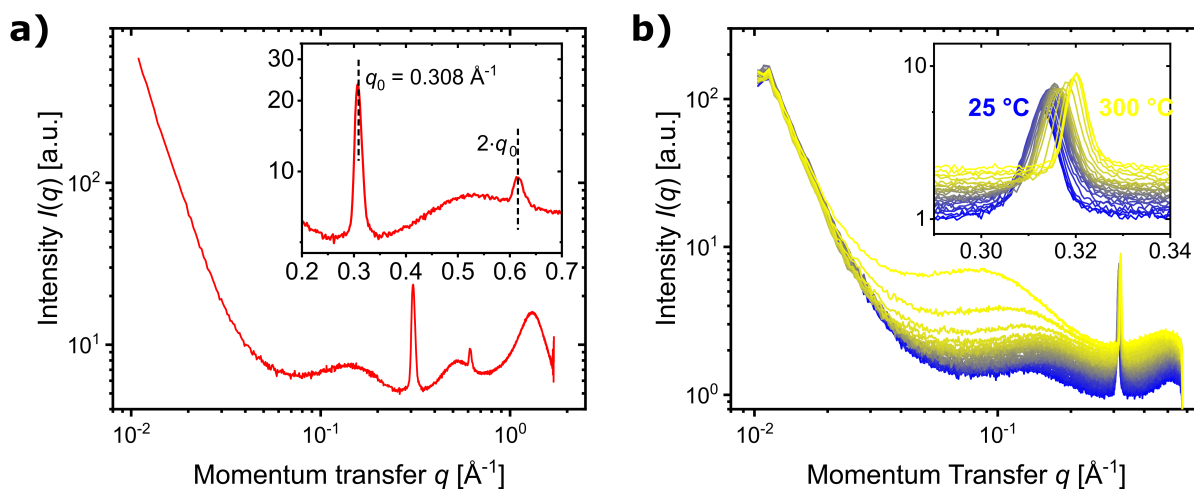


Figure 75: a) SAXS measurement of the ${}^{9.4}\text{PoIF}$ system. b) Temperature dependent SAXS measurement of the ${}^{9.4}\text{PoIF}$ system from 25 °C to 300 °C in steps of 10 °C. The inset shows the scattering curve in the q -range relevant for the Bragg peak at $\sim 0.31 \text{ \AA}^{-1}$.

The scattering curve obtained for the sample without nanoparticles shows weak forward scattering. In deviation from the ATRP samples, two additional peaks are observed at $q_0 = 0.31 \text{ \AA}^{-1}$ and $q_1 = 0.61 \text{ \AA}^{-1}$. The small half-width and intensity of the signals indicate a semi-crystalline polymer. In semi-crystalline polymers, microphase separation occurs when the interblock segregation is sufficiently high and results in the formation of nanoscale structures. Semi-crystalline polymers have two mechanisms of phase separation, microphase separation and crystallization. The interaction between these leads to a morphological richness and kinetic complexity, which makes *a priori* prediction of the structure difficult.[675,676] Four basic structural motifs are commonly observed: cylindrical, spherical, gyroid and lamellar structures. The distances between the SAXS signals of the crystalline blocks allow them to be distinguished (Figure 76).

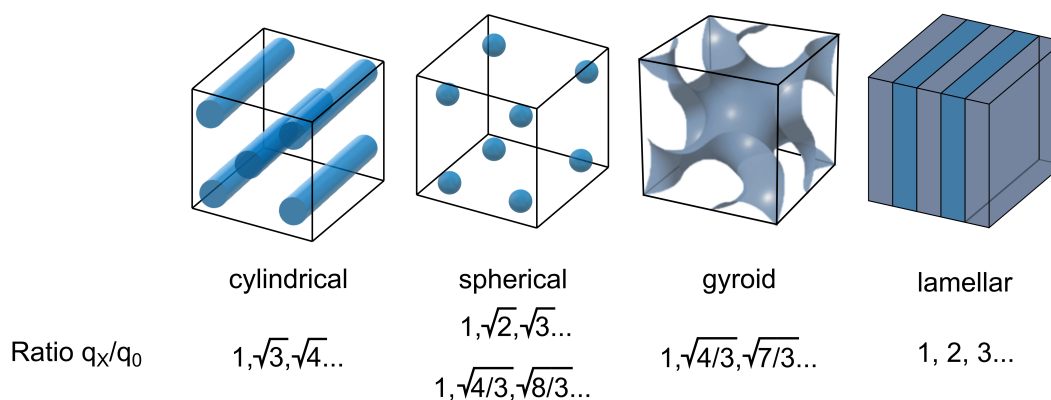


Figure 76: Types of semicrystalline polymers. Adapted from [676–678].

Based on the signal positions ($q_1 = 2 \cdot q_0$), a lamellar structure with a repeat distance of 2.1 nm ($2\pi/q_0$) seems to be present in the polymers.[676] Due to the small increase in the T_g of the polymers with increasing the ionic groups and the absence of a glass transition in the range of poly(SMBS), it seems likely that ionic blocks are responsible for the signal. A similar effect has

been observed for poly(ethylene-co-methacrylic acid).[493,495] The ionic groups of this ionomer tend to aggregate. These so-called multiplets which in contrast to the results here are of spherical shape, consist of fewer than 10 ion pairs, which in turn overlap to form paracrystalline structures. Since no melting signal was observed in the DSC, the stability of the crystalline regions of the polymer was investigated further exemplarily for the ^{9.4}PolF system. For this purpose, temperature dependent SAXS measurements were performed. The results are shown in Figure 75 b). The signal at 0.31 Å⁻¹ is still observed even at temperatures where decomposition of the polymer begins, which is astonishing as these multiplets are usually much more unstable.[496] The high temperature stability of these crystalline regions explains the absence of a melting signal in DSC. It can also be observed that the signal shifts to higher *q* values with increasing temperature, most likely due to evaporation of the comprised water.

The next step was to investigate the mechanical properties of the polymers. Uniaxial tensile tests were performed on the polymers to determine E-modulus, maximum stress, maximum strain and the 0.2 % yield point. First however, the reproducibility of the samples was examined. For this purpose, three samples of the ^{9.4}PolF system were prepared and measured. The stress-strain diagrams obtained are shown in Figure 77 a). In comparison to the rheology study, tensile testing required larger specimens which are more prone to inhomogeneities. These inhomogeneities in the material vastly influence the results, as they potentially lead to crack formation. The triplicate differences in the tensile test are greater than those observed in the rheology studies. Therefore, the data should be regarded with caution. The differences between the FRP triplicates are larger than those observed for the ATRP systems, indicating a second structural influence in addition to the macroscopic inhomogeneities of the specimens, which further reduces the reproducibility of the tensile test results. The stress-strain diagrams are shown in Figure 77 b). The parameters E-modulus, σ_{\max} , ϵ_{\max} and $R_{p0.2}$ were determined from the stress-strain curves and are shown in Figure 77 c) and d).

Results and Discussion

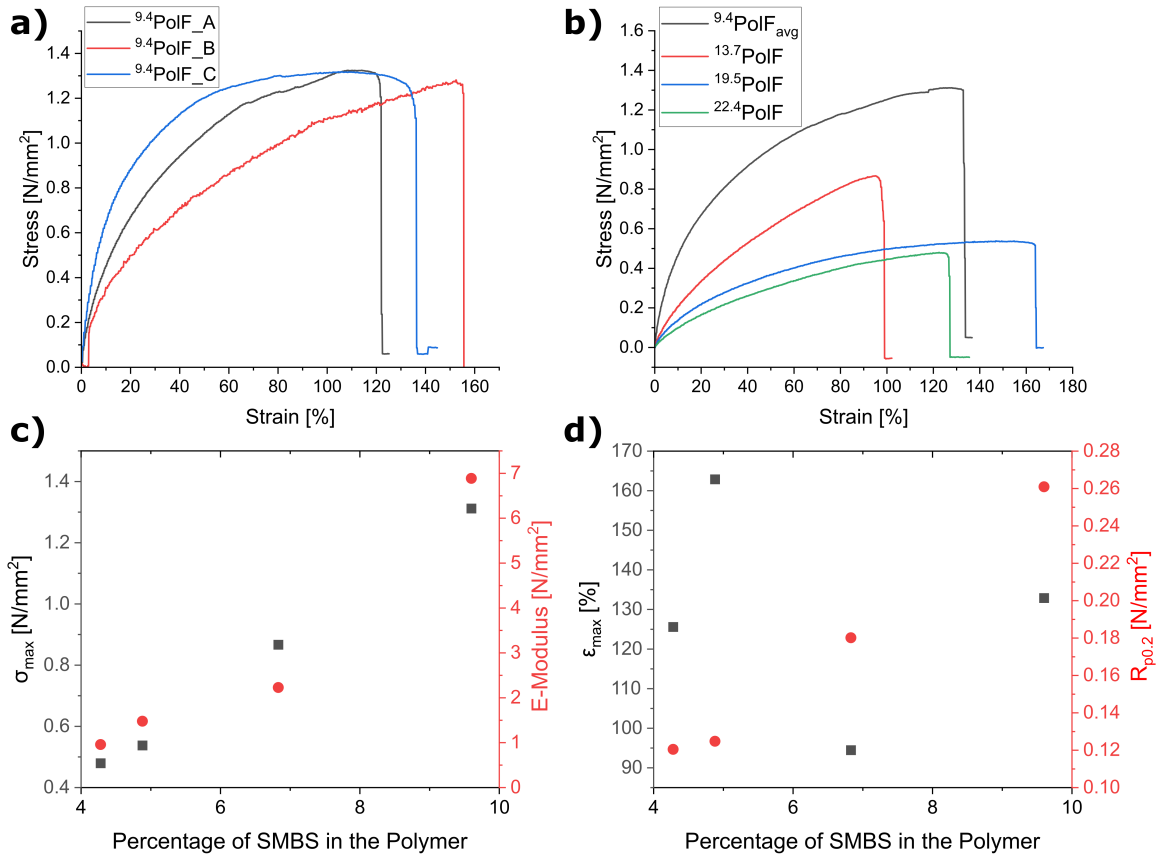


Figure 77: Stress-strain curves of a) the ${}^9.4\text{PoIF}$ triplicates, b) the FRP polymers, as well as c) σ_{max} and E-modulus and d) ϵ_{max} and $R_{p0.2}$ of the polymers as a function of the polymer composition.

While the E-modulus, σ_{max} and $R_{p0.2}$ increase almost linearly with increasing the SMBS content from 0.96 N/mm² to 6.89 N/mm², 0.48 N/mm² to 1.31 N/mm² and 0.12 N/mm² to 0.26 N/mm² respectively, no trend is observed for the maximum strain. The results are in good agreement with the obtained increase in shear modulus from the rheology tests. Since the polymers with lower ionic content are rather soft and thus their areas of application are quite limited, the ${}^9.4\text{PoIF}$ system was used for further composite synthesis.

It can be concluded that the polymers produced by FRP differ significantly in structure from ATRP systems and have a semi-crystalline character. It has also been shown that the polymer composition is not as easily tunable as in ATRP systems. As a result, thermal properties such as T_{95} and T_g can only be controlled within a narrower range. However, the mechanical properties are again tunable via the SMBS content. All polymers show a high affinity towards water, which significantly reduces the mechanical properties upon adsorption. Due to the most promising thermal and mechanical properties, ${}^9.4\text{PoIF}$ was chosen for the synthesis of the self-healing nanocomposites.

3.5.6. Synthesis and Characterization of Ionic Nanocomposites based on the FRP Polymers

To prepare the composite samples, the polymer was dissolved as well as possible in a mixture of water and THF. Then the respective amounts of the $^{0.200}\text{P@Fe}_x\text{O}_y$ particles were added. Three different particle loadings were considered: 2 wt%, 10 wt% and 20 wt%. These are hereafter referred to as NC2, NC10, and NC20. The samples were dried under vacuum at 40 °C for two days and then at 80 °C for two hours. The samples were stored in a desiccator over phosphorus pentoxide for at least two weeks prior to use. For a second batch of samples, the 80 °C drying step was omitted to examine the influence of the increased temperature on the agglomeration process. The composite samples were first examined by FTIR spectroscopy. The spectra obtained are shown in Figure 78.

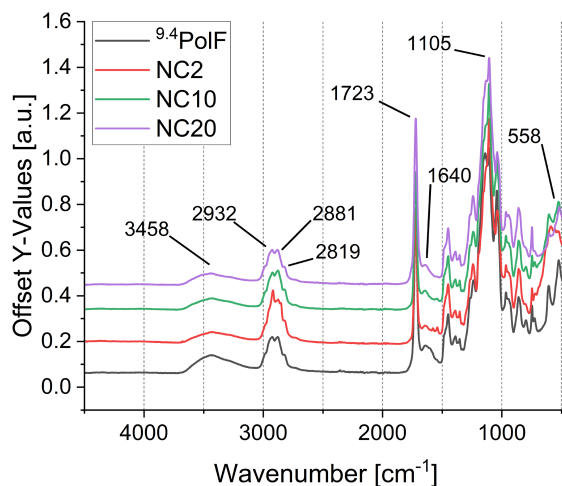


Figure 78: FTIR spectra of $^{9.4}\text{PolF}$, NC2, NC10 and NC20.

The FTIR spectra show the expected signals of the polymer. Mainly the signals of the asymmetric C=O and C-O stretching vibrations at 1723 cm^{-1} and 1105 cm^{-1} , respectively, as well as the C-H stretching vibrations at 2819 – 2932 cm^{-1} . In addition, the signal of the Fe-O-Fe vibration of the iron oxide particles appears at 558 cm^{-1} .

In the next step, the samples were examined by TGA to evaluate their thermal stability. Figure 79 shows the TGA curves as well as the determined T_{95} values.

Results and Discussion

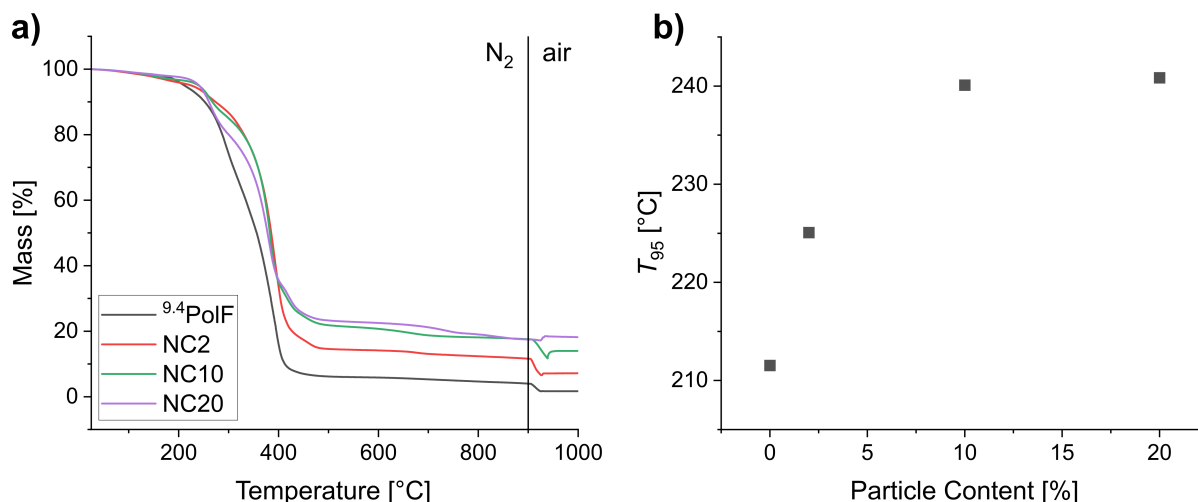


Figure 79: a) TGA curves and b) T_{95} values of the ${}^{9.4}\text{PoIF}$, NC2, NC10 and NC20 composites. The samples were heated from room temperature to 900 °C under nitrogen atmosphere, followed by heating to 1000 °C under a mixture of nitrogen and oxygen (4:1) with a rate of 10 K/min.

The TGA curves show the expected trends. The TGA curves of the composites are shaped by the decomposition of the poly(DEGMA) and the associated mass loss starting above 250 °C. Since no decomposition or sublimation of the particles is expected, the more particles included, the higher the char yields after the nitrogen segment. A residual mass of 17.6 % is observed for the NC20 system, while the polymer sample shows only a residual mass of 3.9 % at 900 °C. In the subsequent air segment, a further mass loss can be observed in the composites analogous to the polymers. However, this loss is less pronounced with increasing particle content. This can be explained by two aspects. First, a smaller decrease in mass is to be expected, as a smaller proportion of the sample is polymer, which is further decomposed in this step and accounts for the decrease in mass, and secondly the particles are oxidized to Fe_2O_3 , which further counteracts the decrease in mass. As a result, NC20 even shows a slight increase in mass upon contact with oxygen. Regarding the thermal stability, again the T_{95} values were considered. When 2 wt% particles are incorporated into the polymer matrix, the T_{95} values increase steeply from 212 °C to 225 °C. Thereafter, at a particle content of 10 wt%, the thermal stability appears to reach a plateau at about 240 °C, as further amounts of particles do not significantly increase the T_{95} values. Nonetheless, the results show that the thermal stability of the polymer can be significantly improved by incorporating the ionic nanoparticles.

DSC studies were also carried out on the composites produced. The DSC curves and the T_g s determined from them as a function of the particle content are shown in Figure 80.

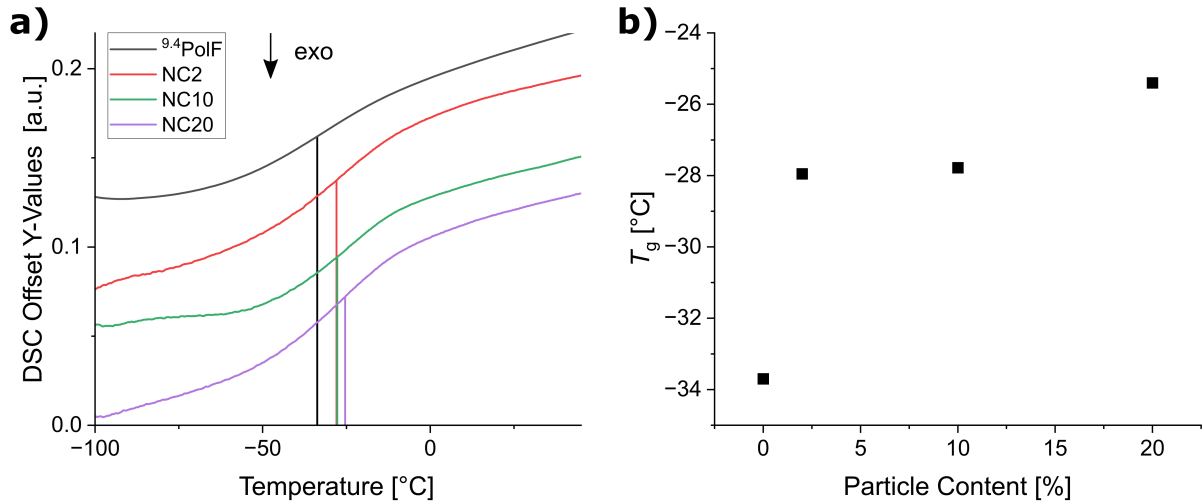


Figure 80: a) DSC curves of the ${}^9\text{PoIF}$ (black), NC2 (red), NC10 (green) and NC20 (purple) samples and b) comparison of the T_g s.

DSC measurements revealed an increase in the T_g s from -33.7 °C to -28.0 °C upon integration of 2 wt% particles. This is due to the reduced chain mobility resulting from the relatively strong ionic interactions between the particles and the polymer matrix. A maximum T_g of -25.4 °C is reached at a particle content of 20 wt%. No further signals were observed in DSC. The glass transition temperatures are therefore all relatively low, indicating high chain mobility and thus good prospects for high efficiency in the healing experiments.

Since strong agglomeration of the particles was already observed in the ATRP systems, this should also be checked for the FRP systems. Again, the distribution of the particles in the polymer was investigated with SAXS and BSE SEM. The samples dried at 40 °C and 80 °C were examined comparatively. In Figure 81 the SAXS curves of the composite samples are shown.

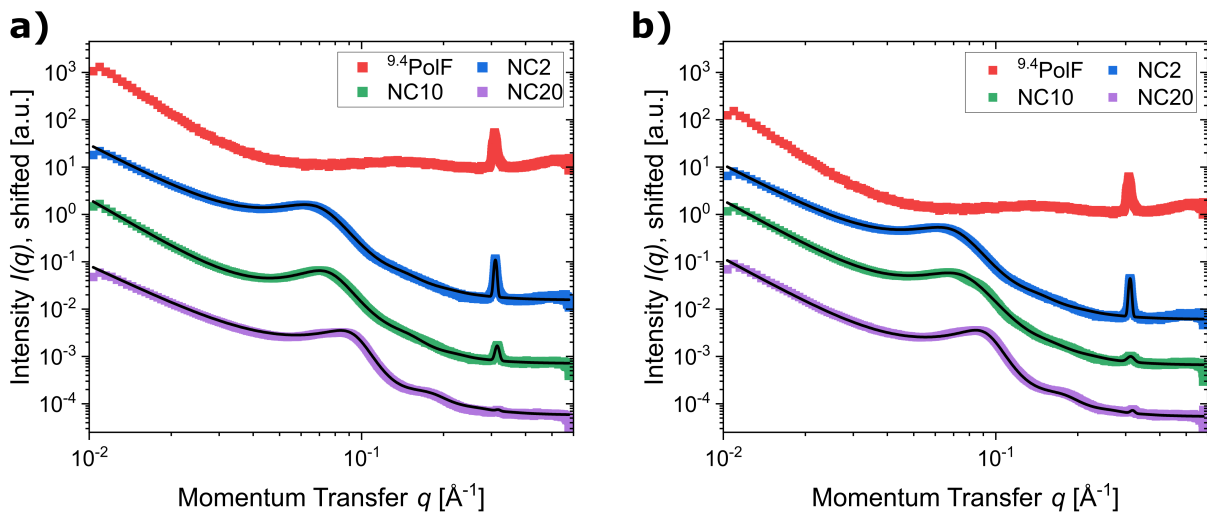


Figure 81: SAXS measurements of the composite samples dried at a) 40 °C and b) 80 °C with particle wt% as indicated in the graph. Black lines are fits to the data according to eq. (12).

Results and Discussion

The scattering curves obtained for the samples which include nanoparticles show a broad peak at $0.05 - 0.1 \text{ \AA}^{-1}$, indicating that the nanoparticles have well-defined and short inter-distances. At small q -values, a strong increase in intensity is observed, which shows that the nanoparticles form agglomerates with sizes of at least 100 nm. Moreover, the sharp peak at $\sim 0.31 \text{ \AA}^{-1}$, resulting from the crystalline polymer parts, decreases in intensity with increasing nanoparticle content to a much larger extent than expected by reducing the polymer content in the sample. Therefore, it can be concluded that the initially crystalline areas become disordered due to the preferential coordination of the ionic groups of the polymers to the cationic functionalized particles.

To quantify the structural properties of the nanoparticles in the polymer matrix as a function of the particle content and drying temperature, the data is modelled using the function:

$$I(q) = I_P(q) + S_{HS}(q)P_{ps}(q) + I_G(q) + I_{bkg} \quad (12)$$

This is an extension of Equation (11), in which the term $I_G(q)$ was introduced. $I_G(q)$ is a Gaussian distribution, that accounts for the Bragg peak at $\sim 0.31 \text{ \AA}^{-1}$, resulting from the paracrystalline structure of the polymers. In accordance with Equation (11), $P_{ps}(q)$ is the form factor of polydisperse spheres, which gives the radius R of the nanoparticles.[656] $S_{HS}(q)$ is the disordered hard sphere structure factor, accounting for the nanoparticle arrangement, which is used to determine the hard sphere radius R_{HS} , and the volume fraction η .[657] The generalized Porod law $I_P(q)$ is again used to account for large-scale structures with the fractal dimension m . I_{bkg} is a constant background.

m , resulting from the fits and shown in Figure 82 a) as a function of the particle content for both drying temperatures, adopts values of ~ 3 for all particle contents, which marks the transition from mass fractals ($m < 3$) to surface fractals ($m > 3$). Therefore, it can be concluded that agglomerates with a loose inner structure are present for all particle contents. R_{HS} (Figure 82 b) decreases from 4.3 nm at 2 wt% nanoparticle content to 3.4 nm with increasing particle content up to 20 wt%, while η (Figure 82 c) increases from $\sim 25 \%$ to $\sim 33 \%$ for the same particle contents. From these observations, it can be concluded that the agglomerates densify with increasing particle content for both drying temperatures.

Results and Discussion

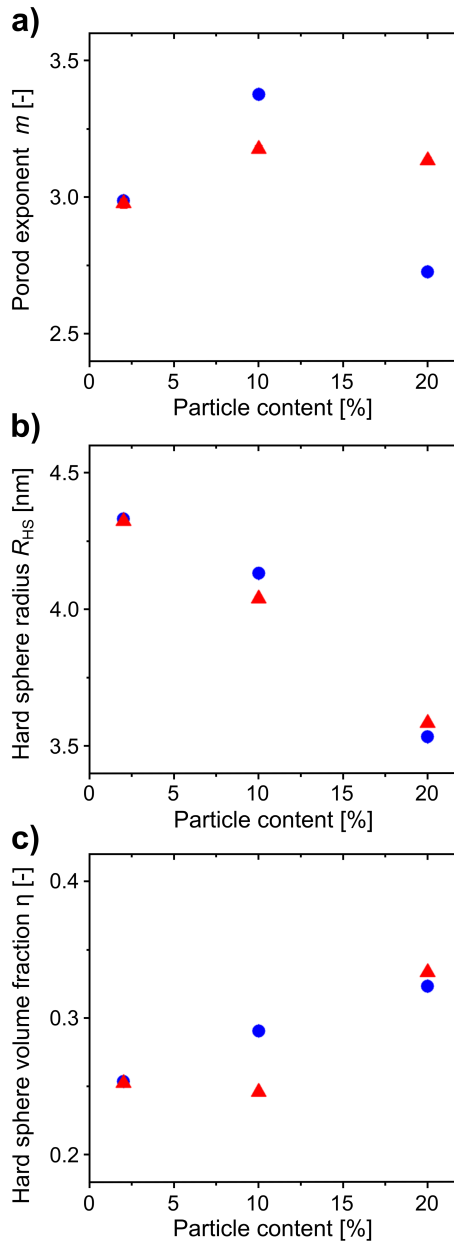


Figure 82: a) Porod exponent, b) hard sphere radius, and c) hard sphere volume fraction of the composite samples dried at 40 °C (blue) and 80 °C (red).

Figure 83 shows the BSE micrographs of the composite samples synthesized at 40 °C and 80 °C respectively. The particles can be seen as lighter areas in the micrographs. Due to the often uneven sample surface, it is difficult to distinguish between particles and surface effects. Nevertheless, some information can be extracted. Consistent with the SAXS results, agglomerates are observed in all cases, regardless of the particle content and the drying temperature. Thus, especially in the composites with 2 wt%, larger areas of the polymer are observed where no particles are present. While smaller spherical agglomerates with a diameter of about 100 nm are observed at low particle concentrations, the size of the agglomerates continues to increase with increasing particle concentration to 10 wt% up to a diameter of approx. 1 μm . The samples prepared at 40 °C appear less compact. In contrast,

Results and Discussion

the particles appear to be sintered together after treatment at 80 °C. When the particle content is further increased to 20 wt%, the differences become even more pronounced. For the samples prepared at 40 °C, the size of the agglomerates decreases again, while for the 80 °C sample the agglomerate size increases even further.

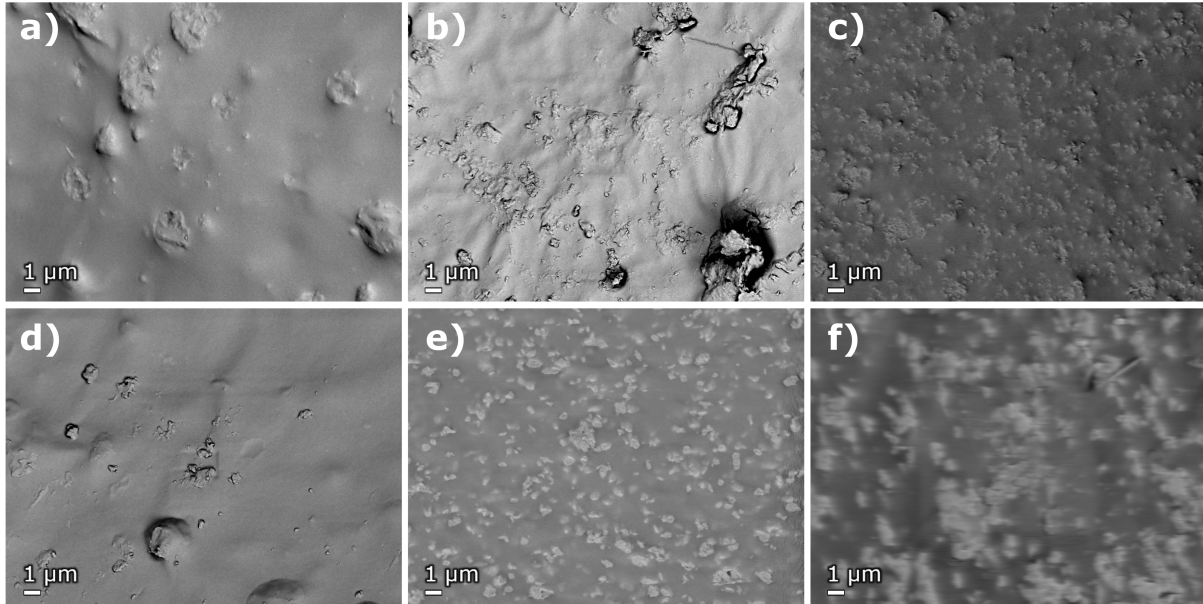


Figure 83: BSE SEM of the a) NC2, b) NC10, c) NC20 composites dried at 40 °C and d) NC2, e) NC10 and f) NC20 dried at 80 °C.

Again, the water absorption and its influence on the mechanical properties of the composites was examined. Water absorption was determined by TGA studies. The dried composites were stored in a desiccator over water at 600 mbar for various periods of time. Figure 84 shows the summarized results of the water adsorption tests. Like the polymers, the composites also show a high affinity towards water. The water content increases to almost 50 % for a storage time of 24 hours. The rate and amount of water absorption does not correlate with the number of particles in the system.

Results and Discussion

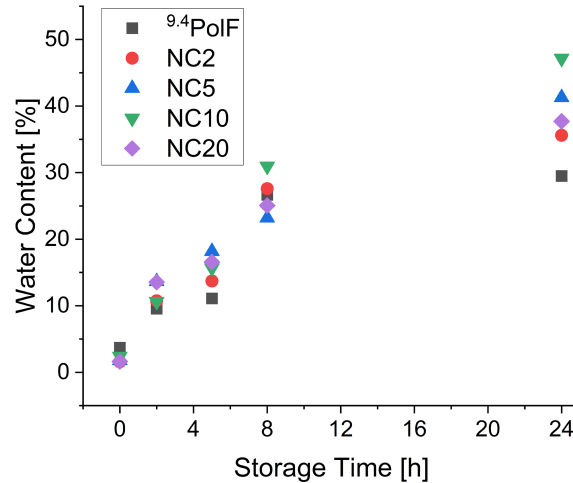


Figure 84: Determined water content of the composite samples after varying storage periods under increased humidity.

The water absorption of the composite is higher than that of the polymer. This is surprising at first, since it was determined from the ATRP systems that the anionic groups are largely responsible for water absorption and the negative groups in the polymer would be neutralized by the positive charges on the particle surface. However, the fact that this is not the case is consistent with the observations made in the case of the FRP polymer systems, where the content of SMBS in the polymer could not be correlated with the amount of water adsorbed. Hence the cause of this effect also seems to originate from the structure of the polymers. Although, the temperature dependent SAXS measurements suggest that water is trapped in the crystalline areas, it is possible that this is less than what could coordinate to the ionic group in an open chain. When these crystalline areas become disordered by the addition of particles, some ionic groups are neutralized by the particles, but some ionic groups remain uncoordinated in the polymer and are now freely available for water adsorption. This counteracting effect results in an initial increase in the amount of water adsorbed when only a small number of particles are added. As more particles are added, the free ionic groups are gradually neutralized by the particles and the water uptake decreases again.

Rheology measurements were performed to assess the influence of the water content on the shear modulus. Figure 85 a) shows the correlation of the shear modulus at 50 °C with the water content of the samples. For all systems the shear modulus decreases with increasing water absorption. The absorbed solvent acts as a plasticizer in the composites.

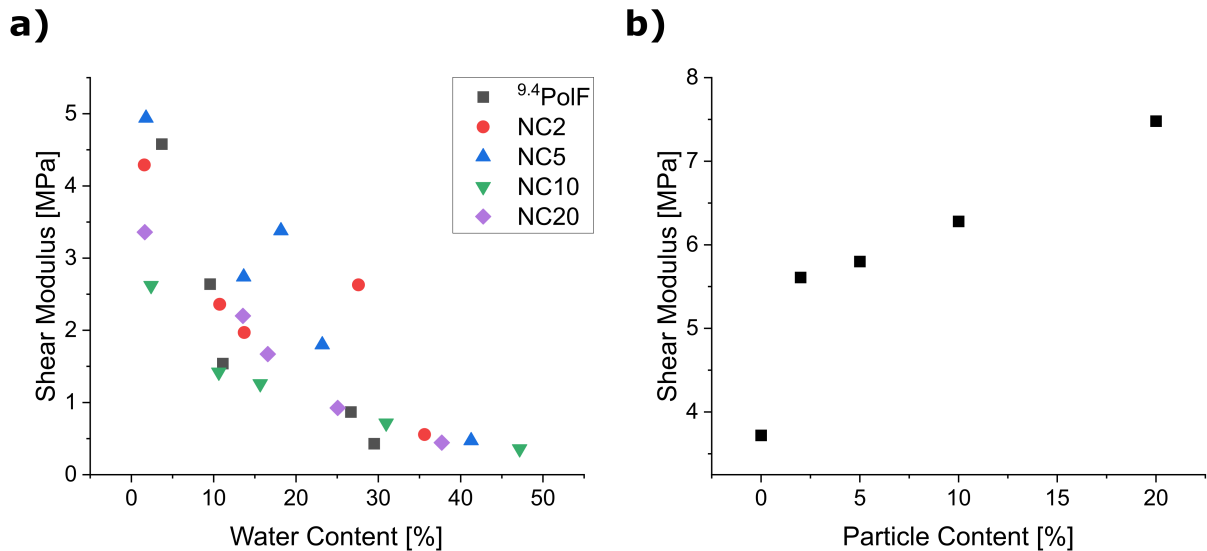


Figure 85: Shear modulus at 50 °C a) in dependency of the water content and b) the composite composition.

As with the polymer, small differences in water content have a very strong influence on the shear modulus. The composite systems obtained from the synthesis show shear moduli between 2.5 and 5 MPa. When stored under high humidity, these moduli decrease to approx. 0.5 MPa for all systems, again stressing the necessity for rigorous drying of the nanocomposites. Initially, no correlation of the shear modulus with the particle content was observed, though after undergoing the developed drying procedure not only significantly higher shear moduli were found but also a clear correlation between shear modulus and particle content was observed. With 5.6 MPa for the composites with 2 wt% and 7.5 MPa for the composites with 20 wt% particle content, the shear moduli are also significantly higher than that of the pristine polymer (3.7 MPa). In addition to the thermal properties, the mechanical properties of the composites can also be flexibly adjusted via the particle content.

In the next step, it was tested whether the mobility of the particles in the polymer is increased by swelling and whether this changes the particle distribution within the matrix. SAXS measurements were used for this purpose. Composite samples that were stored for 2 hours under elevated humidity, resulting in a water content of approx. 10 wt%, were tested. The SAXS curves obtained are shown in Figure 86 a). The overall appearance of the scattering curves is similar to that of the dry systems, indicating that the nanoparticles are strongly agglomerated. As shown in Figure 86 b), the hard sphere radius decreases with increasing nanoparticle content, while the hard sphere volume fraction increases. Both parameters are in the same range as for the dry systems. Therefore, the agglomerates densify with increasing nanoparticle content, largely independent of the water content of the films.

Results and Discussion

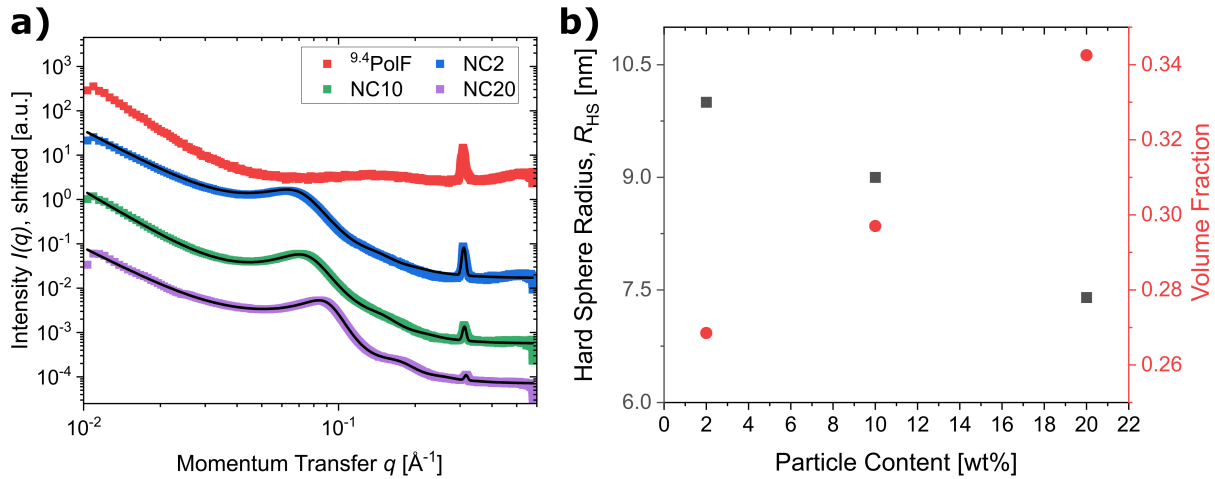


Figure 86: a) SAXS measurements of the composite samples under humid conditions for 2 hours with particle wt% as indicated in the graph. Black lines are fits to the data according to eq. (12). b) Exponent of power law and volume fraction of the composite samples stored under high humidity.

Tensile tests were also carried out on the dried composites. The results are summarized in Figure 87. The E-modulus initially increases from 3.0 N/mm² to 7.4 N/mm² upon increasing the particle content from 2 wt% to 10 wt%. This effect is commonly described in literature. Further it is described that there is also an increase in E-modulus as the particle size decreases.[679] As a result, the increasing agglomeration of the particles counteracts the increase in the E-modulus, which explains its slight decrease in the later stage. Both the fracture stress and the fracture strain decrease almost linearly with increasing particle content from 2.5 to 1.2 N/mm² and 333 to 93 % respectively. The material becomes harder, but tears faster. This is in good agreement with the rheology studies. Jordan *et al.* describe in their review paper that the ultimate stress and strain increase with strong interactions between filler and matrix and decrease upon weak interactions.[679] This indicates a poor interaction between the polymers and particles used in this study, which is rather surprising. However, systems are also described where a strong interaction is expected but a reduction in yield stress and tensile strength is still observed.[680,681] No trends are observable for the $R_{p0.2}$.

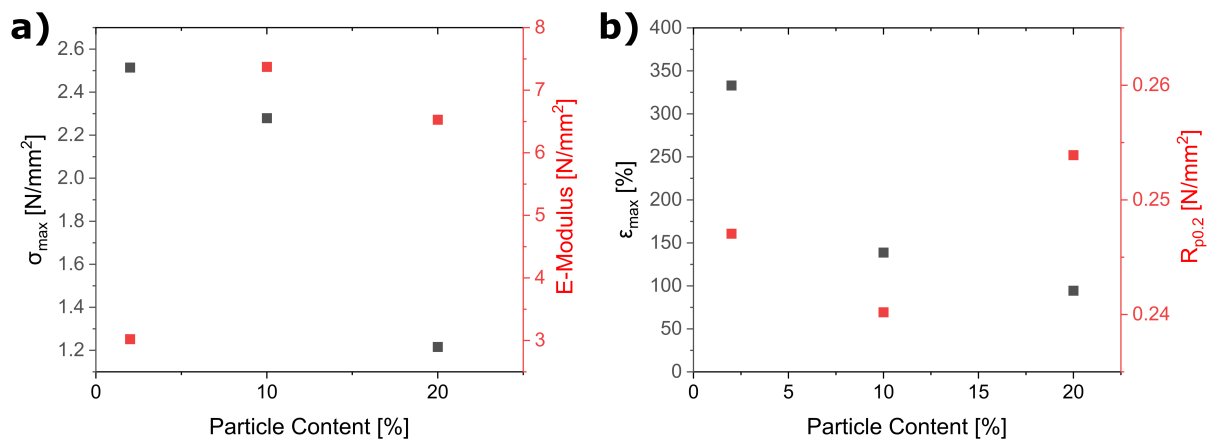


Figure 87: σ_{max} , E-modulus, ϵ_{max} and $R_{p0.2}$ of the composites NC2, NC10 and NC20 as a function of the particle content.

In summary, it has been shown that the crystalline regions of the FRP polymers become disordered by the introduction of the particles. Both an increase in thermal stability and an improvement in mechanical properties were observed. At the same time, however, the glass transition temperature increases due to the rigidification of the system as a result of the ionic interactions, potentially hampering self-healing. Therefore, the influence of the particle content on the self-healing of the composites was investigated.

3.5.7. Self-Healing Studies on the Ionic Nanocomposites based on the FRP Polymers

For the investigation of the self-healing behavior, the composites were cut to half their thickness and allowed to heal in an oven at 80 °C for 24 hours. Healing was observed phenomenologically using a microscope. To determine the efficiency of healing, the specimens were subjected to tensile testing after healing. The material constants were then compared before and after the healing process. The microscope images of the healing process for NC2 are shown exemplarily in Figure 88.

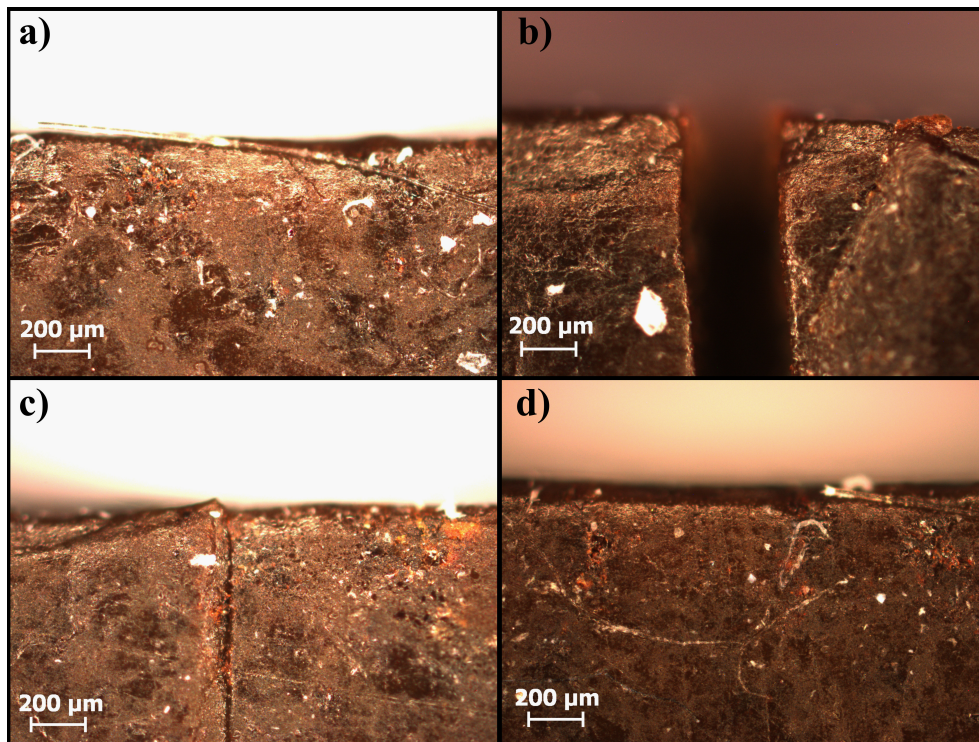


Figure 88: Microscope images of a) NC2, b) cut through half thickness, c) healed at 80 °C for 24 hours and d) another 24 hours at 80 °C in a Teflon mold.

The microscope images show almost complete healing for all composite systems examined. Only with the NC20 composite a slight mark can still be observed after 48 hours. This is due to the higher rigidity associated with the increasing particle content, which hampers the healing process. In all cases, a slight discoloration remains at point of incision compared to the initial composite. Overall, rather long healing times were observed. This indicates a restricted cleavage and reconnection of the ionic bonds, which is a known challenge in the field of ionic

Results and Discussion

self-healing polymers.[505,506] Therefore, wetting, especially with salt water, is the preferred healing trigger for these systems. This healing effect is based on the screening of the polymer charges, which improves the dynamics of bond formation. However, this was not applicable for the system used here due to the high water affinity and the associated strong swelling and loss of mechanical properties of the samples. With this in mind, one approach for future work would be to modify the polymer system to be less water affine, for example by exchange of the anionic group or the matrix polymer. This approach has the potential to address two challenges simultaneously: the problem of changing mechanical properties upon contact with ambient humidity and the limited usability of wetting for self-healing.

Tensile tests were then performed to quantify the healing efficiency. The stress-strain curves show a similar pattern for the initial and the healed samples. Figure 89 shows the σ_{max} , E-modulus, ϵ_{max} and $R_{p0.2}$ values of the healed composites determined from the stress-strain curves in comparison with the initial composites.

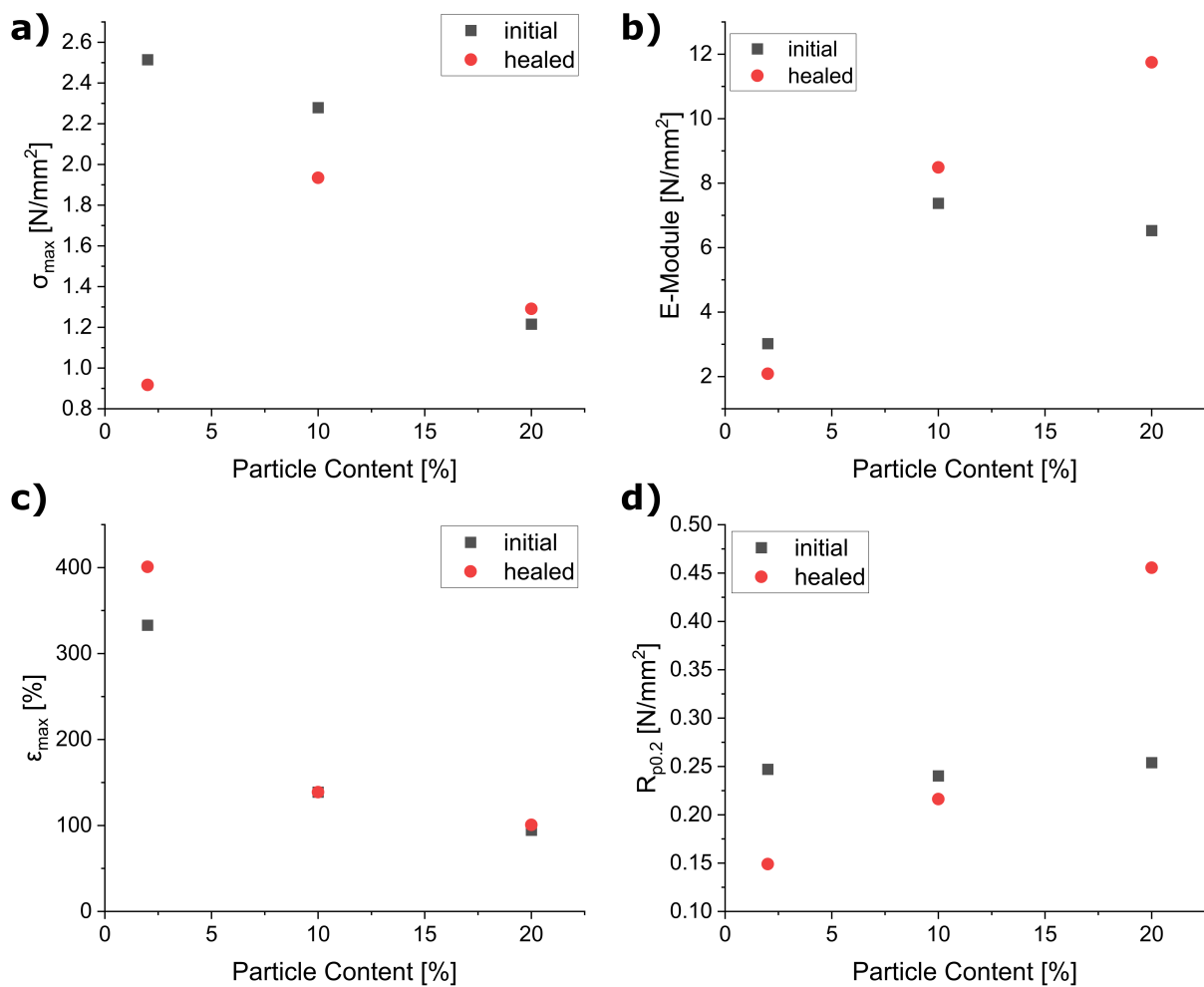


Figure 89: a) σ_{max} , b) E-modulus, c) ϵ_{max} and $R_{p0.2}$ of the healed composites and the composites as synthesized (NC2, NC10 and NC20).

Results and Discussion

For the maximum strain the material properties are fully recovered upon healing for all composite samples. This is not the case for the maximum stress, E-modulus and $R_{p0.2}$, primarily at low particle concentrations (2 wt%). While a recovery of 69 % and 60 % was observed for E-modulus and $R_{p0.2}$ respectively, σ_{max} decreased even more, recovering only 36 % of the initial value. At a particle content of 10 wt%, all properties were largely restored. For σ_{max} 85 %, for $R_{p0.2}$ 90 % and for ϵ_{max} 100 % of the initial properties were retrieved. The E-modulus was found to be even slightly higher for the healed sample. Surprisingly, this was also the case for all properties of the NC20 composite, where a slight incision was still visible after healing. While stress and strain at break for the healed specimens were very close to the initial values and thus in the range of the reproducibility errors of the specimens, values of up to 180 % of the initial value were obtained for E-modulus and $R_{p0.2}$ for the healed specimens. Since the unhealed specimens were also subjected to the same temperature profile and storage conditions, differences in water content can be ruled out as the reason for the increase in both parameters. The cause of the observed increase has not yet been identified. However, it should be noted that healing efficiencies > 100 % have commonly been reported in the literature, though mostly, but not exclusively, in the context of capsule-based healing.[682–684]

Finally, the particle distribution in the polymer after tensile testing was studied to investigate the influence of mechanical stress on the size and shape of the agglomerates. BSE SEM measurements were performed for this purpose. The micrographs are shown in Figure 90.

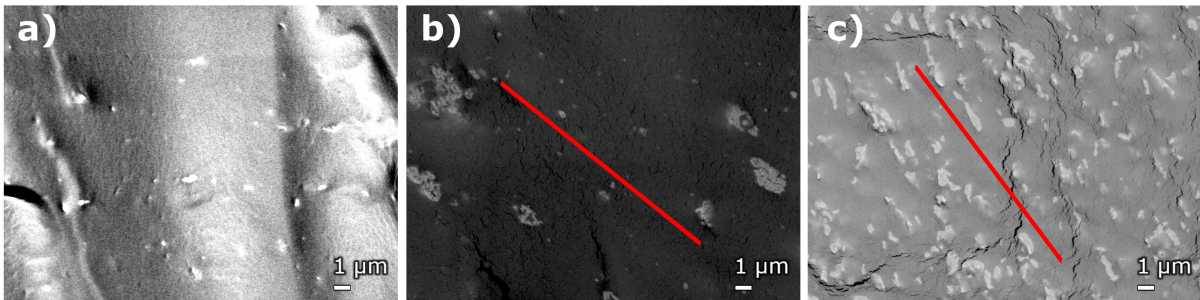


Figure 90: BSE SEM of the a) NC2, b) NC10 and c) NC20 samples after tensile testing (red = preferred orientation).

It is noticeable that an alignment of the agglomerates takes place, especially in the NC10 and NC20 systems. Whether this occurs along the tensile axis could not be determined, but it seems likely. In addition, SAXS measurements were carried out on the composites after the tensile tests. No evidence of anisotropic scattering was observed in the 2D scattering images. Therefore, they were likewise azimuthally averaged. The results are shown in Figure 91.

Results and Discussion

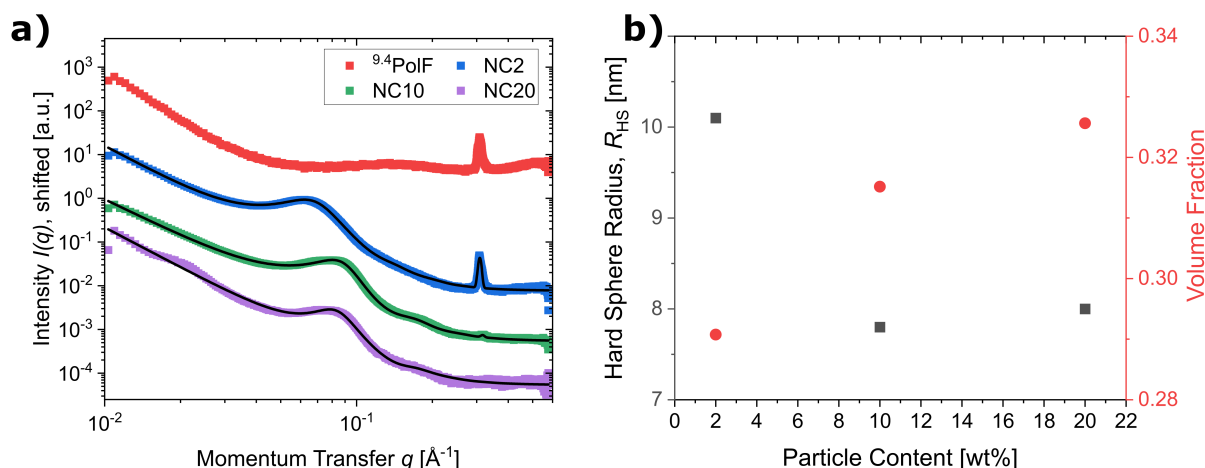


Figure 91: a) SAXS measurements of the composite samples after tensile testing with particle vol% as indicated in the graph. Black lines are fits to the data according to eq.(12). b) Exponent of power law and volume fraction of the composite samples after tensile testing.

The fitting parameters do not differ significantly from those of the dry samples, as is shown in Table 10. This indicates, that although the macroscopic orientation of the agglomerates has changed after tensile testing, they remain largely unchanged on length scales probed by SAXS.

Table 10: Results of the SAXS measurements of the samples stored at high humidity and after tensile testing.

Drying Temperature	40°C			80°C		
Parameter	R_{HS}	m	η [%]	R_{HS}	m	η [%]
NC2	10.1	2.7	32.3	10.2	3.1	33.3
NC10	9.0	3.1	26.4	9.4	3.2	24.6
NC20	7.5	2.9	25.4	7.4	3.0	25.2
	Samples with High Water content			Samples After Tensile Testing		
Parameter	R_{HS}	m	η [%]	R_{HS}	m	η [%]
NC2	10.0	3.0	26.9	10.1	3.1	26.9
NC10	9.0	3.4	29.7	7.8	2.8	31.5
NC20	7.4	2.9	34.3	8.0	3.0	32.6

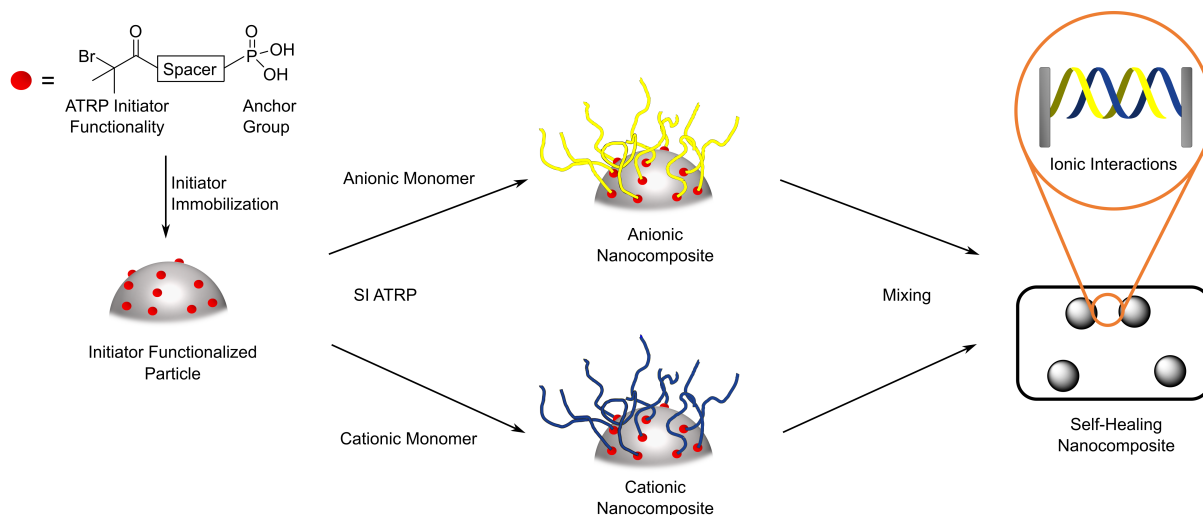
In the course of the studies, SMBS-DEGMA-based copolymers were prepared via ARGET ATRP and FRP. The SMBS:DEGMA ratios in the polymer composition were varied. The polymers were characterized by ^1H NMR, CHN analysis, FTIR and DSC. This revealed that for the FRP polymers the incorporation of the ionic species into the polymer was lower than expected based on the initial monomer ratios. In contrast the ATRP polymers reflected the initially used monomer ratios. As a result, the T_g s for the ATRP systems could be tuned over a wide range of 68 °C, while for the FRP systems, the T_g s could only be varied in a range of 5 °C. SAXS measurements indicate different structures for the obtained polymers. In contrast to the ATRP polymers, the FRP polymers show signs of block-like structures, with the ionic

components forming paracrystalline domains that are very stable up to high temperatures. Like the ATRP systems, the FRP systems exhibit a high affinity towards moisture and absorb water from ambient air. Rheological investigations and tensile tests in combination with TGA revealed that even small amounts of contained water strongly deteriorate the mechanical properties, with the water acting as a plasticizer. As a result, a drying and storage procedure was developed to allow reliable studies. The mechanical properties and thermal stability of the polymers can be improved by incorporation of cationic functionalized iron oxide particles in the polymer matrix. Despite the expected attracting ionic interactions between the polymer matrix and the particles, the synthesized composites showed particle agglomeration in SAXS and BSE SEM, regardless of the polymer composition, preparation method and particle content. When the particles are incorporated into the FRP polymer matrix, the initially crystalline polymer regions become disordered. The composites showed the ability to heal scratches in a μm -scale in a conventional oven. Tensile tests for the FRP composites showed almost complete recovery of mechanical properties after healing within the measurement accuracy, especially at higher particle contents. The ATRP-based composites were further used to demonstrate, that the composites can be healed in an AMF, not only spatially resolved but also faster and under milder conditions.

3.6. Synthesis of Nanocomposites via SI ATRP

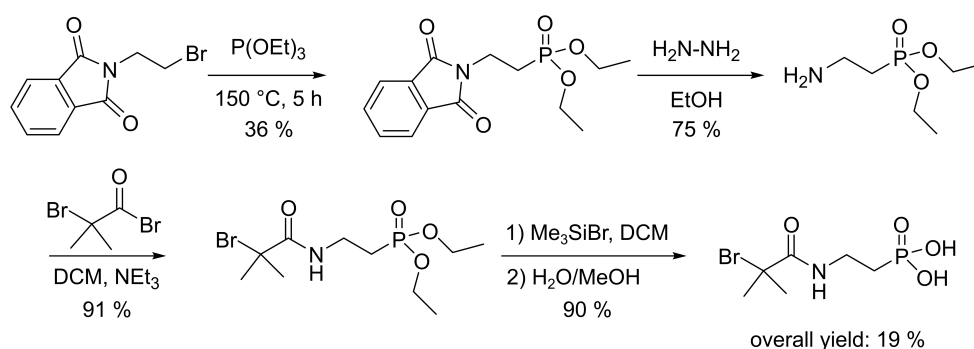
In this chapter, a second approach to self-healing nanocomposites is examined. Here, the self-healing mechanism is completely transferred to the polymer network. The polymer is covalently bound to the particle surface. This approach can be done by grafting-from, grafting-to and grafting-through polymerization. Here the focus is on grafting-from method, as it usually allows higher grafting densities.[26,27] This approach also offers the advantage that the steric repulsion of the polymer strands growing from the particle surface should better suppress agglomeration of the particles. The procedure for this approach is shown in Scheme 23. SI ATRP was chosen as the polymerization technique in order to ensure good controllability of the polymerization and to avoid polymerization in solution, which inevitably occurs with free radical polymerization.

Results and Discussion



Scheme 23: SI ATRP approach to ionic self-healing nanocomposites.

The preparatory studies for these nanocomposites are described in this section. First, an initiator was synthesized which both can covalently bind to the iron oxide particle surface via a phosphonic acid group and features an ATRP initiator group. Scheme 24 shows the initial synthetic approach.



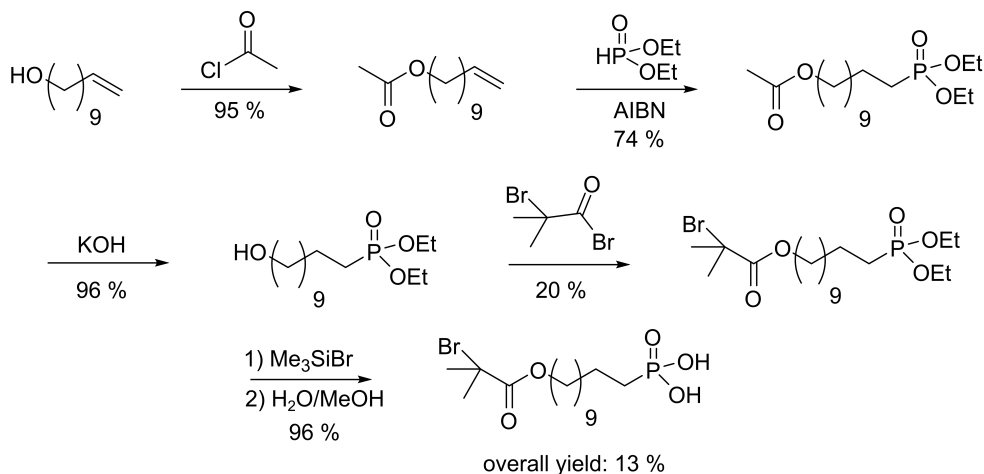
Scheme 24: Synthesis route for (2-(2-bromo-2-methylpropanamido)ethyl)phosphonic acid.

The synthesis was carried out in four steps starting with the commercially available N -(2-bromoethyl)phthalimide, which was converted into the corresponding phosphonic acid ester in a Michaelis-Arbusow reaction. This was followed by hydrazinolysis of the diethyl (2-aminoethyl) phosphonate. Subsequently, the ATRP initiator functionality was introduced in the form of BIBB. The phosphonate ester was then hydrolyzed to give the initiator with an overall yield of 19%. The product obtained was characterized by 1H , ^{13}C , ^{31}P and FTIR spectroscopy. Initial investigations confirmed the suitability of the system to initiate ATRP polymerization both in solution and from the particle surface. However, the particles showed strong agglomeration upon functionalization due to the short spacer length. Therefore, a second generation of initiators with longer spacers was prepared, which showed more promising results. To accustom for different monomer polarities two different initiator systems were synthesized one

utilizing a non-polar alkyl spacer and one using a more polar ethylene glycol-based spacer. The synthesis of these systems is described in more detail below.

3.6.1. Synthesis of a Phosphonic Acid-Based ATRP Initiator with a Non-Polar Linker

The synthesis followed known literature procedures with some modifications.[305,685] The synthesis route is shown in Scheme 25.



Scheme 25: Synthesis route for 11-((2-bromo-2-methylpropanoyl)oxy)undecyl)phosphonic acid.[305,685]

The synthesis was carried out in five steps. The starting material was the commercially available undec-10-en-1-ol. In the first step, an acetyl protection group was introduced to the alcohol by reaction with acetyl chloride. The successful conversion was confirmed by NMR spectroscopy and the disappearance of the O-H stretching vibration and appearance of the C=O stretching vibration in the FTIR spectrum. The synthesis was carried out in 95 % yield. In the next step, the phosphonic ester functionality was introduced by a radical addition of diethyl phosphite to the double bond. AIBN was used as the radical initiator. The product was obtained in 74 % yield. Subsequently, the alcohol was deprotected with potassium hydroxide. Again, the product was obtained in high yield (96 %). The initiator functionality was then introduced by a nucleophilic attack of the OH group on BIBB. The product was obtained in 20 % yield. Finally, the phosphonic acid ester was hydrolyzed with bromotrimethylsilane and methanol. The synthesis was carried out in 96 % yield, resulting in an overall yield of 13 %. The product was characterized by ^1H , ^{13}C , ^{31}P , FTIR spectroscopy and CHN analysis.

In preparation for the planned surface-initiated polymerization, an ATRP polymerization was first carried out in solution to investigate the suitability of the compound as an ATRP initiator. For this purpose, butyl methacrylate was chosen as a model monomer. The synthesis was carried out using CuBr/HMTETA as the redox active complex in toluene. 70 °C was chosen as the reaction temperature. After various reaction times (0.5 h, 1 h, 2 h, 4 h, 7 h, 24 h) samples were taken directly from the solution. The solvent was removed at room temperature under

Results and Discussion

reduced pressure. In Figure 92 the ^1H crude NMR after 30 minutes and 4 hours reaction time are shown as an example.

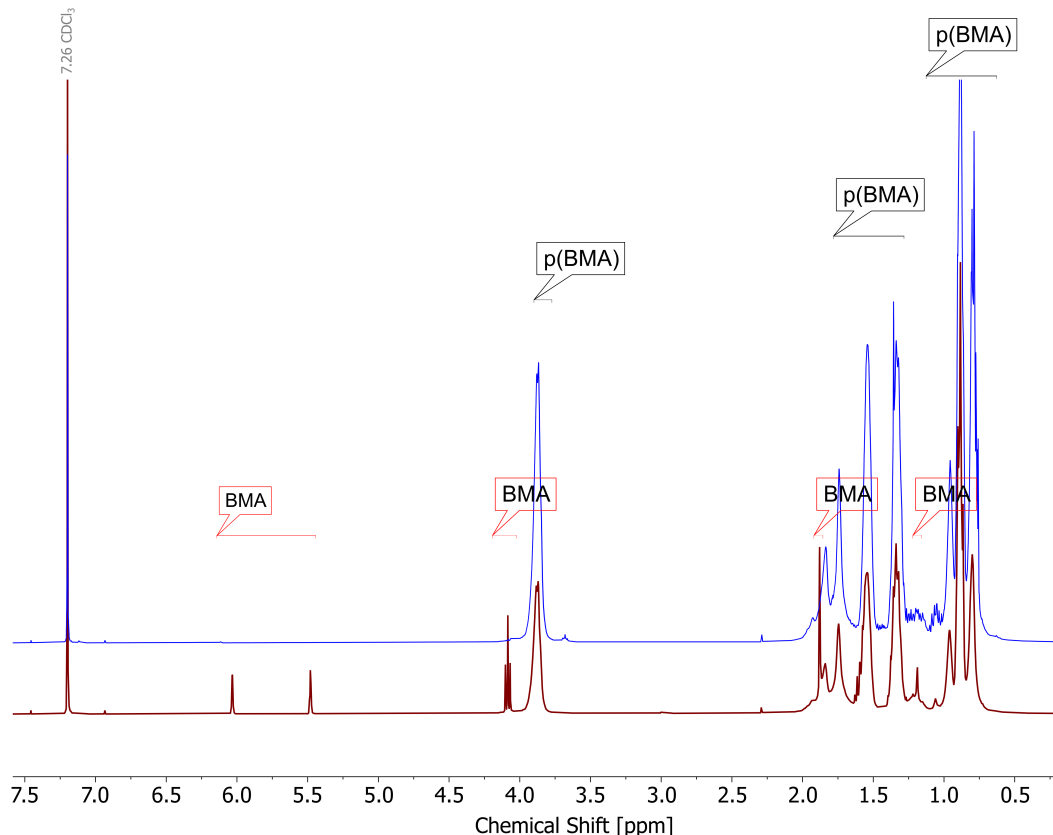


Figure 92: ^1H crude NMR spectrum after 0.5 hours (red) and 4 hours (blue) of the polymerization of BMA using 11-((2-bromo-2-methylpropanoyl)oxy)undecyl)phosphonic acid as initiator.

The NMR spectra clearly show that educt is still present after 30 minutes. This can be seen in particular in the signals of the double bond of the BMA at 6.10 ppm and 5.54 ppm. Nevertheless, the emerging signals of the polymer are clearly visible. The integrals of the signals shows that 90 % of the monomer is already converted after 30 minutes, indicating a high activation rate. Control experiments without the use of the initiator showed almost no conversion (< 2 %). The polymer samples taken after different reaction times were purified by repeated precipitation in *n*-hexane. During this work-up, the copper complex could not be separated, as evidenced by the characteristic blue color of the polymer. Several approaches were taken to remove the copper complex. Initially the polymers were dispersed in water under ultrasonication. Since this was not successful, it seems likely that the phosphonic acid group binds directly to the copper.[686–688] Therefore, an attempt was made to add a stronger complexing agent by adding ethylenediaminetetraacetate to replace the phosphonic acid in the complex. In a similar approach, an attempt was made to prevent the interaction through the protonation of the phosphonic acid by lowering the pH, but no discoloration of the product was observed. The sample was also dissolved in DMF and sodium diethyldithiocarbamate was added, which is commonly used as a copper eliminator.[689] Since the corresponding copper

Results and Discussion

complex is soluble in DMF, the brownish complex was precipitated by adding water. However, the polymer obtained also precipitated when water was added. Therefore, it could not be successfully separated. Further attempts were made to purify the products by column chromatography. First, aluminum oxide (active neutral/basic) was used. Here, the copper is clearly retained within the first centimeter of the separation column. However, also the phosphonic acid group is known to strongly bind to the alumina surface.[690] As a result, the polymer could only be eluted under harsh conditions. A yellow-green product was obtained, which was significantly softer than the initial polymer. An NMR spectrum was recorded of the product obtained. This is shown in Figure 93. In addition to the signals of the polymer, a multitude of additional signals appear that could not be assigned so far. Thus, it seems that the phosphonic acid polymer is decomposing on the alumina column under the harsh conditions. Since it was not possible to measure copper-containing samples by GPC, the samples obtained after the column were measured. The GPC clearly shows the signals of low-molecular decomposition products. Polymer signals appeared only in low intensities and did not allow a reliable evaluation.

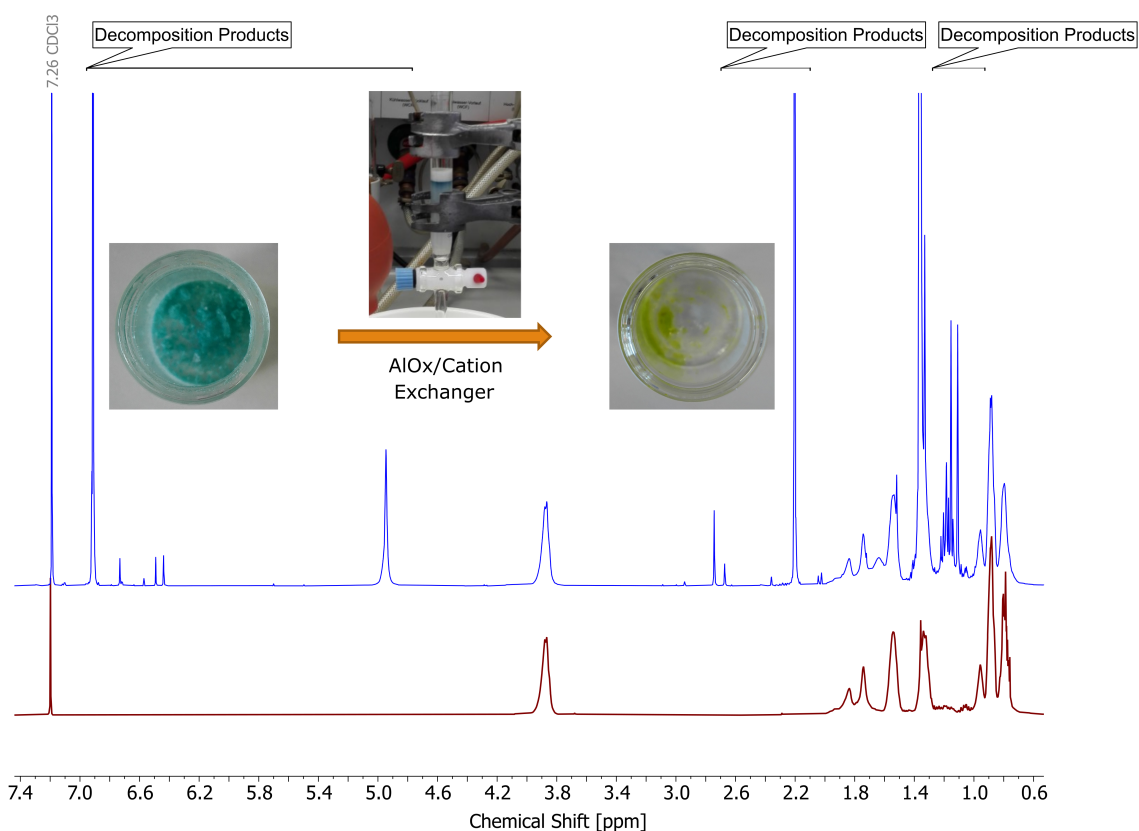


Figure 93: ¹H NMR Spektrum of the polymer sample before (red) and after (blue) passing through aluminum oxide.

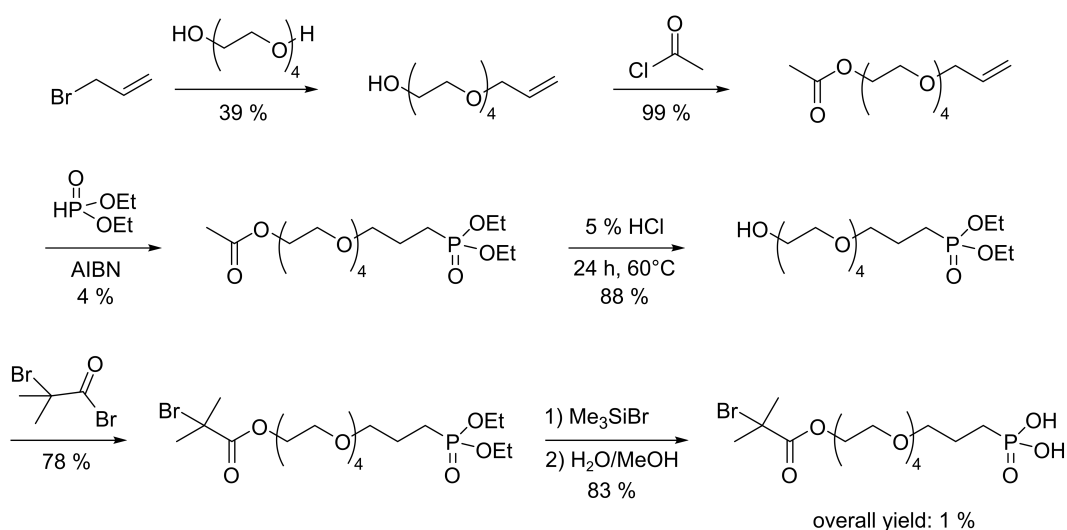
In the next step, silica was used instead of alumina as the stationary phase, as the stability of the Si-O-P bond is reported to be much weaker. This is due to the lower electronegativity of the silicon atom and the presence of the valence 3d orbitals, which make the silicon atom more

susceptible to nucleophilic attack and thus bond cleavage.[691] Nevertheless, some stable bonds of phosphonic acids to silica particle surfaces have been described.[692–694] THF, ethyl acetate and water were used as the eluents. Here, the blue copper complex also remained at the upper edge of the column. However, neither the polymer nor any decomposition products were found in the mobile phase. Thus, a strong binding of the phosphonic acid seems to take place. The reason for this might be, that the phosphonic acid remains bound to the copper cation, which is bound by the Si-O functionalities of the silica gel. This results in a copper-bridged bond that prevents elution. The separation with a sulfonate-based cation exchanger, which should allow a good separation since the solid phase has a high affinity to copper but not to the phosphonic acid, was also unsuccessful. The ^1H NMR spectrum recorded from the product showed degradation products as after the alumina column, again preventing the characterization of the intact polymer.

In summary, it can be said that the synthesized phosphonic acid is suitable as an ATRP initiator and shows high activity. So far, however, no precise characterization of the molecular weight distribution could be carried out, as the separation of the copper complex from the polymer could not be achieved without causing decomposition of the polymer. Since no free phosphonic acid is present during SI ATRP the separation of the copper complex should therefore be easier. For this reason, no further work-up optimization was performed at this time.

3.6.2. Synthesis of a Phosphonic Acid-Based ATRP Initiator with a Polar Linker

A tetraethylene glycol chain was used as a spacer for the polar initiator. The synthesis route used is shown in Scheme 26. The synthesis was carried out on the basis of the works of Traina and Schwartz.[306]



Scheme 26: Synthesis route for (18-bromo-18-methyl-17-oxo-4,7,10,13,16-pentaoxonadecyl)phosphonic acid.[306]

Results and Discussion

The synthesis of the polar initiator was analogous to the non-polar system. However, the 3,6,9,12-tetraoxapentadec-14-en-1-ol is not commercially available and therefore had to be prepared from tetraethylene glycol and allyl bromide. The synthesis was carried out in 39 % yield. Subsequently, the alcohol protecting group was introduced under alkaline conditions. The introduction was carried out in 99 % yield. The radical addition to introduce the phosphonic acid ester was only possible in very low yields. Only 4 % product was obtained. In a further deviation from the non-polar system, the deprotected alcohol could not be isolated after deprotection under alkaline conditions. Though, a cleavage with 88 % yield could be achieved under acidic conditions. For this purpose, a 5 % hydrochloric acid was used, and the reaction mixture was heated to 60 °C for 24 hours. The introduction of the initiator group was carried out in 78 % yield. Finally, the phosphonic acid ester was hydrolyzed. The product was obtained in 83 % yield. The overall yield is therefore approx. 1 %, whereby the low yield is primarily determined by the step of introducing the phosphonic acid ester. The product was characterized by ^1H , ^{13}C , ^{31}P , FTIR spectroscopy and CHN analysis.

A polymerization test in solution with the polar initiator system was also performed. Acrylamide was used as the model monomer. The synthesis was carried out in water at 70 °C, using $\text{CuBr}/2,2'$ -Bipy as the redox active complex. After one hour, a sample was taken and characterized by ^1H NMR spectroscopy. The experiment was conducted analogously without initiator. Figure 94 shows the spectra obtained.

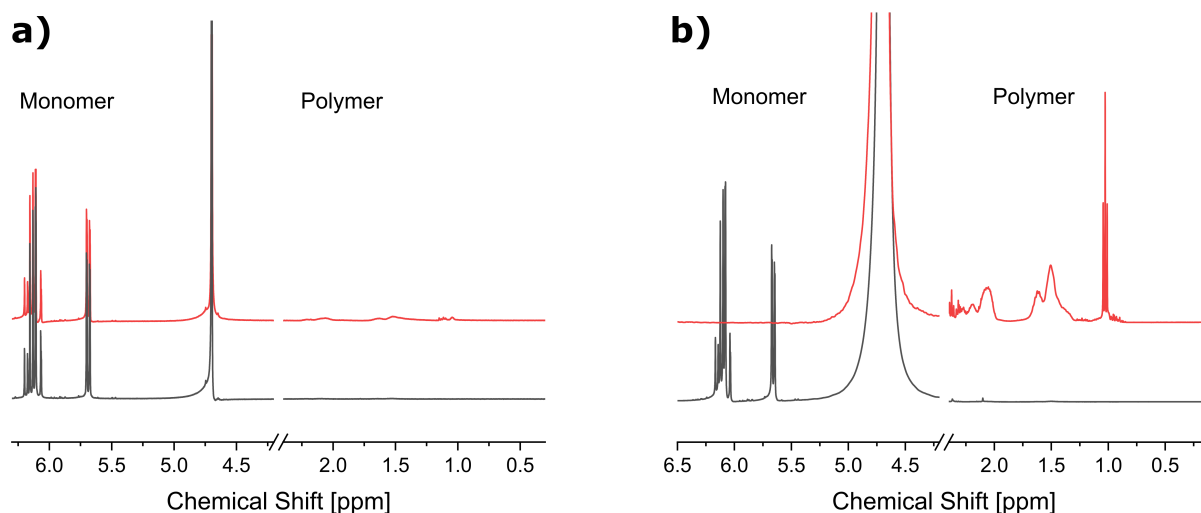


Figure 94: ^1H NMR spectra for the initial reaction solutions (red) and after 1 hour polymerization time (grey) of acrylamide a) without and b) with (18-bromo-18-methyl-17-oxo-4,7,10,13,16-pentaoxonanadecyl)phosphonic acid.

The initial NMR spectra clearly show the signals of the double bond protons of the acrylamide at 5.6 and 6.2 ppm. Without the use of the initiator system, no change in the NMR signal can be detected after one hour, whereas with the use of 1 mol% initiator, a complete conversion is already observed at that time, confirming the suitability of the synthesized initiator system. Due to the problem of separation of the copper complex already observed with the non-polar

initiator system, no further processing and characterization was carried out at this point. In the following chapter, the iron oxide particles were functionalized with the synthesized initiator molecules.

3.6.3. Synthesis of ATRP Initiator Functionalized Particles

An exchange protocol for (11-((2-bromo-2-methylpropanoyl)oxy)undecyl)phosphonic acid and (18-bromo-18-methyl-17-oxo-4,7,10,13,16-pentaoxonadecyl)phosphonic acid was developed to obtain the respective initiator functionalized particles. Here, too, the oleic acid functionalized nanoparticles obtained from the thermal decomposition were used as the starting point. The amount of coupling reagent used was optimized. A range of 0.003 to 0.210 mmol phosphonic acid per 150 mg nanoparticle was investigated. The functionalization was carried out in ethanol, as it provides both stable particle dispersions and good solubility of the phosphonic acids. Functionalization was carried out within 24 hours at room temperature. Subsequently, the particles were magnetically decanted off and washed several times with ethanol to remove excess ligand. The particle systems obtained in this way are referred to in the following as $^{0.003}\text{PIP}@Fe_xO_y$ - $^{0.210}\text{PIP}@Fe_xO_y$ and $^{0.003}\text{AIP}@Fe_xO_y$ - $^{0.210}\text{AIP}@Fe_xO_y$ for the polar and non-polar initiator system, respectively. In Figure 95 the obtained FTIR spectra of the dried particle systems are shown exemplarily for the non-polar system. The spectra were normalized to the Fe-O-Fe vibration at 536 cm^{-1} for better comparability.

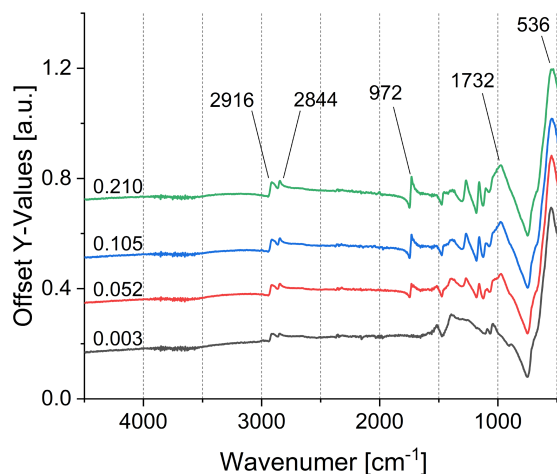


Figure 95: FTIR spectra of the 11-((2-bromo-2-methylpropanoyl)oxy)undecyl)phosphonic acid functionalized iron oxide nanoparticles.

The spectra confirm the successful functionalization. The FTIR spectra show the signal of the PO_3 vibration at 972 cm^{-1} already at low concentrations of phosphonic acid. In addition, the intensity of the symmetric and asymmetric C-H stretching vibrations at 2844 cm^{-1} and 2916 cm^{-1} increases with the amount of phosphonic acid added. The particle size was investigated by XRD, DLS and TEM. The results are shown exemplary for the sample $^{0.105}\text{AIP}@Fe_xO_y$ in Figure 96. The DLS measurements were recorded in methanol for the polar

Results and Discussion

systems and in toluene for the non-polar systems. While no changes in the crystallite size and composition of the particles with increasing functionalization were observed in the XRD, samples $^{0.003}\text{PIP}@Fe_xO_y$ and $^{0.003}\text{AIP}@Fe_xO_y$ clearly show agglomerate formation in the DLS. These agglomerates disappear with increasing degree of functionalization. From the TEM images, 100 particles were measured and used to calculate the size distribution. A mean diameter of 6.5 ± 1.8 nm was determined. The mean particle size therefore agrees well with that obtained from the original particle synthesis and the crystallite sizes determined with XRD. Nevertheless, some larger agglomerates of approx. $1.5 \mu\text{m}$ diameter were also observed in the TEM, although these are probably due to drying effects.

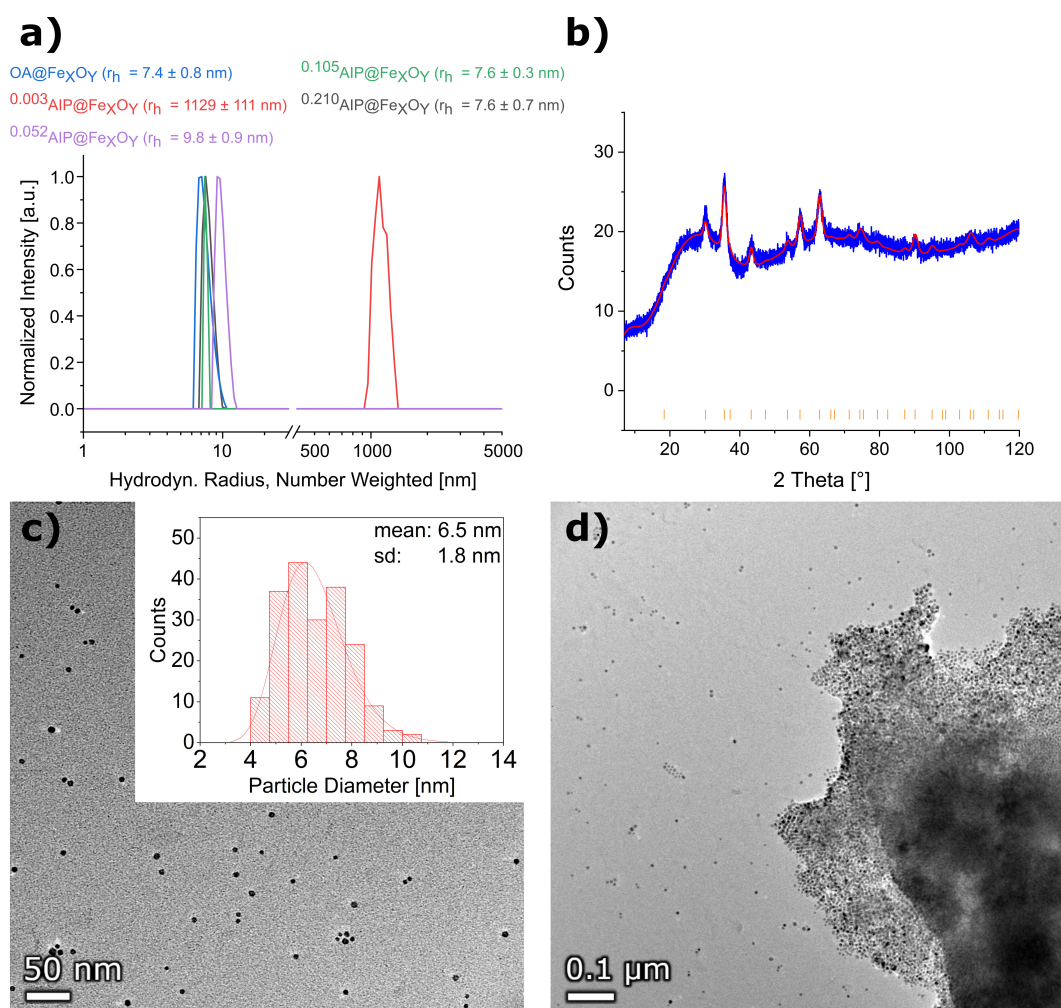


Figure 96: a) DLS measurements of OA@Fe_xO_y (blue), $^{0.003}\text{AIP}@Fe_xO_y$ (red), $^{0.052}\text{AIP}@Fe_xO_y$ (purple), $^{0.105}\text{AIP}@Fe_xO_y$ (green) and $^{0.210}\text{AIP}@Fe_xO_y$ (black) in *n*-hexane, as well as b) XRD and c) d) TEM images of $^{0.105}\text{AIP}@Fe_xO_y$.

For the polymerizations, an accurate determination of the surface loading is necessary. This was first done for the polar initiator system. To calculate the amount of bound phosphonic acid, it was assumed that the oleic acid on the particle surface is completely replaced by the phosphonic acid. In addition, it was assumed that the phosphonate group remains on the particle surface. To calculate the number of molecules per nm² of surface area, the mean

Results and Discussion

surface area per particle was determined from TEM images. Furthermore, the assumption was made, that the particles are completely composed of Fe_3O_4 . The results are summarized in Table 11.

Table 11: TGA and CHN results of the polar initiator-modified particles ($^{0.003}\text{PIP}@Fe_xO_y$ - $^{0.210}\text{PIP}@Fe_xO_y$).

Sample	TGA Mass Loss 900°C, N ₂ [%]	CHN [%]		Surface Loading [Molecules/nm ²]		
		C	H	TGA	C	H
$^{0.003}\text{PIP}@Fe_xO_y$	23.16	10.35	2.13	2.85	3.08	4.11
$^{0.052}\text{PIP}@Fe_xO_y$	24.70	10.81	2.25	3.05	3.27	4.47
$^{0.105}\text{PIP}@Fe_xO_y$	27.12	11.15	2.36	3.37	3.41	4.81
$^{0.210}\text{PIP}@Fe_xO_y$	27.11	11.70	2.62	3.36	3.65	5.07

When the carbon content of the sample determined by CHN analysis is used to calculate the surface loading, values in the range 3.55 to 3.08 molecules per nm² are obtained. This is in good agreement with the particle loading determined from thermogravimetry. Surprisingly, the values determined by means of hydrogen content are significantly higher. In the literature, loadings in the range of 0.9 to 3 phosphonic acid groups per nm² are typically described. In these cases, the formation of a monolayer is assumed.[296,347] Based on the typical space requirement of the phosphonic acid anchor group of 25 Å² [297], a maximum loading of 4.2 molecules per nm² is possible for a dense monolayer. The loading observed, especially at high amounts of phosphonic acid used, suggest that either multilayers are formed, or that the exchange of oleic acid is not complete. To investigate this further, the samples were analyzed by ICP-MS. For this purpose, the functionalized particles were dissolved in a mixture of 37 % hydrochloric acid and aqua regia. The bromine content was used to calculate the surface loading, as it is contained only in the initiator functionality. Figure 97 shows the bromine/particle ratio determined by ICP-MS versus the ratio used for functionalization.

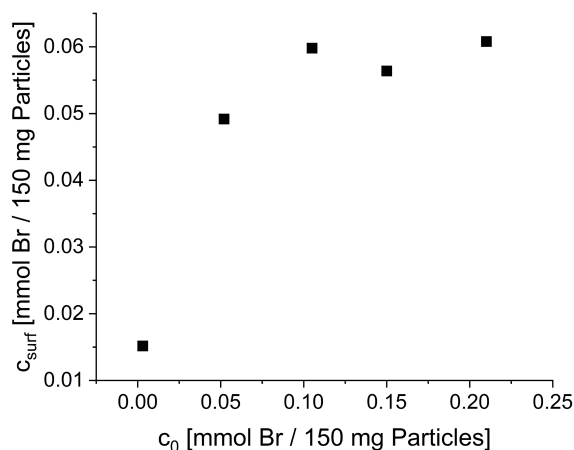


Figure 97: Plot of the bromine/particle ratio determined by ICP-MS against the initial bromine/particle ratio used (polar initiator).

Results and Discussion

Initially, a strong increase of the initiator concentration at the surface can be observed with increasing amount of initiator used. However, a saturation of the surface at a value of approximately 0.06 mmol bromine per 150 mg particles is observed. Further increase in the initial amount of phosphonic acid added does not result in further incorporation of phosphonic acid. This is in contrast to the observations from CHN and TGA measurements, where an increase in carbon and hydrogen content as well as a mass loss in TGA was still observed at high initiator to particle ratios. In addition to the bromine content, the iron content of the samples was also determined. From these values, a loading density in molecules per nm² surface area was calculated. The results are shown in Table 12 in comparison to the values determined by CHN and TGA.

Table 12: Summary of the calculated surface loadings of the polar initiator-modified particles based on ICP-MS, TGA and CHN analysis (^{0.003}PIP@Fe_xO_y-^{0.210}PIP@Fe_xO_y).

Sample	Surface Loading [Molecules/nm ²]			
	ICP-MS	CHN (C)	CHN (H)	TGA
^{0.003} PIP@Fe _x O _y	0.62	3.08	4.11	2.85
^{0.052} PIP@Fe _x O _y	2.10	3.27	4.47	3.05
^{0.105} PIP@Fe _x O _y	2.72	3.41	4.81	3.37
^{0.210} PIP@Fe _x O _y	2.79	3.65	5.70	3.36

Compared to the results of the CHN and TGA analyses, the surface loadings determined by ICP-MS are significantly lower. The surface appears to be saturated at a loading of approximately 2.6 molecules per nm², which is within the range typically described in the literature.[296,347] Furthermore, based on the determined iron and bromine content of the samples, only 75 % of the total sample mass is covered by the initiator and the particles themselves. This indicates that, in addition to the initiator molecules, further organic matter remains on the surface.

Analogous to the polar initiator system, CHN and TGA measurements were also performed on the non-polar functionalized systems. The results are presented in Table 13.

Table 13: TGA and CHN results of the non-polar initiator-modified particles (^{0.003}AIP@Fe_xO_y-^{0.210}AIP@Fe_xO_y).

Sample	TGA Mass Loss 900°C, N ₂ [%]	CHN [%]		Surface Loading [Molecules/nm ²]		
		C	H	TGA	C	H
^{0.003} AIP@Fe _x O _y	21.38	9.28	1.73	3.17	2.55	2.91
^{0.052} AIP@Fe _x O _y	23.83	11.15	2.02	3.56	3.23	3.58
^{0.105} AIP@Fe _x O _y	30.75	12.57	2.26	4.70	3.80	4.19
^{0.210} AIP@Fe _x O _y	36.05	13.25	2.39	5.60	4.09	4.54

Results and Discussion

The CHN analysis yields a surface loading of 2.55 to 4.54 molecules of phosphonic acid per nm^2 of particle surface, depending on the amount of phosphonic acid used. As with the particles functionalized with the polar initiator system, the loadings calculated from the specific hydrogen content are always higher than those calculated based on the carbon content. However, the differences are somewhat smaller here and seem to be constant at approx. 0.4 molecules per nm^2 . In contrast to the polar system, the loadings calculated based on the TGA data are significantly higher in all cases. Especially when high amounts of phosphonic acid are used, the loading increases beyond the maximum possible loading of a monolayer. Analogous to the polar system, studies were also carried out here using ICP-MS. Figure 98 shows the amounts of bromine in mmol per 150 mg particle calculated as a function of the ratio used for the synthesis.

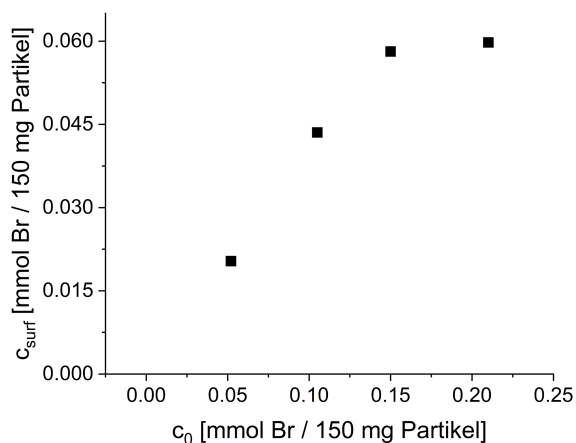


Figure 98: Plot of the bromine/particle ratio determined by ICP-MS against the initial bromine/particle ratio used (non-polar initiator).

Compared to the polar system, the bromine concentrations are significantly lower at low starting concentrations. At an applied concentration of 0.03 mmol bromine per 150 mg particles, the bromine concentration was even below the limit of quantification (LOQ). While in the polar system saturation is already reached at an initial ratio of 0.105 mmol bromine per 150 mg particles, a significant increase in the bromine content at the surface can be observed here when the concentration is increased to 0.150 mmol bromine per 150 mg particles. The saturation concentrations of the two phosphonic acid systems coincide at 0.06 mmol per 150 mg particles. Thus, the polarity of the spacer appears to have very little effect on the maximum binding. Again, the loading density in molecules per nm^2 was calculated and compared with the results of the thermal analysis (Table 14).

Results and Discussion

Table 14: Summary of the calculated surface loadings of the polar initiator-modified particles based on ICP-MS, TGA and CHN analysis ($^{0.003}\text{AIP@Fe}_x\text{O}_y$ - $^{0.210}\text{AIP@Fe}_x\text{O}_y$).

Sample	Surface Loading [Molecules/nm ²]			
	ICP-MS	CHN (C)	CHN (H)	TGA
$^{0.003}\text{AIP@Fe}_x\text{O}_y$	<LOQ	2.55	2.91	3.17
$^{0.052}\text{AIP@Fe}_x\text{O}_y$	0.79	3.23	3.58	3.56
$^{0.105}\text{AIP@Fe}_x\text{O}_y$	1.97	3.80	4.19	4.70
$^{0.210}\text{AIP@Fe}_x\text{O}_y$	2.49	4.09	4.54	5.60

Analogous to the polar initiator, the calculated surface loading based on the CHN and TGA measurements is significantly higher than that determined by ICP-MS. Again, it appears that other organic is present on the surface in addition to the initiator. The comparison between the polar and non-polar initiator systems shows that the surface loading calculated from the thermal analysis is significantly higher in the non-polar system despite a comparable amount of initiator. This indicates that there is more additional organic matter on the particle surface here. Since this is presumably oleic acid, it is reasonable to assume that it comes from the interaction of the non-polar spacer of the initiator with the hydrophobic end of the oleic acid, promoting its additional attachment. The increased polarity of the first initiator system leads to stronger repulsions, leaving less oleic acid attached. The suitability of the functionalized particle systems for initiating SI-ATRP was then tested.

3.6.4. SI ATRP of Model Monomers

Since the ATRP polymerization of ionic monomers often presents its own set of challenges, the basic suitability of the prepared initiator particles was first tested by polymerizing nonionic model monomers. Butyl methacrylate and acrylamide were used for this purpose. Initiator functionalized particles were freshly prepared prior to use. Using ICP-MS, 0.38 mmol of initiator per 150 mg particles was determined for the polar system and 0.39 mmol initiator per 150 mg particles for the non-polar system. For ease of handling, an 8.25 mmol/L concentrated aqueous dispersion of particles was prepared for the polar system and a toluene dispersion of the same concentration was prepared for the non-polar system. In both cases, the solvent used was degassed prior to preparation to prevent unwanted oxidation of the copper complex and radical deactivation during polymerization.

The SI polymerizations were carried out analogously to the solution polymerizations described earlier. The polymerization was carried out at 70 °C for 24 hours. Unreacted monomer and other low molecular weight components were separated by dialysis. Subsequently, the samples were dried. Separation of the particles by magnetic decantation or centrifugation was unsuccessful. Since the initiator functionalized particles were readily separated in the

respective solvents, this suggests that the particles are stabilized in solution by the polymer shell. The crude product obtained could not be analyzed by NMR spectroscopy because of the superparamagnetic particles contained. The samples were compression molded at heating 60 °C to specimens measuring 1 cm x 1 cm x 0.2 cm using a vice (see Figure 99). The composites show a uniform black coloration, indicating that no larger agglomerates are formed. This is confirmed by the TEM images, which despite a few smaller agglomerates (< 15 particles per agglomerate) visible in the BMA-based composites, showed largely well-distributed particles. Since no larger agglomerates of the particles were formed during drying, this at least indicates that the particles are less mobile, further suggesting that they are fixed in the polymer. In addition to the homogeneous polymer layer covering the entire TEM grid, core shell structures were also observed in some cases. Since it has not yet been possible to separate polymer and particles from each other it seems likely that surface-initiated polymerization has been successful and that covalent bonding of the polymer to the particle surface is present. However, since the TEM grids mostly show a continuous polymer film rather than a core-shell systems, thermal polymerization or cleavage of the initiator groups and subsequent polymerization in solution cannot be completely ruled out.

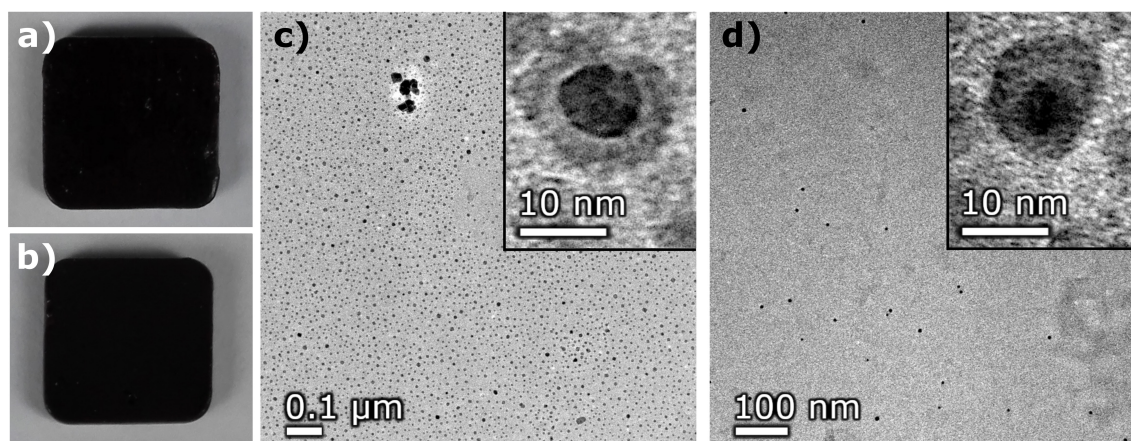


Figure 99: Pictures of the a) BMA- and b) acrylamide-based nanocomposites obtained by SI ATRP, as well as c/d) the respective TEM images of the samples.

In summary, polymerization was successfully carried out and highly magnetic composites were obtained, although it could not be conclusively determined at this time whether the polymerization proceeds from the surface or in solution. Therefore, polymerizations have to be performed with shorter reaction times or larger initiator/monomer ratios to definitively confirm that polymerization originates from the particle surface. In this case, distinct core-shell structures should be observed. Furthermore, the study provides the basis for a subsequent transfer to ionic monomers, which can be applied for self-healing, and for comparison with self-healing systems in which the healing mechanism is localized at the phase interface. So far, the well-dispersed particles in the polymer matrix obtained by the SI ATRP approach are a

promising result, as stress concentration points due to agglomerates are minimized, which might lead to better results in tensile tests compared to the previously described composites.

3.7. Self-Healing Nanocomposites Based on Two Healing Mechanisms

So far, two strategies for the synthesis of self-healing nanocomposites have been considered, both utilizing ionic interactions as the healing mechanism. First, the healing mechanism has been moved to the phase boundary between the polymer and the particles, and second, preliminary studies have been carried out to produce systems in which a covalent bond is used between the particles and the polymer, and healing takes place purely in the polymer. Another promising strategy is the use of multiple healing mechanisms, allowing healing both at the phase interface, as well as in the polymer matrix. These systems are often referred to as fourth-generation self-healing materials and have been increasingly studied since their first description by Burattini *et al.* in 2010.[475] In this approach, dynamic covalent bonds are usually combined with supramolecular interactions, due to the orthogonality of the healing mechanisms. In this way a material can autonomously and instantaneously respond to damage via the supramolecular interactions, while the mechanical properties are improved via the reversible covalent crosslink, further allowing a trigger based second healing. In a recent study, Schäfer and KICKELBICK showed that high healing efficiencies for a double self-healing network could be achieved by combining hydrogen bonding and DA chemistry. This was achieved by combining urea group-containing spherosilicates with butyl methacrylate-based polymers, which carry both DA moieties and self-assembling hydrogen bonds.[73] Due to the improvement in healing efficiency observed in the ionic systems by applying induction heating as a trigger, the spherosilicate based composites from Schäfer and KICKELBICK were transferred to iron oxide particles-based ones in this work. This allows for not only homogeneous inherent temperature generation resulting in milder healing conditions, but also spatially resolved healing. Furthermore, based on the previously demonstrated suitability of the ionic interaction for self-healing in nanocomposites, an analogous composite system should be prepared in which the hydrogen bonding is replaced by the ionic interactions.

3.7.1. Synthesis and Characterization of Double Self-Healing Polymers Based on DA and Hydrogen Bond Chemistry

The polymer systems were adopted from Schäfer and KICKELBICK.[73] They are composed of four methacrylate-based components. BMA was used as the backbone polymer, providing an overall low T_g . The remaining monomers are responsible for the healing mechanisms. A protected maleimide derivative (MIMA), a furan derivative (FMA) and hydrogen bond donor acceptor functionalities bearing monomers were used. Two hydrogen bonding monomers were investigated, a urea and an amide group bearing methacrylate. The two components are hereafter referred to as H1 and H2. The iron oxide nanoparticles were functionalized with (10-

Results and Discussion

(3-propylureido)decyl)phosphonic acid allowing for hydrogen bonding between the organic and inorganic components. The structure of the composite systems is shown in Figure 100.

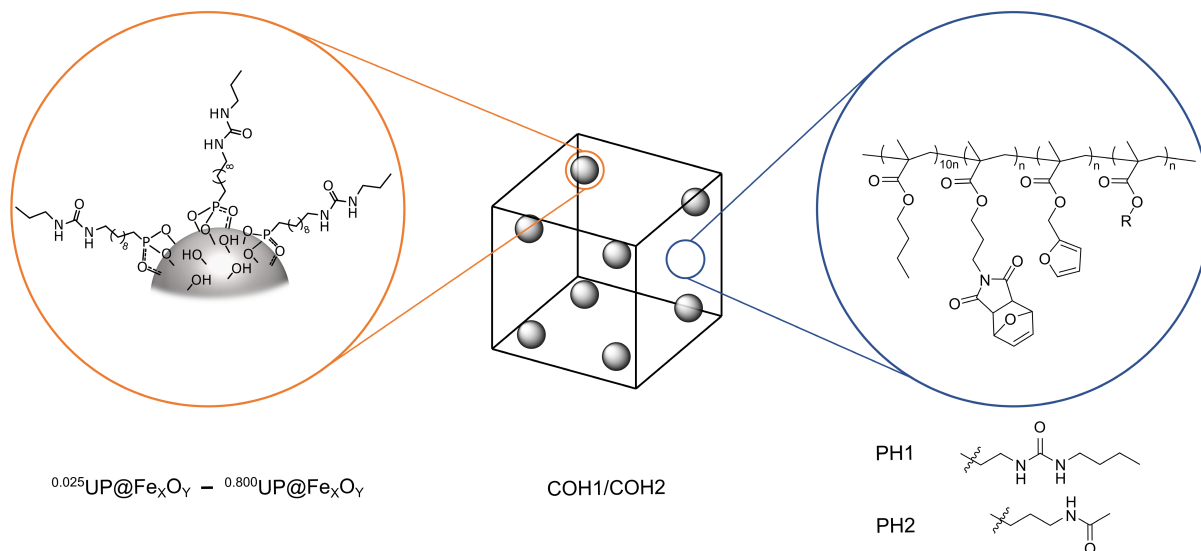
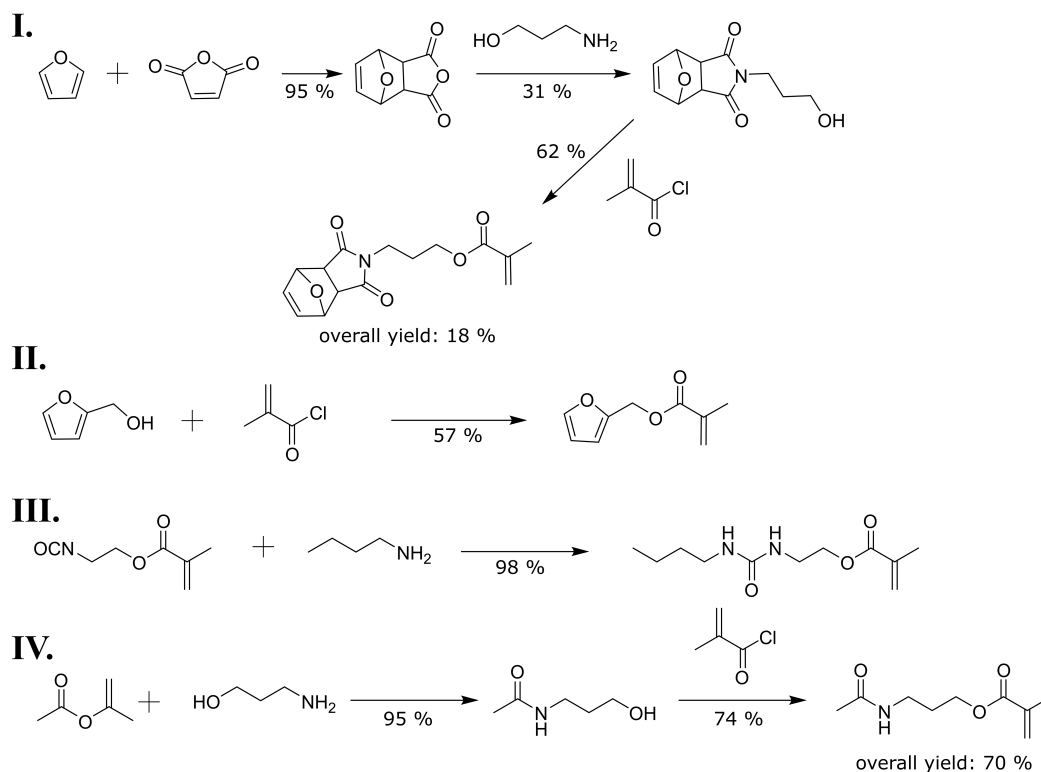


Figure 100: Composition of the double self-healing nanocomposites based on DA chemistry and hydrogen bonding.

The synthesis of the functional monomers used was carried out according to literature procedure.[73] The routes of the individual components are outlined in Scheme 27. The products were characterized by ¹H, ¹³C and FTIR spectroscopy, as well as CHN analysis.

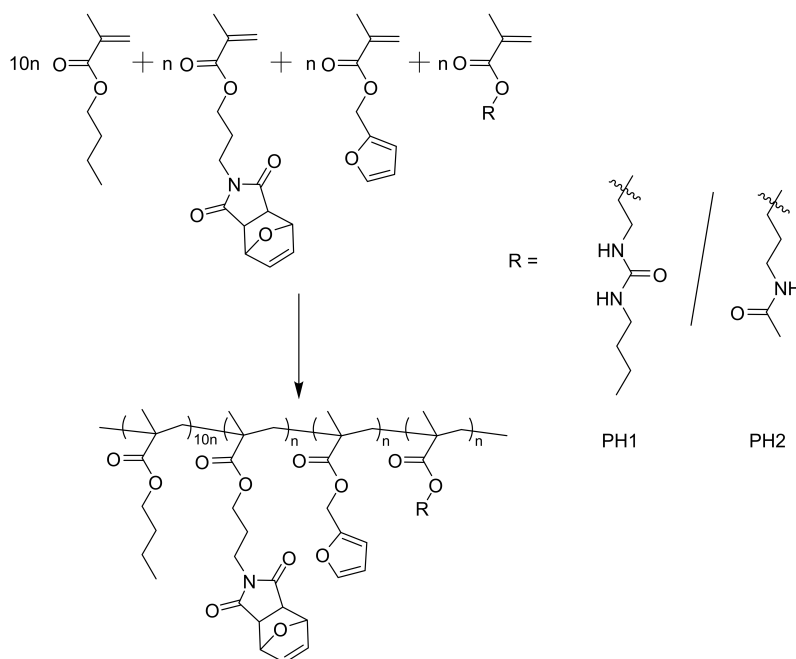


Scheme 27: Synthesis routes for the monomers for the double self-healing system.[73]

Results and Discussion

The synthesis of the protected maleimide derivative was carried out in three steps. The starting point is maleic anhydride, which is protected by reaction with furan. This step is necessary to prevent a reaction of the double bond of the maleimide in the subsequent polymerization. The reaction is carried out in 95 % yield. The maleimide is then obtained by reaction with 3-aminopropanol. The intermediate product was obtained in 31 % yield. Finally, the methacrylate group is introduced via reaction with freshly prepared methacryloyl chloride. With a yield of 62 % for the last step, an overall yield of 18 % is obtained. The furan component is prepared from commercially available furfuryl alcohol, which is also converted into the methacrylate derivative by reaction with methacryloyl chloride. The step is performed out in 57 % yield. The monomer H1 was prepared in two steps. The first step is the ammonolysis of isopropenyl acetate with 3-aminopropanol. The reaction step occurs almost quantitative (95 %). Again, the methacrylate group is introduced by reacting the alcohol group of *N*-(3-hydroxypropyl)acetamide with methacryloyl chloride. A yield of 74 % was determined for this reaction step, resulting in an overall yield of 70 %. The monomer H2 is synthesized by reacting the acetoisocyanate methacrylate with butylamine. The urea derivative is obtained in 98 % yield.

The preparation and characterization of DA/rDA and hydrogen bond based self-healing polymer systems are described below. Scheme 28 shows the target polymer compounds.



Scheme 28: Composition of the double self-healing polymers based on hydrogen bonds and DA chemistry.

The synthesis was carried out in the form of an ARGET ATRP, based on the synthesis described by Schäfer and Kickelbick.[73] A monomer ratio of 1:1:1:10 (FMA:H1:MIMA:BMA) was used. The urea-based polymer will be referred to as PH1 and the amide-based polymer as PH2. Figure 101 shows the ^1H NMR spectrum of PH1.

Results and Discussion

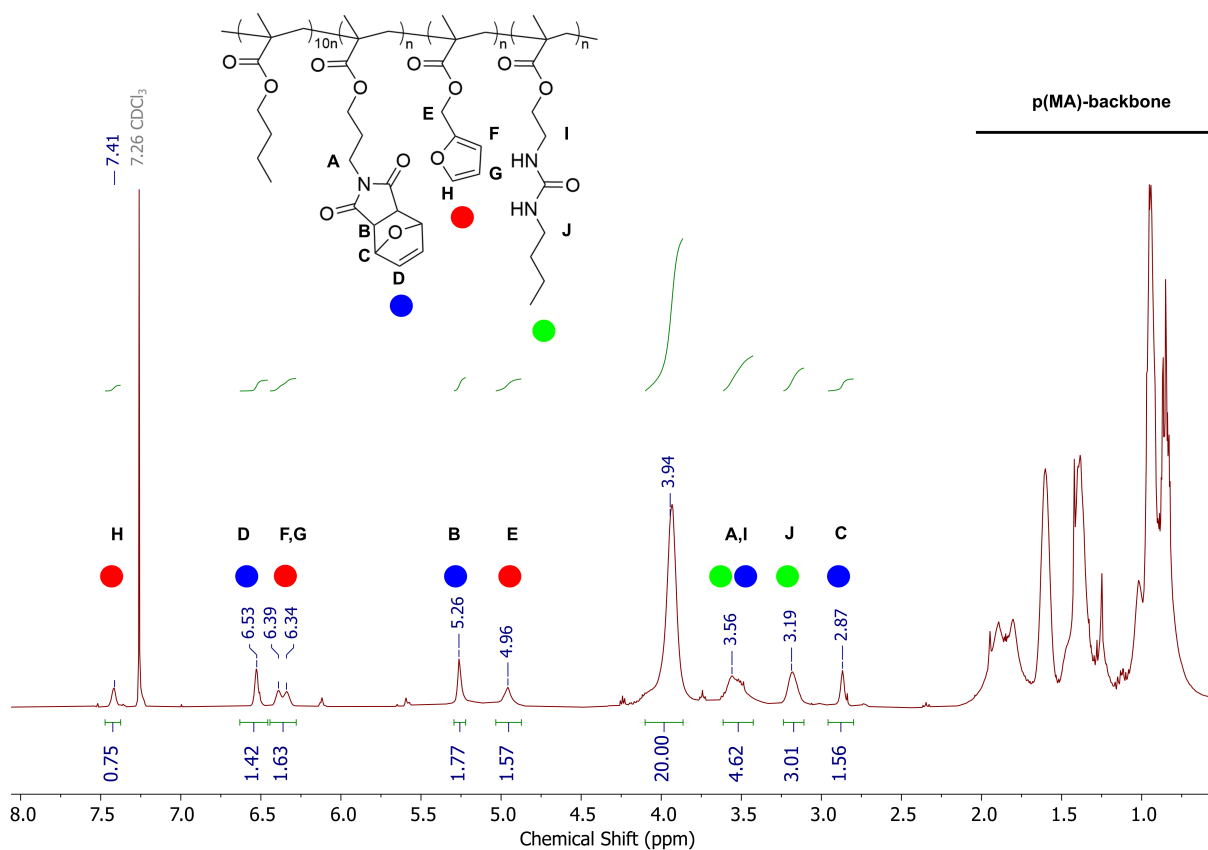


Figure 101: ^1H NMR spectrum of PH1.

The NMR spectrum shows the expected signals with minor impurities. The spectrum was normalized to the signal of CH_2 next to the ester group of the BMA at 3.94 ppm. The comparison of the integrals of the signals of the DA components, as well as the H1 group, shows that the original monomer ratio of 1:10 (functional monomers:BMA) is not exactly reflected in the polymer. While slightly more H1 is incorporated into the polymer (H1:BMA= 1.5:10), slightly less is found in the polymer for the DA components (FMA:MIMA:BMA = 0.8:0.9:10). The FTIR spectrum shows the expected signals. In particular, the signals of the N-H and amide vibrations reconfirm the incorporation of the H1 component. DSC measurements were performed to determine the T_g , as well as to verify the DA activity of the polymer. The results are shown in Figure 102.

Results and Discussion

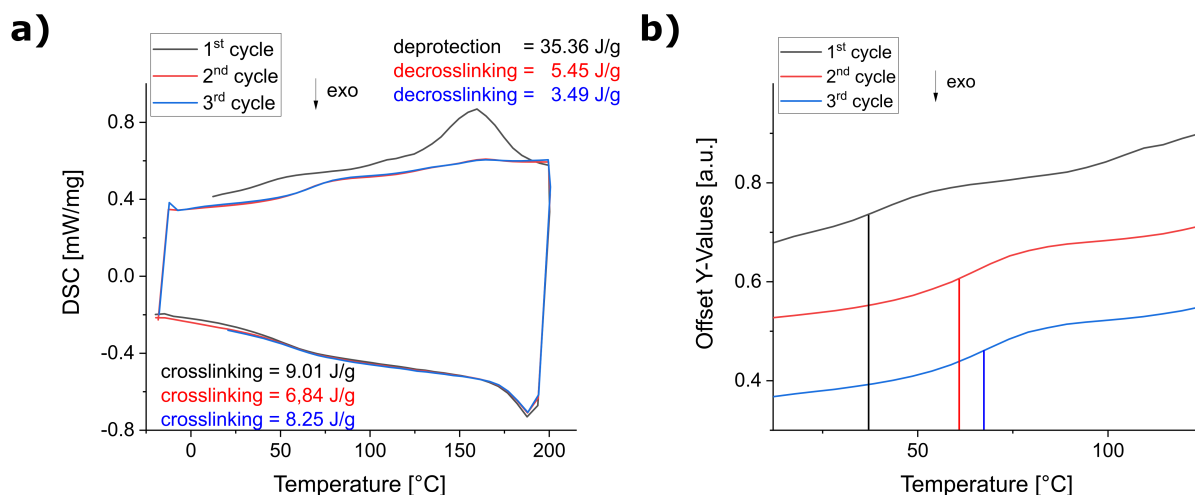


Figure 102: a) DSC curves of PH1 and b) T_g values determined in the three heating cycles.

A temperature range of -20 °C to 200 °C was investigated. A total of three heating cycles were performed. In the first cycle, DSC shows the deprotection of the maleimide component and the subsequent evaporation of the furan formed as a peak in the range of 120 °C – 200 °C. The latter is in particularly strong endothermic, yielding a heat flow of 35 J/g. In the subsequent cooling segment, crosslinking of the maleimide and furan components occurs due to the DA reaction at about 75 °C. The maleimide and furan components undergo a rDA reaction in the second and third heating segments. The endothermic signal is much smaller than in the run-in cycle, as no further furan is released. The heat flux further decreases from 5.45 J/g to 3.49 J/g from the second to the third cycle, indicating a decrease in crosslinking with increasing cycle number. In the second and third heating segments, a slightly increased T_g of 66 °C is observed. This confirms the crosslinking by the DA reaction.

Subsequently the PH2 system was investigated. In contrast to PH1, PH2 has a much lower solubility and can no longer be completely dissolved after drying. Nevertheless, a ¹H NMR could be recorded, but since the sample was not completely dissolved, it is not guaranteed that the NMR is representative of the complete sample. The NMR spectrum obtained is shown in Figure 103.

Results and Discussion

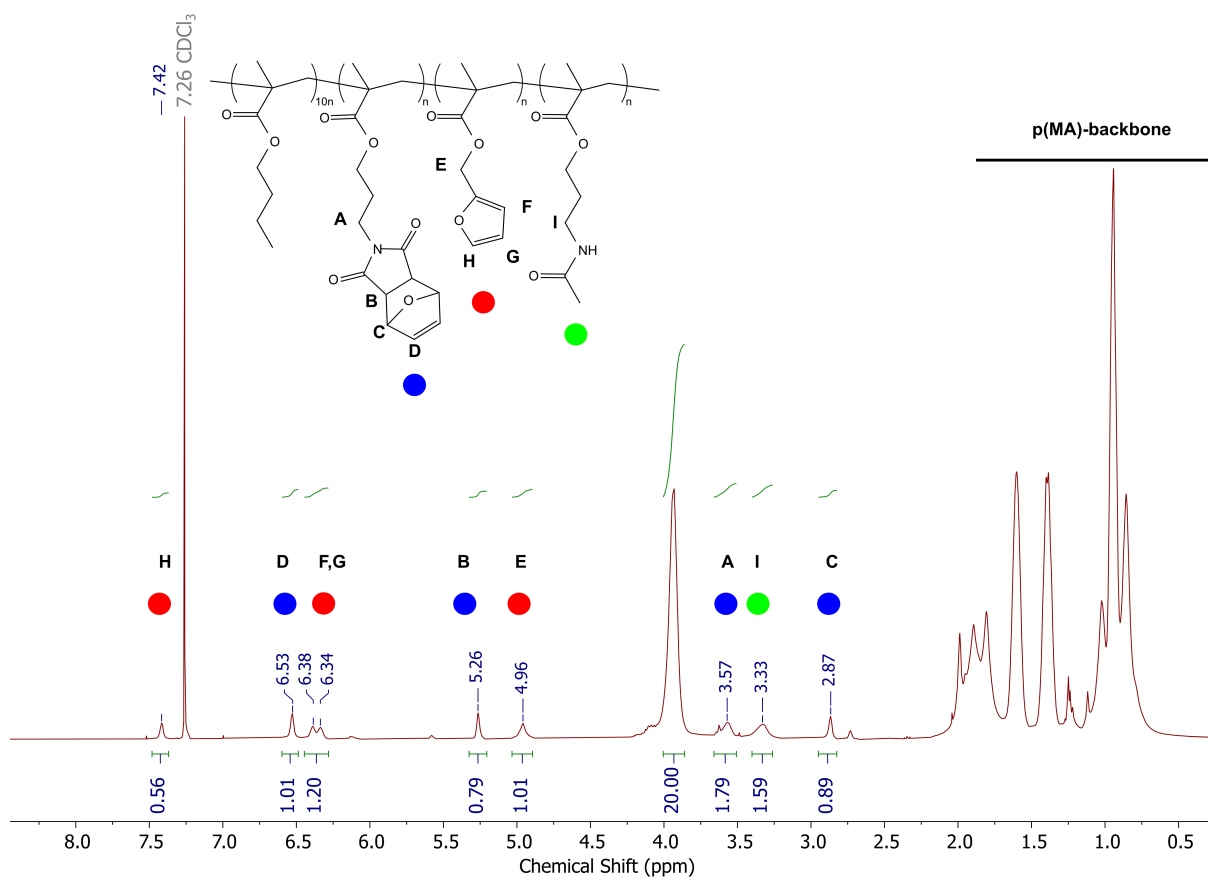


Figure 103: ¹H NMR spectrum of PH2.

The spectrum of PH2 shows the expected signals and confirms the successful synthesis of the copolymer. The polymer composition was again examined using the integrals of the signals of the respective components. All functional monomers, but in particular the DA components, are found in significantly lower concentrations in the polymer than expected based on the initial monomer ratios used (FMA:H2:MIMA:BMA = 0.6 : 0.8 : 0.5 : 10). Whether this is the case for the whole system or whether these polymer strands are overrepresented due to better solubility could not be clarified so far. Subsequently the polymer was investigated by DSC. The results are shown in Figure 104.

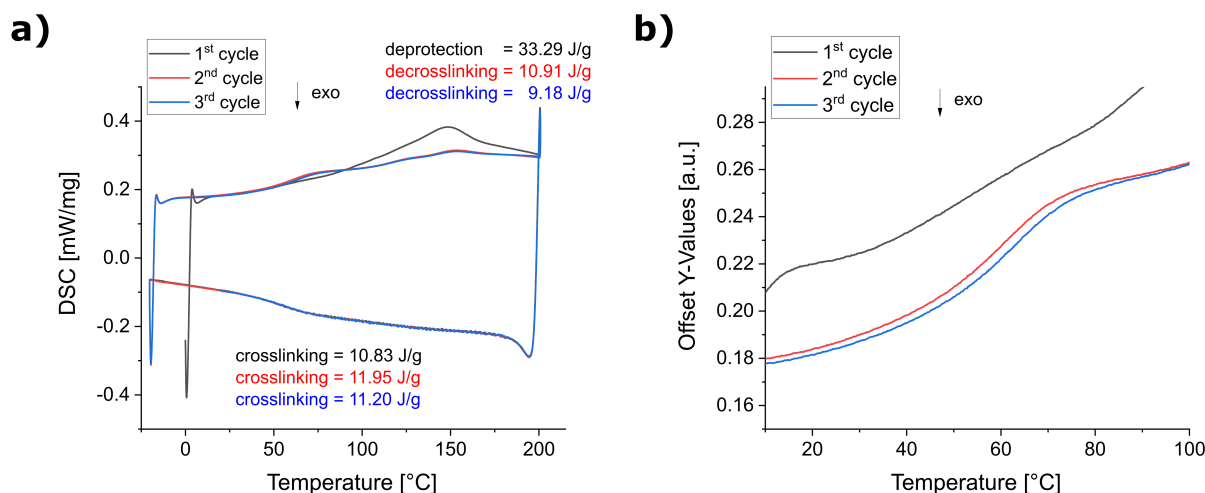


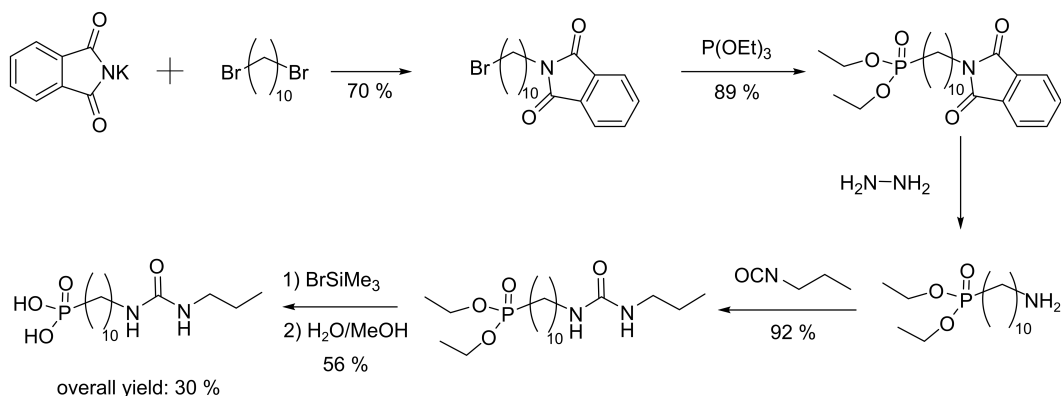
Figure 104 a) DSC curves of PH2 and b) T_g values determined in the three heating cycles.

For polymer PH2, the expected signals were observed. In the first cycle, the maleimide group is deprotected and the released furan is evaporated. On subsequent cooling, crosslinking occurs via the DA reaction, and on reheating, decrosslinking takes place via the rDA reaction. Compared to the polymer PH1, the determined heat flows are slightly higher. This is surprising, since according to NMR there should be fewer DA groups. The reason for this could be the slightly lower T_g of 56 °C. This leads to a higher chain mobility allowing more DA groups to come together and react.

3.7.2. Synthesis and Characterization of the Ureylene Functionalized Iron Oxide Nanoparticles

Subsequently, the synthesis of a suitable phosphonic acid was performed, which can bind to the iron oxide particles and exhibits hydrogen bonding donor-acceptor functionalities. A phosphonic acid containing a urea group was prepared, as this group has already been proven suitable as a good hydrogen bond donor-acceptor in previous studies. A C_{10} carbon chain was chosen as the spacer. Initially, a synthesis route was followed in which the ω -bromophosphonic ester was prepared from a dibromo alkane. This was converted to the corresponding diethyl azidoalkyl phosphonate by reaction with sodium azide. The azide was then reduced to the amine using palladium on activated carbon and hydrogen gas. While the first reaction steps were carried out in higher yields than the reaction route used later, the experiments showed that the hydrogenation step led to by-products that could not be separated in the subsequent synthesis steps, which is why the reaction route was changed later on. The revised synthesis route of the phosphonic acid is shown in Scheme 29. For the synthesis, known literature procedures were applied.[271,370]

Results and Discussion



Scheme 29: Synthesis route for (10-(3-propylureido)decyl)phosphonic acid.

The synthesis consists of five steps. The starting point was 1,10-dibromodecane, which is brought to reaction with potassium phthalimide. The aim was to introduce an amine group in the form of a Gabriel synthesis. The first step was carried out in 70 % yield. Before the phthalimide was cleaved off, the phosphonic acid group was introduced by a Michaelis-Arbusow reaction. The product was obtained in 89 % yield. Subsequently, hydrazinolysis was carried out to give the amine-terminated phosphonic acid esters. Even after long reaction times and excess of hydrazine, no complete conversion to the amine was achieved. The educt could not be completely removed. Therefore, the impure product was used without further processing. Separation of the impurity was possible in the final reaction step. First, however, the urea group was introduced by nucleophilic addition of the amine to 1-propyl isocyanate. The reaction was carried out with a yield of 92 %. Finally, the phosphonic acid ester was hydrolyzed. In this step, a yield of 56 % was obtained. This is rather low for the hydrolysis and is mainly due to impurities carried over from the educt. Overall, a yield of 30 % was obtained.

The phosphonic acid was then used to functionalize iron oxide nanoparticles. A systematic study was conducted to determine an optimal phosphonic acid to particle ratio. A concentration range from 0.025 mmol phosphonic acid per 150 mg particles to 0.8 mmol per 150 mg particles was investigated. Functionalization was carried out in ethanol within 24 hours at room temperature. Since magnetic separation of the particles was not possible, they were separated by centrifugation. Subsequently, the particles were washed several times with ethanol to remove excess phosphonic acid. The particle samples are referred to below as $^{0.025}\text{UP@Fe}_x\text{O}_y$ - $^{0.800}\text{UP@Fe}_x\text{O}_y$. Figure 105 shows the FTIR spectra obtained for the dried particle samples. The spectra were normalized to the Fe-O-Fe particle vibration at 573 cm^{-1} . All samples show the C-H stretching vibrations at 2922 and 2852 cm^{-1} , which increase with the amount of phosphonic acid used. Similarly, the N-H stretching vibration at 3325 cm^{-1} also increase, indicating the successful functionalization. The binding of the phosphonic acid is further confirmed by the appearance of the phosphonate vibration at 1041 cm^{-1} . At 1626 and 1576 cm^{-1} , the amide I and II vibrations of the urea component are visible. Furthermore, a

Results and Discussion

decrease of the carbonyl vibration at 1406 cm^{-1} can be seen, which results from the successive exchange of the oleic acid. However, the vibration remains visible in all systems with low intensity, indicating an incomplete exchange.

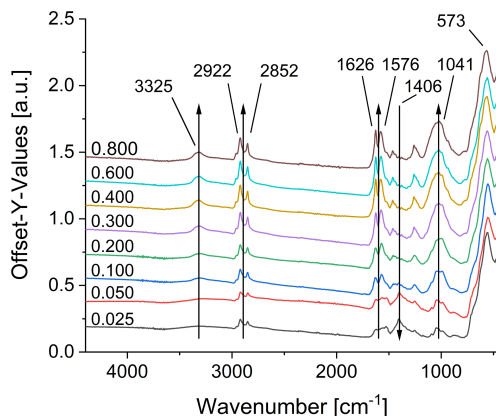


Figure 105: FTIR spectra of the urea functionalized particles ($^{0.025}\text{UP@Fe}_x\text{O}_y$ - $^{0.800}\text{UP@Fe}_x\text{O}_y$).

The particle size was determined by DLS. The results are shown in Figure 106. The measurements were performed in methanol.

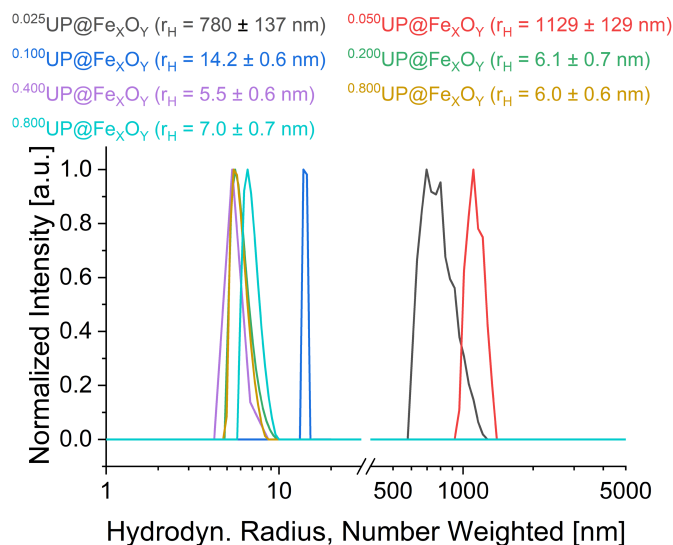


Figure 106: DLS measurements of $^{0.025}\text{UP@Fe}_x\text{O}_y$ (black), $^{0.050}\text{UP@Fe}_x\text{O}_y$ (red), $^{0.100}\text{UP@Fe}_x\text{O}_y$ (blue), $^{0.200}\text{UP@Fe}_x\text{O}_y$ (green), $^{0.400}\text{UP@Fe}_x\text{O}_y$ (purple), $^{0.600}\text{UP@Fe}_x\text{O}_y$ (yellow) and $^{0.800}\text{UP@Fe}_x\text{O}_y$ (teal) in methanol.

The DLS measurements show large agglomerates for particles with low phosphorus content. For instance, a hydrodynamic radius of 780 nm and 1129 nm is obtained for samples $^{0.025}\text{UP@Fe}_x\text{O}_y$ and $^{0.050}\text{UP@Fe}_x\text{O}_y$, respectively. Subsequently, the observed hydrodynamic radius decreases until well-dispersed particles are obtained starting from sample $^{0.200}\text{UP@Fe}_x\text{O}_y$. This is most likely due to larger amounts of the oleic acid still present at the particle surface at the lower phosphonic acid concentrations. This leads to a lower polarity of the particles, which are therefore poorly dispersed in methanol.

Results and Discussion

To quantify the phosphonic acid, present on the surface, TGA and CHN measurements were first performed. The TGA data obtained, as well as the mass losses obtained after the N₂ segment as a function of the amount of phosphonic acid used, are shown in Figure 107.

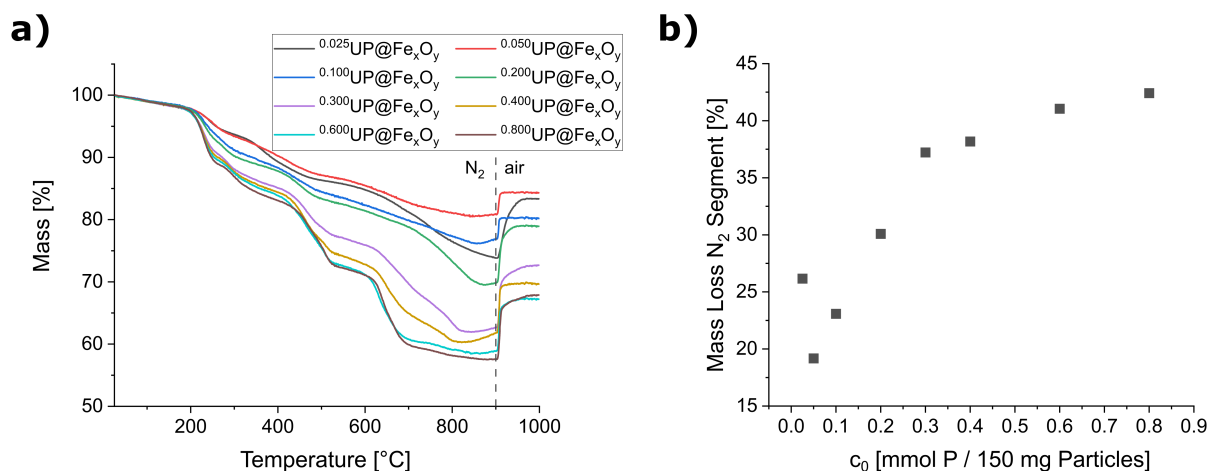


Figure 107: a) TGA curves of the urea functionalized particles, and b) the mass losses obtained after the N₂ segment as a function of the amount of phosphonic acid used.

The mass loss in the N₂ segment increases with increasing amounts of phosphonic acid. While initially the increase in mass increases sharply with the amount of phosphonic acid added, a saturation of the surface appears to take place at higher concentrations. The CHN data also shows an increase in the organic content with increasing amounts of phosphonic acid. The TGA and CHN results were used to quantify surface occupancy applying Equation (10). The results are shown in Table 15.

Table 15: TGA and CHN results of the urea functionalized nanoparticles (^{0.025}UP@Fe_xO_y - ^{0.800}UP@Fe_xO_y).

Sample	TGA Residual Mass [%] 25-900°C N ₂	CHN [%]			Surface Coverage [mmol/g]		
		C	H	N	C	H	N
^{0.025} PA@Fe _x O _y	73.83	11.15	1.88	0.27	0.90	0.87	0.13
^{0.050} PA@Fe _x O _y	80.82	10.61	1.82	0.46	0.78	0.77	0.20
^{0.100} PA@Fe _x O _y	76.92	13.14	2.33	1.13	1.02	1.04	0.52
^{0.200} PA@Fe _x O _y	69.91	14.51	2.62	1.68	1.23	1.28	0.86
^{0.300} PA@Fe _x O _y	62.78	18.49	3.39	2.35	1.75	1.85	1.34
^{0.400} PA@Fe _x O _y	61.82	23.25	4.08	2.56	2.24	2.26	1.48
^{0.600} PA@Fe _x O _y	58.95	21.10	3.89	2.89	2.13	2.26	1.75
^{0.800} PA@Fe _x O _y	57.58	22.36	4.14	3.14	2.31	2.46	1.95

The surface coverage calculated based on the carbon and hydrogen content are in good agreement, whereas the surface coverage calculated based on the nitrogen content is always

Results and Discussion

significantly lower. This confirms the assumption that other organic substances besides phosphonic acid remain on the surface. As the amount of phosphonic acid added increases, the loading calculated from the nitrogen content approaches the values calculated from the carbon and hydrogen contents, indicating a successive replacement of the organic matter bound to the surface by the phosphonic acid. ICP-MS measurements were also performed. The phosphorus content was determined. Due to the high LOQ of phosphorus, most determined concentrations are below the LOQ and should therefore be viewed with caution. These points are highlighted in red. In addition, surface occupancies in molecules per nm² were calculated based on the assumption, that the particles are present entirely as Fe₃O₄. The surface area of the particles was calculated from TEM assuming a perfect spherical shape. The results are listed in Table 16.

Table 16: Surface coverage of the urea functionalized nanoparticles (^{0.025}UP@Fe_xO_y - ^{0.800}UP@Fe_xO_y).

Sample	Surface Coverage [mmol/g]		Surface Coverage [Molecules/nm ²]	
	CHN/TGA	ICP-MS	CHN/TGA	ICP-MS
^{0.025} UP@Fe _x O _y	0.13	0.05	0.62	0.25
^{0.050} UP@Fe _x O _y	0.20	0.06	0.97	0.28
^{0.100} UP@Fe _x O _y	0.52	0.28	2.49	1.33
^{0.200} UP@Fe _x O _y	0.86	0.32	4.07	1.52
^{0.300} UP@Fe _x O _y	1.34	0.41	6.35	1.93
^{0.400} UP@Fe _x O _y	1.48	0.44	7.02	2.09
^{0.600} UP@Fe _x O _y	1.75	0.54	8.31	2.56
^{0.800} UP@Fe _x O _y	1.95	0.54	9.25	2.56

As before for the initiator functionalized particles, the surface loadings calculated from the MS data are also significantly lower for the urea functionalized particles than those determined from CHN and TGA. Consideration of the CHN/TGA data suggests the formation of multi layers, as the calculated loading from ^{0.300}PA@Fe_xO_y exceeds the space requirement of the phosphonic acid group to form a densely packed monolayer. The MS based surface loadings, with a maximum occupancy of about 2.6 molecules per nm² were still well below the theoretically determined maximum occupancy density of 4.2 molecules per nm². This result is in good agreement with the previously determined maximum loading densities of the polar and non-polar initiator systems, which were at 2.8 and 2.5 molecules per nm² respectively. The ^{0.400}PA@Fe_xO_y particle system was used for the further experiments because it showed the best dispersibility in most solvents.

3.7.3. Synthesis and Characterization of the Double Self-Healing Composites Based on DA and Hydrogen Bond Chemistry

For the preparation of the composite samples, a particle content of 20 wt% was used to achieve maximum high temperatures in the AFM, without the composites becoming too brittle. The goal was to reach the required temperatures for the rDA reaction ($\approx 150\text{ }^{\circ}\text{C}$). For the synthesis the polymers and the corresponding amount of particles were dissolved/dispersed in a 1:1 mixture of methanol and *n*-hexane. The solvent was removed under stirring at room temperature under reduced pressure. The urea-based composite will be referred to as COH1 and the amide-based system as COH2. Figure 108 shows the FTIR spectra obtained for the two composite samples.

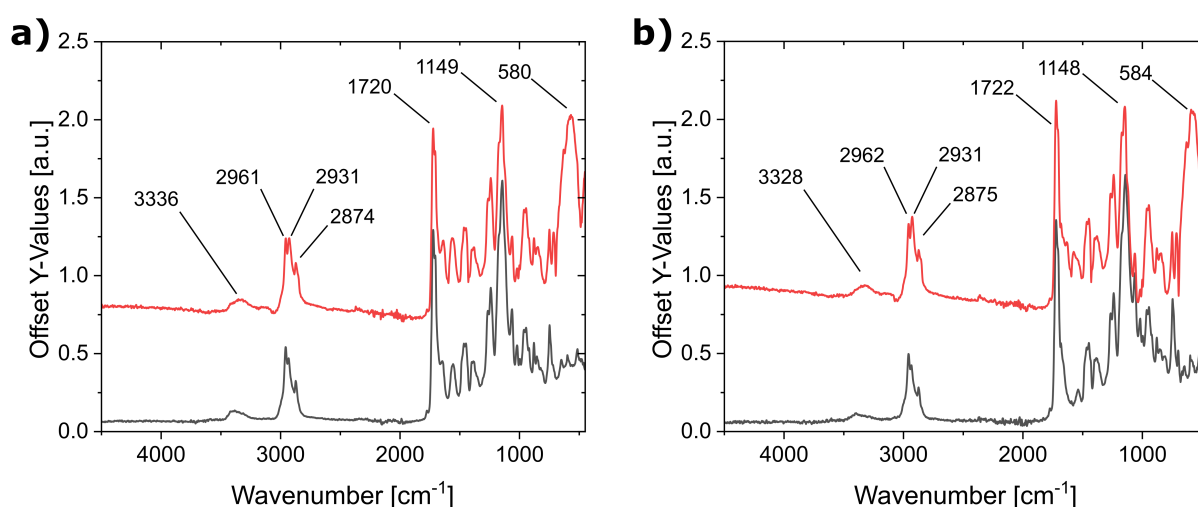


Figure 108: FTIR spectra of a) COH1 (red) and b) COH2 (red) in comparison with the respective polymers (black).

The obtained FTIR spectra of the composites generally exhibit the signals of the respective polymers. In particular, the signals of the N-H stretching vibration at 3336 cm^{-1} , the C-H vibrations at 2900 cm^{-1} , the C=O stretching vibration at 1720 cm^{-1} and the C-O-C stretching vibration at 1149 cm^{-1} are prominent. The location of the N-H stretching vibration at 3300 cm^{-1} rather than 3400 cm^{-1} , which is usually observed in solution, indicates hydrogen bonding.[695–697] In addition, the signals of the Fe-O-Fe particle vibration at 580 cm^{-1} and a shoulder of the N-H stretching vibration at 3100 cm^{-1} also appear. The phosphonate vibration is not detectable due to the superposition of the intense signals of the polymer. Furthermore, TGA and DSC measurements were performed on the composites, though no change in thermal stability or in T_g was observed compared to the polymers within the measurement accuracy.

Subsequently, self-healing experiments were carried out. For this purpose, specimens with a geometry of $5\text{ mm} \times 0.5\text{ mm} \times 2\text{ mm}$ were prepared in a hot press at $70\text{ }^{\circ}\text{C}$. The specimens were then cut to half thickness and the ends were gently pressed together at approx. $40\text{ }^{\circ}\text{C}$. The specimen was then heated by induction in the TruHeat HF 5010 system. The power was

Results and Discussion

increased to 5400 W in four steps. The alternating field was turned on for five minutes at a time. The study was conducted in an open system to allow any furan that may have been formed in the deprotection step to escape. The macroscopic temperature of the sample was recorded. After each heating step, the sample was cooled to room temperature as quickly as possible to prevent crosslinking via DA reaction. The samples were characterized by FTIR spectroscopy. Crack healing was also evaluated by microscopy. The results for COH1 in Figure 109.

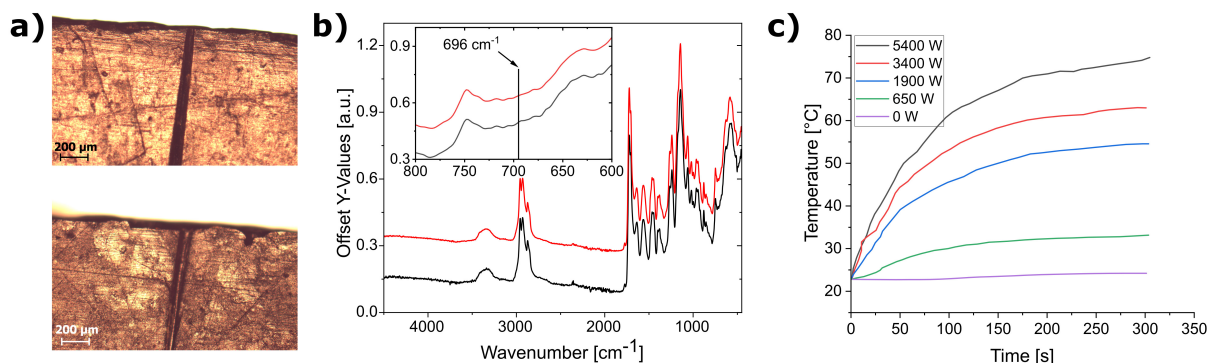


Figure 109: a) Microscope images and b) FTIR spectra of COH1 before (black) and after (red) treatment in the alternating magnetic field (5400 W). c) Macroscopic sample temperature at different field strengths.

Only slight healing is visible in the microscope images after treatment in the high-frequency furnace. The cut edges are slightly rounded, as a consequence of exceeding the T_g during heating (Figure 109 a). The measured macroscopic temperature shows that the temperature of 150 °C required for rDA was not met even with 20 wt% particle content. At maximum power, a temperature of 75 °C was achieved. Since no temperature plateau was reached after five minutes, this does not represent the maximum achievable temperature, but the required 150 °C are not attainable. However, since induction heating results in significantly higher local temperatures than those determined macroscopically, the samples were still characterized by FTIR spectroscopy to determine if rDA can be observed. However, the spectra did not show the ring deformation vibration of the free maleimide ring at 696 cm⁻¹ (Figure 109 b). Furthermore, DSC measurements on the sample heated in the magnetic field clearly show the strong endothermic signal due to the evaporation of the released furan in the first heating cycle at 150 °C (Figure 110). In addition, an increase in the T_g from 54 °C to 65 °C is observed between the first and subsequent heating cycles, indicating crosslinking exclusively after the run-in cycle via the DA reaction and not during induction heating. This shows that the observed healing is only due to hydrogen bonding effects or interflow due to the elevated temperature, which explains the low healing efficiency.

Results and Discussion

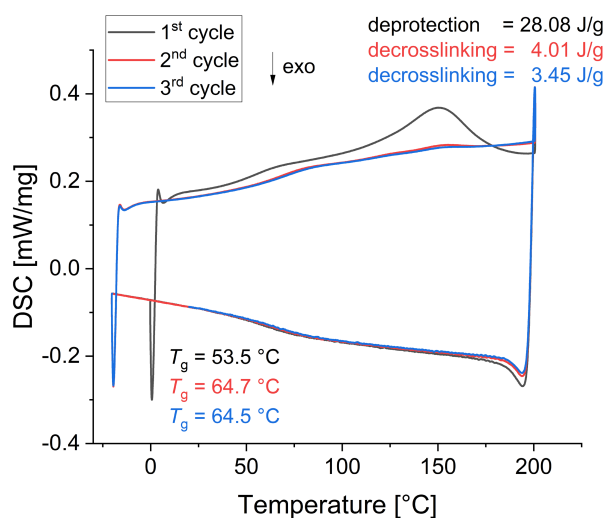


Figure 110: DSC curve of COH1 after heating in the alternating magnetic field for 5 minutes (power =5400 W).

Since both the rDA and the DA reaction were observed in the DSC of the composites, it was subsequently tested whether the DA reaction can be induced by a magnetic field. For this purpose, samples were again prepared, incised and the ends gently pressed together at 40 °C. The samples were then heated in an oven at 150 °C for 20 minutes. The samples were cooled to room temperature as quickly as possible. The specimens were then heated in a magnetic field for 24 hours. A power of 5400 W was used, resulting in a macroscopic temperature of 75 °C. After each step FTIR spectra were recorded. These are shown for both the COH1, as well as the COH2 system in Figure 111.

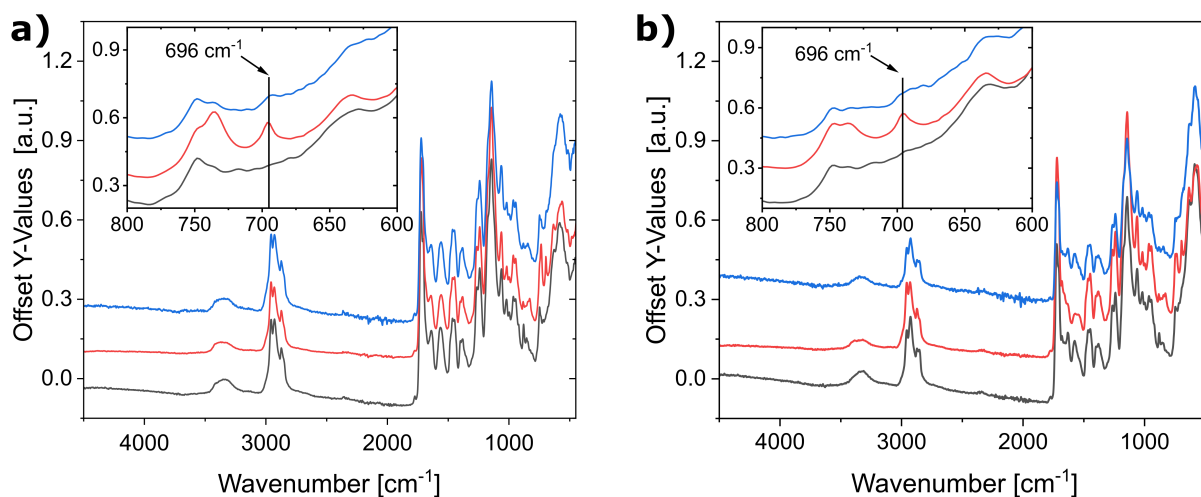


Figure 111: FTIR spectra of a) COH1 and b) COH2 before (black) and after (red) heating to 150 °C, as well after heating in the AMF (blue).

The rDA/DA reactions can again be traced by the signal of the oscillation of the maleimide ring at 696 cm^{-1} . After oven treatment at 150 °C, the signal of the maleimide is clearly visible in both composites, confirming the successful deprotection. Following the subsequent heating step in the AMF, a significant decrease in the signal can be observed. However, even after the long reaction time of 24 hours, the signal of the maleimide oscillation is still recognizable, indicating

a low reaction rate. Microscope images were also taken after every step to observe macroscopic healing (Figure 112).

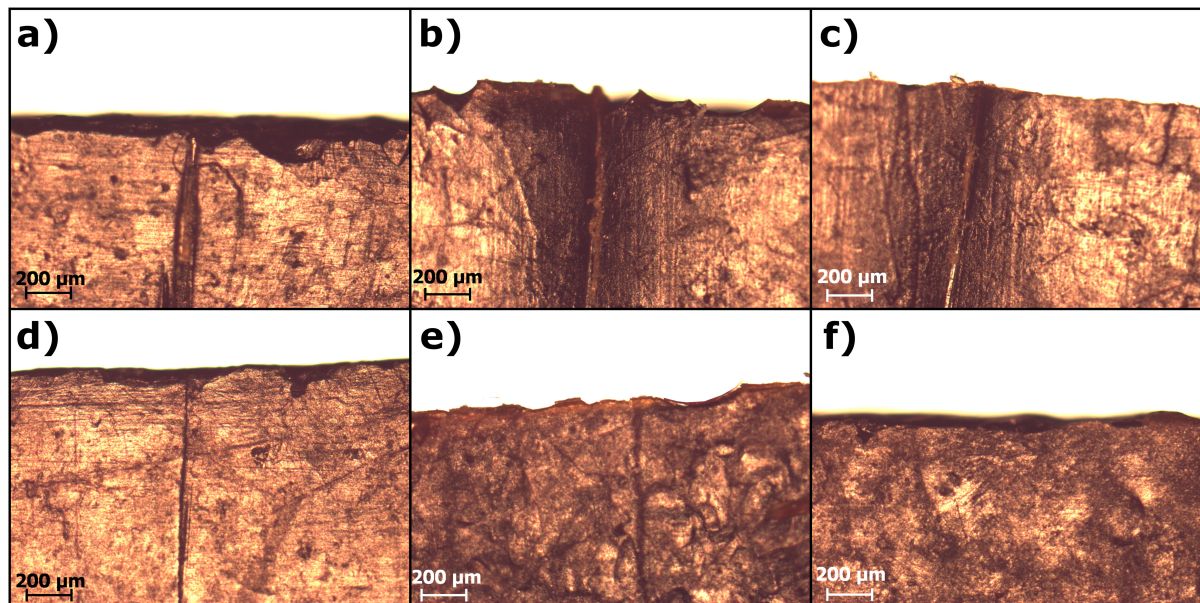


Figure 112: Microscope images of the composites COH1/COH2 after cutting through half thickness and a)/d) heating to 150 °C, followed by treatment in the AFM (5400 W / 75 °C) for b)/e) 12 hours and c)/f) 24 hours.

After heating the samples to 150 °C for 30 minutes, the incisions are still clearly visible. In contrast to the initial experiments where no healing was observed during induction heating, healing was observed in the alternating magnetic field after this deprotection step. After 12 hours, a clear narrowing of the cut occurs. In the case of COH2, the cut disappears completely after 24 hours. The result is consistent with the increased heat transfers observed in the DSC data for the COH2 system due to the DA/rDA reactions, again emphasizing the advantage of the lower T_g of the polymer matrix for self-healing. The series of experiments was then repeated on the same sample. The sample again showed no signs of the rDA reaction or healing in the crosslinked state in the magnetic field but efficient healing after decrosslinking in the conventional oven. This confirms the observations of earlier studies that the mobility of the polymer chains obtained by decrosslinking during the rDA reaction is necessary for subsequent healing.[73] In general, it seems that the interlocking by hydrogen bonds as well as the crosslinking by DA leads to a rigidization of the system, which hampers self-healing. The healing by hydrogen bonds at room temperature, as often described in literature, does not occur here even during induction heating. In view of this, one approach for future work could be to increase the BMA content in the polymer in order to further reduce the T_g . Another interesting point for further investigation would be to study the influence of heat dissipation through the polymer and its effect on the different healing mechanisms. It is plausible that in systems where healing takes place exclusively at the particle surface, poorer heat transfer may be advantageous because more energy is available at the healing site, whereas it might

become a disadvantage when energy has to be transported into the polymer, as in this case for the rDA/DA reactions.

In summary, a phosphonic acid suitable for the functionalization of superparamagnetic iron oxide nanoparticles was successfully prepared. Due to the built-in urea functionality of the phosphonic acid, the particles can be incorporated into the polymer systems that also contain hydrogen bonding donor-acceptor functionalities. After embedding the particles, the composites were successfully heated in an alternating magnetic field. However, the AMF-induced healing could only be applied for self-healing to a limited extent. Initially, no complete healing was observed. Closer examination showed that the alternating magnetic field did not provide sufficient energy for the rDA reaction. After deprotection in a conventional oven, a significant improvement in healing in the AMF was achieved. The DA could be induced by the alternating magnetic field, although low reaction rates were observed. Quantification of the healing efficiency by rheology or tensile tests was not carried out within the scope of this work. The materials are significantly harder than the ionic systems investigated previously. As a result, the systems exhibit lower chain mobility, which limits self-healing. For this reason, composites consisting of the earlier described soft ionic copolymers and DA groups are a particularly promising approach. In the following, the first attempts to synthesize these systems will be presented.

3.7.4. Advances in the Synthesis of Double Self-Healing Polymers Based on DA and Ionic Bond Chemistry

In analogy to the previously discussed double self-healing system, double self-healing nanocomposites based on DA/rDA reactions and ionic interactions should now be prepared. The basic structure of the systems is shown in Figure 113.

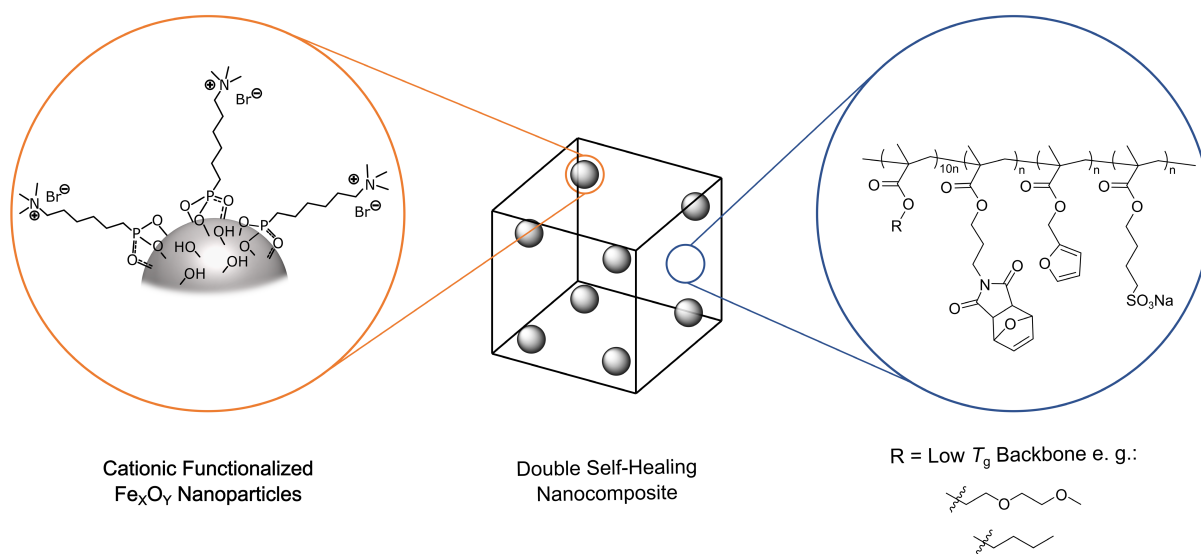


Figure 113: Composition of the double self-healing nanocomposite based on DA chemistry and ionic interactions.

Results and Discussion

The cationic particles from section 3.2.2. can be used as the inorganic component. Therefore, only the polymer synthesis will be described here. Despite great efforts made in the synthesis of the polymers containing both DA and ionic functionalities, the synthesis remains very challenging due to the vastly differing polarity of the functional monomers. Since no reproducible synthesis of the targeted polymer systems has been achieved so far, the considered approaches are briefly described here. A selection of the polymerization experiments and their results are summarized in Table 23 in the experimental. The following parameters have been investigated: The polymerization technique (including ATRP, FRP and RAFT polymerization), the used solvent compositions and in the case of ATRP, the ligand of the copper complex used. Furthermore, the matrix polymer was varied and post functionalization strategies for the introduction of the ionic component were tested. The individual steps and the most important findings obtained are described in more detail below.

Initially, BMA-based polymer systems were used. FRP was carried out using AIBN as the initiator. Since the copolymerization of BMA with the DA components is well known in the literature, the focus was laid on the copolymerization with SMBS. The polymerization in toluene resulted only in the BMA homopolymer, while the SMBS remained dispersed in the reaction medium without conversion. Therefore, the solvent composition was subsequently optimized to allow the complete dissolution of both components. First progress was made by using a solvent composition of methanol and water of 2:3. A solid precipitated during the reaction. The solid was insoluble in all common solvents and was therefore characterized only by FTIR spectroscopy and CHN analysis. The product spectrum is shown in Figure 114 in comparison with the FTIR spectra of poly(BMA) and poly(SMBS).

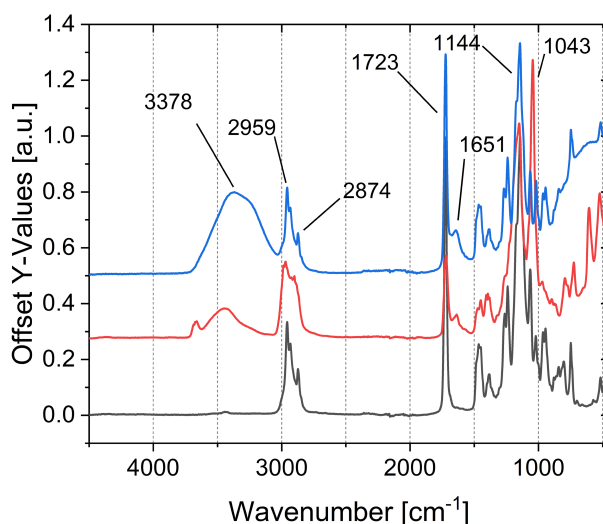
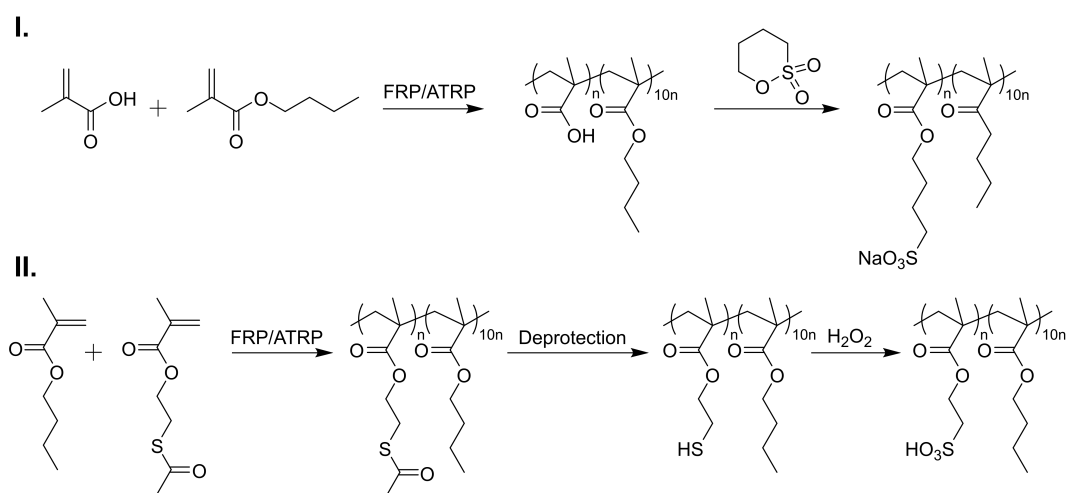


Figure 114: FTIR spectra of poly(BMA) (black), poly(SMBS) (red) and poly(SMBS-co-BMA) (blue).

The FTIR spectrum of the copolymer shows the signals of the poly(BMA). In addition, oscillations of the ionic component appear (e.g. 1651 cm⁻¹), which are not present in the poly(BMA). The intense signal at 3378 cm⁻¹, in the spectra of the ionic homopolymer and the

prepared copolymer originates from adsorbed water which could not be removed. CHN analysis showed a sulfur content of 1.76 %, suggesting the incorporation of the ionic group. Reducing the polarity of the solvent, for example by using a methanol:isopropanol:water mixture (1:1:1), again resulted in the BMA homopolymer. During polymerization, small amounts of a solid precipitated, which showed trace amounts of sulfur. When the methanol-water mixture was used, an analogous result was also obtained by ATRP, both when 2,2'-Bipy and when HMTETA was used as a ligand for the copper complex. Subsequently, copolymerization of BMA, SMBS, FMA and MIMA was attempted under the same reaction conditions. Regardless of the polymerization technique (ARGET ATRP, FRP or RAFT), only poly(BMA) was obtained as the product, while the remaining components were not present in the polymer according to CHN analysis. As a result, two post functionalization strategies were applied. These are shown in Scheme 30.



Scheme 30: Post modification strategies for the synthesis of poly(SMBS-co-BMA).

On the one hand, methacrylic acid was used as a precursor monomer, and on the other hand, 2-(acetylthio)ethyl methacrylate was used. Both enable the subsequent introduction of the sulfonate group. 2-(acetylthio)ethyl methacrylate was synthesized according to literature procedure in two steps.[698] In the first step, S-(2-hydroxyethyl) ethanethioate was prepared by reacting 2-bromoethanol with potassium thioacetate, followed by the introduction of the methacrylate group by reaction with methacryloyl chloride. The resulting monomer was successfully copolymerized with BMA. This was possible both via FRP and ATRP. In Figure 115, the ¹H NMR spectrum of the polymer prepared by FRP is shown.

Results and Discussion

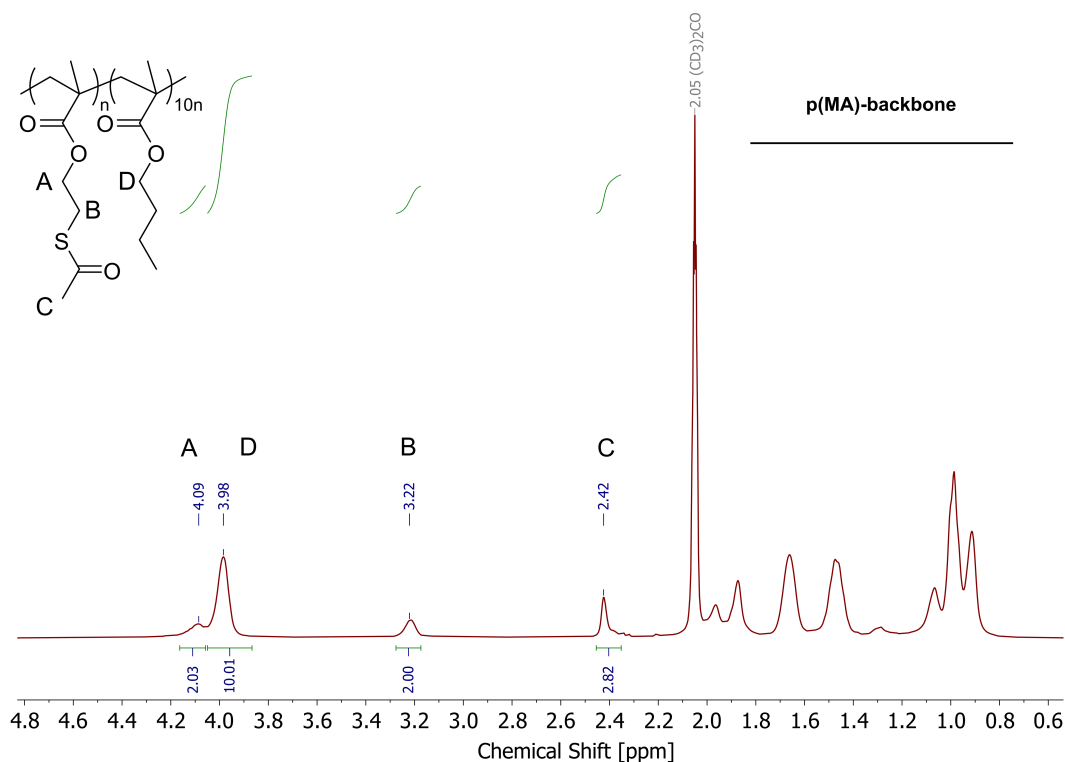


Figure 115: ^1H NMR spectrum of poly(2-(acetylthio)ethyl methacrylate-co-BMA).

Subsequently, the thioester was cleaved to yield the thiol. Four reaction conditions were used for this purpose:

1. Reaction under alkaline conditions with hydrazine [698]
2. Reaction under acidic conditions with hydrochloric acid [698]
3. Reaction under alkaline conditions with sodium methoxide [699]
4. Reaction under alkaline conditions with potassium hydroxide

In all four approaches, the solvent was removed to record an NMR spectrum of the crude product. However, all samples were insoluble in the common NMR solvents. An accurate characterization by FTIR spectroscopy was also not possible due to the superposition of the intense signals of the BMA and since the S-H vibration is hardly detectable in FTIR spectroscopy. Due to the changing properties (solubility and odor), which occur during the deprotection, it can be assumed that this step proceeds at least partially. Therefore, an attempt was made to oxidize the thiol groups with hydrogen peroxide to sulfonic acid and thus achieve better solubility by increasing the polarity. Indeed, a soluble polymer was obtained after this reaction. The ^1H NMR spectrum of the oxidized polymer previously obtained by deprotection with sodium methoxide is shown in Figure 116.

Results and Discussion

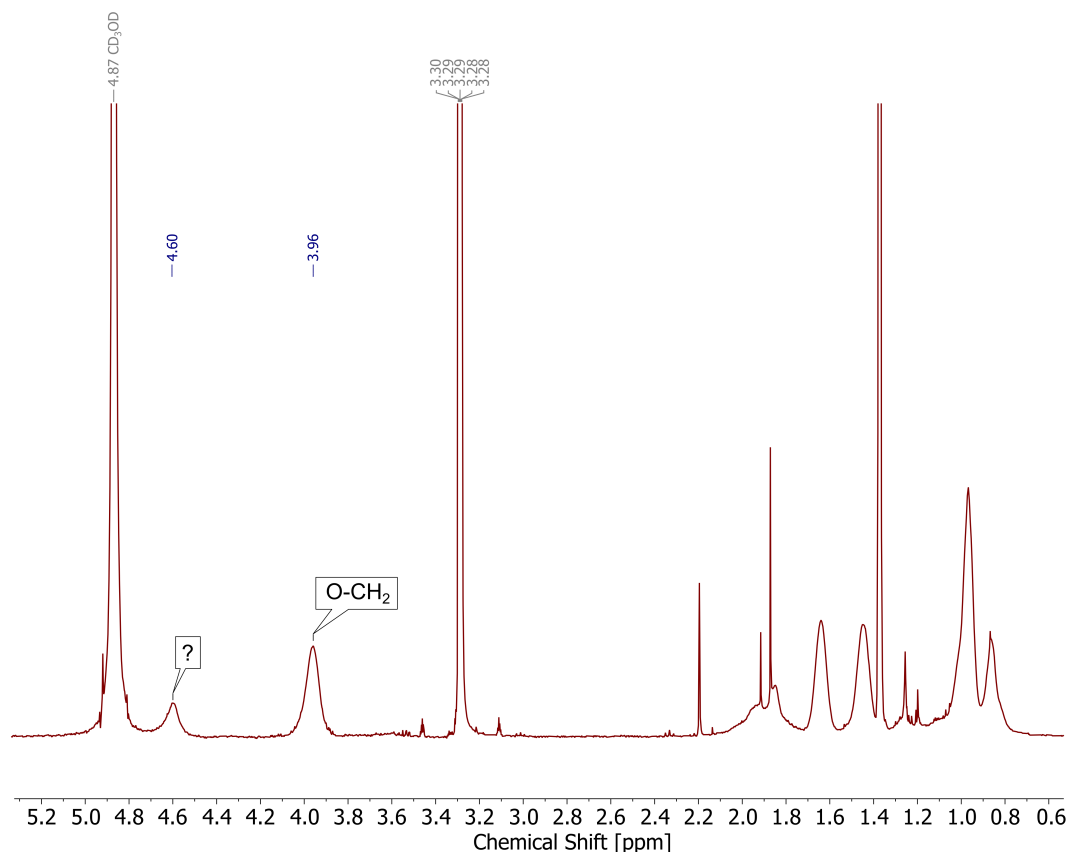


Figure 116: ¹H NMR spectrum of poly(2-(acetylthio)ethyl methacrylate-co-BMA) after treatment with sodium methoxide and H₂O₂.

The NMR spectrum shows neither the expected signals of the CH₂-S (2.8 - 2.9 ppm) nor the CH₂-O (3.9-4.0 ppm) protons of the SMBS. In addition to the expected signal of the CH₂-O group of the BMA at 3.96 ppm, another high intensity signal appears at 4.60 ppm, indicating a partial decomposition of the polymer. As a result, the synthesis route was not pursued any further.

The copolymerization of MA and BMA was also carried out successfully. Subsequently, the copolymer was reacted with 1,4-butane sultone to obtain the sulfonic acid copolymer by ring opening. An NMR spectrum of the product was recorded, which is shown in Figure 117.

Results and Discussion

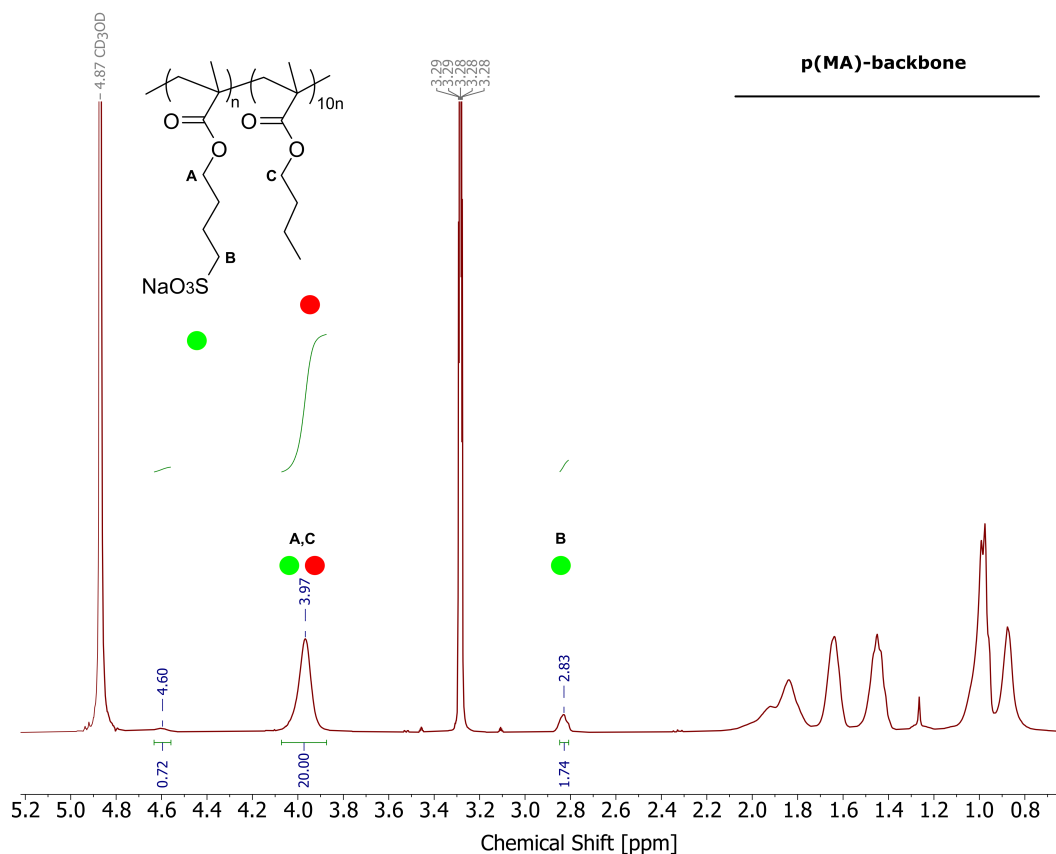


Figure 117: ^1H NMR spectrum von poly(SMBS-co-BMA) via post modification of poly(MA-co-BMA).

The NMR spectrum shows the signal of the S-CH₂ group at 2.83 ppm. The signal of the O-CH₂ group of the SMBS is completely superimposed by the signal of the BMA. Moreover, the signal at 4.6 ppm, which was already observed in the first post modification pathway, indicates a partial decomposition. Nevertheless, a first important step towards the copolymerization of the anionic groups with the DA monomers was achieved, although a synthesis of poly(FMA-co-MIMA-co-SMBS-co-BMA) has not been carried out successfully yet.

DEGMA-based copolymers have also been studied. The polarity of poly(DEGMA) lies in between the DA and ionic components. Since the copolymerization with SMBS has already been successfully demonstrated in the previous studies, the initial focus was on the DA components. ARGET ATRP was performed, using 2,2'-Bipy as the complex ligand. The FMA-co-DEGMA polymer was synthesized in high yield in a solvent mixture of MEK and methanol (3:1). In the same solvent, copolymerization of MIMA and DEGMA was not possible. When non-polar solvents were used (e.g. toluene), the desired copolymer was obtained at least in low yield (< 10 %). The ^1H NMR of the most promising result of the synthesis of a polymer containing both DA components as well as the anionic component is shown in Figure 118.

Results and Discussion

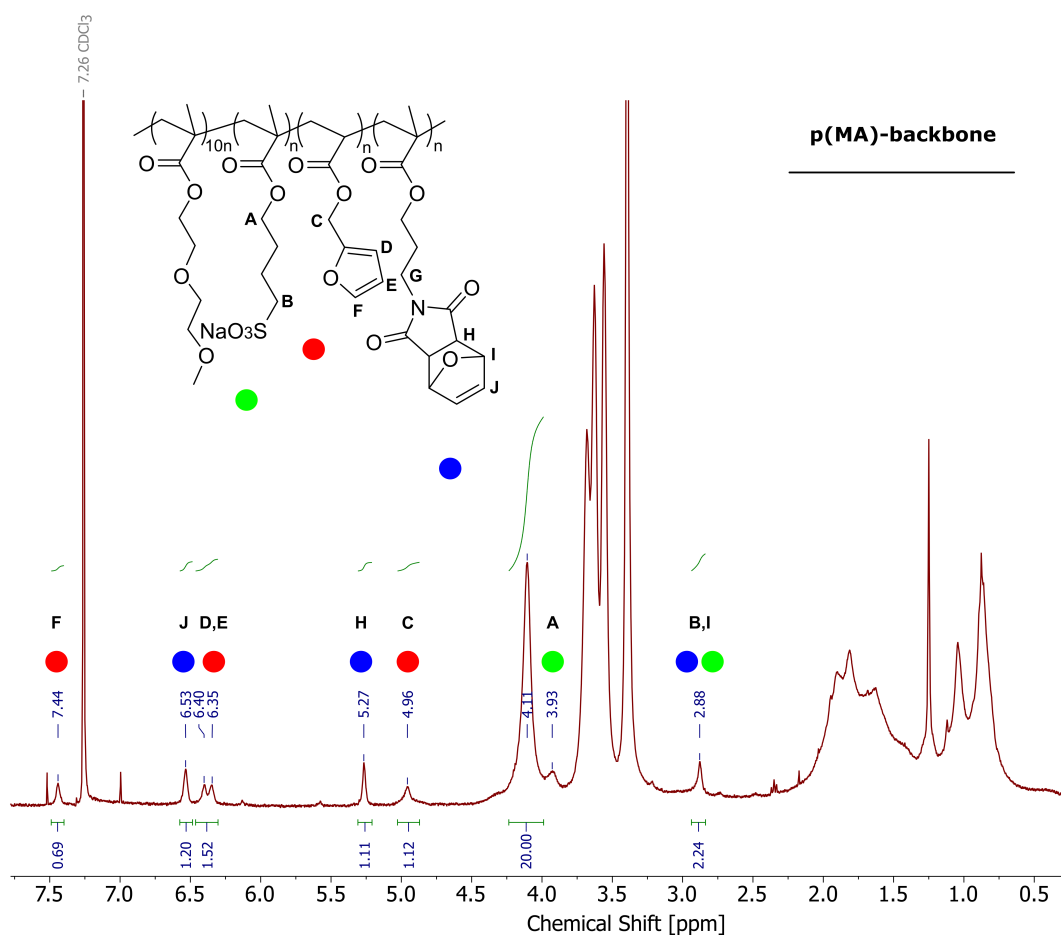


Figure 118: ^1H NMR spectrum of poly(FMA-co-MA-co-MIMA-co-DEGMA).

A solvent ratio of 10: 3:1 of MEK, water and ethanol was used. The NMR spectrum shows the expected signals of both the DA groups and the ionic component. The used monomer ratio of 1:1:1:10 (FMA:MIMA:SMBS:DEGMA) is not fully reflected in the polymer. Instead, a composition of 0.5 : 0.6 : 0.8 : 10 was determined. Despite this promising result, the synthesis shows very poor reproducibility, so that the systems could not be prepared reliably so far. The main problem is that the polymer often precipitates during polymerization and in most cases cannot be redissolved. In addition, the integration of the MIMA component is often not successful. Therefore, the synthesis of poly(FMA-co-SMBS-co-DEGMA) was carried out in a final approach, which showed a much better reproducibility. Here too, the synthesis was carried out in the solvent mixture of MEK, water and ethanol. The NMR spectrum of the product obtained is shown in Figure 119.

Results and Discussion

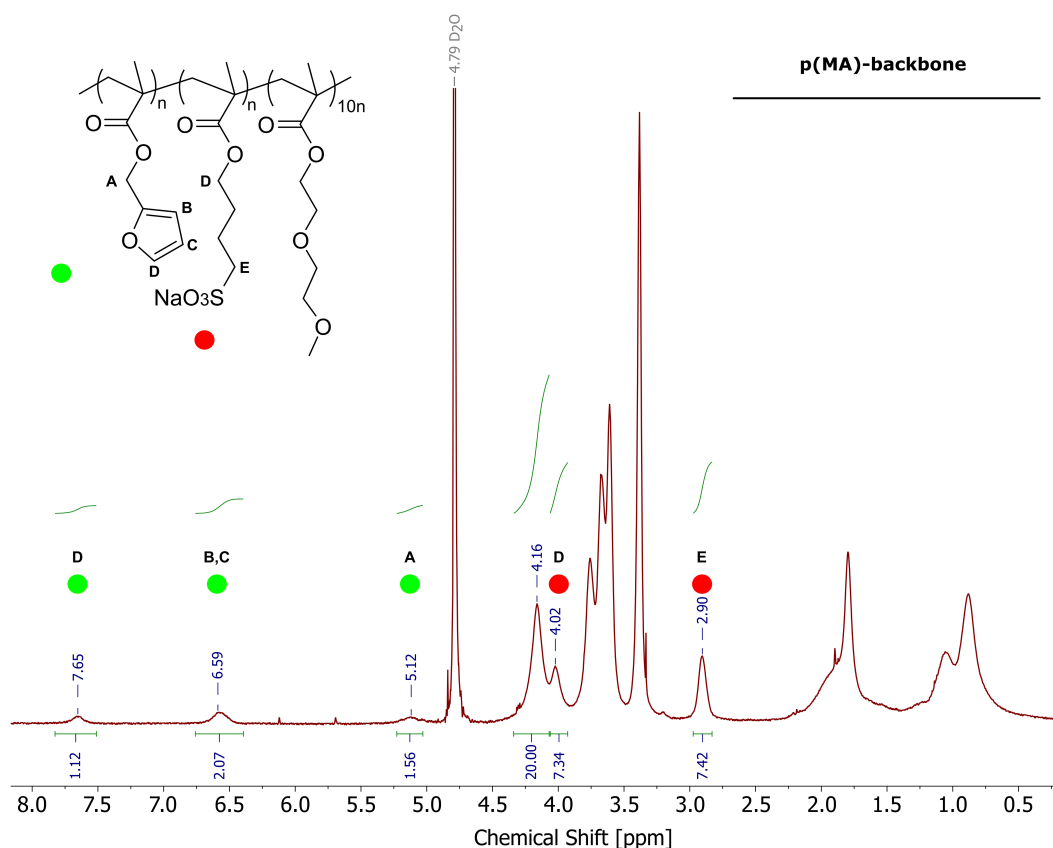


Figure 119: ^1H NMR spectrum of poly(FMA-co-SMBS-co-DEGMA).

Using the signal integrals, the ratio of the components in the polymer was determined to be 0.6 : 3.7 : 10 (FMA:SMBS:DEGMA). Thus, a significantly higher proportion of ionic groups was found in the polymer than in the monomer ratio used. In contrast to the four-component system approach, the syntheses showed good reproducibility on the gram scale. The polymer prepared in this way could potentially serve as a basis for self-healing materials by combination with dendrimer-like maleimide linkers.

The investigations have laid the groundwork for the preparation of double self-healing materials based on ionic interactions and DA chemistry. Despite the challenging synthesis of the copolymers, synthesis strategies were developed for both BMA and DEGMA based copolymers. In the case of BMA based synthesis, post-functionalization approaches seem to be the means of choice to bridge the polarity differences of the functional groups in the polymer. The copolymerization of the DA monomer and the BMA matrix with MA and the subsequent introduction of the sulfonate group by reaction with 1,4-butanediol in a ring opening seems most promising. The use of poly(DEGMA) as a polymer matrix, which serves as a mediator between the functional monomers also appears to be an adequate approach. For the first time, a copolymer of all four components has been prepared in this way, although the reproducibility is poor so far and further attention needs to be paid to optimizing the reaction conditions. Furthermore, systems containing only the furan component, SMBS and DEGMA

Results and Discussion

are more accessible, so that the use of dendrimer like maleimide crosslinkers can possibly lead to access to two component self-healing materials. In addition, previous studies have also shown that the use of a mixture of three separate polymers, each containing one functional component, exhibits similar healing properties as systems in which all functional groups are statistically contained in one polymer.[73,548] Since the two component polymers were also prepared successfully, the polymer blends poly(SMBS-co-DEGMA)/poly(FMA-co-DEGMA)/poly(MIMA-co-DEGMA) and poly(SMBS-co-BMA)/ poly(FMA-co-BMA)/poly(MIMA-co-BMA) are interesting candidates for the double self-healing materials.

4. Conclusion and Perspective

In this work, several nanocomposites were prepared. For this purpose, methacrylate-based copolymers were synthesized and combined with iron oxide nanoparticles specifically tailored for these respective matrices. Their physical and chemical properties were investigated. The focus of this work is the phenomenon of self-healing and the possibility of triggering it by magnetic field induced heating of the integrated particles.

In the first part of the work, the nanoparticle system was selected and synthesized. A series of mixed iron oxides, namely Fe_xO_y , as well as $\text{Mn}_{1-x}\text{Fe}_{2+x}\text{O}_4$ and $\text{Co}_{1-y}\text{Fe}_{2+y}\text{O}_4$ were investigated. Oleic acid functionalized particles were synthesized by thermal decomposition of acetylacetonate precursors, yielding nanoparticles in the 10 nm size range. While the cobalt and manganese mixed oxides showed ferrimagnetic behavior the iron oxide nanoparticles are superparamagnetic at room temperature. All three systems showed the ability to be heated in an alternating magnetic field. In addition to the advantageous magnetic properties the Fe_xO_y particles exhibited a high heating rate, with a SAR value of 63.5 W/g and were therefore used as nano heaters in the further steps.

The next chapter focused on the synthesis of self-healing nanocomposites based on ionic interactions. Here, self-healing was achieved by electrostatic interactions between the particles and the polymer matrix. For this purpose, ionic functionalized nanoparticles were prepared by ligand exchange of the oleic acid by either *N,N,N*-trimethyl-6-phosphonohexan-1-ammonium bromide or 6-phosphono-hexylsulfonic acid to obtain positively and negatively charged particle surfaces, respectively. The cationic functionalized particles showed stable surface charges up to pH 10.6 at which point a desorption of the phosphonic acid occurs. The anionic particles showed strong agglomeration due to the binding of both the sulfonate and phosphonic acid groups to the particle surface. Since agglomerates often act as stress concentration points and thus centers for damage in composites, the focus in the following was on the cationic particle systems. Further, it was also possible to generate switchable surface charges via DA/rDA chemistry, although cyclability is rather restricted. A set of polymer matrices was obtained by ARGET ATRP of SMBS and DEGMA. The polymers carry negative charges over a wide pH range due to the sulfonic acid groups of the SMBS. The mechanical and thermal stability, as well as the T_g s can be adjusted by the polymer composition. This allows to obtain low T_g s, which is necessary for sufficient self-healing. Highly magnetic and thermally more stable composites were obtained by integrating the cationic iron oxide particles. SAXS and BSE SEM revealed particle agglomeration within the polymer matrix independent of the particle content. Nevertheless, an increase in mechanical strength was observed upon particle addition. The systems showed excellent healing of cuts on a μm scale at 80 °C. Further spatially resolved

Conclusion and Perspective

healing at macroscopically lower temperatures was possible in an alternating electromagnetic field, allowing a material-friendly self-healing.

The ionic systems showed a high affinity towards moisture, which is readily adsorbed from the ambient air. The water acts as a plasticizer and even slight differences in the water content significantly alter the material's properties. As a result, a comprehensive storage and drying procedure was developed. In this, FRP was used as the polymerization technique due to the better scalability. Despite the comparable compositions, the obtained polymers exhibited a divergent polymer structure. In the case of FRP semi-crystalline polymers were obtained, indicated by a sharp signal at $q_0 = 0.31 \text{ \AA}^{-1}$ in the SAXS measurements. A second peak at $2 \cdot q_0$, indicates the presence of a lamellar structure with a repeat distance of 2.1 nm. In contrast to the previous systems only a small dependence of the T_g on the polymer composition is observed. Combined with the fact that no glass transition is observed in the expected range of the SMBS homopolymer, this strongly suggests, that the ionic components form the paracrystalline structures, which are remarkably stable even at temperatures up to 300 °C. When iron oxide nanoparticles are added, an improvement in mechanical properties is again observed. Furthermore, the crystalline regions become disordered. The FRP composites also showed good healing ability and almost completely recovered the original properties in tensile tests, especially at high particle contents. Despite the good healing efficiency, long healing times were necessary. For forthcoming studies, it would be beneficial to modify the polymer to exhibit a reduced water affinity, such as by replacing the sulfonate group with other anionic groups. This adjustment could potentially enable wetting based healing, which is the favorable healing trigger for ionic polymers. So far, a contact with water was not possible without compromising the positive mechanical properties.

In the next section, preparatory studies were carried out for synthesis of ionic self-healing nanocomposites in which the healing is completely transferred to the polymer matrix. A grafting-from approach was chosen to allow high loading densities. Two ATRP initiators were prepared, one with a non-polar alkyl linker and the other with a more polar ethylene glycol linker. This allows polymerization in both organic and aqueous media. Again, a phosphonic acid was used for functionalization. α -Bromoisbutyrate functionalities were implemented as the ATRP initiator group. In solution both initiators showed high activity for the polymerization of the model monomers butyl methacrylate and acrylamide. Moreover, the initiators were successfully immobilized on the surface of iron oxide particles. Initial polymerization experiments showed promising results for the SI ATRP, yielding well-dispersed particles in the polymer matrix. This forms the basis for the synthesis of self-healing nanocomposites by transferring the SI ATRP protocol to ionic monomers.

Conclusion and Perspective

Based on the promising results of magnetic field-induced healing, steps were taken to transfer induction-based healing to fourth-generation self-healing materials, which exhibit two healing mechanisms. For this purpose, two BMA based literature-known polymer systems featuring both maleimide and furan functionalities as the DA/rDA components and either urea or amide functionalities as hydrogen bond donors/acceptors were combined with ureylene functionalized iron oxide particles. In this way, self-healing materials were obtained, which could be healed based on two orthogonal healing mechanisms. It was confirmed that only after decrosslinking of the polymer strands healing could be performed successfully by combination of DA reactions and hydrogen bonding. However, rDA had to be carried out thermally, whereas the subsequent magnetic field-induced healing via DA was possible. In comparison to the ionic systems investigated previously, the healing efficiency appears to be inferior. The reason for this is that these materials are significantly more rigid and therefore exhibit lower chain mobility. In order to improve the healing efficiency, the T_g could be lowered in future studies by increasing the BMA content. In addition, the optimization of the particles regarding their heating efficiency could avoid the need to perform rDA in the oven. In addition, especially for the fourth-generation self-healing materials investigations into heat transfer and its impact on the two differently localized healing mechanisms hold significant importance and are interesting for further investigation.

Finally, preparatory studies were carried out on the production of nanocomposites featuring both ionic- and DA-based healing. The synthesis of the polymers represents a central challenge, due to the strongly deviating polarity of the SMBS and MIMA component in particular. To date, BMA-based systems containing both groups have not been directly prepared. A post polymerization introduction of the ionic group via copolymerization of the DA monomers with BMA and MA followed by a ring-opening reaction with 1,4-butanediol showed promising results to circumvent the polarity problem during polymerization. DEGMA based polymers, that feature both DA as well as ionic components were also synthesized, although the results remained poorly reproducible. To overcome this, copolymers of SMBS, FMA, and DEGMA were synthesized, potentially allowing the use of maleimide dendrimers as crosslinkers to obtain a self-healing two-component polymer. The use of different polymer blends containing the polymer backbone and only one functional monomer are also promising candidates for new self-healing materials. In particular, BMA-based systems might be interesting, as the non-polar backbone could reduce the water affinity while maintaining excellent healing ability.

5. Experimental

5.1. Materials

Fe(acac)₃ (97 %), Mn(acac)₂ (98 %), Co(acac)₂ (97 %), 1,2-dodecandiol (90 %), oleic acid (≥ 99 %), CuBr₂ (99 %), di(ethylene glycol) methyl ether methacrylate (95 %), 1,6-dibromhexane (96 %), triethyl phosphite (98 %), trimethylamine solution in ethanol (31-35 %), bromtrimethylsilane (97 %), triethylamine (≥ 99.5 %), acetylchloride (98 %), furan (98 %), 1,10-dibromdecane (97 %), 1,4-dibrombutane (99 %), 10-undecen-1-ol (98 %), sodium hydride (90 %, dry), dimethyl phosphite (98 %), *N*-(3-bromopropyl)phthalimide (98 %), phthalimide potassium salt (98 %), maleic anhydride (99 %), *p*-toluenesulfonic acid monohydrate (≥ 98.5 %), Diethylene glycol (99 %), tetraethylene glycol (99 %), α -bromoisobutyryl bromide (98 %), isopropenyl acetate (99 %), butyl methacrylate (99 %), sodium sulfite (> 97 %), propyl isocyanate (99 %), potassium thioacetate (98 %) and *n*-butyllithium (2.5 M in *n*-hexane, the exact concentration was determined by titration prior to use) were purchased from Sigma-Aldrich. Methacrylic acid (≥ 99 %) and potassium hydroxide (≥ 85 %) were purchased from Merck. Aluminium oxide 90 active neutral (70-230 mesh ASTM), DBPO (72-77 %, 25 % water), AIBN (≥ 99.5 %) and 2-bromoethanol (≥ 96 %) were purchased from Merck Millipore. 2,2'-Bipyridine (> 99 %), 2-Isocyanatoethyl methacrylate (≥ 99 %), hydroquinone (> 99 %) and (98 %) and hydrazine monohydrate (98 %) were purchased from Alfa Aesar. Sodium bicarbonate (> 99 %) was purchased from Fluka. Hydrochloric acid (37 %) and NH₄OH (32 %) were purchased from Bernd Kraft GmbH. Dry dichloromethane (99.8 %) and methanol (99.8 %) were purchased from Acros Organics. Sodium sulfate (99%, dry), 4-methoxyphenol (99 %), pyridine (99 %), 3-aminopropanol (99 %), furfuryl alcohol (98 %), *N*-butylamine (> 99 %), CuBr₂ (99 %) and pre-wetted cellulose regenerated tubing membranes with a 3500 D MWCO were purchased from Fisher Scientific. Sodium chloride (> 99 %), Ammonium chloride (> 99 %), sodium acetate (99 %) and magnesium sulfate (99 %, dry) were purchased from Grüssing GmbH Analytica. Sodium carbonate (97 %) was bought from VWR International GmbH. Acetic anhydride (≥ 99 %) and thionylchloride (≥ 98%) were obtained from Carl Roth GmbH.

CuBr was synthesized by reduction of CuBr₂ with equimolar amounts of NaSO₃ in distilled water at room temperature. The precipitating colorless solid was stirred for 30 minutes in glacial acetic acid and then washed three times with methanol and subsequently three times with diethyl ether. The obtained solid was dried under vacuum and stored under argon atmosphere. AIBN was recrystallized from methanol prior to use. The stabilizers of DEGMA and BMA were removed by passing it through active neutral alumina. The monomers were distilled afterwards for purification. All other chemicals were used without further purification.

5.2. Characterization

Fourier transform infrared (FTIR) spectra were recorded with a Bruker Vertex 70 spectrometer (Bruker Karlsruhe, Germany) under ambient air (16 scans at a resolution of 4 cm⁻¹) in attenuated total reflectance (ATR) mode.

Differential scanning calorimetry (DSC) measurements were performed using a Netzsch DSC 204 F1 Phoenix (NETZSCH-Gerätebau GmbH, Selb, Germany). Samples were prepared in aluminum crucibles with pierced lids and heated under nitrogen at a rate of 5 K/min, 10 K/min or 20 K/min.

Solution nuclear magnetic resonance spectra (NMR) were recorded with a Bruker Advance III HD 300/400 spectrometer (Bruker, Billerica, USA) at 25 °C using CDCl₃, D₂O and the residual protons of solvent and carbon as reference (¹H at 300/400 MHz, ¹³C at 75/ 101 MHz, ³¹P at 121/162 MHz).

Elemental analysis (CHN) was performed with a Vario Micro Cube (Elementar Analysensysteme GmbH, Langenselbold, Germany).

Thermogravimetric analysis (TGA) was performed with a Netzsch Iris TG 209C (NETZSCH-Gerätebau GmbH, Selb, Germany). Measurements were conducted in aluminum oxide crucibles, heating from room temperature to 880 °C under nitrogen atmosphere, followed by heating to 1000 °C under a mixture of nitrogen and oxygen (4:1) with a rate of 10 K/min.

Thermogravimetric analysis - mass spectrometry (TGA-MS) experiments were performed using a Mettler-Toledo TGA/DSC Star System 1 (Mettler-Toledo, Greifensee, Switzerland) applying a heating rate of 10 K/min from 30 to 400 °C and a nitrogen gas flow of 40 ml/min. The TGA was coupled with a ThermoStar GSD 300 T2 to a quadrupole mass spectrometer (QMS 200, Prisma™), both from Pfeiffer Vacuum (Pfeiffer Vacuum GmbH, Aßlar, Germany). Measurements were performed in multiple ion detection mode with a channel electron multiplier detector using a dwell time of 0.2 s and an applied SEM voltage of 1150 V.

ICP-MS measurements were conducted either with an Agilent 8900 Triple Quad or an Agilent 7500cx ICP-MS system (Agilent Technologies, Santa Clara, USA). The detector dwell time for the first one was 100 µs and for the second one 300 ms. The repetition was 3 times. Between 2 and 7 mg particles were dissolved in ultra-pure hydrochloric acid/nitric acid and diluted with ultra-pure water. Additionally, 10 µg/L internal standard (*scandium*) and HNO₃ were added to reach an acid concentration of 3 to 5 % for the measurement. Single element ICP-MS standards of iron, manganese, cobalt, phosphorous and bromine with a concentration of 1 g/L each were used for calibration. The measured isotopes were ⁵⁵Mn, ⁵⁶Fe, ⁵⁹Co, ³¹P and ⁷⁹Br, using He or H₂ as collision gas. ⁴⁵Sc was used as internal standard.

Experimental

Tensile testing: The samples were tested displacement controlled with a uniaxial testing device. Measurements were performed in a heat chamber at 20 °C. Samples were preheated in the unstrained state for at least 15 minutes to guarantee a uniform temperature. Samples were prepared in a hot press at 80 °C using Teflon molds. Samples with an initial sample, width and thickness of 27 mm, 3 mm and 2 mm respectively were used. A waisted sample geometry (R60) was used whereby a smallest cross-section area in the center of the specimen with highest stresses obtained which generates a replicable predetermined breaking point. Measurements were performed with a displacement rate of 0.2 mm/s.[700]

Transmission electron micrographs (TEM) were measured with a JEOL JEM-2010 (JEOL Germany GmbH, Freising, Germany) with 200 kV used for electron acceleration. Samples were prepared on Plano S160–3 copper grids with carbon film.

Powder X-ray diffraction (PXRD) patterns were recorded with a Bruker D8 Advance diffractometer (Bruker, Karlsruhe, Germany) in a Bragg-Brentano θ - θ -geometry (goniometer radius 280 mm). A 2θ range from 7 to 120° (step size 0.013°) was recorded in 1 hour scan time. Cu-K α radiation ($\lambda = 154.0596$ pm, 40 kV, 40 mA) was used with a 12 μ m Ni foil to reduce K β radiation. A variable divergence slit was mounted at the primary beam side (irradiated sample area: 10 \times 7 mm). A LYNXEYE 1D detector was used at the secondary beam side. Background caused by white radiation and sample fluorescence was reduced by limiting the energy range of the detection. Interpretation of the XRD data was performed via Rietveld analysis using TOPAS 5. Crystallographic structure and micro-structure were refined, while instrumental line broadening was included in a fundamental parameters approach. The mean crystallite size $\langle L \rangle$ was calculated at the mean volume weighted column height derived from the integral breadth. The background of standard measurements was fitted by a Chebyshev polynomial function of 15th degree.

X-ray crystallography: The data set was collected using a Bruker D8 Venture diffractometer (Bruker, Karlsruhe, Germany) with a microfocus sealed tube and a Photon II detector. Monochromated Mo-K α radiation ($\lambda = 0.71073$ Å) was used. Data were collected at 273(2) K and corrected for absorption effects using the multi-scan method. The structure was solved by direct methods using SHELXT [701] and was refined by full matrix least squares calculations on F^2 (SHELXL2018 [702]) in the graphical user interface Shelxle [703]. All non H-atoms were located on the electron density maps and refined anisotropically. C-bound H atoms were placed in positions of optimized geometry and treated as riding atoms. Their isotropic displacement parameters were coupled to the corresponding carrier atoms by a factor of 1.2 (CH, CH₂) or 1.5 (CH₃).

Small-angle X-ray scattering (SAXS) experiments were performed on a Xeuss 2.0 system (Xenocs SA., Grenoble, France). A collimated X-ray beam from a Cu-K α source ($\lambda = 1.54$ Å)

Experimental

was used to irradiate the sample, focused on a split size of 0.25 mm². 2D scattering intensity patterns were recorded using a Pilatus 300 K detector from Dectris (Baden, Switzerland) with pixel sizes of 172 × 172 μm², at a sample-to-detector distance of ~1050 mm, calibrated using a silver behenate standard. All samples scattered purely isotropic. Therefore, the 2D scattering patterns were azimuthally averaged to obtain the q -dependent scattered intensity, $I(q)$, where q is the absolute value of the momentum transfer, given by $q = 4\pi \times \sin(\theta/2)/\lambda$, and θ the scattering angle. All samples were measured for 1800 s.

Zeta potential measurements were performed with a Malvern Panalytical Zetasizer Nano ZSP (Malvern Panalytical, Nürnberg, Germany). For the measurement, the solid particle sample was dispersed in deionized water under ultra-sonication for 15 minutes. Sample concentration was ~0.05 wt%. Titration was performed from the initial pH, once to alkaline and once to acidic conditions. At every pH value three measure points were taken each consisting of 20 separate measurements.

Dynamic light scattering (DLS) studies were performed on an ALV/CGS-3 compact goniometer system with an ALV/LSE-5003 correlator (ALV-Laser Vertriebsgesellschaft mbH., Langen, Germany) at a 90° goniometer angle, using noninvasive backscattering ($\lambda = 632.8$ nm). Samples from reaction solution were diluted, homogenized in an ultrasound bath, and equilibrated for about five minutes before measurement.

Microscope images were recorded under polarized light using an Olympus BX60 microscope equipped with a Sony CCD-Iris color camera.

Inductive heating experiments: To generate the external alternating magnetic fields either a TRUMPF Hüttinger high frequency generator 1997 1G 5/3000 or a TruHeat HF 5010 (TRUMPF Hüttinger Elektronik GmbH + Co. KG, Freiburg, Germany) were used. Measurements were carried out with a 3-winded copper coil ($d = 50$ mm) with water cooling at a constant frequency of 1.95 MHz and 3000 W generator power for the first system. For the TruHeat system a 5-winded copper coil ($d = 40$ mm) with water cooling at a constant frequency of 313 kHz and generator power of 5000 W were used. Temperatures in the high frequency oven were measured with a Weidmann Optocon Fotemp1 (Weidmann Technologies Deutschland GmbH, Dresden, Germany) with a TS2 fiber optic temperature sensor. For temperature measurements the samples are pricked with a needle. The tip of the sensor is placed into the resulting hole and the polymer is pressed together at slightly elevated temperature to assure best possible contact. The whole sample is placed into the induction coil.

Mößbauer spectroscopy: A ⁵⁷Co/Rh source was used for the ⁵⁷Fe Mößbauer spectroscopic investigations. The measurements were conducted in usual transmission geometry. The samples were mixed with glucose (anhydrous) to ensure an even distribution of the samples

Experimental

within the thin-walled PMMA containers at a thickness of about 10 mg Sn cm^{-2} . For the 293 K measurements the samples and the source were kept at room temperature. For the measurements at 78 K the samples were placed inside a liquid nitrogen-bath cryostat during the experiments. Data was fitted using the WinNormos for Igor6 program package.[704]

Rheology measurements were performed with an Anton Paar MCR 301 modular compact rheometer (Anton Paar Germany GmbH, Ostfildern-Scharnhausen, Germany). Oscillation measurements with an amplitude of 0.05 % and a frequency of 1 Hz were carried out. The specimens were held under tension with a force of 1 N. The samples were heated to $52.5 \text{ }^\circ\text{C}$ and then cooled back to room temperature.

5.3. Synthetic Procedures

The NMR and FTIR spectra of the synthesized compounds are presented in a separate appendix.

Synthesis and Characterization of the Metal Oxide Nanoparticles

The synthesis was performed according to literature procedure.[261] The particles are synthesized by thermal decomposition of $\text{Fe}(\text{acac})_3$. Therefore 3.53 g (10 mmol) $\text{Fe}(\text{acac})_3$, 10.12 g (10 mmol) dodecane diol, 10 mL oleic acid and 10 mL oleyl amine were dissolved in 100 mL benzyl ether. The reaction mixture was heated to $200 \text{ }^\circ\text{C}$ for 30 minutes, followed by a second heating step at $300 \text{ }^\circ\text{C}$ for another 30 minutes. After cooling to room temperature, the particles were decanted magnetically and washed several times with ethanol (4 x 100 mL). The obtained black solid was then redispersed in 96 mL ethanol for storage. An aliquot of 2 mL was withdrawn, dried under vacuum, and weighted to estimate the concentration and reaction yield (19.0 mg / 2 mL \triangleq 912 mg total mass, TGA: 78.04 % after N_2 Segment).

Yield: 711 mg, 3.1 mmol, 92 %, black solid.

For the cobalt mixed oxide 0.86 g (3.3 mmol) $\text{Co}(\text{acac})_2$ and 2.35 g (6.6 mmol) $\text{Fe}(\text{acac})_3$ were used.

Yield: 644 mg, 2.7 mmol, 83 %, black solid.

For the manganese mixed oxide 0.85 g (3.3 mmol) $\text{Mn}(\text{acac})_2$ and 2.35 g (6.6 mmol) $\text{Fe}(\text{acac})_3$ were used.

Yield: 567 mg, 2.4 mmol, 72 %, black solid.

Synthesis of Permanent Ionic Functionalized Nanoparticles

The synthesis of the two phosphonic acids was performed according to literature procedure.[269]

Diethyl(6-bromohexyl) phosphonate: 24.40 g (100 mmol) 1,6-dibromohexane was heated to 150 °C. Within one hour 16.60 g (100 mmol) triethyl phosphite was added. The reaction mixture was kept at 150 °C for a further 5 hours and then cooled to room temperature. The crude product was fractionally distilled at reduced pressure (Bpt_{0.08 mbar}: 123 °C).

Yield: 19.97 g, 66 mmol, 66 %, colorless oil.

¹H NMR δ (CDCl₃): 3.99-4.12 (4H, O-CH₂-CH₃), 3.34-3.43 (2H, CH₂-Br), 1.34-1.92 (10H, CH₂), 1.24-1.33 (6H, O-CH₂-CH₃) ppm.

¹³C NMR δ (CDCl₃): 61.25 d (O-CH₂), 33.60 (CH₂-Br), 32.28 (CH₂-CH₂), 29.50 d, 27.47, 25.41 d (CH₂-P), 22.13 (CH₂-CH₂), 32.68 (O-CH₂-CH₃) ppm.

³¹P NMR δ (CDCl₃): 32.14 ppm.

FTIR: 2982 (ν_{as} C-H₂), 2933 (ν_s C-H₂), 2864 (ν_s C-H₂), 1439 (δ C-H₂), 1394, 1242 (ν P=O), 1167, 1101, 1024, 955 (ν P-OH), 787, 644 cm⁻¹.

6-(Diethoxyphosphoryl)-N,N,N-trimethylhexan-1-ammonium bromide: 4.20 g (14 mmol) of diethyl- (6-bromohexyl) phosphonate and 10 mL (42 mmol) of trimethylamine (33 % in ethanol) was stirred for 24 hours at room temperature. The crude product was filtered, and the filtrate was freed from the solvent with a rotary evaporator.

Yield: 3.82 g, 11 mmol, 76 %, white solid.

¹H NMR δ (CDCl₃) = 4.00-4.12 m (4H, O-CH₂-CH₃), 3.59-3.71 m (2H, CH₂-Br), 3.45 s (9H, CH₃), 1.36-1.82 m (10H, CH₂), 1.27-1.33 t (6H, O-CH₂) ppm.

¹³C NMR δ (CDCl₃): 66.61 (N-CH₃), 61.45 d (O-CH₂), 53.32 (N-CH₃), 29.84 d (CH₂-P), 25.61, 25.27 d (CH₂P), 22.84, 22.14 (CH₂-CH₂), 16.43 (O-CH₂-CH₃) ppm.

³¹P NMR δ (CDCl₃): 32.14 ppm.

FTIR: 2983 (ν_{as} C-H₂), 2941 (ν_{as} C-H₂), 2858 (ν_s C-H₂), 1488, 1394 (δ C-H₂), 1389, 1246 (ν P=O), 1163, 1095, 1026, 953 (ν P-OH), 792, 521 cm⁻¹.

Experimental

N,N,N-Trimethyl-6-phosphonhexan-1-ammonium bromide: 2.35 g (6 mmol) of 6-(diethoxyphosphoryl)-*N,N,N*-trimethylhexan-1-ammonium bromide was dissolved in 10 mL dry dichloromethane at room temperature under argon atmosphere. 1.5 mL (12 mmol) of bromotrimethylsilane was added dropwise over an hour. The mixture was stirred at room temperature for further 24 hours until the conversion to the silyl ester was completed (verified by ^1H NMR spectroscopy). The solvent was then removed. Subsequently 10 mL of a methanol:water mixture (3:2) was added and the solution was stirred at room temperature for another for 24 hours. Methanol was removed with a rotary evaporator and the product was dried in vacuo. The resulting solid was recrystallized from 2-propanol.

Yield: 1.60 g, 5 mmol, 88 %, white solid.

^1H NMR δ (D_2O) = 3.24-3.31 m (2H, N- CH_2), 3.07 s (9H, $\text{N}(\text{CH}_3)_3$), 1.28-1.83 m (10H, CH_2) ppm.

^{13}C NMR δ (D_2O): 66.61 (N- CH_2), 52.71 (N- CH_3), 29.13 d (CH_2 -P), 27.18, 25.84, 24.86, 21.97 (CH_2 - CH_2) ppm.

^{31}P NMR δ (D_2O): 30.04 ppm.

FTIR: 2943 (ν_{as} C-H₂), 2933 (ν_{as} C-H₂), 2858 (ν_{s} C-H₂), 2156, 1637 (H_2O) 1481 (δ C-H₂), 1217 (ν P=O), 1105, 1055 (ν C-N), 989, 970, 933 (ν P-OH), 914, 768, 717, 660 cm^{-1} .

CHN_{theo} ($\text{C}_9\text{H}_{23}\text{BrNO}_3\text{P}$): C: 35.54; H: 7.62; N: 4.61, CHN_{exp} : C: 33.90, H: 7.07, N: 4.48

6-Bromohexylphosphonic acid: 13.68 g (45 mmol) of diethyl (ω -bromoethyl) phosphonate was dissolved in 40 mL of dry dichloromethane under argon atmosphere and 11.9 mL (91 mmol) of bromotrimethylsilane was slowly added. Stirring was carried out for 24 hours at room temperature. The highly volatile by-products and solvent were removed under vacuum. Then 40 mL of a mixture of methanol and water (3:2) was added and the reaction mixture was stirred over two days. The solvent was removed and the remaining solid was dried in vacuo.

Yield: 10.14 g, 44 mmol, 98 %, pale yellow solid.

^1H NMR δ (CDCl_3) = 9.15 s (2H, OH), 3.39–3.42 m (2H, CH_2 -Br), 1.36-1.91 m (10H, CH_2) ppm.

^{13}C NMR δ (CDCl_3): 33.77 (CH_2 -Br), 32.43, 29.45 d, 27.61 (CH_2 - CH_2), 25.00 d (CH_2 -P), d 21.86 (CH_2 - CH_2) ppm.

^{31}P NMR δ (CDCl_3): 37.36 ppm.

FTIR: 2939 (ν_{as} C-H₂), 2859 (ν_{s} C-H₂), 2705, 2269, 1624 ($\text{H}_2\text{O}/\text{PO-H}$) 1467 (δ C-H₂), 1220 (ν P=O), 1186, 1046, 1012, 940 (ν P-OH), 799, 715, 647, 533 cm^{-1} .

Experimental

6-Mercaptohexyl phosphonic acid: 2.7 g (11 mmol) 6-bromohexylphosphonic acid was dissolved in 25 mL ethanol. 3.7 g (49 mmol) thiourea was dissolved in 25 mL dist. water and added. The reaction mixture was stirred for 18 hours under reflux. Subsequently, the ethanol was removed, 40 mL NH₄OH (32 %) was added, and the reaction mixture was heated to 75 °C for another 2 hours. After cooling to room temperature, the pH was adjusted to 1 using half-conc. HCl. The now acidic solution was extracted three times with 40 mL diethyl ether. The combined organic phase was washed with 40 mL 1 N HCl and dried over magnesium sulfate. The solvent was removed with a rotary evaporator and the remaining waxy solid was dried in vacuo.

Yield: 1.0 g, 6 mmol, 51 %, colorless oil.

¹H NMR δ (CDCl₃) = 8.70 s (2H, OH), 2.50-2.55 m (2H, CH₂-SH), 1.39-1.84 m (10H, CH₂) ppm.

¹³C NMR δ (CDCl₃): 33.79 (CH₂-SH), d 29.90, 28.99, 27.89, 24.65, 21.98 d (CH₂-CH₂) ppm.

³¹P NMR δ (CDCl₃): 37.60 ppm.

FTIR: 2926 (v_{as} C-H₂), 2851 (v_s C-H₂), 2741, 2308 (v_s S-H), 2220, 1576 (H₂O/PO-H) 1452 (δ C-H₂), 1251 (v P=O), 1146, 1098, 993 (v P-OH), 940, 782, 712, 541 cm⁻¹.

6-Phosphonohexylsulfonic acid: 1.71 g of 6-mercaptohexylphosphonic acid (8.6 mmol) was dissolved in 40 mL of acetonitrile. In a second flask, 8.60 g of an aqueous H₂O₂ solution (35 wt% \triangleq 88 mmol) was diluted in 40 mL acetonitrile and then added to the reaction flask in portions. Stirring was carried out overnight. The solvent was removed and the solid obtained was dried in vacuo.

Yield: 1.51 g, 6 mmol, 71 %, white solid.

¹H NMR δ (CD₃OD) = 2.75-2.84 m (2H, CH₂-SO₃H), 1.38-1.84 m (10H, CH₂).

¹³C NMR δ (CD₃OD): 52.55 (CH₂-SO₃), 31.19 d, 29.21, 27.70 d, 25.73, 23.58 d (CH₂-CH₂) ppm.

³¹P NMR δ (CD₃OD) = 31.32 ppm.

FTIR: 2947 (v_{as} C-H₂), 2864 (v_s C-H₂), 2658, 2193, 1681 (H₂O/PO-H) 1470 (δ C-H₂), 1141 (v P=O/S=O), 975 (v P-OH/S-OH), 800, 725, 602, 502, 467 cm⁻¹.

CHN_{theo} (C₉H₂₃BrNO₃P): C: 29.27; H: 6.14; N: 0.00, CHN_{exp}: C: 29.04, H: 6.05, N: 0.00

Experimental

Diethyl (6-mercaptohexyl)phosphonate: 7.49 g (24.8 mmol) diethyl 6-bromohexyl phosphonate was dissolved in 56 mL ethanol. Under gentle heating, 8.37 g (109.9 mmol) of thiourea was dissolved in 56 mL of water and added to the phosphonic acid solution. It was heated under reflux for 18 hours. Then 90 mL of a 32 % NH₄OH solution was added and heated for another 2 hours under reflux. The pH was adjusted to 7 with a half-concentrated HCl. The aqueous phase was extracted twice with 250 mL of diethyl ether. The combined organic phase was washed with a 1 N HCl solution and dried over sodium sulfate.

Yield: 5.78 g, 23 mmol, 92 %, pale yellow liquid.

¹H NMR δ (CDCl₃) = 4.05-4.11 m (4H, O-CH₂-CH₃), 2.48-2.53 m (2H, CH₂-SH), 1.48-1.75 m (10H, CH₂), 1.26-1.46 m (7H, S-H, O-CH₂-CH₃) ppm.

¹³C NMR δ (CDCl₃) = 61.51 d (CH₂-O), 33.76, 30.07 (CH₂-P), 27.88, 26.35, 24.95, 22.50, 16.56 (CH₃) ppm.

³¹P NMR δ (CDCl₃) = 32.37 ppm.

S-(6-(diethoxyphosphoryl)hexyl) ethanethioate: 5.78 g (23 mmol) diethyl (6-mercaptohexyl) phosphonate was dissolved in 12 mL DCM. At 0 °C, 4.1 mL (30 mmol) of triethylamine was added. The reaction mixture was stirred for a further 20 minutes. Then 2.8 mL (39 mmol) acetyl chloride in 14 mL DCM was added dropwise. Stirring was carried out for one hour at 0 °C and one hour at room temperature. The reaction mixture was then stirred overnight at 40 °C. The precipitating CINEt₃ was filtered off. The crude product was washed with a 5 % sodium bicarbonate and then several times with water until pH 4 is reached for the aqueous phase. The organic phase was dried over sodium sulfate, and the solvent was removed under vacuum.

Yield: 3.03 g, 10 mmol, 44 %, yellow liquid.

¹H NMR δ (CDCl₃): 4.12-4.03 m (4H, O-CH₂-CH₃), 2.86-2.83 m (2H, CH₂-S), 2.31 s (C-CH₃), 1.75-1.36 m (10H, CH₂), 1.33-1.29 (6H, O-CH₂-CH₃) ppm.

¹³C NMR δ (CDCl₃): 196.12 (C=O), 61.53 d (O-CH₂), 30.77 30.17 d, 29.21 d, 28.34, 26.43, 25.00, 22.38 d (CH₂), 16.60 d (O-CH₂-CH₃) ppm.

³¹P NMR δ (CDCl₃): 32.37 ppm.

Experimental

(6-(acetylthio)hexyl)phosphonic acid: 3.03 g (11 mmol) diethyl (6-mercaptohexyl) phosphonate was dissolved in 10 mL DCM. Then 2.9 mL (22 mmol) bromotrimethylsilane in 5 mL DCM was added dropwise. Stirring was carried out for 24 hours at room temperature. After removing the solvent, 10 mL of a water methanol mixture (3:2, v:v) was added and the mixture was stirred for another 24 hours at room temperature. The product obtained was dried in vacuo and recrystallized from 2-propanol. As the side product could not be removed, the yield was estimated from the NMR spectrum.

Yield: 815 mg, 3 mmol, 31 %, pale yellow solid.

^1H NMR δ (CDCl_3): 2.86-2.83 m (2H, $\text{CH}_2\text{-S}$), 2.31 s (C-CH_3), 1.76-1.36 m (24H, CH_2) ppm. The signal at 2.50 ppm and the increased signal intensity at 1.76-1.36 ppm originate from an impurity that could not be removed.

6-Phosphonohexylsulfonic acid via *(6-(acetylthio)hexyl)phosphonic acid*: For the initial hydrolysis procedure the 0.50 g (2 mmol) (6-(acetylthio)hexyl)phosphonic was stirred overnight at 40 °C in 50 mL of a saturated KOH solution (1:1 mixture of water and methanol). The pH of the reaction mixture was adjusted to 1 with conc. HCl. The now acidic solution was extracted with diethyl ether, the combined organic phases washed with 1 N HCl and dried over magnesium sulfate. The solvent was removed with a rotary evaporator. The obtained solid was dissolved in 40 mL acetonitrile and 8.6 g of an aqueous H_2O_2 solution (35 wt% \triangleq 88 mmol) was added to the reaction flask in portions. Stirring was carried out overnight. The solvent was removed and the solid obtained was dried in vacuo.

Yield: 0.11 g, 0.5 mmol, 22 %, white solid.

For characterization, see above.

6-Phosphonohexylsulfonic acid via *6-bromohexylphosphonic acid*:

The synthesis was carried out according to literature procedure.[635] 0.57 g (2.3 mmol) (6-bromohexyl)phosphonic acid and 0.87 g (6.9 mmol) Na_2SO_3 was dissolved in 5 mL water. The reaction mixture was heated for 72 hours under reflux. The pH of the solution was adjusted to 1.5 and the solution was extracted with DCM. The organic phase was dried over magnesium sulfate. The solvent was removed.

Yield: 0.07 g, 0.30 mmol, 13 %, white solid.

For characterization, see above.

Synthesis of Functionalized Nanoparticles with Switchable Surface Polarity

Approach 1:

The synthesis of the furane decyl phosphonic acid was carried out according to literature procedure.[271]

2-(10-Bromodecyl)furan: 180 mL of absolute THF was cooled to 0 °C under argon atmosphere. To the cooled solvent 44 mL (96 mmol) of *n*-butyllithium and then 6.8 mL (100 mmol) of furan was added under stirring. The reaction mixture was stirred at 0 °C for 30 minutes and then again at room temperature for an additional 30 minutes. Subsequently, 24.06 g (80 mmol) of 1,10- dibromodecane, dissolved in a little THF, was quickly added to the reaction mixture at -20 – 0 °C under vigorous stirring. After addition, the mixture was stirred overnight at room temperature. The reaction was quenched by adding 80 mL of saturated ammonium chloride solution and then extracted three times with 80 mL of ethyl acetate. The combined organic phase was dried using magnesium sulfate and the solvent was removed using a rotary evaporator. The residue obtained was purified by column chromatography.

Yield: 14.64 g, 51 mmol, 64 %, pale yellow solid.

^1H NMR δ (CDCl_3) = 7.30-7.29 m (1H, CH-O), 6.30-6.27 m (1H, C-H), 5.98-5.97 m (1H, C-H), 3.43-3.39 t (2H, $\text{CH}_2\text{-Br}$), 2.64-2.60 t (2H, CH_2), 1.90-1.82 m (2H, CH_2), 1.64-1.61 m (2H, CH_2), 1.37-1.24 m (12H, CH_2) ppm.

^{13}C NMR δ (CDCl_3) = 156.71 (C-O), 140.72 (CH-O), 110.13 (C-H), 104.62 (C-H), 34.16, 32.95, 29.61, 29.51, 29.42, 29.26, 28.86, 28.83, 28.28, 28.14 (CH_2) ppm.

FTIR: 2923 (ν_{as} C-H₂), 2849 (ν_{s} C-H₂), 1594 (ν C=C), 1508 (ν C=C), 1252, 1135, 1012, 920, 890, 791, 724 (δ Furane), 645, 602, 559 (ν C-Br) cm^{-1} .

Dimethyl (10-(furan-2-yl)decyl)phosphonate: Under argon atmosphere, 0.43 g (18 mmol) of sodium hydride was suspended in 50 mL of absolute THF. To this suspension 1.5 mL (16 mmol) of dimethyl phosphite was added dropwise at 0 °C. The reaction mixture was stirred at 0 °C for 1.5 hours to obtain sodium dimethyl phosphonate. H₂ evolution was observed during this step. The obtained solution was then added dropwise to a solution of 5.85 g (15 mmol) 2-(10-bromodecyl)furan in 130 mL absolute THF. The resulting reaction mixture was stirred overnight at room temperature. The next day, the success of the reaction was checked by ^1H NMR. Low conversion was observed. Therefore, a suspension of 0.43 g sodium hydride in 50 mL THF was prepared again. To this suspension 1.46 mL (15.8 mmol) of dimethyl phosphite was slowly added at 0 °C and the mixture was stirred at 0 °C for 1.5 hours. The

Experimental

reaction mixture was added dropwise to the initial reaction solution and again stirred overnight at room temperature. The precipitated solid was filtered off and the solvent was completely removed. The resulting residue was cleaned up by silica column chromatography. A solvent gradient of *n*-hexane/THF from 1:10 to 1:1 was used.

Yield: 1.80 g, 6 mmol, 38 %, pale yellow oil.

^1H NMR δ (CDCl_3) = 7.23-7.22 m (1H, CH-O), 6.17-6.18 m (1H, C-H), 5.89-5.88 m (1H, C-H), 3.65-3.63 d (6H, CH_3), 2.53-2.49 m (2H, CH_2), 1.75-1.67 (2H, CH_2), 1.57-1.42 (4H, CH_2), 1.35-1.22 m (12H, CH_2) ppm.

^{13}C NMR δ (CDCl_3) = 156.75 (C-O), 140.77 (CH-O), 110.17 (C-H), 104.66 (C-H), 52.39 d (O- CH_3), 30.84, 30.62, 29.58, 29.45, 29.29, 29.21, 28.14 d, 25.77, 23.92, 22.45 d (CH_2) ppm.

^{31}P NMR δ (CDCl_3) = 36.38 ppm.

FTIR: 2917 (ν_{as} C-H₂), 2853 (ν_{s} C-H₂), 1598 (ν C=C), 1504 (ν C=C), 1257, 1239 (ν P=O), 1048, 1022 (ν P-O-C) 929, 895, 822 (δ P-O-C), 724 (δ Furane), 597, 546, 494 cm^{-1} .

(10-(Furan-2-yl)decyl)phosphonic acid: 1.02 g (3.2 mmol) dimethyl (10-(furan-2-yl)decyl) phosphonate was dissolved in 35 mL DCM at 0 °C. Subsequently 0.98 mL (7.4 mmol) bromotrimethylsilane was added dropwise. The reaction mixture was stirred for 16 hours at room temperature. The solvent was removed, and the obtained pale-yellow oil was stirred in 40 mL methanol overnight. The product was precipitated by addition of *n*-hexane and cooling the solution to -25 °C. The product was filtered off and washed with *n*-hexane.

Yield: 1.80 g, 5.7 mmol, 38 %, pale yellow oil.

^1H NMR δ (CDCl_3) = 7.32-7.31 m (1H, CH-O), 6.27-6.26 m (1H, C-H), 6.98-5.99 m (1H, C-H), 2.53-2.49 m (2H, CH_2), 1.72-1.29 m (18 H, CH_2) ppm.

^{13}C NMR δ (CDCl_3) = 156.54 (C-O), 140.88 (CH-O), 110.53 (C-H), 104.88 (C-H), 31.01, 30.04, 29.96, 29.42, 29.27, 29.15, 28.64, 28.35, 27.13, 23.21 ppm.

^{31}P NMR δ (CDCl_3) = 30.13 ppm.

3-(1,3-dioxoisindolin-2-yl)-N,N,N-trimethylpropan-1-ammonium bromide: 7.51 g (28 mmol) of N-(3-bromopropyl)phthalimide was dissolved in 10 mL of dichloromethane and combined with 20 mL (84 mmol) of trimethylamine (31-35 % in ethanol). The reaction mixture was stirred for 24 hours at room temperature. The white solid formed during the reaction was filtered off and the filtrate was washed with dichloromethane. The product was dried in vacuo.

Experimental

Yield: 8.95 g, 27 mmol, 98 %, white solid.

^1H NMR δ (CDCl_3) = 7.93-7.87 m (2H, C-H), 7.86-7.81 m (2H, C-H), 3.82 m (2H, N- CH_2), 3.52-3.44 m (2H, N- CH_2), 3.13 s (9H, N- CH_3), 2.23-2.16 m (2H, CH_2) ppm.

^{13}C NMR δ (CDCl_3) = 169.80 (C=O), 135.50, 133.41, 124.26 (arom.), 65.42 ($\text{CH}_2\text{-N}$), 53.58 ($\text{CH}_3\text{-N}$), 35.72 ($\text{CH}_2\text{-N}$), 23.70 (CH_2) ppm.

FTIR: 3004 (ν_{as} C-H₂), 2953 (ν_{s} C-H₂), 1763 (ν C=O), 1708 (ν C=O), 1472, 1395 (phthalimide ring vibration), 1348, 1163, 1117, 1027, 933, 890, 787, 715, 603, 530, 505 cm^{-1} .

3-Amino-N,N,N-trimethylpropan-1-ammonium bromide: 4.26 g (13 mmol) 3-(1,3-dioxoisindolin-2-yl)-*N,N,N*-trimethylpropan-1-ammonium bromide was added to 500 mL absolute ethanol. To the reaction mixture 1.78 g (37 mmol) of hydrazine monohydrate was added under stirring at 0 °C. The reaction mixture was then stirred for 30 minutes at room temperature and then refluxed for 10 hours. After cooling to room temperature, the precipitated solid phthalhydrazide was filtered off. The solvent was removed, and the residue obtained was taken up again in warm ethanol to just dissolve the residue. After slow cooling, the precipitated solid phthalhydrazide was filtered off and the solvent was completely removed.

Yield: 1.73 g, 5 mmol, 39 %, green sticky solid.

^1H NMR δ (CDCl_3) = 3.59-3.55 m (2H, N- CH_2), 3.31 s (9H, N- CH_3), 2.96-2.93 m (2H, N- CH_2), 2.16-2.09 m (2H, CH_2)

^{13}C NMR δ = 66.65 (N- CH_2), 53.67(N- CH_3), 39.05 (N- CH_2), 26.22 (CH_2) ppm.

FTIR: 3389 (N-H), 2925 (ν_{as} C-H₂), 2855 (ν_{s} C-H₂), 1763 (ν C=O), 1645, 1572, 1480 (ν C-N), 1248, 1053, 956, 909 (δ N-H), 775, 692, 506 cm^{-1} .

3-(1,3-Dioxo-1,3,3a,4,7,7a-hexahydro-2H-4,7-epoxyisoindol-2-yl)-N,N,N-trimethylpropan-1-ammonium bromide: 1.44 g (8.7 mmol) of a protected maleic anhydride in 30 mL of absolute methanol under argon atmosphere. 1.70 g (8.7 mmol) of 3- amino-*N,N,N*-trimethylpropan-1-ammonium bromide was then dissolved in 5 mL absolute methanol and added dropwise. The reaction mixture was stirred at room temperature until all components were dissolved and then refluxed overnight. The solvent was removed, and the residue obtained was recrystallized from methanol. The white crystals obtained were filtered off and washed with small amounts of cold methanol. The product was dried in vacuo.

Yield: 1.08 g, 5.5 mmol, 63 %, white solid.

Experimental

^1H NMR δ (CDCl_3) = 6.57 s (2H, C=CH), 5.20 s (2H, O-CH), 3.62-3.59 m (2H, N-CH₂), 3.10 s (9H, CH₃), 2.98 s (2H, N-CH₂), 2.12-2.04 m (2H, CH₂) ppm.

^{13}C NMR δ (CDCl_3) = 178.49 (C=O), 137.59 (C=C), 82.48 (C-O), 65.21 (N-CH₂), 65.18 (C-H), 53.60 (N-CH₃), 36.21 (N-CH₂), 22.67 (CH₂) ppm.

FTIR: 3010 (ν_{as} C-H₂), 2957 (ν_{s} C-H₂), 1766 (C=O), 1695 (C=O), 1436, 1392, 1360, 1188 (ν C-N), 1135, 1077, 1024, 881, 848, 805, 719 (δ C-O), 651 (ring vibration), 585 cm^{-1} .

Approach 2:

The synthesis of the maleimide decylphosphonic acid was carried out according to the literature procedure.[271]

N-(10-Bromodecyl)phthalimide: 54.84 g (183 mmol) 1,10-dibromodecane was dissolved in 80 mL DMF under argon atmosphere. 7.79 g (42 mmol) potassium phthalimide was added. The reaction mixture was stirred at 160 °C overnight. Then 155 mL petroleum ether, 155 mL diethyl ether and 155 mL saturated sodium chloride solution was added. The organic phase was separated and washed twice with 155 mL saturated sodium chloride solution. The organic phase was dried over sodium sulfate. The solvent was removed and the crude product was purified by column chromatography with a solvent gradient (*n*-hexane:ethyl acetate from 1:0 to 7:3). The product was dried under vacuum.

Yield: 8.51 g, 23 mmol, 55 %, colorless solid.

^1H NMR δ (CDCl_3) = 7.85-7.83 m (2H, C-H), 7.72-7.70 m (2H, C-H), 3.69-3.65 t (2H, N-CH₂), 3.42-3.38 t (2H, Br-CH₂), 1.87-1.80 m (2H, CH₂), 1.42-1.28 m (12H, CH₂) ppm.

^{13}C NMR δ (CDCl_3) = 168.65 (C=O), 134.00, 132.31, 123.31 (arom.), 38.19 (N-CH₂), 34.24 (Br-CH₂), 32.96, 29.48, 29.47, 29.26, 28.85, 28.72, 28.29, 26.96 (CH₂) ppm.

FTIR: 2915 (ν_{as} C-H₂), 2847 (ν_{s} C-H₂), 1767, 1691 (C=O), 1468, 1443, 1401 (phthalimide ring vibration), 1375 (ν C-N), 1228, 1778, 1077, 1047, 1005, 955, 901, 799, 720, 660, 534 cm^{-1} .

N-(10-Phthalimidodecyl)diethyl phosphonate: 3.26 g (9 mmol) *N*-(bromodecyl)phthalimide and 6.2 mL (36 mmol) triethylphosphite was stirred for 18 hours at 150 °C under argon. Excess triethyl phosphite and other by-products were distilled off under reduced pressure.

Yield: 3.78 g, 9 mmol, 100 %, colorless oil.

Experimental

^1H NMR δ (CDCl_3) = 7.83-7.81 m (2H, C-H), 7.70-7.68 m (2H, C-H), 4.09-4.04 m (4H, O-CH₂), 3.67-3.63 t (2H, N-CH₂), 2.01-1.54 m (6H, CH₂), 1.31-1.24 m (18H, CH₂/CH₃) ppm.

^{13}C NMR δ (CDCl_3) = 168.56 (C=O), 133.93, 132.25, 123.23 (arom.), 61.47 d (O-CH₂-CH₃), 38.13 (N-CH₂), 30.68 d, 29.43 d, 29.22, 29.13, 28.67, 26.92, 26.45, 25.05, 22.49 d, 16.56 d (O-CH₂-CH₃) ppm.

^{31}P NMR δ (CDCl_3) = 32.66 ppm.

FTIR: 2987 (ν_{as} C-H₃), 2927 (ν_{as} C-H₂), 2854 (ν_{s} C-H₂), 1770, 1701 (C=O), 1474, 1441, 1393 (phthalimide ring vibration), 1364 (C-N), 1241 (P=O), 1026 (P-OC), 956, 794, 720, 534 cm^{-1} .

N-(10-Aminoalkyl)diethylphosphonate: 7.42 g (17.5 mmol) *N*-(10-phthalimidodecyl)diethyl phosphonate was dissolved in 700 mL ethanol and cooled to 0 °C. Dropwise 2.4 mL of hydrazine monohydrate was added. The reaction was stirred for 30 minutes at 0 °C, 30 minutes at room temperature and then refluxed overnight. The solvent was removed. The sample was collected with DCM and extracted with an aqueous sodium carbonate solution. The organic phase was dried over sodium sulfate. The product was obtained after removal of the solvent.

Yield: 2.43 g, 8 mmol, 47 %, colorless oil.

^1H NMR δ (CDCl_3) = 4.11-3.97 m (4H, O-CH₂), 2.65-3.62 t (2H, N-CH₂), 1.71-1.63 m (2H, P-CH₂), 1.61-1.35 m (6H, CH₂), 1.35-1.22 m (18H, CH₂/CH₃) ppm.

^{13}C NMR δ (CDCl_3) = 61.41 d (O-CH₂-CH₃), 42.23 (N-CH₂), 33.71, 30.65 d, 29.49, 29.47 d, 29.12, 26.91, 26.42, 25.03, 22.45 d, 16.54d (O-CH₂-CH₃) ppm.

^{31}P NMR δ (CDCl_3) = 32.62 ppm.

FTIR: 3495 (ν N-H₂), 2980 (ν_{as} C-H₃), 2924 (ν_{as} C-H₂), 2854 (ν_{s} C-H₂), 1609 (δ C-H), 1462 (ν C-N), 1396, 1241 (P=O), 1025 (P-OC), 955, 796, 621, 543 cm^{-1} .

4-((10-(diethoxyphosphoryl)decyl)amino)-4-oxobut-2-enoic acid: 1.25 g (12 mmol) maleic anhydride was dissolved in 55 mL DCM. 3.75 g (12 mmol) *N*-(10-aminoalkyl)diethylphosphonate was dissolved in 55 mL DCM and added dropwise. Stirring was continued for 1 hour at room temperature. The solvent was removed. The reaction yielded the opened maleimide.

Yield: 4.99 g, 12 mmol, 100 %, colorless oil.

Experimental

^1H NMR δ (CDCl_3) = 6.54 d (1H, =C-H), 6.27 d (1H, =C-H), 4.13-3.99 m (4H, O-CH₂), 3.34-3.29 m (2H, N-CH₂), 1.76-1.55 m (6H, CH₂), 1.38-1.26 m (18H, CH₂/CH₃) ppm.

^{13}C NMR δ = 166.30 (HOC=O), 166.26 (NC=O), 135.21 (C=C), 132.54 (C=C), 61.75 d (O-CH₂-CH₃), 40.47 (N-CH₂), 30.40, 29.13 d, 29.07, 28.62, 26.83, 26.05, 24.66, 22.28, 16.53 d (O-CH₂-CH₃) ppm.

^{31}P NMR δ (CDCl_3) = 32.56 ppm.

FTIR: 3459, 3239 (NH/OH), 2986 (ν_{as} C-H₃), 2927 (ν_{as} C-H₂), 2853 (ν_{s} C-H₂), 1719 (C=O), 1637, 1572, 1402, 1305, 1218 (P=O), 1025 (PO-C), 962 (P-OC), 855, 787, 727, 631, 594, 543 cm^{-1} .

N-(10-Maleimide decyl)phosphonic acid: 2.55 g (6.5 mmol) 4-((10-(diethoxyphosphoryl) decyl)amino)-4-oxobut-2-enoic acid was dissolved in 43 mL acetic anhydride and 0.52 g sodium acetate was added. The mixture was heated overnight. After cooling to room temperature, 45 mL ethyl acetate and 50 mL water were added. The organic phase was separated and extracted with a saturated sodium chloride solution. The solvent was separated by distillation. The subsequent step was carried out under argon atmosphere. The intermediate was dissolved in 20 mL dry acetonitrile and 1.7 mL (13.5 mmol) bromotrimethylsilane was added dropwise. The reaction mixture was stirred overnight. Then 20 mL of methanol was added and stirred again overnight. The reaction mixture was concentrated, and the product precipitated after addition of 20 mL cold *n*-hexane. The product was recrystallized from a mixture of *n*-hexane and ethanol.

Yield: 1.86 g, 5.9 mmol, 90 %, colorless solid.

^1H NMR δ (CD_3OD) = 6.77 s (=C-H), 3.47-3.44 t (2H, N-CH₂), 1.69-1.50 m (6H, CH₂), 1.40-1.23 m (14H, CH₂) ppm.

^{13}C NMR δ = 172.60 (C=O), 135.33 (C=C), 38.52 (N-CH₂), 31.81 d, 30.49 d, 30.27, 30.15, 29.48, 28.89, 27.75, 27.53 ppm.

^{31}P NMR δ (CDCl_3) = 29.95 ppm.

2-(4-bromobutyl)furan: 1.7 mL (23 mmol) furan was dissolved 40 mL dry THF under argon atmosphere. 10 mL of a 2.5 M *n*-butyllithium solution was added dropwise at 0 °C. The sample was stirred 30 minutes at 0 °C then 30 minutes at RT followed for 30 minutes at 40 °C. The mixture was then cooled to -20 °C and 17.27 g (80 mmol) of 1,4-dibromobutane was added dropwise. The mixture was stirred at 0 °C for 30 minutes. The mixture was stirred overnight at

Experimental

room temperature. The reaction mixture was quenched with 80 mL of a saturated ammonium chloride solution. The aqueous phase was extracted three times with 80 mL ethyl acetate. The combined organic phase was dried over sodium sulfate and freed from solvent. The product was purified by silica column chromatography using *n*-hexane as the solvent.

Yield: 2.40 g, 12 mmol, 51 %, colorless solid.

^1H NMR δ (CD_3OD) = 7.31-7.30 m (1H, C-H), 6.30-6.28 m (1H, C-H), 6.01-5.98 m (1H, CH), 3.44-3.41 m (2H, Br- CH_2), 2.67-2.65 m (2H, OC- CH_2) 2.04-1.70 m (4H, CH_2) ppm.

^{13}C NMR δ = 156.15, 141.03, 110.21, 105.18 (arom.), 33.53, 32.17, 27.70, 26.92 (CH_2) ppm.

FTIR: 2944 (ν_{as} C- H_2), 2860 (ν_{s} C- H_2), 1602 (C=C), 1505, 1434, 1253, 1207, 1148 (δ C-H), 1072, 1004, 925, 883, 975, 926, 728 (δ furane), 648, 598, 560 cm^{-1} .

4-(furan-2-yl)-N,N,N-trimethylbutan-1-ammonium bromide: 8.81 g (43 mmol) 2-(4-bromobutyl)furan was stirred in 15.5 mL of a 4.2 M trimethylamine solution in ethanol overnight. The solvent was removed, and the white solid was taken up with *n*-hexane and extracted with water. After removal of the water under reduced pressure, the product was recrystallized from 2-propanol.

Yield: 9.18 g, 35 mmol, 81 %, colorless solid.

^1H NMR δ (CD_3OD) = 7.36-7.35 m (1H, C-H), 6.30-6.29 m (1H, C-H), 6.09-6.08 m (1H, CH), 3.38-3.34 m (2H, N- CH_2), 2.75-2.71 m (2H, OC- CH_2), 1.88-1.81 m (2H, CH_2), 1.75-1.67 m (2H, CH_2) ppm.

^{13}C NMR δ = 156.23, 142.38, 111.20, 106.47 (arom.), 67.42 (N- CH_2), 53.54 (CH_3) 28.05 25.94 23.31 (CH_2) ppm.

FTIR: 3106 (NC- H_3), 3013 (NC- H_3), 2920 (ν_{as} C- H_2), 2864 (ν_{s} C- H_2), 1589 (C=C), 1483 (NC), 1407, 1390, 1333, 1230, 1170, 1143 (δ C-H), 1066, 1004, 996, 965, 917, 875, 776, 748 (δ furane), 605, 529 cm^{-1} .

After re-crystallization of the product, colorless crystals could be obtained, which allowed the determination of a single crystal structure. Due to crystal twinning, not all reflections could be assigned. Furthermore, the measurement was performed at 0°C, which affects the quality of the determinability of the atomic spacings.

Experimental

Table 17: Crystal data and structure refinement for 4-(furan-2-yl)-N,N,N-trimethylbutan-1-ammonium bromide (4761_a).

Identification code	4761_a	
Empirical formula	C ₁₁ H ₂₀ Br N O	
Formula weight	262.19	
Temperature	273(2) K	
Wavelength	0.71073 Å	
Crystal system	Monoclinic	
Space group	<i>P2₁/m</i>	
Unit cell dimensions	a = 5.5709(10) Å b = 7.3592(12) Å c = 15.460(3) Å	α = 90°. β = 90.160(6)°. γ = 90°.
Volume	633.80(19) Å ³	
Z	2	
Density (calculated)	1.374 g/cm ³	
Absorption coefficient	3.216 mm ⁻¹	
F(000)	272	
Crystal size	0.425 x 0.415 x 0.094 mm ³	
Theta range for data collection	2.635 to 26.371°.	
Index ranges	-5 ≤ h ≤ 6, -9 ≤ k ≤ 9, -19 ≤ l ≤ 19	
Reflections collected	4486	
Independent reflections	1163 [R _{int} = 0.0383]	
Completeness to theta = 25.242°	81.7 %	
Absorption correction	Semi-empirical from equivalents	
Max. and min. transmission	0.7456 and 0.6069	
Refinement method	Full-matrix least-squares on F ²	
Data / restraints / parameters	1163 / 0 / 83	
Goodness-of-fit on F ²	1.099	
Final R indices [I > 2σ(I)]	R ₁ = 0.0383, wR ₂ = 0.0903	
R indices (all data)	R ₁ = 0.0448, wR ₂ = 0.0928	
Extinction coefficient	n/a	
Largest diff. peak and hole	0.512 and -0.377 e/Å ⁻³	

Experimental

Table 18: Atomic coordinates ($\times 10^3$) and equivalent isotropic displacement parameters ($\text{\AA}^2 \times 10^5$) for 4761_a. $U(\text{eq})$ is defined as one third of the trace of the orthogonalized U^{ij} tensor.

	x	y	z	U(eq)
Br(1)	0.1390(1)	0.7500	0.1177(1)	0.42(1)
O(1)	0.5457(10)	0.2500	0.6111(3)	0.70(1)
N(1)	0.5180(7)	0.2500	0.1315(2)	0.35(1)
C(1)	0.3966(19)	0.2500	0.6809(4)	0.77(2)
C(2)	0.1735(19)	0.2500	0.6575(5)	0.84(2)
C(3)	0.1741(14)	0.2500	0.5631(4)	0.68(2)
C(4)	0.4003(14)	0.2500	0.5395(4)	0.60(2)
C(8)	0.3783(10)	0.2500	0.2145(3)	0.46(1)
C(9)	0.3422(10)	0.2500	0.588(3)	0.44(1)
C(10)	0.6737(7)	0.4160(4)	0.1234(2)	0.44(1)
C(7)	0.5302(11)	0.2500	0.2955(3)	0.55(1)
C(6)	0.3670(12)	0.2500	0.3772(3)	0.61(2)
C(5)	0.5304(12)	0.2500	0.4556(3)	0.60(2)

Table 19: Bond lengths [\AA] and angles [$^\circ$] for 4761_a.

O(1)-C(1)	1.364(9)	C(1)-O(1)-C(4)	106.2(6)
O(1)-C(4)	1.370(7)	C(9)-N(1)-C(8)	107.7(4)
N(1)-C(9)	1.490(6)	C(9)-N(1)-C(10)#1	108.3(2)
N(1)-C(8)	1.502(6)	C(8)-N(1)-C(10)#1	111.9(2)
N(1)-C(10)#1	1.504(4)	C(9)-N(1)-C(10)	108.3(2)
N(1)-C(10)	1.504(4)	C(8)-N(1)-C(10)	111.9(2)
C(1)-C(2)	1.294(12)	C(10)#1-N(1)-C(10)	108.6(4)
C(2)-C(3)	1.459(10)	C(2)-C(1)-O(1)	111.4(7)
C(3)-C(4)	1.313(10)	C(1)-C(2)-C(3)	106.0(7)
C(4)-C(5)	1.488(8)	C(4)-C(3)-C(2)	106.4(7)
C(8)-C(7)	1.509(7)	C(3)-C(4)-O(1)	110.0(6)
C(7)-C(6)	1.559(8)	C(3)-C(4)-C(5)	135.5(6)
C(6)-C(5)	1.513(8)	O(1)-C(4)-C(5)	114.6(6)
		N(1)-C(8)-C(7)	114.7(4)
		C(8)-C(7)-C(6)	110.2(5)
		C(5)-C(6)-C(7)	107.3(5)
		C(4)-C(5)-C(6)	113.9(6)

Symmetry transformations used to generate equivalent atoms:

#1 $x, -y+1/2, z$

Experimental

Table 20: Anisotropic displacement parameters ($\text{\AA}^2 \times 10^3$) for 4761_a. The anisotropic displacement factor exponent takes the form: $-2 \cdot \pi^2 [h^2 \cdot a^{*2} \cdot U^{11} + \dots + 2 \cdot h \cdot k \cdot a^* \cdot b^* \cdot U^{12}]$.

	U ¹¹	U ²²	U ³³	U ²³	U ¹³	U ¹²
Br(1)	35(1)	42(1)	50(1)	0	7(1)	0
O(1)	84(4)	76(3)	49(2)	0	-8(2)	0
N(1)	29(2)	35(2)	40(2)	0	5(2)	0
C(1)	117(8)	70(4)	44(3)	0	2(4)	0
C(2)	112(8)	89(5)	52(4)	0	33(4)	0
C(3)	63(5)	97(5)	45(3)	0	7(3)	0
C(4)	79(5)	54(3)	47(3)	0	1(3)	0
C(8)	39(3)	57(3)	43(3)	0	13(2)	0
C(9)	38(3)	51(3)	44(3)	0	-2(2)	0
C(10)	39(2)	43(2)	50(2)	2(1)	5(2)	-7(1)
C(7)	55(4)	64(3)	46(3)	0	4(3)	0
C(6)	68(5)	70(4)	45(3)	0	9(3)	0
C(5)	73(5)	67(4)	42(3)	0	11(3)	0

Table 21: Hydrogen coordinates ($\times 10^3$) and isotropic displacement parameters ($\text{\AA}^2 \times 10^5$) for 4761_a.

	x	y	z	U(eq)
H(1)	0.4487	0.2500	0.7381	0.93
H(2)	0.0399	0.2500	0.6935	1.01
H(3)	0.0406	0.2500	0.5269	0.82
H(8A)	0.2755	0.1437	0.2154	0.55
H(8B)	0.2755	0.3563	0.2154	0.55
H(9A)	0.4268	0.2500	0.0048	0.67
H(9B)	0.2432	0.1435	0.0623	0.67
H(9C)	0.2432	0.3565	0.0623	0.67
H(9D)	0.1820	0.2500	0.0815	0.67
H(9E)	0.3656	0.3565	0.0240	0.67
H(9F)	0.3656	0.1435	0.0240	0.67
H(10A)	0.7887	0.4179	0.1697	0.66
H(10B)	0.5755	0.5230	0.1261	0.66
H(10C)	0.7564	0.4129	0.0690	0.66
H(7A)	0.6324	0.3567	0.2961	0.66
H(7B)	0.6324	0.1433	0.2961	0.66
H(6A)	0.2653	0.3570	0.3775	0.73
H(6B)	0.2653	0.1430	0.3775	0.73
H(5A)	0.6330	0.1436	0.4532	0.72
H(5B)	0.6330	0.3564	0.4532	0.72

Experimental

Table 22: Torsion angles [°] for 4761_a.

C(4)-O(1)-C(1)-C(2)	0.000(4)
O(1)-C(1)-C(2)-C(3)	0.000(4)
C(1)-C(2)-C(3)-C(4)	0.000(4)
C(2)-C(3)-C(4)-O(1)	0.000(3)
C(2)-C(3)-C(4)-C(5)	180.000(3)
C(1)-O(1)-C(4)-C(3)	0.000(3)
C(1)-O(1)-C(4)-C(5)	180.000(2)
C(9)-N(1)-C(8)-C(7)	180.000(1)
C(10)#1-N(1)-C(8)-C(7)	61.1(3)
C(10)-N(1)-C(8)-C(7)	-61.1(3)
N(1)-C(8)-C(7)-C(6)	180.000(1)
C(8)-C(7)-C(6)-C(5)	180.000(1)
C(3)-C(4)-C(5)-C(6)	0.000(3)
O(1)-C(4)-C(5)-C(6)	180.000(2)
C(7)-C(6)-C(5)-C(4)	180.000(2)

Symmetry transformations used to generate equivalent atoms:

#1 x,-y+1/2,z

Synthesis of Ionic Self-Healing Nanocomposites

The synthesis of the ionic monomer was carried out according to Niederhauser with minor changes.[644]

Sodium 4-(methacryloyloxy)butan-1-sulfonate: Sodium methacrylate was prepared freshly before synthesis by stirring 10.20 g (119 mmol) methacrylic acid and 9.9 g (118 mmol) sodium bicarbonate at room temperature. Completion of the reaction was determined with ^1H NMR spectroscopy. The obtained white solid was dried under vacuum and used without further purification. 3.60 g (33 mmol) sodium methacrylate was dissolved in 35 mL ethanol and heated to reflux. Subsequently 5.00 g (37 mmol) 1,4-butane sultone was added dropwise. Heating was continued for 8 hours. After cooling to room temperature, the solvent was removed under vacuum. The obtained white solid was washed with small amounts of xylene (3x) and ethanol (3x) and dried under vacuum.

Yield: 5.43 g, 22 mmol, 67 %, white solid.

^1H NMR δ (D_2O) = 6.08 s (1H, =C-H), 5.63-5.67 m (1H, =C-H), 4.14-4.21 m (2H, O-CH₂), 2.88-2.95 m (2H, S-CH₂), 1.88 s (3H, CH₃), 1.78-1.82 m (4H, CH₂) ppm.

^{13}C NMR δ (D_2O): 170.06 (C=O), 136.07 (C=CH₂), 126.50 (CH₂=C), 64.95 (C-O), 50.51 (C-S), 26.68, 20.89, 17.34 (CH₂-CH₂, CH₃), ppm.

Experimental

FTIR: 3535 ($\nu_{\text{as}} \text{C}=\text{O}$), 3493 ($\nu_{\text{as}} \text{C}=\text{O}$), 2956 ($\nu_{\text{as}} \text{C}-\text{H}_2$), 2931 ($\nu_{\text{as}} \text{C}-\text{H}_3$), 2860 ($\nu_{\text{as}} \text{C}-\text{H}_3$), 1716 ($\nu_{\text{as}} \text{C}=\text{O}$), 1630, 1570 ($\nu_{\text{as}} \text{C}=\text{C}$), 1450, 1416 ($\delta \text{C}=\text{C}$), 1348, 1327, 1296, 1165 ($\nu_{\text{as}} \text{C}-\text{O}$), 1049, 906 ($\delta =\text{CH}_2$), 779 cm^{-1} .

CHN_{theo} ($\text{C}_8\text{H}_{13}\text{NaO}_5\text{S}$): C: 39.34; H: 5.37, CHN_{exp} : C: 37.24; H: 5.65.

2-(2-Hydroxyethoxy)ethyl methacrylate: 380 mg (2 mmol) p-toluenesulfonic acid monohydrate and 7.67 mL (80 mmol) diethylene glycol was dissolved in 130 mL toluene and placed in a two-neck flask with water separator. Furthermore, 5 mg (0.2 mol%) of 4-methoxyphenol was added as a stabilizer. The reaction mixture was heated for 1 hour under reflux to remove water. Then, 1.7 mL (20 mmol) of methacrylic acid was added and heated for another 1.5 hours. The solvent was then removed and the crude product obtained was purified by column chromatography over silica (*n*-hexane:EE, 3:2). Before removal of the solvent, a few crystals 4-methoxyphenol were added for stabilization.

Yield: 2.67 g, 15 mmol, 76%, colorless liquid.

^1H NMR δ (CDCl_3) = 6.13 s (1H, =CH), 5.58 s (1H, =CH), 4.29–4.34 m (2H, $\text{CO}_2\text{-CH}_2$), 3.71–3.78 m (4H, CH_2), 3.59–3.64 m (2H, CH_2), 1.95 s (3H, CH_3) ppm.

^{13}C NMR δ (CDCl_3): 167.51 ($\text{C}=\text{O}$), 136.16 ($\text{C}=\text{CH}_2$), 126.04 ($\text{CH}_2=\text{C}$), 72.46, 69.22, 63.87, 61.81 (CH_2), 18.43 (CH_3) ppm.

ATRP based Systems:

Synthesis of the poly(SMBS-co-DEGMA): Various amounts of sodium 4-(methacryloyloxy)butan-1-sulfonate (1.02–3.41 mmol) and 1.93 g (10.24 mmol) DEGMA were dissolved in 18 mL water. The pH was adjusted to 9 with a 1 M NaOH solution. The solution was degassed with 3 freeze-pump-thaw cycles. In a second flask, 6.5 mL methanol was also degassed with 3 freeze pump thaw cycles. Then 14.86 mg (0.102 mmol) CuBr and 32.00 mg (0.205 mmol) 2,2'-bipyridine was added. The solutions were combined and 15.03 μL degassed EBriB (0.1024 mmol) was added. The reaction solution was stirred at 70 °C for 12 hours. Then 32.00 mg of 2,2'-bipyridine and 23 μL of hydrazine monohydrate was added and the mixture was heated for a further 12 hours. The crude product obtained was concentrated and dialyzed against water for 3 days. Like the homopolymer, the sample was not completely decolorized, and the copper was removed by dialyzing against diluted HCl. The product was freed from the solvent. Mean yield 70 % (± 7 %).

Experimental

^1H NMR δ (D_2O) = 4.13 s (20H, $\text{COOCH}_2/\text{DEGMA}$), 3.99 s (2H, $\text{COOCH}_2/\text{anionic}$), 3.59-3.73 m (66H, $\text{CH}_2\text{-CH}_2/\text{DEGMA}$), 3.36 s (34H, O- CH_3), 2.85 s (2H, S- CH_2), 1.75-1.99 m (24H, CH_2), 0.84-1.09 m (34H, CH_3) ppm.

FTIR: 3595 ($\nu_{\text{as}} \text{C=O}$), 3440 ($\nu_{\text{as}} \text{C=O}$), 2990 ($\nu_{\text{as}} \text{C-H}_2$), 2934 ($\nu_{\text{as}} \text{C-H}_3$), 2871, 2821 ($\nu_{\text{as}} \text{C-H}_3$), 1725 ($\nu_{\text{as}} \text{C=O}$), 1458, 1402, 1353, 1233, 1099 ($\nu_{\text{as}} \text{C-O}$), 1043, 952, 861, 741, 601, 530 cm^{-1} .

Synthesis of the composite materials: 0.5 g of the polymer is dissolved in 14 mL of a mixture of THF and H_2O (1:1) under ultrasonication. The appropriate amount of functionalized nanoparticles (2 wt%, 5 wt%, 10 wt% and 20 wt%) is added. The solvent is slowly removed under stirring.

Sample preparation: Polymer and composite films were prepared by compression molding at 80 °C for 24 hours in a Teflon form which was held using a vice.

Self-healing tests: Self-healing experiments were performed by cutting the samples through half thickness. Afterwards the edges were gently pressed together at room temperature. Then the samples were heated to 80 °C for 24 hours. Afterwards the samples were put back into the Teflon molds and heated to 80 °C for another 24 hours. For the self-healing by induction heating the generator power was adjusted to obtain a macroscopic temperature of 58 °C. Healing was performed for two segments of 24 hours duration.

FTIR: 3580 ($\nu_{\text{as}} \text{C=O}$), 3433 ($\nu_{\text{as}} \text{C=O}$), 2998 ($\nu_{\text{as}} \text{C-H}_2$), 2934 ($\nu_{\text{as}} \text{C-H}_3$), 2885, 2821 ($\nu_{\text{as}} \text{C-H}_3$), 1725 ($\nu_{\text{as}} \text{C=O}$), 1458, 1395, 1353, 1240, 1107 ($\nu_{\text{as}} \text{C-O}$), 1043, 966, 861, 587 (Fe-O-Fe) cm^{-1} .

FRP based systems:

Optimization of polymerization conditions:

Polymerization with AIBN: Initially kinetic studies were performed to evaluate the ideal reaction time. SMBS and DEGMA ($n_{\text{ges}} = 32.7$ mmol) were placed in a 100 mL two-necked flask in the desired ratio and dissolved in 43 mL water and 9 mL methanol. 1 mL pyridine was added as a tracer. The reaction mixture was flushed with argon for 10 minutes. 1 mol% AIBN was added. The reaction mixture was flushed with argon for a further 10 minutes before heating to 70 °C. After 30 min, 1 h, 2 h, 3 h, 4 h and 5 h of heating, a sample was taken each time and analyzed with ^1H NMR spectroscopy. Studies on the initiator concentration were performed under the same conditions.

Polymerization with DBPO: SMBS and DEGMA were placed in a 100 mL two-necked flask in the desired ratio ($n_{\text{ges}} = 32.7$ mmol) and dissolved in 43 mL water and 9 mL methanol. 1 mL

Experimental

pyridine was added as a tracer. The reaction mixture was flushed with argon for 10 minutes. 1 mol% DBPO was added. The reaction mixture was flushed with argon for a further 10 minutes before heating to 85 °C. After 30 min, 1 h, 2 h, 3 h, 4 h and 5 h of heating, a sample was taken each time and analyzed with ¹H NMR spectroscopy. Temperature studies were performed under the same conditions.

Optimized Polymerization procedure: SMBS and DEGMA ($n_{\text{ges}} = 65.4$ mmol) were placed in a 250 mL two-necked flask in the desired ratio and dissolved in 86 mL water and 18 mL methanol. The reaction mixture was flushed with argon for 20 minutes. 1 mol% DBPO was added. The reaction mixture was flushed with argon for a further 20 minutes before heating to 60 °C for 5 hours. All polymer samples were dried in vacuo at 40 °C for two days, then 5 hours at 80 °C and were then stored in a desiccator over phosphorus pentoxide for at least two weeks.

Studies on water uptake: The storage under increased humidity took place in a desiccator over water. To further increase the humidity, the pressure is initially reduced to 600 mbar. The water content of the samples was determined after 1 h, 2 h, 4 h, 8 h, 16 h, 32 h and 64 h with TGA.

Studies on water removal: The samples were placed in an oven at 80 °C for 2 h, 5 h, 8 h and 24 hours. After that the samples were immediately placed in closed, cold-welded aluminum crucibles, which were pierced right before TGA to avoid reuptake of water.

Composite synthesis, sample preparation and self-healing tests were performed as described earlier for the ATRP systems.

Synthesis of Phosphonic Acid Based Initiators for SI ATRP

Non-polar initiator:

Undec-10-en-1-yl acetate: The synthesis was carried out under inert gas. To introduce the acetyl protecting group, 17.03 g (100 mmol) of undec-10-en-1-ol was dissolved in 45 mL of DCM. Then 18 mL (130 mmol) of triethylamine was added and the reaction mixture was cooled to 0°C. Subsequently, 10 mL (140 mol) of acetyl chloride in 22 mL of DCM was added dropwise and stirred for another 2 hours. Subsequently, heating was carried out overnight under reflux. The precipitating white solid was filtered off and the filtrate was washed twice with 100 mL of a 5 wt% sodium bicarbonate solution and with 100 mL of water. The organic phase was dried over sodium sulfate. The remaining solvent was then removed.

Yield: 20.13 g, 95 mmol, 95 %, colorless liquid.

Experimental

^1H NMR δ (CDCl_3) = 5.79-5.86 m (1H, C=CH), 4.92-5.01 m (2H, C=CH₂), 4.03-4.07 m (2H, O-CH₂), 2.04-2.06 m (5H, C=C-CH₂), 1.60-1.63 m (2H, CH₂), 1.26-1.38 m (12H, CH₂) ppm.

^{13}C NMR δ (CDCl_3) = 171.23 (C=O), 139.16 (C=C-H), 114.10 (C=CH₂), 64.62 (O-CH₂), 33.76, 29.41, 29.35, 29.19, 29.05, 25.86, 21.00 (CH₂/CH₃) ppm.

FTIR: 2926 (ν_{as} C-H₂), 2855 (ν_{s} C-H₂), 1741 (C=O), 1640, 1468, 1367, 1232, 1035 (C-O), 909 (C=C), 732, 639, 606 cm^{-1} .

11-(Diethoxyphosphoryl)undecyl acetate: The synthesis was carried out under inert gas. 47.68 g diethyl phosphite (345 mmol) was introduced and heated to 120 °C. 0.81 g (4.9 mmol) AIBN and 19.86 g (94 mmol) of the synthesized undec-10-en-1-yl acetate were dissolved in 13.48 g (98 mmol) diethyl phosphite and added dropwise. Stirring was continued for 2 hours at 120 °C. Excess diethyl phosphite was distilled off.

Yield: 24.14 g, 69 mmol, 74 %, yellow oil.

^{13}C NMR δ (CDCl_3) = 171.24 (C=O), 64.60 (O=C-O-CH₂) 61.44, 61.38 (O=P-O-CH₂), 30.64, 30.47, 29.42, 29.29, 29.19, 29.04, 29.02, 28.53, 26.30, 25.85, 24.09, 22.35, 22.30, 21.00 (CH₂/CH₃), 16.47, 16.41 (P-O-CH₂-CH₃) ppm.

^{31}P NMR δ (CDCl_3) = 32.69 ppm.

FTIR: 2926 (ν_{as} C-H₂), 2852 (ν_{s} C-H₂), 1732 (C=O), 1640, 1450, 1363, 1240, 1035 (C-O), 950, (P-O), 795, 610, 547 cm^{-1} .

Diethyl (11-hydroxyundecyl) phosphonate: A mixture of 22.17 g (63 mmol) 11-(diethoxyphosphoryl)undecyl acetate, 0.69 g (12 mmol) KOH and 86 mL dry methanol was heated at reflux for three days. The solvent was removed, and the obtained pale-yellow oil was taken up with 75 mL of a 5 wt% sodium bicarbonate solution. The aqueous phase was extracted three times with 40 mL of DCM. The combined organic phase was washed with 20 mL of water and dried over sodium sulfate. The remaining DCM was removed.

Yield: 18.74 g, 61 mmol, 96 %, pale yellow oil.

^1H NMR δ (CDCl_3) = 4.00-4.13 m (4H, P-O-CH₂), 3.59-3.68 m (2H, HO-CH₂), 2.25 s (1H, OH), 1.53-1.78 m (6H, CH₂), 1.22-1.37 m (20H, CH₂, O-CH₂-CH₃) ppm.

^{13}C NMR δ (CDCl_3) = 62.89 (H-O-CH₂) 61.41, 61.35 (O=P-O-CH₂), 32.71, 30.60, 30.42, 29.46, 29.33, 29.24, 28.99, 26.27, 25.67, 24.88, 22.32, 22.27 (CH₂/CH₃), 16.45, 16.39 (P-O-CH₂-CH₃) ppm.

Experimental

^{31}P NMR δ (CDCl_3) = 32.76 ppm.

FTIR: 3410 (OH), 2923 (ν_{as} C-H₂), 2852 (ν_{s} C-H₂), 1456, 1396, 1222, 1026 (C-O), 958, (P-O), 787, 719, 543 cm^{-1} .

11-(Diethoxyphosphoryl)undecyl 2-bromo-2-methylpropanoate: The synthesis was carried out under inert gas. 17.06 g (55 mmol) diethyl (11-hydroxyundecyl) phosphonate and 6.16 g (61 mmol) triethylamine were dissolved in 250 mL dry DCM. The reaction mixture was cooled with a water bath. Then 6.8 mL of α -bromoisobutyryl bromide was added dropwise and stirred overnight at room temperature. The solvent was then removed ($T < 30\text{ }^\circ\text{C}$). The purification was carried out by column chromatography. For this, a solvent gradient from *n*-hexane:EE (96:4) to *n*-hexane:EE (80:20) was used. To remove residual α -bromoisobutyryl bromide, the product was taken up with 50 mL DCM and washed three times each with 5 wt% sodium bicarbonate and with 15 mL water. The organic phase was dried over sodium sulfate and the solvent was removed.

Yield: 5.06 g, 11 mmol, 20 %, yellow oil.

^1H NMR δ (CDCl_3) = 4.00-4.17 m (6H, O=C-O-CH₂, P-O-CH₂), 1.92 s (6H, Br-C-(CH₃)₂), 1.53-1.76 m (6H, CH₂), 1.22-1.37 m (20H, CH₂, O-CH₂-CH₃) ppm.

^{13}C NMR δ (CDCl_3) = 171.71, 66.11 (H-O-CH₂) 61.45, 61.39 (O=P-O-CH₂), 55.97 (Br-C), 32.71 (Br-C-(CH₃)₂), 30.73, 30.47, 29.40, 29.37, 29.28, 29.10, 29.02, 28.27, 26.27, 25.71, 24.88, 22.33, 22.28 (CH₂/CH₃), 16.46, 16.40 (P-O-CH₂-CH₃) ppm.

^{31}P NMR δ (CDCl_3) = 32.76 ppm.

FTIR: 2927 (ν_{as} C-H₂), 2855 (ν_{s} C-H₂), 1733 (C=O), 1463, 1388, 1232, 1164, 1126, 1022 (C-O), 955, (P-O), 787, 723, 639, 538, 484 cm^{-1} .

(11-((2-Bromo-2-methylpropanoyl)oxy)undecyl)phosphonic acid: The synthesis was carried out under inert gas. 7.21 g (16 mmol) 11-(diethoxyphosphoryl)undecyl 2-bromo-2-methylpropanoate was dissolved in 27 mL dry dichloromethane. 4.2 mL (32 mmol) of bromotrimethylsilane was added slowly over the period of 30 minutes. The reaction mixture was stirred overnight at room temperature. The solvent was removed and the residue was taken up with a mixture of methanol and water (30 mL, methanol:water = 3:2). Again, stirring was carried out overnight at room temperature. Subsequently, the solvent was removed under reduced pressure.

Yield: 6.07 g, 15 mmol, 96 %, yellow solid.

Experimental

^1H NMR δ (CDCl_3) = 8.09 (2H, OH), 4.15-4.19 m (2H, O=CO-CH₂), 1.94 s (6H, CH₃-C-Br), 1.19-1.83 m (20H, CH₂) ppm.

^{13}C NMR δ (CDCl_3) = 171.75 (C=O), 66.15, 56.00, 30.77, 29.45, 29.43, 29.34, 29.15, 29.05, 28.32, 25.77 ppm.

^{31}P NMR δ (CDCl_3) = 37.88 ppm.

FTIR: 2916 (ν_{as} C-H₂), 2847 (ν_{s} C-H₂), 2778 (ν_{as} PO-H), 2286 (ν_{s} PO-H), 1729 (C=O), 1461, 1381, 1281, 1217, 1167, 1108, 1073, 1048 (C-O), 989, (P-O), 944, 785, 715, 637, 527, 482 cm^{-1} .

CHN_{theo} ($\text{C}_9\text{H}_{23}\text{BrNO}_3\text{P}$): C: 44.90; H: 7.54; CHN_{exp} : C: 46.67, H: 7.77

Polar initiator:

3,6,9,12-Tetraoxapentadec-14-en-1-ol: The synthesis was carried out under inert gas. 20 g (103 mmol) of tetraethylene glycol and 5.33 g (133 mmol) of sodium hydroxide were placed in 67 mL of dry THF. Dropwise, 8.8 mL of allyl bromide (102 mmol) in 33 mL of THF was added. The reaction mixture was then heated for 3 hours to reflux. The precipitating solid was separated, and the filtrate was concentrated. The crude product was taken up with 50 mL of water and washed twice with 50 mL toluene followed by eight extractions with 40 mL of DCM. The combined organic phase, was washed two more times with 25 mL of water. The product was dried over sodium sulfate and residual DCM was removed.

Yield: 9.20 g, 39 mmol, 39 %, colorless oil.

^1H NMR δ (CDCl_3) = 5.82-5.91 m (1H, C=CH), 5.12-5.25 m (2H, C=CH₂), 3.97-3.98 d (2H, CH-CH₂), 3.53-3.70 m (16H, CH₂, O-CH₂-CH₃), 2.93 s (1H, OH) ppm.

^{13}C NMR δ (CDCl_3) = 134.57 (C-H), 116.93 (C=CH₂), 72.35, 72.04, 70.43, 70.38, 70.16, 69.22, 69.17 (CH₂), 61.49 (HO-CH₂) ppm.

FTIR: 3453 (O-H), 3078 (ν =C-H), 2863 ($\nu_{\text{as}}/\nu_{\text{s}}$ C-H₂), 1455, 1350, 1291, 1250, 1093 (C-O), 993, 925, 880, 845, 563, 522 cm^{-1} .

3,6,9,12-Tetraoxapentadec-14-en-1-yl acetate: 8.7346 g of 3,6,9,12-tetraoxapentadec-14-en-1-ol and 6.72 mL (48 mmol) of triethylamine were dissolved in 20 mL of dry DCM. The reaction mixture was cooled to 0 °C and 3.7 mL (52 mmol) of acetyl chloride was added dropwise to 10 mL of DCM. Stirring was continued for one hour at 0 °C and two hours at room temperature.

Experimental

The precipitating solid was removed, and the filtrate was washed twice each time with 33 mL of a 5 wt% sodium bicarbonate solution and water. The product was dried over sodium sulfate and the remaining solvent was removed.

Yield: 10.25 g, 37 mmol, 99.5 %, colorless oil.

^1H NMR δ (CDCl_3) = 5.82-5.96 m (1H, C=CH), 5.14-5.29 m (2H, C=CH₂), 4.19-4.22 m (2H, O=C-O-CH₂), 4.02-3.98 d (2H, CH-CH₂), 3.55-3.73 m (14H, CH₂, O-CH₂-CH₃), 2.06 s (3H, CH₃) ppm.

^{13}C NMR δ (CDCl_3) = 170.98 (C=O), 134.62 (C=C-H), 117.03 (C=CH₂), 72.12, 70.55, 70.50, 70.45, 69.29, 69.00 (CH₂), 63.50 (O=C-O-CH₂) 20.87 (CH₃) ppm.

FTIR: 3078 (ν =C-H), 2863 ($\nu_{\text{as}}/\nu_{\text{s}}$ C-H₂), 1737 (C=O), 1451, 1371, 1236, 1102 (C-O), 1056, 997, 926, 850, 639, 606, 555, 509 cm^{-1} .

15-(Diethoxyphosphoryl)-3,6,9,12-tetraoxapentadecyl acetate: The synthesis was carried out under inert gas. 19.87 g diethylphosphite (144 mmol) was heated to 120 °C. 0.34 g (2.0 mmol) AIBN and 9.14 g (39 mmol) of the synthesized 3,6,9,12-tetraoxapentadec-14-en-1-yl acetate were dissolved in 5.62 g (41 mmol) diethylphosphite and added dropwise. Stirring was continued for an additional 2 hours at 120 °C. Excess diethyl phosphite was distilled off. The product was purified by column chromatography (solvent gradient: ethyl acetate:methanol, 100:0 to 50:50).

Yield: 0.75 g, 1.8 mmol, 4.5 %, pale yellow oil.

^1H NMR δ (CDCl_3) = 4.19-4.23 m (2H, O=C=CH₂), 4.05-4.08 m (4H, P-(O-CH₂)₂), 3.44-3.74 m (16H, CH₂), 2.08 s (3H, O=C-CH₃), 1.75-1.90 m (4H, CH₂, P-CH₂-CH₂), 1.28-1.32 m (6H, P-(O-CH₂-CH₃)₂) ppm.

^{13}C NMR δ (CDCl_3) = 170.03 (C=O), 70.82 d, 70.53, 70.49, 70.03, 69.06 (CH₂), 63.54 (O=C-O-CH₂), 61.48 d (P-O-(CH₂)₂), 22.94, 22.72, 22.67, 21.52 (CH₂), 20.92 (O=C-CH₃), 16.36 d (P-O-(CH₂-CH₃)₂) ppm.

^{31}P NMR δ (CDCl_3) = 32.35 ppm.

FTIR: 2865 ($\nu_{\text{as}}/\nu_{\text{s}}$ C-H₂), 1457, 1347, 1289, 1248, 1096 (C-O/P-O), 991, 923, 885, 844, 561, 519 cm^{-1} .

Experimental

Diethyl(1-hydroxy-3,6,9,12-tetraoxapentadecan-15-yl)phosphonate: 12.32 g (30 mmol) of 15-(diethoxyphosphoryl)-3,6,9,12-tetraoxapentadecyl acetate was added to 42.5 mL of a 5 % HCl solution. The reaction mixture was heated to 60 °C. A sample was taken after 30 minutes, 150 minutes, and 24 hours, and checked for complete conversion. Solvent and volatile by-products were distilled off via a U-tube. The product was dried under high vacuum.

Yield: 9.77 g, 26 mmol, 88 %, pale yellow oil.

^1H NMR δ (D_2O) = 4.08-4.15 m (4H, PO-CH₂), 3.55-3.72 m (18H, CH₂), 1.79-1.97 m (4H, P-CH₂-CH₂), 1.30-1.33 t (6H, CH₃) ppm.

^{13}C NMR δ (D_2O) = 71.83, 70.27 d, 69.78, 69.69, 69.57, 69.29, 63.20 d (P-O-(CH₂)₂), 60.45, 21.75 d, 21.37, 19.97, 15.76 d (P-O-(CH₂-CH₃)₂) ppm.

^{31}P NMR δ (D_2O) = 35.62 ppm.

FTIR: 3456 (O-H), 2868 ($\nu_{\text{as}}/\nu_{\text{s}}$ C-H₂), 1459, 1346, 1296, 1250, 1094 (C-O/P-O), 997, 925, 883, 844, 555, 526 cm⁻¹.

15-(Diethoxyphosphoryl)-3,6,9,12-tetraoxapentadecyl-2-bromo-2-methylpropanoat: The synthesis was carried out under inert gas. 6.86 g (18 mmol) of diethyl (1-hydroxy-3,6,9,12-tetraoxapentadecan-15-yl) phosphonate and 2.23 g (22 mmol) of triethylamine were dissolved in 40 mL of dry THF. Subsequently, 4.24 g (18 mmol) α -bromoisobutyryl bromide in 8 mL THF was added. The reaction mixture was stirred for 48 hours at room temperature. The resulting triethylammonium bromide was filtered off and the solvent was removed under high vacuum. The crude product was taken up with 60 mL of dichloromethane and washed three times with 30 mL of a 5 % sodium bicarbonate solution, and three times with 30 mL of water. The organic phase was dried over sodium sulfate and the solvent was removed.

Yield: 7.49 g, 14 mmol, 78 %, pale yellow liquid.

^1H NMR δ (CDCl_3) = 4.30-4.33 m (2H, O=CO-CH₂), 4.20-4.08 m (4H, P-O-CH₂), 3.46-3.75 m (14H, CH₂), 1.93 s (6H, CH₃-C-Br), 1.73-1.85 m (4H, CH₂), 1.28-1.33 t (6H, O-CH₂-CH₃) ppm.

^{13}C NMR δ (CDCl_3) = 171.54, 70.79 d, 70.62, 70.55, 70.52, 70.48, 68.65, 65.05, 61.44, 61.37, 55.64, 30.67, 22.78 d, 22.67, 21.52, 16.39 d (O-CH₂-CH₃) ppm.

^{31}P NMR δ (CDCl_3) = 32.33 ppm.

FTIR: 2868 ($\nu_{\text{as}}/\nu_{\text{s}}$ C-H₂), 1733 (C=O), 1459, 1388, 1275, 1240, 1098, 1022, 955, 820, 644, 539, 476 cm⁻¹.

Experimental

(18-Bromo-18-methyl-17-oxo-4,7,10,13,16-pentaoxanonadecyl)phosphonic acid: The synthesis was carried out under inert gas. 6.28 g (12 mmol) 15-(diethoxyphosphoryl)-3,6,9,12-tetraoxapentadecyl 2-bromo-2-methylpropanoate was dissolved in 26 mL dry dichloromethane. 3.69 g (24 mmol) of bromotrimethylsilane was added slowly over the period of 30 minutes. The reaction mixture was stirred overnight at room temperature. The solvent was removed and the residue was taken up with a mixture of methanol and water (30 mL, methanol:water = 3:2). Again, stirring was carried out overnight at room temperature. Subsequently, the solvent was removed in vacuo.

Yield: 4.64 g, 10 mmol, 83 %, pale yellow oil.

$^1\text{H NMR } \delta$ (CD_3OD) = 4.27-4.29 m (2H, O=CO-CH₂), 3.49-3.73 m (14H, CH₂), 1.89 s (6H, CH₃-C-Br), 1.73-1.81 m (4H, CH₂) ppm.

$^{13}\text{C NMR } \delta$ (CD_3OD) = 173.29 (C=O), 72.11 d, 71.64, 71.49, 71.45, 69.83, 66.44, 57.24, 54.99, 49.99, 31.22, 25.51, 24.25 d, 24.13 (CH₂/CH₃) ppm.

$^{31}\text{P NMR } \delta$ (CD_3OD) = 29.89 ppm.

FTIR: 3421 (O-H), 2933 (ν_{as} C-H₂), 2875 (ν_{s} C-H₂), 2737 (ν_{as} PO-H), 2290 (ν_{s} PO-H), 1737 (C=O), 1456, 1351, 1278, 1099 (C-O), 986, (P-O), 937, 859, 762, 721, 643, 522 cm⁻¹.

CHN_{theo} (C₁₅H₃₀BrNO₉P): C: 38.72, H: 6.50; CHN_{exp}: C: 39.34; H: 6.70

Self-Healing Nanocomposites Based on Hydrogen Bonding and DA Chemistry

Monomer Synthesis:

The syntheses was performed according to literature procedure with minor changes.[73]

3a,4,7,7a-Tetrahydro-4,7-epoxyisobenzofuran-1,3-dion: A solution of 48.08 g maleic anhydride (447 mmol) in 250 mL furan was stirred for 24 hours at room temperature. The precipitated solid was filtered off and washed with cold diethyl ether.

Yield: 76.93 g, 472 mmol, 95 %, white solid.

$^1\text{H NMR } \delta$ (CDCl_3) = 6.58 s (2H, =C-H), 5.46 s (2H, H-C-O), 3.18 s (2H, CHCO) ppm.

$^{13}\text{C NMR } \delta$ (CDCl_3) = 169.88 (C=O), 136.96 (C=C), 82.16 (C-O), 48.68 (C-H) ppm.

FTIR: 3088-3195 (ν C-H), 2854-3162 (ν =C-H, ν C=O), 1778 (ν C=O) cm⁻¹.

Experimental

2-(2-Hydroxyethyl)-3a,4,7,7a-tetrahydro-1H-4,7-epoxyisoindol-1,3(2H)-dione: 30.00 g
3a,4,7,7a-tetrahydro-4,7-epoxyisobenzofuran-1,3-dione (180 mmol) was dissolved in 80 mL dry methanol. Then, 50 mL of 3-aminopropanol (659 mmol) in 12 mL of methanol was added dropwise and stirred at room temperature until complete dissolution. The reaction mixture was then heated for 4 hours to reflux. The solvent was removed in vacuo and the residue was stored overnight at -25 °C. The precipitating solid was separated and washed with small amounts of cold methanol.

Yield: 12.62 g, 56 mmol, 31 %, white solid.

^1H NMR δ (CDCl_3) = 6.52 s (2H, =C-H), 5.28 s (2H, H-C-O), 3.65 t (2H, CH_2OH), 3.52 t (2H, CH_2OH) 2.88 s (2H, CHCO), 1.77 m (2H, CH_2) ppm.

^{13}C NMR δ (CDCl_3) = 176.98 (C=O), 136.51 (HC=CH), 80.96 (HC-O), 58.58 (C-OH) , 47.48 (C-H), 35.11 (C-N), 30.29 (CH_2) ppm.

FTIR: 3510 (ν O-H), 3010 (ν =C-H), 2835-2962 (ν C-H), 1687 (ν C=O) cm^{-1} .

2-(1,3-Dioxo-1,3,3a,4,7,7a-hexahydro-2H-4,7-epoxyisoindol-2-yl)ethylmethacrylat: The synthesis was carried out under argon atmosphere. The methacryloyl chloride used was freshly prepared. For this purpose, 16.9 mL of methacrylic acid (200 mmol) and a few drops of DMF were placed in a three-neck flask equipped with a reflux condenser and dropping funnel. Then, 15.3 mL of thionyl chloride (210 mmol) was added dropwise. The reaction mixture was heated to 50 °C for 2 hours. After cooling to room temperature, the crude product was fractionally distilled. (Bpt_{100 mbar}: 35 °C).

14.05 g of 2-(2-hydroxyethyl)-3a,4,7,7a-tetrahydro-1H-4,7-epoxyisoindole-1,3(2H)-dione (63 mmol) was dissolved in 100 mL of dry DCM and cooled to 0°C. 6.6 mL of distilled methacryloyl chloride (68 mmol) was slowly added. Then, 13 mL (94 mmol) of triethylamine was added. The reaction mixture was stirred overnight at room temperature. The precipitated solid was filtered off and the filtrate was washed three times with 75 mL of a saturated sodium bicarbonate solution and three times with water. The crude product was dried over magnesium sulfate and purified by column chromatography (ethyl acetate:dichloromethane = 1:1).

Yield: 11.37 g, 39 mmol, 62 %, pale yellow solid.

^1H NMR δ (CDCl_3) = 6.51 s (2H, =C-H Maleimide), 6.13 m (1H, =C-H methacryl), 5.57 m (1H, =C-H methacryl), 5.26 m (2H, H-C-O), 4.12 t (2H, CH_2OH), 3.61 t (2H, CH_2OH) 2.84 s (2H, CHCO), 1.95-2.01 m (5H, CH_2) ppm.

Experimental

^{13}C NMR δ (CDCl_3) = 176.14 (N-C=O), 167.26 (O-C=O), 136.54, 136.54 (C=CH₂/HC=CH), 125.68 (H₂C=C), 80.96 (HC-O), 61.56 (H₂C-O), 47.42 (C-H), 35.82 (C-N), 26.73 (CH₂), 18.35 (CH₃) ppm.

FTIR: 3510 (v O-H), 3010 (v =C-H), 2835-2962 (v C-H), 1687 (v C=O) cm^{-1} .

CHN_{theo} ($\text{C}_{15}\text{H}_{17}\text{NO}_5$): C: 61.85, H: 5.88, N: 4.81; CHN_{exp} : C: 61.82; H: 5.87, N: 4.80

Furan-2-ylmethyl methacrylate:

14.9 mL furfuryl alcohol (172 mmol) was dissolved in 150 mL dry DCM and cooled to 0 °C. After 10 minutes, 18 mL of freshly distilled methacryloyl chloride (187 mmol) in 20 mL DCM was slowly added. Then 35 mL of triethylamine (252 mmol) was added. The reaction mixture is stirred overnight at room temperature. The resulting trimethylammonium chloride is filtered off and the filtrate is removed from the solvent. The liquid obtained is fractionally distilled on vacuum (Bpt_{2 mbar}: 85 °C).

Yield: 16.42 g, 99 mmol, 57%, colorless oil.

^1H NMR δ (CDCl_3) = 7.42 m (1H, furan), 6.35-6.43 m (2H, furan), 6.36 m (1H, furan), 6.13 m (1H, =CH₂), 5.57-5.58 m (1H, C=H₂), 5.13 s (2H, -CH₂), 1.94 m (3H, -CH₃) ppm.

^{13}C NMR δ (CDCl_3) = 167.06 (C=O), 149.60 (HC=C), 143.23 (HC-O), 136.00 (C=CH₂), 126.10 (CH₂=C), 110.63 (C-H), 110.55 (C-H), 58.29 (CH₂), 18.34 (CH₃) ppm.

FTIR: 3186-3097 (v =C-H), 2902-3012 (v C-H), 1716 (v C=O), 1155 (v C-O) cm^{-1} .

CHN_{theo} ($\text{C}_9\text{H}_{10}\text{O}_3$): C: 65.05, H: 6.07; CHN_{exp} : C: 64.61; H: 6.01

3-Acetylaminoopropanol: 85.7 mL (778 mmol) of isopropenyl acetate and 15 g of 3-aminopropanol were placed in a Schlenk flask and heated to 60 °C for 3 hours. Excess isopropenyl acetate and acetone formed were distilled off. The crude product obtained was fractionally distilled. (Bpt_{0.007 mbar}: 170 °C)

Yield: 22.23 g, 190 mmol, 95 %, yellow oil.

^1H NMR δ (CDCl_3) = 6.67 s (1H, N-H), 3.84 s (1H, O-H), 3.60 t (2H, CH₂-OH), 3.34 td (2H, CH₂-N), 1.98 s (3H, CH₃), 1.66 m (2H, CH₂) ppm.

^{13}C NMR δ (CDCl_3) = 171.71 (C=O), 59.36 (C-O), 36.53 (C-N), 32.09 (CH₂), 23.12 (CH₃) ppm.

FTIR: 3043-3635 (v O-H/N-H), 2809-2990 (v C-H), 1631 (Amid I, v C=O), 1551 (Amid II, v C-N) cm^{-1} .

Experimental

3-Acetamidopropyl methacrylate (H2): 16.86 g (143 mmol) 3-acetylaminoopropanol and 23.9 mL (173 mmol) triethylamine were dissolved in 300 mL DCM and cooled to 0 °C. 16.6 mL (173 mmol) freshly prepared methacryloyl chloride in 40 mL DCM was added dropwise. The reaction mixture was stirred overnight at room temperature. The reaction solution was concentrated to 50 % and stored at -25 °C overnight. The precipitated solid was filtered off and the filtrate was washed twice with 50 mL of water. The organic phase was dried over magnesium sulfate. The crude product was fractionally distilled (Bpt_{0.003 mbar}: 100 °C). To remove final impurities, the product was purified by column chromatography (ethyl acetate).

Yield: 23.79 g, 128 mmol, 74 %, colorless oil.

¹H NMR δ (CDCl₃) = 6.37 s (1H, N-H), 6.05 m (1H, H₂C=C), 5.53 m (1H, H₂C=C), 4.16 t (2H, H₂C-O), 3.28 m (2H, H₂C-N), 1.92 s (3H, CH₃), 1.81-1.93 m (5H, CH₃/CH₂) ppm.

¹³C NMR δ (CDCl₃) = 170.23 (N-C=O), 167.40 (O-C=O), 136.96 (C=CH₂), 125.63 (CH₂=C), 62.05 (H₂C-O), 36.21 (H₂C-N), 28.50 (CH₂), 23.04, 18.14 (CH₃) ppm.

FTIR: 3492-3062 (ν N-H), 2809-2990 (ν C-H/ν =C-H), 1716 (ν C=O), 1631 (Amid I, ν C=O), 1551 (Amid II, ν C-N) cm⁻¹.

CHN_{theo} (C₉H₁₅NO₃): C: 58.36, H: 8.16, N: 7.56; CHN_{exp}: C: 57.55; H: 8.08, N: 8.09

2-(3-Butylureido)ethyl methacrylate (H1): The synthesis was carried out under inert gas. 10 g (64 mmol) acetoisocyanate methacrylate was dissolved in 250 mL DCM. Then 6.4 mL (65 mmol) of butylamine was added dropwise. Stirring was carried out for 1.5 hours at room temperature. The reaction solution was concentrated to 50 mL and cooled to -25 °C. The precipitating solid was filtered off and dried under vacuum.

Yield: 14.34 g, 63 mmol, 98 %, white solid.

¹H NMR δ (CDCl₃) = 6.11 m (1H, H₂C=C), 5.58 m (1H, H₂C=C), 4.72 brs (2H, N-H), 4.22 t (2H, H₂C-O), 3.49 t (2H, H₂C-N), 3.14 t (2H, H₂C-N), 1.94 m (3H, CH₃) 1.29-1.50 m (4H, CH₂), 0.91 t (3H, CH₃) ppm.

¹³C NMR δ (CDCl₃) = 167.60 (O-C=O), 158.24 (N-C=O), 136.03 (C=CH₂), 126.07 (CH₂=C), 64.16 (H₂C-O), 40.39, 39.67 (H₂C-N), 32.20, 10.02, 18.32 (CH₂), 13.77 (CH₃) ppm.

FTIR: 3116-3462 (ν N-H), 2833-3006 (ν C-H/ν =C-H), 1709 (ν C=O), 1618 (Amid I, ν C=O), 1574 (Amid II, ν C-N) cm⁻¹.

CHN_{theo} (C₁₁H₂₀N₂O₃): C: 57.87, H: 8.83, N: 12.27; CHN_{exp}: C: 57.92; H: 8.72, N: 12.05

Experimental

Synthesis of the double self-healing polymers:

PH1: The ARGET ATRP was carried out under inert gas atmosphere. For this purpose, 13.9 mL of BMA (87 mmol), 1.96 g of H1 (8.6 mmol), 1.34 g of FMA (8.1 mmol), and 2.49 g of MIMA (8.5 mmol) were dissolved in 54 mL of toluene and 3 mL of methanol. The solution was degassed with 3 freeze-pump-thaw cycles. Subsequently, 124 mg CuBr (0.86 mmol) and 224 μ L HMTETA (0.82 mmol) were added. The solution was degassed with two more cycles and 126 μ L of degassed EBriB (0.86 mmol) was added. The reaction solution was stirred for 15 hours at 70 °C. Then, 224 μ L of HMTETA and 200 μ L of hydrazine were added again and heating was continued for another 12 hours. The copper complex was removed by column chromatography (alumina active basic, solvent: toluene). To remove unreacted monomer, the polymer was taken up several times with a little THF and precipitated in cold *n*-hexane.

PH2: The ARGET ATRP was carried out under inert gas atmosphere. For this purpose, 13.9 mL BMA (87 mmol), 1.59 g H1 (8.6 mmol), 1.34 g FMA (8.1 mmol), and 2.49 g MIMA (8.5 mmol) were dissolved in 54 mL toluene and 3 mL methanol. The solution was degassed with 3 freeze-pump-thaw cycles. Then, 124 mg of CuBr (0.86 mmol) and 224 μ L of HMTETA (0.82 mmol) were added. The solution was degassed with two more cycles and 126 μ L of degassed EBriB (0.86 mmol) was added. The reaction solution was stirred for 15 hours at 70 °C. Then, 224 μ L of HMTETA and 200 μ L of hydrazine were added again and heating was continued for another 12 hours. The copper complex was removed by column chromatography (alumina active basic, solvent: toluene). To remove unreacted monomer, the polymer was taken up several times with a little THF and precipitated in cold *n*-hexane.

Synthesis of the hydrogen bond-forming phosphonic acid:

N-(10-Bromodecyl) phthalimide: The synthesis was carried out under inert gas. 42.06 g of 1,10-dibromodecane (140 mmol) was dissolved in 59 mL of previously dried DMF. Then, 5.97 g of potassium phthalimide (32 mmol) was added. The reaction mixture was heated under reflux for 8 hours and then stirred overnight at room temperature. The precipitating solid was filtered off and 240 mL of a 1:1:1 mixture of petroleum ether, diethyl ether and a saturated sodium chloride solution was added to the filtrate. The organic phase was separated and concentrated. The crude product obtained was purified by column chromatography (silica, PE:Et₂O = 4:1).

Yield: 8.25 g, 22.52 mmol, 70 %, white solid.

Experimental

^1H NMR δ (CDCl_3) = 7.83-7.85 m (2H, Ar-H), 7.69-7.71 m (2H, Ar-H), 3.67 t (2H, N- CH_2), 3.40 t (2H, Br- CH_2), 1.27-1.87 m (16H, CH_2) ppm.

^{13}C NMR δ (CDCl_3) = 168.64 (C=O), 134.00 (Ar), 132.31 (Ar), 123.30 (Ar), 38.19 (C-N), 34.23 (C-Br), 32.96, 29.48, 29.47, 29.26, 28.85, 28.73, 28.29, 26.96 (CH_2) ppm.

FTIR = 2908 (s, CH_2), 2848 (s, CH_2), 1695 (s, C=O), 1375 (m, C-N) cm^{-1} .

FTIR: 2908 (ν_{as} C-H₂), 2848 (ν_{s} C-H₂), 1763, 1695 (C=O), 1472, 1440, 1375 (C-N), 1193, 1067, 896, 789, 720, 644, 618, 529 cm^{-1} .

N-(10-Phthalimidoalkyl)diethyl phosphonate: 6.62 g of *N*-(10-bromodecyl) phthalimide (18 mmol) was dissolved in 14 mL of triethyl phosphite (80 mmol) and heated at 150 °C for 24 hours. Subsequently, excess triethyl phosphite and the volatile by-products were distilled off. The product was used without further workup.

Yield: 6.77 g, 16 mmol, 89 %, pale yellow oil.

^1H NMR δ (CDCl_3) = 7.77-7.82 m (2H, Ar-H), 7.65-7.69 m (2H, Ar-H), 3.98-4.12 m (4H, O- CH_2) 3.63 t (2H, N- CH_2), 1.19-1.35 m (18H, CH_2) ppm.

^{13}C NMR δ (CDCl_3) = 168.51 (C=O), 133.90 (Ar), 132.22 (Ar), 123.20 (Ar), 61.45, 61.39 (O- CH_2), 38.09 (N- CH_2), 30.72, 30.55, 29.44, 29.33, 29.18, 29.10, 28.63, 26.88, 26.41, 25.02, 22.48, 22.42, 16.58, 16.52 (CH_3) ppm.

^{31}P NMR δ (CDCl_3) = 32.62 ppm.

FTIR: 2928 (ν_{as} C-H₂), 2854 (ν_{s} C-H₂), 1772, 1709 (C=O), 1474, 1440, 1399 (C-N), 1237 (P=O), 1021 (C-O), 951, (P-O), 789, 719, 623, 528 cm^{-1} .

Diethyl (10-aminodecyl) phosphonate: The synthesis was carried out under inert gas. 3.85 g *N*-(10-phthalimidoalkyl) diethyl phosphonate (9 mmol) was dissolved in 394 mL ethanol. The reaction mixture was cooled to 0 °C and then 1.2 mL of hydrazine monohydrate was added dropwise. After an additional 30 minutes at 0 °C, the mixture was refluxed overnight. The precipitating solid was filtered off and washed with small amounts of DCM. The ^1H and ^{13}C NMR still showed minor signals of the educt. These were also observed after another 24 hours reaction time with fresh hydrazine. Due to the similar polarity and the very high boiling points of both substances, they could not be separated by column chromatography or distillation.

Yield: 2.57 g, 8.74 mmol, 89 %, yellow oil.

Experimental

^1H NMR δ (CDCl_3) = 3.99-4.13 m (4H, O- CH_2), 3.55 brs (2H, NH_2), 2.70 t (2H, N- CH_2), 1.24-1.73 m (24H, N- CH_2) ppm.

^{13}C NMR δ (CDCl_3) = 61.51, 61.44 (O- CH_2), 41.84 (N- CH_2), 32.77, 30.78, 30.61, 29.59, 29.46, 29.39, 29.16, 26.92, 26.46, 25.07, 22.51, 22.46, 16.62, 16.56 (CH_3) ppm.

^{31}P NMR δ (CDCl_3) = 32.65 ppm.

FTIR: 3575-3259 (ν N-H), 2926 (ν_{as} C-H $_2$), 2855 (ν_{s} C-H $_2$), 1646, 1572, 1452, 1243 (P=O), 1025 (C-O), 955, (P-O), 782, 700, 544, 490 cm^{-1} .

Diethyl (10-(3-propylureido) decyl) phosphonate: The synthesis was carried out under inert gas. 1.36 g diethyl (10-aminodecyl) phosphonate (4.6 mmol) was dissolved in 10 mL dry DCM. The reaction mixture was cooled to 0 °C and 0.4 mL of propyl isocyanate was added dropwise. Stirring was then continued for another hour at room temperature. The solvent was removed. Here, too, the product still contains the impurity from the precursor.

Yield: 1.61 g, 4.26 mmol, 92 %, yellow oil.

^1H NMR δ (CDCl_3) = 4.01-4.15 m (4H, O- CH_2), 3.10-3.16 m (4H, N- CH_2), 0.94-1.76 m (26H, CH_2 /O- CH_2 - CH_3), 0.92 t (3H, CH_3) ppm.

^{13}C NMR δ (CDCl_3) = 158.69 (C=O), 61.63, 61.56 (O- CH_2), 42.50 (N- CH_2), 40.75 (N- CH_2), 30.58, 30.42, 30.21, 29.34, 29.22, 29.08, 28.96, 26.85, 26.38, 24.98, 23.53, 22.39, 22.34, 16.65 (O- CH_2 - CH_3), 16.59 (O- CH_2 - CH_3), 11.51(CH_3) ppm.

^{31}P NMR δ (CDCl_3) = 32.65 ppm.

FTIR: 3323 (N-H), 2927 (ν_{as} C-H $_2$), 2854 (ν_{s} C-H $_2$), 1620 (Amid I, ν C=O), 1577 (Amid II, ν C-N) (C=O), 1474, 1380, 1233 (P=O), 1030 (C-O), 965, (P-O), 811, 615, 537, 490 cm^{-1} .

(10-(3-Propylureido) decyl) phosphonic acid: The synthesis was carried out under inert gas. 1.59 g diethyl (10-(3-propylureido) decyl) phosphonate (4.2 mmol) was dissolved in 10 mL dichloromethane. Then, 1.1 mL of bromotrimethylsilane was added dropwise (8.4 mmol). The reaction mixture was stirred for 6 hours at room temperature. The solvent was removed and 10 mL of a methanol/water mixture was added (6:4). The mixture was stirred overnight at room temperature. The precipitating solid was filtered off washed with a little cold dichloromethane and dried. The product shows a small impurity in the ^{31}P NMR spectrum.

Yield: 0.75 g, 2.33 mmol, 56 %, pale yellow solid.

Experimental

^1H NMR δ (MeOH- d_4) = 3.10-3.08 m (4H, N-CH₂), 1.26-1.71 m (22H, CH₂), 0.88 t (3H, CH₃) ppm.

^{13}C NMR δ (MeOH- d_4) = 161.40 (C=O), 42.80 (N-CH₂), 41.00 (N-CH₂), 31.84, 31.68, 31.35, 30.65, 30.45, 30.27, 28.78, 27.92, 27.41, 24.51, 23.94, 23.90 (CH₂), 11.61 (CH₃) ppm.

^{31}P NMR δ (MeOH- d_4) = 30.23 ppm.

FTIR: 3325 (N-H), 2922 (ν_{as} C-H₂), 2849 (ν_{s} C-H₂), 2771 (ν_{as} PO-H), 2265 (ν_{s} PO-H), 1616 (Amid I, ν C=O), 1577 (Amid II, ν C-N) (C=O), 1469, 1326, 1261, 1223, 1101, 1053, 993, 941, 781, 730, 625, 534, 500 cm^{-1} .

Self-Healing Nanocomposites Based on Ionic Interactions and DA Chemistry

S-(2-Hydroxyethyl) ethanethioat: The synthesis was carried out according to Kröger.[698] 4 g of potassium thioacetate (35 mmol) was dissolved in 55 mL of acetone. Then 2.4 mL of 2-bromoethanol (34 mmol) in 15 mL of acetone was added dropwise. Stirring was carried out overnight at room temperature. The resulting solid was filtered off and the filtrate was freed from the solvent. The product obtained was taken up with dichloromethane and washed with water. The organic phase was dried over sodium sulfate and the solvent was removed.

Yield: 2.41 g, 20 mmol, 59 %, yellow liquid.

^1H NMR δ (CDCl₃) = 3.77 t (2H, CH₂O), 3.08 t (2H, CH₂S), 2.36 s (3H, CH₃) ppm.

2-(Acetylthio)ethyl methacrylate: The synthesis was carried out according to Kröger.[698] 2.39 g *S*-(2-hydroxyethyl) ethanethioat (20 mmol) was dissolved in 24 mL dry dichloromethane. Then, 3.5 mL of triethylamine was injected directly into the solution via a syringe and the solution was cooled to 0 °C. Then, 2.7 mL of freshly prepared methacryloyl chloride in 10 mL of dry dichloromethane was added dropwise. Stirring was performed for one hour at 0 °C and overnight at room temperature. The reaction mixture was extracted twice with 45 mL of water and 0.5 M HCl. The still highly contaminated product was purified by vacuum distillation in the presence of hydroquinone as a radical scavenger.

Yield: 2.11 g, 11 mmol, 56 %, yellow liquid.

^1H NMR δ (CDCl₃) = 6.11 m (1H, =CH₂), 5.58 m (1H, =CH₂), 4.25 t (2H, CH₂S), 3.18 t (2H, CH₂O) 2.35 s (3H, CH₃), 1.93 s (3H, CH₃) ppm.

Experimental

Table 23: Approaches towards ionic /DA-double self-healing systems.

Polym. Technique	Monomer	Initiator	Cu-Ligand/CTA	Solvent	Result
ATRP	SMBS co BMA	EBriB	HMTETA	Toluene	Main Product: poly(BMA), no reaction of SMBS was observed
ATRP	SMBS co BMA	EBriB	2,2'-Bipyridine	Methanol:Water (2:3)	Insoluble solid, FTIR shows signals of both components
ATRP	SMBS co BMA	EBriB	HMTETA	Methanol:Water (2:3)	Insoluble solid, FTIR shows signals of both components
FRP	SMBS co BMA	AIBN	-	Toluene	Main Product: poly(BMA), no reaction of SMBS was observed
FRP	SMBS co BMA	AIBN	-	Methanol:Water (2:3)	Insoluble solid, FTIR shows signals of both components
FRP	SMBS co BMA	AIBN	-	Methanol:2-Propanol:Water (1:1:1)	poly(BMA), second insoluble phase shows signals of both components
ARGET ATRP	FMA co MIMA co SMBS co BMA	EBriB	HMTETA	Toluene	Main product: poly(BMA); no copolymer was observed
FRP	FMA co MIMA co SMBS co BMA	AIBN	-	Methanol:Water (2:3)	Main product: poly(BMA) (in solution); Traces of poly(FMA-co-MIMA-co-SMBS-co-BMA) were obtained as precipitate
RAFT	FMA co MIMA co SMBS co BMA	AIBN	2-Cyanoprop-2-ylidithiobenzoat	Methanol:Water (2:3)	Main product: poly(BMA); no copolymer was observed
ARGET ATRP	MA co BMA	EBriB	HMTETA	Toluene:Methanol (1:1)	Successful copolymerization; Successful synthesis of poly(SMBS-co-BMA) after reaction with 1,4-butanedisulfone
FRP	MA co BMA	AIBN	-	Toluene:Methanol (1:2)	Successful copolymerization; Successful synthesis of poly(SMBS-co-BMA) after reaction with 1,4-butanedisulfone
ATRP	2-(Acetylthio)ethylmethacrylat co BMA	EBriB	HMTETA	Toluene:Methanol (1:1)	Successful polymerization; Product insoluble after deprotection; oxidation yields a soluble product but not the desired copolymer (decomposition)
FRP	2-(Acetylthio)ethylmethacrylat co BMA	EBriB	HMTETA	Toluene:Methanol (1:1)	Successful polymerization; Product insoluble after deprotection; oxidation yields a soluble product but not the desired copolymer (decomposition)
ARGET ATRP	FMA co DEGMA	EBriB	2,2'-Bipyridine	MEK:Methanol (3:1)	Successful synthesis of the copolymer
ARGET ATRP	MIMA co DEGMA	EBriB	2,2'-Bipyridine	MEK:Methanol (3:1)	No copolymer obtained
ARGET ATRP	MIMA co DEGMA	EBriB	2,2'-Bipyridine	Toluene	Successful synthesis of the copolymer, yield < 10 %
ARGET ATRP	FMA co MIMA co SMBS co DEGMA	EBriB	2,2'-Bipyridine	MEK:Water:Ethanol (10:3:1)	Successful synthesis of the copolymer, but poor reproducibility
ARGET ATRP	FMA co SMBS co DEGMA	EBriB	2,2'-Bipyridine	MEK:Water:Ethanol (10:3:1)	Successful synthesis of the copolymer

6. References

- [1] Alkaç, İ.M.; Çerçi, B.; Timuralp, C.; Şen, F. *Nanomaterials and Their Classification*. In *Nanomaterials for Direct Alcohol Fuel Cells*; Elsevier, **2021**. DOI: 10.1016/B978-0-12-821713-9.00011-1.
- [2] Bayda, S.; Adeel, M.; Tuccinardi, T.; Cordani, M.; Rizzolio, F. The History of Nanoscience and Nanotechnology: From Chemical–Physical Applications to Nanomedicine. *Molecules*, **2019**, *25*, 112. DOI: 10.3390/molecules25010112.
- [3] Schaming, D.; Remita, H. Nanotechnology: From the Ancient Time to Nowadays. *Found. Chem.*, **2015**, *17*, 187–205. DOI: 10.1007/s10698-015-9235-y.
- [4] Ostwald, W. *Die Welt Der Vernachlässigten Dimensionen: Eine Einführung in Die Kolloidchemie, Mit Besonderer Berücksichtigung Ihrer Anwendungen.*; Verlag Theodor Steinkopff Dresden, **1914**.
- [5] Work, W.J.; Horie, K.; Hess, M.; Stepto, R.F.T. Definition of Terms Related to Polymer Blends, Composites, and Multiphase Polymeric Materials (IUPAC Recommendations 2004). *Pure Appl. Chem.*, **2004**, *76*, 1985–2007. DOI: 10.1351/pac200476111985.
- [6] Omanović-Miklićanin, E.; Badnjević, A.; Kazlagić, A.; Hajlovac, M. Nanocomposites: A Brief Review. *Health Technol.*, **2020**, *10*, 51–59. DOI: 10.1007/s12553-019-00380-x.
- [7] Folarin, O.M.; Sadiku, E.R.; Maity, A. Polymer-Noble Metal Nanocomposites: Review. *Int. J. Phys. Sci.*, **2011**, *6*, 4869–4882.
- [8] Siva Prasanna, S.R.V.; Balaji, K.; Pandey, S.; Rana, S. *Metal Oxide Based Nanomaterials and Their Polymer Nanocomposites*; Elsevier Inc., **2018**. DOI: 10.1016/B978-0-12-814615-6.00004-7.
- [9] Panahi-Sarmad, M.; Noroozi, M.; Abrisham, M.; Eghbalinia, S.; Teimoury, F.; Bahramian, A.R.; Dehghan, P.; Sadri, M.; Goodarzi, V. A Comprehensive Review on Carbon-Based Polymer Nanocomposite Foams as Electromagnetic Interference Shields and Piezoresistive Sensors. *ACS Appl. Electron. Mater.*, **2020**, *2*, 2318–2350. DOI: 10.1021/acsaelm.0c00490.
- [10] Zhang, Z.; Zhang, P.; Wang, Y.; Zhang, W. Recent Advances in Organic-Inorganic Well-Defined Hybrid Polymers Using Controlled Living Radical Polymerization Techniques. *Polym. Chem.*, **2016**, *7*, 3950–3976. DOI: 10.1039/c6py00675b.
- [11] Thostenson, E.T.; Li, C.; Chou, T.W. Nanocomposites in Context. *Compos. Sci. Technol.*, **2005**, *65*, 491–516. DOI: 10.1016/j.compscitech.2004.11.003.
- [12] Schaefer, D.W.; Justice, R.S. How Nano Are Nanocomposites? *Macromolecules*, **2007**, *40*, 8501–8517. DOI: 10.1021/ma070356w.
- [13] Harito, C.; Bavykin, D. V.; Yuliarto, B.; Dipojono, H.K.; Walsh, F.C. Polymer Nanocomposites Having a High Filler Content: Synthesis, Structures, Properties, and Applications. *Nanoscale*, **2019**, *11*, 4653–4682. DOI: 10.1039/c9nr00117d.
- [14] Ates, B.; Koytepe, S.; Ulu, A.; Gurses, C.; Thakur, V.K. Chemistry, Structures, and Advanced Applications of Nanocomposites from Biorenewable Resources. *Chem. Rev.*, **2020**, *120*, 9304–9362. DOI: 10.1021/acs.chemrev.9b00553.
- [15] Wang, G.T.; Liu, H.Y.; Saintier, N.; Mai, Y.W. Cyclic Fatigue of Polymer Nanocomposites. *Eng. Fail. Anal.*, **2009**, *16*, 2635–2645. DOI: 10.1016/j.engfailanal.2009.04.022.

References

- [16] Xu, P.-P.; Zhang, S.-M.; Huang, H.-D.; Xu, L.; Zhong, G.-J.; Li, Z.-M. Highly Efficient Three-Dimensional Gas Barrier Network for Biodegradable Nanocomposite Films at Extremely Low Loading Levels of Graphene Oxide Nanosheets. *Ind. Eng. Chem. Res.*, **2020**, *59*, 5818–5827. DOI: 10.1021/acs.iecr.9b06810.
- [17] Merritt, S.M.J.; Wemyss, A.M.; Farris, S.; Patole, S.; Patias, G.; Haddleton, D.M.; Shollock, B.; Wan, C. Gas Barrier Polymer Nanocomposite Films Prepared by Graphene Oxide Encapsulated Polystyrene Microparticles. *ACS Appl. Polym. Mater.*, **2020**, *2*, 725–731. DOI: 10.1021/acsapm.9b01041.
- [18] Shifrina, Z.B.; Matveeva, V.G.; Bronstein, L.M. Role of Polymer Structures in Catalysis by Transition Metal and Metal Oxide Nanoparticle Composites. *Chem. Rev.*, **2020**, *120*, 1350–1396. DOI: 10.1021/acs.chemrev.9b00137.
- [19] Gelaw, T.B.; Sarojini, B.K.; Kodoth, A.K. Review of the Advancements on Polymer/Metal Oxide Hybrid Nanocomposite-Based Adsorption Assisted Photocatalytic Materials for Dye Removal. *ChemistrySelect*, **2021**, *6*, 9300–9310. DOI: 10.1002/slct.202102020.
- [20] Hossain, S.K.S.; Hoque, M.E. *Polymer Nanocomposite Materials in Energy Storage: Properties and Applications*; Elsevier Ltd., **2018**. DOI: 10.1016/B978-0-08-102262-7.00009-X.
- [21] Li, S.; Meng Lin, M.; Toprak, M.S.; Kim, D.K.; Muhammed, M. Nanocomposites of Polymer and Inorganic Nanoparticles for Optical and Magnetic Applications. *Nano Rev.*, **2010**, *1*, 5214. DOI: 10.3402/nano.v1i0.5214.
- [22] Emam, H.E.; Ahmed, H.B.; Abdelhameed, R.M. Melt Intercalation Technique for Synthesis of Hetero-Metallic@chitin Bio-Composite as Recyclable Catalyst for Prothiofos Hydrolysis. *Carbohydr. Polym.*, **2021**, *266*, 118163. DOI: 10.1016/j.carbpol.2021.118163.
- [23] Khvan, S.; Kim, J.; Lee, S.-S. Fabrication of Pre-Exfoliated Clay Masterbatch via Exfoliation-Adsorption of Polystyrene Nanobeads. *Macromol. Res.*, **2007**, *15*, 51–58. DOI: 10.1007/BF03218752.
- [24] Zhang, Y.; Zhu, B.; Cai, X.; Yuan, X.; Zhao, S.; Yu, J.; Qiao, K.; Qin, R. Rapid In Situ Polymerization of Polyacrylonitrile/Graphene Oxide Nanocomposites as Precursors for High-Strength Carbon Nanofibers. *ACS Appl. Mater. Interfaces*, **2021**, *13*, 16846–16858. DOI: 10.1021/acsami.1c02643.
- [25] Guo, Q.; Ghadiri, R.; Weigel, T.; Aumann, A.; Gurevich, E.; Esen, C.; Medenbach, O.; Cheng, W.; Chichkov, B.; Ostendorf, A. Comparison of in Situ and Ex Situ Methods for Synthesis of Two-Photon Polymerization Polymer Nanocomposites. *Polymers*, **2014**, *6*, 2037–2050. DOI: 10.3390/polym6072037.
- [26] Macchione, M.A.; Biglione, C.; Strumia, M. Design, Synthesis and Architectures of Hybrid Nanomaterials for Therapy and Diagnosis Applications. *Polymers*, **2018**, *10*, 527. DOI: 10.3390/polym10050527.
- [27] Rubio, N.; Au, H.; Leese, H.S.; Hu, S.; Clancy, A.J.; Shaffer, M.S.P.P. Grafting from versus Grafting to Approaches for the Functionalization of Graphene Nanoplatelets with poly(Methyl Methacrylate). *Macromolecules*, **2017**, *50*, 7070–7079. DOI: 10.1021/acs.macromol.7b01047.
- [28] Benoit, D.N.; Zhu, H.; Lillierose, M.H.; Verm, R.A.; Ali, N.; Morrison, A.N.; Fortner, J.D.; Avendano, C.; Colvin, V.L. Measuring the Grafting Density of Nanoparticles in Solution by Analytical Ultracentrifugation and Total Organic Carbon Analysis. *Anal. Chem.*, **2012**, *84*, 9238–9245. DOI: 10.1021/ac301980a.
- [29] Zdyrko, B.; Luzinov, I. Polymer Brushes by the “Grafting to” Method. *Macromol. Rapid*

References

- Commun.*, **2011**, 32, 859–869. DOI: 10.1002/marc.201100162.
- [30] Lechner, M.D.; Gehrke, K.; Nordmeier, E.H. *Makromolekulare Chemie*; Springer Berlin Heidelberg: Berlin, Heidelberg, **2014**. DOI: 10.1007/978-3-642-41769-6.
- [31] Moad, G.; Solomon, D.H. *The Chemistry of Radical Polymerization*; 2nd ed.; Elsevier Science Ltd, Amsterdam, **2005**.
- [32] Odian, G. *Radical Chain Polymerization in Principles of Polymerization*; 4th ed.; John Wiley & Sons, Hoboken, **2004**.
- [33] Szwarc, M. Living Polymers. *Nature*, **1956**, 178, 1168–1169. DOI: 10.1038/1781168a0.
- [34] Jenkins, A.D.; Kratochvíl, P.; Stepto, R.F.T.; Suter, U.W. Glossary of Basic Terms in Polymer Science (IUPAC Recommendations 1996). *Pure Appl. Chem.*, **1996**, 68, 2287–2311. DOI: 10.1351/pac199668122287.
- [35] Webster, O.W. Living Polymerization Methods. *Science*, **1991**, 251, 887–893. DOI: 10.1126/science.251.4996.887.
- [36] Höcker, H. Directed Polymer Synthesis for Industrial Application. *Macromol. Symp.*, **1996**, 101, 1–9. DOI: 10.1002/masy.19961010103.
- [37] Smith, Q.A.; Storey, R.F. Quasiliving Cationic Polymerization of Styrene and Isobutylene: Run Number and Apparent Rate Constant of Ionization by TiCl₄ and Energies of Activation of Elementary Reactions. *Macromolecules*, **2005**, 38, 4983–4988. DOI: 10.1021/ma050470j.
- [38] Jenkins, A.D.; Jones, R.G.; Moad, G. Terminology for Reversible-Deactivation Radical Polymerization Previously Called “Controlled” Radical or “Living” Radical Polymerization (IUPAC Recommendations 2010). *Pure Appl. Chem.*, **2009**, 82, 483–491. DOI: 10.1351/PAC-REP-08-04-03.
- [39] Otsu, T.; Yoshida, M.; Tazaki, T. A Model for Living Radical Polymerization. *Die Makromol. Chemie, Rapid Commun.*, **1982**, 3, 133–140. DOI: 10.1002/marc.1982.030030209.
- [40] Otsu, T.; Yoshida, M. Efficient Synthesis of Two or Multi Component Block Copolymers through Living Radical Polymerization with Polymeric Photoiniferters. *Polym. Bull.*, **1982**, 7, 197–203. DOI: 10.1007/BF00255315.
- [41] Otsu, T.; Yoshida, M. Role of Initiator-Transfer Agent-Terminator (Iniferter) in Radical Polymerizations: Polymer Design by Organic Disulfides as Iniferters. *Die Makromol. Chemie, Rapid Commun.*, **1982**, 3, 127–132. DOI: 10.1002/marc.1982.030030208.
- [42] Otsu, T. Iniferter Concept and Living Radical Polymerization. *J. Polym. Sci. Part A Polym. Chem.*, **2000**, 38, 2121–2136. DOI: 10.1002/(SICI)1099-0518(20000615)38:12<2121::AID-POLA10>3.0.CO;2-X.
- [43] Meijs, G.F.; Rizzardo, E. Chain Transfer by an Addition-Fragmentation Mechanism The Use of α -Benzyloxystyrene for the Preparation of Low- Molecular-Weight poly(Methyl Methacrylate) and Polystyrene. *Macromolecules*, **1988**, 9, 547–551. DOI: 10.1002/marc.1988.030090807.
- [44] Meijs, G.F.; Rizzardo, E.; Thang, S.H. Preparation of Controlled Molecular Weight, Olefin-Terminated Polymers by Free Radical Methods. Chain Transfer Using Allylic Sulfides. *Macromolecules*, **1988**, 21, 3122–3124. DOI: 10.1021/ma00188a039.
- [45] Moad, G.; Rizzardo, E. A 20th Anniversary Perspective on the Life of RAFT (RAFT Coming of Age). *Polym. Int.*, **2020**, 69, 658–661. DOI: 10.1002/pi.5944.

References

- [46] Perrier, S. 50th Anniversary Perspective: RAFT Polymerization—A User Guide. *Macromolecules*, **2017**, *50*, 7433–7447. DOI: 10.1021/acs.macromol.7b00767.
- [47] Goto, A.; Ohno, K.; Fukuda, T. Mechanism and Kinetics of Iodide-Mediated Polymerization of Styrene. *Macromolecules*, **1998**, *31*, 2809–2814. DOI: 10.1021/ma9712007.
- [48] Boyer, C.; Valade, D.; Sauguet, L.; Ameduri, B.; Boutevin, B. Iodine Transfer Polymerization (ITP) of Vinylidene Fluoride (VDF). Influence of the Defect of VDF Chaining on the Control of ITP. *Macromolecules*, **2005**, *38*, 10353–10362. DOI: 10.1021/ma051349f.
- [49] Hawker, C.J.; Bosman, A.W.; Harth, E. New Polymer Synthesis by Nitroxide Mediated Living Radical Polymerizations. *Chem. Rev.*, **2001**, *101*, 3661–3688. DOI: 10.1021/cr990119u.
- [50] Wang, J.-S.; Matyjaszewski, K. Controlled /“ Living ” Radical Polymerization . Atom Transfer Radical Polymerization in the Presence of Transition-Metal Complexes. *J. Am. Chem. Soc.*, **1995**, *117*, 5614–5615. DOI: 10.1021/ma980725b.
- [51] Kato, M.; Kamigaito, M.; Sawamoto, M.; Higashimura, T. Polymerization of Methyl Methacrylate with the Carbon Tetrachloride/Dichlorotris(Triphenylphosphine)-Ruthenium(II)/Methylaluminum Bis(2,6-Di-Tert-Butylphenoxide) Initiating System: Possibility of Living Radical Polymerization. *Macromolecules*, **1995**, *28*, 1721–1723. DOI: 10.1021/ma00109a056.
- [52] Matyjaszewski, K. Mechanistic and Synthetic Aspects of Atom Transfer Radical Polymerization. *J. Macromol. Sci. Part A*, **1997**, *34*, 1785–1801. DOI: 10.1080/10601329708010308.
- [53] Kabachii, Y.A.; Kochev, S.Y.; Bronstein, L.M.; Blagodatskikh, I.B.; Valetsky, P.M. Atom Transfer Radical Polymerization with Ti(III) Halides and Alkoxides. *Polym. Bull.*, **2003**, *50*, 271–278. DOI: 10.1007/s00289-003-0157-9.
- [54] Poli, R.; Allan, L.E.N.; Shaver, M.P. Iron-Mediated Reversible Deactivation Controlled Radical Polymerization. *Prog. Polym. Sci.*, **2014**, *39*, 1827–1845. DOI: 10.1016/j.progpolymsci.2014.06.003.
- [55] Dadashi-Silab, S.; Matyjaszewski, K. Iron Catalysts in Atom Transfer Radical Polymerization. *Molecules*, **2020**, *25*, 1648. DOI: 10.3390/molecules25071648.
- [56] Cruz, T.F.C.; Machado, P.M.M.; Gomes, C.S.B.; Ascenso, J.R.; Lemos, M.A.N.D.A.; Bordado, J.C.; Gomes, P.T. Bis(Formylpyrrolyl) Cobalt Complexes as Mediators in the Reversible-Deactivation Radical Polymerization of Styrene and Methyl Methacrylate. *New J. Chem.*, **2018**, *42*, 5900–5913. DOI: 10.1039/C8NJ00350E.
- [57] Weiser, M.-S.; Mülhaupt, R. Cobalt(II) Octanoate and Cobalt(II) Perfluorooctanoate Catalyzed Atom Transfer Radical Polymerization of Styrene in Toluene and Fluorous Media—A Versatile Route to Catalyst Recycling and Oligomer Formation. *J. Polym. Sci. Part A Polym. Chem.*, **2005**, *43*, 3804–3813. DOI: 10.1002/pola.20873.
- [58] Duquesne, E.; Habimana, J.; Degée, P.; Dubois, P. Nickel-Catalyzed Supported ATRP of Methyl Methacrylate Using Cross-Linked Polystyrene Triphenylphosphine as Ligand. *Macromolecules*, **2005**, *38*, 9999–10006. DOI: 10.1021/ma051413t.
- [59] Le Grogneec, E.; Claverie, J.; Poli, R. Radical Polymerization of Styrene Controlled by Half-Sandwich Mo(III)/Mo(IV) Couples: All Basic Mechanisms Are Possible. *J. Am. Chem. Soc.*, **2001**, *123*, 9513–9524. DOI: 10.1021/ja010998d.
- [60] Maria, S.; Stoffelbach, F.; Mata, J.; Daran, J.-C.; Richard, P.; Poli, R. The Radical Trap in Atom Transfer Radical Polymerization Need Not Be Thermodynamically Stable. A

References

- Study of the $\text{MoX}_3(\text{PMe}_3)_3$ Catalysts. *J. Am. Chem. Soc.*, **2005**, *127*, 5946–5956. DOI: 10.1021/ja043078e.
- [61] Idehara, A.H.S.; Gois, P.D.S.; Fernandez, H.; Goi, B.E.; Machado, A.E.H.; Lima-Neto, B.S.; Carvalho, V.P. Accessible Ring Opening Metathesis and Atom Transfer Radical Polymerization Catalysts Based on Dimethyl Sulfoxide Ruthenium(II) Complexes Bearing N-Heterocyclic Carbene Ligands. *Mol. Catal.*, **2018**, *448*, 135–143. DOI: 10.1016/j.mcat.2018.01.032.
- [62] Delaude, L.; Delfosse, S.; Richel, A.; Demonceau, A.; Noels, A.F. Tuning of Ruthenium N-Heterocyclic Carbene Catalysts for ATRP. *Chem. Commun.*, **2003**, *3*, 1526–1527. DOI: 10.1039/b301733h.
- [63] Sunjuk, M.; Abu-Surrah, A.S.; Abu Safieh, K.A.; Qaroush, A.K.; Al-Qaisi, F.M. γ -Diimine Palladium(II) Based Complexes Mediated Polymerization of Methyl Methacrylate. *Arab. J. Chem.*, **2017**, *10*, S1209–S1215. DOI: 10.1016/j.arabjc.2013.02.019.
- [64] Ye, J.; Ye, Z. “Living” Polymerization of Ethylene and 1-Hexene Using Novel Binuclear Pd–Diimine Catalysts. *Polymers*, **2017**, *9*, 282. DOI: 10.3390/polym9070282.
- [65] Kotani, Y.; Kamigaito, M.; Sawamoto, M. Re(V)-Mediated Living Radical Polymerization of Styrene: $^1\text{ReO}_2\text{I}(\text{PPh}_3)_2/\text{R-I}$ Initiating Systems. *Macromolecules*, **1999**, *32*, 2420–2424. DOI: 10.1021/ma981614f.
- [66] Seeliger, F.; Matyjaszewski, K. Temperature Effect on Activation Rate Constants in ATRP: New Mechanistic Insights into the Activation Process. *Macromolecules*, **2009**, *42*, 6050–6055. DOI: 10.1021/ma9010507.
- [67] Braunecker, W.A.; Tsarevsky, N. V.; Gennaro, A.; Matyjaszewski, K. Thermodynamic Components of the Atom Transfer Radical Polymerization Equilibrium: Quantifying Solvent Effects. *Macromolecules*, **2009**, *42*, 6348–6360. DOI: 10.1021/ma901094s.
- [68] Tang, W.; Matyjaszewski, K. Effect of Ligand Structure on Activation Rate Constants in ATRP. *Macromolecules*, **2006**, *39*, 4953–4959. DOI: 10.1021/ma0609634.
- [69] Tang, W.; Matyjaszewski, K. Effects of Initiator Structure on Activation Rate Constants in ATRP. *Macromolecules*, **2007**, *40*, 1858–1863. DOI: 10.1021/ma062897b.
- [70] Wang, J.-S.; Matyjaszewski, K. “Living”/Controlled Radical Polymerization. Transition-Metal-Catalyzed Atom Transfer Radical Polymerization in the Presence of a Conventional Radical Initiator. *Macromolecules*, **1995**, *28*, 7572–7573. DOI: 10.1021/ma00126a041.
- [71] Jakubowski, W.; Min, K.; Matyjaszewski, K. Activators Regenerated by Electron Transfer for Atom Transfer Radical Polymerization of Styrene. *Macromolecules*, **2006**, *39*, 39–45. DOI: 10.1021/ma0522716.
- [72] Jakubowski, W.; Matyjaszewski, K. Activators Regenerated by Electron Transfer for Atom-Transfer Radical Polymerization of (Meth)Acrylates and Related Block Copolymers. *Angew. Chemie*, **2006**, *118*, 4594–4598. DOI: 10.1002/ange.200600272.
- [73] Schäfer, S.; Kickelbick, G. Double Reversible Networks: Improvement of Self-Healing in Hybrid Materials via Combination of Diels–Alder Cross-Linking and Hydrogen Bonds. *Macromolecules*, **2018**, *51*, 6099–6110. DOI: 10.1021/acs.macromol.8b00601.
- [74] Matyjaszewski, K.; Jakubowski, W.; Min, K.; Tang, W.; Huang, J.; Braunecker, W.A.; Tsarevsky, N. V. Diminishing Catalyst Concentration in Atom Transfer Radical Polymerization with Reducing Agents. *Proc. Natl. Acad. Sci.*, **2006**, *103*, 15309–15314. DOI: 10.1073/pnas.0602675103.
- [75] Dong, H.; Matyjaszewski, K. ARGET ATRP of 2-(Dimethylamino)Ethyl Methacrylate as

References

- an Intrinsic Reducing Agent. *Macromolecules*, **2008**, *41*, 6868–6870. DOI: 10.1021/ma8017553.
- [76] Kwak, Y.; Magenau, A.J.D.; Matyjaszewski, K. ARGET ATRP of Methyl Acrylate with Inexpensive Ligands and Ppm Concentrations of Catalyst. *Macromolecules*, **2011**, *44*, 811–819. DOI: 10.1021/ma102665c.
- [77] Coca, S.; Jasieczek, C.B.; Beers, K.L.; Matyjaszewski, K. Polymerization of Acrylates by Atom Transfer Radical Polymerization. Homopolymerization of 2-Hydroxyethyl Acrylate. *J. Polym. Sci. Part A Polym. Chem.*, **1998**, *36*, 1417–1424. DOI: 10.1002/(SICI)1099-0518(19980715)36:9<1417::AID-POLA9>3.0.CO;2-P.
- [78] Jewrajka, S.K.; Mandal, B.M. Living Radical Polymerization. II. Improved Atom Transfer Radical Polymerization of Acrylamide in Aqueous Glycerol Media with a Novel Pentamethyldiethylenetriamine-Based Soluble Copper(I) Complex Catalyst System. *J. Polym. Sci. Part A Polym. Chem.*, **2004**, *42*, 2483–2494. DOI: 10.1002/pola.20062.
- [79] Fantin, M.; Isse, A.A.; Gennaro, A.; Matyjaszewski, K. Understanding the Fundamentals of Aqueous ATRP and Defining Conditions for Better Control. *Macromolecules*, **2015**, *48*, 6862–6875. DOI: 10.1021/acs.macromol.5b01454.
- [80] Smolne, S.; Buback, M. Kinetic Investigations of Cu-Mediated ATRP in Aqueous Solution. *Macromol. Chem. Phys.*, **2015**, *216*, 894–902. DOI: 10.1002/macp.201400589.
- [81] Tsarevsky, N. V.; Pintauer, T.; Matyjaszewski, K. Deactivation Efficiency and Degree of Control over Polymerization in ATRP in Protic Solvents. *Macromolecules*, **2004**, *37*, 9768–9778. DOI: 10.1021/ma048438x.
- [82] Li, J.; Xiao, H.; Kim, Y.S.; Lowe, T.L. Synthesis of Water-Soluble Cationic Polymers with Star-like Structure Based on Cyclodextrin Core via ATRP. *J. Polym. Sci. Part A Polym. Chem.*, **2005**, *43*, 6345–6354. DOI: 10.1002/pola.21058.
- [83] Mendonça, P. V.; Konkolewicz, D.; Averick, S.E.; Serra, A.C.; Popov, A. V.; Guliashvili, T.; Matyjaszewski, K.; Coelho, J.F.J. Synthesis of Cationic poly((3-Acrylamidopropyl)Trimethylammonium Chloride) by SARA ATRP in Ecofriendly Solvent Mixtures. *Polym. Chem.*, **2014**, *5*, 5829–5836. DOI: 10.1039/c4py00707g.
- [84] Cho, H.Y.; Averick, S.E.; Paredes, E.; Wegner, K.; Averick, A.; Jurga, S.; Das, S.R.; Matyjaszewski, K. Star Polymers with a Cationic Core Prepared by ATRP for Cellular Nucleic Acids Delivery. *Biomacromolecules*, **2013**, *14*, 1262–1267. DOI: 10.1021/bm4003199.
- [85] Scott, C.; Mitrovic, B.; Eastwood, S.; Kinsel, G. Stimuli Response of Cationic Polymer Brush Prepared by ATRP: Application in Peptide Fractionation. *Polymer*, **2014**, *55*, 3551–3556. DOI: 10.1016/j.polymer.2014.06.075.
- [86] Matyjaszewski, K. Atom Transfer Radical Polymerization (ATRP): Current Status and Future Perspectives. *Macromolecules*, **2012**, *45*, 4015–4039. DOI: 10.1021/ma3001719.
- [87] Mori, H.; Müller, A.H.E. New Polymeric Architectures with (Meth)Acrylic Acid Segments. *Prog. Polym. Sci.*, **2003**, *28*, 1403–1439. DOI: 10.1016/S0079-6700(03)00076-5.
- [88] Iddon, P.D.; Robinson, K.L.; Armes, S.P. Polymerization of Sodium 4-Styrenesulfonate via Atom Transfer Radical Polymerization in Protic Media. *Polymer*, **2004**, *45*, 759–768. DOI: 10.1016/j.polymer.2003.11.030.
- [89] Dimitrov, I.; Jankova, K.; Hvilsted, S. Synthesis and ATRP of Novel Fluorinated Aromatic Monomer with Pendant Sulfonate Group. *J. Fluor. Chem.*, **2013**, *149*, 30–35. DOI: 10.1016/j.jfluchem.2013.02.008.

References

- [90] Dimitrov, I.; Jankova, K.; Hvilsted, S. Controlled Synthesis of Fluorinated Copolymers with Pendant Sulfonates. *J. Polym. Sci. Part A Polym. Chem.*, **2008**, *46*, 7827–7834. DOI: 10.1002/pola.23087.
- [91] Oikonomou, E.K.; Pefkianakis, E.K.; Bokias, G.; Kallitsis, J.K. Direct Synthesis of Amphiphilic Block Copolymers, Consisting of poly(Methyl Methacrylate) and poly(Sodium Styrene Sulfonate) Blocks through Atom Transfer Radical Polymerization. *Eur. Polym. J.*, **2008**, *44*, 1857–1864. DOI: 10.1016/j.eurpolymj.2008.03.005.
- [92] Fantin, M.; Isse, A.A.; Venzo, A.; Gennaro, A.; Matyjaszewski, K. Atom Transfer Radical Polymerization of Methacrylic Acid: A Won Challenge. *J. Am. Chem. Soc.*, **2016**, *138*, 7216–7219. DOI: 10.1021/jacs.6b01935.
- [93] Fu, L.; Simakova, A.; Fantin, M.; Wang, Y.; Matyjaszewski, K. Direct ATRP of Methacrylic Acid with Iron-Porphyrin Based Catalysts. *ACS Macro Lett.*, **2018**, *7*, 26–30. DOI: 10.1021/acsmacrolett.7b00909.
- [94] Ford, J.F.; Vickers, T.J.; Mann, C.K.; Schlenoff, J.B. Polymerization of a Thiol-Bound Styrene Monolayer. *Langmuir*, **1996**, *12*, 1944–1946. DOI: 10.1021/la950913k.
- [95] Bialk, M.; Prucker, O.; R uhe, J. Grafting of Polymers to Solid Surfaces by Using Immobilized Methacrylates. *Colloids Surfaces A Physicochem. Eng. Asp.*, **2002**, *198–200*, 543–549. DOI: 10.1016/S0927-7757(01)00958-X.
- [96] Nollen, K.; Kaden, V.; Hamann, K. Polymerisationsreaktionen an Adsorptionsschichten von Feststoffpulvern. *Die Angew. Makromol. Chemie*, **1969**, *6*, 1–23. DOI: 10.1002/apmc.1969.050060101.
- [97] Prucker, O.; R uhe, J. Synthesis of poly(Styrene) Monolayers Attached to High Surface Area Silica Gels through Self-Assembled Monolayers of Azo Initiators. *Macromolecules*, **1998**, *31*, 592–601. DOI: 10.1021/ma970660x.
- [98] Prucker, O.; R uhe, J. Mechanism of Radical Chain Polymerizations Initiated by Azo Compounds Covalently Bound to the Surface of Spherical Particles. *Macromolecules*, **1998**, *31*, 602–613. DOI: 10.1021/ma970661p.
- [99] Zhang, J.; Jin, J.; Zhao, H. Surface-Initiated Free Radical Polymerization at the Liquid–Liquid Interface: A One-Step Approach for the Synthesis of Amphiphilic Janus Silica Particles. *Langmuir*, **2009**, *25*, 6431–6437. DOI: 10.1021/la9000279.
- [100] Advincula, R.C. Surface Initiated Polymerization from Nanoparticle Surfaces. *J. Dispers. Sci. Technol.*, **2003**, *24*, 343–361. DOI: 10.1081/DIS-120021794.
- [101] Tsubokawa, N.; Funaki, A.; Hada, Y.; Sone, Y. Grafting Polyesters onto Carbon Black. I. Polymerization of β -Propiolactone Initiated by Alkali Metal Carboxylate Group on the Surface of Carbon Black. *J. Polym. Sci. Part A Polym. Chem. Ed.*, **1982**, *20*, 3297–3304. DOI: 10.1002/pol.1982.170201204.
- [102] Braun, D.; Kamprath, A. Versuche Zur Pflropfung von Polystyrol Auf Ru oberfl achen. *Die Angew. Makromol. Chemie*, **1984**, *120*, 1–41. DOI: 10.1002/apmc.1984.051200101.
- [103] Quirk, R.P.; Mathers, R.T. Surface-Initiated Living Anionic Polymerization of Isoprene Using a 1,1-Diphenylethylene Derivative and Functionalization with Ethylene Oxide. *Polym. Bull.*, **2001**, *45*, 471–477. DOI: 10.1007/s002890170100.
- [104] Zhou, Q.; Fan, X.; Xia, C.; Mays, J.; Advincula, R. Living Anionic Surface Initiated Polymerization (SIP) of Styrene from Clay Surfaces. *Chem. Mater.*, **2001**, *13*, 2465–2467. DOI: 10.1021/cm0101780.
- [105] Ru igaj, A.; Krajnc, M.;  ebenik, U. Polymerization of Octamethylcyclotetrasiloxane between Montmorillonite Nanoplatelets Initiated by Surface Anions. *Polym. Bull.*, **2015**,

References

- 72, 1863–1878. DOI: 10.1007/s00289-015-1377-5.
- [106] Schomaker, E.; Zwarteveen, A.J.; Challa, G.; Capka, M. Synthesis of Isotactic poly(Methyl Methacrylate) Covalently Bound to Microparticulate Silica. *Polym. Commun.*, **1988**, *29*, 158–160.
- [107] Oosterling, M.L.C.M.; Sein, A.; Schouten, A.J. Anionic Grafting of Polystyrene and poly(Styrene-Block-Isoprene) onto Microparticulate Silica and Glass Slides. *Polymer*, **1992**, *33*, 4394–4400. DOI: 10.1016/0032-3861(92)90286-6.
- [108] Zhou, Q.; Wang, S.; Fan, X.; Advincula, R.; Mays, J. Living Anionic Surface-Initiated Polymerization (LASIP) of a Polymer on Silica Nanoparticles. *Langmuir*, **2002**, *18*, 3324–3331. DOI: 10.1021/la015670c.
- [109] Kim, C.J.; Sondergeld, K.; Mazurowski, M.; Gallei, M.; Rehahn, M.; Spehr, T.; Frielinghaus, H.; Stühn, B. Synthesis and Characterization of Polystyrene Chains on the Surface of Silica Nanoparticles: Comparison of SANS, SAXS, and DLS Results. *Colloid Polym. Sci.*, **2013**, *291*, 2087–2099. DOI: 10.1007/s00396-013-2923-z.
- [110] Hawker, C.J. Molecular Weight Control by a “Living” Free-Radical Polymerization Process. *J. Am. Chem. Soc.*, **1994**, *116*, 11185–11186. DOI: 10.1021/ja00103a055.
- [111] Zoppe, J.O.; Ataman, N.C.; Mocny, P.; Wang, J.; Moraes, J.; Klok, H.-A. Surface-Initiated Controlled Radical Polymerization: State-of-the-Art, Opportunities, and Challenges in Surface and Interface Engineering with Polymer Brushes. *Chem. Rev.*, **2017**, *117*, 1105–1318. DOI: 10.1021/acs.chemrev.6b00314.
- [112] Mocny, P.; Klok, H.A. Complex Polymer Topologies and Polymer—Nanoparticle Hybrid Films Prepared via Surface-Initiated Controlled Radical Polymerization. *Prog. Polym. Sci.*, **2020**, *100*, 101185. DOI: 10.1016/j.progpolymsci.2019.101185.
- [113] Badoux, M.; Billing, M.; Klok, H.-A. Polymer Brush Interfaces for Protein Biosensing Prepared by Surface-Initiated Controlled Radical Polymerization. *Polym. Chem.*, **2019**, *10*, 2925–2951. DOI: 10.1039/C9PY00163H.
- [114] Li, M.; Fromel, M.; Ranaweera, D.; Rocha, S.; Boyer, C.; Pester, C.W. SI-PET-RAFT: Surface-Initiated Photoinduced Electron Transfer-Reversible Addition–Fragmentation Chain Transfer Polymerization. *ACS Macro Lett.*, **2019**, *8*, 374–380. DOI: 10.1021/acsmacrolett.9b00089.
- [115] Pyun, J.; Matyjaszewski, K. Synthesis of Nanocomposite Organic/Inorganic Hybrid Materials Using Controlled/“Living” Radical Polymerization. *Chem. Mater.*, **2001**, *13*, 3436–3448. DOI: 10.1021/cm011065j.
- [116] Pyun, J.; Kowalewski, T.; Matyjaszewski, K. Synthesis of Polymer Brushes Using Atom Transfer Radical Polymerization. *Macromol. Rapid Commun.*, **2003**, *24*, 1043–1059. DOI: 10.1002/marc.200300078.
- [117] Matyjaszewski, K.; Dong, H.; Jakubowski, W.; Pietrasik, J.; Kusumo, A. Grafting from Surfaces for “Everyone”: ARGET ATRP in the Presence of Air. *Langmuir*, **2007**, *23*, 4528–4531. DOI: 10.1021/la063402e.
- [118] Matyjaszewski, K.; Tsarevsky, N. V. Macromolecular Engineering by Atom Transfer Radical Polymerization. *J. Am. Chem. Soc.*, **2014**, *136*, 6513–6533. DOI: 10.1021/ja408069v.
- [119] Ejaz, M.; Yamamoto, S.; Ohno, K.; Tsujii, Y.; Fukuda, T. Controlled Graft Polymerization of Methyl Methacrylate on Silicon Substrate by the Combined Use of the Langmuir-Blodgett and Atom Transfer Radical Polymerization Techniques. *Macromolecules*, **1998**, *31*, 5934–5936. DOI: 10.1021/ma980240n.

References

- [120] Pnias, D.; Taxiarchou, M.; Paspaliaris, I.; Kontopoulos, A. Mechanisms of Dissolution of Iron Oxides in Aqueous Oxalic Acid Solutions. *Hydrometallurgy*, **1996**, *42*, 257–265. DOI: 10.1016/0304-386X(95)00104-O.
- [121] Pietrasik, J.; Hui, C.M.; Chaladaj, W.; Dong, H.; Choi, J.; Jurczak, J.; Bockstaller, M.R.; Matyjaszewski, K. Silica-Polymethacrylate Hybrid Particles Synthesized Using High-Pressure Atom Transfer Radical Polymerization. *Macromol. Rapid Commun.*, **2011**, *32*, 295–301. DOI: 10.1002/marc.201000531.
- [122] Wang, Y.; Teng, X.; Wang, J.S.; Yang, H. Solvent-Free Atom Transfer Radical Polymerization in the Synthesis of Fe₂O₃@polystyrene Core-Shell Nanoparticles. *Nano Lett.*, **2003**, *3*, 789–793. DOI: 10.1021/nl034211o.
- [123] Gravano, S.M.; Dumas, R.; Liu, K.; Patten, T.E. Methods for the Surface Functionalization of γ -Fe₂O₃ Nanoparticles with Initiators for Atom Transfer Radical Polymerization and the Formation of Core-Shell Inorganic-Polymer Structures. *J. Polym. Sci. Part A Polym. Chem.*, **2005**, *43*, 3675–3688. DOI: 10.1002/pola.20823.
- [124] Sun, Y.; Ding, X.; Zheng, Z.; Cheng, X.; Hu, X.; Peng, Y. Surface Initiated ATRP in the Synthesis of Iron Oxide/Polystyrene Core/Shell Nanoparticles. *Eur. Polym. J.*, **2007**, *43*, 762–772. DOI: 10.1016/j.eurpolymj.2006.10.021.
- [125] Mao, X.; Sun, H.; He, X.; Chen, L.; Zhang, Y. Well-Defined Sulfamethazine-Imprinted Magnetic Nanoparticles via Surface-Initiated Atom Transfer Radical Polymerization for Highly Selective Enrichment of Sulfonamides in Food Samples. *Anal. Methods*, **2015**, *7*, 4708–4716. DOI: 10.1039/C5AY00590F.
- [126] Babu, K.; Dhamodharan, R. Grafting of poly(Methyl Methacrylate) Brushes from Magnetite Nanoparticles Using a Phosphonic Acid Based Initiator by Ambient Temperature Atom Transfer Radical Polymerization (ATATRP). *Nanoscale Res. Lett.*, **2008**, *3*, 109. DOI: 10.1007/s11671-008-9121-9.
- [127] Basti, H.; Tahar, L. Ben; Smiri, L.S.; Herbst, F.; Nowak, S.; Mangeney, C.; Ammar, S. Surface Modification of γ -Fe₂O₃ Nanoparticles by Grafting from Poly-(Hydroxyethylmethacrylate) and Poly-(Methacrylic Acid): Qualitative and Quantitative Analysis of the Polymeric Coating. *Colloids Surfaces A Physicochem. Eng. Asp.*, **2016**, *490*, 222–231. DOI: 10.1016/j.colsurfa.2015.11.013.
- [128] Yan, J.; Li, S.; Cartieri, F.; Wang, Z.; Hitchens, T.K.; Leonardo, J.; Averick, S.E.; Matyjaszewski, K. Iron Oxide Nanoparticles with Grafted Polymeric Analogue of Dimethyl Sulfoxide as Potential Magnetic Resonance Imaging Contrast Agents. *ACS Appl. Mater. Interfaces*, **2018**, *10*, 21901–21908. DOI: 10.1021/acsami.8b06416.
- [129] Vasquez, E.S.; Nicholson, W.B.; Walters, K.B. Surface Modification of Iron Oxide (Fe₃O₄) Micro- and Nano-Particles with Stimuli Responsive Polymers. *2011 Nanotech Conf. Expo.*, **2011**, *1*, 612–615.
- [130] Yao, X.; Jing, J.; Liang, F.; Yang, Z. Polymer-Fe₃O₄ Composite Janus Nanoparticles. *Macromolecules*, **2016**, *49*, 9618–9625. DOI: 10.1021/acs.macromol.6b02004.
- [131] Matyjaszewski, K.; Miller, P.J.; Shukla, N.; Immaraporn, B.; Gelman, A.; Luokala, B.B.; Siclován, T.M.; Kickelbick, G.; Vallant, T.; Hoffmann, H.; Pakula, T. Polymers at Interfaces: Using Atom Transfer Radical Polymerization in the Controlled Growth of Homopolymers and Block Copolymers from Silicon Surfaces in the Absence of Untethered Sacrificial Initiator. *Macromolecules*, **1999**, *32*, 8716–8724. DOI: 10.1021/ma991146p.
- [132] von Werne, T.A.; Germack, D.S.; Hagberg, E.C.; Sheares, V. V.; Hawker, C.J.; Carter, K.R. A Versatile Method for Tuning the Chemistry and Size of Nanoscopic Features by Living Free Radical Polymerization. *J. Am. Chem. Soc.*, **2003**, *125*, 3831–3838.

References

- DOI: 10.1021/ja028866n.
- [133] Wang, Y.; Schroeder, H.; Morick, J.; Buback, M.; Matyjaszewski, K. High-Pressure Atom Transfer Radical Polymerization of n-Butyl Acrylate. *Macromol. Rapid Commun.*, **2013**, *34*, 604–609. DOI: 10.1002/marc.201200752.
- [134] Kagawa, Y.; Zetterlund, P.B.; Minami, H.; Okubo, M. Compartmentalization in Atom Transfer Radical Polymerization (ATRP) in Dispersed Systems. *Macromol. Theory Simulations*, **2006**, *15*, 608–613. DOI: 10.1002/mats.200600049.
- [135] Bombalski, L.; Min, K.; Dong, H.; Tang, C.; Matyjaszewski, K. Preparation of Well-Defined Hybrid Materials by ATRP in Miniemulsion. *Macromolecules*, **2007**, *40*, 7429–7432. DOI: 10.1021/ma071408k.
- [136] Cordero, R.; Jawaid, A.; Hsiao, M.-S.; Lequeux, Z.; Vaia, R.A.; Ober, C.K. Mini Monomer Encapsulated Emulsion Polymerization of PMMA Using Aqueous ARGET ATRP. *ACS Macro Lett.*, **2018**, *7*, 459–463. DOI: 10.1021/acsmacrolett.8b00038.
- [137] Loiko, O.P.; Heuts, J.P.A.; van Herk, A.M. Synthesis of Polymer-Vesicle Latex Particles through an ATRP-Based Approach. *Colloid Polym. Sci.*, **2022**, *300*, 387–396. DOI: 10.1007/s00396-022-04951-9.
- [138] Magenau, A.J.D.; Strandwitz, N.C.; Gennaro, A.; Matyjaszewski, K. Electrochemically Mediated Atom Transfer Radical Polymerization. In *Science*; **2011**; Vol. 332, pp. 81–84. DOI: 10.1126/science.1202357.
- [139] Bortolamei, N.; Isse, A.A.; Magenau, A.J.D.; Gennaro, A.; Matyjaszewski, K. Controlled Aqueous Atom Transfer Radical Polymerization with Electrochemical Generation of the Active Catalyst. *Angew. Chemie Int. Ed.*, **2011**, *50*, 11391–11394. DOI: 10.1002/anie.201105317.
- [140] Magenau, A.J.D.; Bortolamei, N.; Frick, E.; Park, S.; Gennaro, A.; Matyjaszewski, K. Investigation of Electrochemically Mediated Atom Transfer Radical Polymerization. *Macromolecules*, **2013**, *46*, 4346–4353. DOI: 10.1021/ma400869e.
- [141] Rabea, A.M.; Zhu, S. Ultrasonically Enhanced Bulk ATRP of Methyl Methacrylate at High Conversion with Good Livingness and Control. *Am. Inst. Chem. Eng.*, **2016**, *62*, 1683–1687. DOI: 10.1002/aic15165.
- [142] Zaborniak, I.; Chmielarz, P. Ultrasound-Mediated Atom Transfer Radical Polymerization (ATRP). *Materials*, **2019**, *12*, 3600. DOI: 10.3390/ma12213600.
- [143] Cho, H.Y.; Bielawski, C.W. Atom Transfer Radical Polymerization in the Solid-State. *Angew. Chemie Int. Ed.*, **2020**, *59*, 13929–13935. DOI: 10.1002/anie.202005021.
- [144] Tasdelen, M.A.; Uygun, M.; Yagci, Y. Photoinduced Controlled Radical Polymerization in Methanol. *Macromol. Chem. Phys.*, **2010**, *211*, 2271–2275. DOI: 10.1002/macp.201000445.
- [145] Chen, M.; Zhong, M.; Johnson, J.A. Light-Controlled Radical Polymerization: Mechanisms, Methods, and Applications. *Chem. Rev.*, **2016**, *116*, 10167–10211. DOI: 10.1021/acs.chemrev.5b00671.
- [146] Ribelli, T.G.; Konkolewicz, D.; Bernhard, S.; Matyjaszewski, K. How Are Radicals (Re)Generated in Photochemical ATRP? *J. Am. Chem. Soc.*, **2014**, *136*, 13303–13312. DOI: 10.1021/ja506379s.
- [147] Yan, W.; Dadashi-Silab, S.; Matyjaszewski, K.; Spencer, N.D.; Benetti, E.M. Surface-Initiated Photoinduced ATRP: Mechanism, Oxygen Tolerance, and Temporal Control during the Synthesis of Polymer Brushes. *Macromolecules*, **2020**, *53*, 2801–2810. DOI: 10.1021/acs.macromol.0c00333.

References

- [148] Osborne, V.L.; Jones, D.M.; Huck, W.T.S. Controlled Growth of Triblock Polyelectrolyte Brushes. *Chem. Commun.*, **2002**, 1838–1839. DOI: 10.1039/b204737c.
- [149] Dunlop, I.E.; Briscoe, W.H.; Titmuss, S.; Jacobs, R.M.J.; Osborne, V.L.; Edmondson, S.; Huck, W.T.S.; Klein, J. Direct Measurement of Normal and Shear Forces between Surface-Grown Polyelectrolyte Layers. *J. Phys. Chem. B*, **2009**, *113*, 3947–3956. DOI: 10.1021/jp807190z.
- [150] Ramos, J.I.; Moya, S.E. Effect of the Density of ATRP Thiol Initiators in the Yield and Water Content of Grafted-From PMETAC Brushes. A Study by Means of QCM-D and Spectroscopic Ellipsometry Combined in a Single Device. *Macromol. Chem. Phys.*, **2012**, *213*, 549–556. DOI: 10.1002/macp.201100501.
- [151] Dunlop, I.E.; Thomas, R.K.; Titmus, S.; Osborne, V.; Edmondson, S.; Huck, W.T.S.; Klein, J. Structure and Collapse of a Surface-Grown Strong Polyelectrolyte Brush on Sapphire. *Langmuir*, **2012**, *28*, 3187–3193. DOI: 10.1021/la204655h.
- [152] Gao, T.; Wang, X.; Yu, B.; Wei, Q.; Xia, Y.; Zhou, F. Noncovalent Microcontact Printing for Grafting Patterned Polymer Brushes on Graphene Films. *Langmuir*, **2013**, *29*, 1054–1060. DOI: 10.1021/la304385r.
- [153] Li, B.; Yu, B.; Zhou, F. In Situ AFM Investigation of Electrochemically Induced Surface-Initiated Atom-Transfer Radical Polymerization. *Macromol. Rapid Commun.*, **2013**, *34*, 246–250. DOI: 10.1002/marc.201200653.
- [154] Ma, S.; Liu, J.; Ye, Q.; Wang, D.; Liang, Y.; Zhou, F. A General Approach for Construction of Asymmetric Modification Membranes for Gated Flow Nanochannels. *J. Mater. Chem. A*, **2014**, *2*, 8804–8814. DOI: 10.1039/C4TA00126E.
- [155] Tan, K.Y.; Gautrot, J.E.; Huck, W.T.S. Formation of Pickering Emulsions Using Ion-Specific Responsive Colloids. *Langmuir*, **2011**, *27*, 1251–1259. DOI: 10.1021/la102904r.
- [156] Chen, X.; Randall, D.P.; Perruchot, C.; Watts, J.F.; Patten, T.E.; von Werne, T.; Armes, S.P. Synthesis and Aqueous Solution Properties of Polyelectrolyte-Grafted Silica Particles Prepared by Surface-Initiated Atom Transfer Radical Polymerization. *J. Colloid Interface Sci.*, **2003**, *257*, 56–64. DOI: 10.1016/S0021-9797(02)00014-0.
- [157] Fielding, L.A.; Edmondson, S.; Armes, S.P. Synthesis of pH-Responsive Tertiary Amine Methacrylate Polymer Brushes and Their Response to Acidic Vapour. *J. Mater. Chem.*, **2011**, *21*, 11773. DOI: 10.1039/c1jm11412c.
- [158] Topham, P.D.; Glidle, A.; Toolan, D.T.W.; Weir, M.P.; Skoda, M.W.A.; Barker, R.; Howse, J.R. The Relationship between Charge Density and Polyelectrolyte Brush Profile Using Simultaneous Neutron Reflectivity and In Situ Attenuated Total Internal Reflection FTIR. *Langmuir*, **2013**, *29*, 6068–6076. DOI: 10.1021/la4005592.
- [159] Cheesman, B.T.; Neilson, A.J.G.; Willott, J.D.; Webber, G.B.; Edmondson, S.; Wanless, E.J. Effect of Colloidal Substrate Curvature on pH-Responsive Polyelectrolyte Brush Growth. *Langmuir*, **2013**, *29*, 6131–6140. DOI: 10.1021/la4004092.
- [160] Wang, W.; Tang, J.; Jia, Z.; Li, X.; Xiao, Z. Grafting of Amphiphilic Polymers Containing Quaternary Ammonium Group on SiO₂ Surface via Surface-Initiated ATRP. *J. Polym. Res.*, **2012**, *19*, 9804. DOI: 10.1007/s10965-011-9804-2.
- [161] Kang, M.K.; Mao, W.; Yoo, H.S. Surface-Initiated Atom Transfer Radical Polymerization of Cationic Corona on Iron Oxide Nanoparticles for Magnetic Sorting of Macrophages. *Biomater. Sci.*, **2018**, *6*, 2248–2260. DOI: 10.1039/C8BM00418H.
- [162] Dong, H.; Huang, J.; Koepsel, R.R.; Ye, P.; Russell, A.J.; Matyjaszewski, K. Recyclable Antibacterial Magnetic Nanoparticles Grafted with Quaternized poly(2-

References

- (Dimethylamino)Ethyl Methacrylate) Brushes. *Biomacromolecules*, **2011**, *12*, 1305–1311. DOI: 10.1021/bm200031v.
- [163] Kirillova, A.; Stoychev, G.; Ionov, L.; Synytska, A. Self-Assembly Behavior of Hairy Colloidal Particles with Different Architectures: Mixed versus Janus. *Langmuir*, **2014**, *30*, 12765–12774. DOI: 10.1021/la503455h.
- [164] Masci, G.; Bontempo, D.; Tiso, N.; Diociaiuti, M.; Mannina, L.; Capitani, D.; Crescenzi, V. Atom Transfer Radical Polymerization of Potassium 3-Sulfopropyl Methacrylate: Direct Synthesis of Amphiphilic Block Copolymers with Methyl Methacrylate. *Macromolecules*, **2004**, *37*, 4464–4473. DOI: 10.1021/ma0497254.
- [165] Wan, F.; Pei, X.; Yu, B.; Ye, Q.; Zhou, F.; Xue, Q. Grafting Polymer Brushes on Biomimetic Structural Surfaces for Anti-Algae Fouling and Foul Release. *ACS Appl. Mater. Interfaces*, **2012**, *4*, 4557–4565. DOI: 10.1021/am300912w.
- [166] Lattuada, M.; Hatton, T.A. Functionalization of Monodisperse Magnetic Nanoparticles. *Langmuir*, **2007**, *23*, 2158–2168. DOI: 10.1021/la062092x.
- [167] Li, C.; Yang, J.; Wang, P.; Liu, J.; Yang, Q. An Efficient Solid Acid Catalyst: Poly-p-Styrenesulfonic Acid Supported on SBA-15 via Surface-Initiated ATRP. *Microporous Mesoporous Mater.*, **2009**, *123*, 228–233. DOI: 10.1016/j.micromeso.2009.04.005.
- [168] Liu, X.; He, S.; Song, G.; Jia, H.; Shi, Z.; Liu, S.; Zhang, L.; Lin, J.; Nazarenko, S. Proton Conductivity Improvement of Sulfonated poly(Ether Ether Ketone) Nanocomposite Membranes with Sulfonated Halloysite Nanotubes Prepared via Dopamine-Initiated Atom Transfer Radical Polymerization. *J. Memb. Sci.*, **2016**, *504*, 206–219. DOI: 10.1016/j.memsci.2016.01.023.
- [169] Yuan, J.; Wang, C.; Wei, Y. High-Capacity Strong Cation Exchanger Prepared from an Inactivated Immobilized Enzyme and Its Application to the Removal of Methylene Blue from Water. *RSC Adv.*, **2016**, *6*, 61013–61020. DOI: 10.1039/c6ra10243c.
- [170] Foster, R.N.; Johansson, P.K.; Tom, N.R.; Koelsch, P.; Castner, D.G. Experimental Design and Analysis of Activators Regenerated by Electron Transfer-Atom Transfer Radical Polymerization Experimental Conditions for Grafting Sodium Styrene Sulfonate from Titanium Substrates. *J. Vac. Sci. Technol. A Vacuum, Surfaces, Film.*, **2015**, *33*, 05E131. DOI: 10.1116/1.4929506.
- [171] Bondar, Y. V.; Kim, H.J.; Lim, Y.J. Sulfonation of (Glycidyl Methacrylate) Chains Grafted onto Nonwoven Polypropylene Fabric. *J. Appl. Polym. Sci.*, **2007**, *104*, 3256–3260. DOI: 10.1002/app.25887.
- [172] Makowski, H.S.; Lundberg, R.D.; Singhal, G.H. Flexible Polymeric Compositions Comprising a Normally Plastic Polymer Sulfonated to About 0.2 to About 10 Mole % Sulfonate, US3870841A, **1975**.
- [173] Jalal, N.M.; Jabur, A.R.; Hamza, M.S.; Allami, S. The Effect of Sulfonation Reaction Time on Polystyrene Electrospun Membranes as Polymer Electrolyte. In *AIP Conference Proceedings*; **2020**; Vol. 2290, p. 020049. DOI: 10.1063/5.0027514.
- [174] Ngadiwiyana; Ismiyanto; Gunawan; Purbowatiningrum, R.; Prasetya, N.B.A.; Kusworo, T.D.; Susanto, H. Sulfonated Polystyrene and Its Characterization as a Material of Electrolyte Polymer. *J. Phys. Conf. Ser.*, **2018**, *1025*, 012133. DOI: 10.1088/1742-6596/1025/1/012133.
- [175] Coughlin, J.E.; Reisch, A.; Markarian, M.Z.; Schlenoff, J.B. Sulfonation of Polystyrene: Toward the “Ideal” Polyelectrolyte. *J. Polym. Sci. Part A Polym. Chem.*, **2013**, *51*, 2416–2424. DOI: 10.1002/pola.26627.
- [176] Hermann, A.; Diesner, M.-O.; Abel, J.; Greßmann, A. Assessment of Impacts of a

References

- European Register of Products Containing Nanomaterials, Umweltbundesamt. **2014**.
- [177] *Risk & Policy Analysis Limited, Impact Assessment of the REACH Implementation Project on Substance ID for Nanomaterials; 2012.*
- [178] *REACH Implementation Project Substance Identification of Nanomaterials (RIP-oN 1), European Commission Joint Research Centre; 2011.*
- [179] Asmatulu, R.; Nguyen, P.; Asmatulu, E. Nanotechnology Safety in the Automotive Industry. In *Nanotechnology Safety*; Elsevier, **2013**; pp. 57–72. DOI: 10.1016/B978-0-444-59438-9.00005-9.
- [180] Chavali, M.S.; Nikolova, M.P. Metal Oxide Nanoparticles and Their Applications in Nanotechnology. *SN Appl. Sci.*, **2019**, *1*, 607. DOI: 10.1007/s42452-019-0592-3.
- [181] Keller, A.A.; Wang, H.; Zhou, D.; Lenihan, H.S.; Cherr, G.; Cardinale, B.J.; Miller, R.; Ji, Z. Stability and Aggregation of Metal Oxide Nanoparticles in Natural Aqueous Matrices. *Environ. Sci. Technol.*, **2010**, *44*, 1962–1967. DOI: 10.1021/es902987d.
- [182] Zhang, Y.; Chen, Y.; Westerhoff, P.; Hristovski, K.; Crittenden, J.C. Stability of Commercial Metal Oxide Nanoparticles in Water. *Water Res.*, **2008**, *42*, 2204–2212. DOI: 10.1016/j.watres.2007.11.036.
- [183] Stankic, S.; Suman, S.; Haque, F.; Vidic, J. Pure and Multi Metal Oxide Nanoparticles: Synthesis, Antibacterial and Cytotoxic Properties. *J. Nanobiotechnology*, **2016**, *14*, 73. DOI: 10.1186/s12951-016-0225-6.
- [184] Helms, C.R.; Poindexter, E.H. The Silicon-Silicon Dioxide System: Its Microstructure and Imperfections. *Reports Prog. Phys.*, **1994**, *57*, 791–852. DOI: 10.1088/0034-4885/57/8/002.
- [185] Getzlaff, M.; Leifels, M.; Weber, P.; Kökcam-Demir, Ü.; Janiak, C. Nanoparticles in Toner Material. *SN Appl. Sci.*, **2019**, *1*, 489. DOI: 10.1007/s42452-019-0501-9.
- [186] Zhang, X.; Wang, M.; Guo, S.; Zhang, Z.; Li, H. Effects of Weathering and Rainfall Conditions on the Release of SiO₂, Ag, and TiO₂ Engineered Nanoparticles from Paints. *J. Nanoparticle Res.*, **2017**, *19*, 338. DOI: 10.1007/s11051-017-4022-4.
- [187] Dhapte, V.V.; Kadam, S.; Pokharkar, V.; Khanna, P.K.; Dhapte, V.V. Versatile SiO₂ Nanoparticles@Polymer Composites with Pragmatic Properties. *ISRN Inorg. Chem.*, **2014**, *2014*, 1–8. DOI: 10.1155/2014/170919.
- [188] Zhang, L.; Tian, A.; Wang, C.; Bai, F.; Fu, S. Formulation of Nanoscale Copolymer-SiO₂ Dispersion via Miniemulsion Polymerization for Application in White Inkjet Ink. *Pigment Resin Technol.*, **2017**, *46*, 48–55. DOI: 10.1108/PRT-08-2015-0074.
- [189] Huang, Y.; Li, P.; Zhao, R.; Zhao, L.; Liu, J.; Peng, S.; Fu, X.; Wang, X.; Luo, R.; Wang, R.; Zhang, Z. Silica Nanoparticles: Biomedical Applications and Toxicity. *Biomed. Pharmacother.*, **2022**, *151*, 113053. DOI: 10.1016/j.biopha.2022.113053.
- [190] Dubey, R.S.; Rajesh, Y.B.R.D.; More, M.A. Synthesis and Characterization of SiO₂ Nanoparticles via Sol-Gel Method for Industrial Applications. *Mater. Today Proc.*, **2015**, *2*, 3575–3579. DOI: 10.1016/j.matpr.2015.07.098.
- [191] Zhuang, C.; Chen, Y. The Effect of Nano-SiO₂ on Concrete Properties: A Review. **2019**, *8*, 562–572. DOI: 10.1515/ntrev-2019-0050.
- [192] Braun, J.H.; Baidins, A.; Marganski, R.E. TiO₂ Pigment Technology: A Review. *Prog. Org. Coatings*, **1992**, *20*, 105–138. DOI: 10.1016/0033-0655(92)80001-D.
- [193] Tian, C.; Huang, S.; Yang, Y. Anatase TiO₂ White Pigment Production from Unenriched Industrial Titanyl Sulfate Solution via Short Sulfate Process. *Dye. Pigment.*, **2013**, *96*,

References

- 609–613. DOI: 10.1016/j.dyepig.2012.09.016.
- [194] Sharma, S.; Sharma, R.K.; Gaur, K.; Torres, J.F.C.; Loza-Rosas, S.A.; Torres, A.; Saxena, M.; Julin, M.; Tinoco, A.D. Fueling a Hot Debate on the Application of TiO₂ Nanoparticles in Sunscreen. *Materials*, **2019**, *12*. DOI: 10.3390/ma12142317.
- [195] Yoon, H.; Kim, D.; Park, M.; Kim, J.J.; Kim, J.J.; Srituravanich, W.; Shin, B.; Jung, Y.; Jeon, S. Extraordinary Enhancement of UV Absorption in TiO₂ Nanoparticles Enabled by Low-Oxidized Graphene Nanodots. *J. Phys. Chem. C*, **2018**, *122*, 12114–12121. DOI: 10.1021/acs.jpcc.8b03329.
- [196] Manda, A.A.; Drmosh, Q.A.; Elsayed, K.A.; Al-Alotaibi, A.L.; Olanrewaju Alade, I.; Onaizi, S.A.; Dafalla, H.D.M.; Elhassan, A. Highly Efficient UV–Visible Absorption of TiO₂/Y₂O₃ Nanocomposite Prepared by Nanosecond Pulsed Laser Ablation Technique. *Arab. J. Chem.*, **2022**, *15*, 1–10. DOI: 10.1016/j.arabjc.2022.104004.
- [197] Lee, B.Y.; Jayapalan, A.R.; Bergin, M.H.; Kurtis, K.E. Photocatalytic Cement Exposed to Nitrogen Oxides: Effect of Oxidation and Binding. *Cem. Concr. Res.*, **2014**, *60*, 30–36. DOI: 10.1016/j.cemconres.2014.03.003.
- [198] Amor, F.; Baudys, M.; Racova, Z.; Scheinherrová, L.; Ingrisova, L.; Hajek, P. Contribution of TiO₂ and ZnO Nanoparticles to the Hydration of Portland Cement and Photocatalytic Properties of High Performance Concrete. *Case Stud. Constr. Mater.*, **2022**, *16*, e00965. DOI: 10.1016/j.cscm.2022.e00965.
- [199] Hou, Y.; Yang, S.; Li, C.; Zhao, H.; Yang, H.G. TiO₂ Cement for High-Performance Dye-Sensitized Solar Cells. *RSC Adv.*, **2016**, *6*, 83802–83807. DOI: 10.1039/C6RA20039G.
- [200] Ding, Y.; Ding, B.; Kanda, H.; Usiobo, O.J.; Gallet, T.; Yang, Z.; Liu, Y.; Huang, H.; Sheng, J.; Liu, C.; Yang, Y.; Queloz, V.I.E.; Zhang, X.; Audinot, J.-N.; Redinger, A.; Dang, W.; Mosconic, E.; Luo, W.; De Angelis, F.; Wang, M.; Dörflinger, P.; Armer, M.; Schmid, V.; Wang, R.; Brooks, K.G.; Wu, J.; Dyakonov, V.; Yang, G.; Dai, S.; Dyson, P.J.; Nazeeruddin, M.K. Single-Crystalline TiO₂ Nanoparticles for Stable and Efficient Perovskite Modules. *Nat. Nanotechnol.*, **2022**, *17*, 598–605. DOI: 10.1038/s41565-022-01108-1.
- [201] Janczarek, M.; Klapiszewski, Ł.; Jędrzejczak, P.; Klapiszewska, I.; Ślosarczyk, A.; Jesionowski, T. Progress of Functionalized TiO₂-Based Nanomaterials in the Construction Industry: A Comprehensive Review. *Chem. Eng. J.*, **2022**, *430*, 132062. DOI: 10.1016/j.cej.2021.132062.
- [202] Bullen, K.E. Cores of the Terrestrial Planets. *Nature*, **1973**, *243*, 68–70. DOI: 10.1038/243068a0.
- [203] Roth, W.L. Magnetic Structures of MnO, FeO, CoO, and NiO. *Phys. Rev.*, **1958**, *110*, 1333–1341. DOI: 10.1103/PhysRev.110.1333.
- [204] Sharma, V.K.; Waldner, F. Superparamagnetic and Ferrimagnetic Resonance of Ultrafine Fe₃O₄ Particles in Ferrofluids. *J. Appl. Phys.*, **1977**, *48*, 4298–4302. DOI: 10.1063/1.323418.
- [205] Ashby, M.F. *Materials and the Environment*; Elsevier, **2009**.
- [206] Li, Q.; Kartikowati, C.W.; Horie, S.; Ogi, T.; Iwaki, T.; Okuyama, K. Correlation between Particle Size/Domain Structure and Magnetic Properties of Highly Crystalline Fe₃O₄ Nanoparticles. *Sci. Rep.*, **2017**, *7*, 9894. DOI: 10.1038/s41598-017-09897-5.
- [207] Lak, A. Synthesis and Characterization of Magnetic Iron Oxide Nanoparticles (Dissertation), **2013**.
- [208] Santoyo Salazar, J.; Perez, L.; de Abril, O.; Truong Phuoc, L.; Ihiwakrim, D.; Vazquez,

References

- M.; Greneche, J.-M.; Begin-Colin, S.; Pourroy, G. Magnetic Iron Oxide Nanoparticles in 10–40 Nm Range: Composition in Terms of Magnetite/Maghemite Ratio and Effect on the Magnetic Properties. *Chem. Mater.*, **2011**, *23*, 1379–1386. DOI: 10.1021/cm103188a.
- [209] Qiao, L.; Fu, Z.; Li, J.; Ghosen, J.; Zeng, M.; Stebbins, J.; Prasad, P.N.; Swihart, M.T. Standardizing Size- and Shape-Controlled Synthesis of Monodisperse Magnetite (Fe₃O₄) Nanocrystals by Identifying and Exploiting Effects of Organic Impurities. *ACS Nano*, **2017**, *11*, 6370–6381. DOI: 10.1021/acsnano.7b02752.
- [210] Vreeland, E.C.; Watt, J.; Schober, G.B.; Hance, B.G.; Austin, M.J.; Price, A.D.; Fellows, B.D.; Monson, T.C.; Hudak, N.S.; Maldonado-Camargo, L.; Bohorquez, A.C.; Rinaldi, C.; Huber, D.L. Enhanced Nanoparticle Size Control by Extending LaMer's Mechanism. *Chem. Mater.*, **2015**, *27*, 6059–6066. DOI: 10.1021/acs.chemmater.5b02510.
- [211] Gupta, R.; Pancholi, K.; De Sa, R.; Murray, D.; Huo, D.; Droubi, G.; White, M.; Njuguna, J. Effect of Oleic Acid Coating of Iron Oxide Nanoparticles on Properties of Magnetic Polyamide-6 Nanocomposite. *JOM*, **2019**, *71*, 3119–3128. DOI: 10.1007/s11837-019-03622-5.
- [212] Mikhaylova, M.; Kim, D.K.; Bobrysheva, N.; Osmolowsky, M.; Semenov, V.; Tsakalagos, T.; Muhammed, M. Superparamagnetism of Magnetite Nanoparticles: Dependence on Surface Modification. *Langmuir*, **2004**, *20*, 2472–2477. DOI: 10.1021/la035648e.
- [213] Abenojar, E.C.; Wickramasinghe, S.; Bas-Concepcion, J.; Samia, A.C.S. Structural Effects on the Magnetic Hyperthermia Properties of Iron Oxide Nanoparticles. *Prog. Nat. Sci. Mater. Int.*, **2016**, *26*, 440–448. DOI: 10.1016/j.pnsc.2016.09.004.
- [214] Butler, R.F.; Banerjee, S.K. Theoretical Single-Domain Grain Size Range in Magnetite and Titanomagnetite. *J. Geophys. Res.*, **1975**, *80*, 4049–4058. DOI: 10.1029/JB080i029p04049.
- [215] Leslie-Pelecky, D.L.; Rieke, R.D. Magnetic Properties of Nanostructured Materials. *Chem. Mater.*, **1996**, *8*, 1770–1783. DOI: 10.1021/cm960077f.
- [216] Ali, S.; Khan, S.A.; Yamani, Z.H.; Qamar, M.T.; Morsy, M.A.; Sarfraz, S. Shape- and Size-Controlled Superparamagnetic Iron Oxide Nanoparticles Using Various Reducing Agents and Their Relaxometric Properties by Xigo Acorn Area. *Appl. Nanosci.*, **2019**, *9*, 479–489. DOI: 10.1007/s13204-018-0907-5.
- [217] Gutiérrez, L.; de la Cueva, L.; Moros, M.; Mazarío, E.; de Bernardo, S.; de la Fuente, J.M.; Morales, M.P.; Salas, G. Aggregation Effects on the Magnetic Properties of Iron Oxide Colloids. *Nanotechnology*, **2019**, *30*, 112001. DOI: 10.1088/1361-6528/aafbff.
- [218] Bakuzis, A.F.; Branquinho, L.C.; Luiz e Castro, L.; de Amaral e Eloi, M.T.; Miotto, R. Chain Formation and Aging Process in Biocompatible Polydisperse Ferrofluids: Experimental Investigation and Monte Carlo Simulations. *Adv. Colloid Interface Sci.*, **2013**, *191–192*, 1–21. DOI: 10.1016/j.cis.2012.12.003.
- [219] Serantes, D.; Baldomir, D. Nanoparticle Size Threshold for Magnetic Agglomeration and Associated Hyperthermia Performance. *Nanomaterials*, **2021**, *11*, 2786. DOI: 10.3390/nano11112786.
- [220] Torres-Lugo, M.; Rinaldi, C. Thermal Potentiation of Chemotherapy by Magnetic Nanoparticles. *Nanomedicine*, **2013**, *8*, 1689–1707. DOI: 10.2217/nnm.13.146.
- [221] Kandasamy, G.; Maity, D. Recent Advances in Superparamagnetic Iron Oxide Nanoparticles (SPIONs) for in Vitro and in Vivo Cancer Nanotheranostics. *Int. J. Pharm.*, **2015**, *496*, 191–218. DOI: 10.1016/j.ijpharm.2015.10.058.
- [222] Sutens, B.; Swusten, T.; Zhong, K.; Jochum, J.; Van Bael, M.; Van der Eycken, E.;

References

- Brullot, W.; Bloemen, M.; Verbiest, T. Tunability of Size and Magnetic Moment of Iron Oxide Nanoparticles Synthesized by Forced Hydrolysis. *Materials*, **2016**, *9*, 554. DOI: 10.3390/ma9070554.
- [223] Maldonado-Camargo, L.; Unni, M.; Rinaldi, C. Magnetic Characterization of Iron Oxide Nanoparticles for Biomedical Applications. In *Methods Mol Biol.*; **2017**; Vol. 1570, pp. 47–71. DOI: 10.1007/978-1-4939-6840-4_4.
- [224] Rosensweig, R.E. Heating Magnetic Fluid with Alternating Magnetic Field. *J. Magn. Magn. Mater.*, **2002**, *252*, 370–374. DOI: 10.1016/S0304-8853(02)00706-0.
- [225] Nemati, Z.; Alonso, J.; Martinez, L.M.; Khurshid, H.; Garaio, E.; Garcia, J.A.; Phan, M.H.; Srikanth, H. Enhanced Magnetic Hyperthermia in Iron Oxide Nano-Octopods: Size and Anisotropy Effects. *J. Phys. Chem. C*, **2016**, *120*, 8370–8379. DOI: 10.1021/acs.jpcc.6b01426.
- [226] Das, R.; Alonso, J.; Nemati Porshokouh, Z.; Kalappattil, V.; Torres, D.; Phan, M.-H.; Garaio, E.; García, J.Á.; Sanchez Llamazares, J.L.; Srikanth, H. Tunable High Aspect Ratio Iron Oxide Nanorods for Enhanced Hyperthermia. *J. Phys. Chem. C*, **2016**, *120*, 10086–10093. DOI: 10.1021/acs.jpcc.6b02006.
- [227] Dennis, C.L.; Ivkov, R. Physics of Heat Generation Using Magnetic Nanoparticles for Hyperthermia. *Int. J. Hyperth.*, **2013**, *29*, 715–729. DOI: 10.3109/02656736.2013.836758.
- [228] Lee, J.-H.H.; Jang, J.T.; Choi, J.S.; Moon, S.H.; Noh, S.H.; Kim, J.W.J.-G.G.; Kim, J.W.J.-G.G.; Kim, I.-S.S.; Park, K.I.; Cheon, J. Exchange-Coupled Magnetic Nanoparticles for Efficient Heat Induction. *Nat. Nanotechnol.*, **2011**, *6*, 418–422. DOI: 10.1038/nnano.2011.95.
- [229] Bauer, L.M.; Situ, S.F.; Griswold, M.A.; Samia, A.C.S. High-Performance Iron Oxide Nanoparticles for Magnetic Particle Imaging – Guided Hyperthermia (HMPI). *Nanoscale*, **2016**, *8*, 12162–12169. DOI: 10.1039/C6NR01877G.
- [230] Song, L.; Yan, C.; Zhang, W.; Wu, H.; Jia, Z.; Ma, M.; Xie, J.; Gu, N.; Zhang, Y. Influence of Reaction Solvent on Crystallinity and Magnetic Properties of MnFe₂O₄ Nanoparticles Synthesized by Thermal Decomposition. *J. Nanomater.*, **2016**, *2016*, 1–8. DOI: 10.1155/2016/4878935.
- [231] Arbain, R.; Othman, M.; Palaniandy, S. Preparation of Iron Oxide Nanoparticles by Mechanical Milling. *Miner. Eng.*, **2011**, *24*, 1–9. DOI: 10.1016/j.mineng.2010.08.025.
- [232] Kang, Y.S.; Risbud, S.; Rabolt, J.F.; Stroeve, P. Synthesis and Characterization of Nanometer-Size Fe₃O₄ and γ-Fe₂O₃ Particles. *Chem. Mater.*, **1996**, *8*, 2209–2211. DOI: 10.1021/cm960157j.
- [233] Hariani, P.L.; Faizal, M.; Ridwan, R.; Marsi, M.; Setiabudidaya, D. Synthesis and Properties of Fe₃O₄ Nanoparticles by Co-Precipitation Method to Removal Procion Dye. *Int. J. Environ. Sci. Dev.*, **2013**, *4*, 336–340. DOI: 10.7763/IJESD.2013.V4.366.
- [234] Giannouli, C. Magnetite: Synthesis and Characterization. *Key Eng. Mater.*, **2013**, *543*, 460–463. DOI: 10.4028/www.scientific.net/KEM.543.460.
- [235] Celis, J.A.; Olea Mejía, O.F.; Cabral-Prieto, A.; García-Sosa, I.; Derat-Escudero, R.; Baggio Saitovitch, E.M.; Alzamora Camarena, M. Synthesis and Characterization of Nanometric Magnetite Coated by Oleic Acid and the Surfactant CTAB: Surfactant Coated Nanometric Magnetite/Maghemite. *Hyperfine Interact.*, **2017**, *238*, 43. DOI: 10.1007/s10751-017-1414-x.
- [236] Morey, G.W.; Ingerson, E. The Pneumatolytic and Hydrothermal Alteration and Synthesis of Silicates. *Econ. Geol.*, **1937**, *32*, 607–750.

References

- DOI: 10.2113/gsecongeo.32.5_Suppl.607.
- [237] Li, H.; Lu, Z.; Cheng, G.; Rong, K.; Chen, F.; Chen, R. HEPES-Involved Hydrothermal Synthesis of Fe₃O₄ Nanoparticles and Their Biological Application. *RSC Adv.*, **2015**, *5*, 5059–5067. DOI: 10.1039/C4RA12536C.
- [238] Soria, J.; Sanz, J.; Sobrados, I.; Coronado, J.M.; Hernández-Alonso, M.D.; Fresno, F. Water–Hydroxyl Interactions on Small Anatase Nanoparticles Prepared by the Hydrothermal Route. *J. Phys. Chem. C*, **2010**, *114*, 16534–16540. DOI: 10.1021/jp105131w.
- [239] Ge, S.; Shi, X.; Sun, K.; Li, C.; Uher, C.; Baker, J.R.; Banaszak Holl, M.M.; Orr, B.G. Facile Hydrothermal Synthesis of Iron Oxide Nanoparticles with Tunable Magnetic Properties. *J. Phys. Chem. C*, **2009**, *113*, 13593–13599. DOI: 10.1021/jp902953t.
- [240] Ebelmen, J.-J. Sur Une Production Artificielle de Silice Diaphane. *Comptes Rendus Acad. Sci. Fr.*, **1844**, *19*, 398.
- [241] Livage, J.; Henry, M.; Sanchez, C. Sol-Gel Chemistry of Transition Metal Oxides. *Prog. Solid State Chem.*, **1988**, *18*, 259–341. DOI: 10.1016/0079-6786(88)90005-2.
- [242] Hench, L.L.; West, J.K. The Sol-Gel Process. *Chem. Rev.*, **1990**, *90*, 33–72. DOI: 10.1021/cr00099a003.
- [243] Lee, Y.; Lee, J.; Bae, C.J.; Park, J.-G.; Noh, H.-J.; Park, J.-H.; Hyeon, T. Large-Scale Synthesis of Uniform and Crystalline Magnetite Nanoparticles Using Reverse Micelles as Nanoreactors under Reflux Conditions. *Adv. Funct. Mater.*, **2005**, *15*, 503–509. DOI: 10.1002/adfm.200400187.
- [244] Dresco, P.A.; Zaitsev, V.S.; Gambino, R.J.; Chu, B. Preparation and Properties of Magnetite and Polymer Magnetite Nanoparticles. *Langmuir*, **1999**, *15*, 1945–1951. DOI: 10.1021/la980971g.
- [245] Zhou, Z.H.; Wang, J.; Liu, X.; Chan, H.S.O. Synthesis of Fe₃O₄ Nanoparticles from Emulsions. *J. Mater. Chem.*, **2001**, *11*, 1704–1709. DOI: 10.1039/b100758k.
- [246] Lassenberger, A.; Grünwald, T.A.; van Oostrum, P.D.J.; Rennhofer, H.; Amenitsch, H.; Zirbs, R.; Lichtenegger, H.C.; Reimhult, E. Monodisperse Iron Oxide Nanoparticles by Thermal Decomposition: Elucidating Particle Formation by Second-Resolved in Situ Small-Angle X-Ray Scattering. *Chem. Mater.*, **2017**, *29*, 4511–4522. DOI: 10.1021/acs.chemmater.7b01207.
- [247] Xu, Z.; Shen, C.; Hou, Y.; Gao, H.; Sun, S. Oleylamine as Both Reducing Agent and Stabilizer in a Facile Synthesis of Magnetite Nanoparticles. *Chem. Mater.*, **2009**, *21*, 1778–1780. DOI: 10.1021/cm802978z.
- [248] Wilson, D.; Langell, M.A. XPS Analysis of Oleylamine/Oleic Acid Capped Fe₃O₄ Nanoparticles as a Function of Temperature. *Appl. Surf. Sci.*, **2014**, *303*, 6–13. DOI: 10.1016/j.apsusc.2014.02.006.
- [249] Muraishi, K.; Takano, T.; Nagase, K.; Tanaka, N. Thermal Decomposition of Fe(II) Carboxylates: Comparison of Decomposition Process between the Formate and Malonate. *J. Inorg. Nucl. Chem.*, **1981**, *43*, 2293–2297. DOI: 10.1016/0022-1902(81)80252-7.
- [250] Frison, R.; Cernuto, G.; Cervellino, A.; Zaharko, O.; Colonna, G.M.; Guagliardi, A.; Masciocchi, N. Magnetite–Maghemite Nanoparticles in the 5–15 Nm Range: Correlating the Core–Shell Composition and the Surface Structure to the Magnetic Properties. A Total Scattering Study. *Chem. Mater.*, **2013**, *25*, 4820–4827. DOI: 10.1021/cm403360f.
- [251] Gatteschi, D.; Caneschi, A.; Pardi, L.; Sessoli, R. Large Clusters of Metal Ions: The

References

- Transition from Molecular to Bulk Magnets. *Science*, **1994**, *265*, 1054–1058. DOI: 10.1126/science.265.5175.1054.
- [252] Kwon, S.G.; Piao, Y.; Park, J.; Angappane, S.; Jo, Y.; Hwang, N.-M.; Park, J.-G.; Hyeon, T. Kinetics of Monodisperse Iron Oxide Nanocrystal Formation by “Heating-Up” Process. *J. Am. Chem. Soc.*, **2007**, *129*, 12571–12584. DOI: 10.1021/ja074633q.
- [253] LaMer, V.K.; Dinegar, R.H. Theory, Production and Mechanism of Formation of Monodispersed Hydrosols. *J. Am. Chem. Soc.*, **1950**, *72*, 4847–4854. DOI: 10.1021/ja01167a001.
- [254] Ho, C.-H.; Tsai, C.-P.; Chung, C.-C.; Tsai, C.-Y.; Chen, F.-R.; Lin, H.-J.; Lai, C.-H. Shape-Controlled Growth and Shape-Dependent Cation Site Occupancy of Monodisperse Fe₃O₄ Nanoparticles. *Chem. Mater.*, **2011**, *23*, 1753–1760. DOI: 10.1021/cm102758u.
- [255] Kulpa-Greszta, M.; Tomaszewska, A.; Dziedzic, A.; Pązik, R. Rapid Hot-Injection as a Tool for Control of Magnetic Nanoparticle Size and Morphology. *RSC Adv.*, **2021**, *11*, 20708–20719. DOI: 10.1039/D1RA02977K.
- [256] Sharma, P.; Holliger, N.; Pfromm, P.H.; Liu, B.; Chikan, V. Size-Controlled Synthesis of Iron and Iron Oxide Nanoparticles by the Rapid Inductive Heating Method. *ACS Omega*, **2020**, *5*, 19853–19860. DOI: 10.1021/acsomega.0c02793.
- [257] Mourdikoudis, S.; Liz-Marzán, L.M. Oleylamine in Nanoparticle Synthesis. *Chem. Mater.*, **2013**, *25*, 1465–1476. DOI: 10.1021/cm4000476.
- [258] Mourdikoudis, S.; Menelaou, M.; Fiuza-Maneiro, N.; Zheng, G.; Wei, S.; Pérez-Juste, J.; Polavarapu, L.; Sofer, Z. Oleic Acid/Oleylamine Ligand Pair: A Versatile Combination in the Synthesis of Colloidal Nanoparticles. *Nanoscale Horizons*, **2022**, *7*, 941–1015. DOI: 10.1039/D2NH00111J.
- [259] Klokkenburg, M.; Hilhorst, J.; Ern , B.H. Surface Analysis of Magnetite Nanoparticles in Cyclohexane Solutions of Oleic Acid and Oleylamine. *Vib. Spectrosc.*, **2007**, *43*, 243–248. DOI: 10.1016/j.vibspec.2006.09.008.
- [260] Harris, R.A.; Shumbula, P.M.; van der Walt, H. Analysis of the Interaction of Surfactants Oleic Acid and Oleylamine with Iron Oxide Nanoparticles through Molecular Mechanics Modeling. *Langmuir*, **2015**, *31*, 3934–3943. DOI: 10.1021/acs.langmuir.5b00671.
- [261] Sun, S.; Zeng, H.; Robinson, D.B.; Raoux, S.; Rice, P.M.; Wang, S.X.; Li, G. Monodisperse MFe₂O₄ (M = Fe, Co, Mn) Nanoparticles. *J. Am. Chem. Soc.*, **2004**, *126*, 273–279. DOI: 10.1021/ja0380852.
- [262] Raza, M.; Bachinger, A.; Zahn, N.; Kickelbick, G. Interaction and UV-Stability of Various Organic Capping Agents on the Surface of Anatase Nanoparticles. *Materials*, **2014**, *7*, 2890–2912. DOI: 10.3390/ma7042890.
- [263] Kickelbick, G.; Schubert, U. Organic Functionalization of Metal Oxide Nanoparticles. *ChemInform*, **2004**, *35*. DOI: 10.1002/chin.200401218.
- [264] Schmidt, H. Inorganic-Organic Composites by Sol-Gel Techniques. *J. Sol-Gel Sci. Technol.*, **1994**, *1*, 217–231. DOI: 10.1007/BF00486165.
- [265] Wang, Y.; Zhang, J.; Shen, X.; Shi, C.; Wu, J.; Sun, L. Dispersion Investigation of TiO₂ Nanoparticles Coated by Pulsed RF Plasma Polymer. *Mater. Chem. Phys.*, **2006**, *98*, 217–224. DOI: 10.1016/j.matchemphys.2005.09.010.
- [266] Becker, D.; Haberkorn, R.; Kickelbick, G. Reactive Milling Induced Structure Changes in Phenylphosphonic Acid Functionalized LiMn₂O₄ Nanocrystals – Synthesis, Rietveld Refinement, and Thermal Stability. *Eur. J. Inorg. Chem.*, **2019**, *2019*, 4835–4845.

References

- DOI: 10.1002/ejic.201900946.
- [267] Sperling, R.A.; Parak, W.J. Surface Modification, Functionalization and Bioconjugation of Colloidal Inorganic Nanoparticles. *Philos. Trans. R. Soc. A Math. Phys. Eng. Sci.*, **2010**, *368*, 1333–1383. DOI: 10.1098/rsta.2009.0273.
- [268] Li, D.; Jones, G.L.; Dunlap, J.R.; Hua, F.; Zhao, B. Thermosensitive Hairy Hybrid Nanoparticles Synthesized by Surface-Initiated Atom Transfer Radical Polymerization. *Langmuir*, **2006**, *22*, 3344–3351. DOI: 10.1021/la053103+.
- [269] Heinrich, C.; Niedner, L.; Oberhausen, B.; Kickelbick, G. Surface-Charged Zirconia Nanoparticles Prepared by Organophosphorus Surface Functionalization with Ammonium or Sulfonate Groups. *Langmuir*, **2019**, *35*, 11369–11379. DOI: 10.1021/acs.langmuir.9b01093.
- [270] Liu, Y.; Purich, D.L.; Wu, C.; Wu, Y.; Chen, T.; Cui, C.; Zhang, L.; Cansiz, S.; Hou, W.; Wang, Y.; Yang, S.; Tan, W. Ionic Functionalization of Hydrophobic Colloidal Nanoparticles To Form Ionic Nanoparticles with Enzymelike Properties. *J. Am. Chem. Soc.*, **2015**, *137*, 14952–14958. DOI: 10.1021/jacs.5b08533.
- [271] Schäfer, S.; Kickelbick, G. Diels–Alder Reactions on Surface-Modified Magnetite/Maghemite Nanoparticles: Application in Self-Healing Nanocomposites. *ACS Appl. Nano Mater.*, **2018**, *1*, 2640–2652. DOI: 10.1021/acsnm.8b00308.
- [272] Neouze, M.-A.; Schubert, U. Surface Modification and Functionalization of Metal and Metal Oxide Nanoparticles by Organic Ligands. *Monatshefte für Chemie - Chem. Mon.*, **2008**, *139*, 183–195. DOI: 10.1007/s00706-007-0775-2.
- [273] Boyer, C.; Whittaker, M.R.; Bulmus, V.; Liu, J.; Davis, T.P. The Design and Utility of Polymer-Stabilized Iron-Oxide Nanoparticles for Nanomedicine Applications. *NPG Asia Mater.*, **2010**, *2*, 23–30. DOI: 10.1038/asiamat.2010.6.
- [274] Zhang, X.; Yang, D.; Yang, R.; Zhu, X.; Feng, J.; Wang, Z.; Zuo, S.; Niu, J.; Liu, S. Exposed the Mechanism of Lead Chloride Dopant for High Efficiency Planar-Structure Perovskite Solar Cells. *Org. Electron.*, **2018**, *62*, 499–504. DOI: 10.1016/j.orgel.2018.06.020.
- [275] Davis, K.; Qi, B.; Witmer, M.; Kitchens, C.L.; Powell, B.A.; Mefford, O.T. Quantitative Measurement of Ligand Exchange on Iron Oxides via Radiolabeled Oleic Acid. *Langmuir*, **2014**, *30*, 10918–10925. DOI: 10.1021/la502204g.
- [276] Nara, M.; Torii, H.; Tasumi, M. Correlation between the Vibrational Frequencies of the Carboxylate Group and the Types of Its Coordination to a Metal Ion: An Ab Initio Molecular Orbital Study. *J. Phys. Chem.*, **1996**, *100*, 19812–19817. DOI: 10.1021/jp9615924.
- [277] Deacon, G.B. Relationships between the Carbon-Oxygen Stretching Frequencies of Carboxylate Complexes and the Type of Carboxylate Coordination. *Coord. Chem. Rev.*, **1980**, *33*, 227–250. DOI: 10.1016/S0010-8545(00)80455-5.
- [278] Dobson, K.D.; McQuillan, A.J. In Situ Infrared Spectroscopic Analysis of the Adsorption of Aromatic Carboxylic Acids to TiO₂, ZrO₂, Al₂O₃, and Ta₂O₅ from Aqueous Solutions. *Spectrochim. Acta Part A Mol. Biomol. Spectrosc.*, **2000**, *56*, 557–565. DOI: 10.1016/S1386-1425(99)00154-7.
- [279] Palacios, E.G.; Juárez-López, G.; Monhemius, A.J. Infrared Spectroscopy of Metal Carboxylates: II. Analysis of Fe(III), Ni and Zn Carboxylate Solutions. *Hydrometallurgy*, **2004**, *72*, 139–148. DOI: 10.1016/S0304-386X(03)00137-3.
- [280] Corr, S.A.; Gun'ko, Y.K.; Tekoriute, R.; Meledandri, C.J.; Brougham, D.F. poly(Sodium-4-Styrene)Sulfonate–Iron Oxide Nanocomposite Dispersions with Controlled Magnetic

References

- Resonance Properties. *J. Phys. Chem. C*, **2008**, *112*, 13324–13327. DOI: 10.1021/jp805519n.
- [281] Shultz, M.D.; Reveles, J.U.; Khanna, S.N.; Carpenter, E.E. Reactive Nature of Dopamine as a Surface Functionalization Agent in Iron Oxide Nanoparticles. *J. Am. Chem. Soc.*, **2007**, *129*, 2482–2487. DOI: 10.1021/ja0651963.
- [282] Wang, L.; Yang, Z.; Gao, J.; Xu, K.; Gu, H.; Zhang, B.; Zhang, X.; Xu, B. A Biocompatible Method of Decorporation: Bisphosphonate-Modified Magnetite Nanoparticles to Remove Uranyl Ions from Blood. *J. Am. Chem. Soc.*, **2006**, *128*, 13358–13359. DOI: 10.1021/ja0651355.
- [283] Borghi, E.B.; Morando, P.J.; Blesa, M.A. Dissolution of Magnetite by Mercaptocarboxylic Acids. *Langmuir*, **1991**, *7*, 1652–1659. DOI: 10.1021/la00056a018.
- [284] Amirbahman, A.; Sigg, L.; Gunten, U. von. Reductive Dissolution of Fe(III) (Hydr)Oxides by Cysteine: Kinetics and Mechanism. *J. Colloid Interface Sci.*, **1997**, *194*, 194–206. DOI: 10.1006/jcis.1997.5116.
- [285] Cohen, H.; Gedanken, A.; Zhong, Z. One-Step Synthesis and Characterization of Ultrastable and Amorphous Fe₃O₄ Colloids Capped with Cysteine Molecules. *J. Phys. Chem. C*, **2008**, *112*, 15429–15438. DOI: 10.1021/jp805090y.
- [286] Bini, R.A.; Marques, R.F.C.; Santos, F.J.; Chaker, J.A.; Jafellicci, M. Synthesis and Functionalization of Magnetite Nanoparticles with Different Amino-Functional Alkoxysilanes. *J. Magn. Magn. Mater.*, **2012**, *324*, 534–539. DOI: 10.1016/j.jmmm.2011.08.035.
- [287] Zhang, C.; Wängler, B.; Morgenstern, B.; Zentgraf, H.; Eisenhut, M.; Untenecker, H.; Krüger, R.; Huss, R.; Seliger, C.; Semmler, W.; Kiessling, F. Silica- and Alkoxysilane-Coated Ultrasmall Superparamagnetic Iron Oxide Particles: A Promising Tool To Label Cells for Magnetic Resonance Imaging. *Langmuir*, **2007**, *23*, 1427–1434. DOI: 10.1021/la061879k.
- [288] Wu, W.; He, Q.; Jiang, C. Magnetic Iron Oxide Nanoparticles: Synthesis and Surface Functionalization Strategies. *Nanoscale Res. Lett.*, **2008**, *3*, 397. DOI: 10.1007/s11671-008-9174-9.
- [289] Larsen, B.A.; Hurst, K.M.; Ashurst, W.R.; Serkova, N.J.; Stoldt, C.R. Mono and Dialkoxysilane Surface Modification of Superparamagnetic Iron Oxide Nanoparticles for Application as Magnetic Resonance Imaging Contrast Agents. *J. Mater. Res.*, **2012**, *27*, 1846–1852. DOI: 10.1557/jmr.2012.160.
- [290] Mutin, P.H.; Guerrero, G.; Vioux, A. Hybrid Materials from Organophosphorus Coupling Molecules. *J. Mater. Chem.*, **2005**, *15*, 3761. DOI: 10.1039/b505422b.
- [291] Sahoo, Y.; Pizem, H.; Fried, T.; Golodnitsky, D.; Burstein, L.; Sukenik, C.N.; Markovich, G. Alkyl Phosphonate/Phosphate Coating on Magnetite Nanoparticles: A Comparison with Fatty Acids. *Langmuir*, **2001**, *17*, 7907–7911. DOI: 10.1021/la010703+.
- [292] Guerrero, G.; Mutin, P.H.; Vioux, A. Anchoring of Phosphonate and Phosphinate Coupling Molecules on Titania Particles. *Chem. Mater.*, **2001**, *13*, 4367–4373. DOI: 10.1021/cm001253u.
- [293] Pujari, S.P.; Scheres, L.; Marcelis, A.T.M.; Zuilhof, H. Covalent Surface Modification of Oxide Surfaces. *Angew. Chemie Int. Ed.*, **2014**, *53*, 6322–6356. DOI: 10.1002/anie.201306709.
- [294] Brodard-Severac, F.; Guerrero, G.; Maquet, J.; Florian, P.; Gervais, C.; Mutin, P.H. High-Field ¹⁷O MAS NMR Investigation of Phosphonic Acid Monolayers on Titania. *Chem. Mater.*, **2008**, *20*, 5191–5196. DOI: 10.1021/cm8012683.

References

- [295] Jespersen, M.L.; Inman, C.E.; Kearns, G.J.; Foster, E.W.; Hutchison, J.E. Alkanephosphonates on Hafnium-Modified Gold: A New Class of Self-Assembled Organic Monolayers. *J. Am. Chem. Soc.*, **2007**, *129*, 2803–2807. DOI: 10.1021/ja065598a.
- [296] Breucker, L.; Landfester, K.; Taden, A. Phosphonic Acid-Functionalized Polyurethane Dispersions with Improved Adhesion Properties. *ACS Appl. Mater. Interfaces*, **2015**, *7*, 24641–24648. DOI: 10.1021/acsami.5b06903.
- [297] Gao, W.; Dickinson, L.; Grozinger, C.; Morin, F.G.; Reven, L. Self-Assembled Monolayers of Alkylphosphonic Acids on Metal Oxides. *Langmuir*, **1996**, *12*, 6429–6435. DOI: 10.1021/la9607621.
- [298] Hong, H.G.; Sackett, D.D.; Mallouk, T.E. Adsorption of Well-Ordered Zirconium Phosphonate Multilayer Films on High Surface Area Silica. *Chem. Mater.*, **1991**, *3*, 521–527. DOI: 10.1021/cm00015a030.
- [299] Paszternák, A.; Felhősi, I.; Pászti, Z.; Kuzmann, E.; Vértes, A.; Kálmán, E.; Nyikos, L. Surface Analytical Characterization of Passive Iron Surface Modified by Alkyl-Phosphonic Acid Layers. *Electrochim. Acta*, **2010**, *55*, 804–812. DOI: 10.1016/j.electacta.2009.09.023.
- [300] Queffélec, C.; Petit, M.; Janvier, P.; Knight, D.A.; Bujoli, B. Surface Modification Using Phosphonic Acids and Esters. *Chem. Rev.*, **2012**, *112*, 3777–3807. DOI: 10.1021/cr2004212.
- [301] Michaelis, A.; Kaehne, R. Über das Verhalten der Jodalkyle Gegen die Sogen. Phosphorigsäureester oder O -Phosphine. *Berichte der Dtsch. Chem. Gesellschaft*, **1898**, *31*, 1048–1055. DOI: 10.1002/cber.189803101190.
- [302] Arbusow, A.J. On the Structure of Phosphonic Acid and Its Derivates: Isometization and Transition of Bonds from Trivalent to Pentavalent Phosphorus. *J. Russ. Phys. Chem. Soc.*, **1906**, *38*, 687.
- [303] Iorga, B.; Eymery, F.; Carmichael, D.; Savignac, P. Dialkyl 1-Alkynylphosphonates: A Range of Promising Reagents. *European J. Org. Chem.*, **2000**, 3103–3115. DOI: 10.1002/1099-0690(200009)2000:18<3103::AID-EJOC3103>3.0.CO;2-V.
- [304] Griffin, C.E.; Wells, H.J. Phosphonic Acids and Esters. I. Radical Initiated Addition of Phosphorous Acid to Olefins. *J. Org. Chem.*, **1959**, *24*, 2049–2051. DOI: 10.1021/jo01094a624.
- [305] Francová, D.; Kickelbick, G. Synthesis of Methacrylate-Functionalized Phosphonates and Phosphates with Long Alkyl-Chain Spacers and Their Self-Aggregation in Aqueous Solutions. *Monatshette für Chemie - Chem. Mon.*, **2009**, *140*, 413–422. DOI: 10.1007/s00706-008-0045-y.
- [306] Traina, C.A.; Schwartz, J. Surface Modification of Y₂O₃ Nanoparticles. *Langmuir*, **2007**, *23*, 9158–9161. DOI: 10.1021/la701653v.
- [307] McKenna, C.E.; Higa, M.T.; Cheung, N.H.; McKenna, M.-C. The Facile Dealkylation of Phosphonic Acid Dialkyl Esters by Bromotrimethylsilane. *Tetrahedron Lett.*, **1977**, *18*, 155–158. DOI: 10.1016/S0040-4039(01)92575-4.
- [308] Matter, F.; Luna, A.L.; Niederberger, M. From Colloidal Dispersions to Aerogels: How to Master Nanoparticle Gelation. *Nano Today*, **2020**, *30*, 100827. DOI: 10.1016/j.nantod.2019.100827.
- [309] Liu, T.; Wei, J.; Fu, G.; Zhang, P.; Zhang, Z.; Guo, D.-S.; Yang, X. Surface Charge Switchable Nanoparticles Capable of Controlled Nitric Oxide Release for the Treatment of Acidity-Associated Bacterial Infections. *Polym. Chem.*, **2021**, *12*, 1023–1029.

References

- DOI: 10.1039/D0PY01460E.
- [310] Odent, J.; Raquez, J.-M.; Dubois, P.; Giannelis, E.P. Ultra-Stretchable Ionic Nanocomposites: From Dynamic Bonding to Multi-Responsive Behavior. *J. Mater. Chem. A*, **2017**, *5*, 13357–13363. DOI: 10.1039/C7TA04101B.
- [311] Krieger, A.; Zika, A.; Gröhn, F. Functional Nano-Objects by Electrostatic Self-Assembly: Structure, Switching, and Photocatalysis. *Front. Chem.*, **2022**, *9*, 1–46. DOI: 10.3389/fchem.2021.779360.
- [312] Dirani, A.; Fernandes, A.E.; Ramirez Wong, D.; Lipnik, P.; Poleunis, C.; Nysten, B.; Glinel, K.; Jonas, A.M. Layers over Layer-by-Layer Assemblies: Silanization of Polyelectrolyte Multilayers. *Langmuir*, **2014**, *30*, 10057–10065. DOI: 10.1021/la502729z.
- [313] Wen, K.; Maoz, R.; Cohen, H.; Sagiv, J.; Gibaud, A.; Desert, A.; Ocko, B.M. Postassembly Chemical Modification of a Highly Ordered Organosilane Multilayer: New Insights into the Structure, Bonding, and Dynamics of Self-Assembling Silane Monolayers. *ACS Nano*, **2008**, *2*, 579–599. DOI: 10.1021/nn800011t.
- [314] Lindgren, E.B.; Derbenev, I.N.; Khachatourian, A.; Chan, H.-K.; Stace, A.J.; Besley, E. Electrostatic Self-Assembly: Understanding the Significance of the Solvent. *J. Chem. Theory Comput.*, **2018**, *14*, 905–915. DOI: 10.1021/acs.jctc.7b00647.
- [315] Iler, R.K. Multilayers of Colloidal Particles. *J. Colloid Interface Sci.*, **1966**, *21*, 569–594. DOI: 10.1016/0095-8522(66)90018-3.
- [316] Katagiri, K.; Yamazaki, S.; Inumaru, K.; Koumoto, K. Anti-Reflective Coatings Prepared via Layer-by-Layer Assembly of Mesoporous Silica Nanoparticles and Polyelectrolytes. *Polym. J.*, **2015**, *47*, 190–194. DOI: 10.1038/pj.2014.104.
- [317] Nuraje, N.; Asmatulu, R.; Cohen, R.E.; Rubner, M.F. Durable Antifog Films from Layer-by-Layer Molecularly Blended Hydrophilic Polysaccharides. *Langmuir*, **2011**, *27*, 782–791. DOI: 10.1021/la103754a.
- [318] Qiao, Z.; Yao, Y.; Su, Y.; Song, S.; Yin, M.; Luo, J. Layer-by-Layer Assembled Multilayer Films with Multiple Antibacterial and pH-Induced Self-Cleaning Activities Based on Polyurethane Micelles. *ACS Appl. Bio Mater.*, **2019**, *2*, 4583–4593. DOI: 10.1021/acsbm.9b00678.
- [319] Hutin, A. Difference between Isoelectric Point (IEP), Point of Zero Charge (PZC), and Isoionic Point (IIP). *little corner Sci. Appl. Notes $\phi - \chi$* , **2022**. DOI: 10.5281/zenodo.6346860.
- [320] Grancarić, A.M.; Ristić, N.; Tarbuk, A.; Ristić, I. Electrokinetic Phenomena of Cationised Cotton and Its Dyeability with Reactive Dyes. *Fibres Text. East. Eur.*, **2013**, *21*, 106–110.
- [321] Parks, G.A. The Isoelectric Points of Solid Oxides, Solid Hydroxides, and Aqueous Hydroxo Complex Systems. *Chem. Rev.*, **1965**, *65*, 177–198. DOI: 10.1021/cr60234a002.
- [322] Clavier, A.; Seijo, M.; Carnal, F.; Stoll, S. Surface Charging Behavior of Nanoparticles by Considering Site Distribution and Density, Dielectric Constant and pH Changes – a Monte Carlo Approach. *Phys. Chem. Chem. Phys.*, **2015**, *17*, 4346–4353. DOI: 10.1039/C4CP04733H.
- [323] Barisik, M.; Atalay, S.; Beskok, A.; Qian, S. Size Dependent Surface Charge Properties of Silica Nanoparticles. *J. Phys. Chem. C*, **2014**, *118*, 1836–1842. DOI: 10.1021/jp410536n.

References

- [324] Bachinger, A.; Kickelbick, G. Pickering Emulsions Stabilized by Anatase Nanoparticles. *Monatshefte für Chemie - Chem. Mon.*, **2010**, *141*, 685–690. DOI: 10.1007/s00706-010-0273-9.
- [325] Bachinger, A.; Ivanovici, S.; Kickelbick, G. Formation of Janus TiO₂ Nanoparticles by a Pickering Emulsion Approach Applying Phosphonate Coupling Agents. *J. Nanosci. Nanotechnol.*, **2011**, *11*, 8599–8608. DOI: 10.1166/jnn.2011.4745.
- [326] Kosmulski, M. The pH Dependent Surface Charging and Points of Zero Charge. VIII. Update. *Adv. Colloid Interface Sci.*, **2020**, *275*, 102064. DOI: 10.1016/j.cis.2019.102064.
- [327] Xiong, Y.; Liu, X.; Xiong, H. Aggregation Modeling of the Influence of pH on the Aggregation of Variably Charged Nanoparticles. *Sci. Rep.*, **2021**, *11*, 17386. DOI: 10.1038/s41598-021-96798-3.
- [328] Delgado, A.V.; González-Caballero, F.; Hunter, R.J.; Koopal, L.K.; Lyklema, J. Measurement and Interpretation of Electrokinetic Phenomena. *J. Colloid Interface Sci.*, **2007**, *309*, 194–224. DOI: 10.1016/j.jcis.2006.12.075.
- [329] Kaszuba, M.; Corbett, J.; Watson, F.M.; Jones, A. High-Concentration Zeta Potential Measurements Using Light-Scattering Techniques. *Philos. Trans. R. Soc. A Math. Phys. Eng. Sci.*, **2010**, *368*, 4439–4451. DOI: 10.1098/rsta.2010.0175.
- [330] Yeh, Y.; Cummins, H.Z. Localized Fluid Flow Measurements with an He-Ne Laser Spectrometer. *Appl. Phys. Lett.*, **1964**, *4*, 176–178. DOI: 10.1063/1.1753925.
- [331] Miller, J.F.; Schätzel, K.; Vincent, B. The Determination of Very Small Electrophoretic Mobilities in Polar and Nonpolar Colloidal Dispersions Using Phase Analysis Light Scattering. *J. Colloid Interface Sci.*, **1991**, *143*, 532–554. DOI: 10.1016/0021-9797(91)90286-H.
- [332] Marsalek, R. Zeta Potential - Applications. In *International Proceedings of Chemical, Biological and Environmental Engineering*; **2012**; Vol. 35, pp. 15–19.
- [333] Xian-Ju, W.; Xin-Fang, L. Influence of pH on Nanofluids' Viscosity and Thermal Conductivity. *Chinese Phys. Lett.*, **2009**, *26*, 056601. DOI: 10.1088/0256-307X/26/5/056601.
- [334] Gulicovski, J.J.; Čerović, L.S.; Milonjić, S.K. Point of Zero Charge and Isoelectric Point of Alumina. *Mater. Manuf. Process.*, **2008**, *23*, 615–619. DOI: 10.1080/10426910802160668.
- [335] Zhang, W.-D.; Xu, L.-X.; Shi, W.; Wang, C.-C.; Hui, Y.-H.; Xie, Z.-F. Oxidation of Aldehydes to Carboxylic Acids in Water Catalyzed by Cobalt(II) Schiff-Base Complex Anchored to SBA-15/MCM-41. *Russ. J. Gen. Chem.*, **2014**, *84*, 782–788. DOI: 10.1134/S1070363214040306.
- [336] Karthikeyan, P.; Aswar, S.A.; Muskawar, P.N.; Bhagat, P.R.; Kumar, S.S. A Novel CuCl₂/BIL Catalyst for Direct Oxidation of Alcohol to Acid at Ambient Temperature. *Catal. Commun.*, **2012**, *26*, 189–193. DOI: 10.1016/j.catcom.2012.05.020.
- [337] Lagodzinskaya, G. V.; Laptinskaya, T. V.; Kazakov, A.I.; Kurochkina, L.S.; Manelis, G.B. Slow Large-Scale Supramolecular Structuring as a Cause of Kinetic Anomalies in the Liquid-Phase Oxidation with Nitric Acid. *Russ. Chem. Bull.*, **2016**, *65*, 984–992. DOI: 10.1007/s11172-016-1401-4.
- [338] Correa, A.; Martín, R. Metal-Catalyzed Carboxylation of Organometallic Reagents with Carbon Dioxide. *Angew. Chemie Int. Ed.*, **2009**, *48*, 6201–6204. DOI: 10.1002/anie.200900667.

References

- [339] Pawsey, S.; Yach, K.; Reven, L. Self-Assembly of Carboxyalkylphosphonic Acids on Metal Oxide Powders. *Langmuir*, **2002**, *18*, 5205–5212. DOI: 10.1021/la015749h.
- [340] Pawsey, S.; McCormick, M.; De Paul, S.; Graf, R.; Lee, Y.S.; Reven, L.; Spiess, H.W. ¹H Fast MAS NMR Studies of Hydrogen-Bonding Interactions in Self-Assembled Monolayers. *J. Am. Chem. Soc.*, **2003**, *125*, 4174–4184. DOI: 10.1021/ja029008u.
- [341] Braissant, O.; Decho, A.W.; Dupraz, C.; Glunk, C.; Przekop, K.M.; Visscher, P.T. Exopolymeric Substances of Sulfate-Reducing Bacteria: Interactions with Calcium at Alkaline pH and Implication for Formation of Carbonate Minerals. *Geobiology*, **2007**, *5*, 401–411. DOI: 10.1111/j.1472-4669.2007.00117.x.
- [342] Sokolov, I.; Smith, D.S.; Henderson, G.S.; Gorby, Y.A.; Ferris, F.G. Cell Surface Electrochemical Heterogeneity of the Fe(III)-Reducing Bacteria *Shewanella Putrefaciens*. *Environ. Sci. Technol.*, **2001**, *35*, 341–347. DOI: 10.1021/es001258s.
- [343] Guthrie, J.P. Hydrolysis of Esters of Oxy Acids. *Can. J. Chem.*, **1978**, *56*, 2342–2354. DOI: 10.1139/v78-385.
- [344] Takei, K.; Tsuto, K.; Miyamoto, S.; Wakatsuki, J. Anionic Surfactants: Lauric Products. *J. Am. Oil Chem. Soc.*, **1985**, *62*, 341–347. DOI: 10.1007/BF02541402.
- [345] Xu, Z.; Ma, X.; Ma, Y.; Wang, Q.; Zhou, J. Zirconium Phosphonates-Supported Chiral Mn(III) Salen Complexes for the Asymmetric Epoxidation of Unfunctionalized Olefins. *Catal. Commun.*, **2009**, *10*, 1261–1266. DOI: 10.1016/j.catcom.2009.02.002.
- [346] Taffa, D.; Kathiresan, M.; Walder, L. Tuning the Hydrophilic, Hydrophobic, and Ion Exchange Properties of Mesoporous TiO₂. *Langmuir*, **2009**, *25*, 5371–5379. DOI: 10.1021/la8038126.
- [347] Mohapatra, S.; Pramanik, P. Synthesis and Stability of Functionalized Iron Oxide Nanoparticles Using Organophosphorus Coupling Agents. *Colloids Surfaces A Physicochem. Eng. Asp.*, **2009**, *339*, 35–42. DOI: 10.1016/j.colsurfa.2009.01.009.
- [348] Xu, B.; Gonella, G.; DeLacy, B.G.; Dai, H.-L. Adsorption of Anionic Thiols on Silver Nanoparticles. *J. Phys. Chem. C*, **2015**, *119*, 5454–5461. DOI: 10.1021/jp511997w.
- [349] Kumal, R.R.; Karam, T.E.; Haber, L.H. Determination of the Surface Charge Density of Colloidal Gold Nanoparticles Using Second Harmonic Generation. *J. Phys. Chem. C*, **2015**, *119*, 16200–16207. DOI: 10.1021/acs.jpcc.5b00568.
- [350] Maoz, R.; Mattis, S.; DiMasi, E.; Ocko, B.M.; Sagiv, J. Self-Replicating Amphiphilic Monolayers. *Nature*, **1996**, *384*, 150–153. DOI: 10.1038/384150a0.
- [351] Maoz, R.; Cohen, H.; Sagiv, J. Specific Nonthermal Chemical Structural Transformation Induced by Microwaves in a Single Amphiphilic Bilayer Self-Assembled on Silicon. *Langmuir*, **1998**, *14*, 5988–5993. DOI: 10.1021/la980223r.
- [352] Soloway, S.; Lipschitz, A. Basicity of Some Nitrilated Amines. *J. Org. Chem.*, **1958**, *23*, 613–615. DOI: 10.1021/jo01098a603.
- [353] Hassan, S.S.M.; Tadros, F.; Selig, W. Microdetermination and PKa Measurement of Some Aliphatic Amines Using the Copper-Ion-Selective Electrode. *Microchem. J.*, **1981**, *26*, 426–435. DOI: 10.1016/0026-265X(81)90121-1.
- [354] Sabesan, A.; Venkatasubramanian, N. Oxidation of Aromatic Secondary and Tertiary Amines by Peroxydisulphate. A Kinetic Study. *Aust. J. Chem.*, **1971**, *24*, 1633. DOI: 10.1071/CH9711633.
- [355] Gabriel, S. Über eine Darstellungsweise Primärer Amine aus den Entsprechenden Halogenverbindungen. *Berichte der Dtsch. Chem. Gesellschaft*, **1887**, *20*, 2224–2236. DOI: 10.1002/cber.18870200227.

References

- [356] Delépine, M. Sur une Nouvelle Méthode de Préparation des Amines Primaires. *C. R. Hebd. Seances Acad. Sci.*, **1895**, *124*, 292–295.
- [357] He, S.-M.; Luo, Y.; Hove-Jensen, B.; Zechel, D.L. A Fluorescent Substrate for Carbon–Phosphorus Lyase: Towards the Pathway for Organophosphonate Metabolism in Bacteria. *Bioorg. Med. Chem. Lett.*, **2009**, *19*, 5954–5957. DOI: 10.1016/j.bmcl.2009.08.035.
- [358] Mercklé, L.; de Andrés-Gómez, A.; Dick, B.; Cox, R.J.; Godfrey, C.R.A. A Fragment-Based Approach to Understanding Inhibition of 1-Deoxy-D-Xylulose-5-Phosphate Reductoisomerase. *ChemBioChem*, **2005**, *6*, 1866–1874. DOI: 10.1002/cbic.200500061.
- [359] Allen, C.F.H.; VanAllen, J. 2-Amino-p-Cymen. *Org. Synth.*, **1942**, *3*, 63. DOI: 10.15227/orgsyn.022.0009.
- [360] Ram, S.; Ehrenkauf, R.E. A General Procedure for Mild and Rapid Reduction of Aliphatic and Aromatic Nitro Compounds Using Ammonium Formate as a Catalytic Hydrogen Transfer Agent. *Tetrahedron Lett.*, **1984**, *25*, 3415–3418. DOI: 10.1016/S0040-4039(01)91034-2.
- [361] Hofmann, A.W. Über die Einwirkung des Broms in Alkalischer Lösung auf die Amine. *Berichte der Dtsch. Chem. Gesellschaft*, **1883**, *16*, 558–560. DOI: 10.1002/cber.188301601120.
- [362] Afanasyev, O.I.; Kuchuk, E.; Usanov, D.L.; Chusov, D. Reductive Amination in the Synthesis of Pharmaceuticals. *Chem. Rev.*, **2019**, *119*, 11857–11911. DOI: 10.1021/acs.chemrev.9b00383.
- [363] Cai, L.; Xu, R.; Guo, X.; Pike, V.W. Rapid Room-Temperature ¹¹C-Methylation of Arylamines with [¹¹C]Methyl Iodide Promoted by Solid Inorganic-Bases in DMF. *European J. Org. Chem.*, **2012**, *2012*, 1303–1310. DOI: 10.1002/ejoc.201101499.
- [364] Eschweiler, W. Ersatz von an Stickstoff Gebundenen Wasserstoffatomen durch die Methylgruppe mit Hilfe von Formaldehyd. *Berichte der Dtsch. Chem. Gesellschaft*, **1905**, *38*, 880–882. DOI: 10.1002/cber.190503801154.
- [365] Kowalczyk, B.; Walker, D.A.; Soh, S.; Grzybowski, B.A. Nanoparticle Supracrystals and Layered Supracrystals as Chemical Amplifiers. *Angew. Chemie*, **2010**, *122*, 5873–5877. DOI: 10.1002/ange.201002295.
- [366] Kowalczyk, B.; Kalsin, A.M.; Orlik, R.; Bishop, K.J.M.; Patashinskii, A.Z.; Mitus, A.; Grzybowski, B.A. Size Selection During Crystallization of Oppositely Charged Nanoparticles. *Chem. - A Eur. J.*, **2009**, *15*, 2032–2035. DOI: 10.1002/chem.200802334.
- [367] Tien, J.; Terfort, A.; Whitesides, G.M. Microfabrication through Electrostatic Self-Assembly. *Langmuir*, **1997**, *13*, 5349–5355. DOI: 10.1021/la970454i.
- [368] Hong, L.; Cacciuto, A.; Luijten, E.; Granick, S. Clusters of Charged Janus Spheres. *Nano Lett.*, **2006**, *6*, 2510–2514. DOI: 10.1021/nl061857i.
- [369] Siek, M.; Kandere-Grzybowska, K.; Grzybowski, B.A. Mixed-Charge, pH-Responsive Nanoparticles for Selective Interactions with Cells, Organelles, and Bacteria. *Accounts Mater. Res.*, **2020**, *1*, 188–200. DOI: 10.1021/accountsmr.0c00041.
- [370] Schäfer, S.; Kickelbick, G. Simple and High Yield Access to Octafunctional Azido, Amine and Urea Group Bearing Cubic Spherosilicates. *Dalt. Trans.*, **2017**, *46*, 221–226. DOI: 10.1039/C6DT03872G.
- [371] Balachander, N.; Sukenik, C.N. Monolayer Transformation by Nucleophilic Substitution:

References

- Applications to the Creation of New Monolayer Assemblies. *Langmuir*, **1990**, *6*, 1621–1627. DOI: 10.1021/la00101a001.
- [372] Lehnfeld, J.; Gruening, M.; Kronseder, M.; Mueller, R. Comparison of Protein-Repellent Behavior of Linear versus Dendrimer-Structured Surface-Immobilized Polymers. *Langmuir*, **2020**, *36*, 5880–5890. DOI: 10.1021/acs.langmuir.0c00625.
- [373] Butler, G.B.; Angelo, R.J. Preparation and Polymerization of Unsaturated Quaternary Ammonium Compounds. VIII. A Proposed Alternating Intramolecular-Intermolecular Chain Propagation. *J. Am. Chem. Soc.*, **1957**, *79*, 3128–3131. DOI: 10.1021/ja01569a037.
- [374] Rabiee, A.; Ershad-Langroudi, A.; Zeynali, M.E. A Survey on Cationic Polyelectrolytes and Their Applications: Acrylamide Derivatives. *Rev. Chem. Eng.*, **2015**, *31*, 239–261. DOI: 10.1515/revce-2014-0056.
- [375] Ooi, Y.J.; Wen, Y.; Zhu, J.; Song, X.; Li, J. Surface Charge Switchable Polymer/DNA Nanoparticles Responsive to Tumor Extracellular pH for Tumor-Triggered Enhanced Gene Delivery. *Biomacromolecules*, **2020**, *21*, 1136–1148. DOI: 10.1021/acs.biomac.9b01521.
- [376] Griffith, A.A. VI. The Phenomena of Rupture and Flow in Solids. *Philos. Trans. R. Soc. London. Ser. A, Contain. Pap. a Math. or Phys. Character*, **1921**, *221*, 163–198. DOI: 10.1098/rsta.1921.0006.
- [377] Stern, T. Mechanism of Micro-Crack Propagation in Semicrystalline Polymers. *J. Res. Updat. Polym. Sci.*, **2014**, *3*, 57–62. DOI: 10.6000/1929-5995.2014.03.02.1.
- [378] Fekete, E.; Molnár, S.; Kim, G.-M.; Michler, G.H.; Pukánszky, B. Aggregation, Fracture Initiation, and Strength of PP/CaCO₃ Composites. *J. Macromol. Sci. Part B*, **1999**, *38*, 885–899. DOI: 10.1080/00222349908248146.
- [379] Zare, Y.; Rhee, K.Y.; Hui, D. Influences of Nanoparticles Aggregation/Agglomeration on the Interfacial/Interphase and Tensile Properties of Nanocomposites. *Compos. Part B Eng.*, **2017**, *122*, 41–46. DOI: 10.1016/j.compositesb.2017.04.008.
- [380] Shin, H.; Yang, S.; Choi, J.; Chang, S.; Cho, M. Effect of Interphase Percolation on Mechanical Behavior of Nanoparticle-Reinforced Polymer Nanocomposite with Filler Agglomeration: A Multiscale Approach. *Chem. Phys. Lett.*, **2015**, *635*, 80–85. DOI: 10.1016/j.cplett.2015.06.054.
- [381] Blaiszik, B.J.; Kramer, S.L.B.; Olugebefola, S.C.; Moore, J.S.; Sottos, N.R.; White, S.R. Self-Healing Polymers and Composites. *Annu. Rev. Mater. Res.*, **2010**, *40*, 179–211. DOI: 10.1146/annurev-matsci-070909-104532.
- [382] Thakur, V.K.; Kessler, M.R. Self-Healing Polymer Nanocomposite Materials: A Review. *Polymer*, **2015**, *69*, 369–383. DOI: 10.1016/j.polymer.2015.04.086.
- [383] Billiet, S.; Hillewaere, X.K.D.; Teixeira, R.F.A.; Du Prez, F.E. Chemistry of Crosslinking Processes for Self-Healing Polymers. *Macromol. Rapid Commun.*, **2013**, *34*, 290–309. DOI: 10.1002/marc.201200689.
- [384] White, S.R.; Sottos, N.R.; Geubelle, P.H.; Moore, J.S.; Kessler, M.R.; Sriram, S.R.; Brown, E.N.; Viswanathan, S. Autonomic Healing of Polymer Composites. *Nature*, **2001**, *409*, 794–797. DOI: 10.1038/35057232.
- [385] Wu, X.-F.; Rahman, A.; Zhou, Z.; Pelot, D.D.; Sinha-Ray, S.; Chen, B.; Payne, S.; Yarin, A.L. Electrospinning Core-Shell Nanofibers for Interfacial Toughening and Self-Healing of Carbon-Fiber/Epoxy Composites. *J. Appl. Polym. Sci.*, **2013**, *129*, 1383–1393. DOI: 10.1002/app.38838.

References

- [386] Olugebefola, S.C.; Hamilton, A.R.; Fairfield, D.J.; Sottos, N.R.; White, S.R. Structural Reinforcement of Microvascular Networks Using Electrostatic Layer-by-Layer Assembly with Halloysite Nanotubes. *Soft Matter*, **2014**, *10*, 544–548. DOI: 10.1039/C3SM52288A.
- [387] Brown, E.N.; Kessler, M.R.; Sottos, N.R.; White, S.R. In Situ poly(Urea-Formaldehyde) Microencapsulation of Dicyclopentadiene. *J. Microencapsul.*, **2003**, *20*, 719–730. DOI: 10.3109/02652040309178083.
- [388] Blaiszik, B.J.; Caruso, M.M.; McIlroy, D.A.; Moore, J.S.; White, S.R.; Sottos, N.R. Microcapsules Filled with Reactive Solutions for Self-Healing Materials. *Polymer*, **2009**, *50*, 990–997. DOI: 10.1016/j.polymer.2008.12.040.
- [389] Burnworth, M.; Tang, L.; Kumpfer, J.R.; Duncan, A.J.; Beyer, F.L.; Fiore, G.L.; Rowan, S.J.; Weder, C. Optically Healable Supramolecular Polymers. *Nature*, **2011**, *472*, 334–337. DOI: 10.1038/nature09963.
- [390] Jia, X.-Y.; Mei, J.-F.; Lai, J.-C.; Li, C.-H.; You, X.-Z. A Highly Stretchable Polymer That Can Be Thermally Healed at Mild Temperature. *Macromol. Rapid Commun.*, **2016**, *37*, 952–956. DOI: 10.1002/marc.201600142.
- [391] Cordier, P.; Tournilhac, F.; Soulié-Ziakovic, C.; Leibler, L. Self-Healing and Thermoreversible Rubber from Supramolecular Assembly. *Nature*, **2008**, *451*, 977–980. DOI: 10.1038/nature06669.
- [392] Xu, C.; Cao, L.; Lin, B.; Liang, X.; Chen, Y. Design of Self-Healing Supramolecular Rubbers by Introducing Ionic Cross-Links into Natural Rubber via a Controlled Vulcanization. *ACS Appl. Mater. Interfaces*, **2016**, *8*, 17728–17737. DOI: 10.1021/acsami.6b05941.
- [393] Utrera-Barrios, S.; Verdejo, R.; López-Manchado, M.A.; Hernández Santana, M. Evolution of Self-Healing Elastomers, from Extrinsic to Combined Intrinsic Mechanisms: A Review. *Mater. Horizons*, **2020**, *7*, 2882–2902. DOI: 10.1039/D0MH00535E.
- [394] Kamand, F.Z.; Mehmood, B.; Ghunem, R.; Hassan, M.K.; El-Hag, A.; Al-Sulaiti, L.; Abdala, A. Self-Healing Silicones for Outdoor High Voltage Insulation: Mechanism, Applications and Measurements. *Energies*, **2022**, *15*, 1677. DOI: 10.3390/en15051677.
- [395] Wool, R.P.; O'Connor, K.M. A Theory Crack Healing in Polymers. *J. Appl. Phys.*, **1981**, *52*, 5953–5963. DOI: 10.1063/1.328526.
- [396] Malinskii, Y.M.; Prokopenko, V. V.; Ivanova, N.A.; Kargin, V.A. Investigation of Self-Healing of Cracks in Polymers - 1. Effect of Temperature and Crosslinks on Self-Healing of Cracks in Polyvinyl Acetate. *Polym. Mech.*, **1970**, *6*, 240–244. DOI: 10.1007/BF00859196.
- [397] Malinskii, Y.M.; Prokopenko, V. V.; Ivanova, N.A.; Kargin, V.A. Investigation of Self-Healing of Cracks in Polymers - 2. Effect of Molecular Weight of a Polymer and the Environment on Self-Healing of Cracks in Polyvinyl Acetate. *Polym. Mech.*, **1970**, *6*, 382–384. DOI: 10.1007/BF00858197.
- [398] Malinskii, Y.M.; Prokopenko, V. V.; Kargin, V.A. Investigation of Self-Healing of Cracks in Polymers - 3. Effect of Medium and Layer Thickness on Self-Healing in Polyvinyl Acetate. *Polym. Mech.*, **1970**, *6*, 969–972. DOI: 10.1007/BF00856916.
- [399] Jud, K.; Kausch, H.H.; Williams, J.G. Fracture Mechanics Studies of Crack Healing and Welding of Polymers. *J. Mater. Sci.*, **1981**, *16*, 204–210. DOI: 10.1007/BF00552073.
- [400] Wool, R.P.; O'Connor, K.M. Time Dependence of Crack Healing. *J. Polym. Sci. Polym. Lett. Ed.*, **1982**, *20*, 7–16. DOI: 10.1002/pol.1982.130200102.

References

- [401] de Gennes, P.G. Reptation of a Polymer Chain in the Presence of Fixed Obstacles. *J. Chem. Phys.*, **1971**, *55*, 572–579. DOI: 10.1063/1.1675789.
- [402] Prager, S.; Tirrell, M. The Healing Process at Polymer–Polymer Interfaces. *J. Chem. Phys.*, **1981**, *75*, 5194–5198. DOI: 10.1063/1.441871.
- [403] Dahlke, J.; Zechel, S.; Hager, M.D.; Schubert, U.S. How to Design a Self-Healing Polymer: General Concepts of Dynamic Covalent Bonds and Their Application for Intrinsic Healable Materials. *Adv. Mater. Interfaces*, **2018**, *5*, 1800051. DOI: 10.1002/admi.201800051.
- [404] Skene, W.G.; Lehn, J.-M.P. Dynamers: Polyacylhydrazone Reversible Covalent Polymers, Component Exchange, and Constitutional Diversity. *Proc. Natl. Acad. Sci.*, **2004**, *101*, 8270–8275. DOI: 10.1073/pnas.0401885101.
- [405] Lehn, J.-M. Dynamers: Dynamic Molecular and Supramolecular Polymers. *Aust. J. Chem.*, **2010**, *63*, 611. DOI: 10.1071/CH10035.
- [406] Kuhl, N.; Bode, S.; Bose, R.K.; Vitz, J.; Seifert, A.; Hoepfener, S.; Garcia, S.J.; Spange, S.; van der Zwaag, S.; Hager, M.D.; Schubert, U.S. Acylhydrazones as Reversible Covalent Crosslinkers for Self-Healing Polymers. *Adv. Funct. Mater.*, **2015**, *25*, 3295–3301. DOI: 10.1002/adfm.201501117.
- [407] Kuhl, N.; Bode, S.; Hager, M.D.; Schubert, U.S. Self-Healing Polymers Based on Reversible Covalent Bonds. In *Advances in Polymer Science*; **2015**; Vol. 273, pp. 1–58. DOI: 10.1007/12_2015_336.
- [408] Cho, S.; Hwang, S.Y.; Oh, D.X.; Park, J. Recent Progress in Self-Healing Polymers and Hydrogels Based on Reversible Dynamic B–O Bonds: Boronic/Boronate Esters, Borax, and Benzoxaborole. *J. Mater. Chem. A*, **2021**, *9*, 14630–14655. DOI: 10.1039/D1TA02308J.
- [409] Wang, Y.; Yu, H.; Yang, H.; Hao, X.; Tang, Q.; Zhang, X. An Injectable Interpenetrating Polymer Network Hydrogel with Tunable Mechanical Properties and Self-Healing Abilities. *Macromol. Chem. Phys.*, **2017**, *218*, 1700348. DOI: 10.1002/macp.201700348.
- [410] Pepels, M.; Filot, I.; Klumperman, B.; Goossens, H. Self-Healing Systems Based on Disulfide–Thiol Exchange Reactions. *Polym. Chem.*, **2013**, *4*, 4955. DOI: 10.1039/c3py00087g.
- [411] Krishnakumar, B.; Singh, M.; Parthasarthy, V.; Park, C.; Sahoo, N.G.; Yun, G.J.; Rana, S. Disulfide Exchange Assisted Self-Healing Epoxy/PDMS/Graphene Oxide Nanocomposites. *Nanoscale Adv.*, **2020**, *2*, 2726–2730. DOI: 10.1039/D0NA00282H.
- [412] Hodgson, J.L.; Roskop, L.B.; Gordon, M.S.; Lin, C.Y.; Coote, M.L. Side Reactions of Nitroxide-Mediated Polymerization: N–O versus O–C Cleavage of Alkoxyamines. *J. Phys. Chem. A*, **2010**, *114*, 10458–10466. DOI: 10.1021/jp1064165.
- [413] Zhang, Z.P.; Rong, M.Z.; Zhang, M.Q.; Yuan, C. Alkoxyamine with Reduced Homolysis Temperature and Its Application in Repeated Autonomous Self-Healing of Stiff Polymers. *Polym. Chem.*, **2013**, *4*, 4648. DOI: 10.1039/c3py00679d.
- [414] Li, Y.; Jin, Y.; Fan, W.; Zhou, R. A Review on Room-Temperature Self-Healing Polyurethane: Synthesis, Self-Healing Mechanism and Application. *J. Leather Sci. Eng.*, **2022**, *4*, 24. DOI: 10.1186/s42825-022-00097-0.
- [415] Chao, A.; Negulescu, I.; Zhang, D. Dynamic Covalent Polymer Networks Based on Degenerative Imine Bond Exchange: Tuning the Malleability and Self-Healing Properties by Solvent. *Macromolecules*, **2016**, *49*, 6277–6284. DOI: 10.1021/acs.macromol.6b01443.

References

- [416] Hu, J.; Mo, R.; Sheng, X.; Zhang, X. A Self-Healing Polyurethane Elastomer with Excellent Mechanical Properties Based on Phase-Locked Dynamic Imine Bonds. *Polym. Chem.*, **2020**, *11*, 2585–2594. DOI: 10.1039/D0PY00151A.
- [417] Mukherjee, S.; Hill, M.R.; Sumerlin, B.S. Self-Healing Hydrogels Containing Reversible Oxime Crosslinks. *Soft Matter*, **2015**, *11*, 6152–6161. DOI: 10.1039/C5SM00865D.
- [418] Zhang, L.; You, Z. Dynamic Oxime-Urethane Bonds, a Versatile Unit of High Performance Self-Healing Polymers for Diverse Applications. *Chinese J. Polym. Sci.*, **2021**, *39*, 1281–1291. DOI: 10.1007/s10118-021-2625-9.
- [419] Zheng, P.; McCarthy, T.J. A Surprise from 1954: Siloxane Equilibration Is a Simple, Robust, and Obvious Polymer Self-Healing Mechanism. *J. Am. Chem. Soc.*, **2012**, *134*, 2024–2027. DOI: 10.1021/ja2113257.
- [420] Putnam-Neeb, A.A.; Kaiser, J.M.; Hubbard, A.M.; Street, D.P.; Dickerson, M.B.; Nepal, D.; Baldwin, L.A. Self-Healing and Polymer Welding of Soft and Stiff Epoxy Thermosets via Silanolates. *Adv. Compos. Hybrid Mater.*, **2022**, *5*, 3068–3080. DOI: 10.1007/s42114-022-00558-4.
- [421] Lu, Y.-X.; Guan, Z. Olefin Metathesis for Effective Polymer Healing via Dynamic Exchange of Strong Carbon–Carbon Double Bonds. *J. Am. Chem. Soc.*, **2012**, *134*, 14226–14231. DOI: 10.1021/ja306287s.
- [422] Neal, J.A.; Mozhdghi, D.; Guan, Z. Enhancing Mechanical Performance of a Covalent Self-Healing Material by Sacrificial Noncovalent Bonds. *J. Am. Chem. Soc.*, **2015**, *137*, 4846–4850. DOI: 10.1021/jacs.5b01601.
- [423] Kuhl, N.; Geitner, R.; Bose, R.K.; Bode, S.; Dietzek, B.; Schmitt, M.; Popp, J.; Garcia, S.J.; van der Zwaag, S.; Schubert, U.S.; Hager, M.D. Self-Healing Polymer Networks Based on Reversible Michael Addition Reactions. *Macromol. Chem. Phys.*, **2016**, *217*, 2541–2550. DOI: 10.1002/macp.201600353.
- [424] Fan, B.; Zhang, K.; Liu, Q.; Eelkema, R. Self-Healing Injectable Polymer Hydrogel via Dynamic Thiol-Alkynone Double Addition Cross-Links. *ACS Macro Lett.*, **2020**, *9*, 776–780. DOI: 10.1021/acsmacrolett.0c00241.
- [425] Kuhl, N.; Geitner, R.; Vitz, J.; Bode, S.; Schmitt, M.; Popp, J.; Schubert, U.S.; Hager, M.D. Increased Stability in Self-Healing Polymer Networks Based on Reversible Michael Addition Reactions. *J. Appl. Polym. Sci.*, **2017**, *134*, 44805. DOI: 10.1002/app.44805.
- [426] Abdallah, M.; Yoshikawa, C.; Hearn, M.T.W.; Simon, G.P.; Saito, K. Photoreversible Smart Polymers Based on $2\pi + 2\pi$ Cycloaddition Reactions: Nanofilms to Self-Healing Films. *Macromolecules*, **2019**, *52*, 2446–2455. DOI: 10.1021/acs.macromol.8b01729.
- [427] Kim, S.; Kim, B.-H.; Oh, M.; Park, D.H.; Lee, S. Repeatable Crack Self-Healing by Photochemical [2+2] Cycloaddition of TCE-Co-DCE Monomers Enclosed in Homopolymer Microcapsules. *Polymers*, **2019**, *11*, 104. DOI: 10.3390/polym11010104.
- [428] Chung, C.; Roh, Y.; Cho, S.; Kim, J. Crack Healing in Polymeric Materials via Photochemical [2+2] Cycloaddition. *Chem. Mater.*, **2004**, *16*, 3982–3984. DOI: 10.1021/cm049394+.
- [429] Xu, J.-F.; Chen, Y.-Z.; Wu, L.-Z.; Tung, C.-H.; Yang, Q.-Z. Dynamic Covalent Bond Based on Reversible Photo [4+4] Cycloaddition of Anthracene for Construction of Double-Dynamic Polymers. *Org. Lett.*, **2013**, *15*, 6148–6151. DOI: 10.1021/ol403015s.
- [430] Hoffmann, R.; Woodward, R.B. Orbital Symmetries and Endo-Exo Relationships in Concerted Cycloaddition Reactions. *J. Am. Chem. Soc.*, **1965**, *87*, 4388–4389. DOI: 10.1021/ja00947a033.

References

- [431] Wang, J.; Liu, Z.; Li, J.; Song, Z.; Hu, C.; Su, Z. Exo/Endo Selectivity Control in Diels–Alder Reactions of Geminal Bis(Silyl) Dienes: Theoretical and Experimental Studies. *J. Org. Chem.*, **2019**, *84*, 3940–3952. DOI: 10.1021/acs.joc.8b03090.
- [432] Sakata, K.; Fujimoto, H. Origin of the Endo Selectivity in the Diels-Alder Reaction between Cyclopentadiene and Maleic Anhydride. *European J. Org. Chem.*, **2016**, *2016*, 4275–4278. DOI: 10.1002/ejoc.201600676.
- [433] Stille, J.K.; Plummer, L. Polymerization by the Diels-Alder Reaction. *J. Org. Chem.*, **1961**, *26*, 4026–4029. DOI: 10.1021/jo01068a092.
- [434] Staudinger, H.; Bruson, H.A. Über Die Polymerisation Des Cyclopentadiens. *Justus Liebig's Ann. der Chemie*, **1926**, *447*, 110–122. DOI: 10.1002/jlac.19264470111.
- [435] Kennedy, J.P.; Castner, K.F. Thermally Reversible Polymer Systems by Cyclopentadienylation. I. A Model for Termination by Cyclopentadienylation of Olefin Polymerization. *J. Polym. Sci. Polym. Chem. Ed.*, **1979**, *17*, 2039–2054. DOI: 10.1002/pol.1979.170170714.
- [436] Kennedy, J.P.; Castner, K.F. Thermally Reversible Polymer Systems By Cyclopentadienylation - II. the Synthesis of Cyclopentadiene-Containing Polymers. *J. Polym. Sci. Polym. Chem. Ed.*, **1979**, *17*, 2055–2070. DOI: 10.1002/pol.1979.170170715.
- [437] Bergman, S.D.; Wudl, F. Mendable Polymers. *J. Mater. Chem.*, **2008**, *18*, 41–62. DOI: 10.1039/B713953P.
- [438] Murphy, E.B.; Bolanos, E.; Schaffner-Hamann, C.; Wudl, F.; Nutt, S.R.; Auad, M.L. Synthesis and Characterization of a Single-Component Thermally Remendable Polymer Network: Staudinger and Stille Revisited. *Macromolecules*, **2008**, *41*, 5203–5209. DOI: 10.1021/ma800432g.
- [439] Vedejs, E.; Eberlein, T.H.; Mazur, D.J.; McClure, C.K.; Perry, D.A.; Ruggeri, R.; Schwartz, E.; Stults, J.S.; Varie, D.L. Thioaldehyde Diels-Alder Reactions. *J. Org. Chem.*, **1986**, *51*, 1556–1562. DOI: 10.1021/jo00359a034.
- [440] Inglis, A.J.; Sinnwell, S.; Stenzel, M.H.; Barner-Kowollik, C. Ultrafast Click Conjugation of Macromolecular Building Blocks at Ambient Temperature. *Angew. Chemie Int. Ed.*, **2009**, *48*, 2411–2414. DOI: 10.1002/anie.200805993.
- [441] Inglis, A.J.; Nebhani, L.; Altintas, O.; Schmidt, F.G.; Barner-Kowollik, C. Rapid Bonding/Debonding on Demand: Reversibly Cross-Linked Functional Polymers via Diels–Alder Chemistry. *Macromolecules*, **2010**, *43*, 5515–5520. DOI: 10.1021/ma100945b.
- [442] Glassner, M.; Delaittre, G.; Kaupp, M.; Blinco, J.P.; Barner-Kowollik, C. (Ultra)Fast Catalyst-Free Macromolecular Conjugation in Aqueous Environment at Ambient Temperature. *J. Am. Chem. Soc.*, **2012**, *134*, 7274–7277. DOI: 10.1021/ja301762y.
- [443] McGregor, W.M.; Sherrington, D.C. Some Recent Synthetic Routes to Thioketones and Thioaldehydes. *Chem. Soc. Rev.*, **1993**, *22*, 199. DOI: 10.1039/cs9932200199.
- [444] Zhou, J.; Guimard, N.K.; Inglis, A.J.; Namazian, M.; Lin, C.Y.; Coote, M.L.; Spyrou, E.; Hilf, S.; Schmidt, F.G.; Barner-Kowollik, C. Thermally Reversible Diels–Alder-Based Polymerization: An Experimental and Theoretical Assessment. *Polym. Chem.*, **2012**, *3*, 628–639. DOI: 10.1039/C1PY00356A.
- [445] Guimard, N.K.; Ho, J.; Brandt, J.; Lin, C.Y.; Namazian, M.; Mueller, J.O.; Oehlschlaeger, K.K.; Hilf, S.; Lederer, A.; Schmidt, F.G.; Coote, M.L.; Barner-Kowollik, C. Harnessing Entropy to Direct the Bonding/Debonding of Polymer Systems Based on Reversible Chemistry. *Chem. Sci.*, **2013**, *4*, 2752. DOI: 10.1039/c3sc50642h.

References

- [446] Oehlenschlaeger, K.K.; Guimard, N.K.; Brandt, J.; Mueller, J.O.; Lin, C.Y.; Hilf, S.; Lederer, A.; Coote, M.L.; Schmidt, F.G.; Barner-Kowollik, C. Fast and Catalyst-Free Hetero-Diels–Alder Chemistry for on Demand Cyclable Bonding/Debonding Materials. *Polym. Chem.*, **2013**, *4*, 4348. DOI: 10.1039/c3py00476g.
- [447] Oehlenschlaeger, K.K.; Mueller, J.O.; Brandt, J.; Hilf, S.; Lederer, A.; Wilhelm, M.; Graf, R.; Coote, M.L.; Schmidt, F.G.; Barner-Kowollik, C. Adaptable Hetero Diels-Alder Networks for Fast Self-Healing under Mild Conditions. *Adv. Mater.*, **2014**, *26*, 3561–3566. DOI: 10.1002/adma.201306258.
- [448] Engel, T.; KICKELBICK, G. Thermally Remendable Polymers. In *Self-Healing Polymers*; Binder, W.H., Ed.; Wiley, **2013**; pp. 153–171. DOI: 10.1002/9783527670185.ch6.
- [449] Rulíšek, L.; Šebek, P.; Havlas, Z.; Hrabal, R.; Čapek, P.; Svatoš, A. An Experimental and Theoretical Study of Stereoselectivity of Furan–Maleic Anhydride and Furan–Maleimide Diels–Alder Reactions. *J. Org. Chem.*, **2005**, *70*, 6295–6302. DOI: 10.1021/jo050759z.
- [450] Craven, J.M. Cross-Linked Thermally Reversible Polymers Produced from Condensation Polymers with Pendant Furan Groups Cross-Linked with Maleimides, US3435003A, **1969**.
- [451] Stevens, M.P.; Jenkins, A.D. Crosslinking of Polystyrene via Pendant Maleimide Groups. *J. Polym. Sci. Polym. Chem. Ed.*, **1979**, *17*, 3675–3685. DOI: 10.1002/pol.1979.170171123.
- [452] Goussé, C.; Gandini, A.; Hodge, P. Application of the Diels–Alder Reaction to Polymers Bearing Furan Moieties. 2. Diels–Alder and Retro-Diels–Alder Reactions Involving Furan Rings in Some Styrene Copolymers. *Macromolecules*, **1998**, *31*, 314–321. DOI: 10.1021/ma9710141.
- [453] Chujo, Y.; Sada, K.; Saegusa, T. Reversible Gelation of Polyoxazoline by Means of Diels-Alder Reaction. *Macromolecules*, **1990**, *23*, 2636–2641. DOI: 10.1021/ma00212a007.
- [454] Canary, S.A.; Stevens, M.P. Thermally Reversible Crosslinking of Polystyrene via the Furan–Maleimide Diels–Alder Reaction. *J. Polym. Sci. Part A Polym. Chem.*, **1992**, *30*, 1755–1760. DOI: 10.1002/pola.1992.080300829.
- [455] Chen, X.; Dam, M.A.; Ono, K.; Mal, A.; Shen, H.; Nutt, S.R.; Sheran, K.; Wudl, F. A Thermally Re-Mendable Cross-Linked Polymeric Material. *Science*, **2002**, *295*, 1698–1702. DOI: 10.1126/science.1065879.
- [456] Chen, X.; Wudl, F.; Mal, A.K.; Shen, H.; Nutt, S.R. New Thermally Remendable Highly Cross-Linked Polymeric Materials. *Macromolecules*, **2003**, *36*, 1802–1807. DOI: 10.1021/ma0210675.
- [457] Raffa, P.; Kassi, A.; Gosschalk, J.; Migliore, N.; Polgar, L.M.; Picchioni, F. A Structure-Properties Relationship Study of Self-Healing Materials Based on Styrene and Furfuryl Methacrylate Cross-Linked via Diels–Alder Chemistry. *Macromol. Mater. Eng.*, **2021**, *306*, 2000755. DOI: 10.1002/mame.202000755.
- [458] Brancart, J.; Scheltjens, G.; Muselle, T.; Van Mele, B.; Terryn, H.; Van Assche, G. Atomic Force Microscopy–Based Study of Self-Healing Coatings Based on Reversible Polymer Network Systems. *J. Intell. Mater. Syst. Struct.*, **2014**, *25*, 40–46. DOI: 10.1177/1045389X12457100.
- [459] Araya-Hermosilla, R.; Broekhuis, A.A.; Picchioni, F. Reversible Polymer Networks Containing Covalent and Hydrogen Bonding Interactions. *Eur. Polym. J.*, **2014**, *50*, 127–134. DOI: 10.1016/j.eurpolymj.2013.10.014.

References

- [460] Rivero, G.; Nguyen, L.-T.T.; Hillewaere, X.K.D.; Du Prez, F.E. One-Pot Thermo-Remendable Shape Memory Polyurethanes. *Macromolecules*, **2014**, *47*, 2010–2018. DOI: 10.1021/ma402471c.
- [461] Fortunato, G.; Marroccoli, V.; Corsini, F.; Turri, S.; Griffini, G. A Facile Approach to Durable, Transparent and Self-Healing Coatings with Enhanced Hardness Based on Diels-Alder Polymer Networks. *Prog. Org. Coatings*, **2020**, *147*, 105840. DOI: 10.1016/j.porgcoat.2020.105840.
- [462] Okhay, N.; Mignard, N.; Jegat, C.; Taha, M. Diels-Alder Thermoresponsive Networks Based on High Maleimide- Functionalized Urethane Prepolymers. *Des. Monomers Polym.*, **2013**, *16*, 475–487. DOI: 10.1080/15685551.2012.747166.
- [463] Jin, K.; Kim, S.; Xu, J.; Bates, F.S.; Ellison, C.J. Melt-Blown Cross-Linked Fibers from Thermally Reversible Diels–Alder Polymer Networks. *ACS Macro Lett.*, **2018**, *7*, 1339–1345. DOI: 10.1021/acsmacrolett.8b00685.
- [464] Yilmaz, D.; Lansande, D.; Lewandowski, S.; Perraud, S.; Llevot, A.; Carlotti, S. Combination of Permanent Hydrosilylation and Reversible Diels–Alder Reactions for Self-Healing poly(Dimethylsiloxane) Materials with Enhanced Ageing Properties. *Mater. Today Chem.*, **2022**, *24*, 100860. DOI: 10.1016/j.mtchem.2022.100860.
- [465] Zhao, J.; Xu, R.; Luo, G.; Wu, J.; Xia, H. A Self-Healing, Re-Moldable and Biocompatible Crosslinked Polysiloxane Elastomer. *J. Mater. Chem. B*, **2016**, *4*, 982–989. DOI: 10.1039/c5tb02036k.
- [466] Kim, S.Y.; Lee, T.H.; Park, Y. II; Nam, J.H.; Noh, S.M.; Cheong, I.W.; Kim, J.C. Influence of Material Properties on Scratch-Healing Performance of Polyacrylate-Graft-Polyurethane Network That Undergo Thermally Reversible Crosslinking. *Polymer*, **2017**, *128*, 135–146. DOI: 10.1016/j.polymer.2017.09.021.
- [467] Magana, S.; Zerroukhi, A.; Jegat, C.; Mignard, N. Thermally Reversible Crosslinked Polyethylene Using Diels-Alder Reaction in Molten State. *React. Funct. Polym.*, **2010**, *70*, 442–448. DOI: 10.1016/j.reactfunctpolym.2010.04.007.
- [468] Liu, Y.-L.; Chen, Y.-W. Thermally Reversible Cross-Linked Polyamides with High Toughness and Self-Repairing Ability from Maleimide- and Furan-Functionalized Aromatic Polyamides. *Macromol. Chem. Phys.*, **2007**, *208*, 224–232. DOI: 10.1002/macp.200600445.
- [469] Peng, Y.J.; He, X.; Wu, Q.; Sun, P.C.; Wang, C.J.; Liu, X.Z. A New Recyclable Crosslinked Polymer Combined Polyurethane and Epoxy Resin. *Polymer*, **2018**, *149*, 154–163. DOI: 10.1016/j.polymer.2018.06.082.
- [470] García-Astrain, C.; Gandini, A.; Coelho, D.; Mondragon, I.; Retegi, A.; Eceiza, A.; Corcuera, M.A.; Gabilondo, N. Green Chemistry for the Synthesis of Methacrylate-Based Hydrogels Crosslinked through Diels-Alder Reaction. *Eur. Polym. J.*, **2013**, *49*, 3998–4007. DOI: 10.1016/j.eurpolymj.2013.09.004.
- [471] Yan, Q.; Zhao, L.; Cheng, Q.; Zhang, T.; Jiang, B.; Song, Y.; Huang, Y. Self-Healing Polysiloxane Elastomer Based on Integration of Covalent and Reversible Networks. *Ind. Eng. Chem. Res.*, **2019**, *58*, 21504–21512. DOI: 10.1021/acs.iecr.9b04355.
- [472] Dello Iacono, S.; Martone, A.; Pastore, A.; Filippone, G.; Acierno, A.; Zarrelli, M.; Giordano, M. Thermally Activated Multiple Self-Healing Diels-Alder Epoxy System. *Polym. Eng. Sci.*, **2017**, *57*, 674–679. DOI: 10.1002/pen.24570.
- [473] Burattini, S.; Colquhoun, M.; Greenland, B.W.; Hayes, W. A Novel Self-Healing Supramolecular Polymer System. *Faraday Discuss.*, **2009**, *143*, 251–264. DOI: 10.1039/B900859D.

References

- [474] Burattini, S.; Colquhoun, H.M.; Fox, J.D.; Friedmann, D.; Greenland, B.W.; Harris, P.J.F.; Hayes, W.; MacKay, M.E.; Rowan, S.J. A Self-Repairing, Supramolecular Polymer System: Healability as a Consequence of Donor-Acceptor π - π Stacking Interactions. *Chem. Commun.*, **2009**, *44*, 6717–6719. DOI: 10.1039/b910648k.
- [475] Burattini, S.; Greenland, B.W.; Merino, D.H.; Weng, W.; Seppala, J.; Colquhoun, H.M.; Hayes, W.; Mackay, M.E.; Hamley, I.W.; Rowan, S.J. A Healable Supramolecular Polymer Blend Based on Aromatic π - π Stacking and Hydrogen-Bonding Interactions. *J. Am. Chem. Soc.*, **2010**, *132*, 12051–12058. DOI: 10.1021/ja104446r.
- [476] Hart, L.R.; Nguyen, N.A.; Harries, J.L.; Mackay, M.E.; Colquhoun, H.M.; Hayes, W. Perylene as an Electron-Rich Moiety in Healable, Complementary π - π Stacked, Supramolecular Polymer Systems. *Polymer*, **2015**, *69*, 293–300. DOI: 10.1016/j.polymer.2015.03.028.
- [477] Mei, J.; Jia, X.; Lai, J.; Sun, Y.; Li, C.; Wu, J.; Cao, Y.; You, X.; Bao, Z. A Highly Stretchable and Autonomous Self-Healing Polymer Based on Combination of Pt \cdots Pt and π - π Interactions. *Macromol. Rapid Commun.*, **2016**, *37*, 1667–1675. DOI: 10.1002/marc.201600428.
- [478] Meurer, J.; Hniopek, J.; Ahner, J.; Schmitt, M.; Popp, J.; Zechel, S.; Peneva, K.; Hager, M.D. In-Depth Characterization of Self-Healing Polymers Based on π - π Interactions. *Beilstein J. Org. Chem.*, **2021**, *17*, 2496–2504. DOI: 10.3762/bjoc.17.166.
- [479] Rao, Y.-L.; Chortos, A.; Pfattner, R.; Lissel, F.; Chiu, Y.-C.; Feig, V.; Xu, J.; Kurosawa, T.; Gu, X.; Wang, C.; He, M.; Chung, J.W.; Bao, Z. Stretchable Self-Healing Polymeric Dielectrics Cross-Linked Through Metal-Ligand Coordination. *J. Am. Chem. Soc.*, **2016**, *138*, 6020–6027. DOI: 10.1021/jacs.6b02428.
- [480] Mozhdzhi, D.; Ayala, S.; Cromwell, O.R.; Guan, Z. Self-Healing Multiphase Polymers via Dynamic Metal-Ligand Interactions. *J. Am. Chem. Soc.*, **2014**, *136*, 16128–16131. DOI: 10.1021/ja5097094.
- [481] Bode, S.; Enke, M.; Bose, R.K.; Schacher, F.H.; Garcia, S.J.; Van Der Zwaag, S.; Hager, M.D.; Schubert, U.S. Correlation Between Scratch Healing and Rheological Behavior for Terpyridine Complex Based Metallopolymers. *J. Mater. Chem. A*, **2015**, *3*, 22145–22153. DOI: 10.1039/c5ta05545h.
- [482] Shi, L.; Ding, P.; Wang, Y.; Zhang, Y.; Ossipov, D.; Hilborn, J. Self-Healing Polymeric Hydrogel Formed by Metal-Ligand Coordination Assembly: Design, Fabrication, and Biomedical Applications. *Macromol. Rapid Commun.*, **2019**, *40*, 1800837. DOI: 10.1002/marc.201800837.
- [483] Dzhardimalieva, G.I.; Yadav, B.C.; Singh, S.; Uflyand, I.E. Self-Healing and Shape Memory Metallopolymers: State-of-the-Art and Future Perspectives. *Dalt. Trans.*, **2020**, *49*, 3042–3087. DOI: 10.1039/c9dt04360h.
- [484] Wathier, M.; Grinstaff, M.W. Synthesis and Properties of Supramolecular Ionic Networks. *J. Am. Chem. Soc.*, **2008**, *130*, 9648–9649. DOI: 10.1021/ja803248q.
- [485] Porcel, C.H.; Schlenoff, J.B. Compact Polyelectrolyte Complexes: “Saloplastic” Candidates for Biomaterials. *Biomacromolecules*, **2009**, *10*, 2968–2975. DOI: 10.1021/bm900373c.
- [486] Sun, T.L.; Kurokawa, T.; Kuroda, S.; Ihsan, A. Bin; Akasaki, T.; Sato, K.; Haque, M.A.; Nakajima, T.; Gong, J.P. Physical Hydrogels Composed of Polyampholytes Demonstrate High Toughness and Viscoelasticity. *Nat. Mater.*, **2013**, *12*, 932–937. DOI: 10.1038/nmat3713.
- [487] Reisch, A.; Tirado, P.; Roger, E.; Boulmedais, F.; Collin, D.; Voegel, J.-C.; Frisch, B.;

References

- Schaaf, P.; Schlenoff, J.B. Compact Saloplastic poly(Acrylic Acid)/poly(Allylamine) Complexes: Kinetic Control Over Composition, Microstructure, and Mechanical Properties. *Adv. Funct. Mater.*, **2013**, *23*, 673–682. DOI: 10.1002/adfm.201201413.
- [488] Barcellona, M.N.; Johnson, N.; Bernards, M.T. Characterizing Drug Release from Nonfouling Polyampholyte Hydrogels. *Langmuir*, **2015**, *31*, 13402–13409. DOI: 10.1021/acs.langmuir.5b03597.
- [489] Cao, S.; Barcellona, M.N.; Pfeiffer, F.; Bernards, M.T. Tunable Multifunctional Tissue Engineering Scaffolds Composed of Three-Component Polyampholyte Polymers. *J. Appl. Polym. Sci.*, **2016**, *133*, 43985. DOI: 10.1002/app.43985.
- [490] Huang, Y.; King, D.R.; Sun, T.L.; Nonoyama, T.; Kurokawa, T.; Nakajima, T.; Gong, J.P. Energy-Dissipative Matrices Enable Synergistic Toughening in Fiber Reinforced Soft Composites. *Adv. Funct. Mater.*, **2017**, *27*, 1605350. DOI: 10.1002/adfm.201605350.
- [491] Kolmakov, G. V.; Matyjaszewski, K.; Balazs, A.C. Harnessing Labile Bonds between Nanogel Particles to Create Self-Healing Materials. *ACS Nano*, **2009**, *3*, 885–892. DOI: 10.1021/nn900052h.
- [492] Kalista, S.J.; Ward, T.C.; Oyetunji, Z. Self-Healing of poly(Ethylene-co-Methacrylic Acid) Copolymers Following Projectile Puncture. *Mech. Adv. Mater. Struct.*, **2007**, *14*, 391–397. DOI: 10.1080/15376490701298819.
- [493] Varley, R.J.; van der Zwaag, S. Towards an Understanding of Thermally Activated Self-Healing of an Ionomer System During Ballistic Penetration. *Acta Mater.*, **2008**, *56*, 5737–5750. DOI: 10.1016/j.actamat.2008.08.008.
- [494] Eisenberg, A.; Rinaudo, M. Polyelectrolytes and Ionomers. *Polym. Bull.*, **1990**, *24*, 671. DOI: 10.1007/BF00300165.
- [495] Eisenberg, A.; Hird, B.; Moore, R.B. A New Multiplet-Cluster Model for the Morphology of Random Ionomers. *Macromolecules*, **1990**, *23*, 4098–4107. DOI: 10.1021/ma00220a012.
- [496] Eisenberg, A. Clustering of Ions in Organic Polymers. A Theoretical Approach. *Macromolecules*, **1970**, *3*, 147–154. DOI: 10.1021/ma60014a006.
- [497] Marx, C.L.; Caulfield, D.F.; Cooper, S.L. Morphology of Ionomers. *Macromolecules*, **1973**, *6*, 344–353. DOI: 10.1021/ma60033a007.
- [498] Yarusso, D.J.; Cooper, S.L. Microstructure of Ionomers: Interpretation of Small-Angle X-Ray Scattering Data. *Macromolecules*, **1983**, *16*, 1871–1880. DOI: 10.1021/ma00246a013.
- [499] Boyarsky, A.; Go'ra, P. A Model for the Structure of Spacetime. *Chaos, Solitons & Fractals*, **1996**, *7*, 611–630. DOI: 10.1016/0960-0779(95)00113-1.
- [500] Roche, E.J.; Stein, R.S.; Russell, T.P. Small- Angle X-Ray Scattering Study of Ionomer Deformation. *J. Polym. Sci. Polym. Phys. Ed.*, **1980**, *18*, 1497–1512. DOI: 10.1002/pol.1980.180180702.
- [501] Kalista, S.J.; Pflug, J.R.; Varley, R.J. Effect of Ionic Content on Ballistic Self-Healing in EMAA Copolymers and Ionomers. *Polym. Chem.*, **2013**, *4*, 4910. DOI: 10.1039/c3py00095h.
- [502] Zhang, J.; Huo, M.; Li, M.; Li, T.; Li, N.; Zhou, J.; Jiang, J. Shape Memory and Self-Healing Materials from Supramolecular Block Polymers. *Polymer*, **2018**, *134*, 35–43. DOI: 10.1016/j.polymer.2017.11.043.
- [503] Das, A.; Sallat, A.; Böhme, F.; Suckow, M.; Basu, D.; Wießner, S.; Stöckelhuber, K.W.; Voit, B.; Heinrich, G. Ionic Modification Turns Commercial Rubber into a Self-Healing

References

- Material. *ACS Appl. Mater. Interfaces*, **2015**, *7*, 20623–20630. DOI: 10.1021/acsami.5b05041.
- [504] Wang, X.; Wang, Y.; Bi, S.; Wang, Y.; Chen, X.; Qiu, L.; Sun, J. Optically Transparent Antibacterial Films Capable of Healing Multiple Scratches. *Adv. Funct. Mater.*, **2014**, *24*, 403–411. DOI: 10.1002/adfm.201302109.
- [505] Reisch, A.; Roger, E.; Phoeung, T.; Antheaume, C.; Orthlieb, C.; Boulmedais, F.; Lavallo, P.; Schlenoff, J.B.; Frisch, B.; Schaaf, P. On the Benefits of Rubbing Salt in the Cut: Self-Healing of Saloplastic PAA/PAH Compact Polyelectrolyte Complexes. *Adv. Mater.*, **2014**, *26*, 2547–2551. DOI: 10.1002/adma.201304991.
- [506] Cuthbert, T.J.; Jadischke, J.J.; de Bruyn, J.R.; Ragogna, P.J.; Gillies, E.R. Self-Healing Polyphosphonium Ionic Networks. *Macromolecules*, **2017**, *50*, 5253–5260. DOI: 10.1021/acs.macromol.7b00955.
- [507] Zhang, H.; Wang, C.; Zhu, G.; Zacharia, N.S. Self-Healing of Bulk Polyelectrolyte Complex Material as a Function of pH and Salt. *ACS Appl. Mater. Interfaces*, **2016**, *8*, 26258–26265. DOI: 10.1021/acsami.6b06776.
- [508] Ihsan, A. Bin; Sun, T.L.; Kurokawa, T.; Karobi, S.N.; Nakajima, T.; Nonoyama, T.; Roy, C.K.; Luo, F.; Gong, J.P. Self-Healing Behaviors of Tough Polyampholyte Hydrogels. *Macromolecules*, **2016**, *49*, 4245–4252. DOI: 10.1021/acs.macromol.6b00437.
- [509] Zhang, W.; Wu, B.; Sun, S.; Wu, P. Skin-like Mechanoresponsive Self-Healing Ionic Elastomer from Supramolecular Zwitterionic Network. *Nat. Commun.*, **2021**, *12*, 4082. DOI: 10.1038/s41467-021-24382-4.
- [510] Brunsveld, L.; Folmer, B.J.B.; Meijer, E.W.; Sijbesma, R.P. Supramolecular Polymers. *Chem. Rev.*, **2001**, *101*, 4071–4098. DOI: 10.1021/cr990125q.
- [511] Diesendruck, C.E.; Sottos, N.R.; Moore, J.S.; White, S.R. Biomimetic Self-Healing. *Angew. Chemie Int. Ed.*, **2015**, *54*, 10428–10447. DOI: 10.1002/anie.201500484.
- [512] Xie, Z.; Hu, B.-L.; Li, R.-W.; Zhang, Q. Hydrogen Bonding in Self-Healing Elastomers. *ACS Omega*, **2021**, *6*, 9319–9333. DOI: 10.1021/acsomega.1c00462.
- [513] Zhang, G.; Sun, Z.; Li, M. Recent Developments: Self-Healing Polymers Based on Quadruple Hydrogen Bonds. *E3S Web Conf.*, **2021**, *290*, 01037. DOI: 10.1051/e3sconf/202129001037.
- [514] Gadwal, I. A Brief Overview on Preparation of Self-Healing Polymers and Coatings via Hydrogen Bonding Interactions. *Macromol*, **2020**, *1*, 18–36. DOI: 10.3390/macromol1010003.
- [515] Fouquey, C.; Lehn, J.-M.; Levelut, A.-M. Molecular Recognition Directed Self-Assembly of Supramolecular Liquid Crystalline Polymers from Complementary Chiral Components. *Adv. Mater.*, **1990**, *2*, 254–257. DOI: 10.1002/adma.19900020506.
- [516] Hentschel, J.; Kushner, A.M.; Ziller, J.; Guan, Z. Self-Healing Supramolecular Block Copolymers. *Angew. Chemie Int. Ed.*, **2012**, *51*, 10561–10565. DOI: 10.1002/anie.201204840.
- [517] Li, G.; Wie, J.J.; Nguyen, N.A.; Chung, W.J.; Kim, E.T.; Char, K.; MacKay, M.E.; Pyun, J. Synthesis, Self-Assembly and Reversible Healing of Supramolecular Perfluoropolyethers. *J. Polym. Sci. Part A Polym. Chem.*, **2013**, *51*, 3598–3606. DOI: 10.1002/pola.26777.
- [518] Liu, M.; Liu, P.; Lu, G.; Xu, Z.; Yao, X. Multiphase-Assembly of Siloxane Oligomers with Improved Mechanical Strength and Water-Enhanced Healing. *Angew. Chemie Int. Ed.*, **2018**, *57*, 11242–11246. DOI: 10.1002/anie.201805206.

References

- [519] Song, Y.; Liu, Y.; Qi, T.; Li, G.L. Towards Dynamic but Supertough Healable Polymers through Biomimetic Hierarchical Hydrogen-Bonding Interactions. *Angew. Chemie Int. Ed.*, **2018**, *57*, 13838–13842. DOI: 10.1002/anie.201807622.
- [520] Xia, L.; Tu, H.; Zeng, W.; Yang, X.; Zhou, M.; Li, L.; Guo, X. A Room-Temperature Self-Healing Elastomer with Ultra-High Strength and Toughness Fabricated via Optimized Hierarchical Hydrogen-Bonding Interactions. *J. Mater. Chem. A*, **2022**, *10*, 4344–4354. DOI: 10.1039/d1ta08748g.
- [521] Zhou, Z.; Chen, S.; Xu, X.; Chen, Y.; Xu, L.; Zeng, Y.; Zhang, F. Room Temperature Self-Healing Crosslinked Elastomer Constructed by Dynamic Urea Bond and Hydrogen Bond. *Prog. Org. Coatings*, **2021**, *154*, 106213. DOI: 10.1016/j.porgcoat.2021.106213.
- [522] Lv, C.; Zhao, K.; Zheng, J. A Highly Stretchable Self-Healing poly(Dimethylsiloxane) Elastomer with Reprocessability and Degradability. *Macromol. Rapid Commun.*, **2018**, *39*, 1700686. DOI: 10.1002/marc.201700686.
- [523] Lee, S.H.; Shin, S.R.; Lee, D.S. Self-Healing of Cross-Linked PU via Dual-Dynamic Covalent Bonds of a Schiff Base from Cystine and Vanillin. *Mater. Des.*, **2019**, *172*, 107774. DOI: 10.1016/j.matdes.2019.107774.
- [524] Dai, X.; Du, Y.; Wang, Y.; Liu, Y.; Xu, N.; Li, Y.; Shan, D.; Xu, B. Bin; Kong, J. Stretchable Self-Healing Polymeric Networks with Recyclability and Dual Responsiveness. *ACS Appl. Polym. Mater.*, **2020**, *2*, 1065–1072. DOI: 10.1021/acsapm.9b01073.
- [525] Deng, G.; Li, F.; Yu, H.; Liu, F.; Liu, C.; Sun, W.; Jiang, H.; Chen, Y. Dynamic Hydrogels with an Environmental Adaptive Self-Healing Ability and Dual Responsive Sol–Gel Transitions. *ACS Macro Lett.*, **2012**, *1*, 275–279. DOI: 10.1021/mz200195n.
- [526] Chen, J.; Su, Q.; Guo, R.; Zhang, J.; Dong, A.; Lin, C.; Zhang, J. A Multitasking Hydrogel Based on Double Dynamic Network with Quadruple-Stimuli Sensitiveness, Autonomic Self-Healing Property, and Biomimetic Adhesion Ability. *Macromol. Chem. Phys.*, **2017**, *218*, 1700166. DOI: 10.1002/macp.201700166.
- [527] Liu, H.; Xiong, C.; Tao, Z.; Fan, Y.; Tang, X.; Yang, H. Zwitterionic Copolymer-Based and Hydrogen Bonding-Strengthened Self-Healing Hydrogel. *RSC Adv.*, **2015**, *5*, 33083–33088. DOI: 10.1039/c4ra15003a.
- [528] Guo, H.; Fang, X.; Zhang, L.; Sun, J. Facile Fabrication of Room-Temperature Self-Healing, Mechanically Robust, Highly Stretchable, and Tough Polymers Using Dual Dynamic Cross-Linked Polymer Complexes. *ACS Appl. Mater. Interfaces*, **2019**, *11*, 33356–33363. DOI: 10.1021/acsami.9b11166.
- [529] Sattar, M.A.; Gangadharan, S.; Patnaik, A. Design of Dual Hybrid Network Natural Rubber–SiO₂ Elastomers with Tailored Mechanical and Self-Healing Properties. *ACS Omega*, **2019**, *4*, 10939–10949. DOI: 10.1021/acsomega.9b01243.
- [530] Sun, H.; Liu, X.; Liu, S.; Yu, B.; Ning, N.; Tian, M.; Zhang, L. Silicone Dielectric Elastomer with Improved Actuated Strain at Low Electric Field and High Self-Healing Efficiency by Constructing Supramolecular Network. *Chem. Eng. J.*, **2019**, *384*, 123242. DOI: 10.1016/j.cej.2019.123242.
- [531] Stein, S.; Mordvinkin, A.; Voit, B.; Komber, H.; Saalwächter, K.; Böhme, F. Self-Healing and Reprocessable Bromo Butylrubber Based on Combined Ionic Cluster Formation and Hydrogen Bonding. *Polym. Chem.*, **2020**, *11*, 1188–1197. DOI: 10.1039/c9py01630a.
- [532] Wang, X.; Liang, D.; Cheng, B. Preparation and Research of Intrinsic Self-Healing Elastomers Based on Hydrogen and Ionic Bond. *Compos. Sci. Technol.*, **2020**, *193*, 108127. DOI: 10.1016/j.compscitech.2020.108127.

References

- [533] Zhong, M.; Liu, X.Y.; Shi, F.K.; Zhang, L.Q.; Wang, X.P.; Cheetham, A.G.; Cui, H.; Xie, X.M. Self-Healable, Tough and Highly Stretchable Ionic Nanocomposite Physical Hydrogels. *Soft Matter*, **2015**, *11*, 4235–4241. DOI: 10.1039/c5sm00493d.
- [534] Ye, G.; Song, Z.; Yu, T.; Tan, Q.; Zhang, Y.; Chen, T.; He, C.; Jin, L.; Liu, N. Dynamic Ag–N Bond Enhanced Stretchable Conductor for Transparent and Self-Healing Electronic Skin. *ACS Appl. Mater. Interfaces*, **2020**, *12*, 1486–1494. DOI: 10.1021/acsami.9b17354.
- [535] Gerth, M.; Bohdan, M.; Fokkink, R.; Voets, I.; van der Gucht, J.; Sprakel, J. Supramolecular Assembly of Self-Healing Nanocomposite Hydrogels. *Macromol. Rapid Commun.*, **2014**, *35*, 2065–2070. DOI: 10.1002/marc.201400543.
- [536] Das, S.; Martin, P.; Vasilyev, G.; Nandi, R.; Amdursky, N.; Zussman, E. Processable, Ion-Conducting Hydrogel for Flexible Electronic Devices with Self-Healing Capability. *Macromolecules*, **2020**, *53*, 11130–11141. DOI: 10.1021/acs.macromol.0c02060.
- [537] Rekondo, A.; Martin, R.; Ruiz De Luzuriaga, A.; Cabañero, G.; Grande, H.J.; Odriozola, I. Catalyst-Free Room-Temperature Self-Healing Elastomers Based on Aromatic Disulfide Metathesis. *Mater. Horizons*, **2014**, *1*, 237–240. DOI: 10.1039/c3mh00061c.
- [538] Xu, W.M.; Rong, M.Z.; Zhang, M.Q. Sunlight Driven Self-Healing, Reshaping and Recycling of a Robust, Transparent and Yellowing-Resistant Polymer. *J. Mater. Chem. A*, **2016**, *4*, 10683–10690. DOI: 10.1039/c6ta02662a.
- [539] Jian, X.; Hu, Y.; Zhou, W.; Xiao, L. Self-Healing Polyurethane Based on Disulfide Bond and Hydrogen Bond. *Polym. Adv. Technol.*, **2018**, *29*, 463–469. DOI: 10.1002/pat.4135.
- [540] Li, X.; Yu, R.; He, Y.; Zhang, Y.; Yang, X.; Zhao, X.; Huang, W. Self-Healing Polyurethane Elastomers Based on a Disulfide Bond by Digital Light Processing 3D Printing. *ACS Macro Lett.*, **2019**, *8*, 1511–1516. DOI: 10.1021/acsmacrolett.9b00766.
- [541] Guo, H.; Han, Y.; Zhao, W.; Yang, J.; Zhang, L. Universally Autonomous Self-Healing Elastomer with High Stretchability. *Nat. Commun.*, **2020**, *11*, 2037. DOI: 10.1038/s41467-020-15949-8.
- [542] Roy, N.; Buhler, E.; Lehn, J.M. Double Dynamic Self-Healing Polymers: Supramolecular and Covalent Dynamic Polymers Based on the Bis-Iminocarbohydrazide Motif. *Polym. Int.*, **2014**, *63*, 1400–1405. DOI: 10.1002/pi.4646.
- [543] Yan, H.; Dai, S.; Chen, Y.; Ding, J.; Yuan, N. A High Stretchable and Self-Healing Silicone Rubber with Double Reversible Bonds. *ChemistrySelect*, **2019**, *4*, 10719–10725. DOI: 10.1002/slct.201902244.
- [544] Yang, Z.; Li, H.; Zhang, L.; Lai, X.; Zeng, X. Highly Stretchable, Transparent and Room-Temperature Self-Healable Polydimethylsiloxane Elastomer for Bending Sensor. *J. Colloid Interface Sci.*, **2020**, *570*, 1–10. DOI: 10.1016/j.jcis.2020.02.107.
- [545] Li, Y.; Guo, W.; Li, W.; Liu, X.; Zhu, H.; Zhang, J. Tuning Hard Phase Towards Synergistic Improvement of Toughness and Self-Healing Ability of poly(Urethane Urea) by Dual Chain Extenders and Coordinative Bonds. *Chem. Eng. J.*, **2020**, *393*, 124583. DOI: 10.1016/j.cej.2020.124583.
- [546] Lin, C.; Sheng, D.; Liu, X.; Xu, S.; Ji, F.; Dong, L.; Zhou, Y.; Yang, Y. Coordination Bonds and Diels–Alder Bonds Dual Crosslinked Polymer Networks of Self-healing Polyurethane. *J. Polym. Sci. Part A Polym. Chem.*, **2019**, *57*, 2228–2234. DOI: 10.1002/pola.29508.
- [547] Araya-Hermosilla, R.; Lima, G.M.R.; Raffa, P.; Fortunato, G.; Pucci, A.; Flores, M.E.; Moreno-Villoslada, I.; Broekhuis, A.A.; Picchioni, F. Intrinsic Self-Healing Thermoset through Covalent and Hydrogen Bonding Interactions. *Eur. Polym. J.*, **2016**, *81*, 186–

References

197. DOI: 10.1016/j.eurpolymj.2016.06.004.
- [548] Zhang, B.; Digby, Z.A.; Flum, J.A.; Foster, E.M.; Sparks, J.L.; Konkolewicz, D. Self-Healing, Malleable and Creep Limiting Materials Using Both Supramolecular and Reversible Covalent Linkages. *Polym. Chem.*, **2015**, *6*, 7368–7372. DOI: 10.1039/C5PY01214G.
- [549] Zhao, J.; Xu, R.; Luo, G.; Wu, J.; Xia, H. Self-Healing poly(Siloxane-Urethane) Elastomers with Remoldability, Shape Memory and Biocompatibility. *Polym. Chem.*, **2016**, *7*, 7278–7286. DOI: 10.1039/c6py01499b.
- [550] Willocq, B.; Khelifa, F.; Brancart, J.; Van Assche, G.; Dubois, P.; Raquez, J.-M. One-Component Diels–Alder Based Polyurethanes: A Unique Way to Self-Heal. *RSC Adv.*, **2017**, *7*, 48047–48053. DOI: 10.1039/C7RA09898G.
- [551] Cummings, S.C.; Dodo, O.J.; Hull, A.C.; Zhang, B.; Myers, C.P.; Sparks, J.L.; Konkolewicz, D. Quantity or Quality: Are Self-Healing Polymers and Elastomers Always Tougher with More Hydrogen Bonds? *ACS Appl. Polym. Mater.*, **2020**, *2*, 1108–1113. DOI: 10.1021/acsapm.9b01095.
- [552] Lindenmeyer, K.M.; Johnson, R.D.; Miller, K.M. Self-Healing Behaviour of Furan-Maleimide poly(Ionic Liquid) Covalent Adaptable Networks. *Polym. Chem.*, **2020**, *11*, 5321–5326. DOI: 10.1039/d0py00016g.
- [553] Osada, T.; Kamoda, K.; Mitome, M.; Hara, T.; Abe, T.; Tamagawa, Y.; Nakao, W.; Ohmura, T. A Novel Design Approach for Self-Crack-Healing Structural Ceramics with 3D Networks of Healing Activator. *Sci. Rep.*, **2017**, *7*, 17853. DOI: 10.1038/s41598-017-17942-6.
- [554] Grabowski, B.; Tasan, C.C. Self-Healing Metals. In *Advances in Polymer Science*; **2016**; Vol. 273, pp. 387–407. DOI: 10.1007/12_2015_337.
- [555] Arslan, M.; Tasdelen, M. Polymer Nanocomposites via Click Chemistry Reactions. *Polymers*, **2017**, *9*, 499. DOI: 10.3390/polym9100499.
- [556] Khan, N.I.; Halder, S.; Gunjan, S.B.; Prasad, T. A Review on Diels-Alder Based Self-Healing Polymer Composites. *IOP Conf. Ser. Mater. Sci. Eng.*, **2018**, *377*, 012007. DOI: 10.1088/1757-899X/377/1/012007.
- [557] Thangavel, G.; Tan, M.W.M.; Lee, P.S. Advances in Self-Healing Supramolecular Soft Materials and Nanocomposites. *Nano Converg.*, **2019**, *6*, 29. DOI: 10.1186/s40580-019-0199-9.
- [558] Sanka, R.V.S.P.; Krishnakumar, B.; Letierrier, Y.; Pandey, S.; Rana, S.; Michaud, V. Soft Self-Healing Nanocomposites. *Front. Mater.*, **2019**, *6*, 1–20. DOI: 10.3389/fmats.2019.00137.
- [559] Song, T.; Jiang, B.; Li, Y.; Ji, Z.; Zhou, H.; Jiang, D.; Seok, I.; Murugadoss, V.; Wen, N.; Colorado, H. Self-Healing Materials: A Review of Recent Developments. *ES Mater. Manuf.*, **2021**, *14*, 1–19. DOI: 10.30919/esmm5f465.
- [560] Corten, C.C.; Urban, M.W. Repairing Polymers Using Oscillating Magnetic Field. *Adv. Mater.*, **2009**, *21*, 5011–5015. DOI: 10.1002/adma.200901940.
- [561] Yoonessi, M.; Lerch, B.A.; Peck, J.A.; Rogers, R.B.; Solá-Lopez, F.J.; Meador, M.A. Self-Healing of Core–Shell Magnetic Polystyrene Nanocomposites. *ACS Appl. Mater. Interfaces*, **2015**, *7*, 16932–16937. DOI: 10.1021/acsami.5b04314.
- [562] Yang, Y.; He, J.; Li, Q.; Gao, L.; Hu, J.; Zeng, R.; Qin, J.; Wang, S.X.; Wang, Q. Self-Healing of Electrical Damage in Polymers Using Superparamagnetic Nanoparticles. *Nat. Nanotechnol.*, **2019**, *14*, 151–155. DOI: 10.1038/s41565-018-0327-4.

References

- [563] Ahmed, A.S.; Ramanujan, R. V. Magnetic Field Triggered Multicycle Damage Sensing and Self Healing. *Sci. Rep.*, **2015**, *5*, 13773. DOI: 10.1038/srep13773.
- [564] Post, W.; Bose, R.; García, S.; van der Zwaag, S. Healing of Early Stage Fatigue Damage in Ionomer/Fe₃O₄ Nanoparticle Composites. *Polymers*, **2016**, *8*, 436. DOI: 10.3390/polym8120436.
- [565] Hohlbein, N.; Shaaban, A.; Schmidt, A.M. Remote-Controlled Activation of Self-Healing Behavior in Magneto-Responsive Ionomeric Composites. *Polymer*, **2015**, *69*, 301–309. DOI: 10.1016/j.polymer.2015.04.024.
- [566] Hohlbein, N.; Shaaban, A.; Bras, A.R.; Pyckhout-Hintzen, W.; Schmidt, A.M. Self-Healing Dynamic Bond-Based Rubbers: Understanding the Mechanisms in Ionomeric Elastomer Model Systems. *Phys. Chem. Chem. Phys.*, **2015**, *17*, 21005–21017. DOI: 10.1039/c5cp00620a.
- [567] Zhang, Y.; Wang, Y.; Wen, Y.; Zhong, Q.; Zhao, Y. Self-Healable Magnetic Structural Color Hydrogels. *ACS Appl. Mater. Interfaces*, **2020**, *12*, 7486–7493. DOI: 10.1021/acscami.9b22579.
- [568] Engel, T.; Kickelbick, G. Self-Healing Nanocomposites from Silica-Polymer Core-Shell Nanoparticles. *Polym. Int.*, **2014**, *63*, 915–923. DOI: 10.1002/pi.4642.
- [569] Schäfer, S.; Kickelbick, G. Self-Healing Polymer Nanocomposites Based on Diels-Alder-Reactions with Silica Nanoparticles: The Role of the Polymer Matrix. *Polymer*, **2015**, *69*, 357–368. DOI: 10.1016/j.polymer.2015.03.017.
- [570] Engel, T.; Kickelbick, G. Thermoreversible Reactions on Inorganic Nanoparticle Surfaces: Diels–Alder Reactions on Sterically Crowded Surfaces. *Chem. Mater.*, **2013**, *25*, 149–157. DOI: 10.1021/cm303049k.
- [571] Bourlinos, A.B.; Herrera, R.; Chalkias, N.; Jiang, D.D.; Zhang, Q.; Archer, L.A.; Giannelis, E.P. Surface-Functionalized Nanoparticles with Liquid-Like Behavior. *Adv. Mater.*, **2005**, *17*, 234–237. DOI: 10.1002/adma.200401060.
- [572] Rodriguez, R.; Herrera, R.; Archer, L.A.; Giannelis, E.P. Nanoscale Ionic Materials. *Adv. Mater.*, **2008**, *20*, 4353–4358. DOI: 10.1002/adma.200801975.
- [573] Fernandes, N.J.; Akbarzadeh, J.; Peterlik, H.; Giannelis, E.P. Synthesis and Properties of Highly Dispersed Ionic Silica–poly(Ethylene Oxide) Nanohybrids. *ACS Nano*, **2013**, *7*, 1265–1271. DOI: 10.1021/nn304735r.
- [574] Fernandes, N.J.; Wallin, T.J.; Vaia, R.A.; Koerner, H.; Giannelis, E.P. Nanoscale Ionic Materials. *Chem. Mater.*, **2014**, *26*, 84–96. DOI: 10.1021/cm402372q.
- [575] Wu, J.; Li, D.; Zeng, H.; Zhou, Z.; Yang, S.; Zhao, N.; Xu, J. TiO₂ Nanoscale Ionic Materials Using Mussel Adhesive Proteins Inspired Ligand. *Appl. Surf. Sci.*, **2018**, *29*, 606–611. DOI: 10.1016/j.apsusc.2018.08.039.
- [576] Voevodin, A.A.; Vaia, R.A.; Patton, S.T.; Diamanti, S.; Pender, M.; Yoonessi, M.; Brubaker, J.; Hu, J.-J.; Sanders, J.H.; Phillips, B.S.; MacCuspie, R.I. Nanoparticle-Wetted Surfaces for Relays and Energy Transmission Contacts. *Small*, **2007**, *3*, 1957–1963. DOI: 10.1002/smll.200700500.
- [577] Comenencia Ortiz, L.; Kwon, H.-K.; Rodriguez, J.; Chen, Y.; Vukasin, G.D.; Heinz, D.B.; Shin, D.D.; Kenny, T.W. Low-Power Dual Mode MEMS Resonators With PPB Stability Over Temperature. *J. Microelectromechanical Syst.*, **2020**, *29*, 190–201. DOI: 10.1109/JMEMS.2020.2970609.
- [578] Zheng, J.; Xiao, P.; Liu, W.; Zhang, J.; Huang, Y.; Chen, T. Mechanical Robust and Self-Healable Supramolecular Hydrogel. *Macromol. Rapid Commun.*, **2016**, *37*, 265–270.

References

- DOI: 10.1002/marc.201500571.
- [579] Odent, J.; Raquez, J.-M.; Samuel, C.; Barrau, S.; Enotiadis, A.; Dubois, P.; Giannelis, E.P. Shape-Memory Behavior of Polylactide/Silica Ionic Hybrids. *Macromolecules*, **2017**, *50*, 2896–2905. DOI: 10.1021/acs.macromol.7b00195.
- [580] Moghimikheirabadi, A.; Karatrantos, A. V.; Kröger, M. Ionic Polymer Nanocomposites Subjected to Uniaxial Extension: A Nonequilibrium Molecular Dynamics Study. *Polymers*, **2021**, *13*, 4001. DOI: 10.3390/polym13224001.
- [581] Mugemana, C.; Moghimikheirabadi, A.; Arl, D.; Addiego, F.; Schmidt, D.F.; Kröger, M.; Karatrantos, A. V. Ionic poly(Dimethylsiloxane)–Silica Nanocomposites: Dispersion and Self-Healing. *MRS Bull.*, **2022**, *47*, 1185–1197. DOI: 10.1557/s43577-022-00346-x.
- [582] Bhattacharya, S.; Samanta, S.K. Soft-Nanocomposites of Nanoparticles and Nanocarbons with Supramolecular and Polymer Gels and Their Applications. *Chem. Rev.*, **2016**, *116*, 11967–12028. DOI: 10.1021/acs.chemrev.6b00221.
- [583] Han, L.; Lu, X.; Wang, M.; Gan, D.; Deng, W.; Wang, K.; Fang, L.; Liu, K.; Chan, C.W.; Tang, Y.; Weng, L.-T.; Yuan, H. A Mussel-Inspired Conductive, Self-Adhesive, and Self-Healable Tough Hydrogel as Cell Stimulators and Implantable Bioelectronics. *Small*, **2017**, *13*, 1601916. DOI: 10.1002/smll.201601916.
- [584] Guadagno, L.; Vertuccio, L.; Naddeo, C.; Calabrese, E.; Barra, G.; Raimondo, M.; Sorrentino, A.; Binder, W.H.; Michael, P.; Rana, S. Self-Healing Epoxy Nanocomposites via Reversible Hydrogen Bonding. *Compos. Part B*, **2019**, *157*, 1–13. DOI: 10.1016/j.compositesb.2018.08.082.
- [585] Jiang, H.; Zhang, G.; Feng, X.; Liu, H.; Li, F.; Wang, M.; Li, H. Room-Temperature Self-Healing Tough Nanocomposite Hydrogel Crosslinked by Zirconium Hydroxide Nanoparticles. *Compos. Sci. Technol.*, **2017**, *140*, 54–62. DOI: 10.1016/j.compscitech.2016.12.027.
- [586] Hu, X.; Liang, R.; Li, J.; Liu, Z.; Sun, G. Highly Stretchable Self-Healing Nanocomposite Hydrogel Reinforced by 5 Nm Particles. *ES Mater. Manuf.*, **2018**, *2*, 16–23. DOI: 10.30919/esmm5f158.
- [587] Bian, W.; Wang, W.; Yang, Y. A Self-Healing and Electrical-Tree-Inhibiting Epoxy Composite with Hydrogen-Bonds and SiO₂ Particles. *Polymers*, **2017**, *9*, 431. DOI: 10.3390/polym9090431.
- [588] Iyer, B.V.S.; Salib, I.G.; Yashin, V. V.; Kowalewski, T.; Matyjaszewski, K.; Balazs, A.C. Modeling the Response of Dual Cross-Linked Nanoparticle Networks to Mechanical Deformation. *Soft Matter*, **2013**, *9*, 109–121. DOI: 10.1039/c2sm27121d.
- [589] Lu, C.-H.; Yu, C.-H.; Yeh, Y.-C. Engineering Nanocomposite Hydrogels Using Dynamic Bonds. *Acta Biomater.*, **2021**, *130*, 66–79. DOI: 10.1016/j.actbio.2021.05.055.
- [590] Tsai, T.-Y.; Shen, K.-H.; Chang, C.-W.; Jovanska, L.; Wang, R.; Yeh, Y.-C. In Situ Formation of Nanocomposite Double-Network Hydrogels with Shear-Thinning and Self-Healing Properties. *Biomater. Sci.*, **2021**, *9*, 985–999. DOI: 10.1039/D0BM01528H.
- [591] Shao, C.; Chang, H.; Wang, M.; Xu, F.; Yang, J. High-Strength, Tough, and Self-Healing Nanocomposite Physical Hydrogels Based on the Synergistic Effects of Dynamic Hydrogen Bond and Dual Coordination Bonds. *ACS Appl. Mater. Interfaces*, **2017**, *9*, 28305–28318. DOI: 10.1021/acsami.7b09614.
- [592] Wu, M.; Chen, J.; Ma, Y.; Yan, B.; Pan, M.; Peng, Q.; Wang, W.; Han, L.; Liu, J.; Zeng, H. Ultra Elastic, Stretchable, Self-Healing Conductive Hydrogels with Tunable Optical Properties for Highly Sensitive Soft Electronic Sensors. *J. Mater. Chem. A*, **2020**, *8*, 24718–24733. DOI: 10.1039/D0TA09735G.

References

- [593] Rasband, W. ImageJ (Version 1.54k).
- [594] Urian, Y.A.; Atoche-Medrano, J.J.; Quispe, L.T.; León Félix, L.; Coaquira, J.A.H. Study of the Surface Properties and Particle-Particle Interactions in Oleic Acid-Coated Fe₃O₄ Nanoparticles. *J. Magn. Magn. Mater.*, **2021**, *525*, 167686. DOI: 10.1016/j.jmmm.2020.167686.
- [595] Lai, C.W.; Low, F.W.; Tai, M.F.; Abdul Hamid, S.B. Iron Oxide Nanoparticles Decorated Oleic Acid for High Colloidal Stability. *Adv. Polym. Technol.*, **2018**, *37*, 1712–1721. DOI: 10.1002/adv.21829.
- [596] Ferreira, F.F.; Granado, E.; Carvalho Jr, W.; Kycia, S.W.; Bruno, D.; Droppa Jr, R. X-Ray Powder Diffraction Beamline at D10B of LNLS: Application to the Ba₂FeReO₆ Double Perovskite. *J. Synchrotron Radiat.*, **2006**, *13*, 46–53. DOI: 10.1107/S0909049505039208.
- [597] Solano, E.; Frontera, C.; Puig, T.; Obradors, X.; Ricart, S.; Ros, J. Neutron and X-Ray Diffraction Study of Ferrite Nanocrystals Obtained by Microwave-Assisted Growth. A Structural Comparison with the Thermal Synthetic Route. *J. Appl. Crystallogr.*, **2014**, *47*, 414–420. DOI: 10.1107/S1600576713032895.
- [598] Ferreira, T.A.S.; Waerenborgh, J.C.; Mendonça, M.H.R.M.; Nunes, M.R.; Costa, F.M. Structural and Morphological Characterization of FeCo₂O₄ and CoFe₂O₄ Spinel Prepared by a Coprecipitation Method. *Solid State Sci.*, **2003**, *5*, 383–392. DOI: 10.1016/S1293-2558(03)00011-6.
- [599] Jette, E.R.; Foote, F. An X-Ray Study of the Wüstite (FeO) Solid Solutions. *J. Chem. Phys.*, **1933**, *1*, 29–36. DOI: 10.1063/1.1749215.
- [600] Wood, I.G.; Vočadlo, L.; Dobson, D.P.; Price, G.D.; Fortes, A.D.; Cooper, F.J.; Neale, J.W.; Walker, A.M.; Marshall, W.G.; Tucker, M.G.; Francis, D.J.; Stone, H.J.; McCammon, C.A. Thermoelastic Properties of Magnesiowüstite, (Mg_{1-x}Fe_x)O: Determination of the Anderson–Grüneisen Parameter by Time-of-Flight Neutron Powder Diffraction at Simultaneous High Pressures and Temperatures. *J. Appl. Crystallogr.*, **2008**, *41*, 886–896. DOI: 10.1107/S0021889808025417.
- [601] Mahdavi, M.; Ahmad, M.; Haron, M.; Namvar, F.; Nadi, B.; Rahman, M.; Amin, J. Synthesis, Surface Modification and Characterisation of Biocompatible Magnetic Iron Oxide Nanoparticles for Biomedical Applications. *Molecules*, **2013**, *18*, 7533–7548. DOI: 10.3390/molecules18077533.
- [602] Chen, R.; Christiansen, M.G.; Anikeeva, P. Maximizing Hysteretic Losses in Magnetic Ferrite Nanoparticles via Model-Driven Synthesis and Materials Optimization. *ACS Nano*, **2013**, *7*, 8990–9000. DOI: 10.1021/nn4035266.
- [603] Varanda, L.C.; Souza, C.G.S.; Moraes, D.A.; Neves, H.R.; Souza Junior, J.B.; Silva, M.F.; Bini, R.A.; Albers, R.F.; Silva, T.L.; Beck Junior, W. Size and Shape-Controlled Nanomaterials Based on Modified Polyol and Thermal Decomposition Approaches. A Brief Review. *An. Acad. Bras. Cienc.*, **2019**, *91*, e20181180. DOI: 10.1590/0001-3765201920181180.
- [604] Song, Q.; Ding, Y.; Wang, Z.L.; Zhang, Z.J. Tuning the Thermal Stability of Molecular Precursors for the Nonhydrolytic Synthesis of Magnetic MnFe₂O₄ Spinel Nanocrystals. *Chem. Mater.*, **2007**, *19*, 4633–4638. DOI: 10.1021/cm070990o.
- [605] Lasheras, X.; Insausti, M.; de la Fuente, J.M.; Gil de Muro, I.; Castellanos-Rubio, I.; Marcano, L.; Fernández-Gubieda, M.L.; Serrano, A.; Martín-Rodríguez, R.; Garaio, E.; García, J.A.; Lezama, L. Mn-Doping Level Dependence on the Magnetic Response of Mn_xFe_{3-x}O₄ Ferrite Nanoparticles. *Dalt. Trans.*, **2019**, *48*, 11480–11491. DOI: 10.1039/C9DT01620A.

References

- [606] Chaudhuri, A.; Mandal, K. Dynamic Magnetic Properties of Monodisperse CoFe_2O_4 Nanoparticles Synthesized by a Facile Solvothermal Technique. *Phys. B Condens. Matter*, **2019**, *575*, 311640. DOI: 10.1016/j.physb.2019.08.017.
- [607] Kalaiselvan, C.R.; Laha, S.S.; Somvanshi, S.B.; Tabish, T.A.; Thorat, N.D.; Sahu, N.K. Manganese Ferrite (MnFe_2O_4) Nanostructures for Cancer Theranostics. *Coord. Chem. Rev.*, **2022**, *473*, 214809. DOI: 10.1016/j.ccr.2022.214809.
- [608] Schuele, W.J.; Shtrikman, S.; Treves, D. Observation of Superparamagnetism by the Mössbauer Effect. *J. Appl. Phys.*, **1965**, *36*, 1010–1011. DOI: 10.1063/1.1714075.
- [609] Kopcewicz, M.; Grabias, A.; Kuryliszyn-Kudelska, I.; Dobrowolski, W. Mössbauer Effect Study of Superparamagnetic Behavior of ZnFe_2O_4 Nanoparticles Formed in ZnO Doped with Fe_2O_3 . *Phys. status solidi*, **2019**, *256*, 1800223. DOI: 10.1002/pssb.201800223.
- [610] Knyazev, Y. V.; Balaev, D.A.; Kirillov, V.L.; Bayukov, O.A.; Mart'yanov, O.N. Mössbauer Spectroscopy Study of the Superparamagnetism of Ultrasmall $\epsilon\text{-Fe}_2\text{O}_3$ Nanoparticles. *JETP Lett.*, **2018**, *108*, 527–531. DOI: 10.1134/S0021364018200092.
- [611] Joos, A.; Rümenapp, C.; Wagner, F.E.; Gleich, B. Characterisation of Iron Oxide Nanoparticles by Mössbauer Spectroscopy at Ambient Temperature. *J. Magn. Magn. Mater.*, **2016**, *399*, 123–129. DOI: 10.1016/j.jmmm.2015.09.060.
- [612] Mamani, J.B.; Gamarra, L.F.; Brito, G.E. de S. Synthesis and Characterization of Fe_3O_4 Nanoparticles with Perspectives in Biomedical Applications. *Mater. Res.*, **2014**, *17*, 542–549. DOI: 10.1590/S1516-14392014005000050.
- [613] Rondinone, A.J.; Samia, A.C.S.; Zhang, Z.J. Superparamagnetic Relaxation and Magnetic Anisotropy Energy Distribution in CoFe_2O_4 Spinel Ferrite Nanocrystallites. *J. Phys. Chem. B*, **1999**, *103*, 6876–6880. DOI: 10.1021/jp9912307.
- [614] Liu, C.; Zhang, Z.J. Size-Dependent Superparamagnetic Properties of Mn Spinel Ferrite Nanoparticles Synthesized from Reverse Micelles. *Chem. Mater.*, **2001**, *13*, 2092–2096. DOI: 10.1021/cm0009470.
- [615] Okada, Y.; Asama, H.; Koike, N.; Yamashita, S.; Maeta, N.; Uesaka, A.; Kamiya, H. Direct Ordering of Anchoring Events at the Surface of Iron Oxide Nanoparticles Enabled by A Stepwise Phase-Transfer Strategy. *ChemistrySelect*, **2018**, *3*, 8458–8461. DOI: 10.1002/slct.201801416.
- [616] Han, S.; Hagiwara, M.; Ishizone, T. Synthesis of Thermally Sensitive Water-Soluble Polymethacrylates by Living Anionic Polymerizations of Oligo(Ethylene Glycol) Methyl Ether Methacrylates. *Macromolecules*, **2003**, *36*, 8312–8319. DOI: 10.1021/ma0347971.
- [617] Schmitt, C. Surface Modification of Oxide Nanoparticles Using Phosphonic Acids: Characterization, Surface Dynamics, and Dispersion in Sols and Nanocomposites (Dissertation), **2017**.
- [618] Walter, A.; Garofalo, A.; Parat, A.; Martinez, H.; Felder-Flesch, D.; Begin-Colin, S. Functionalization Strategies and Dendronization of Iron Oxide Nanoparticles. *Nanotechnol. Rev.*, **2015**, *4*. DOI: 10.1515/ntrev-2015-0014.
- [619] Wang, N.; Hsu, C.; Zhu, L.; Tseng, S.; Hsu, J.-P. Influence of Metal Oxide Nanoparticles Concentration on Their Zeta Potential. *J. Colloid Interface Sci.*, **2013**, *407*, 22–28. DOI: 10.1016/j.jcis.2013.05.058.
- [620] Kirby, B.J.; Hasselbrink, E.F. Zeta Potential of Microfluidic Substrates: 1. Theory, Experimental Techniques, and Effects on Separations. *Electrophoresis*, **2004**, *25*, 187–202. DOI: 10.1002/elps.200305754.

References

- [621] Lobato, N.C.C.; Mansur, M.B.; Ferreira, A. de M. Characterization and Chemical Stability of Hydrophilic and Hydrophobic Magnetic Nanoparticles. *Mater. Res.*, **2017**, *20*, 736–746. DOI: 10.1590/1980-5373-mr-2016-0707.
- [622] Baalousha, M. Aggregation and Disaggregation of Iron Oxide Nanoparticles: Influence of Particle Concentration, pH and Natural Organic Matter. *Sci. Total Environ.*, **2009**, *407*, 2093–2101. DOI: 10.1016/j.scitotenv.2008.11.022.
- [623] Tombácz, E.; Farkas, K.; Földesi, I.; Szekeres, M.; Illés, E.; Tóth, I.Y.; Nesztor, D.; Szabó, T. Polyelectrolyte Coating on Superparamagnetic Iron Oxide Nanoparticles as Interface between Magnetic Core and Biorelevant Media. *Interface Focus*, **2016**, *6*, 20160068. DOI: 10.1098/rsfs.2016.0068.
- [624] O'Brien, R.W.; White, L.R. Electrophoretic Mobility of a Spherical Colloidal Particle. *J. Chem. Soc. Faraday Trans. 2*, **1978**, *74*, 1607. DOI: 10.1039/f29787401607.
- [625] López-García, J.J.; Grosse, C.; Horno, J. Influence of the Counterion and Co-Ion Diffusion Coefficient Values on Some Dielectric and Electrokinetic Properties of Colloidal Suspensions. *J. Phys. Chem. B*, **2005**, *109*, 11907–11912. DOI: 10.1021/jp050918i.
- [626] García-Salinas, M.; de las Nieves, F.. Influence of Counterion Type and Diffusion on the Primary Electroviscous Effect. *Colloids Surfaces A Physicochem. Eng. Asp.*, **2003**, *222*, 65–77. DOI: 10.1016/S0927-7757(03)00235-8.
- [627] Kawaguchi, Y.; Itamura, Y.; Onimura, K.; Oishi, T. Effects of the Chemical Structure on the Heat Resistance of Thermoplastic Expandable Microspheres. *J. Appl. Polym. Sci.*, **2005**, *96*, 1306–1312. DOI: 10.1002/app.21429.
- [628] Lee, W.-H.; Kim, J.-O. Effect of Coexisting Components on Phosphate Adsorption Using Magnetite Particles in Water. *Environ. Sci. Pollut. Res.*, **2019**, *26*, 1054–1060. DOI: 10.1007/s11356-017-8528-1.
- [629] Chitrakar, R.; Tezuka, S.; Sonoda, A.; Sakane, K.; Ooi, K.; Hirotsu, T. Phosphate Adsorption on Synthetic Goethite and Akaganeite. *J. Colloid Interface Sci.*, **2006**, *298*, 602–608. DOI: 10.1016/j.jcis.2005.12.054.
- [630] Geelhoed, J.S.; Hiemstra, T.; Van Riemsdijk, W.H. Phosphate and Sulfate Adsorption on Goethite: Single Anion and Competitive Adsorption. *Geochim. Cosmochim. Acta*, **1997**, *61*, 2389–2396. DOI: 10.1016/S0016-7037(97)00096-3.
- [631] Yu, Z.; Zhang, C.; Zheng, Z.; Hu, L.; Li, X.; Yang, Z.; Ma, C.; Zeng, G. Enhancing Phosphate Adsorption Capacity of SDS-Based Magnetite by Surface Modification of Citric Acid. *Appl. Surf. Sci.*, **2017**, *403*, 413–425. DOI: 10.1016/j.apsusc.2017.01.163.
- [632] Pauly, C.S.; Genix, A.-C.; Alauzun, J.G.; Sztucki, M.; Oberdisse, J.; Hubert Mutin, P. Surface Modification of Alumina-Coated Silica Nanoparticles in Aqueous Sols with Phosphonic Acids and Impact on Nanoparticle Interactions. *Phys. Chem. Chem. Phys.*, **2015**, *17*, 19173–19182. DOI: 10.1039/C5CP01925G.
- [633] Yee, C.; Kataby, G.; Ulman, A.; Prozorov, T.; White, H.; King, A.; Rafailovich, M.; Sokolov, J.; Gedanken, A. Self-Assembled Monolayers of Alkanesulfonic and -Phosphonic Acids on Amorphous Iron Oxide Nanoparticles. *Langmuir*, **1999**, *15*, 7111–7115. DOI: 10.1021/la990663y.
- [634] Odinets, I.L.; Vinogradova, N.M.; Lyssenko, K.A.; Antipin, M.Y.; Petrovskii, P. V.; Mastyukova, T.A. Intramolecular Cyclization of α -Haloalkylsubstituted Thiophosphorylacetonitriles: Synthesis and Stereochemistry of 3-Cyano-2-Oxo-1,2-Thiaphosphacyclanes. *Heteroat. Chem.*, **2002**, *13*, 1–21. DOI: 10.1002/hc.1101.
- [635] Bouillot, A.M.J. Triazole Derivatives as Scd Inhibitors, WO2009/016216. **2009**.

References

- [636] Han, D.-D.; Cai, Q.; Chen, Z.-D.; Li, J.-C.; Mao, J.-W.; Lv, P.; Gao, B.-R. Bioinspired Surfaces With Switchable Wettability. *Front. Chem.*, **2020**, *8*. DOI: 10.3389/fchem.2020.00692.
- [637] Osicka, J.; Ilčíková, M.; Popelka, A.; Filip, J.; Bertok, T.; Tkac, J.; Kasak, P. Simple, Reversible, and Fast Modulation in Superwettability, Gradient, and Adsorption by Counterion Exchange on Self-Assembled Monolayer. *Langmuir*, **2016**, *32*, 5491–5499. DOI: 10.1021/acs.langmuir.6b01084.
- [638] Sun, T.; Wang, G.; Feng, L.; Liu, B.; Ma, Y.; Jiang, L.; Zhu, D. Reversible Switching between Superhydrophilicity and Superhydrophobicity. *Angew. Chemie Int. Ed.*, **2004**, *43*, 357–360. DOI: 10.1002/anie.200352565.
- [639] Xia, F.; Jiang, L. Bio-Inspired, Smart, Multiscale Interfacial Materials. *Adv. Mater.*, **2008**, *20*, 2842–2858. DOI: 10.1002/adma.200800836.
- [640] Li, S.; Fan, Y.; Liu, Y.; Niu, S.; Han, Z.; Ren, L. Smart Bionic Surfaces with Switchable Wettability and Applications. *J. Bionic Eng.*, **2021**, *18*, 473–500. DOI: 10.1007/s42235-021-0038-7.
- [641] Reddy, P.Y.; Kondo, S.; Toru, T.; Ueno, Y. Lewis Acid and Hexamethyldisilazane-Promoted Efficient Synthesis of N -Alkyl- and N -Arylimide Derivatives. *J. Org. Chem.*, **1997**, *62*, 2652–2654. DOI: 10.1021/jo962202c.
- [642] Göksu, H.; Topal, M.; Keskin, A.; Gültekin, M.S.; Çelik, M.; Gülçin, I.; Tanc, M.; Supuran, C.T. 9,10-Dibromo-N-Aryl-9,10-Dihydro-9,10-[3,4]Epi pyrroloanthracene-12,14-Diones: Synthesis and Investigation of Their Effects on Carbonic Anhydrase Isozymes I, II, IX, and XII. *Arch. Pharm. (Weinheim)*, **2016**, *349*, 466–474. DOI: 10.1002/ardp.201600047.
- [643] Mandal, R.; Emayavaramban, B.; Sundararaju, B. Cp*Co(III)-Catalyzed C-H Alkylation with Maleimides Using Weakly Coordinating Carbonyl Directing Groups. *Org. Lett.*, **2018**, *20*, 2835–2838. DOI: 10.1021/acs.orglett.8b00761.
- [644] Niederhauser, W.D.; Broderick, E.; Owings, F.F. Method for Preparing Salts of Sulfoalkyl Methacrylates, US2964557, **1960**.
- [645] David, S.E.; Timmins, P.; Conway, B.R. Impact of the Counterion on the Solubility and Physicochemical Properties of Salts of Carboxylic Acid Drugs. *Drug Dev. Ind. Pharm.*, **2012**, *38*, 93–103. DOI: 10.3109/03639045.2011.592530.
- [646] Bamford, D.; Dlubek, G.; Dommet, G.; Höring, S.; Lüpke, T.; Kilburn, D.; Alam, M.A. Positron/Positronium Annihilation as a Probe for Chemical Environments of Free Volume Holes in Fluoropolymers. *Polymer*, **2006**, *47*, 3486–3493. DOI: 10.1016/j.polymer.2006.03.044.
- [647] Schneider, H.A. Polymer Class Specificity of the Glass Temperature. *Polymer*, **2005**, *46*, 2230–2237. DOI: 10.1016/j.polymer.2004.07.054.
- [648] Liu, W.; Yi, P.; Tang, Z. QSPR Models for Various Properties of Polymethacrylates Based on Quantum Chemical Descriptors. *QSAR Comb. Sci.*, **2006**, *25*, 936–943. DOI: 10.1002/qsar.200510177.
- [649] Théneau, C.; Salmerón Sánchez, M.; Rodríguez Hernández, J.C.; Monleón Pradas, M.; Saiter, J.M.; Gómez Ribelles, J.L. The Kinetics of the Structural Relaxation Process in PHEMA-Silica Nanocomposites Based on an Equation for the Configurational Entropy. *Eur. Phys. J. E*, **2007**, *24*, 69–77. DOI: 10.1140/epje/i2007-10214-4.
- [650] Dolan, C.; Drouet, F.; Ware, D.C.; Brothers, P.J.; Jin, J.; Brimble, M.A.; Williams, D.E. A New High-Capacity Metal Ion-Complexing Gel Containing Cyclen Ligands. *RSC Adv.*, **2016**, *6*, 23645–23652. DOI: 10.1039/C6RA00604C.

References

- [651] Kelley, F.N.; Bueche, F. Viscosity and Glass Temperature Relations for Polymer-Diluent Systems. *J. Polym. Sci.*, **1961**, *50*, 549–556. DOI: 10.1002/pol.1961.1205015421.
- [652] Gordon, M.; Taylor, J.S. Ideal Copolymers and the Second-Order Transitions of Synthetic Rubbers. I. Noncrystalline Copolymers. *Rubber Chem. Technol.*, **1953**, *26*, 323–335. DOI: 10.5254/1.3539818.
- [653] Moll, J.; Kumar, S.K. Glass Transitions in Highly Attractive Highly Filled Polymer Nanocomposites. *Macromolecules*, **2012**, *45*, 1131–1135. DOI: 10.1021/ma202218x.
- [654] Eriksson, M.; Goossens, H.; Peijs, T. Influence of Drying Procedure on Glass Transition Temperature of PMMA Based Nanocomposites. *Nanocomposites*, **2015**, *1*, 36–45. DOI: 10.1179/2055033214Y.0000000005.
- [655] Ash, B.J.; Siegel, R.W.; Schadler, L.S. Glass-Transition Temperature Behavior of Alumina/PMMA Nanocomposites. *J. Polym. Sci. Part B Polym. Phys.*, **2004**, *42*, 4371–4383. DOI: 10.1002/polb.20297.
- [656] Lindner, P.; Zemb, T. *Neutrons, X-Rays and Light: Scattering Methods Applied to Soft Condensed Matter*; North Holland, **2002**.
- [657] Percus, J.K.; Yevick, G.J. Analysis of Classical Statistical Mechanics by Means of Collective Coordinates. *Phys. Rev.*, **1958**, *110*, 1–13. DOI: 10.1103/PhysRev.110.1.
- [658] Dong, J.; Zink, J.I. Taking the Temperature of the Interiors of Magnetically Heated Nanoparticles. *ACS Nano*, **2014**, *8*, 5199–5207. DOI: 10.1021/nn501250e.
- [659] Hu, Y.; Shen, J.; Li, N.; Ma, H.; Shi, M.; Yan, B.; Huang, W.; Wang, W.; Ye, M. Comparison of the Thermal Properties between Composites Reinforced by Raw and Amino-Functionalized Carbon Materials. *Compos. Sci. Technol.*, **2010**, *70*, 2176–2182. DOI: 10.1016/j.compscitech.2010.08.020.
- [660] Kochetov, R.; Korobko, A. V; Andritsch, T.; Morshuis, P.H.F.; Picken, S.J.; Smit, J.J. Modelling of the Thermal Conductivity in Polymer Nanocomposites and the Impact of the Interface between Filler and Matrix. *J. Phys. D. Appl. Phys.*, **2011**, *44*, 395401. DOI: 10.1088/0022-3727/44/39/395401.
- [661] Zhou, Y.; Wang, L.; Zhang, H.; Bai, Y.; Niu, Y.; Wang, H. Enhanced High Thermal Conductivity and Low Permittivity of Polyimide Based Composites by Core-Shell Ag@SiO₂ Nanoparticle Fillers. *Appl. Phys. Lett.*, **2012**, *101*. DOI: 10.1063/1.4733324.
- [662] Yang, J.; Yang, Y.; Waltermire, S.W.; Wu, X.; Zhang, H.; Gutu, T.; Jiang, Y.; Chen, Y.; Zinn, A.A.; Prasher, R.; Xu, T.T.; Li, D. Enhanced and Switchable Nanoscale Thermal Conduction Due to van Der Waals Interfaces. *Nat. Nanotechnol.*, **2012**, *7*, 91–95. DOI: 10.1038/nnano.2011.216.
- [663] Steele, C.W. Eddy Current Problem. In *Numerical Computation of Electric and Magnetic Fields*; Springer Netherlands: Dordrecht, **1987**; pp. 175–196. DOI: 10.1007/978-94-015-7143-2_10.
- [664] Karlsson, J.O.; Gatenholm, P. Solid-Supported Wettable Hydrogels Prepared by Ozone Induced Grafting. *Polymer*, **1996**, *37*, 4251–4256. DOI: 10.1016/0032-3861(96)00277-7.
- [665] Kittle, J.; Levin, J.; Levin, N. Water Content of Polyelectrolyte Multilayer Films Measured by Quartz Crystal Microbalance and Deuterium Oxide Exchange. *Sensors*, **2021**, *21*, 771. DOI: 10.3390/s21030771.
- [666] An, H.; Habib, T.; Shah, S.; Gao, H.; Patel, A.; Echols, I.; Zhao, X.; Radovic, M.; Green, M.J.; Lutkenhaus, J.L. Water Sorption in MXene/Polyelectrolyte Multilayers for Ultrafast Humidity Sensing. *ACS Appl. Nano Mater.*, **2019**, *2*, 948–955.

References

- DOI: 10.1021/acsanm.8b02265.
- [667] Liu, T.; An, Q.; Zhao, Q.; Wu, J.; Song, Y.; Zhu, B.; Gao, C. Synergistic Strengthening of Polyelectrolyte Complex Membranes by Functionalized Carbon Nanotubes and Metal Ions. *Sci. Rep.*, **2015**, *5*, 7782. DOI: 10.1038/srep07782.
- [668] Hariri, H.H.; Lehaf, A.M.; Schlenoff, J.B. Mechanical Properties of Osmotically Stressed Polyelectrolyte Complexes and Multilayers: Water as a Plasticizer. *Macromolecules*, **2012**, *45*, 9364–9372. DOI: 10.1021/ma302055m.
- [669] Ostendorf, A.; Schönhoff, M.; Cramer, C. Ionic Conductivity of Solid Polyelectrolyte Complexes with Varying Water Content: Application of the Dynamic Structure Model. *Phys. Chem. Chem. Phys.*, **2019**, *21*, 7321–7329. DOI: 10.1039/C8CP05853A.
- [670] Matyjaszewski, K.; Xia, J. Atom Transfer Radical Polymerization. *Chem. Rev.*, **2001**, *101*, 2921–2990. DOI: 10.1021/cr940534g.
- [671] Minoura, Y.; Ueda, M.; Mizunuma, S.; Oba, M. The Reaction of Polypropylene with Maleic Anhydride. *J. Appl. Polym. Sci.*, **1969**, *13*, 1625–1640. DOI: 10.1002/app.1969.070130805.
- [672] Stickler, M. Free-Radical Polymerization Kinetics of Methyl Methacrylate at Very High Conversions. *Die Makromol. Chemie*, **1983**, *184*, 2563–2579. DOI: 10.1002/macp.1983.021841216.
- [673] Saadat, Y.; Kim, K.; Foudazi, R. Initiator-Dependent Kinetics of Lyotropic Liquid Crystal-Templated Thermal Polymerization. *Polym. Chem.*, **2021**, *12*, 2236–2252. DOI: 10.1039/D1PY00127B.
- [674] Capponi, S.; Alvarez, F.; Račko, D. Free Volume in a PVME Polymer-Water Solution. *Macromolecules*, **2020**, *53*, 4770–4782. DOI: 10.1021/acs.macromol.0c00472.
- [675] Loo, Y.; Register, R.A. Crystallization Within Block Copolymer Mesophases. In *Developments in Block Copolymer Science and Technology*; Wiley, **2004**; pp. 213–243. DOI: 10.1002/0470093943.ch6.
- [676] Hamley, I.W.; Castelletto, V. Small-Angle Scattering of Block Copolymers. *Prog. Polym. Sci.*, **2004**, *29*, 909–948. DOI: 10.1016/j.progpolymsci.2004.06.001.
- [677] Capretti, A.; Auriemma, F.; De Rosa, C.; Di Girolamo, R.; Forestiere, C.; Miano, G.; Pepe, G.P. Block-Copolymer-Based Plasmonic Metamaterials. *Metamaterials VIII*, **2013**, 87710V. DOI: 10.1117/12.2018492.
- [678] Dolan, J.A.; Wilts, B.D.; Vignolini, S.; Baumberg, J.J.; Steiner, U.; Wilkinson, T.D. Optical Properties of Gyroid Structured Materials: From Photonic Crystals to Metamaterials. *Adv. Opt. Mater.*, **2015**, *3*, 12–32. DOI: 10.1002/adom.201400333.
- [679] Jordan, J.; Jacob, K.I.; Tannenbaum, R.; Sharaf, M.A.; Jasiuk, I. Experimental Trends in Polymer Nanocomposites - A Review. *Mater. Sci. Eng. A*, **2005**, *393*, 1–11. DOI: 10.1016/j.msea.2004.09.044.
- [680] Richard, S.; Rajadurai, J.S.; Manikandan, V. Influence of Particle Size and Particle Loading on Mechanical and Dielectric Properties of Biochar Particulate-Reinforced Polymer Nanocomposites. *Int. J. Polym. Anal. Charact.*, **2016**, *21*, 462–477. DOI: 10.1080/1023666X.2016.1168602.
- [681] Chan, C.-M.; Wu, J.; Li, J.-X.; Cheung, Y.-K. Polypropylene/Calcium Carbonate Nanocomposites. *Polymer*, **2002**, *43*, 2981–2992. DOI: 10.1016/S0032-3861(02)00120-9.
- [682] Wu, P.; Liu, L.; Wu, Z. Synthesis of Diels-Alder Reaction-Based Remendable Epoxy

References

- Matrix and Corresponding Self-healing Efficiency to Fibrous Composites. *Macromol. Mater. Eng.*, **2020**, *305*, 2000359. DOI: 10.1002/mame.202000359.
- [683] Romero-Sabat, G.; Gago-Benedí, E.; Roa Rovira, J.J.; González-Gálvez, D.; Mateo, A.; Medel, S.; Tolentino Chivite, A. Development of a Highly Efficient Extrinsic and Autonomous Self-Healing Polymeric System at Low and Ultra-Low Temperatures for High-Performance Applications. *Compos. Part A Appl. Sci. Manuf.*, **2021**, *145*, 106335. DOI: 10.1016/j.compositesa.2021.106335.
- [684] Wang, Y.; Pham, D.T.; Zhang, Z.; Li, J.; Ji, C.; Liu, Y.; Leng, J. Sustainable Self-Healing at Ultra-Low Temperatures in Structural Composites Incorporating Hollow Vessels and Heating Elements. *R. Soc. Open Sci.*, **2016**, *3*, 160488. DOI: 10.1098/rsos.160488.
- [685] Gietter, A.A.S.; Gildner, P.G.; Cinderella, A.P.; Watson, D.A. General Route for Preparing β -Nitrocarbonyl Compounds Using Copper Thermal Redox Catalysis. *Org. Lett.*, **2014**, *16*, 3166–3169. DOI: 10.1021/ol5014153.
- [686] Chausson, S.; Rueff, J.M.; Lepetit, M.B.; Perez, O.; Retoux, R.; Simon, C.; Le Pluart, L.; Jaffrès, P.A. Copper(II) n-Alkylphosphonates Used as Nanofillers: Single Crystal, Powder Structure Studies and Influence of the Alkyl Chain Length on the Magnetic Properties. *Eur. J. Inorg. Chem.*, **2012**, 2193–2202. DOI: 10.1002/ejic.201101218.
- [687] Gnatowski, A.; Jelonkiewicz, J.; Laskowski, Ł.; Laskowska, M. Influence of the Copper-Containing SBA-15 Silica Fillers on the Mechanical Properties of High Density Polyethylene. *J. Nanomater.*, **2016**, *2016*. DOI: 10.1155/2016/3291719.
- [688] Laskowski, L.; Laskowska, M. Functionalization of SBA-15 Mesoporous Silica by Cu-Phosphonate Units: Probing of Synthesis Route. *J. Solid State Chem.*, **2014**, *220*, 221–226. DOI: 10.1016/j.jssc.2014.08.034.
- [689] Ebbesen, M.F.; Itskalov, D.; Baier, M.; Hartmann, L. Cu Elimination from Cu-Coordinating Macromolecules. *ACS Macro Lett.*, **2017**, *6*, 399–403. DOI: 10.1021/acsmacrolett.7b00124.
- [690] Hector Jr, L.G.; Opalka, S.M.; Nitowski, G.A.; Wieserman, L.; Siegel, D.J.; Yu, H.; Adams, J.B. Investigation of Vinyl Phosphonic Acid/Hydroxylated α -Al₂O₃(0001) Reaction Enthalpies. *Surf. Sci.*, **2001**, *494*, 1–20. DOI: 10.1016/S0039-6028(01)01387-5.
- [691] D'yakov, V.M.; Voronkov, M.G.; Orlov, N.F. Mechanism of the Hydrolysis of Trialkylsilyl Esters of Oxygen Acids of Phosphorus. *Bull. Acad. Sci. USSR Div. Chem. Sci.*, **1972**, *21*, 2417–2420. DOI: 10.1007/BF00850083.
- [692] Davidowski, S.K.; Holland, G.P. Solid-State NMR Characterization of Mixed Phosphonic Acid Ligand Binding and Organization on Silica Nanoparticles. *Langmuir*, **2016**, *32*, 3253–3261. DOI: 10.1021/acs.langmuir.5b03933.
- [693] Weinberger, C.; Heckel, T.; Schnippering, P.; Schmitz, M.; Guo, A.; Keil, W.; Marsmann, H.C.; Schmidt, C.; Tiemann, M.; Wilhelm, R. Straightforward Immobilization of Phosphonic Acids and Phosphoric Acid Esters on Mesoporous Silica and Their Application in an Asymmetric Aldol Reaction. *Nanomaterials*, **2019**, *9*, 249. DOI: 10.3390/nano9020249.
- [694] Hanson, E.L.; Schwartz, J.; Nickel, B.; Koch, N.; Danisman, M.F. Bonding Self-Assembled, Compact Organophosphonate Monolayers to the Native Oxide Surface of Silicon. *J. Am. Chem. Soc.*, **2003**, *125*, 16074–16080. DOI: 10.1021/ja035956z.
- [695] Mido, Y. An Infrared Study of Various Dialkylureas in Solution. *Spectrochim. Acta Part A Mol. Spectrosc.*, **1973**, *29*, 431–438. DOI: 10.1016/0584-8539(73)80025-X.
- [696] Rao, C.N.R.; Chaturvedi, G.C.; Gosavi, R.K. Infrared Spectra and Configurations of

References

- Alkylurea Derivatives: Normal Vibrations on *N,N'*-Dimethyl- and Tetramethylurea. *J. Mol. Spectrosc.*, **1968**, *28*, 526–535. DOI: 10.1016/0022-2852(68)90184-7.
- [697] Bala, S.S.; Ghosh, P.N. Fermi Resonance, Hydrogen Bonding and Hot Bands in the IR Spectra of Thiourea and Urea. *J. Mol. Struct.*, **1983**, *101*, 69–77. DOI: 10.1016/S0022-2860(83)80001-5.
- [698] Kröger, A.P.P.; Boonen, R.J.E.A.; Paulusse, J.M.J. Well-Defined Single-Chain Polymer Nanoparticles via Thiol-Michael Addition. *Polymer*, **2017**, *120*, 119–128. DOI: 10.1016/j.polymer.2017.05.040.
- [699] Liras, M.; García, O.; Guarrotxena, N.; Palacios-Cuesta, M.; Quijada-Garrido, I. Versatile Thiolated Thermosensitive Polymers Synthesized by ATRP of MEO₂MA and AcSEMA, a New Methacrylic Monomer with a Protected Thiol Group. *Polym. Chem.*, **2013**, *4*, 5751. DOI: 10.1039/c3py00773a.
- [700] Neuhaus, S.; Seibert, H.; Diebels, S. Investigation of the Damage Behavior of Polyurethane in Stress Relaxation Experiments and Estimation of the Stress-at-Break σ_b with a Failure Envelope. In *Engineering Design Applications II Structures, Materials and Processes*; Öchsner, A.; Altenbach, H., Eds.; Springer Nature Switzerland, **2020**; pp. 1–15. DOI: 10.1007/978-3-030-20801-1_1.
- [701] Sheldrick, G.M. SHELXT - Integrated Space-Group and Crystal-Structure Determination. *Acta Crystallogr. Sect. A Found. Crystallogr.*, **2015**, *71*, 3–8. DOI: 10.1107/S2053273314026370.
- [702] Sheldrick, G.M. Crystal Structure Refinement with SHELXL. *Acta Crystallogr. Sect. C Struct. Chem.*, **2015**, *71*, 3–8. DOI: 10.1107/S2053229614024218.
- [703] Hübschle, C.B.; Sheldrick, G.M.; Dittrich, B. ShelXle: A Qt Graphical User Interface for SHELXL. *J. Appl. Crystallogr.*, **2011**, *44*, 1281–1284. DOI: 10.1107/S0021889811043202.
- [704] Brand, R.A. WINNORMOS for IGOR6 (Version for Igor 6.2 or Above: 22/02/2017).